THE EFFECT OF FREE-STREAM TURBULENCE ON TURBULENT BOUNDARY LAYERS

by

PHILIP ERNEST HANCOCK

DEPARTMENT OF AERONAUTICS,
IMPERIAL COLLEGE,
UNIVERSITY OF LONDON.

A Thesis submitted for the degree of Doctor of Philosophy at the University of London, July 1980.

ABSTRACT

Mean flow and turbulence measurements of a two-dimensional, incompressible, constant-pressure, flat-plate turbulent boundary layer beneath a nearly homogeneous, nearly isotropic (grid-generated) turbulent free stream are presented. $1600 \lesssim Re_\theta \lesssim 5000$.

Thomas & Hancock (1977, appendix 1) have shown experimentally that for high Reynolds numbers the impermeable-surface condition $v = 0$ on uniformly-convected grid-generated turbulence primarily affects the large scale motion; the condition affects a layer approximately $2L_e$ in thickness, where L_e is the free-stream length scale. It is shown in the present thesis that the ratio between free-stream and boundary layer length scales, L_e/δ, has a large effect, at least when $L_e/\delta = O[1]$. This effect was largely obscured in previous work.

A careful set of mean velocity profiles and skin-friction measurements have substantially clarified the quantitative effect on the mean flow. The law of the wall is unaffected while the defect law is dependent upon both the free-stream intensity, $(u'/U)_e$ (strictly u'_e/u_τ), and L_e/δ. An empirically-derived correlation for the skin friction is given.

A slightly heated boundary layer and a three-wire probe (comprising a conventional X-wire probe and a fluctuating-temperature probe) enabled conditionally-sampled as well as conventional turbulence measurements. Digital signal processing was used. The conditionally-sampled fluctuations were measured with respect to conventionally-averaged means.

The turbulent/turbulent interface is even more contorted with increased penetration by external (i.e. 'cold') fluid towards the wall, and with wisps of boundary layer (i.e. 'hot') fluid reaching well beyond the boundary layer edge. These wisps contain negligible shear stress but some quantities, most notably $\gamma\overline{v^3}_H$ and $\gamma\overline{u^2}_H$, are by no means negligible. Structural parameters based on either conventional or hot-zone turbulence quantities are generally dependent upon both $(u'/U)_e$ and L_e/δ. For a non-turbulent free stream the cold-zone ratios $-\overline{uv}_C/\sqrt{(\overline{u^2}_C\ \overline{v^2}_C)}$ and $-\overline{uv}_C/\overline{q^2}_C$ reach values larger than the corresponding ratios for turbulent motion, and are only slowly reduced by free-stream turbulence.

Balances of the turbulent kinetic energy and shear-stress transport equations are presented.

Implications for calculation methods are very briefly discussed.

ACKNOWLEDGEMENTS

I would like to thank my supervisor, Prof. P. Bradshaw, for suggesting and guiding the course of this study.

I also wish to express my thanks to the members of the Department of Aeronautics for useful discussions and their general interest and support, especially to Dr N.H. Thomas for his collaboration in the work included in appendix 1. I would like to thank too, Mr J. Coles in particular and the workshop staff as a whole for the construction of and assistance with various pieces of equipment, Mr L. Eals for efficient construction and renovation of electronic apparatus, and Mr J. O'Leary for taking the photographs.

I am grateful to Mrs A. Davidson for patient and skillful typing of the bulk of the manuscript, and to Mrs L. Simovic for ably typing the remainder.

Finally, I wish to thank my wife, Jan, for her continued and enthusiastic support (sometimes amidst rampant gloom or frustration); she will be more than pleased to see this ended.

DECLARATION

The work reported by Thomas & Hancock (1977) and included here as appendix 1 was equally supported by Dr N.H. Thomas and the present author. Had there not been joint interest in that work a similar experimental program would have been followed by the present author and incorporated in the main body of this thesis.

The main data-reduction computer programs employed were taken from those generally available within the Department of Aeronautics. The more important modifications made to them are discussed in the text.

The remainder of the work reported herein was conducted solely by the present author under the guidance of his supervisor.

CONTENTS

TABLE TITLES

FIGURE TITLES

CHAPTER 1

CHAPTER 2

CHAPTER 3

4.13 Transport velocities V_τ and V_q

a) No grid

b) $(u'/U)_e \approx 0.025$

c) $(u'/U)_e \approx 0.040$

d) $(u'/U)_e = 0.0575$

e) 15.2 cm grid, $X_{LE} = 2.06$ m, stns 6, 8, 10, 12, 14, 16

4.14 Smoke-filled boundary layer (photographs of)

4.15 Calcomp-plot samples

a) No grid, stn 6

b) " stn 14

c) $(u'/U)_e = 0.0240$, $L_e^u/\delta_{995} = 1.88$

d) " 0.0255, " 0.67

e) " 0.0410, " 1.90

f) " 0.0399, " 0.71

g) " 0.0575 " 1.83

h) " 0.0575 " 1.34

4.16 Intermittency factor profiles

a) No grid

b) Comparison of no-grid measurements with those of other workers

c) $(u'/U)_e \approx 0.025$

d) $(u'/U)_e \approx 0.040$

e) $(u'/U)_e = 0.0575$

f) 15.2 cm grid, $X_{LE} = 2.06$ m, stns 6, 8, 10, 12, 14, 16

4.17 Average position $\overline{y}$ of the interface

a) Values of $\overline{y}/\delta_{995}$ displayed at appropriate $(u'/U)_e$ and L_e^u/δ_{995}

b) Values of $\overline{y}/\delta_{05}$ displayed at appropriate $(u'/U)_e$ and L_e^u/δ_{05}

4.18 Average burst frequency and average burst lengths

a) No grid

b) $(u'/U)_e \approx 0.025$

c) $(u'/U)_e \approx 0.040$

d) $(u'/U)_e \approx 0.0575$

e) Average burst frequency, 15.2 cm grid, $X_{LE} = 2.06$ m

f) " " length, " "

4.19 Conditionally-averaged mean velocities

a) No grid, stn 14

b) 7.6 cm grid, $X_{LE} = 2.06$ m, stn 6

c) 7.6 cm grid, $X_{LE} = 0.30$ m, stn 16

d) 15.2 cm grid, $X_{LE} = 2.06$ m, stn 10

c) $(u'/U)_e \approx 0.040$

d) $(u'/U)_e = 0.0575$

4.43 Diffusion function

a) No grid

b) $(u'/U)_e \approx 0.025$

c) $(u'/U)_e \approx 0.040$

d) $(u'/U)_e = 0.0575$

e) 15.2 cm grid, $X_{LE} = 2.06$ m, stns 6, 8, 10, 12, 14, 16

NOMENCLATURE

		Example equation
a	Convergence/divergence origin of the boundary layer	3.3.3
a_1	Stress ratio $\equiv -\overline{uv}/\overline{q^2}$	
B	Hot-wire calibration constant	2.4.6
B'	Hot-wire calibration constant	2.4.2
C	Constant in decay law	3.1.20
C	Constant in logarithmic law of velocity profile	2.2.3
C_θ	Constant in logarithmic law of temperature profile	1.2.25
C_f	Skin-friction coefficient $\equiv 2\tau_w/(\rho U_e^2)$	
E	Mean voltage (unless otherwise stated) from hot-wire anemometer	2.4.2
E_o	Hot-wire calibration constant	2.4.2
e	Fluctuating voltage, $\overline{e} \equiv 0$	
F_u	Flatness factor $\equiv \overline{u^4}/(\overline{u^2})^2$	
F_v	" " $\equiv \overline{v^4}/(\overline{v^2})^2$	
$F_{u,H}$	Hot-zone flatness factor $\equiv \overline{u_H^4}/(\overline{u_H^2})^2$	
$F_{v,H}$	" " " " $\equiv \overline{v_H^4}/(\overline{v_H^2})^2$	
$F_{u,C}$	Cold-zone flatness factor $\equiv \overline{u_C^4}/(\overline{u_C^2})^2$	
$F_{v,C}$	" " " " $\equiv \overline{v_C^4}/(\overline{v_C^2})^2$	
f_γ	Half of interface average crossing frequency	
G	Clauser shape parameter	
G	Diffusion function	4.8.10
G'	Approximation for diffusion function	4.8.12
Gr	Grashof number	
g	Wake function	3.3.6
g	Gravitational acceleration	
H	Shape parameter $\equiv \delta^*/\theta$	
ID	Intermittency function generated by LAGTHR	
k	von Karman's constant	2.2.3
k_θ	Constant in logarithmic temperature law of the wall	1.2.25
L	A length scale of the energy-containing eddies	
L_τ	Dissipation length scale $\equiv (-\overline{uv})^{3/2}/\varepsilon$	
L_q	Dissipation length scale $\equiv \overline{q^2}^{3/2}/\varepsilon$	
L_e^q	Dissipation length scale of free-stream turbulence $= 2(\overline{q_e^2})^{3/2}/(U_e.d\overline{q_e^2}/dx)$	
L_e^u	Dissipation length scale of free-stream turbulence $= (\overline{u_e^2})^{3/2}/(U_e.d\overline{u_e^2}/dx)$	

$L_{x_{11}}$	Integral length scale	3.2.10
$L_{x_{22}}$	" " "	"
$L_{x_{33}}$	" " "	"
L_γ	Hot-burst average length	4.5.3
$L_{(1-\gamma)}$	Cold-burst average length	4.5.4
ℓ	Mixing length	4.8.2
M	Turbulence-grid mesh size	
M	Mach number	
N_u	Nusselt number	
n	Exponent in hot-wire calibration	2.4.2
n	Exponent in decay law	3.1.17
p	Mean static pressure	
p'	Fluctuating static pressure, $\overline{p'} \equiv 0$	
Q	Arbitrary quantity	4.2.1
q	Velocity fluctuation, $q^2 \equiv u^2 + v^2 + w^2$	
R	Probe resistance	
Re_δ	Reynolds number $\equiv U_e\delta/\nu$	
Re_{δ^*}	Reynolds number $\equiv U_e\delta^*/\nu$	
Re_θ	Reynolds number $\equiv U_e\theta/\nu$	
S_u	Skewness factor $\equiv \overline{u^3}/(\overline{u^2})^{3/2}$	
S_v	" " $\equiv \overline{v^3}/(\overline{v^3})^{3/2}$	
$S_{u,H}$	Hot-zone skewness factor $\equiv \overline{u_H^3}/(\overline{u_H^2})^{3/2}$	
$S_{v,H}$	" " " " $\equiv \overline{v_H^3}/(\overline{v_H^2})^{3/2}$	
$S_{u,C}$	Cold-zone skewness factor $\equiv \overline{u_C^3}/(\overline{u_C^2})^{3/2}$	
$S_{v,C}$	" " " " $\equiv \overline{v_C^3}/(\overline{v_C^2})^{3/2}$	
T	Mean temperature	
T_e	Free-stream mean temperature	
T_W	Wall mean temperature	
T_W	Hot-wire temperature	
T_τ	Friction temperature	1.2.25
t	Time	
U	Mean velocity in x (or X) direction	
V	" " " y direction	
W	" " " z direction	
U_e	Free-stream mean velocity	
u	Fluctuating velocity in x (or X) direction, $\overline{u} \equiv 0$	

v	Fluctuating velocity in y direction	
w	" " " z direction	
u'	R.M.S. of $u \equiv \sqrt{\overline{u^2}}$	
v'	" " $v \equiv \sqrt{\overline{v^2}}$	
w'	" " $w \equiv \sqrt{\overline{w^2}}$	
U_{eff}	Effective velocity over hot wire	2.4.3
u_τ	Friction velocity $\equiv \sqrt{\tau_w/\rho}$	
V_E	Entrainment velocity	4.4.2
V_q	Transport velocity of turbulent kinetic energy	4.4.3
V_τ	" " " " shear stress	4.4.4
W	Wake function	3.3.9
X	Distance downstream from turbulence grid/turbulence generator mid plane	
x	Distance downstream from plate leading edge	
y	Distance above plate	
z	Distance from plate centre line	
$\overline{y}$	Average position of intermittency interface, defined by the position at which $\gamma = 0.5$	
α	Temperature coefficient of resistance	2.4.9
γ	Intermittency factor	
δ	A boundary layer thickness based on the mean velocity profile	
δ	Correction to effective wire angles	
δ_{99}	Boundary layer thickness defined by the position at $U/U_e = 0.99$	
δ_{995}	Boundary layer thickness defined by the position at which $U/U_e = 0.995$	
δ_{05}	Boundary layer thicnkess defined by the position at which $-\overline{uv}/u_\tau^2 = 0.05$	
δ^*	Displacement thickness $\equiv \int_0^\infty (1-U/U_e)dy$	
ε	Dissipation rate of turbulent kinetic energy	3.1.3
ε	Hot-wire temperature correction factor	2.4.10
θ	Fluctuating temperature, $\overline{\theta} \equiv 0$	
θ	Moment thickness $\equiv \int_0^\infty (1-U/U_e)U/U_e dy$	
μ	Viscosity	
ν	Kinematic viscosity	

ν_T	Eddy viscosity	4.8.1
Π	Velocity profile 'wake' strength (or parameter)	3.3.6
Π_θ	Temperature profile 'wake' strength	1.2.25
ρ	Density	
σ	Hot-wire overheat ratio	2.4.10
σ	Standard deviation of intermittency factor profile	
τ	Shear stress $\equiv -\rho\overline{uv} + \mu\partial U/\partial y$	
τ_W	Wall shear stress	
ϕ	Rotation (following r.h. screw rule) of x-wire probe about its longitudinal axis (ϕ = 0 when wires parallel with x-y plane. $\phi = \pi/2$ when wires parallel with x-z plane.)	2.4.3
ϕ_{11}	Spectral density	3.2.5
ϕ_{22}	" "	"
ϕ_{33}	" "	"
ψ_{eff}	Effective wire angle	2.4.3
$\Delta\psi$	Rotation ('yaw') of probe about the y-axis used for wire angle measurement	

Subscripts:

e	Free-stream value
C	Cold-zone conditional average
H	Hot-zone conditional average
0(zero)	Value in the absence of free-stream turbulence but (and unless otherwise stated) at the same Reynolds number, Re_θ
1,2	Respectively, wire-1 and wire-2 of x-wire probe

CHAPTER 1

INTRODUCTION

1.1 GENERAL COMMENTS

For a long time, fluctuations in the free-stream velocity have been known to promote transition from laminar to turbulent flow and to affect the development of fully-turbulent shear layers. In considering the effect of free-stream velocity fluctuations on turbulent shear layers it is important to note that the fluctuations may be a combination of genuine turbulence (random unsteadiness of three-dimensional vortex lines) and "ordered" unsteadiness of irrotational or highly two-dimensional motions. In multi-stage axial-flow turbomachinery, for example, the mixing of the wakes of successive blade rows leads to a roughly homogeneous, roughly isotropic field of turbulence with length scales of the same order as the wake dimensions, in much the same way that the wakes of the bars of a turbulence grid generate nearly homogeneous, nearly isotropic turbulence. Superimposed on this will be the periodic or "ordered" unsteadiness of the pressure fields and wake velocity defects of the blade rows immediately upstream, due to the relative motion between rotors and stators. The flow around boiler tubes is a similar example except that the "ordered" unsteadiness is produced by flow instabilities or vibration of the tubes rather than by blade motion, while the intensity of the background turbulence would be larger because of the rather bluff nature of boiler tubes compared with the aerofoil shape of rotors and stators. The presence of free-stream turbulence in wind tunnels can lead to discrepancies between model and full-size tests (see for example, Milligan & Klein, 1933), in addition to those due to Reynolds number effects. Downstream of a reattachment point a new sub-boundary layer will develop with fluid from the reattached mixing layer approximating to a field of relatively unsheared "external" turbulence

(Chandrsuda, 1975).

For wavelengths of the free-stream turbulence (or ordered unsteadiness, or both) very much larger than the shear layer thickness, the shear layer will respond in a quasi-steady manner. In a review by Bradshaw (1974), from which some of the present chapter is taken, it is pointed out that in the exact transport equations (for, say, Reynolds stresses) the proportion of temporal to spatial derivatives of the total rates of change - appearing on the left-hand side of the equations - is immaterial. Calculation methods which can deal with large spatial gradients in steady flow are thus better equipped to deal with additional temporal derivatives in unsteady flow. Free-stream turbulence which has a length scale small in comparison with the thickness of the shear layer will decay rapidly and consequently be expected to affect only a small streamwise distance of the shear layer. In shear flows where upstream history effects are important it is likely that the upstream history of the free-stream turbulence over the length of the shear layer will be equally important. The length scales of free-stream turbulence or ordered unsteadiness which are expected to have the most effect on the shear layer turbulence structure are scales of order the shear layer thickness.

1.2 A REVIEW OF THE LITERATURE

Subsection 1.2.1 is concerned with boundary layer flows. Mean flow measurements in isothermal boundary layers are discussed first, followed next by a very brief discussion of the effects of free-stream turbulence on heat transfer, and finally by a discussion of turbulence measurements. Subsection 1.2.2 briefly discusses the effects of free-stream turbulence on free shear layers. Subsection 1.2.3 asserts that the effect of free-stream pressure fluctuations is negligible in low Mach number flows and small even in high subsonic flows. Subsection 1.2.4 discusses

engineering shear layer calculation methods and more theoretical analyses that are relevant to boundary layer flows.

1.2.1 Boundary layer flows

Although it is obvious that free-stream turbulence will increase mixing by reinforcing the existing shear layer turbulence, it is not obvious that the increased mixing results in a corresponding increase in the rate of transfer of momentum. That is, it is not obvious that, say, the skin friction will increase. Bradshaw (1974) has pointed out that because the half-wake thickness of a point source scalar in the free stream grows typically 4 times faster than the thickness of a boundary layer under the influence of the same field of free-stream turbulence, either the ability of the existing shear layer to transfer momentum or scalars is reduced, or the shear-layer turbulence or the boundary beneath reduces the mixing ability of the free-stream turbulence in the vicinity of the boundary.

Now, disregarding the boundary layer itself, the effect of the boundary impermeability on the free-stream turbulence near it must be to reduce the normal component of fluctuating velocity to zero at the boundary. Viscosity demands that the tangential fluctuations are also zero at the boundary. At high Reynolds numbers the extent of viscous effects will be small when compared with the length scale of the free-stream energy-containing eddies. Just outside a thin viscous layer the normal component velocity fluctuations will be small compared with the free-stream value, and the extent over which their magnitude is reduced will depend upon the length scale of the free-stream eddies. Furthermore, the continuity equation suggests (but does not insist) that as a consequence of the reduction of the normal component the tangential fluctuations will increase in magnitude. The important

effect of boundary impermeability on nearby free-stream turbulence is discussed in more detail in subsection 1.2.4.

Uzkan & Reynolds (1967) have conducted an experiment in which unsheared grid-generated turbulence was passed adjacent to a wall - in fact, an endless belt - moving at the stream mean velocity. The boundary layer upstream of the moving wall was removed by suction, and over the moving wall the mean shear was zero. They found no amplification of streamwise fluctuating velocity and showed that the effect of the presence of the wall on the external turbulence extended over a distance proportional to $\sqrt{(\nu x/U_e)}$ (i.e. as for a laminar boundary layer) where x is the distance along the moving wall. Indeed, they considered that any amplification would have indicated turbulence production which because of their low Reynolds number, would probably have been true (Hunt & Graham, 1978). Thomas & Hancock (1977 ; see Appendix 1 of this thesis) have conducted a similar experiment but at a Reynolds number an order of magnitude larger than in Uzkan & Reynolds case, and have measured all three components of fluctuating velocity. They found the damping of the normal velocity fluctuation to be the largest effect of the wall impermeability, extending about two free-stream longitudinal integral length scales from the wall. In their case significant viscous effects on the tangential velocity fluctuations extended only about 5% of the free-stream integral scale from the wall, consistent with Uzkan & Reynolds result. Thomas & Hancock also found that streamwise velocity fluctuation was amplified to as much as twice its mean-square free-stream value.

When the underlying boundary layer thickness is small compared with the length scale of the energy-containing eddies far from the boundary, the magnitude of the normal velocity fluctuations just outside the boundary layer will also be small.

Asymptotically, this is the quasi-steady situation briefly discussed earlier in the chapter. Karlsson (1959) and Cousteix et al (1977) have made measurements in a turbulent boundary layer beneath a free stream oscillating in the longitudinal direction. Karlsson has indicated that the skin friction increases by only 4% for a $\pm$ 30% fluctuation in free stream velocity. This is a very much smaller effect than that observed for a truly-turbulent free-stream of length scale comparable with the boundary layer scale.

Experiments on the effects of free-stream turbulence have mostly consisted - sensibly enough - of measurements downstream of grid-generated turbulence, but unfortunately, quite frequently of an unmeasured degree of homogeneity and isotropy. Nominally two-dimensional constant-pressure flat plate flows have been investigated by Kline et al. (1960), Schlichting & Das (1970), Charnay et al (1971), Huffman et al. (1972), Robertson & Holt (1972), Tsuji & Iida (1972), Charnay (1974), Charnay et al. (1976), Meier (1977), Meier & Kreplin (1978), Simonich & Bradshaw (1978), and Slanciauskas & Pedisius (1979). Green (1972) has analysed the mean velocity data of Huffman et al and some of the data given by Charnay et al. (1971). Robertson & Holt have included for comparison with their own data the data of Wieghardt (1944), Ludwieg & Tillmann (1950), Favre et al. (1954), Edwards & Furber (1956), Kline et al. (1960), Kestin et al. (1961), and Pichal (1966).

For some of the measurements of Robertson & Holt, Tsuji & Iida, and Meier the plate leading edge was less than 4 grid mesh sizes downstream of the grid. At small distances of this order the grid-generated turbulence would quite likely still have had significant non-uniformity and ordered unsteadiness due to the individual bar wakes. Meier (1977) has given some consideration

to the effect of grid proximity and concluded that the effect was only to move the effective origin of the boundary layer forward without further downstream effects. Meier & Kreplin used turbulence grids mounted either within, or upstream of, their (two-dimensional) 15:1 wind tunnel contraction, with the consequence that the free-stream turbulence at the contraction exit must have been grossly anisotropic. The measurements of Evans (1972, 1976) were taken in the wall boundary layer of a sucked-down circular pipe with a turbulence-generating grid just downstream of the inlet. Immediately downstream of the grid the boundary layer would have been subjected to the strong two-dimensional transverse vortices shed from the grid and the longitudinal ("horseshoe") vortices wrapped around the bars of the grid immersed within the boundary layer. (In chapter 2 some smoke flow visualization photographs of a boundary layer passing through a large-mesh turbulence grid, presented in figures 2.1 are discussed.) Although in Evans' case the problem of fluctuating separations at a leading edge due to normal-component velocity fluctuations was avoided, the effect of high intensity unsteadiness very close to the grid would almost certainly have been worse, persisting further downstream. Hoffmann (private communication, 1978) has found that deliberately induced streamwise vortices (for example, by upstream concave curvature) decay only slowly, having a life-time typical of the life-time of laboratory boundary layer flows. Robertson & Holt, Tsuji & Iida, Charnay, Charnay et al., Meier, Meier & Kreplin, Simonich & Bradshaw, and Slanciauskas & Pedisius used square-mesh biplane grids of either round bars or rectangular slats. Kline et al, Schlichting & Das, and Huffman et al used monoplane grids consisting of single rows of round bars. It is likely that the flow downstream of these grids may have maintained significant two-dimensionality for a greater distance than for a square-mesh grid

with, say, the same bar spacing and area blockage. In fact, Schlichting & Das oscillated their grid and used the bar wakes to simulate the effect of upstream blade wakes of axial turbomachinery. They also used the same technique in flow over an isolated aerofoil and flow over a cascade of aerofoils.

The effect on a constant-pressure turbulent boundary layer of a turbulent free stream that also has a small mean velocity gradient, $\lambda \equiv dU_e/dy$, has been investigated by Masuda et al. (1972) and Ahmad et al. (1977), for positive, zero and negative values of λ. The measurements of Masuda et al. were taken on a flat plate in an otherwise open working section, and with the leading edge not less than 18 bar diameters downstream of a row of bars spaced non-uniformly to generate the mean velocity gradient dU_e/dy. The measurements of Ahmad et al. were taken on a flat plate with its leading edge touching a shear flow and turbulence generator similar to that used by Masuda et al.. Between the grid and a transition trip a length of small-sized honeycomb fixed across the whole flow was used to smooth-out the lateral gradient in turbulence length scale. Neither of these authors non-dimensionalised the free-stream velocity gradient, λ, by a typical boundary layer gradient, u_τ/δ say, with the result that Ahmad et al have taken their free stream velocity gradient to be less severe than that of Masuda et al when, in fact, it is about $2\frac{1}{2}$ times larger. Roughly, for Masuda et al. $\lambda\delta/u_\tau \approx +0.76$ and -0.58, while for Ahmad et al $\lambda\delta/u_\tau \approx +2.0$ and -1.6. The inflexion point and further rise in the mean velocity profile just outside the wake region which Ahmad et al. consider rather surprising is no more than the result of plotting a linear variation of free-stream velocity against axes appropriate to the logarithmic law of the wall. Indeed, this is clear from Masuda et al although in their case, because $|\lambda\delta/u_\tau|$ is smaller, the inflexion is less marked.

Free-stream turbulence effects on nominally two-dimensional flat plate flows with an adverse pressure gradient have been investigated by Arnal et al.(1976) and Arnal (1977), and with a strongly favourable pressure gradient by Kearney et al.(1970), although Kearney et al.were mainly interested in the effects on heat transfer. The adverse pressure gradient measurements, obtained in the same rig, employed a slightly rectangular mesh turbulence grid of 'V'-shaped bars positioned approximately 10 mesh lengths upstream of the plate leading edge. The measurements showed free-stream turbulence effects to become much larger as the boundary layer in the absence of free-stream turbulence tended towards separation. By reinforcing the mixing the free-stream turbulence delayed separation.

Measurements of the effects of free-stream turbulence on isolated aerofoils have been obtained by Schlichting & Das, McKeough (1976), Pfeil & Pache (1977) and Barrack (1977). Barrack has well reviewed previous investigations of Reynolds number and free-stream turbulence effects on aerofoil stall, and has experimentally investigated three NACA 23000-series aerofoils for $0.01 \lesssim (u'/U)_e \lesssim 0.08$, integral length scales of $0.005 < L_{x_{II}}/c < 0.12$, and chord (c) Reynolds numbers of 2.7×10^5 and 7.6×10^5. He found that the stall characteristics of a particular aerofoil in the absence of free-stream turbulence determines its response to free-stream turbulence. That is, different stall mechanisms are affected in different ways. Measurements on cascades of aerofoils have been made by Schlichting & Das, Evans (1970), Evans (1976), and Bayley & Milligan (1977). Evans (1976) concluded that in turbomachinery the unsteadiness of blade-wake interactions is as important as the effects of "steady" free-stream t ɔulence. While he shows from his experiments using static grids that cascade performance at first decreases and then increases with increasing free-stream intensity, Schlichting & Das,

using oscillating grids - the oscillation frequency did not seem to be too important - say more or less the opposite.

Comparison of turbulent boundary layers with and without free-stream turbulence is best made using parameters that allow for free-stream turbulence effects on the virtual origin of the layer, such as the Reynolds number $U_e\theta/\nu$, for example.

All of the experimental data show that free-stream turbulence increases the skin friction and the fullness of the velocity profile. Charnay (1974), Huffman et al., and Robertson & Holt show that the boundary layer thickness increases with free-stream turbulence intensity. Charnay gives, at constant streamwise distance,

$$\left(\frac{d\delta_{99}}{dx}\right)\Big/\left(\frac{d\delta_{99}}{dx}\right)_o \approx 1+9.0\left(\frac{u'}{U}\right)_e \quad \text{for } \left(\frac{u'}{U}\right)_e \lesssim 0.06. \tag{1.2.1}$$

Since the rate of growth in the absence of free-stream turbulence is approximately independent of streamwise distance, comparison at, say, constant $U_e\theta/\nu$ is not necessary. Robertson & Holt suggest, at constant $U_e\theta/\nu$,

$$\left(\frac{\delta_{99}}{\theta}\right)\Big/\left(\frac{\delta_{99}}{\theta}\right)_o \approx 1 + 4.9\left(\frac{u'}{U}\right)_e \text{ for } \left(\frac{u'}{U}\right)_e \lesssim 0.06, \tag{1.2.2}$$

$$\approx 1.34 \quad \text{for } 0.06 \lesssim \left(\frac{u'}{U}\right)_e \lesssim 0.10,$$

although the data are rather scattered.

The dimensional argument for the existence of the inner layer "law of the wall" makes no reference to the turbulence in the outer layer, although of course the friction velocity u_τ depends upon the whole flow and the shear stress profile in the inner layer depends on the pressure gradient. Therefore, for free-stream turbulence whose intensity is not too large by comparison with u_τ, the free-stream turbulence and the existing turbulence in the outer layer would be indistinguishible to the inner layer. In such a

case the logarithmic law would still be expected to hold unless the free-stream and boundary layer length scales differ greatly : very small-scale free-stream turbulence could perhaps affect the inner layer. Certainly, all the measurements of skin friction in the data examined have been made either by fitting the velocity profile over an appropriate range to the logarithmic law of the wall or by use of Preston tubes which, in any case, requires the existence of an inner layer law. The data of Robertson & Holt suggest that the logarithmic law holds for $(u'/U)_e \lesssim 0.1$, but the data of Kline et al show the logarithmic law to break down for a free-stream intensity, $(u'/U)_e$, of only 0.05. Such an effect may have been due to a free-stream intensity of $(u'/U)_e \simeq 0.2$ at the leading edge and due possibly to the use of a monoplane grid (of round bars).

The effect of free-stream turbulence on the outer layer is to reduce the so-called wake component $g(y/\delta,\Pi)$, defined by

$$\frac{U}{u_\tau} = \frac{1}{k} \ln\left(\frac{yu_\tau}{\nu}\right) + C + \frac{1}{k} g(y/\delta, \Pi), \qquad (1.2.3)$$

where Π and δ are functions of x. Measurements of Huffman et al, Evans (1972), Slanciauskas & Pedisius, and some of Meier's indicate that the wake component becomes entirely negative for sufficiently large free-stream intensity although the intensity at which this occurs is not the same in each case. The cosine form for $g(y/\delta,\Pi), \Pi\,(1 - \cos(\pi \frac{y}{\delta}))$, put forward by Hinze (1959), is a good fit in many cases but it cannot possibly do well if any substantial part of the wake function is negative. Evans' (1976) measurements on a cascade of aerofoils showed the cosine form to be a rather poor fit in an adverse pressure gradient for $(u'/U)_e \simeq 0.05$, even though the wake function was entirely positive. Parameters deduced from a cosine form of the law-of-the-wake fitted to mean velocity profiles should be viewed cautiously. Huffman et al determined skin friction and boundary layer thickness by fitting the measured velocity

profiles to the logarithmic law and a cosine form for the law of the wake. Some doubt is cast on their values of boundary layer thickness for the larger free-stream intensities.

An extension of the dimensional analysis for the velocity defect law introduces the scale ratios L_e/δ and u'_e/u_τ, where L_e is a free-stream turbulence length scale (of the energy-containing eddies), giving

$$\frac{U_e - U}{u_\tau} = f\left(\frac{y}{\delta}, \frac{L_e}{\delta}, \frac{u'_e}{u_\tau}\right). \tag{1.2.4}$$

If this equation is to overlap the inner layer law then the function on the right hand side must reduce to the form

$$f_1\left(\frac{y}{\delta}\right) + f_2\left(\frac{L_e}{\delta}, \frac{u'_e}{u_\tau}\right)$$

in that region. In order to correlate the free-stream intensity with its effect on the velocity defect, Charnay et al.(1971) found

$$\frac{U_e - U}{u_\tau - \alpha\, u'_e} = f_3\left(\frac{y}{\delta}\right) \quad \text{where } \alpha \approx 0.29 \tag{1.2.5}$$

and

$$\left(1 + 5.0\,\frac{u'_e}{U_e}\right)\left(\frac{U_e - U}{u_\tau}\right) = f_4\left(\frac{y}{\delta}\right) \tag{1.2.6}$$

was obtained by Evans (1972). However, both these correlations are inconsistent with the inner layer law of the wall since they imply that the von Karman constant is a function of free-stream intensity. Therefore, the above two correlations must be regarded as completely empirical, being valid at best only in the outer layer.

Green's analysis of the data of Huffman et al.and Charnay showed that, at constant $U_e\Theta/\nu$, the shape parameter H and the Clauser shape parameter, G, defined by

$$G \equiv \frac{\int_0^\infty \left(\frac{U_e - U}{u_\tau}\right)^2 dy}{\int_0^\infty \frac{U_e - U}{u_\tau} dy} = \frac{H - 1}{H}\sqrt{\frac{2}{c_f}}, \qquad (1.2.7)$$

both decreased with increased free-stream intensity. He gives

$$\frac{H}{H_o} = 1 - (2.4 - 0.25H)\left(\frac{u'}{U}\right)_e \qquad (1.2.8)$$

$$\text{for} \left(\frac{u'}{U}\right)_e \lesssim 0.05$$

$$\frac{G}{G_o} = 1 - \frac{1}{3}\sqrt{\frac{2}{c_f}}\left(\frac{u'}{U}\right)_e \qquad (1.2.9)$$

Bradshaw (1974) gives for the same data and the data of Kline et al.,

$$\frac{H}{H_o} \approx 1 - 2.0\left(\frac{u'}{U}\right)_e \qquad (1.2.10)$$

Robertson & Holt, however, suggest a smaller effect with

$$\frac{H}{H_o} \approx 1 - 1.0\left(\frac{u'}{U}\right)_e \qquad (1.2.11)$$

The data of Slanciauskas & Pedisius are in better agreement with the deductions of Green and Bradshaw. Evidently, from Green's analysis, G/G_o is Reynolds number dependent, even though at high Reynolds numbers ($Re_\theta \gtrsim 5000$) G_o is well established to be independent of Reynolds number. Equation 1.2.9 stems directly from equation 1.2.5 with $\alpha = \frac{1}{3}$ instead of 0.29.

Now, the internally generated turbulent kinetic energy of a (free or bound) shear layer, $\overline{q_{SL}^2}$ say, and the turbulent kinetic energy in the shear layer due to the free-stream turbulence, $\overline{q_e^2}\ f(y)$ say, must be uncorrelated until interaction begins. Non-interaction is only likely if $\overline{q_e^2} \ll \overline{q_{SL}^2}$ over a substantial part of the layer. Thus

$$\overline{q_{TOTAL}^2} = \overline{q_{SL}^2} + \overline{q_e^2}\ f(y), \text{ provided } \overline{q_e^2} \ll \overline{q_{SL}^2} \qquad (1.2.12)$$

Bradshaw (1974) has pointed out that provided the rate of mixing within the shear layer remains proportional to $\overline{q_{TOTAL}^2}$, increase in

mixing rate will be initially proportional to the mean-square free-stream intensity. In confirmation, Meier has found, at constant $U_e\theta/\nu$, that

$$\frac{H}{H_o} = 1 - 90.0\left(\frac{u'}{U}\right)_e^2 \qquad \text{for } 0 \lesssim \left(\frac{u'}{U}\right)_e \lesssim 0.01$$

$$= 1.009 - 1.8\left(\frac{u'}{U}\right)_e \qquad \text{for } 0.01 \lesssim \left(\frac{u'}{U}\right)_e \lesssim 0.02, \tag{1.2.13}$$

$$\text{and } \frac{G}{G_o} = 1 - 0.76\sqrt{\frac{2}{c_f}}\left(\frac{u'}{U}\right)_e^2 \qquad \text{for } 0 \lesssim \left(\frac{u'}{U}\right)_e \lesssim 0.01$$

$$= 1.049 - 0.38\sqrt{\frac{2}{c_f}}\left(\frac{u'}{U}\right)_e^2 \qquad \text{for } 0.01 \lesssim \left(\frac{u'}{U}\right)_e \lesssim 0.02. \tag{1.2.14}$$

The main reason that previous experimenters had not observed such a non-linear dependence of the above form is that nearly all investigations have been for $(u'/U)_e \gtrsim 0.01$. Meier's results have important implications for wind tunnel design and testing in that the linear dependence inferred from previous measurements implies a much larger effect of free-stream turbulence for $(u'/U)_e \lesssim 0.01$, the range of values found in wind tunnels.

Irrespective of the failure of the cosine form of the law-of-the-wake, the reduction of the wake component at constant $\delta u_\tau/\nu$ implies an increase in skin friction, viz

$$\frac{U_e}{u_\tau} = \frac{1}{k}\ln\left(\frac{\delta u_\tau}{\nu}\right) + C + \frac{2\Pi}{k} \quad . \tag{1.2.15}$$

Empirical correlations of the effect of free-stream turbulence intensity on skin friction have mostly been of the simple linear form

$$\frac{c_f}{c_{f_o}} = 1 + \text{constant} \times \left(\frac{u'}{U}\right)_e \quad . \tag{1.2.16}$$

Bradshaw (1974) has shown that the skin friction ratio and change

in wake strength at constant $U_e\delta/\nu$ are related by

$$\frac{c_f}{c_{f_o}} \approx 1 - \frac{4}{k}(\Pi - \Pi_o)\sqrt{\frac{c_{f_o}}{2}}\left(1 - \frac{1}{k}\sqrt{\frac{c_{f_o}}{2}}\right). \qquad (1.2.17)$$

The term $\frac{1}{k}\sqrt{\frac{c_{f_o}}{2}}$ is typically of the order of 0.1 and neglecting it amounts to comparing at constant $u_\tau\delta/\nu$. As will be seen below the scatter in the value of the constant in equation 1.2.16 is much larger than 10%, therefore an adequate approximation of equation 1.2.17 is

$$\frac{c_f}{c_{f_o}} \approx 1 - \frac{4}{k}(\Pi - \Pi_o)\sqrt{\frac{c_{f_o}}{2}} \qquad (1.2.18)$$

So then, if $(\Pi - \Pi_o) \propto u'_e/u_\tau$, c_f/c_{f_o} depends upon $(u'/U)_e$ rather than u'_e/u_τ. On the basis of the data of Charnay et al. (1971) and Robertson & Holt, Bradshaw has suggested that

$$\frac{c_f}{c_{f_o}} = 1 + 3.2\left(\frac{u'}{U}\right)_e \quad \text{for } \left(\frac{u'}{U}\right)_e \lesssim 0.05 \qquad (1.2.19)$$

is a good fit. The limited data of Tsuji & Iida are consistent with this but Green's analysis of the data of Huffman et al. gives

$$\frac{c_f}{c_{f_o}} = 1 + 4.8\left(\frac{u'}{U}\right)_e \quad \text{for } \left(\frac{u'}{U}\right)_e \lesssim 0.05. \qquad (1.2.20)$$

Slanciauskas & Pedisius' results give, at constant $U_e\theta/\nu$,

$$\begin{aligned} \frac{c_f}{c_{f_o}} &\approx 1 + 3.8\left(\frac{u'}{U}\right)_e \quad \text{for } \left(\frac{u'}{U}\right)_e \lesssim 0.05, \\ &\approx 1.1 + 0.8\left(\frac{u'}{U}\right)_e \quad \text{for } 0.05 \lesssim \left(\frac{u'}{U}\right)_e \lesssim 0.10. \end{aligned} \qquad (1.2.21)$$

Evans' (1972) data suggests the constant of equation 1.2.16 is about 6.0 for $(u'/U)_e \lesssim 0.05$ while Simonich & Bradshaw found values lower than 2.0 for the same range of $(u'/U)_e$. The 'constants' of Green and Simonich & Bradshaw fall near the edges of the scatter of the data of previous workers presented by Robertson & Holt. Meier's measurements show that, at constant $U_e\theta/\nu$,

$$\frac{c_f}{c_{f_o}} = 1 + 190\left(\frac{u'}{U}\right)_e^2 \quad \text{for} \quad 0 \lesssim \left(\frac{u'}{U}\right)_e \lesssim 0.01,$$

$$= 0.981 + 3.8\left(\frac{u'}{U}\right)_e \quad \text{for} \quad 0.01 \lesssim \left(\frac{u'}{U}\right)_e \lesssim 0.02 \qquad (1.2.22)$$

In the experiments of Huffman et al. and Slanciauskas & Pedisius the free-stream turbulence intensity, $(u'/U)_e$, in the absence of the turbulence grids was about 1% in each case. Green's evaluation of c_{f_o} for the data of Huffman et al. was based on the linear dependence between G and $(u'/U)_e$ given in equation 1.2.9. The inclusion of an initially parabolic dependence between G and $(u'/U)_e$, say of the form given by Meier, would have resulted in a modified form of equation 1.2.20, namely

$$\frac{c_f}{c_{f_o}} = A + 4.8\left(\frac{u'}{U}\right)_e \quad \text{for} \quad 0.01(\text{say}) \lesssim \left(\frac{u'}{U}\right)_e \lesssim 0.05, \qquad (1.2.23)$$

with A less than unity. Meier's results (equation 1.2.22) suggest A = 0.97. Slanciauskas & Pedisius assumed the relation between c_f/c_{f_o} and $(u'/U)_e$ to be linear for $(u'/U)_e \gtrsim 0$.

Clearly, quantitative agreement between the sets of data just discussed is generally rather poor. Of course, the experimental error in each data set is hard, if not impossible, to determine and experimental errors in evaluating small differences are enlarged; a 1% error band in evaluating skin friction, for example, introduces a possible error of 10% in a difference if the difference is of order 10%. The discrepancies do not seem to show a trend with Reynolds number, although the data could not be said to be conclusive on this. Comparing boundary layers with and without free-stream turbulence at constant Reynolds number removes some, though not necessarily all, Reynolds number dependence.

In the analysis presented earlier it was assumed that the free-stream turbulence can be specified by L_e and u'_e alone,

and formulae like equation 1.2.16 relating c_f/c_{f_o} to u'_e alone imply that the effect of L_e is small. However, other properties may affect the response of a shear layer to free-stream turbulence. For instance, the normal component of fluctuating velocity is probably as important if not more so than the streamwise component, but it would appear that only Huffman et al., Evans, Charnay, and Meier have measured it. In the case of Charnay $(u'/v')_e \approx 1.1$ while for Evans and Meier $(u'/v')_e \approx 1.05$. The tabulated data of Huffman et al. gives a ratio of $(u'/v')_e \approx 0.6$ which may have been a consequence of the type of grid used. Huffman (private communication, 1977) has confirmed that the tabulation does indeed imply such a degree of anisotropy but that it is possibly in error. (Unfortunately, a more detailed record of the experiment apparently no longer exists.) If equation 1.2.16 is based upon v'_e rather than u'_e the 'constant' is about 2.6 instead of 4.8. Meier & Kreplin have measured the effect of the length scale ratio $(L_{x_{11}})_e/\delta$ for a free-stream streamwise intensity $(u'/U)_e$ of only 0.002. Brief reference to their experimental arrangement was made earlier. Unfortunately they did not measure the ratio $(u'/v')_e$ which in their case must have been considerably less than unity because of the effect of the contraction. In fact, the rather large length scale ratio effect that they obtained - for $(u'/U)_e = 0.002$, halving $(L_{x_{11}})_e/\delta$ from approximately 1.7 increased the skin friction by about 1.5% - is only consistent with Meier's results just cited, obtained using the same wind tunnel but with a different grid arrangement, if the normal component of free-stream intensity, v'_e, is much more important than the streamwise intensity, u'_e. Charnay has measured the transverse integral length scale $L_{Y_{11}}$ ($= \frac{1}{2} L_{x_{11}}$ in isotropic turbulence), defined as

$$L_{y_{11}} = \int_0^\infty \frac{\overline{v(y)\ v(y+r)}}{\overline{v^2}}\ dr\ , \qquad (1.2.24)$$

but the length scale was generally still increasing with y at the outermost measurement position. It appears that, at constant free-stream intensity, $L_{y_{11}}/\delta_{99}$ at the boundary layer edge was varied by about a factor 2. (Overall, at the boundary layer edge, $L_{y_{11}}/\delta_{99}$ was varied within 0.2 to 1.2.) Charnay concluded that for the range covered by his measurements the length scale ratio was unimportant. Slanciauskas & Pedisius acknowledged that the ratio of free-stream to boundary layer length scales is likely to be important but they did not make any systematic investigation. They stated, without defining L, that L/δ was within the approximate range of 0.5 to 1.0.

Whereas all the experiments agree that free-stream turbulence increases the skin friction of a turbulent boundary layer the heat transfer measurements do not show such consistency. Edwards & Furber (1956), Reynolds et al. (1958), Kestin et al. (1961), Kestin (1966), Junkhan & Serovy (1967), Brown & Burton (1977), and Consigny et al. (1979) say that heat transfer is not affected by free-stream turbulence. Sugawara et al. (1953), Feiler & Yeager (1962), Simonich & Bradshaw (1978) and Slanciauskas & Pedisius (1979) conclude that there is an increase. Simonich & Bradshaw and Slanciauskas & Pedisius compared heat transfer rates at constant momentum thickness Reynolds number, Re_θ, and have both shown the increase to be about twice the increase in the skin friction compared on the same basis. Their data show that free-stream turbulence reduces the thermal wake strength, Π_θ, defined by

$$\frac{w - T_e}{T_\tau} = \frac{1}{k_\theta} \ln\left(\frac{u_\tau \delta}{\nu}\right) + C_\theta + \frac{2\Pi_\theta}{k_\theta}\ . \qquad (1.2.25)$$

T_τ is the 'friction temperature' equal to $Q_w/(\rho C_p u_\tau)$ where Q_w is

the wall heat transfer rate per unit area, and C_p is the specific heat at constant pressure. Simonich & Bradshaw point out that, at constant $u_\tau\delta/\nu$, a decrease of Π must be accompanied by an increase of Π_θ if the heat transfer were to remain unaffected. Thus, the heat transfer and the temperature profile cannot be simultaneously unaffected by free-stream turbulence.

Extensive boundary layer turbulence measurements have been made by Huffman et al., Charnay, and Charnay et al., in a constant-pressure layer, by Arnal in an adverse pressure gradient, and by Ahmad et al. in a constant-pressure layer with either a small positive, zero or negative free-stream transverse mean velocity gradient, dU_e/dy. Charnay has used a x-wire-plus-temperature-wire probe similar to that used in the present thesis, to obtain temperature-conditioned measurements. Some of the other workers previously mentioned, for example Evans (1972), have made less detailed turbulence measurements.

Huffman et al., Charnay, and Evans show the shear stress profile edge, δ_{05} say, to be moved outwards with respect to the mean velocity profile edge by the action of free-stream turbulence. Charnay and Evans referred to the δ_{99} thickness for the mean velocity profile while Huffman et al. referred to the value derived from fitting the mean velocity profile to the inner layer logarithmic law combined with the cosine form for the wake function. However, the shear stress measurements of Huffman et al. are, for the largest grid, dubiously large near and outside the mean velocity profile edge; at the edge the shear stress is about 0.6 of the wall value. Bradshaw (1974) has pointed out that if the flow is two-dimensional such a large shear stress implies an excessively large entrainment velocity and is inconsistent with the direct stress and static-pressure gradients. Thus, either the quality of the flow downstream of the largest grid was poor, or the shear stress measurements were

in error.

Charnay's measurements of $-\overline{uv}/\sqrt{(\overline{u^2}.\overline{v^2})}$ show that for $y/\delta_{99} \lesssim 0.9$ it is only weakly affected by free-stream turbulence except at the largest intensity quoted of $(u'/U)_e = 0.047$ where it is reduced by about 20%. Between $y/\delta_{99} \approx 0.9$ and $y/\delta_{99} \approx 1.4$ $-\overline{uv}/\sqrt{(\overline{u^2}.\overline{v^2})}$ increases slightly with increasing free-stream intensity. $-\overline{uv}$ is zero outside $y/\delta_{99} \approx 1.4$. The structural parameter $-\overline{uv}/\overline{q^2}$ is shown to decrease more uniformly inside $y/\delta_{99} \approx 0.9$, and to increase outside. In the inner layer $-\overline{uv}/\overline{q^2}$ is decreased by about 20% when $(u'/U)_e = 0.047$. Huffman et al. show $-\overline{uv}/\overline{q^2}$ to increase in the outer layer and, though not conclusively, to be unaffected in the inner layer. Of course, in view of their doubtful shear stress measurements $-\overline{uv}/\overline{q^2}$ must also be doubtful. Moreover, an increase of $-\overline{uv}/\overline{q^2}$ and $-\overline{uv}/\sqrt{(\overline{u^2}.\overline{v^2})}$ near the boundary layer edge is surprising because $-\overline{uv}$ should be unsignificant in a uniform free-stream. Arnal, in agreement with the present measurements, shows $-\overline{uv}/\overline{q^2}$ to decrease everywhere with increasing free-stream intensity.

Charnay gives the correlation coefficients $\overline{u^3}/(\overline{u^2})^{3/2}$, $\overline{u^2v}/(\overline{u^2}\sqrt{\overline{v^2}})$, $\overline{uv^2}/(\overline{v^2}\sqrt{\overline{u^2}})$, $\overline{v^3}/(\overline{v^2})^{3/2}$ and $\overline{w^2u}/(\overline{w^2}\sqrt{\overline{u^2}})$. They are shown to be reduced in magnitude as the free-stream intensity is increased. Measurements of the correlation coefficient outside the mean velocity edge do not all reach zero but are all less than 0.2; in exactly homogeneous turbulence the triple products must be zero. Flatness factors $\overline{u^4}/(\overline{u^2})^2$ and $\overline{v^4}/(\overline{v^2})^2$ are also reduced and tend to the free-stream value (of approximately 3) with increased free-stream intensity.

Both Charnay and Huffman et al. present balances of the turbulent kinetic energy equation. Charnay shows the dominant production term, $-\overline{uv}.\partial U/\partial y.\delta/U_e^3$, to be only slightly affected by free-stream turbulence, implying nearly compensating changes in

the mean velocity gradient and shear stress. Huffman et al. show a slight reduction in $-\overline{uv}.\partial U/\partial y.\delta/U_e^3$ in the outer layer at the highest free-stream intensity. A more plausible shear stress distribution would reduce the production still further but only where it is itself small compared with the other terms. There is no obvious reason why the production should be unaffected by free-stream turbulence. Charnay determined dissipation from spectral measurements and evaluated the pressure diffussion as a small difference. Huffman et al. neglected the pressure diffusion and evaluated dissipation by difference. Both show the dissipation to be increased most in the outer layer. Free-stream turbulence forces the advection in the outer part of the boundary layer to change sign from that which occurs in its absence. Charnay and Huffman et al. observed an increase in turbulent diffusion. Huffman et al. give the diffusion function G and the shear stress dissipation length scale L_τ, as defined by Bradshaw (1967, and quoted in chapter 4, section 4.8), but these quantities depend fairly strongly on the accuracy of the shear stress measurements.

A function which defines instantaneously whether the fluid at a (fixed) point is shear layer or external fluid (perhaps another shear layer) is called an intermittency function. The time-average of the intermittency function is the intermittency factor, γ. Intermittency techniques that use a function of fluctuating velocity as a discriminator between shear layer and external fluid are only usable when the fluctuations in the external fluid are very small in magnitude or consist of a very different band of frequencies compared with the shear layer fluid. Such methods have been considered by Bradbury (1964), Fiedler & Head (1966), Kaplan & Laufer (1968), Wygnanski & Fiedler (1970), Antonia & Bradshaw (1970), Kovasznay et al. (1970), Sunyach (1971), Antonia (1972), Thomas (1973), Castro (1973), Hedley & Keffer (1974),

Bradshaw & Murlis (1974) and Murlis (1975). Murlis gives an extensive review of the discriminating function and its interpretation into an intermittency function.

Velocity discrimination is of no use when free-stream turbulence is present with scales of the order of the underlying boundary layer scales. An alternative and attractive method of slightly heating the shear layer fluid and using temperature as a discriminator has been used by Johnson (1959), Sunyach (1971), Charnay (1974), Charnay et al. (1976), Antonia, Prahbu & Stephenson (1975), Dean & Bradshaw (1976), Weir & Bradshaw (1977), Antonia, Dahn & Prabhu (1977), Andreopoulos (1978) and Chen & Blackwelder (1978).

Charnay uniformly heated his plate, electrically, to about 20^{o}C above the ambient temperature (i.e. a 7% change in absolute temperature across the layer). This causes $(\Delta T/T)\delta_{gg}g/U_e^2$, which is of the order of the gradient Richardson number $-(g/T)\,\partial T/\partial y/(\partial U/\partial y)^2$, to be roughly 0.3×10^{-3}. The instantaneous overheat ratio of the x-wire probe (nominally 0.8) would have varied by about 13%. In removing the fluctuating temperature effects from the x-wire probe only mean sensitivities could be used because of the analogue processing. Fluctuating temperature was measured with a 2μm x 1.5 mm platinum wire operating at a constant current of approximately 1mA. Charnay estimates the '3dB' frequency of his uncompensated temperature wire to be about 200 Hz or equivalently about one boundary layer thickness, although this appears to be a conservative estimate. Fluid was declared to be shear layer fluid only if either the temperature or the square of its derivative or both exceeded threshold levels.

Charnay gives intermittency statistics and conditional averages for three levels of free-stream intensity, $(u'/U)_e$ =

0.018, 0.032 and 0.047, the background, no-grid level being 0.003. The average position of the interface, $\bar{y}$, defined as the position where $\gamma = 0.5$, does not change beyond ± 0.01 from its no-grid value of $0.83\ \delta_{99}$. The standard deviation, σ, of the interface position, determined by fitting

$$\frac{1}{2}\left[1 - \mathrm{erf}\left(\frac{y - \bar{y}}{\sqrt{2}\ \delta_{99}\sigma}\right)\right]$$

(following Corrsin & Kistler, 1955) to the intermittency factor $\gamma(y)$, increases roughly linearly from its no-grid value of $0.22\delta_{99}$ to $0.35\delta_{99}$ at $(u'/U)_e = 0.047$. The change in the intermittency factor profile implies a greater penetration of the free-stream fluid into the boundary layer and a greater excursion of boundary layer fluid into the free-stream. Average burst frequency, $f_\gamma \delta_{99}/U_e$, - which is generally strongly dependent on the intermittency discrimation technique employed (Murlis, 1975), and so should at most only be used comparatively - shows a roughly linear increase with free-stream intensity at constant Reynolds number. At $(u'/U)_e = 0.047$ the peak average burst frequency is about 80% larger than it is for the no-grid case. With only the background free-stream intensity the average burst frequency distribution is comparable with that obtained by Hedley & Keffer (1974) but broader than that obtained by Kovasznay et al. The peak values are all approximately equal. Average burst length, defined as $\gamma U_e/f_\gamma$, decreases with increased free-stream intensity except near the boundary layer edge and outside where it increases, consistent with the outward movement of the interface. Charnay's conditionally-averaged mean velocities are in qualitative agreement with those of other workers. On average the boundary layer fluid moves with a streamwise velocity less than the mean and moves outwards, and the external fluid moves with a streamwise velocity

greater than the mean and moves inwards. Higher order moments of conditionally-averaged velocity fluctuations were measured with reference to conditionally-averaged means rather than conventionally-averaged means. Such averaging tends to ignore the large-scale turbulent motion. The conditionally-averaged turbulence quantities presented in chapter 4 are based upon conditionally-averaged velocity fluctuations measured with respect to conventionally-averaged means.

1.2.2 Free shear layer flows

Although boundary layers are not significantly affected by free-stream fluctuations of wavelength an order of magnitude greater than δ, free shear layers can be bodily convected, with a consequent snaking appearance (Bradshaw, 1976), as sketched in figure 1.1b. Conversely, free-stream turbulence that has a length scale that is small when compared with the shear layer length scale will re-inforce the shear layer turbulence but without bodily convecting it, and cause small-scale distortion of the turbulent/turbulent interface just as in boundary layers (Bradshaw, 1976; Fink, 1977), as sketched in figure 1.1c. Bodily displacement, Δy, (in the direction of shear) of a snaking shear layer when viewed from fixed Eulerian axes will result in an apparent increase in the streamwise velocity equal to $(\partial U/\partial y)\Delta y$, and time-averaged measurements will show an apparent increase in growth rate.

Experiments on free-stream turbulence effects on free shear layers are more difficult than for boundary layers because of the snaking effect and the importance of initial conditions on shear layer development. Brown & Roshko (1974) found that two-stream mixing layers exhibit large orderly structure - similar to the eigenmodes of instability of a laminar boundary layer - persisting for a time considerably larger than the life time of

many typical shear flows (Chandrsuda et al., 1978). They suggest that as such it is the asymptotic fully developed form of a "turbulent" mixing layer. Chandrsuda et al. argue that the structure observed by Brown & Roshko is rare in practice requiring initially laminar boundary layers at separation and low free-stream turbulence or low "still-air" turbulence if the mean velocity on one side is zero. Bradshaw (1977) has attributed the non-linear growth rate of plane turbulent jets as measured by several investigators and documented by Kotsovinos (1976) to self-induced draughts ("still-air" turbulence) occurring within the laboratory.

Effects of free-stream turbulence on free shear layers have been investigated by Peerless (1971), Saiy (1974) and Mohammadian et al. (1976) in a plane two-stream mixing layer; by Patel (1977) in a plane one-stream mixing layer; by Leuchter (1976) in a circular two-stream mixing layer; by Kulik et al. (1969) and Fink (1977) in a circular turbulent jet; and by Komoda (1957) in a turbulent wake.

The measurements of Peerless, Saiy and Mohammadian et al. were obtained using the same rig which consisted of two adjacent rectangular ducts inclined ($8\frac{1}{2}^{o}$) to each other and meeting to form a sharp "trailing edge". Most of the boundary layers upstream of the trailing edge were removed by suction. Peerless and Mohammadian et al. used a system of oscillating grids consisting of single rows of spanwise round bars, situated at the trailing edge. The grid oscillation wavelength was considerably larger than the shear layer scale and probably caused considerable shear layer flapping. Strong vortex shedding was also present at two bar-spacings downstream of the grids. Saiy, in a more extensive repeat of Peerless' measurements used, in preference, stationary square-mesh rectangular-bar grids - though having only two meshes per duct height - inserted about eight mesh sizes

upstream of the trailing edge. At the trailing edge the turbulence spectra were like that expected of nearly homogeneous nearly isotropic turbulences. Saiy's measurements were obtained in the range $40 \lesssim x/\theta \lesssim 60$ for free-stream velocity ratios of 0.48 and 0.72. Except for a slight flattening in the edge region the mean velocity profiles were found to be approximately independent of free-stream intensity for $(u'/U)_e \lesssim 0.06$, when scaled on the momentum thickness (defined $\int_{-\infty}^{+\infty} (U - U_{e_2})/(U_{e_1} - U_{e_2})(1 - (U - U_{e_2})/(U_{e_1} - U_{e_2}))dy, U_{e_1} > U_{e_2}$) and the difference in free-stream velocities. The direct stresses in the layer were increased by free-stream turbulence, roughly equally for each component. The shear stress, $-\overline{uv}$, was also increased in magnitude. Shear layer snaking (and also flapping) could be expected to increase $\overline{u^2}$ and $|-\overline{uv}|$.

Patel observed a rather large increase in spreading rate, as much as 30% for an increase in $(u'/U)_e$ from 0.005 to 0.014. Patel increased the free-stream intensity in an unconventional manner by partially stalling the wind tunnel blower fan.

Leuchter has given some preliminary results for a square-mesh round-rod biplane grid positioned in the external flow at the shear layer separation point. The observed increase in the mixing layer thickness was almost undoubtedly assisted by the streamwise horseshoe vortices wrapped around the bars of the grid immersed in the shear layer. Fink used a somewhat similar rig, but with the grid placed 10 mesh sizes upstream of the jet exit, which had a diameter of 0.15 of the grid mesh size. Measurements were obtained within the range of zero to 150 jet diameters downstream, for which the free-stream intensity, $(u'/U)_e$ decreased from 0.08 to 0.04. The velocity ratio was varied between 3 and 6. The grid mesh size was chosen small enough to avoid bodily convection of the jet as observed by

smoke flow visualization. Free-stream turbulence increased the half-width of the velocity profile by roughly 10%. The results indicate that the jet approaches a wake-like structure more rapidly when free-stream turbulence is present.

1.2.3 Effect of free-stream acoustic disturbances

Physically, free-stream acoustic disturbances would be expected to exert most effect when the characteristic wavelengths of the acoustic disturbances are of the order of those occurring in the shear layer in the absence of the disturbances. If u_o and ℓ are velocity and length scales of the shear layer, and λ and f are wavelength and frequency scales of the acoustic disturbances then

$$\frac{\lambda}{\ell} = \frac{1}{M} \cdot \frac{u_o}{\ell f} , \qquad (1.2.26)$$

where M is the Mach number. λ/ℓ and $u_o/(\ell f)$ can both be of order unity only if the Mach number is of order unity.

Most experiments on the effect of acoustic disturbances have been done in boundary layers. Acoustic disturbances in high subsonic and transonic wind tunnels are of particular importance and recent investigations have been made by Weeks & Hodges (1977) at M = 0.32, 0.60, 0.80 and 0.86; by Benek (1977) at M = 0.50; and by Raghunathan et al. (1979) at M = 0.64, 0.78 and 0.95. Unfortunately, Benek reported only the level of sound and not its spectrum. Weeks & Hodges used a discrete-tone Hartmann generator which produced frequencies typical of those within the boundary layer. Both Weeks & Hodges and Benek found that there was negligible response of the boundary layers for root mean square fluctuating pressure levels up to about 8% of the dynamic pressure. Raghunathan et al. varied the liner porosity of their transonic wind tunnel to vary the sound level between 0.6 and 2.3% of the dynamic pressure. They found only small changes in mean flow parameters but more significant increases in the streamwise

fluctuation intensity - the only component measured - within the layer. The wavelength of the peak of the frequency spectrum was rather larger than the boundary layer thickness.

1.2.4 Calculation methods and theoretical analyses

The experimental data discussed in subsection 1.2.1 show that the effect of free-stream turbulence on boundary layer flow is confined largely to the outer layer and to an uncertain amount of inactive motion in the inner layer. Thus, for the purposes of calculation methods it would appear that allowances for free-stream turbulence in the turbulence modelling can also be confined mainly to the outer layer. Calculation of free shear layer flows, however, will probably present greater difficulty particularly if the free-stream length scale is so large that the layer is bodily convected.

For boundary layer flows Evans & Horlock (1973) have adapted the turbulent kinetic energy integral equation method of Hirst & Reynolds (1968). Because of their experimental evidence that the turbulent shear stress extends well outside the mean velocity edge they have included an additional shear stress term in the momentum integral equation, which they write as

$$\frac{C_f}{2}\left(1 - \frac{\tau_\delta}{\tau_w}\right) = \frac{d\Theta_\delta}{dx} + (H_\delta + 2)\frac{\Theta_\delta}{U_\delta}\cdot\frac{dU_\delta}{dx}, \qquad (1.2.27)$$

where suffix δ denotes quantities evaluated at or as far as the mean velocity edge. They use, on the basis of Evans (1972), $\tau_\delta/\tau_w = 4(u'/U)_\delta$ and a modified version of Hirst & Reynolds' energy equation

$$\frac{d}{dx}\left[\frac{E^2}{2}\int_0^\delta U dy\right] = 0.14\, u_\tau E^2 + \frac{1}{2}E(\overline{q^2})_\delta, \qquad (1.2.28)$$

where $E = \frac{d}{dx}\int_0^\delta U dy$, and $(\overline{q^2})_\delta$ is taken as $3(\overline{u^2})_\delta$. However, because of the effect of the wall on the free-stream turbulence (see later)

the assumption of isotropy at $y = \delta$ and the assumption for τ_δ/τ_{WALL} are open to doubt and may go some way to explain why the calculations overestimate the data of Huffman et al. (1972) and Evans.

McDonald & Kreskovsky (1974) have used the turbulent kinetic energy equation, an algebraic dissipation length scale based on shear stress, an algebraic mixing-length scale and the modified structural parameter

$$a_1(\overline{q^2} - f(\tfrac{y}{\delta})\,\overline{q_e^2}) = -\overline{uv}\,, \qquad (1.2.29)$$

where $a_1 = 0.15$. f was chosen as $\frac{1}{2}(1 - \cos(\pi y/\delta))$, so forcing $-\overline{uv}$ to zero as the free-stream is approached. Arguments put forward in subsection 1.2.1 suggest that $f(y/\delta)$ should scale on a free-stream length scale as well as the boundary layer length scale. McDonald & Kreskovsky have compared their model with the data of Kline et al., Charnay (1971) and Huffman et al. with reasonable agreement.

Arnal (1977) has used a two-equation transport model, similar to that due to Jones & Launder (1972), and an adapted mixing-length integral method. Closure of the two-equation model is by gradient diffusion for the transport of turbulent kinetic energy and turbulent dissipation, and by an eddy viscosity scaled on the turbulent kinetic energy and turbulent dissipation (ie the so-called Prandtl-Kolmogorov hypothesis). Comparison of both methods was made against Arnal's own adverse pressure gradient data and the constant-pressure data of Huffman et al. and Charnay. Both methods were shown to give reasonable prediction of all three sets of data.

Prediction methods for free-stream turbulence effects on free shear layers appear to be confined to turbulence models using eddy viscosity or mixing-length concepts, or both. Peerless and

Mohammadian et al. have used an eddy viscosity expressed as a function of the streamwise intensity of each free-stream and a mixing length proportional to the momentum thickness (defined in subsection 1.2.2). They have also used a two-equation method based on an eddy viscosity hypothesis and transport equations for the turbulent kinetic energy and w, where w is the square of a characteristic shear layer frequency (the so-called Kolmogorov frequency). Both Peerless and Mohammadian et al. obtained reasonable agreement between the two methods and the measurements. Saiy has compared his own data with two-equation methods based on an eddy viscosity hypothesis and transport equations for the turbulent kinetic energy and either w or $\sqrt{w}$. There appeared to be little difference between the methods in reasonably predicting the measurements.

Fink has argued, in analogy with the energy cascade wave number hypothesis, that for a sufficiently large free-stream length scale the increase in eddy viscosity, $\Delta\nu_T$, is

$$\Delta\nu_T \propto \varepsilon^{1/3} b^{4/3}. \qquad (1.2.30)$$

ε is the dissipation in the free-stream and b is the shear layer turbulence length scale. A sufficiently large free-stream length scale ensures, for high Reynolds number flow, that b is comparable with wavenumbers that occur in the inertial subrange of the free-stream turbulence. Predictions of the mean flow development of the jet influenced by free-stream turbulence agree fairly well with the measurements.

The effect of the impermeability of a plane boundary on adjacent unsheared turbulence has been analysed by Graham (1975) and Hunt & Graham (1978). Far from the boundary the turbulence was assumed to be homogeneous and isotropic. Alternatively, the same situation may be visualized as a stationary, infinite "box of turbulence" into which an impermeable boundary is suddenly inserted.

Further assumptions of weak turbulence, permitting the Navier-Stokes equations to be formally linearized, and of high Reynolds number (based on turbulent scales), were made. Hunt & Graham show by use of the continuity equation that if the length scale $\delta_V \sim \sqrt{(\nu x/U)}$ of a viscous-dominated layer adjacent to the boundary is small by comparison with the free-stream length scale, then $\overline{v^2}$ remains very small within the viscous layer; the change in $\overline{v^2}$ must occur in an outer inertial layer. Outside the viscous sublayer $\overline{v^2}$ is calculated to increase monotonically to a value very slightly larger than the free-stream value before decreasing to the free-stream value, reaching $0.95\ \overline{v_e^2}$ at $y/(L_{x_{11}})_e \approx 2.0$. As the boundary is approached from the free-stream, $\overline{u^2}$ ($= \overline{w^2}$) at first decreases slightly but then increases above the free-stream value for $y/(L_{x_{11}})_e \lesssim 0.5$ to a maximum of $1.5\ \overline{u_e^2}$ at the boundary. At $y/(L_{x_{11}})_e = 0.5$, $\overline{v^2} \approx 0.65\ \overline{v_e^2}$. The analysis is an asymptotic one so that close to the wall $\overline{u^2}$ and $\overline{w^2}$ must conform to the condition imposed by the no-slip condition at the boundary. Hunt & Graham calculate the viscous layer thickness, defined by the position where $\sqrt{u^2}$ and $\sqrt{w^2}$ are 0.99 of their asymptotic values, to be $\delta_V = 4.0\ \sqrt{(\nu x/U)}$.[†] The amount by which $\overline{u^2}$ and $\overline{w^2}$ are predicted to amplify decreases as δ_V/L_e increases. Thus, amplification of $\overline{u^2}$ and $\overline{w^2}$ ceases when $\delta_V/(L_{x_{11}})_e \approx 0.5$.

Uzkan & Reynolds (1967) and Thomas & Hancock (1977, Appendix 1) have made measurements of grid turbulence near a wall moving at the stream speed, for which $\delta_V/(L_{x_{11}})_e \approx 0.4$ and 0.1 (according to Hunt & Graham's calculations), respectively. Uzkan & Reynolds measured only $\overline{u^2}$ and deduced the effect of the wall on $\overline{u^2}$ to be purely viscous, consistent with the analysis. They found

---

[†] For a constant-pressure flat-plate laminar boundary layer

$\delta_{99} = 4.9\ \sqrt{(\nu x/U_e)}$

that $\delta_v = 1.8\sqrt{(\nu x/U)}$ which, in view of the difficulty in measuring differences in turbulence intensity of the order of 1%, is in reasonable agreement with the calculated thickness. Thomas & Hancock measured $\overline{u^2}$, $\overline{v^2}$ and $\overline{w^2}$ and confirmed the predicted attenuation of $\overline{v^2}$. However, they found that the amplification of $\overline{u^2}$ agreed with that predicted only for the smallest distance from the grid (x/M = 13). Further downstream the amplification of $\overline{u^2}$ was greater than predicted and at the most downstream station (x/M = 25) the maximum $\overline{u^2}/\overline{u_e^2}$ exceeded 2. Contrary to prediction the measured $\overline{w^2}$ appeared to be little affected by the presence of the boundary, the transfer of energy being almost entirely from $\overline{v^2}$ to $\overline{u^2}$.

Durbin (1977) has extended the analysis of Hunt & Graham to include a constant mean shear of thickness δ, adjacent to the wall. In this case the wall is stationary. (Although a constant mean shear gives a discontinuity in velocity gradient dU/dy at $y = \delta$ a profile that has continuity of velocity gradient renders the analysis intractable.) Only the high Reynolds number case was considered and the thin viscous-dominated layer at the wall was neglected. The boundary layer turbulence was assumed to be statistically independent of the turbulence in the free-stream, and the latter was taken to be weak. Statistical independence is most realistic when the intensity in the free-stream is small or when the free-stream length scale is large with respect to the boundary layer length scale; the latter is analogous to the independence of distant wave-numbers in the energy cascade. No account was taken of the effect of free-stream turbulence on the mean velocity profile. Durbin was able to give a full solution of his equations only with the restriction that the free-stream turbulence remained outside the boundary layer; the velocity fluctuations calculated within the boundary layer are irrotational

fluctuations due to the external turbulence. $\overline{u^2}$, $\overline{w^2}$ and $-\overline{uv}$ develop with time (ie streamwise distance) from the initial conditions specified at time = 0, while $\overline{v^2}$ is independent of time. The development of $\overline{u^2}$, $\overline{w^2}$ and $-\overline{uv}$ is most rapid near $y = \delta$, and a consequence of the discontinuity there in dU/dy is that $\overline{u^2}$, $\overline{w^2}$, $-\overline{uv}$ are also discontinuous at $y = \delta$. $\overline{v^2}$ is continuous everywhere. However, it is not clear how much of the predicted effect on $\overline{u^2}$, $\overline{w^2}$ and $-\overline{uv}$ is due to the discontinuity in dU/dy. Outside $y = \delta$ $\overline{u^2}$ and $\overline{w^2}$ are amplified with respect to their free-stream values and this is accompanied by an attenuation of $\overline{v^2}$. Between $y = 0$ and $y = \delta$ $\overline{u^2}$ and $\overline{w^2}$ are maximum and of the order of the free-stream value just inside $y = \delta$. Inside $y = \delta$ $-\overline{uv}$ is calculated to be positive but outside it is calculated to be negative. The experimental data so far reviewed and the new data presented in the present thesis provide no substantial support for the existence of a negative shear stress (negative $-\overline{uv}$) outside the boundary layer edge.

1.2.5 Conclusion to the review

Mean-flow measurements on nominally two-dimensional flat plate boundary layers in the presence of approximately isotropic free-stream turbulence show that there is an increase in growth rate and momentum transfer, and a fuller mean velocity profile (ie a reduced wake strength in the outer layer). Quantitative agreement between the various sets of measurements is rather poor with some workers indicating changes in skin friction as much as three times those observed by others. The measurements of Meier are particularly important because they confirm that for a small free-stream intensity of $(u'/U)_e \lesssim 0.01$ the turbulence within the boundary layer is mostly uncorrelated with the free-stream turbulence.

Mostly, the effects of free-stream turbulence have been correlated with only the (streamwise) turbulence intensity outside the boundary layer edge, and the length scale of the free-stream

turbulence has, with the exception of Meier & Kreplin, been commonly assumed to be of much less importance. Charnay investigated the possibility of a length scale effect but did not observe any. However, physical arguments, the analyses of Graham and Hunt & Graham and the measurements of Thomas & Hancock have shown that there is a large effect of the boundary impermeability on the free-stream turbulence. This is difficult to reconcile with the conclusion that the length scale ratio L_e/δ is an unimportant parameter, even if it should turn out to be unimportant in the actual interaction between the boundary layer and external turbulence. Meier & Kreplin's measurements in what must have been grossly anisotropic free-stream turbulence do show a length scale effect, but one that is larger than that inferred from the streamwise intensity and Meier's measurements for nearly isotropic free-stream turbulence. Rather, their measurements strongly confirm the idea that the normal component intensity is more important than the streamwise component.

Measurements of the effect of free-stream turbulence on heat transfer through a turbulent boundary layer fall into two categories, one asserting that there is no effect and the other showing an increase. However, the more recent measurements show fairly convincingly that there is an increase and that it is about twice the increase in the skin friction.

Boundary layer turbulence measurements have shown that the effect of free-stream turbulence is confined mainly to the outer layer but with a small uncertain amount of inactive motion within the inner layer. The edge of the shear stress profile has been observed to move out further than the mean velocity edge although the very large movement measured by Huffman et al. is seriously in doubt. Charnay's intermittency measurements using temperature as a passive contaminant show that the penetration of external fluid into the boundary layer fluid is increased and the boundary layer fluid

extends further into the free-stream. The average burst frequency and average burst length show that the interface becomes even more contorted when free-stream turbulence is present. Charnay used an uncompensated temperature probe which filtered-out the finer structure of the interface. Furthermore, his conditional averages have been evaluated with respect to conditionally-averaged mean velocities with the result that the larger-scale motion is ignored.

The effects of free-stream pressure fluctuations are likely to be important only at high subsonic, transonic and supersonic Mach numbers, and are of particular concern in wind tunnels operating in these regimes. Experiments in the high subsonic regime show that the effects are small.

Free shear layers in the presence of large scale free-stream turbulence will be bodily convected in a quasi-steady manner. The consequent snaking appearance will result in an apparent increase in the growth rate of the layer. Small-scale free-stream turbulence will not bodily convect the layer but will cause small-scale corrugations of the turbulent/turbulent interface. Experiments on turbulent shear layers are more complicated than for boundary layers even if the free-stream length scale is small enough to avoid bodily convection. A major complication arises from the highly coherent structure observed in some circumstances as, for example, by Brown & Roshko in a two-stream mixing layer.

A number of calculation methods have been adapted to account for free-stream turbulence effects on boundary and free shear layers by incorporating additional emperical information. Most of them have been demonstrated to give reasonable predictions.

1.3 OUTLINE OF THE FOLLOWING CHAPTERS

In the following chapters the results of an experimental investigation of the effect of nearly homogeneous nearly isotropic free-stream turbulence on a closely two-dimensional nearly constant-pressure flat plate incompressible turbulent boundary layer are presented. Chapter 2 presents some preliminary experimental results that influenced the experimental arrangement for the main measurements but are not worth including in chapters 3 and 4. The major part of chapter 2 gives the details of the experimental techniques used. Chapter 3 discusses the inner and outer layer laws. Decay laws for grid-generated turbulence are discussed as a prelude to a parametric analysis of wind tunnel and boundary layer Reynolds number constraints on the range of free-stream intensity and the ratio of free-stream to boundary layer length scales that may be obtained in laboratory experiments. At this point some parameters that are pertinent to the measurements of other workers are discussed. The free-stream turbulence measurements are presented before the mean flow measurements which are also compared with those of previous workers. Chapter 4 presents the boundary layer turbulence measurements. Conditional-sampling techniques, including the intermittency algorithm employed, are discussed early in the chapter to avoid breaking up the presentation of the measurements. The conventional averages are presented next, followed by the intermittency measurements and the conditional averages. Balances of the turbulent kinetic energy and turbulent shear stress equations are presented. Some implications for calculation methods are discussed. Finally, a conclusion to the thesis is provided in chapter 5.

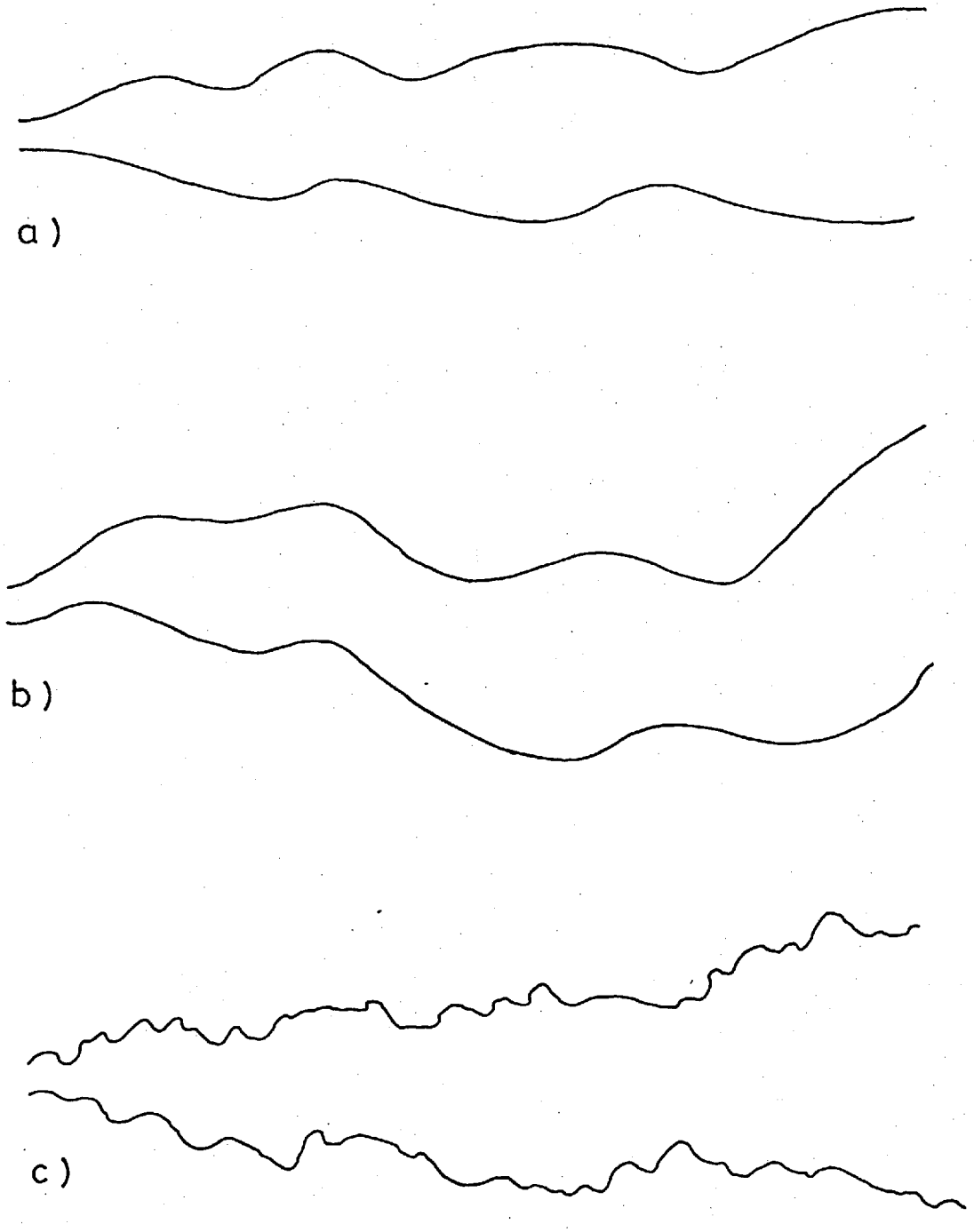

Fig. 1.1 Effect of free-stream turbulence on a turbulent free shear layer; a) Negligible free-stream turbulence; b) Large-scale free-stream turbulence; c) Small-scale free-stream turbulence.

CHAPTER 2

EXPERIMENTAL ARRANGEMENT, TECHNIQUES AND SOME PRELIMINARY EXPERIMENTAL RESULTS

2.1 EXPERIMENTAL ARRANGEMENT

2.1.1 Preliminary experimental considerations and final experimental arrangement

As an early part of the present investigation a smoke-filled boundary layer on a wind tunnel wall was examined just downstream of a square-mesh turbulence grid. Figure 2.1 shows two views of the boundary layer flow behind the grid with an initially laminar boundary layer (a & b) and with an initially turbulent boundary layer (c & d). In each view illumination is by a thin plane of light; in a & c the plane of light is aligned with the flow direction and a vertical bar of the grid, and in b & d it is parallel and adjacent to the wind tunnel wall. With either a laminar or turbulent initial boundary layer, the boundary layer is seen to thicken rapidly after it has passed under the grid. Boundary layer fluid is sucked up behind the vertical bars to about the height of the first horizontal bar. Horseshoe vortices wrapped around the vertical bars of the grid immersed within the boundary layer (seen in the vertical views) are more distinct for an initially laminar boundary layer. A strong two-dimensional structure normal to the plane of the boundary layer is seen to persist for roughly three mesh lengths downstream of the grid for an initially laminar boundary layer. For an initially turbulent boundary layer such persistence is not quite so obvious. Although impossible to include in the present thesis, cine-film records of the flows shown in figure 2.1 were also made and show the motions described above more clearly. The length scale of the large disturbances near the grid are (in this case) of the order of the length scale of the underlying

boundary layer. Thus even though figure 2.2 indicates that the laminar boundary layer becomes fully turbulent quite rapidly it is very likely that either an initially laminar or an initially turbulent boundary layer will still contain significant streamwise mean vorticity and (time-averaged) will not be two-dimensional for some further distance downstream. It was therefore decided to confine attention to a boundary layer flow on a flat plate with its leading edge no closer than about four mesh lengths downstream of the turbulence grid.

The wind tunnel selected for the main quantitative measurements was the Department of Aeronautics 0.91 m × 0.91 m (3 ft × 3 ft) wind tunnel which has a 4.9 m long working section. Just downstream of the (9:1) contraction a slot was provided to enable frames containing turbulence grids to be easily inserted into the air stream. The turbulence grids are discussed in more detail in the next section. Without the turbulence grids the background turbulence and unsteadiness was approximately 0.03% of the mean velocity (Davies, 1975). The maximum wind speed attainable with no turbulence grid and an empty working section was approximately 45 m/s and the fan driving the tunnel was capable of operating over a power factor range of 0.5 to 2.0. For the present measurements a free-stream mean velocity of about 16 m/s was used throughout. A plan view of the wind tunnel is shown in figure 2.2.

A flat plate made of "Beauti-Board" (plywood sandwiched between heat resisting plastic and intended for kitchen furniture) 15 mm thick, 0.91 m wide and 2.4 m long was supported horizontally mid-way between the working section floor and ceiling, by rails fixed to the working section side walls so that it could be fixed at various positions along the length of the working section. A separate profiled leading edge strip, 0.91 m × approximately 75 mm,

was fitted by means of dowels to the upstream end of the plate. Three leading edge profiles were designed using mean flow hodograph methods which are described in more detail in appendix 2. A transition trip wire of diameter 0.79 mm was attached by a fine thread of Araldite to the upper and lower surfaces of each leading edge strip. At the downstream end of the plate a symmetrically tapered trailing edge strip (0.91 m x 90 mm) was also fitted by means of dowels.

Ten 8.9 cm diameter removable instrumentation disks were mounted along the centre-line of the plate flush with the upper measuring surface. (Instrumentation fixed to the plate rather than the working section wall avoided problems due to plate deflection or vibration. Some small-amplitude large-wavelength vibration of the plate when in the presence of high-intensity free-stream turbulence was encountered.) The four upstream-most disks were spaced 0.152 m apart and the remaining six disks 0.305 m apart. The instrumentation disks or measuring stations were numbered 1, 2, 3, 4, 6, 8, 10, 12 and 16. Approximately, the distance from the leading edge (of the leading edge strips) to the n^{th} station is given by

$$x_n \text{ (m)} = 0.152\ n.$$

Surface static pressure holes were provided off the plate centre-line on the lower and upper surface at stations 1, 2, 4 and 16, and on the lower surface at stations 1 and 2.

A reference Pitot-static probe was permanently situated 1.68 m from the grid position, 0.2 m above the plane of the plate and 0.2 m from the plate centre-line, and connected to a Betz manometer. The local free-stream mean velocity was measured using an instrumentation disk static pressure hole and a Pitot probe supported from the permanently fitted working section traverse gear.

Boundary layer measurements were made using a finely-controllable boundary layer traverse gear, of the type shown in figure 2.3, permanently fitted to an instrumentation disk which was also fitted with two static pressure holes. The probe support passed through the instrumentation disk and was attached to the slide of the traverse which was driven via a fine-pitched lead screw. Probe position was recorded by a linear potentiometer which was regularly calibrated by means of slip gauges. Allowance for backlash was made when setting the initial position of the probe and a given position was always reached by moving the probe away from the plate surface.

The use of a flat plate with a sharp leading edge of small included angle minimises pressure gradient effects on the initial boundary layer and provides the layer with a defined origin. When free-stream turbulence is present simple reasoning suggests that the normal component fluctuating velocity will cause fluctuating separation at the leading edge. At an early stage of the present work it was decided to consider a symmetrically-sharp (ogive-shaped) leading edge with a half-apex angle typical of the largest fluctuating incidence to which the leading edge would be subjected. Two sharp leading edge shapes were designed with apex half angles of 10^{o} and 25^{o}. Design and shape details of these and also those of a round-nose leading edge shape (not used) are given in appendix 2. A brief flow visualization exercise using a (much thicker) plate with an ogive-shaped leading edge (of comparable apex half angle) positioned 6 mesh lengths downstream of turbulence grid was performed in the Department's 1.22 m x 0.61 m smoke tunnel. The path followed by a plume of smoke approximately coincident with the mean stagnation stream line switched from side to side of the leading edge but no fluctuating separations were observed.

Preliminary measurements, not reported here, showed a slight rise in skin friction coefficient at the last measuring station (16) apparently due to the proximity of the trailing edge. An extension plate 0.3 m long was therefore inserted between the plate and the tapered trailing edge strip.

A non-zero pressure difference between the plate upper and lower surface static pressure holes at station 1 was used to infer a non-zero mean circulation around the plate. The pressure difference was brought to within 0.5% of the free-stream dynamic pressure by an otherwise insignificant upwards deflection of the extension plate of about 1.5^{o}.

A plan view of the complete plate is shown in figure 2.4 and figure 2.5 shows it mounted in its most forward position in the wind tunnel.

2.1.2 Turbulence grids

Preliminary flow investigations in the 0.91 m × 0.91 m wind tunnel revealed that two of the four existing turbulence grids - the 15.2 cm and 22.8 cm mesh grids - produced long-time randomly unsteady and spatially non-uniform mean velocity profiles throughout the working section. At the streamwise position of the reference Pitot-static probe the spatial non-uniformity in mean velocity was as much as ±10% and the unsteady variations were about ±5%. Varying the wind speed indicated no consistent Reynolds number dependence of the unsteadiness or non-uniformity. A similar problem with a 15.2 cm mesh grid was also encountered by Cherry (1980) using the Aeronautics Department's 0.91 m × 0.61 m wind tunnel. As far as the author is aware there is no direct reference in the literature to this kind of problem.

Initially it was thought that the problem might be related to the fact that the offending grids had only a small number

of meshes per wind tunnel width, but this was later discounted. All of the grids were of biplane construction with one row of bars immediately behind the other perpendicular row. However, the bars of the satisfactory grids were of square cross-section while the bars of the unsatisfactory grids were of rectangular cross-section (of approximately 2:1) with the wider side normal to the stream. The immediate use of a large-mesh square-bar biplane grid of the desired solidity was made difficult because grids were normally slid into the air stream through a 3.8 cm-wide slot provided in the working section wall. As a possible alternative a square-mesh monoplane grid (ie, with the horizontal and vertical bars lying in the same plane) of nearly square bars was made by fitting fillets between the cross-overs of the troublesome 15.2 cm mesh grid. This grid behaved much as it did without the fillets.

A simple flow visualization exercise using pieces of wool about 4 mesh sizes in length showed that the wake flow in the region of the bar intersections of the monoplane grid was not the same for each intersection. Furthermore, the wake flow patterns would occasionally change. Between the intersections wool lengths indicated a very much more steady and uniform behaviour. Repeating the exercise but with the fillets removed showed the wakes of the cross-overs to be similarly non-uniform and unsteady. For either grid the junction wake flow patterns could be altered by disturbing the flow, and a strong correlation between the reference Pitot-static probe and the wake flow patterns was observed. An existing 15.2 cm mesh square-bar biplane grid was cut to fit into the working section of the present wind tunnel. The flow downstream of this grid was found to be uniform and steady. Two new grids each of 15.2 cm mesh and 3.8 cm square cross-section bars were made, one of monoplane construction and the other of biplane construction. The tolerated variation of mesh size was

about 1%, better than the unsatisfactory grids. For the new biplane grid the horizontal bars were fitted to the vertical bars from within the working section. The flow downstream of the carefully-constructed monoplane grid was no better than for the other unsatisfactory grids while downstream of the biplane grid the flow was found to be steady, spatially uniform and also acoustically quieter than the monoplane grid. An obvious difference between the two grids is the difference between the stagnation lines at the junctions of the bars : for the monoplane grid the stagnation lines must also intersect but for the biplane grid they cannot. Possibly, streamwise vortices produced by the shear layer vorticity shed from the upstream bars being wrapped around perpendicular downstream bars have the effect of stabilizing the wakes of the cross-over.

The turbulence grids used for the measurements reported below are listed in table 2.1, and four are shown in figure 2.6. Almost all of the measurements were obtained using the square-mesh square-bar biplane grids although some mean-flow properties and free-stream turbulence measurements were measured with turbulence generators comprising a single row of vertical square bars. (For the main mean flow investigations the horizontal bars of the 15.2 cm mesh biplane grid were separately but consistently fixed to the vertical bars from within the working section. For the later mean flow and main turbulence measurements the wind tunnel grid slot was modified to accommodate the larger grid.) The single row of round bars was used only to measure the degree of anisotropy produced by this type of turbulence generator, primarily as a comparison with the tabulated measurements of Huffman et al. (1972) which indicate a high degree of anisotropy (discussed in subsection 1.2.1 of chapter 1). Direct comparison will, however, not be entirely valid because the present round bar turbulence

generator has only two-thirds the solidity of those used by Huffman et al. The comparison is presented in chapter 3.

2.2 MEAN FLOW MEASUREMENT TECHNIQUES

2.2.1 Measurement of the velocity profiles and the skin friction

Boundary layer mean velocity profiles were measured with single Pitot probes (of diameters 1.00 mm or 1.26 mm) referenced to a static pressure hole in the instrumentation disk. One of the two Pitot probes is shown mounted in the traverse gear in figure 2.3. The Pitot-static pressure difference was measured using one range (0 - 30 mm water) of a Furness multi-range capacitance manometer, type MDC. After further amplification the output of the capacitance manometer was RC low-pass filtered with a time-constant of 4.7 seconds, before input to one channel of a Solartron Data Transfer Unit (DTU) dater logger. (The DTU controls a Solartron LM1420 Digital voltmeter (DVM), sequentially switching it between a preselected number of input channels and outputting to a Teletype typewriter fitted with a paper tape punch.) For the first main set of mean velocity profile measurements the local free-stream velocity was also recorded on a second channel of the DTU using a second capacitance manometer. This was done because at the time the first main data collection was initiated the quality of the flow downstream of the new grids had not been thoroughly proved. However, the free-stream mean velocity was confirmed to be steady and the logged values were not used in the final profile analysis. Subsequently, the free-stream mean velocity was recorded by hand (as well as by the traversing probe). The digital resolution of the Pitot-static pressure difference was 0.07% of the free-stream value. The output of the traverse gear linear potentiometer was monitored using a Solartron LM1619 DVM and logged by the Data Transfer Unit. The digital resolution of the probe position, limited by the LM1420 DVM, was 0.025 mm for the first main

velocity profile data set and 0.050 mm for the subsequent data set. The zero position of the Pitot probe was set visually, and the likely error was of the order of 0.025 mm. A block diagram of the mean velocity measuring apparatus is shown in figure 2.7. Figures 2.8 and 2.9 show typical capacitance manometer and traverse gear position-potentiometer calibrations, respectively.

Skin friction measurements were obtained in four ways; (i) by fitting a portion of the mean velocity profile to the logarithmic law of the wall, (ii) by using Preston tubes, each mounted in an instrumentation disk, (iii) by using the traverse Pitot probe as a Preston tube, (iv) by a Pitot probe resting on the surface and supported from above by the (permanent) working section traverse gear. This latter arrangement allowed the skin friction to be measured at positions off the plate centre-line and served as a means of checking the two-dimensionality of the mean flow. Patel's (1965) Preston tube calibration, as discussed by Wong (1970), but with a slightly different interpolation between the ranges of the two curves, was used.

2.2.2 Mean velocity profile data reduction

The mean velocity profiles, and the displacement and momentum thickness were evaluated from the Pitot traverse data (recorded on punched paper tape) by an existing computer program (Brederode, 1973; Shabaka, 1979) with some small modifications. Some of the more important details of the program are briefly discussed below. Skin friction was deduced by fitting a portion of the velocity profile to the logarithmic law of the wall. Since the inner layer dimensional arguments do not depend upon outer layer length scales it is expected that the inner layer will be unable to distinguish between outer layer turbulence and free-stream turbulence. Therefore, it follows that the logarithmic law of the wall should be unaffected by the free-stream turbulence -

or, at least, that true changes in the skin friction caused by free-stream turbulence will be larger than any changes in measured skin friction caused by changes in the logarithmic law.

To determine the skin friction the computer program first fitted the mean velocity profile, by the method of least squares, to

$$\frac{U}{U_e} = A + B \ln\left(\frac{yU}{\nu}\right) \qquad (2.2.1)$$

in the range $y_L < y < y_U$, where

$$y_L = 100\,\frac{\nu}{u_\tau} \text{ and } y_U = 0.15\ \delta_{995} \qquad (2.2.2)$$

To sufficient accuracy y_L was evaluated using only a first guess for the friction velocity, $u_\tau = 0.04\ U_e$. δ_{995} was determined by a crude but acceptable curve fit to the velocity profile over the range $0.98\ U_e < U < 0.9995\ U_e$. The skin friction was then evaluated by requiring U/U_e given by

$$\frac{U}{U_e} = \frac{u_\tau}{U_e}\left(\frac{1}{k}\ln\left(\frac{yu_\tau}{\nu}\right) + C\right) \qquad (2.2.3)$$

and U/U_e given by equation 2.2.1 to be equal at $y = y_1$, where y_1 was given by

$$\ln\left(\frac{y_1\ 0.04\ U_e}{\nu}\right) = \frac{1}{2}\ \ln(100) + \ln\left(\frac{y_U \times 0.04\ U_e}{\nu}\right). \qquad (2.2.4)$$

$k = 0.41$ and $C = 5.2$ were used throughout. According to Brederode & Bradshaw (1974) the values of $k = 0.41$ and $C = 5.0$ suggested by Coles (1968) give skin friction values consistently about 2% higher than given by a Preston tube using Patel's widely-accepted calibration : Brederode & Bradshaw have argued that the value of $C = 5.0$ deduced by Coles should be amended to $C = 5.2$ to force agreement with Patel's calibration.

Inside $y_+ \approx 100$, high turbulence intensity, the effect of the wall on the probe, the effect of a high mean velocity gradient and inaccuracy in y cause doubts about the accuracy of Pitot tube measurements. Therefore for $y_+ \lesssim 100$ the measured velocity profile

was ignored and replaced by a linear sublayer and buffer layer ($0 \lesssim y_+ \lesssim 50$) and a cubic polynomial transition layer ($50 < y_+ \lesssim 100$) matched to the measured profile outside $y_+ = 100$. Coles' (1968) values of the contributions to the displacement and momentum thickness were used in the region $y_+ < 50$. Simpson's rule was used to integrate the mean velocity profile in the outer layer. To allow for the effect of the mean velocity gradient $\partial U/\partial y$ the effective centre of the Pitot probe, following MacMillan (1957) and confirmed by Patel (1965), was taken to be 0.15 of its outside diameter above its centre, for the whole profile.

As the Reynolds number decreases y_U tends to y_L : for all the profiles taken at station 4 the fitting range was changed to $y_L = 50\ \nu/u_\tau < y < y_V = 0.20\ \delta_{995}$. Calcomp plots of the profile in semi-logarithmic axes showed that the extended region maintained the slope of 1/0.41.

More accurate values of δ_{995} than the estimates yielded by the profile analysis program were obtained by fitting the curve

$$\frac{U}{U_e} = 1 - a(Y_1 - y)^2 \qquad (2.2.5)$$

to the data in the range $0.98 \lesssim U/U_e \lesssim 0.999$. A least-squares fit was used to evaluate a and Y_1, giving

$$\delta_{995} = Y_1 - \sqrt{\frac{0.005}{a}} \,. \qquad (2.2.6)$$

Values of δ_{995} quoted for the present experimental work were evaluated using the method just described. Generally, the accuracy of δ_{995} cannot be expected to be more than one order of magnitude smaller than the interval in y in the region $y = \delta_{995}$.

The following expressions were used where necessary to evaluate the density, kinematic viscosity and velocity:

$$\rho = 348.3\ p_a/(273.2 + \theta) \quad kg/m^3$$

$$\nu = (0.1340 + 0.000879 \times \theta)/p_a \times 10^{-4} \quad m^2/s \qquad (2.27)$$

$$U = 0.2365 \left(\frac{h(\theta + 273.2)}{p_a}\right)^{\frac{1}{2}} \quad m/s \quad ,$$

where p_a(bar) is the atmospheric pressure, θ (^oC) is the working section temperature and h(mm H_2O) is the pressure head.

2.2.3 Remaining remarks

The capacitance manometer(s) was calibrated (against a Betz manometer) before each traverse and the "zero" recorded before and after each traverse. Drift in the zero during a traverse was of the order of 1% of the free-stream dynamic head and was linearly interpolated to determine the zero of the intervening Pitot-static pressure measurements. The probe position potentiometer was calibrated over its whole range from time to time, and more frequently for regions close to the plate surface. Typically, the slope of the calibration of the potentiometer remained within about 0.2% over several weeks and the "zero" remained constant during at least one traverse. Profile measurements were started with the probe just resting on the instrumentation disk surface and then moved outwards until it was certain that the free-stream had been reached. The first-logged points were remeasured before the profile was considered complete. At several positions throughout the profile the measurement was repeated two or three times before moving the probe to its next position. At each new position of the probe 60 seconds (about 12 low pass filter time-constants) were allowed to elapse before the measurement was logged. A small amount of slow drift of the working-section dynamic head was removed by careful manual adjustment of the fan motor thyristor control : the remaining scatter was less than about ±0.5%.

2.3 PASSIVE HEATING OF THE BOUNDARY LAYER AND MEAN TEMPERATURE MEASUREMENT

For the boundary layer turbulence measurements presented in chapter 4 the boundary layer was slightly heated above the free-stream temperature by four 28 s.w.g. (0.38 mm) Nichrome heating wires stretched across the flow just downstream of the leading edge. The wires were at a height of 3-4 mm and spring-loaded† to take up expansion. See figure 2.10. The heating wires were connected in series and power was supplied by a Variac auto-transformer to a maximum of 8 amps x 209 volts. Depending upon the turbulence grid and plate position used the heating power supplied was adjusted so that the maximum temperature in the boundary layer mid-way between stations 6 and 16 was 3-4°C above the free-stream temperature.

A Comark differential thermocouple thermometer was used to measure the boundary layer mean temperature profiles. One of the junctions was held in the free-stream away from the boundary layer and the other was supported by the boundary layer traverse gear.

The temperature of the free-stream was measured by a mercury-in-glass thermometer held near to, but not touching, one of the working section windows. The temperature could be read to an accuracy of about 0.2°C.

Stratification in the working section was negligible.

2.4 TURBULENCE MEASUREMENT TECHNIQUES

The main turbulence measurements were obtained using a three-wire probe. This consisted of a standard Disa 55P 51 x-wire probe, wired locally with 5 μm platinum wire, and a locally

---

†Adjustment of the spring tension was also used to prevent the wires from vibrating.

made constant-current temperature probe fitted to the side of the x-wire probe holder. The resolution volume of the three-wire probe was approximately equal to a cube with sides 1.5 mm long. Disa 5 m coaxial cables were used to connect the x-wire probe to standard Disa 55D01 constant-temperature anemometers operated at a bridge ratio of 20:1 and a DC gain setting of "high". The temperature probe was connected to a locally-made constant-current 'anemometer'. Only a minimum of signal processing was carried out before recording the fluctuating voltages on an Ampex FR1300 frequency-modulated tape recorder. A tape speed of 60 inches per second (1.52 m/s) was used, giving a frequency response of 0 Hz to 20 kHz. Mean voltages for the x-wire probes were recorded by hand. Block diagrams of the electronic units used are shown in figures 2.11 and 2.12. The recorded data were later digitized and recorded on digital tape for analysis on the College's CDC computer. The digital analysis programs are discussed in subsection 2.4.6.

The fluctuating voltages were amplified before recording them in order to keep the signal-to-noise ratio of the tape recorder as high as possible. Care was taken to ensure that the positive and negative peaks of the fluctuations did not exceed the ±1 volt linear range of the tape recorder amplifiers. Signal inversion introduced by the additional amplification was easily removed at the digital analysis stage.

Now, the response θ_W of a slender-wire temperature probe with negligible internal heating to a temperature fluctuation θ_A is given by

$$\theta_A = \theta_W + M \frac{d\theta_W}{dt} . \qquad (2.4.1)$$

M is the time-constant of the wire response and is due to thermal capacity of the wire. M decreases fairly slowly with increasing Reynolds number. Although the damping provided by M reduces the

wire's high frequency response it can be easily compensated, in principle at least, by adding to the anemometer output a proportion M of its derivative.

The circuit shown in figure 2.12b was used to provide frequency compensation and amplification of the constant-current 'anemometer' output. The compensation was set with the probe positioned where the temperature intermittency was about 0.5 and the capacitance C increased until the backs of the hot bursts decreased as rapidly as possible to zero without overshooting the cold level. In error, the 3 dB upper cut-off frequency of the compensator and amplifier shown in figure 2.12b was set to 10 kHz instead of 20 kHz but this should not have significantly affected the results since 10 kHz corresponds approximately to the spatial resolution volume of the three-wire probe in a flow at 16 m/s. Some limitation of the bandwidth of the compensating circuit was necessary to avoid oscillation and reduce large amplification of unwanted high-frequency noise. Compensation could have been carried out as part of the digital analysis but this would have had the disadvantage that the noise of the tape recorder and the noise of the amplifiers shown in figure 2.12b would also have been amplified resulting in a worse signal to noise ratio. The signal level was controlled by the combined attenuator and filter box.

The filter box (due to Dr. A.J. Smits) shown in figure 2.11 was designed specifically for use with the Disa 55D01 anemometer units in order to separate out its mean and fluctuating output voltages : the fluctuating signals were 1 Hz high-pass filtered and the mean values of the fluctuating "dc" were 200 Hz low-pass filtered ("integrated") and measured with a single Solatron LM1420 digital voltmeter switched between either anemometer output. The gain adjustments of the operational amplifiers shown in figure 2.11b were set to nominal integer values of either 2, 3, 4 or 5 depending

upon the signal amplification required.

Measurements of $\overline{u^2}$ were also obtained by using a U-probe and a Datron 1030 r.m.s. meter. Some preliminary unlinearized x-wire analogue measurements of $\overline{u^2}$, $\overline{v^2}$ and $\overline{w^2}$ - not presented here - were obtained by approximately matching the wire calibrations and using a sum-and-difference unit to give signals proportional to u and v, or u and w. The wires were approximately matched by amplifying or attenuating the mean output voltage of one of the anemometers to be equal to the mean output voltage of the other. The output voltages were found to remain closely equal over most of the calibration range. For all analogue fluctuating velocity measurements the unlinearized small-signal sensitivity was used.

2.4.1 Wiring of the probes

The x-wire probe and U-probe were wired by soft-soldering silver-sheathed 5 μm platinum wire (Wollaston wire) to the probe prongs. The prongs were first cleaned and tinned. A short straight length of Wollaston wire was cut from the reel, laid across the prongs, and the soldering iron applied to the underside of each prong in turn. Only a very minimum of solder was used. After the second soldered joint had been made and the surplus wire cut off with a scalpel, the first soldered joint was reheated to release any tension in the wire. When the wires had been attached to the probe they were etched using a pin-head bubble of 10% nitric acid and 90% distilled water issuing from an upwards-facing capillary tube. The etched length varied from wire to wire between about 1.0 and 1.3 mm. Care was taken, particularly for the x-wire probe, to ensure that the etched wires were as straight as possible. Slight curvature is unavoidable when the wires are heated. It was found quite easy to attach the wires close to $\pm 45^{\circ}$ to the probe axis giving approximately equal sensitivity to the longitudinal and transverse components of velocity. The temperature probe was

similarly wired with 1 μm platinum Wollaston wire. The etched length again varied from wire to wire between about 1.0 and 1.3 mm.

2.4.2 Setting-up the constant-temperature anemometers

The output and input bias voltages were set as described in the operating manual, and the HF filter set to position 2. A resistance ratio of 2.0 was used for the platinum wire probes. However, for newly-wired probes the overheat ratio was increased slightly to about 2.1 and the wire(s) left to anneal to avoid an initial calibration drift. A period of about six hours was found to be sufficient although the wires were usually left annealing overnight. After annealing the resistance ratio was returned to 2.0.

The bandwidth of the probe and anemometer increases with the gain of the anemometer internal amplifier and the mean velocity. It is also dependent upon the input bias voltage and the impedance of the probe cable. Anemometer bandwidth was set using the square wave test at a wind speed a little above the maximum at which measurements were to be taken. The gain setting was increased to 7 (giving a maximum bandwidth of the order of 90 kHz) and the 'L' (inductance) and 'Q' (quality) screws set to balance the probe cable impedance and so avoid parasitic oscillation. The input bias control was used as a fine control on the bandwidth; it also affects the anemometer mean output voltage and, once set, was left untouched.

2.4.3 Calibration of the hot-wire probes

In this subsection U, V, W and U_{eff} are instantaneous total velocities and E is the anemometer instantaneous total output voltage, where "total = mean plus fluctuating parts". Here, a mean value will be denoted by an overbar.

In the present work the heat transfer law Nu(Re, Pr, Gr) for a hot wire operating at constant temperature was assumed to be of the form

$$E^2 = E_o^2 + B' \ (U_{eff})^n \qquad (2.4.2)$$

where n = 0.45 was used. (See for example, Bradbury & Castro, 1972). Except in very low speed flows buoyancy forces ($\propto Gr/Re^2$) are negligible.

For the present measurements the probe axis was always aligned parallel to the plate centre-line and (to within about 1^o) parallel to the plate plane. (Allowance for the probe pitch is discussed later.) The effective velocities for each wire of a x-wire probe were therefore

$$U_{eff_{1,2}} = U \cos \psi_{eff_{1,2}} \pm (V \cos \phi + W \sin \phi)\sin \psi_{eff_{1,2}} \qquad (2.4.3)$$

where the suffix 1,2 denotes one or other wire and $\psi_{eff_{1,2}}$ ($\approx 45^o$) are effective wire angles taken to be positive for both wires. The plus sign refers to wire 1 and the minus sign to wire 2. $\psi_{eff_{1,2}}$ are approximately equal to the geometric angles between the wire and the mean (calibration) stream direction. ϕ is the rotation of the parallel planes containing the wires from the vertical (y-axis). For the measurements presented $\phi = 0$ (probe sensitive to u and v) and $\phi = \pi/2$ (probe sensitive to u and w). From equations 2.4.2 and 2.4.3

$$E_{1,2}^2 = E_{o_{1,2}}^2 + B_{1,2} \ (U \pm (V \cos \phi + W \sin \phi)\tan \psi_{eff_{1,2}})^n \qquad (2.4.4)$$

where

$$B = B'(\cos \psi_{eff})^n \ . \qquad (2.4.5)$$

The hot wires were statically calibrated - as opposed to dynamical calibration by sinusoidally oscillating the probe to determine its sensitivities - in the free-stream and with no turbulence grid in the working section. $\overline{V}$ and $\overline{W}$ were assumed to be zero for the calibration. Thus, from equation 2.4.4

$$\overline{E}_{1,2}^2 = \overline{E}_{o_{1,2}}^2 + B_{1,2}\overline{U}^n \ . \qquad (2.4.6)$$

$\overline{E}_o^2$ and B were evaluated by the method of least squares. Small changes of mean temperature often occurred during calibration, for which allowance was made as discussed in subsection 2.4.5. Figure 2.13 shows typical x-wire probe calibrations before and after a set of measurements.

The effective wire angles (for the x-wire probe) were measured with the probe rotated so that $\phi = \pi/2$, in a non-turbulent free-stream. By means of a "saddle" arrangement the instrumentation disk was yawed† through the angles $\pm n\Delta\psi$, where n = 0, 1, 2, 3 and $\Delta\psi = 4.67^o$. For each wire

$$\left[\frac{\overline{E}^2 - \overline{E}_o^2}{B_{\Delta\psi=o}\,\overline{U}^n}\right]^{\frac{1}{n}} - \cos(n\Delta\psi) = -\tan\psi_{eff}\cdot\sin(n\Delta\psi)\ , \qquad (2.4.7)$$

(Bradshaw, 1971, p123). This equation is easily derived from equation 2.4.4. $\tan\psi_{eff}$ was determined by a graphical straight line fit in preference to, say, the method of least squares. A typical 'yaw' calibration is shown in figure 2.14. On a few occasions the graphical best-fit straight line for one or both wires failed to pass through the origin because of slight calibration drift or small calibration errors. Temperature corrections were found to be quite important in this respect.

For the measurements of u and v it was usually found necessary to apply a small correction, $\delta\psi$, to the effective wire angles because of a slight pitch†† of the probe. $\delta\psi$ was obtained by interpolation of the yaw calibration using the values of $\overline{E}_1$ and $\overline{E}_2$ measured to determine $\overline{E}^2_{o_{1,2}}$ and $B_{1,2}$. The method relies on the fact that differences in output voltages are very nearly independent of mean velocity and changes in mean temperature, but sensitive to

---

† rotated about the y-axis

†† rotation about the z-axis

pitch when $\phi = 0$, or yaw when $\phi = \pi/2$ (or pitch and yaw when $\phi \neq n\pi/2$, where n = 0, 1, 2 etc.). An example is given in figure 2.15. The corrections to the effective wire angles were about 1^o, or less.

It was found useful to establish the effects of an error in ψ_{eff} on measured turbulence quantities, particularly the shear stress. In appendix 3 it is shown that

$$\overline{u^2}'' = \overline{u^2}' + C_1^2\,\overline{v^2}' + \overline{uv}'\,2C_1 \ ,$$

$$\overline{v^2}'' = \overline{v^2}'\,C_2^2 \qquad (2.4.7)$$

$$\text{and} \quad \overline{uv}'' = \overline{uv}'\,C_2 + \overline{v^2}'\,C_1C_2 \ ,$$

$$\text{where} \quad C_1 = \frac{\tan\psi_2''.\tan\psi_1' - \tan\psi_2''.\tan\psi_2'}{\tan\psi_1'' + \tan\psi_2''} \qquad (2.4.8)$$

$$\text{and} \quad C_2 = \frac{\tan\psi_1' + \tan\psi_2'}{\tan\psi_1'' + \tan\psi_2''} \ ,$$

Single and double primes denote uncorrected and corrected quantities respectively. Effective wire angles are to be understood. An uncorrected pitch of 1^o, for example, gives an error in $\overline{uv}$ of $0.035\,\overline{v^2}$ - or, very roughly, $0.035\,(-\overline{uv})$.

2.4.4 Calibration of the temperature wire

The temperature coefficient of resistance, $\frac{1}{R}\frac{\partial R}{\partial T}$, of the (platinum) temperature wire was assumed to be 0.0038 $(^oC)^{-1}$ and was found to be consistent with the boundary layer mean temperature profile measurements. The change, e, in the voltage across a constant-current wire due to a change, ΔR, in the resistance is simply $e = I\Delta R$, where I is the current. Therefore, for small fluctuations in R due to small fluctuations, θ, in temperature

$$e = \alpha IR\theta \ ,$$

$$= \alpha E\theta \ ,$$

where $\bar{E}$ is the mean voltage across the wire. For the constant-current 'anemometer' used, both $\bar{E}$ and e were amplified by the internal pre-amplifier. Thus, at the output of the pre-amplifier, using the same notation,

$$e = \alpha\bar{E}\theta \ . \qquad (2.4.9)$$

$\alpha\bar{E}$ is the sensitivity of the wire.

The temperature sensitivity of a constant-current wire increases linearly with current while the velocity sensitivity increases approximately as the cube of the current. (See for example, Hinze, 1975, chapter 2.) The probe current was therefore reduced such that near the wall its sensitivity to velocity fluctuations was negligible by comparison with the temperature fluctuations of the passively heated boundary layer. A wire current of approximately 0.9 mA was used throughout. Even at a current of 1.2 mA a velocity of 1 m/s - a typical fluctuation - was measured to be equivalent to a temperature change of the order of $0.01^{o}C$.

2.4.5 Temperature corrections to the hot-wire measurements

Effects of temperature fluctuations, θ, and mean temperature change, ΔT, on the hot-wire probes were corrected using

$$E^2_{T+\Delta T+\theta} = (1 - \frac{\varepsilon}{\sigma})(\bar{E}^2_o + B\ U^n) \ , \qquad (2.4.10)$$

where $\varepsilon = (\theta + \Delta T)/T$ (Bearman, 1971). Here, E, ε and U are instantaneous quantities. T is the temperature at which $\bar{E}^2_o$ and B where evaluated, and $\sigma = (T_W - T)/T$. T_W is the wire temperature and is independent of T, ΔT, θ or U in a constant-temperature system. Strictly, $\bar{E}^2_o$ and B are functions of stream temperature and, more accurately,

$$E^2_{T+\Delta T+\theta} = (1 - \frac{\varepsilon}{\sigma})\ \bar{E}^2_o(1 - \frac{0.49\varepsilon}{1 + 0.49\sigma}) + B(1 - \frac{0.12\varepsilon}{1 + 0.12\sigma})U^n \qquad (2.4.11)$$

However, equation 2.4.10 was found to be sufficient. For a more detailed discussion see, for example, Comte-Bellot (1977).

No boundary-layer heating was applied for the analogue U-probe (and x-wire) measurements and therefore only mean temperature drift corrections were necessary. In the digital analysis of the three-wire probe measurements the velocities measured by each wire of the x-wire probe were calculated neglecting temperature effects and then corrected using the equation

$$U_c = U_u\left(1 - \frac{E^2}{E^2 - \bar{E}_o^2} \cdot \frac{\varepsilon}{\sigma}\right)^{1/n} \qquad (2.4.12)$$

approximated by

$$U_c = U_u\left(1 - \frac{1}{n}.\frac{E^2}{E^2 - \bar{E}_o^2} \cdot \frac{\varepsilon}{\sigma}\right) , \qquad (2.4.13)$$

where the suffices 'u' and 'c' refer respectively, to uncorrected and corrected values. $U_u = (E^2 - \bar{E}_o^2)/B^{1/n}$. Equation 2.4.12 is easily derived from equation 2.4.10. Note that the temperature sensitivity is dependent upon the instantaneous operating point E of the hot-wire. $\bar{E}_o^2$ and B were corrected for free-stream temperature drift before digital analysis; corrections for the boundary layer heating (mean plus fluctuating) were done as part of the digital analysis.

2.4.6 Digital analysis programs

Two computer programs, CS3W and D3ECOP, were used to calculate turbulence quantities from the recorded velocity and temperature fluctuations. CS3W was an existing conditional-sampling program and is discussed in its standard form by Weir & Bradshaw (1974). For the present work some changes to the standard version of the intermittency subroutine LAGTHR were found necessary. The authors version of LAGTHR is discussed in chapter 4, subsection 4.2.1, and a listing is given in appendix 6.

Program D3ECOP was an adaptation (by the present author) of an existing two-channel 1024 point (maximum) fast-Fourier-transform program COPHASE, constructed by Davies (1974). D3ECOP comprised the

tape-reading subroutines (BUFFIN and UNPACK) and the probe-calibrations inversion subroutines (RESOLV and TDATA) of CS3W combined with the transform subroutines of COPHASE. The program calculated the power spectral density, the co' and quad' spectral densities, and the coherence and phase angle of two components of fluctuating velocity measured with an x-wire probe in a (mildly) heated flow. Only power spectral densities are presented (chapter 3).

The bandwidth and frequency definition of a discrete, digital Fourier transform are limited by the number of samples in each record or block of data. Since a frequency must be defined by at least two samples each record analysed gave a spectrum defined at a maximum of 512 (equally spaced) frequencies. Each record gives only one estimate of the spectral density of its lowest frequency, two estimates of the lowest-but-one frequency, etc. The definition of the spectral density is improved by forming ensemble averages of several transformed records. COPHASE also included frequency smoothing over K estimates either side of each estimate to further smooth the final spectrum. Smoothing over the K lowest frequencies was achieved by reflecting the spectrum about the spectral density axis. However, this distorts the final spectral density for the K lowest frequencies unless the spectral density there is constant. COPHASE was modified so that the frequency smoothing was increased linearly from zero for the estimate at the lowest frequency to K for the estimate at the K+1 frequency. A value of K=4 was used for all of the spectra presented.

2.4.7 Remaining remarks

Turbulence measurements were carried out in pairs of profile traverses corresponding to $\phi = 0$ and $\phi = \pi/2$. The x-wire probe was calibrated for $\overline{E}^2_{o_{1,2}}$ and $B_{1,2}$ before and after each traverse. Drift in $\overline{E}^2_o$ and B, after correction for temperature drift, was less

than about 1% and averaged values were used in the subsequent analysis. The effective wire angles $\psi_{eff_{1,2}}$ were measured before and after each pair of profile traverses. The wire angles measured first were used in the analysis of the first traverse of the pair and the remeasured angles in the analysis of the second traverse. It was usually found that for a particular pair of crossed wires the internal angle between the wires remained within a scatter band of about 0.5^{o} wide over several profile traverses. In the occasional instance of uncertainty in a velocity or angle calibration the calibration was repeated, and if the uncertainty remained one or both wires were replaced.

A build-up of dirt of size of the order of 1 μm on the temperature probe wire caused a degradation of high frequency response. Although a "burn-off" heating current of about 10 mA - a higher current would have burnt-out the wire - was passed through the temperature wire (see figure 2.12) at intervals during a traverse the build-up was not entirely prevented. Washing the wire did not always remove all the dirt and it was found better to rewire the probe frequently. Each wire was used for only two traverses.

A recording of 30 seconds in length was taken at each point in a traverse and the first recorded point (i.e. the point nearest the wall) was recorded again for a further 30 seconds at the end of the traverse. Tape usage was optimised by rewinding the tape over the previous record, sufficient for the tape to have built-up to full (forward) speed when the end of the last record has passed, and the record button then depressed. In the instance that a recording was unwanted it was not over-recorded because a slight distortion - high-frequency rippling near the peaks - was observed when a sine wave was recorded over itself.

1 kHz sinusoidal calibration signals were regularly recorded on to the tape. The calibration signal for the two x-wire

probe channels was simultaneously input to the amplifiers shown in figure 2.11a with the output of the dual filter box disconnected. The calibration signal for the temperature probe channel was separately input to the compensator and amplifier unit shown in figure 2.12b but with the compensator capacitance, C, and the filter box disconnected. Calibration signal amplitudes were measured with a Datron 1030 r.m.s. meter.

MESH SIZE or BAR SPACING	BAR SIZE & SHAPE	TYPE	COMMENT
7.62 cm	1.25 cm SQUARE	BI-PLANE, SQUARE MESH	ALUMINIUM
7.62 cm	1.25 cm SQUARE	ROW OF VERTICAL BARS	WOOD
15.2 cm	3.81 cm SQUARE	BI-PLANE, SQUARE MESH	WOOD (PINE)
15.2 cm	3.81 cm SQUARE	ROW OF VERTICAL BARS*	WOOD (PINE)
11.4 cm	2.86 cm ROUND	ROW OF VERTICAL BARS	BROOMSTICKS (SUPPLIED BY I.C. CENTRAL STORES)

* As previous grid but with horizontal bars removed.

TABLE 2.1 Dimensional details of turbulence-grids and turbulence generators.

a) Side view

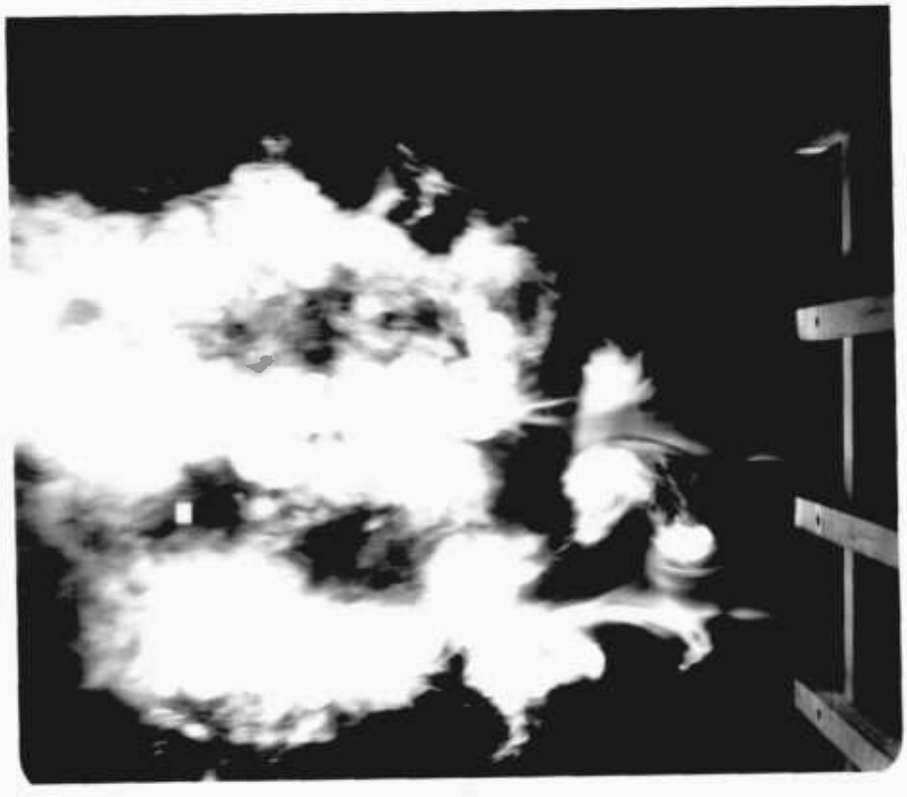

b) Plan view

Fig. 2.1 Boundary layer flow through the base of a turbulence-generating grid. Upstream boundary layer laminar in a) and b) and turbulent in c) and d). M = 15.2cm, bar size = 2.5cm x 2.5cm, $U_e \approx 1$ m/s. Flow right to left.

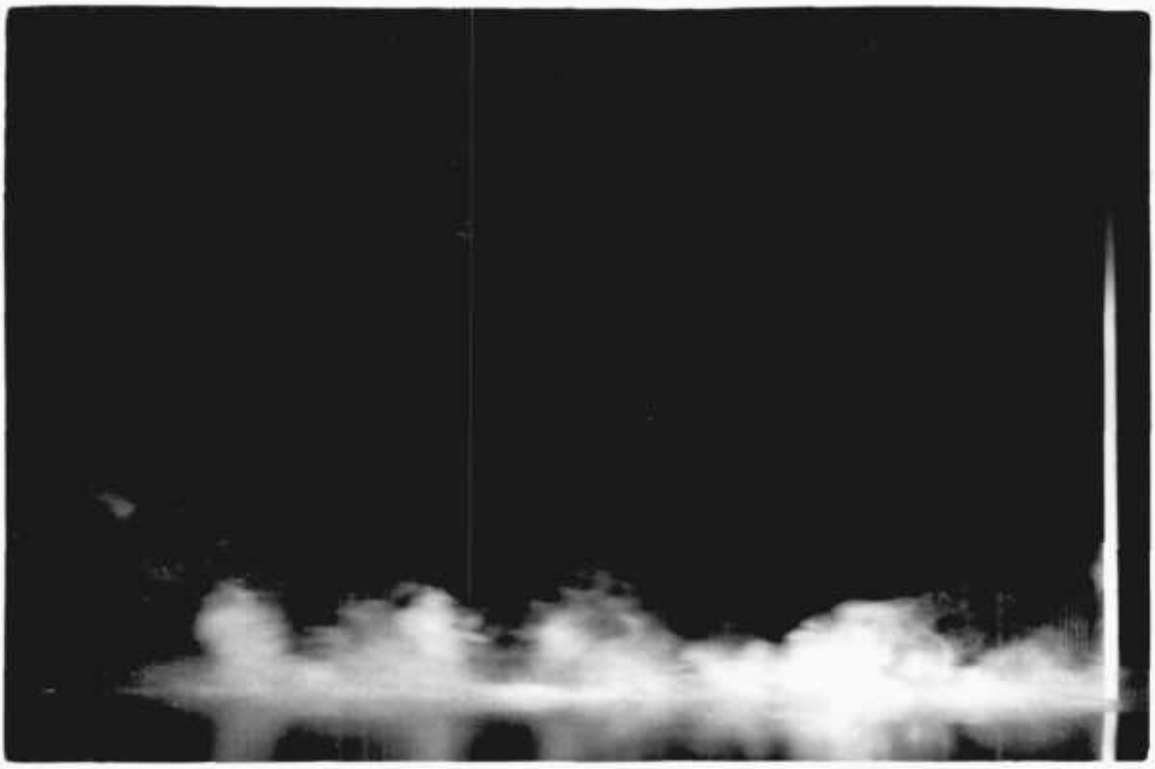

c) Side view

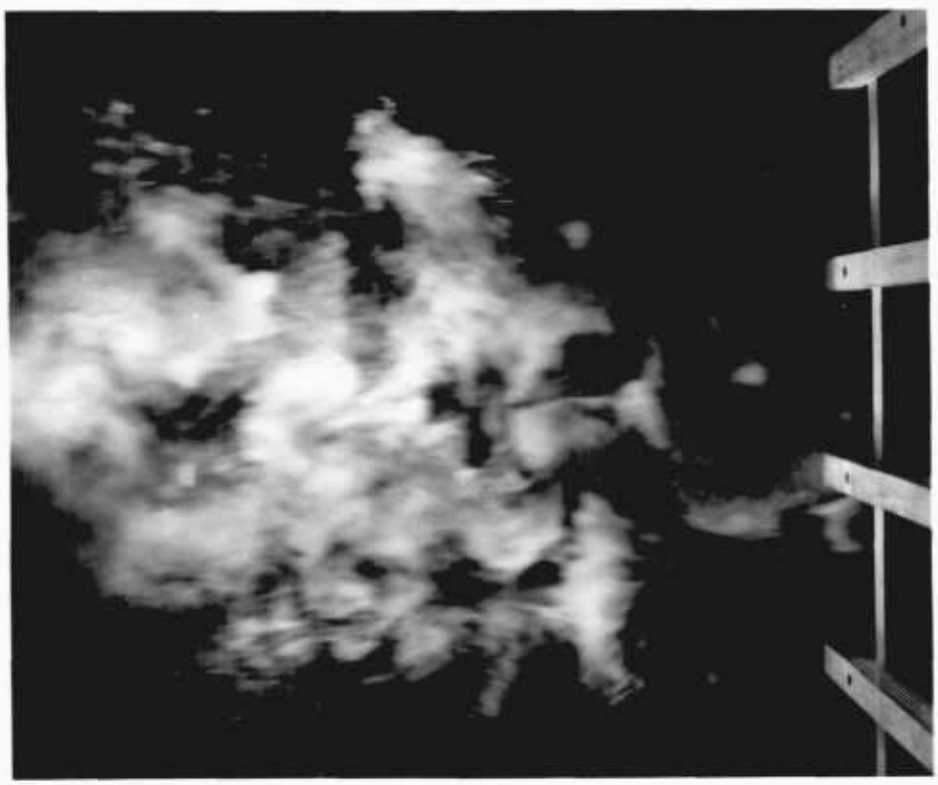

d)

Figs 2.1 c and d,

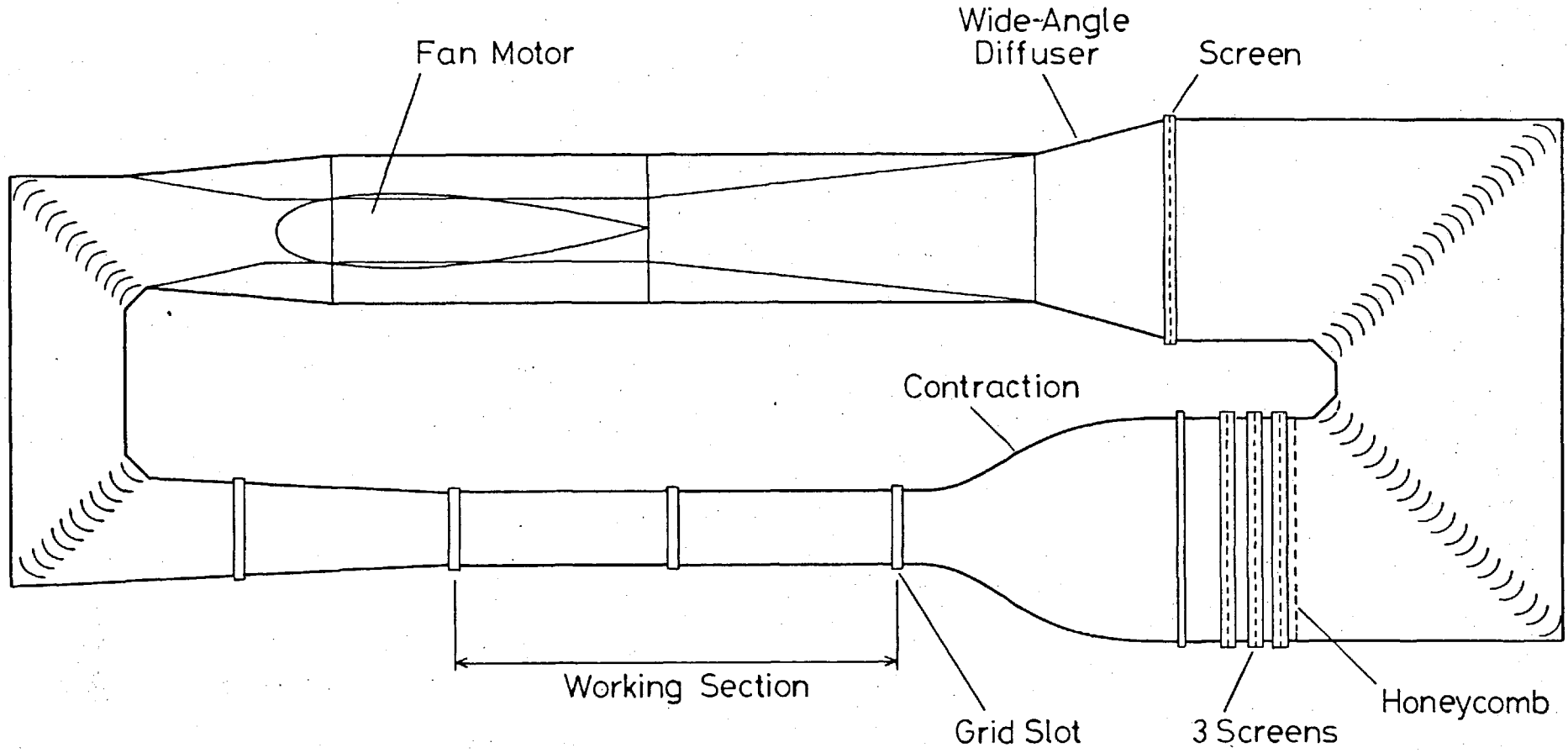

Fig. 2.2 Plan view of wind tunnel

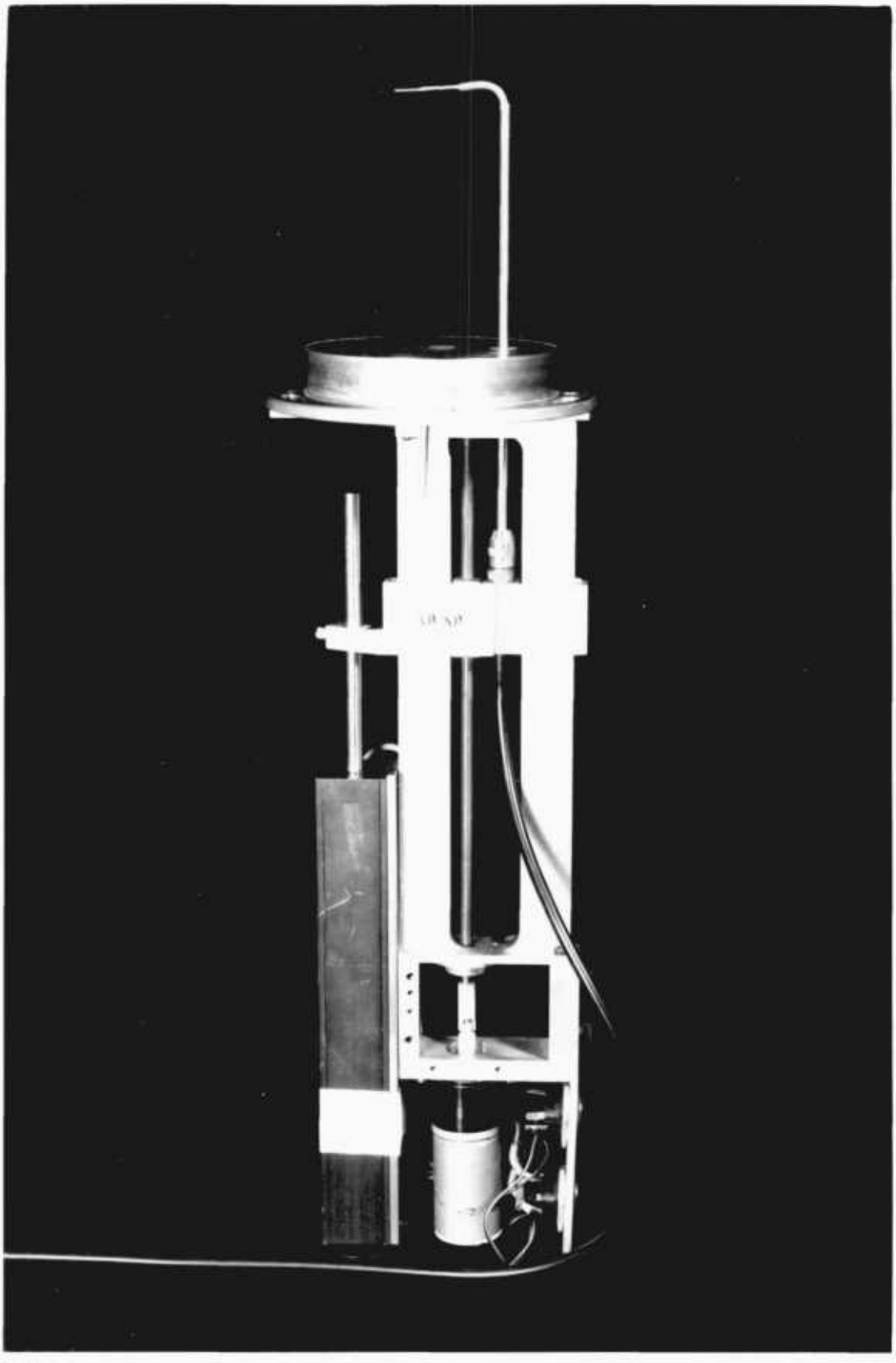

Fig. 2.3 Boundary layer traverse gear

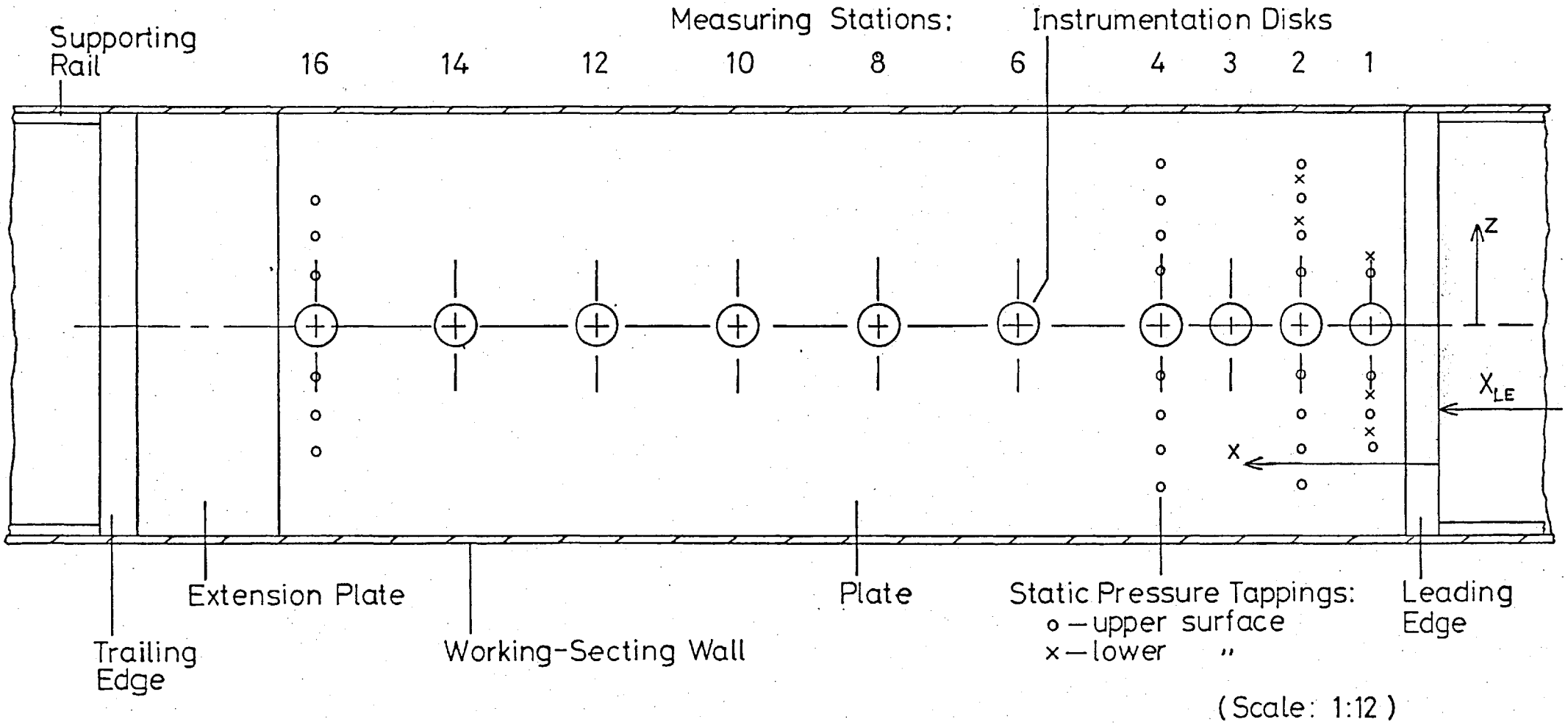

Fig. 2.4 Plan view of flate plate.

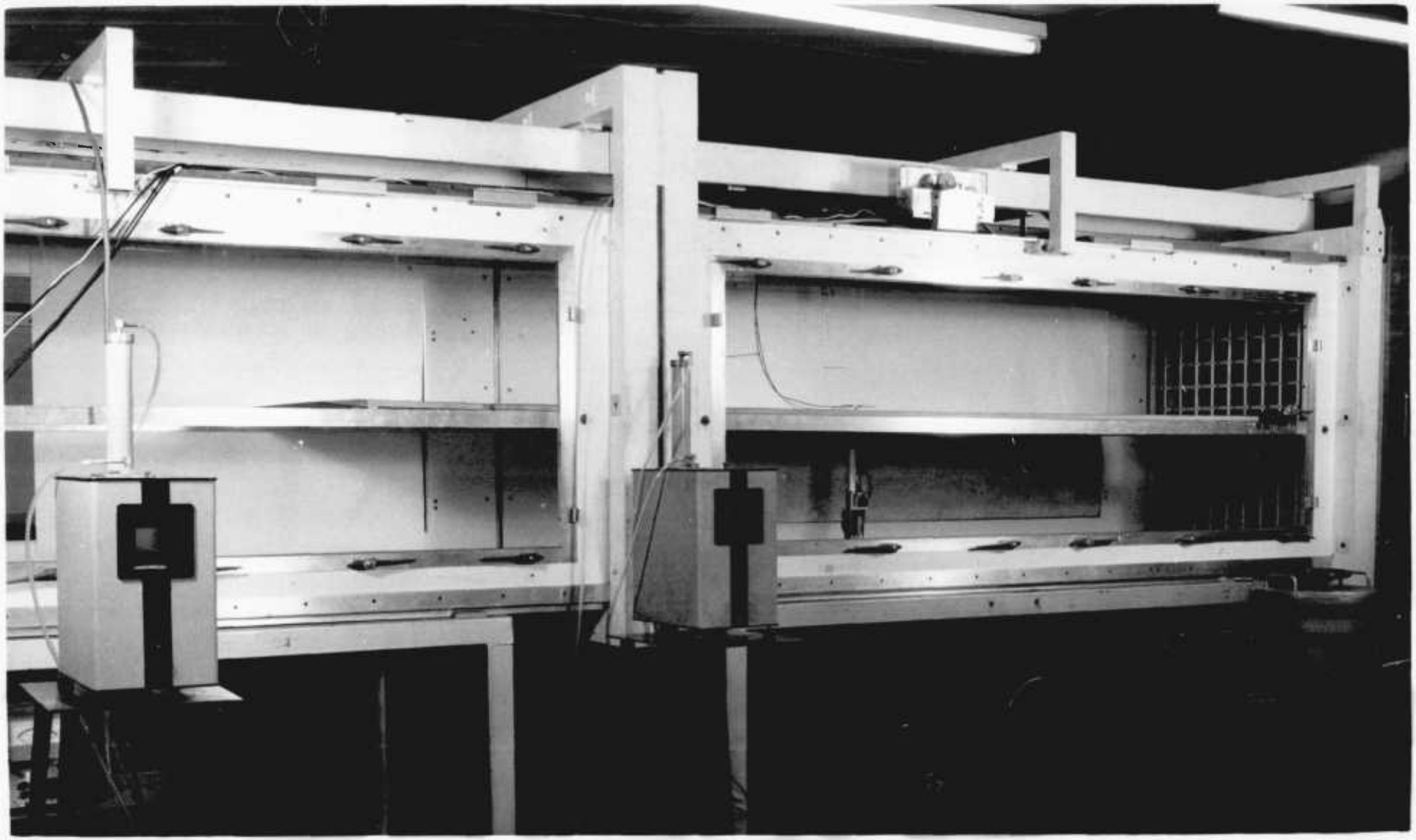

Fig. 2.5 View of flate plate mounted in 3ft x 3ft wind tunnel

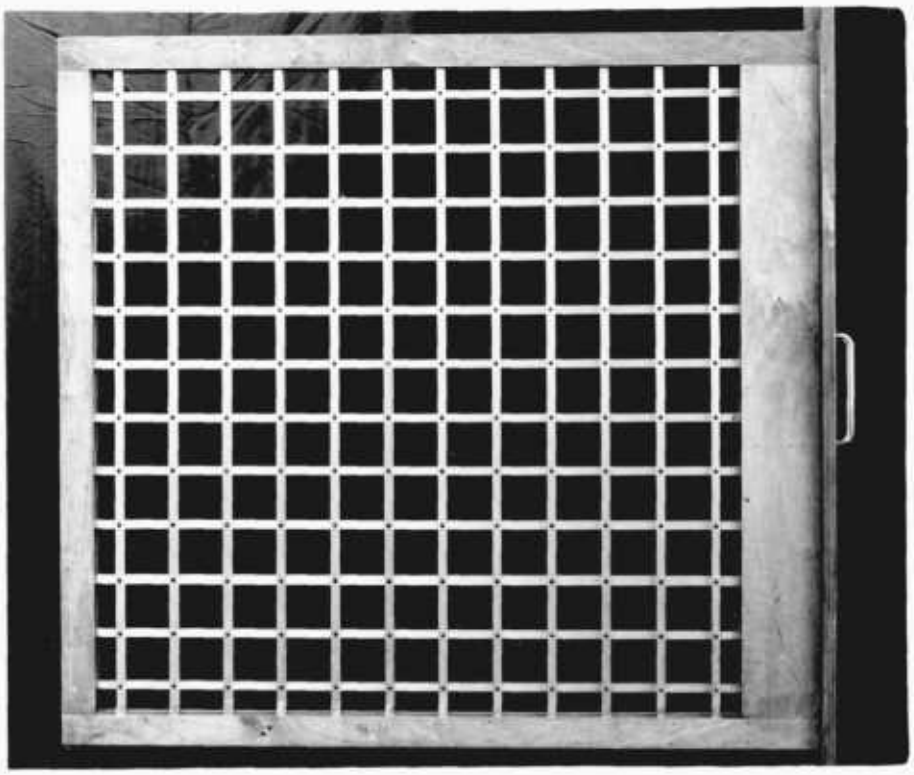

a) Biplane grid. M = 7.62cm

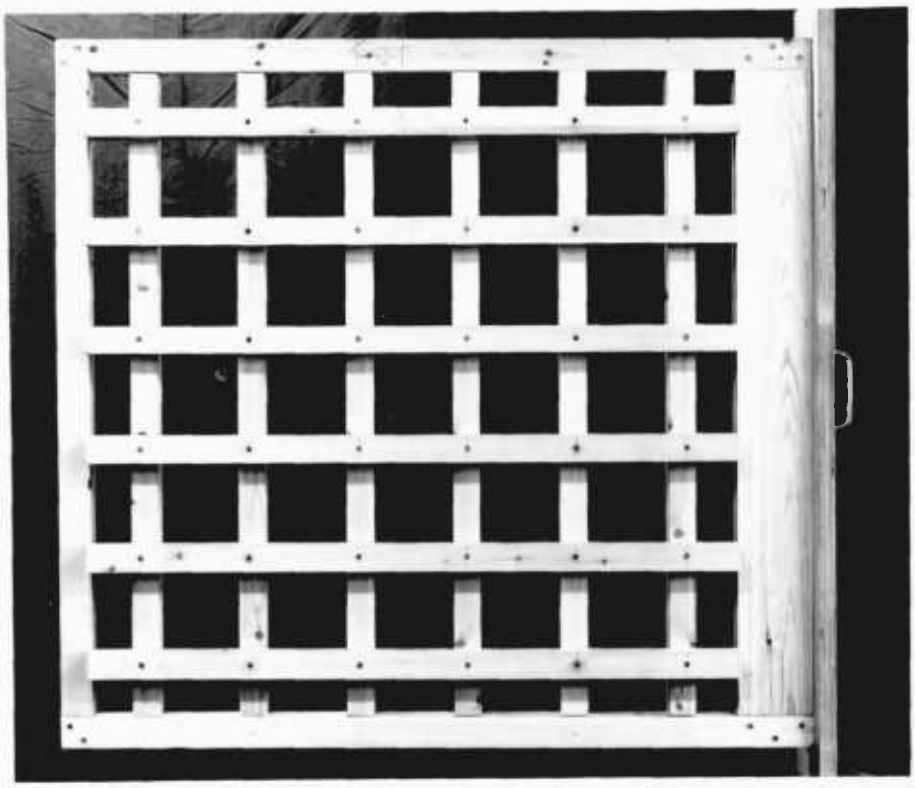

b) Biplane grid. M = 15.2cm

Fig. 2.6 Turbulence grids (a and b) and turbulence generators (c and d)

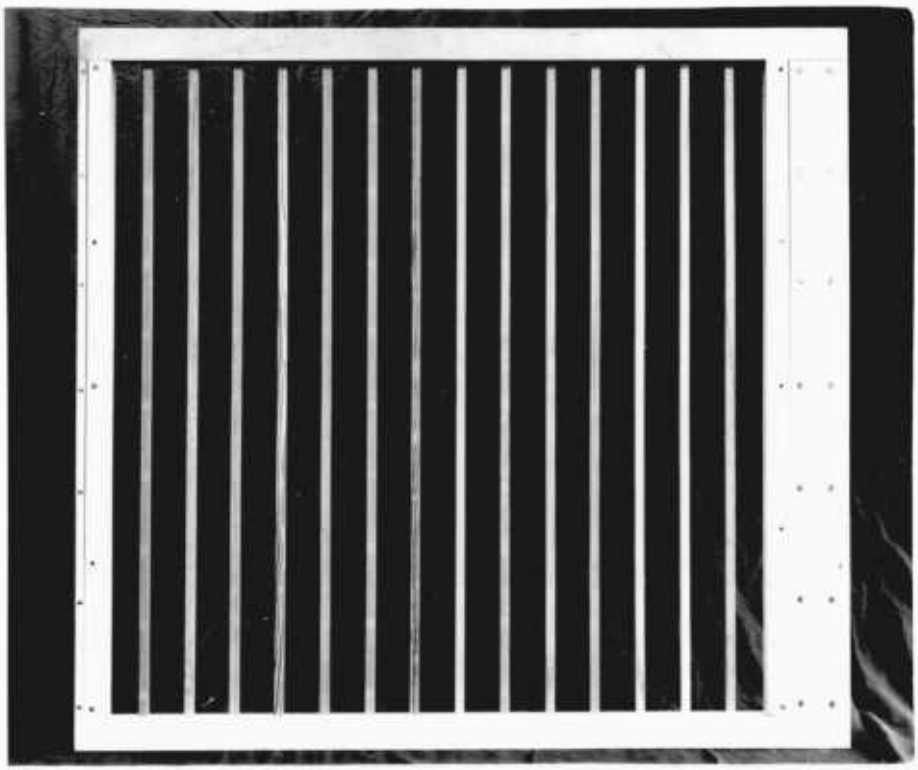

c) 7.6cm-spaced row of square bars

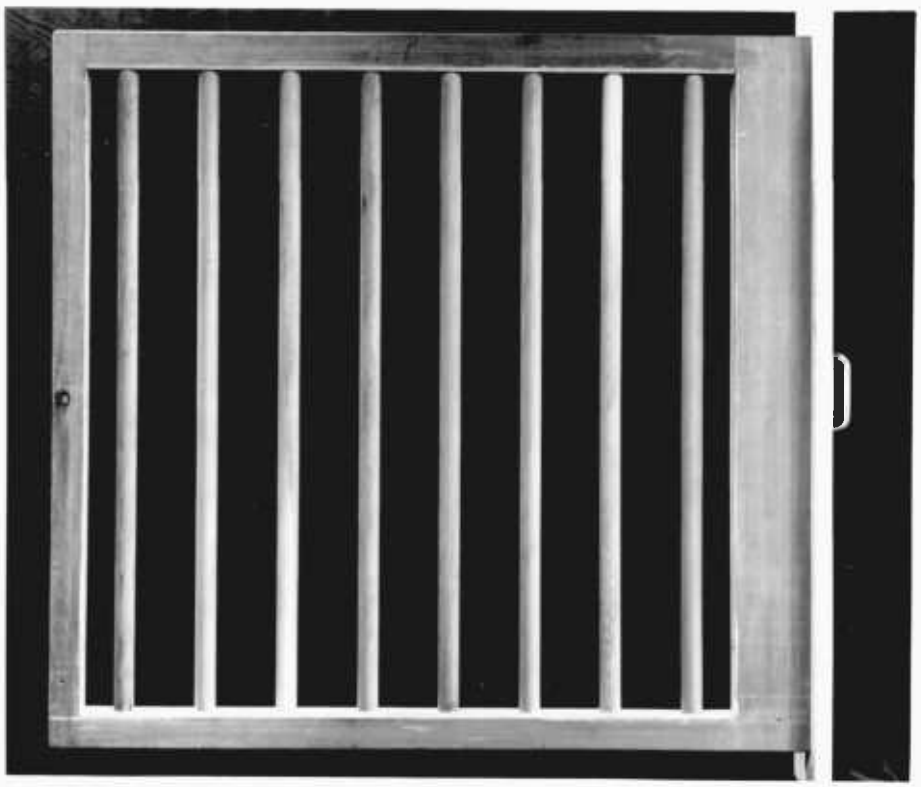

d) 11.4cm-spaced row of round bars

Figs 2.6 c and d,

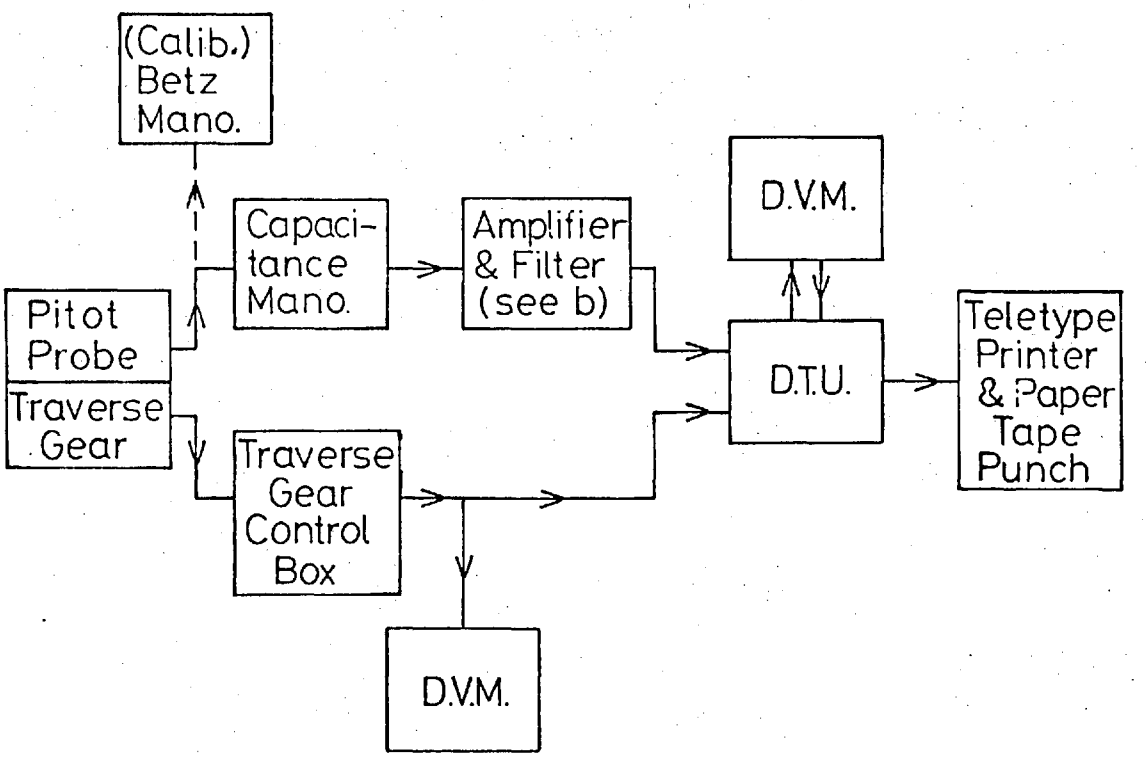

a) Block Diagram of Apparatus

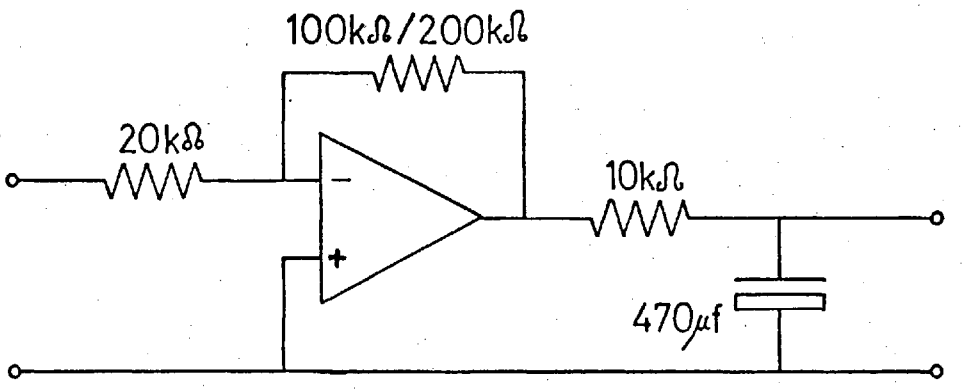

b) Amplifier and Filter in a)

Fig. 2.7 Electronic apparatus for mean velocity profile measurements.

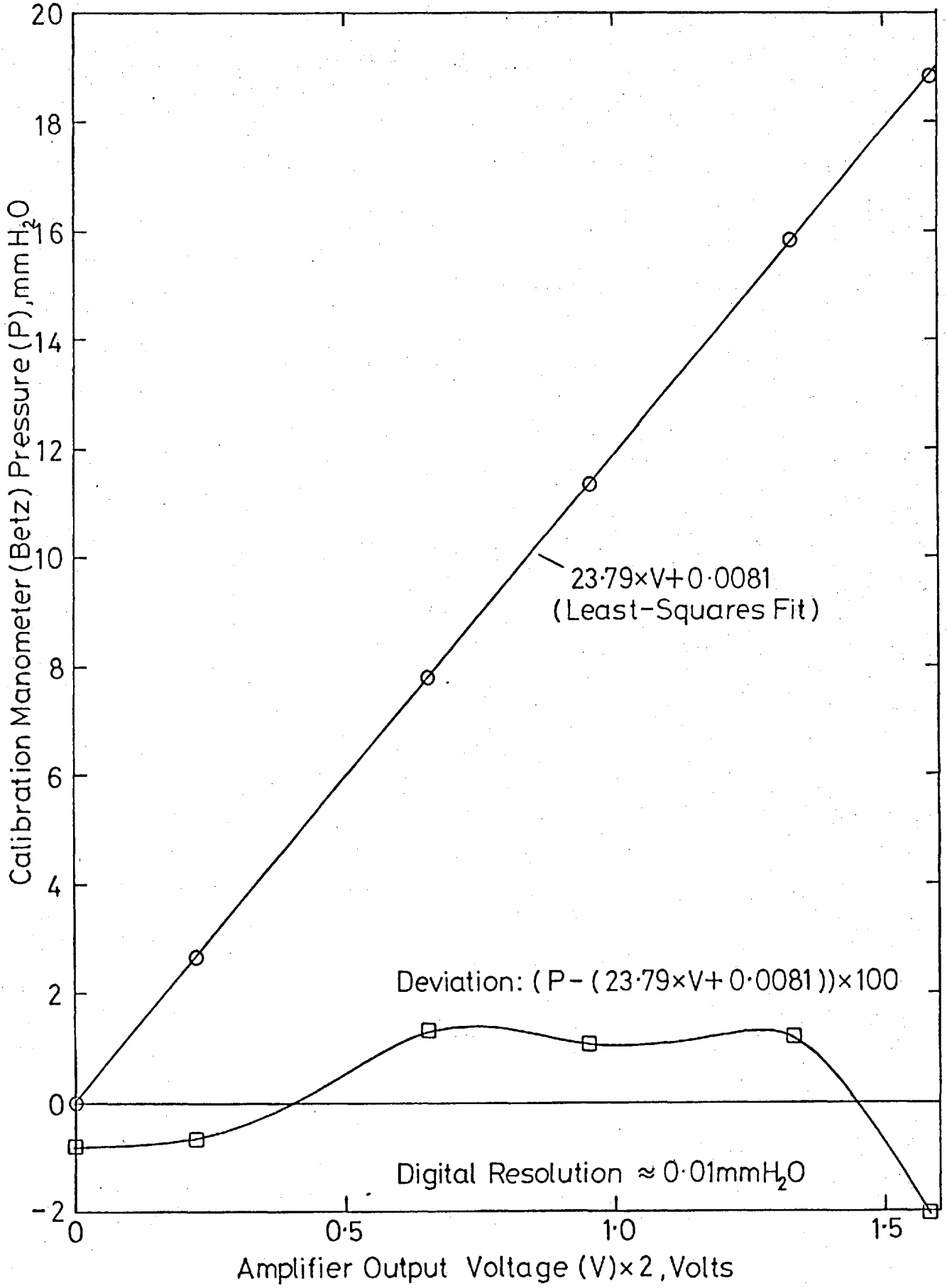

Fig. 2.8 Typical calibration of capacitance manometer.

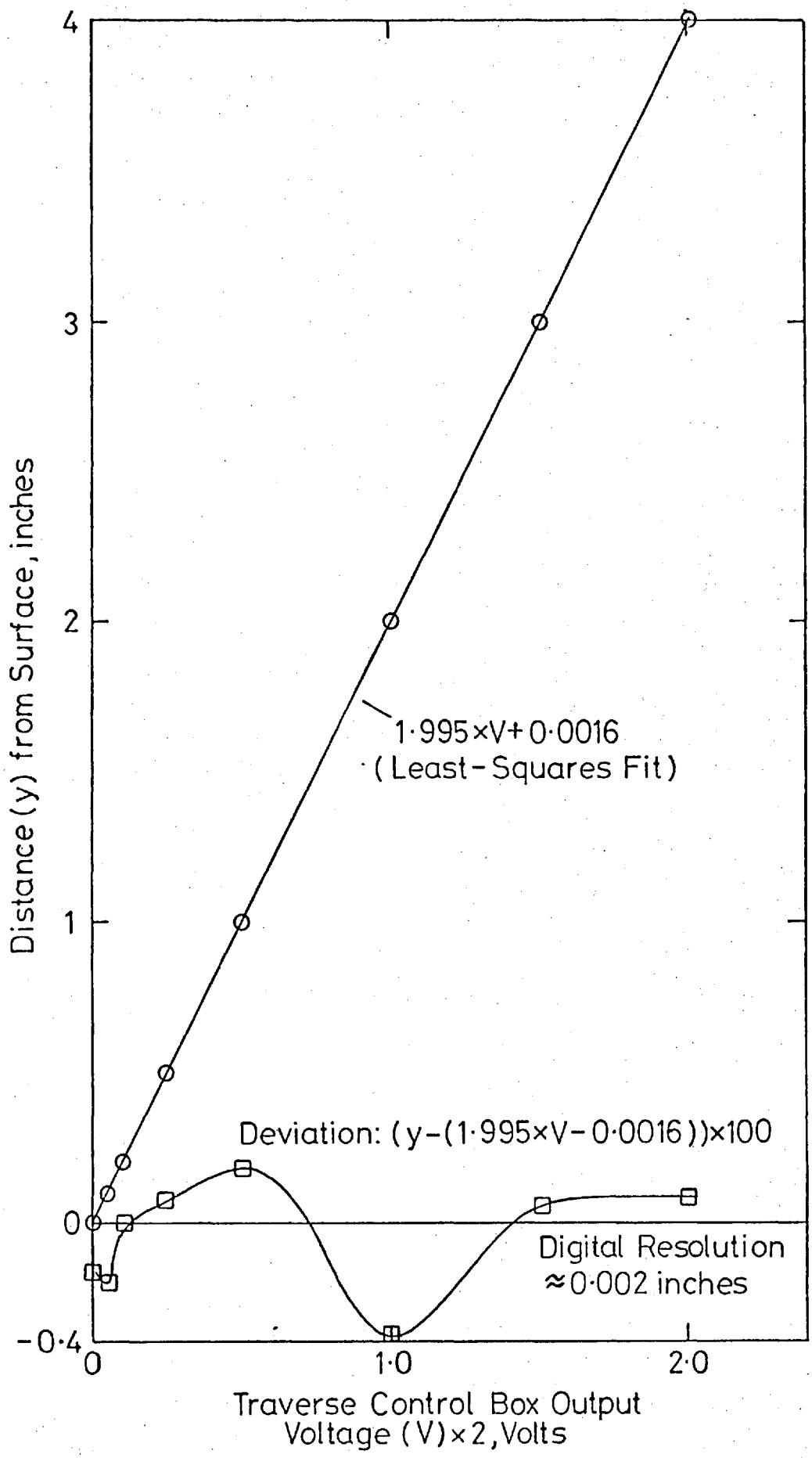

Fig. 2.9 Typical calibration of traverse-gear position potentiometer.

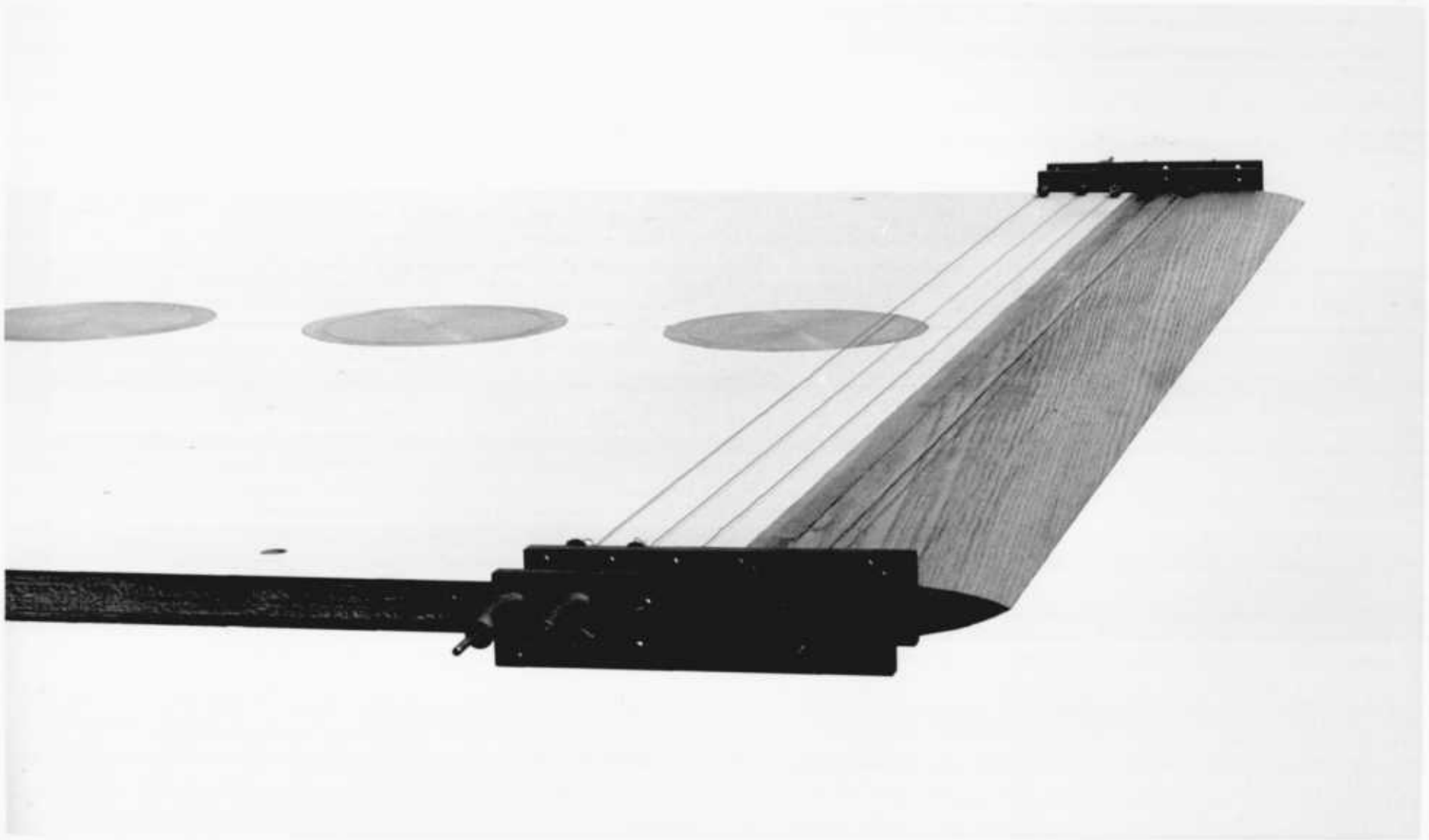

Fig. 2.10 View of plate leading edge and the heating wires. The transition trip wire can be seen just downstream of the first heating wire.

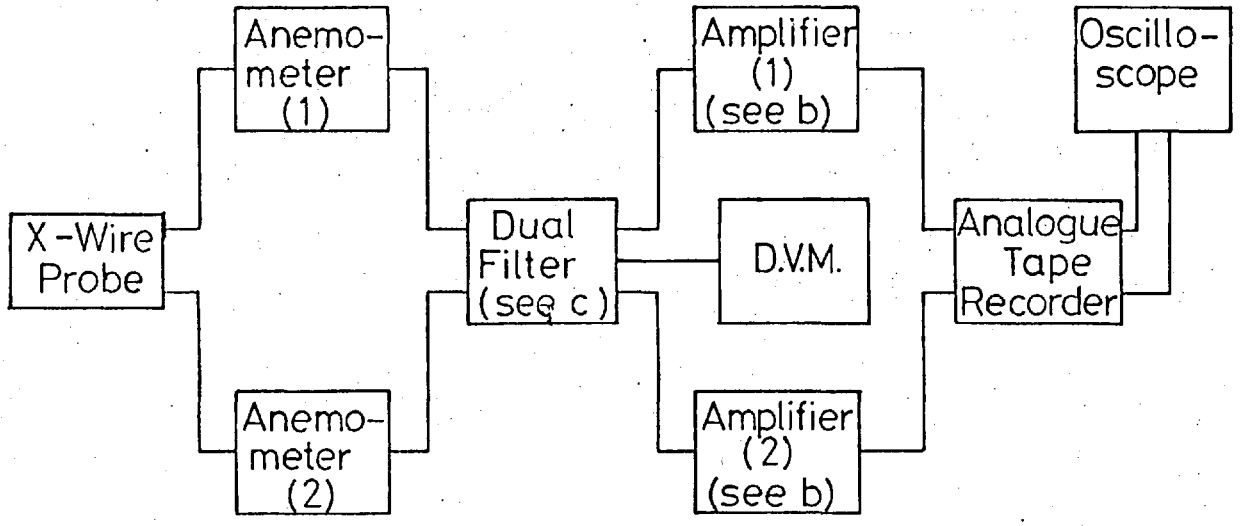

a) Block Diagram of Apparatus

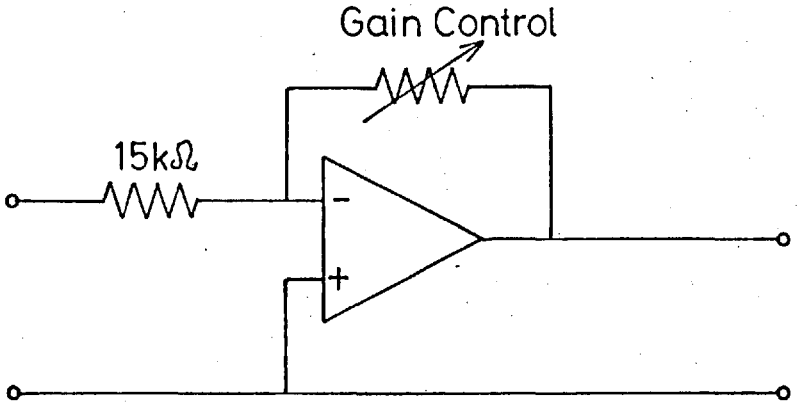

b) Block Diagram of (Operational) Amplifier in a)

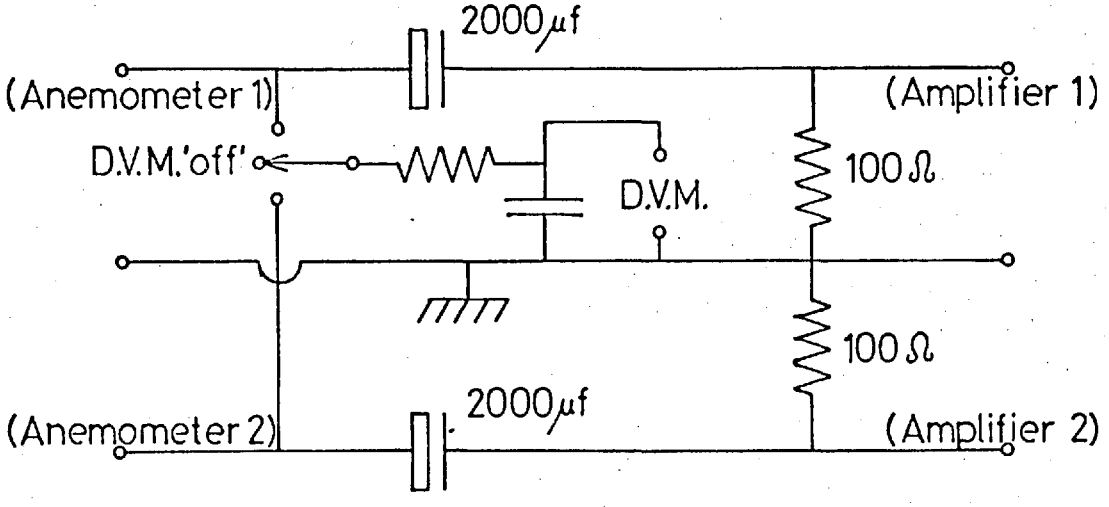

c) Dual Filter in a) (A.J.Smits)

Fig. 2.11 Electronic apparatus for X-wire probe measurements.

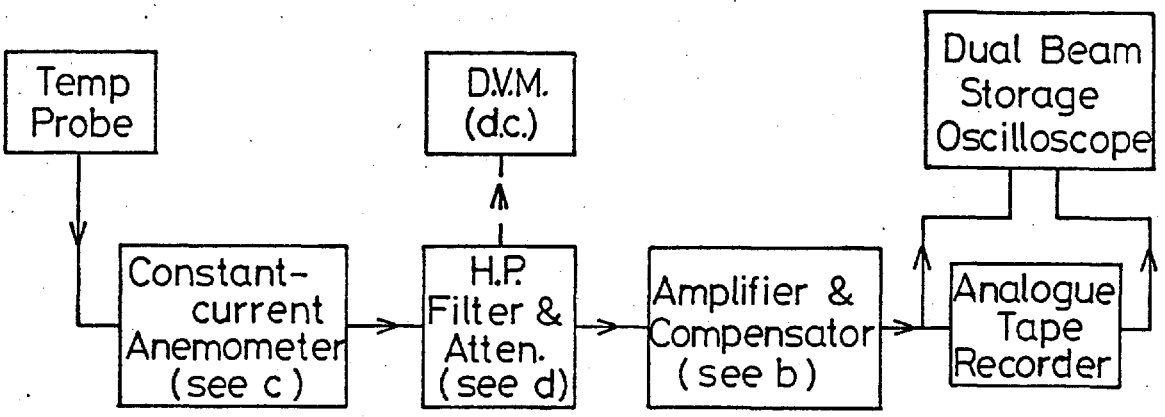

a) Block Diagram of Apparatus

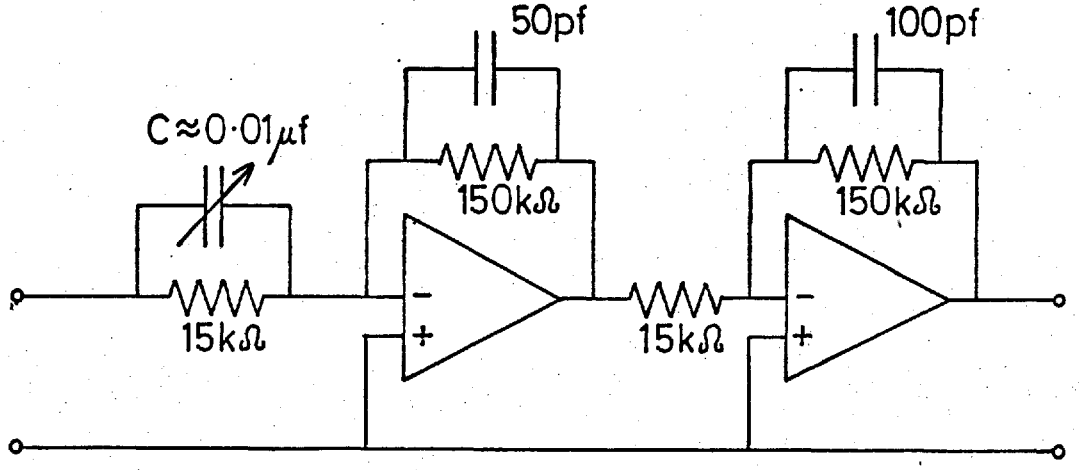

b) Compensator and Amplifier

Fig. 2.12 Electronic apparatus for measuring temperature fluctuations.
(continued next page)

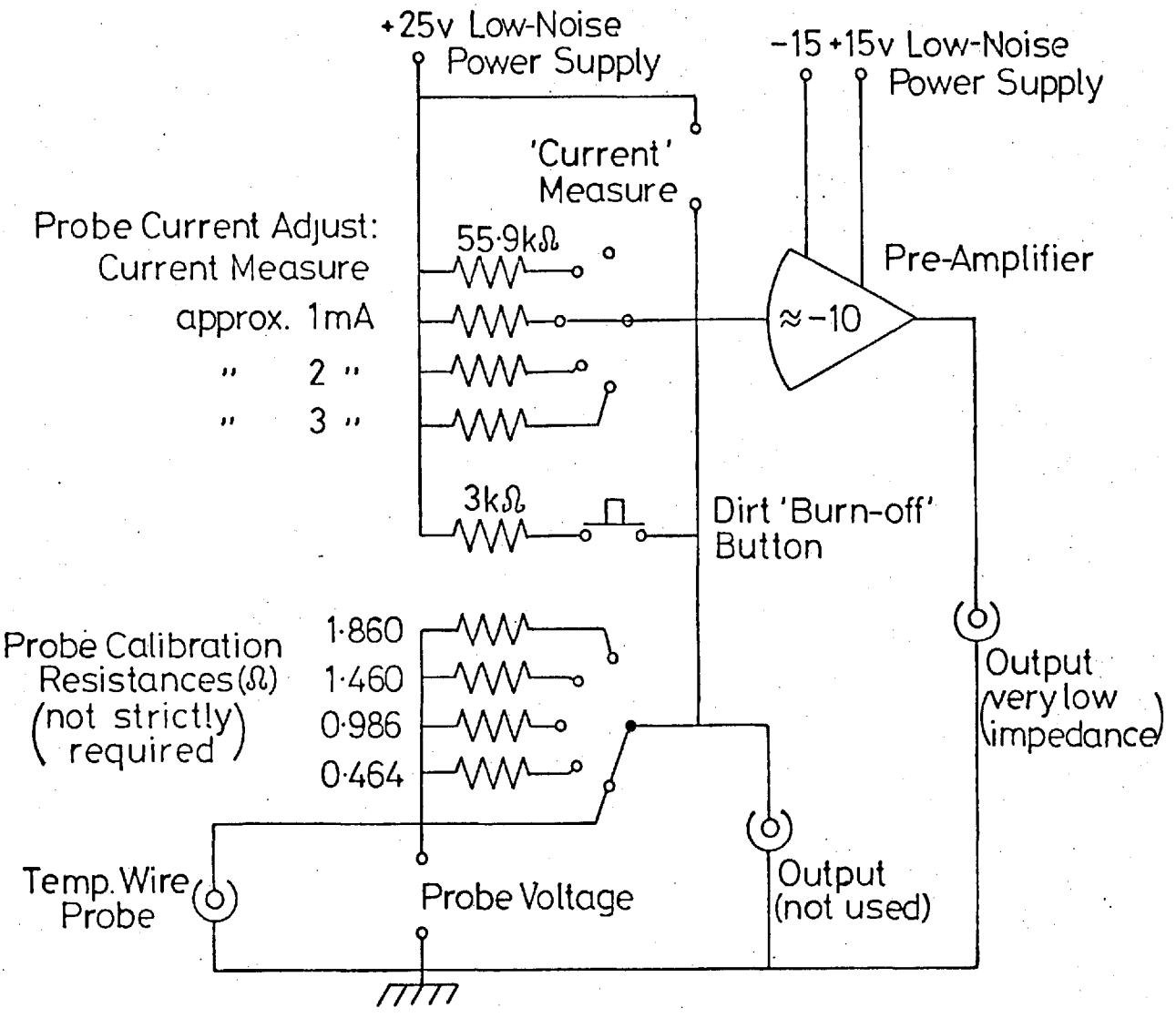

c) Constant-Current Temperature 'Anemometer'

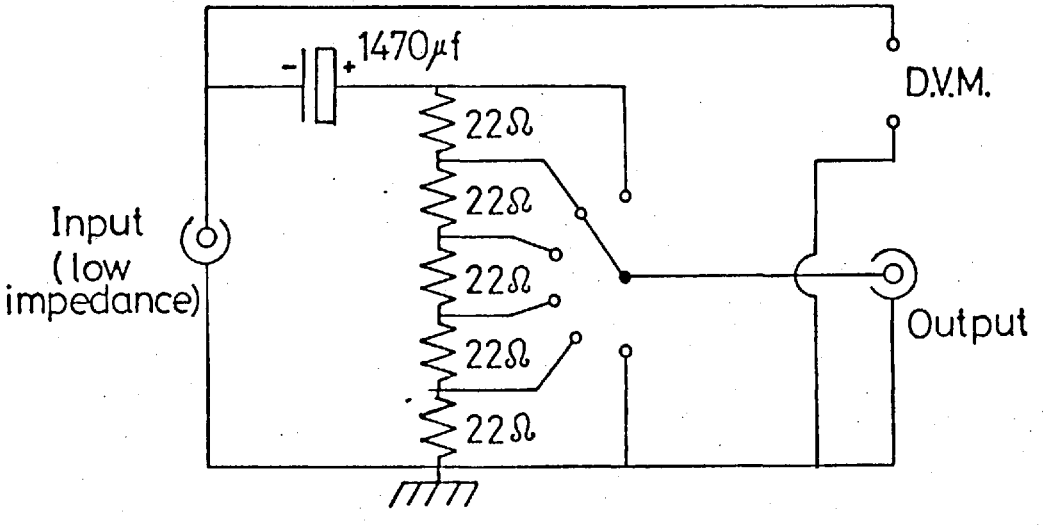

d) High-Pass Filter and Attenuator

Fig. 2.12 (completed)

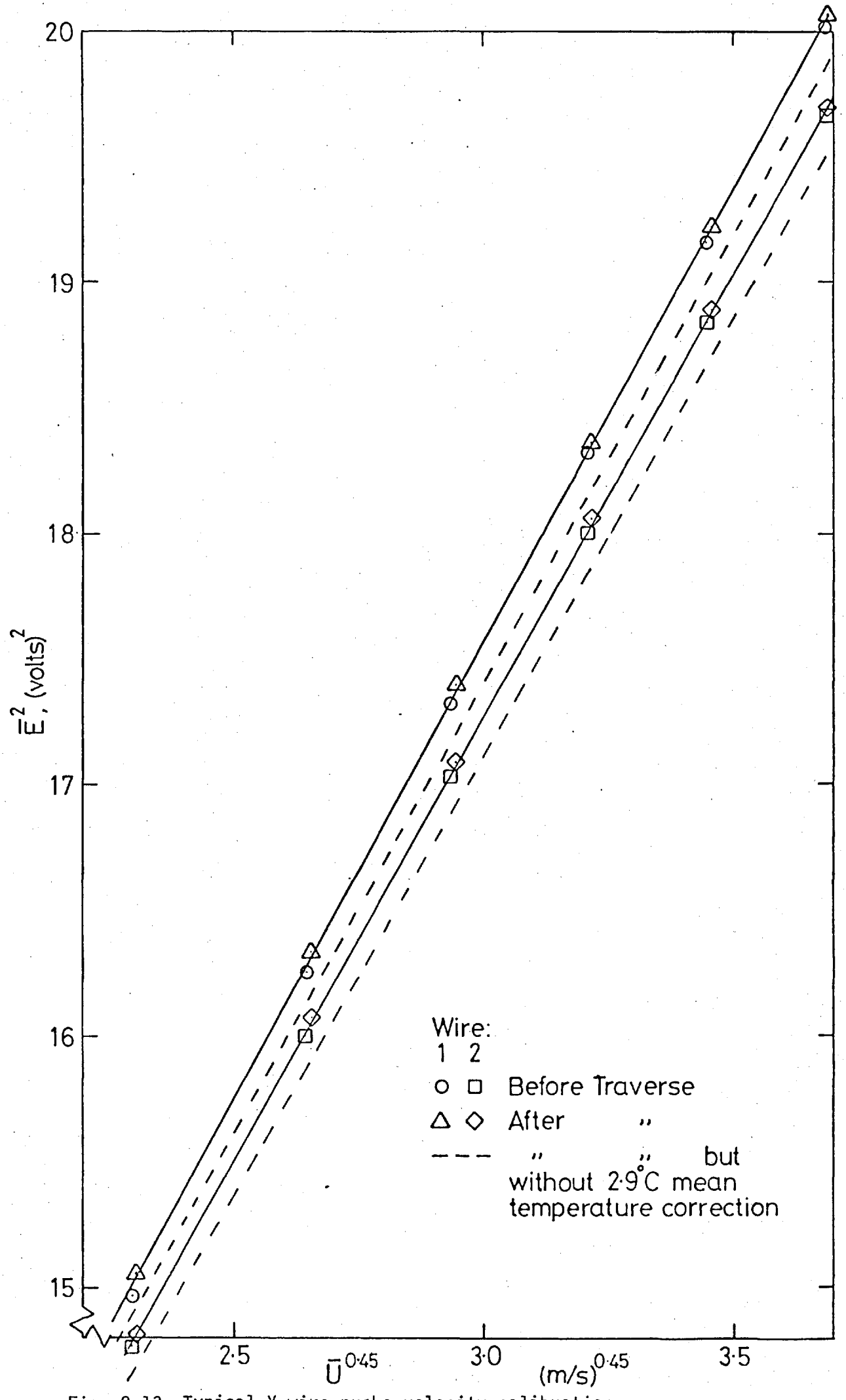

Fig. 2.13 Typical X-wire probe velocity calibration.

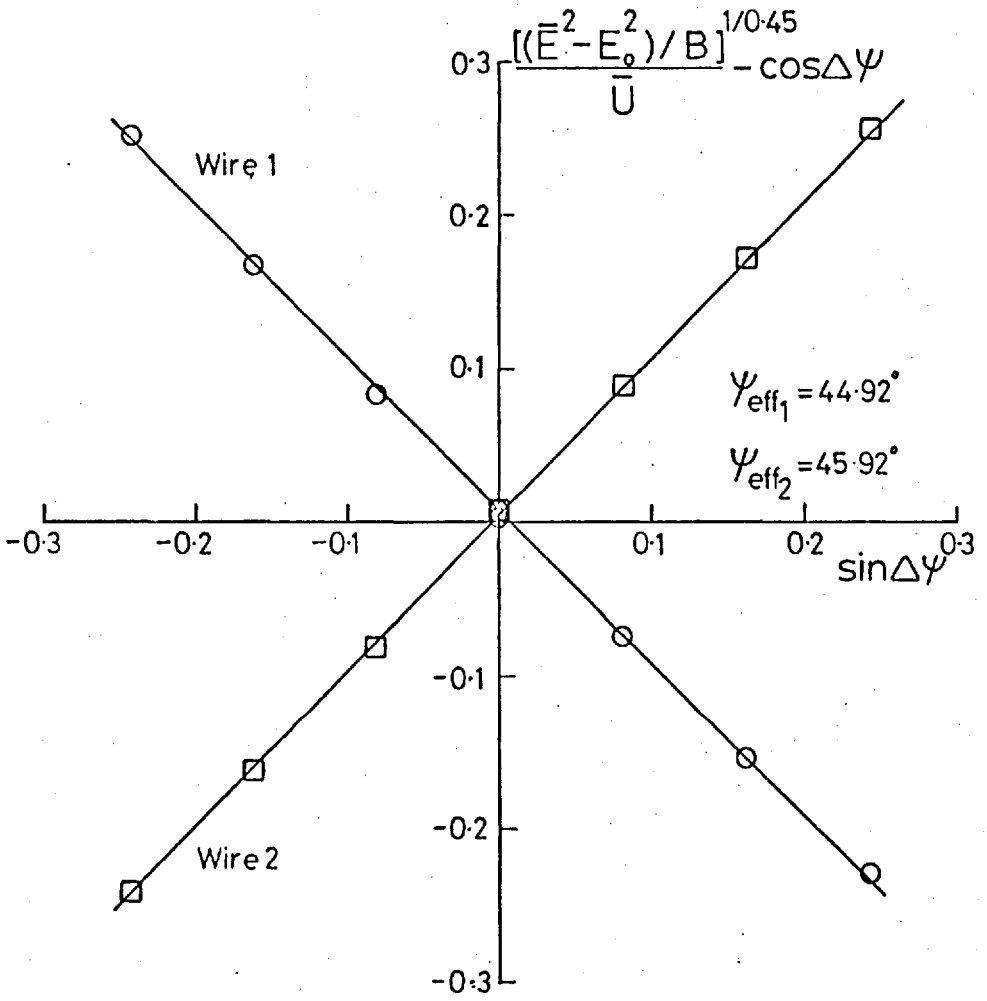

Fig. 2.14 Typical X-wire probe angle calibration.

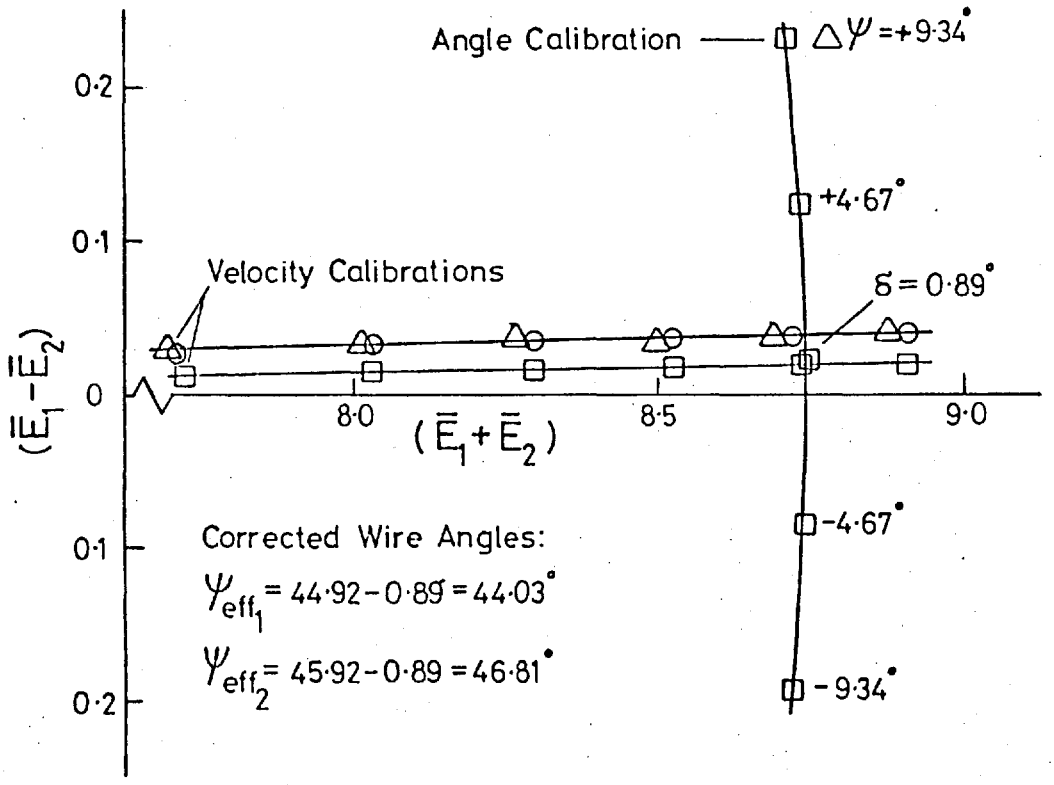

Fig. 2.15 Typical correction to effective wire angles.

CHAPTER 3

MEAN FLOW AND FREE-STREAM TURBULENCE MEASUREMENTS

3.1 INTRODUCTION

As a result of the analysis of Graham (1975), Hunt & Graham (1978), and the measurements of Thomas & Hancock (1977), the free-stream is defined as the region outside the boundary layer where the mean flow and the turbulence quantities are independent of the distance, y, from the surface. For flows where the mean streamlines are not nearly parallel and nearly straight a still more careful definition of free-stream would be needed. Turbulence measurements within the boundary layer and between the boundary layer and the free-stream are presented in chapter 4.

3.1.1 Equations and relevant parameters

The conservation equation for the turbulent kinetic energy is

$$\frac{D\,\frac{1}{2}\overline{q^2}}{Dt} = -\overline{u_i u_j}\,\frac{\partial U_i}{\partial x_j} - \frac{\partial}{\partial x_j}\left(\overline{pu_j} + \frac{1}{2}\overline{q^2 u_j}\right) + \nu\,\overline{u_i \frac{\partial^2 u_i}{\partial x_j^2}} \qquad (3.1.1)$$

Advection = Production - (Pressure + Turbulent)Diffusion + Viscosity effects,

(Townsend, 1976, p38). The viscous term on the right hand side of the equation 3.1.1 may be written as

$$\nu\,\overline{u_i \frac{\partial^2 u_i}{\partial x_j^2}} = \nu\left[\frac{\partial^2}{\partial x_j^2}\left(\frac{1}{2}\overline{q^2}\right) + \frac{\partial^2}{\partial x_i \partial x_j}\left(\overline{u_i u_j}\right)\right] - \varepsilon \qquad (3.1.2)$$

Viscous Diffusion - Viscous Dissipation

where $$\varepsilon = \frac{1}{2}\nu\,\overline{\left(\frac{\partial u_i}{\partial x_j} + \frac{\partial u_j}{\partial x_i}\right)^2} \qquad (3.1.3)$$

Dissipation of turbulent kinetic energy occurs in the highest wave number region of the turbulent kinetic energy spectrum. Energy is transferred between adjacent wave numbers from the low wave number energy-containing range through to the dissipating range. The

cascade hypothesis implies that the energy dissipation is controlled by the large-scale energy-containing motion. If the velocity scale of the turbulence is u and the length scale of the large eddies is L then the viscous dissipation is of the order u^3/L while the viscous diffusion is of the order $\nu u^2/L$ (Townsend 1976, p42). Provided that the Reynolds number of the turbulence, uL/ν, is not small the viscous diffusion may be neglected with respect to the viscous dissipation.

In a constant-velocity free-stream homogeneous in the y-direction and at high Reynolds number, uL/ν, equation 3.1.1 reduces to

$$\frac{D}{Dt}\left(\frac{1}{2}\overline{q^2}\right) = U\frac{\partial}{\partial x}\left(\frac{1}{2}\overline{q^2}\right) = \frac{\partial}{\partial x}\left(\overline{pu} + \frac{1}{2}\overline{q^2 u}\right) - \varepsilon \,. \qquad (3.1.4)$$

The diffusion is of the order of $(\overline{q^2})^{1/2}/U$ times the advection or less and for weak turbulence it is commonly neglected. Using $\sqrt{\overline{q^2}}$ for the velocity scale u and defining L by $L \equiv (\overline{q^2})^{3/2}/\varepsilon$ equation 3.1.4 becomes

$$U\frac{\partial}{\partial x}\left(\frac{1}{2}\overline{q^2}\right) = -\frac{(\overline{q^2})^{3/2}}{L} \,. \qquad (3.1.5)$$

Thus, in the free-stream the dissipation and advection may be described by $\overline{q^2}$ and L.

The velocity profile of a flat two-dimensional constant-pressure boundary layer in the absence of free-stream turbulence is related to U_e, δ, and ν by

$$h_1\,(U, y, U_e, \delta, \nu) = 0, \qquad (3.1.6)$$

and the friction velocity, u_τ, is related by

$$h_2\,(u_\tau, U_e, \delta, \nu) = 0, \qquad (3.1.7)$$

(Rotta, 1962, p99). When free-stream turbulence is present in otherwise similar conditions we may expect

$$h_1\,(U, y, U_e, \delta, \nu, L_e, u_e') = 0, \qquad (3.1.8)$$

and

$$h_2\,(u_\tau, U_e, \delta, \nu, L_e, u_e') = 0, \qquad (3.1.9)$$

where L and u have been replaced by L_e and u'_e to emphasise that they are free-stream scales. Later we shall take u'_e to be equal to $\sqrt{\overline{u_e^2}}$. From the last two equations the outer layer velocity-defect law has the form

$$\frac{U_e - U}{u_\tau} = f\left(\frac{y}{\delta}, \frac{U_e\delta}{\nu}, \frac{L_e}{\delta}, \frac{u'_e}{U_e}\right). \qquad (3.1.10)$$

In the absence of free-stream turbulence the velocity defect profiles will be self-preserving if u_τ/U_e = constant, and $U_e \propto x^a$. Experiment shows that the flat two-dimensional constant-pressure boundary layer is closely self-preserving even though u_τ/U_e slowly decreases with increasing distance, and is strongly Reynolds number dependent only for $U_e\delta/\nu \lesssim 2 \times 10^4$. A boundary layer in the presence of free-stream turbulence could be expected to be self-preserving if L_e/δ and u'_e/U_e changed sufficiently slowly in the streamwise direction which requires L_e/δ to be large. (Self-preservation is not in itself important and is unlikely to exist in many practical flows, but its presence in experimental work enables the quantity of measurements to be reduced.)

3.1.2 Decay of grid-generated turbulence

Conceptually, a truly spatially homogeneous field of turbulence may be thought of as a stationary 'box of turbulence' for which the turbulent kinetic energy equation reduces to

$$\frac{d}{dt}\left(\frac{1}{2}\overline{q^2}\right) = -\varepsilon \qquad (3.1.11)$$

Experimentally, the simplest approximation is grid-generated turbulence convected at constant mean velocity, for which the turbulent kinetic energy equation reduces to equation 3.1.4. For a field of grid turbulence to be approximately homogeneous the length scale of the inhomogeneity, say,

$$L_h = \overline{q^2} \,/\, \left|\frac{d\overline{q^2}}{dx}\right| \qquad (3.1.12)$$

should be large when compared with the scale of the energy-containing eddies. From the turbulent kinetic energy equation, approximate homogeneity requires

$$\sqrt{(\overline{q^2})} \; / \; U \ll 1 \qquad (3.1.13)$$

(Townsend, 1976, p51). Thus,

$$\frac{L_e}{L_h} \approx \frac{2\sqrt{(\overline{q^2})}}{U} \qquad (3.1.14)$$

Early measurements of the decay of grid turbulence, for example those given by Batchelor (1953), were correlated by a decay law of the form

$$\left(\frac{\overline{q^2}}{U^2}\right)_e \propto \left(\frac{x - x_o}{M}\right)^{-1} , \qquad (3.1.15)$$

where M is the grid mesh size or bar periodicity, x_o is a virtual origin (quoted typically as about 10 M), and the constant of proportionality depends upon grid geometry. More recently, Comte-Bellot & Corrsin (1966), proposed the two decay laws

$$\left(\frac{\overline{u^2}}{U^2}\right)_e = C_1^2 \left(\frac{x - x_{o_1}}{M}\right)^{-n_1} , \qquad (3.1.16)$$

and

$$\left(\frac{\overline{v^2}}{U^2}\right)_e = C_2^2 \left(\frac{x - x_{o_2}}{M}\right)^{-n_2} . \qquad (3.1.16)$$

Two equations were proposed in order to account for the general failure of unstrained grid turbulence to be perfectly isotropic; the evidence showed unstrained grid turbulence to be axisymmetric. Their measurements, and their analysis of measurements by other workers showed that for biplane grids of round or square cross-section bars $x_{o_1} \approx x_{o_2}$ and $n_1 \approx n_2 = n$. Typically, $n \approx 1.25$. Departure from true isotropy was such that $1.05 \lesssim \sqrt{(\overline{u^2}/\overline{v^2})} \lesssim 1.3$. Assuming $x_{o_1} = x_{o_2} = x_o$ and $n_1 = n_2 = n$

$$\left(\frac{\overline{q^2}}{U^2}\right)_e = C^2 \left(\frac{x - x_o}{M}\right)^{-n} \qquad (3.1.17)$$

and from equation 3.1.5

$$L_e = 2M\frac{C}{n}\left(\frac{x - x_o}{M}\right)^{1 - \frac{n}{2}} . \qquad (3.1.18)$$

In the case of the measurements presented in this thesis a slightly different dissipation length scale, L_e^u, is used. L_e^u is defined by

$$U_e \frac{d(\overline{u^2})_e}{dx} = \frac{-(\overline{u^2})_e^{3/2}}{L_e^u} . \qquad (3.1.19)$$

Note, that there is no factor of $\frac{1}{2}$ on the left hand side of equation 3.1.19 such as appears on the left hand side of the turbulent kinetic energy equation. For a decay law of the form

$$\left(\frac{\overline{u^2}}{U^2}\right)_e = C^2\left(\frac{x - x_o}{M}\right)^{-n}, \qquad (3.1.20)$$

$$L_e^u = M\frac{C}{n}\left(\frac{x - x_o}{M}\right)^{1 - \frac{n}{2}} . \qquad (3.1.21)$$

3.1.3 Wind tunnel and boundary layer Reynolds number constraints

The combinations of free-stream intensity and (free-stream to boundary layer) length scale ratio for the measurements presented in this thesis were obtained by varying three parameters. These were the grid mesh size M, the distance X_{LE} between the grid and the plate leading edge, and the measuring station (i.e. the distance x). Strong low Reynolds number effects were avoided by requiring $Re_\theta \gtrsim 2000$ which, in the absence of free-stream turbulence, corresponds roughly to $Re_\delta \gtrsim 2 \times 10^4$.

Obviously, the length scale of the free-stream turbulence cannot be larger than a typical transverse dimension of the working section. Consequently, if the measurements are to avoid low Reynolds number effects then there must be an upper limit to the length scale ratio obtainable in a given facility. This upper limit must vary inversely as the boundary layer low Reynolds number limit. Furthermore, combining equations 3.1.20 and 3.1.21,

leads to

$$\frac{L_e^u}{\delta} = \frac{(U_e M/\nu)}{(U_e \delta/\nu)} \quad \frac{C^{2/n}}{n} \left(\frac{u'}{U}\right)_e^{(1-2/n)}. \tag{3.1.22}$$

Thus, for given $(U_e M/\nu)$ and $(U_e \delta/\nu)$, the length scale ratio varies as $(u'/U)_e^{(1-2/n)}$. This equation provides an upper limit on the length scale ratio when $(U_e M/\nu)/(U_e \delta/\nu)$ is as large as permissible. In choosing the largest mesh size it was supposed that a minimum number of meshes across the working section width and height were required to ensure uniform flow downstream: nearly homogeneous, nearly isotropic free-stream turbulence requires the free-stream length scale to be rather less than the working section width or height.

Now, for any given grid, the upper limit on the length scale ratio will be largest where the free-stream intensity is least, that is, at the end of the working section. By writing equation 3.1.20 as

$$M = X \left[\left(\frac{(u'/U)_e}{C}\right)^{-2/n} + \frac{X_o}{M}\right]^{-1} \tag{3.1.23}$$

and combining with equation 3.1.22 leads to

$$\frac{L_e^u}{\delta} = \frac{(U_e\, X/\nu)}{(U_e\, \delta/\nu)} \frac{1}{n} \left(\frac{u'}{U}\right)_e \left[1 + \frac{X_o}{M}\left(\frac{(u'/U)_e}{C}\right)^{2/n}\right]^{-1} \tag{3.1.24}$$

The term $\frac{X_o}{M}\left[\frac{(u'/U)_e}{C}\right]^{2/n}$ may be written as $(X/X_o - 1)^{-1}$ which is small when X is large compared with X_o. Equation 3.1.24 describes, as a function of free-stream intensity, the upper limit on the length scale ratio that is imposed by the working section length, ℓ say, when $X = \ell$. The largest length scale ratio may be realized, for example, by using a flat plate mounted at the end of the working section and just long enough to give the minimum $U_e\delta/\nu$, with a grid of the largest permitted mesh size.

A further constraint on the measurements was imposed by the largest permitted free-stream intensity at the plate leading edge. This limit was chosen to be as low as possible but without severe limitation on the range of free-stream intensity and length scale ratio implied. The limit was $(u'/U)_e \simeq 0.15$.

Figure 3.1 summarises the results deduced above. Boundaries A (equation 3.1.22) and B (equation 3.1.24) are defined by the working section dimensions and by the minimum boundary layer thickness for which measurements are to be obtained. Boundary C is defined by the largest permitted free-stream intensity at the leading edge, the boundary layer development length, and by the largest grid mesh size. (The development length may be reduced by artificially thickening the boundary layer, for example, by surface roughness.) Boundary D is included to emphasise that the minimum free-stream intensity of interest may be excluded by boundary B for large length scale ratios. As we shall see, conscious effort is required to set up flows which cover large ranges of both length scale ratio and free-stream intensity. In most previous work there was a very high coefficient of correlation between length scale ratio and free-stream intensity, larger grids producing higher values of both, and conversely.

3.1.4 Brief review of the range of free-stream turbulence intensity and length scale ratio used by some other workers

In this section the range of free-stream intensity and length scale ratio implied in the data of Robertson & Holt (1972), Huffman et al. (1972), Evans (1972), Charnay (1974) and Meier (1976) are compared .

The degree of anisotropy of the free-stream turbulence for the data of Huffman et al., Evans, Charnay and Meier has been discussed in chapter 1, subsection 1.2.1. Robertson & Holt assumed their free-stream turbulence to be closely isotropic.

Robertson & Holt and Meier give decay laws for their free-stream turbulence from which dissipation length scales may be determined. Free-stream dissipation length scales for the measurements of Huffman et al., Evans and Charnay have been evaluated (by the present author) by fitting a decay law of the form given in equation 3.1.20 to their data.

Boundary layer thicknesses are given explicitly by Huffman et al., Evans and Meier; Charnay gives the boundary layer thicknesses for most, but not all, of his profile measurement sets. Unfortunately, he does not give the boundary layer thicknesses for the sets of measurements that compare the effect of change of free-stream length scale at constant free-stream intensity. (Charnay concluded that halving the free-stream length scale had negligible effect on the boundary layer.) Robertson & Holt do not give the boundary layer thicknesses but they do give F/F_0 where $F = \delta_{99}/\theta$. For the analysis of their data the boundary layer thickness in the absence of free-stream turbulence, δ_0, has been assumed to be given by

$$\delta_0 = 0.37 \times \left(\frac{U_e x}{\nu}\right)^{-0.2} \qquad (3.1.25)$$

(Schlichting 1968, p598). The boundary layer thicknesses calculated are consistent with the momentum thickness Reynolds number range quoted[†].

Figure 3.2 shows L_e^u/δ and $(u'/U)_e$ following the analysis outlined above. At first, it may seem surprising that the five essentially independent sets of measurements fall so close to a single curve. (For these measurements $L_e^u/\delta \approx 0.3 + 16(u'/U)_e$, +0.4, -0.3.) This coincidence is put into perspective on noting that these measurements were all obtained using wind tunnels of comparable dimensions and at comparable Reynolds numbers. From figure 3.2 it is clear that

---

[†]Also for the present purposes, no strong distinction is made between the different definitions for the edge of the mean velocity profile.

the effects of length scale ratio could not have been distinguished from the effects of intensity unless the former were very strong. If, though, the relative scatter of the data shown in figure 3.2 is not important then the measurements of these workers should be consistent. However, as shown in the review in chapter 1, subsection 1.2.1, these data do not appear to be highly consistent.

3.1.5 The present measurements

The main mean-flow measurement sets were obtained using square-mesh square-bar biplane grids. A directory of the combinations of grid sizes, plate positions, and measuring stations is given in table 3.1. Table 3.3 tabulates the corresponding boundary layer and free-stream turbulence parameters. Figure 3.28 shows the values of L_e^u/δ_{995} and $(u'/U)_e$ for these measurements.

A small number of boundary layer mean flow and free-stream turbulence measurements were collected for turbulence generators consisting of single rows of square-section vertical bars. Table 3.2 gives a directory of combinations of generator sizes, plate positions, and measuring stations. Some quantitative evidence is given in section 3.2 for using square-mesh square-bar biplane grids in preference to generators of single rows of round or square bars. The boundary layer mean flow measurements listed in table 3.2 are presented separately in appendix 5.

3.2 FREE-STREAM MEAN VELOCITY GRADIENT AND TURBULENCE MEASUREMENTS

The free-stream mean velocity, $U_e(X)$, normalized by its value at measuring station 4, is given in figure 3.3, for X_{LE} = 0.30 m and X_{LE} = 2.06 m. The velocity variation along the plate is seen to be nearly independent of free-stream turbulence and largely dependent upon the position of the plate within the working section. (A higher mean velocity gradient with the plate in the upstream position in the constant cross-section working section is consistent with the

growth rate of the working section wall boundary layers decreasing with distance along the working section.) No measurements of mean velocity gradient were obtained with the plate in the intermediate positions, X_{LE} = 0.76 m and X_{LE} = 1.37 m, for which only a small number of measurements were collected, but it is anticipated that the mean velocity variation, $U_e(X)$, would have been between the measured values given in figure 3.3. The pressure gradient parameter $\beta = \frac{\delta^*}{\tau_w}\frac{dp}{dx} = \frac{-2}{C_f}\frac{\delta^*}{U_e}\frac{dU_e}{dx}$ has a value of about -0.08 when the plate is in its upstream-most position (X_{LE} = 0.30 m) and a value of about -0.04 when it is in its downstream-most position (X_{LE} = 2.06 m).

Figure 3.4 shows $(\overline{u^2}/U^2)_e^{-0.8}$ plotted against X/M for the 7.6 cm and 15.2 cm grids. The straight-line approximations of the measurements are, for the 7.6 cm grid,

$$\left[\frac{\overline{u^2}}{U^2}\right]_e^{-0.8} = 11.43\left(\frac{X}{M} - 4.81\right) \qquad (3.2.1)$$

or

$$\left[\frac{\overline{u^2}}{U^2}\right]_e = 0.0476\left(\frac{X}{M} - 4.81\right)^{-1.25}$$

and, for the 15.2 cm grid,

$$\left[\frac{\overline{u^2}}{U^2}\right]_e^{-0.8} = 8.39\left(\frac{X}{M} - 3.63\right) \qquad (3.2.2)$$

or

$$\left[\frac{\overline{u^2}}{U^2}\right]_e = 0.0700\left(\frac{X}{M} - 3.63\right)^{-1.25} .$$

The numerical difference in the decay laws is consistent with the higher solidity of the 15.2 cm grid : the pressure drop across the grid, and hence the turbulence intensity, are expected to increase with grid solidity. The smaller relative distance of the virtual origin of the decay law for the 15.2 cm grid is consistent with the larger bar size to mesh size of this grid, causing earlier mixing of the bar

wakes.

The contributions $\overline{u_e^2}$, $\overline{v_e^2}$ and $\overline{w_e^2}$ to the turbulent kinetic energy, $\overline{q_e^2}$, are shown in figure 3.5. (The measurements shown are those obtained during the last wind tunnel session. Although $\overline{u_e^2}$, $\overline{v_e^2}$ and $\overline{w_e^2}$ were measured during a previous wind tunnel session some small errors of the order of the differences between $\overline{u_e^2}$, $\overline{v_e^2}$ and $\overline{w_e^2}$ were incurred, causing some doubt about their reliability. Therefore, they are not presented.) Particularly noticeable, though small and unimportant in the present context, is the difference between $\overline{v_e^2}$ and $\overline{w_e^2}$ for the 15.2 cm grid. Initially $\overline{v_e^2}$ is close to $\overline{u_e^2}$ but with increasing distance $\overline{v_e^2}$ becomes closer to $\overline{w_e^2}$. $(\overline{u^2}/\overline{w^2})_e$ is approximately constant. It is tentatively suggested that the difference in $\overline{v_e^2}$ and $\overline{w_e^2}$ is a result of the biplane construction of the turbulence grid. However, the differences between $\overline{v_e^2}$ and $\overline{w_e^2}$ observed for the 15.2 cm grid are not necessarily supported by the rather fewer measurements of the turbulence generated by the 7.6 cm grid, also shown in figure 3.5.

The algebraic equation (3.1.21) for the growth of the free-stream length scale assumed the free-stream mean velocity gradient to be zero. Re-writing the left hand side of equation 3.1.19 as

$$U_e \frac{d}{dx}(\overline{u^2})_e = U_e^3 \frac{d}{dx}\left(\frac{\overline{u^2}}{U^2}\right)_e + 2\,\overline{u_e^2}\,\frac{dU_e}{dx} = \frac{-(\overline{u^2})_e^{3/2}}{L_e^u} \qquad (3.2.3)$$

and combining with the decay law equation (3.1.20) gives

$$L_e^u = M\frac{C}{n}\left(\frac{X - X_o}{M}\right)^{1-n/2} \Big/ \left(1 - \frac{2(X - X_o)}{n}\,\frac{1}{U_e}\frac{dU_e}{dx}\right) . \qquad (3.2.4)$$

Over the plate the term $2(X - X_o)/(nU_e).dU_e/dx$ is approximately independent of both x and the plate position, and has a value of about 0.08. The dissipation length scales quoted are corrected values.

Although intensity and dissipation length scale are representative scales of the energy containing eddies they are not

unique : in particular they are not sufficient to define the whole wave number distribution of the turbulent kinetic energy. Using Taylor's hypothesis measurements of the one-dimensional wave number spectra, defined as

$$\phi_{11}(k_1) = \frac{1}{2\pi}\int_{-\infty}^{+\infty} \overline{u(x)u(x+r)}e^{-ik_1 r}dr; \quad \phi_{22}(k_1) = \frac{1}{2\pi}\int_{-\infty}^{+\infty} \overline{v(x)v(x+r)}e^{-ik_1 r}dr;$$

$$\phi_{33}(k_1) = \frac{1}{2\pi}\int_{-\infty}^{+\infty} \overline{w(x)w(x+r)}e^{-ik_1 r}dr \qquad (3.2.5\ a,b,c)$$

were obtained from a frequency spectrum Fast Fourier Transform computer program. The frequency spectra were defined in the interval 0 to $+\infty$ such that

$$\int_0^\infty \phi_{11}(f)\,df = \overline{u^2}; \quad \int_0^\infty \phi_{22}(f)\,df = \overline{v^2};$$

$$\int_0^\infty \phi_{33}(f)\,df = \overline{w^2}, \qquad (3.2.6\ a,b,c)$$

where f is the frequency in Hertz. Thus

$$\phi_{11}(k_1) = \frac{1}{2}\phi_{11}(f)/(\frac{2\pi}{U}); \quad \phi_{22}(k_1) = \frac{1}{2}\phi_{22}(f)/(\frac{2\pi}{U});$$

$$\phi_{33}(k_1) = \frac{1}{2}\phi_{33}(f)/(\frac{2\pi}{U}), \qquad (3.2.7\ a,b,c)$$

and $k_1 = f \times (2\pi/U)$. To give what was considered to be a reasonable definition of the lowest frequency of interest 25 (real-time) seconds of data were analysed at approximately 2 Hz intervals in the range 2 Hz to 1000 Hz[†]. Analysis of higher frequencies was achieved by using a larger frequency interval (requiring a higher rate of

---

[†]The 3 dB point of the low-frequency response of the analogue apparatus was 1 Hz.

digitization) of 36 Hz in the range 36 Hz to 18 KHz, on about 1.5 (real-time) seconds of data. These partial spectra have been normalized by separately determined, unfiltered mean square values of the respective fluctuating quantities. About 90% of the free-stream turbulent kinetic energy was found to reside below 1000 Hz.

Figures 3.6 and 3.7 show the spectral analyses for seven positions downstream of the 15.2 cm grid (X/M = 15, 19.5, 21.5, 23.5, 25.5, 27.5 and 29.5), and three positions downstream of the 7.6 cm grid (X/M = 20, 36 and 39). In some cases only the lower part of the spectrum has been analysed and presented. Also, the spectra $\phi_{33}(k_1)$ are not presented at all positions. Where both $\phi_{22}(k_1)$ and $\phi_{33}(k_1)$ have been evaluated two analyses of $\phi_{11}(k_1)$ are available as shown. The extent to which two separate estimates of $\phi_{11}(k_1)$ agree is a result of the number of samples at each frequency; better agreement would be expected for a larger number of samples. For the present purposes the agreement was considered satisfactory.

Some, but not all of the measurements of $\phi_{22}(k_1)$ and $\phi_{33}(k_1)$ confirm a slight rise at low wave numbers prior to their monotonic decrease at higher wave numbers. From the isotropic relation

$$\phi_{22}(k_1) = \phi_{33}(k_1) = \frac{1}{2}\left(\phi_{11}(k_1) - k_1 \frac{d}{dk_1}\phi_{11}(k_1)\right) \qquad (3.2.8)$$

a rise of $\phi_{22}(k_1)$ and $\phi_{33}(k_1)$ with k_1 is possible but not inevitable. All of the spectra exhibit a slope close to the value -5/3 expected in an inertial sub-range despite a fairly low turbulence Reynolds number, $Re_\lambda = u'_e\lambda/\nu$. λ is Taylor's microscale, defined by $\lambda^2 = \overline{u^2}/\overline{(\partial u/\partial x)^2}$. For the 15.2 cm grid $Re_\lambda \approx 230$, and for the 7.6 cm grid $Re_\lambda \approx 130$. Here, the microscale has been evaluated assuming isotropy of the dissipating eddies which leads to $\varepsilon = 15\,\nu\,\overline{u^2}/\lambda^2$, giving

$$\frac{\lambda u'_e}{\nu} = 5\sqrt{\frac{L_e u'_e}{\nu}}\,. \qquad (3.2.9)$$

It is not intended to review in detail the minimum value of Re_λ required for the existence of an inertial subrange. This subject is briefly discussed, for example, by Townsend (1976), and in more detail by Hinze (1975). From the measurements quoted by Townsend the minimum value is $Re_\lambda \approx 100$, while Hinze suggests the value might be somewhat larger but less than $Re_\lambda = 500$. High wave number local isotropy is discussed in detail by Champagne (1978).

Integral length scales, defined as

$$L_{X_{11}} = \int_0^\infty \frac{\overline{u(x)u(x+r)}}{\overline{u^2}} dr \; ; \qquad L_{X_{22}} = \int_0^\infty \frac{\overline{v(x)v(x+r)}}{\overline{v^2}} dr \; ;$$

$$L_{X_{33}} = \int_0^\infty \frac{\overline{w(x)w(x+r)}}{\overline{w^2}} dr \; , \qquad (3.2.10\ a,b,c)$$

have been determined from the 'constant' spectral densities in the low wave number range of the spectra, i.e.

$$L_{X_{11}} = \frac{U_e}{4\overline{u^2}} \phi_{11} \; (f \to 0) \; ; \qquad L_{X_{22}} = \frac{U_e}{4\overline{v^2}} \phi_{22} \; (f \to 0) \; ;$$

$$L_{X_{33}} = \frac{U_e}{4\overline{w^2}} \phi_{33} \; (f \to 0). \qquad (3.2.11\ a,b,c)$$

$L_{X_{11}}$ and the average value of the transverse scales $L_{X_{22}}$ and $L_{X_{33}}$ are shown in figure 3.8 plotted against the dissipation length scale, L_e^u. Since the dissipation length scale has been determined from the decay of the energy-containing eddies and is not strongly dependent upon a portion of the spectrum containing a relatively small amount of energy, it is anticipated that the dissipation length scale will be more accurate than the integral scale determined from spectrum measurements. Scatter about the line of minimum standard deviation† is largely contained within a band of ±10%. This is

†assumed to pass through the origin.

consistent with the expected accuracy of the digitally measured spectra at the lowest wave numbers. An interesting result, considering that the turbulence is not exactly homogeneous or exactly isotropic, is that the ratio of the transverse to longitudinal integral length scales $L_{X_{22}}/L_{X_{11}}$, say, is close to the isotropic value of one-half. From figure 3.8,

$$L_{X_{11}} = 0.626 \times L_e^u \,, \qquad (3.2.12)$$

and $$L_{X_{22}} = 0.313 \times L_e^u \,.$$

The decay of the free-stream turbulence intensity downstream of the turbulence generators comprising a single row of vertical square bars is shown in figure 3.9. The straight-line approximations of the measurements are, for the 7.6 cm-spaced row of bars,

$$\left(\frac{\overline{u^2}}{U^2}\right)_e = 0.0611 \left(\frac{X}{M} - 5.16\right)^{-1.25} \qquad (3.2.13)$$

and, for the 15.2 cm-spaced row of bars,

$$\left(\frac{\overline{u^2}}{U^2}\right)_e = 0.105 \left(\frac{X}{M} - 4.07\right)^{-1.25} \qquad (3.2.14)$$

The larger X_o/M for the single row of bars compared with the corresponding square-mesh grid is likely to be a consequence of the reduced solidity causing delayed mixing of the bar wakes. Compared with the respective square-mesh grid $\overline{u_e^2}$ is larger at constant $(X - X_o)/M$. A higher $\overline{u_e^2}$ can be partly explained by the turbulence being more anisotropic than for the square mesh grids and partly by an unusual spectrum of u_e at low wavenumbers. Approximately, $(\overline{u^2}/\overline{v^2})_e = 1.25$ while for the square mesh grids $(\overline{u^2}/\overline{v^2})_e$ does not much exceed 1.1. Figures 3.10 and 3.11 show spectra at X/M = 19.9 downstream of the 7.6 cm-spaced row of bars and at X/M = 29.5 downstream of the 15.2 cm-spaced row of bars. At low wavenumbers $\phi_{11}(k_1)$ increases with

decreasing k_1 in both cases, while $\phi_{22}(k_1)$ behaves much as for the square-mesh grids except possibly for a small hump at $k_1 \lesssim 8\ m^{-1}$. Neglecting this hump and subtracting $2 \times \phi_{22}(k_1)/\overline{v^2}$ from $\phi_{11}(k_1)/\overline{u^2}$ amounts to about 7% of $\overline{u_e^2}$.

Spectral analyses of the velocity fluctuation at a distance downstream of a turbulence generator consisting of a single row of 2.86 cm diameter bars, spaced 11.4 cm apart, are shown in figure 3.12. This generator has the same solidity as the 15.2 cm-spaced row of square bars just discussed. $\phi_{11}(k_1)$ is well behaved in the low wave number region although, compared with the square-mesh (square-bar) biplane grids, the "knee" of the spectrum is less pronounced. The vortex shedding frequency of an isolated bar of the grid is approximately 110 Hz, or $k_1 = 44\ m^{-1}$, which is not very far from the frequency of the small peak noticeable in the region of the knee of $\phi_{33}(k_1)$.

3.3 BOUNDARY LAYER MEAN FLOW MEASUREMENTS

3.3.1 Preliminary skin friction measurements

Prior to measurement of the boundary layer mean velocity profiles on the plate centre-line, some Preston-tube measurements of skin friction were made on and either side of the centre-line. In a truly two-dimensional flow the wall shear stress is constant in the transverse z-direction. Figure 3.13 shows the cross-stream distribution of the skin friction coefficient C_f normalized by its value at the centre-line $C_{f_{z=0}}$, at stations 4 and 16 for two plate positions (X_{LE} = 2.06 m and X_{LE} = 0.30 m), with and without free-stream turbulence. At station 4 the variation in C_f is within ±1% of the centre-line value. At station 16 the variation is larger but within ±2% over a distance from the centre-line of approximately ±23 cm, roughly four times the largest boundary layer thickness measured (see section 3.3.2). Cross-stream variation of static pressure on the plate surface was of the order of ½% of the free-stream dynamic

head ($\frac{1}{2}\rho U_e^2$). Surface roughness (isolated steps of the order of 0.1 mm high) was present near the plate centre line as a result of tolerances in machining and mounting of the instrumentation disks. A roughness height of k = 0.1 mm corresponds to a Reynolds number of $u_\tau k/\nu \approx 4$ and is therefore unlikely to have significantly affected the boundary layer (see, for example, Bradshaw, 1976, p72). Away from the instrumentation disks the plate surface was smooth. Previous experimenters, for example, Fernholz (1964), have also found cross-stream variations of C_f to increase with streamwise distance. Some of the non-uniformity has been shown to be due to transition effects and flow non-uniformity caused by wind tunnel screens etc., but there does not appear to be a completely clear explanation for the remaining non-uniformity.

No measurements of C_f off the centre line were obtained with the heating wires in position.

3.3.2 Mean velocity profiles, free-stream turbulence intensities and length scale ratios

Mean velocity profiles are shown in figures 3.14 to 3.26 in three pairs of coordinates; $U/U_e \sim y$, $U/u_\tau \sim y$, $U/u_\tau \sim \ln(u_\tau y/\nu)$. With the limitation that u_τ has been determined by use of the logarithmic low of the wall (see subsection 2.2.2 of chapter 2) the hypothesis that the inner layer law of the wall should be unaffected by the presence of moderate free-stream turbulence intensity is supported by these figures. Conversely, of course, the free-stream turbulence might be classed as "moderate" if its presence does not cause the law of the wall to fail. Figures 3.14 to 3.26 do not even show any tendency for the logarithmic region, normally extending to $y \approx 0.15\ \delta_{995}$, to become thinner in the presence of free-stream turbulence.

The boundary layer thickness δ_{995} for the profiles in figures 3.14 to 3.26 are shown in figure 3.27. Corresponding values

of free-stream intensity $(u'/U)_e$ and length scale ratio L_e^u/δ_{995} at which profile measurements were obtained are shown in figure 3.28. The points in figure 3.28 are labelled with the respective profile numbers given in table 3.3. Also shown is the region covered by Robertson & Holt (1972), Huffman et al. (1972), Evans (1972), Charnay (1974) and Meier (1976), as discussed in section 3.1.4.

The analysis discussed in subsection 3.1.3 assumed that the free-stream mean velocity was invariant with streamwise distance, which is not quite true for the present measurements. Figure 3.29 shows the bounding curves of free-stream intensity and length scale ratio given by equations 3.1.22 and 3.1.24 corrected for the free-stream mean velocity gradient, for a lower Reynolds number limit of $Re_\delta = 2 \times 10^4$. Curve 1a gives the constraint implied by the largest grid used, namely M = 15.2 cm. As a comparison, curve 1b gives the constraint implied by the 7.6 cm grid. The constraint implied by the working section length is shown for the 15.2 cm grid, curve 2a, and the 7.6 cm grid, curve 2b. These two curves assume, however, that the plate is just long enough to give the minimum boundary layer Reynolds number permitted (i.e. $Re_\delta = 2 \times 10^4$) at a position coincident with the end of the working section. In the present experiment the plate was too long to satisfy this condition. Therefore curves 3a and 3b have been calculated on the same basis as curves 2a and 2b but for a working section shorter by an amount equal to the plate length for which $Re_\delta > 2 \times 10^4$, assuming the position at which $Re_\delta = 2 \times 10^4$ is roughly independent of free-stream turbulence. Strictly, these new curves cannot be claimed to be limiting although the measured values of $(u'/U)_e$ and L_e^u/δ_{995} do not contradict them. Approximately, the region bounded by curves 2 and 3 is the region excluded as a result of the plate exceeding the length just long enough to give $Re_\delta = 2 \times 10^4$. Figure 3.29 also shows the length scale ratio based upon the free-stream integral length scale $L_{x_{11}}$.

The axis of $L_{x_{11}}/\delta_{995}$ refers to the 'best fit' between L_e^u and $L_{x_{11}}$ given in figure 3.8 rather than the measured values of $L_{x_{11}}$.

3.3.3 Velocity-defect profiles

The mean velocity profiles shown in figures 3.14 to 3.26 are shown re-plotted in outer-layer coordinates in figures 3.30 to 3.41.

Figures 3.30 and 3.31 show the velocity-defect profiles in the absence of free-stream turbulence. Departure from self-preservation, evident in figure 3.30, is consistent with a reduced wake strength at low Reynolds numbers. For equilibrium boundary layers Coles' (1956) wake function, $\frac{\Pi}{k}W(\frac{y}{\delta})$ defined by

$$\frac{U}{u_\tau} = \frac{1}{k} \ln (\frac{yu_\tau}{\nu}) + C + \frac{\Pi}{k} W(\frac{y}{\delta}), \qquad (3.3.1)$$

decreases in strength with decreasing Reynolds number for $Re_\theta \lesssim 5000$ (Coles, 1962). Figure 3.31 shows the velocity defect measured at stations 6 and 14 with the (unheated) boundary layer heating wires mounted close to the leading edge. The velocity defect measured at station 14 agrees well with the measurements at stations 8, 12 and 16, shown in figure 3.30. However, the velocity defect at station 6 ($x = 0.91$ m) is a little larger than expected, from which it must be concluded that the heating wires had a small effect on the development of the boundary layer over and above a change in the effective origin of the boundary layer. The effect of the presence of the heating wires would appear to be insignificant at, and probably upstream of, station 14.

The effect of free-stream turbulence on the velocity defect is shown in figures 3.32 to 3.41. An insert in each figure shows the pertinent values of free-stream intensity and length scale ratio. Also shown in these figures is the 'no-grid' velocity-defect profile for $Re_\theta \gtrsim 2700$. In figures 3.32, 3.33 and 3.40 the length scale ratio

is approximately constant and hence the effect shown is the single effect of free-stream intensity. In agreement with other workers' observations, the velocity defect decreases with increasing free-stream intensity. Note that the decrease at station 4, shown in figure 3.32, is slightly exaggerated by the low Reynolds number at that station. The effect of the heating wires cited earlier would account for the lack of change in the velocity defect measured at stations 6 and 8 shown in figure 3.33.

The velocity-defect profiles shown in figures 3.34 to 3.36 are seen to be closely self-preserving. These figures imply that the effect of free-stream turbulence, which increases with free-stream intensity, decreases with length scale ratio L_e/δ. (Strictly, self-preservation would require the velocity and length scales of the free-stream turbulence to remain in constant proportion to the velocity and length scales of the boundary layer. The self-preservation exhibited is largely fortuitous.) Figures 3.37 to 3.39 demonstrate explicitly the single effect of length scale ratio for three values of free-stream intensity. They show clearly that the response of the boundary layer to free-stream turbulence is strongly dependent on the length scale ratio. The velocity defect decreases with decreasing length scale ratio. Apart from the recent contribution by Meier & Kreplin (1978) other workers have generally assumed or inferred that the effect of length scale ratio (L_e/δ) is negligible compared to that of the free-stream intensity.

Two velocity-defect profiles which have nearly equal values for the free-stream intensity and length scale ratio are shown in figure 3.41. The closeness between these two profiles confirms the general reliability of the measurements and the adequacy of the free-stream intensity (compared, strictly, with u_τ rather than U_e) and the length scale ratio to describe the effect of free-stream turbulence. The slight discrepancy between the two profiles is qualitatively

consistent with the lower u'_e/u_τ for the profile with the higher $(u'/U)_e$. (The slight discrepancy is also consistent with the tentative suggestion in the next subsection that the clauser shape parameter, G, and hence the velocity defect, may be weakly dependent upon the Reynolds number when free-stream turbulence is present even if it is not when free-stream turbulence is absent.)

The effect of free-stream turbulence on the shape parameter H is shown in figure 3.42. Figure 3.43 contains tabulated values of $\Delta H/H_o$ where $\Delta H = H - H_o$. H_o was derived from the curve through the 'no-grid' measurements given in figure 3.42 (and extrapolated for the higher Reynolds numbers effected by the presence of the heating wires). $\Delta H/H_o (< 0)$ decreases with increasing free-stream intensity and decreasing length scale ratio.

3.3.4 Skin friction measurements

Measurements of the skin friction coefficient, C_f, obtained by fitting a portion of the mean velocity profile to the logarithmic law of the wall, are shown in figure 3.44 plotted with respect to the Reynolds number, Re_θ. Preston tube measurements, using Patel's (1965) calibration, (obtained only for the cases without the heating wires at the plate leading edge) are also shown. The Preston tube selected for these measurements gave a skin friction representative of a number of different-sized Preston tubes tried. On average the selected Preston tube gave a skin friction value 1.6% above that obtained by fitting the velocity profile to the logarithmic law (with k = 0.41 and C = 5.2. See chapter 2, subsection 2.2.2). The Preston tube skin friction coefficients quoted in table 3.3 and figure 3.44 are 1.6% smaller than the measured values. The adjusted measurements are consistent with, and hence support, the skin friction values obtained from the logarithmic law velocity profile fit.

In a truly two-dimensional incompressible flow the momentum integral equation reduces to

$$\frac{C_f}{2} = \frac{d\theta}{dx} + (H + 2)\frac{\theta}{U_e}\frac{dU_e}{dx} . \qquad (3.3.2)$$

Figure 3.45 compares the measured friction coefficient C_f with that determined by evaluation of the right hand side of equation 3.3.2. Most of the values of skin friction coefficient so evaluated fall within ±10% of the value obtained using the logarithmic law of the wall. All but one out of twenty two fall within ±20%. A similar approach was used by Coles (1962) in his analysis of constant-pressure boundary layer data to distinguish between what he considered as 'normal' and 'abnormal' boundary layers : for the boundary layers considered as 'normal' the discrepancy between the friction coefficient measured by the two methods was within about ±10%. In the present experimental arrangement exact two-dimensionality is not to be expected, mainly because of the presence of the boundary layers on the working section side walls. Generally, in a converging or diverging flow the velocity W and the velocity $\partial W/\partial z$ are non-zero. For a symmetrically converging or diverging flow the momentum integral equation on the line of symmetry ($W = 0$ but $\partial W/\partial z \neq 0$) is

$$\frac{C_f}{2} = \frac{d\theta}{dx} + (H + 2)\frac{\theta}{U_e}\frac{dU_e}{dx} + \frac{\theta}{x + a} \qquad (3.3.3)$$

(Schlichting 1968, p651) where 'a' is the virtual origin of the convergence ($a + x < 0$) or divergence ($a + x > 0$). Variation of the virtual origin as infered by figure 3.45 and equation 3.3.3 is shown in figure 3.46 in the form $x/(x + a)$ against $x(\geq 0)$. Also shown are lines of constant 'a' corresponding to convergent flow ($a < -x$) and divergent flow ($a > -x$). Of course, any conclusions that may be drawn from either figure 3.45 or figure 3.46 are subject to the accuracy with which $d\theta/dx$ has been determined from the profile measurements.

The effect of free-stream turbulence on the skin friction coefficient, C_f, is shown tabulated on figure 3.47 in the form $\Delta C_f/C_{f_o} = (C_f - C_{f_o})/C_{f_o}$. C_{f_o} was derived from the curve through the 'no-grid' measurements given in figure 3.44. (For the slightly higher Reynolds numbers achieved as a result of the presence of the heating wires C_{f_o} was obtained by extrapolation. Clearly, $\Delta C_f/C_{f_o}$, like $\Delta H/H_o$, depends strongly on both the free-stream intensity and the length scale ratio.

At an intermediate stage of obtaining the present measurements a three-dimensional representation of $\Delta C_f/C_{f_o}$ was constructed in perspex, as shown photographed in figure 3.48. (These measurements were those obtained prior to adding the heating wires.) Also shown are results of Robertson & Holt, Evans, Meier and Huffman et al., the latter as interpreted by the present writer using Meier's results to correct their 'no-grid' measurements. (See subsection 3.3.7.) The inadequacy of a linear correlation between $\Delta C_f/C_{f_o}$ and $(u'/U)_e$, as already confirmed by Meier for $(u'/U)_e \lesssim 0.01$, is clearly demonstrated for $(u'/U)_e \gtrsim 0.01$ also.

A simple empirical correlation which enables the dependence of $\Delta C_f/C_{f_o}$ on intensity and length scale ratio to be expressed as a single curve, with the exception of one data point, is shown in figure 3.49. The single discrepancy, which is too large to be accounted for by the expected errors of measurement, occurs at a high free-stream intensity of $(u'/U)_e \approx 0.06$, a low length scale ratio of $L^u_e/\delta_{995} \approx 1$ and, in particular, a low Reynolds number of $Re_\theta \approx 1800$. An explanation of the discrepancy exists if the disappearance of the so-called "wake" component subsequently limits the increase in the friction coefficient that is due to the presence of free-stream turbulence. Now, for a turbulent boundary layer in the absence of free-stream turbulence the wake strength decreases with decreasing Reynolds number for $Re_\theta \lesssim 5000$. It follows that

for a boundary layer in the presence of free-stream turbulence (such that the free-stream intensity and length-scale ratio are constant) the wake strength will disappear sooner at low Reynolds numbers unless the reduction in wake strength due to the free-stream turbulence is Reynolds-number dependent in an exactly compensatory manner. The remaining data shown in figure 3.49 are contained within a band width of approximately ±1% of the friction coefficient, typical of the likely measurement errors.

The values of $\Delta H/H_o$ and $\Delta C_f/C_{f_o}$ tabulated in figures 3.43 and 3.47, respectively, are compared in figure 3.50. The relationship between $\Delta H/H_o$ and $\Delta C_f/C_{f_o}$ is evidently independent of free-stream intensity and length scale ratio, but, as shown below, probably not independent of Reynolds number. Meier's (1976) measurements for a similar Reynolds number range give $\Delta H/H_o = 0.47\ \Delta C_f/C_{f_o}$. A functional dependence between $\Delta H/H_o$ and $\Delta C_f/C_{f_o}$ alone implies that the Clauser shape parameter, G, (defined in equation 3.3.22) is a function of Reynolds number even if it is not in the absence of free-stream turbulence. For, from the definition of G

$$G = G_o + \Delta G = \left(1 - \frac{1}{H_o}\left(1 + \frac{\Delta H}{H_o}\right)^{-1}\right)\left(1 + \frac{\Delta C_f}{C_{f_o}}\right)^{-1/2}\sqrt{\frac{2}{C_{f_o}}} \qquad (3.3.4)$$

and on retaining only the linear term of the Taylor series expansion

$$\frac{\Delta G}{G_o} = \frac{1}{H_o - 1}\frac{\Delta H}{H_o} - \frac{1}{2}\frac{\Delta C_f}{C_{f_o}}$$

where the second order term $\frac{1}{2}\frac{1}{H_o - 1}\frac{\Delta H}{H_o}\frac{\Delta C_f}{C_{f_o}}$ has also been neglected. H_o is a function of Reynolds number.

3.3.5 A comment on the so-called law of the wake

For a boundary layer in the absence of free-stream turbulence the similarity laws permit the mean velocity profile to be described by

$$\frac{U}{u_\tau} = \frac{1}{k} \ln\left(\frac{yu_\tau}{\nu}\right) + C + \frac{1}{k} g(\Pi, \frac{y}{\delta}) \qquad (3.3.6)$$

where $g(\Pi, y/\delta)$ is the generalized form of the 'wake' function (proposed by Coles, 1956). Normally, Π, is considered as a 'wake' strength (Coles; see equation 3.3.9, below) or as a wake strength cum shape parameter of the wake function (Finley et al., 1966; Dean, 1974). Usually, $g(\Pi,1) = 2\Pi$. The velocity defect is given by

$$\frac{U_e - U}{u_\tau} = -\frac{1}{k} \ln\left(\frac{y}{\delta}\right) + \frac{1}{k} g(\Pi,1) - \frac{1}{k} g(\Pi,\frac{y}{\delta}). \qquad (3.3.7)$$

Neglecting Reynolds-number effects, the effect of free-stream turbulence introduces two additional independent parameters, u_e'/u_τ and L_e/δ, into the defect law to give

$$\frac{U_e - U}{u_\tau} = f\left(\frac{y}{\delta}, \frac{u_e'}{u_\tau}, \frac{L_e}{\delta}\right). \qquad (3.3.8)$$

This equation states that in general the shape of the velocity defect and hence the shape of the wake function is dependent upon both the free-stream intensity and the length scale ratio. That is, equation 3.3.8 implies that the wake function cannot necessarily be characterised by a single parameter, Π.

The usefulness of a wake function depends upon how well $g(\Pi, y/\delta)$ may be fitted by a simple analytic function. In his analysis of velocity profile data Coles (1968) has employed the simplification

$$g(\Pi, \frac{u}{\delta}) = \Pi\, W(\frac{y}{\delta}). \qquad (3.3.9)$$

However, this simplification cannot be strictly valid because at $y = \delta$, where $dU/dy = 0$, equation 3.3.6 requires

$$\left.\frac{d\, g(\Pi, y/\delta)}{d(y/\delta)}\right|_{y=\delta} = -1. \qquad (3.3.10)$$

In constant-pressure layers the discrepancy would appear not to be too important, as exemplified by the general success of Coles' analysis. The form used by Finley et al. and Dean is the simplest polynomial

that satisfies the boundary conditions

$$g(\Pi, 0) = 0 , \qquad g(\Pi, 1) = 2\Pi, \qquad (3.3.11\ a,b)$$

$$\left.\frac{d\, g(\Pi, y/\delta)}{d(y/\delta)}\right|_{y\to 0} = 0 , \qquad \left.\frac{d\, g(\Pi, y/\delta)}{d(y/\delta)}\right|_{y\to \delta} = -1. \qquad (3.3.11\ c,d)$$

That is,

$$g(\Pi,\frac{y}{\delta}) = (1 + 6\Pi)(\frac{y}{\delta})^2 - (1 + 4\Pi)(\frac{y}{\delta})^3. \qquad (3.3.12)$$

The usefulness of the wake function described by equation 3.3.12 was tested by solving the equations

$$\frac{U_e}{u_\tau} = \frac{1}{k} \ln(\frac{\delta u_\tau}{\nu}) + C + \frac{2\Pi}{k} \qquad (3.3.13)$$

and

$$\frac{\delta^*}{\delta} = \frac{1}{k} \frac{u_\tau}{U_e} (\frac{11}{12} + \Pi) \qquad (3.3.14)$$

for δ and Π, given u_τ/U_e, u_τ and δ^*, for the velocity profiles shown in figure 3.51. For the cases when free-stream turbulence is present the analytic wake function given by equation 3.3.12 fails to describe the wake part of the velocity profile very closely, although it is considerably better than the frequently-used cosine function for $W(y/\delta)$ $(= 1 - \cos(\pi\frac{y}{\delta}))$ in equation 3.3.9 which is incapable of describing a negative wake function. No extensive attempt was made to find a generalised analytic wake function. Table 3.3 tabulates, for the outer layer, the maximum departure ΔU of the velocity profile above the logarithmic law where ΔU is defined by

$$\frac{\Delta U}{u_\tau} = \left[\frac{U}{u_\tau} - \frac{1}{k} \ln(\frac{y u_\tau}{\nu}) - C\right]_{MAX} \qquad (3.3.15)$$

Also tabulated is the position, $y_{\Delta U}$, at which the maximum velocity difference occurs.

3.3.6 Boundary layer thickness growth rate and the shape factor δ_{995}/θ

The effect of free-stream turbulence on the boundary layer thickness is evident from figure 3.27. Boundary layer thickness growth

rates for the boundary layers defined by four or more measurements are shown in figure 3.52. Noticeably, the growth rate for the case in which unheated wires were present at the leading edge is significantly larger than the other growth rates. The increase in growth rate at constant Re_θ is tabulated in figure 3.53 in the form

$$\frac{\Delta(d\delta_{995}/dx)}{(d\delta_{995}/dx)_o} \equiv \frac{d\delta_{995}/dx - (d\delta_{995}/dx)_o}{(d\delta_{995}/dx)_o}$$

Evidently, the increase in the growth rate does not follow the monotonic dependence upon the length scale ratio exhibited by, say, the increase in the skin friction coefficient. The growth rate as documented in figure 3.53 behaves rather oddly.

Figure 3.54 shows the shape factor δ_{995}/θ plotted as a function of Reynolds number, Re_θ. The increase in the shape factor at constant Re_θ, tabulated on figure 3.55 in the form

$$\frac{\Delta\delta_{995}/\theta}{(\delta_{995}/\theta)_o} \equiv \frac{\delta_{995}/\theta - (\delta_{995}/\theta)_o}{(\delta_{995}/\theta)_o} , \qquad (3.3.17)$$

does not show the same dependence on the length scale ratio as the growth rate discussed above. Figure 3.56 compares $\Delta(\delta_{995}/\theta)/(\delta_{995}/\theta)_o$ with $\Delta C_f/C_{f_o}$. The scatter (of about ±8%) is much larger than the similarly-based comparison between $\Delta H/H_o$ and $\Delta C_f/C_{f_o}$, and also appears to have no consistent trend with free-stream intensity or length scale ratio. No Reynolds-number dependence is apparent.

Now, the boundary layer growth rate, $d\delta_{995}/dx$, and the shape factor, δ_{995}/θ, are related by

$$\frac{d\delta_{995}}{dx} \equiv \theta \frac{d(\delta_{995}/\theta)}{dx} + \frac{\delta_{995}}{\theta}\frac{d\theta}{dx} . \qquad (3.3.18)$$

Since, as discussed in subsection 3.3.4, departure of the boundary layer from a truly two-dimensional flow affects $d\theta/dx$ (and also C_f), $d\delta_{995}/dx$ is also affected. Thus the inconsistent behaviour of $d\delta_{995}/dx$ can be attributed, at least in part, to the departure of the boundary layer from truly two-dimensional flow. For the present

measurements the effect of free-stream turbulence on the boundary layer thickness, δ_{995}, is better described in relation to the momentum thickness by the shape factor δ_{995}/θ.

3.3.7 Some comparisons with other workers' data

The effect of free-stream turbulence on the skin-friction coefficient, compared at constant Re_θ, as deduced from the measurements of other workers, is shown in figure 3.57. The present measurements are represented by a mean line in this figure. Robertson & Holt (for whose data $400 \lesssim Re_\theta \lesssim 2000$), Charnay as inferred by Bradshaw (1974), and Evans (1972) show consistently lower, though more scattered, values for $\Delta C_f/C_{f_o}$ than the present measurements. Too much emphasis should not be placed on the measurements of Charnay : since Charney would appear not to have measured the momentum thickness, Bradshaw has used the empirical correlation of Robertson & Holt to convert the comparison of skin-friction coefficient at constant $U_e\delta_{99}/\nu$ given by Charnay to a comparison at constant $U_e\theta/\nu$. The results of Meier fit in well with the correlation of the present measurements and with the consensus of the results of Robertson & Holt, Charnay, and Evans. Meier's results have been used to correct the data of Huffman et al. and Evans for the effect of the high "background" free-stream turbulence intensity ($(u'/U)_e \approx 0.01$, in both cases) in the absence of a turbulence-generating grid. The length-scale ratio, L^u_e/δ, inferred from the decay of the background free-stream turbulence turns out to be about 0.5 for the data of Huffman et al. and about 0.3 for Evans' data, both conveniently close to the values covered by Meier. The corrected data of Huffman et al. show a slightly smaller increase in $\Delta C_f/C_{f_o}$ than the present measurements and a significantly smaller increase than that deduced by Green.

Green's analysis employed the skin-friction formula of Nash & MacDonald (1967) and the defect-law correlation of Charnay et al.,

$$\frac{U_e - U}{u_\tau} = (1 - \alpha \frac{u'_e}{u_\tau}) f(\frac{y}{\delta}), \qquad (3.3.19)$$

but used a slightly different value of α. (See chapter 1, subsection 1.2.1.) (The correlation of Charnay et al. cannot be valid in the inner layer since it implies that von Karman's constant k is a function of u'_e/u_τ.) Nash & MacDonald's (1967) skin-friction formula used by Green is

$$\sqrt{\frac{2}{C_f}} = A \ln(Re_\theta) + B + F(G). \qquad (3.3.20)$$

From Nash & MacDonald, A = 2.47, B = 4.75 and

$$F(G) = 1.5G + 1724/(G^2 + 200) - 16.87 \qquad (3.3.21)$$

and G is the Clauser shape parameter, defined by

$$G \equiv \int_0^\infty \left(\frac{U_e - U}{u_\tau}\right)^2 dy \Big/ \int_0^\infty \left(\frac{U_e - U}{u_\tau}\right) dy. \qquad (3.3.22)$$

(Equation 3.3.20 is in fact incompatible with the skin-friction formula

$$\sqrt{\frac{2}{C_f}} = \frac{1}{k} \ln(Re_{\delta^*}) + C + Q(\Pi), \qquad (3.3.23)$$

derived from equations 3.3.13 and 3.3.14, because δ^*/θ varies with Reynolds number whilst, except at low Reynolds numbers, G and Π are supposed not to. The incompatibility is not considered here.) Differentiating equation 3.3.20 leads to

$$\frac{dC_f}{C_f} = -2 \sqrt{\frac{C_f}{2}} F'(G)\, dG. \qquad (3.3.24)$$

For a constant-pressure two-dimensional incompressible boundary layer in the absence of free-stream turbulence F(G) = 0.

Now, F(G) was evaluated by Nash & MacDonald for values of F that were almost exclusively greater than zero. However, all the measurements show that, at constant Re_θ, the presence of free-stream turbulence increases the skin friction whereupon F must always be negative. The present 'no-grid' measurements are probably better

fitted by

$$\sqrt{\frac{2}{C_f}} = 2.47 \ln Re_\theta + 5.24 \qquad (3.3.25)$$

as shown in figure 3.58a. Figure 3.58b shows F(G) due to the effect of free-stream turbulence, determined from the present measurements. The extrapolated correlation of Nash & MacDonald is also shown and is seen to have a slope, F'(G), approximately 18% larger than the straight line passing through the present measurements. The difference between F'(G) given by Nash & MacDonald and F'(G) determined from the present measurements is insufficient to account for the entire difference between Green's method of analysis and the analysis (by the present writer) using Meier's results. Had a linear extrapolation rather than Meier's results been used (by the present writer) to evaluate C_{f_o}, it would have been smaller by about 2% and the remaining difference would have been quite small.

3.4. CONCLUSION TO THE CHAPTER

Simple reasoning shows that the defect law will, in principle at least, depend upon both the free-stream intensity and the free-stream to boundary layer length scale ratio. Constraints imposed by wind tunnel dimensions and Reynolds number range on the boundary layer measurements can easily limit the range of free-stream intensity and length scale ratio obtainable in laboratory flows. These constraints have been partly responsible for the close relationship between the length scale ratio and the free-stream intensity of previous measurements, as shown in figure 3.2. Clearly, in such cases, the effects of varying length scale ratio could not have been distinguished from the effects of varying free-stream intensity unless the former were strong. A special effort has been made in the present thesis to obtain a larger range of length scale than previously.

The present results show, for the first time, that the effect of (nearly isotropic) free-stream turbulence on a turbulent boundary layer depends significantly on both the free-stream intensity and the length scale ratio. That the effect decreases with increasing length scale ratio, at least in the range $5.5 \gtrsim L_e^u/\delta_{995} \gtrsim 0.7$, is consistent firstly with the fact that eddies interact most with eddies of comparable size and secondly with the reduction of the normal component of fluctuating velocity of the free-stream turbulence due to the presence of the boundary, as demonstrated by the measurements of Thomas & Hancock (1977, appendix 1).

It is not obvious from the present measurements just how the effect will vary as the length scale tends to zero. Very small-scale free-stream turbulence will directly affect only a very short fetch. Furthermore, since boundary layers in general do not respond greatly to very small-scale disturbances, for example, surface roughness smaller than the viscous sublayer thickness, the effect of very small-scale free-stream turbulence may similarly be very small. However, for free-stream turbulence that has a length scale of the order of the inner layer scales, the argument that the inner layer would not discern between outer-layer and free-stream turbulence would no longer be applicable. One consolation though is that a moderate free-stream intensity would necessarily be relatively small when compared with the high turbulence intensity that exists within the inner layer.

A simple empirical correlation that relates $\Delta C_f/C_{f_o}$ at constant Re_θ to the parameter $(u'/U)_e/(L_e^u/\delta_{995} + 2.0)$ by a single curve has been found, as shown in figure 3.49. When the effects of free-stream turbulence are large the persistence of the inner-layer logarithmic law would appear to restrict further change in the boundary layer mean flow properties. Slender evidence shows that this restriction is stronger when low Reynolds number effects are

present. Using the above correlation the consensus of results of previous workers shows a slightly smaller effect than the present measurements. Meier's measurements confirm that the boundary layer turbulence and the free-stream turbulence are uncorrelated when the effect of the latter is small, and the present measurements for smaller values of the free-stream intensity support the hypothesis.

Clearly, the data correlations derived from the present measurements apply with any certainty only if the free-stream turbulence is closely isotropic and slightly inhomogeneous in the streamwise direction. Turbulence that is highly anisotropic cannot be adequately described by a single velocity scale and, necessarily, by a single length scale; anisotropy ratios for the intensities, and probably for the length scales also, must be included.

PLATE POSITION, $X_{LE(m)}$	GRID MESH/BAR SIZE	PROFILE MEASUREMENTS AT STATIONS; NO HEATING WIRES AT LEADING EDGE	UNHEATED WIRES AT LEADING EDGE
0.30	NO GRID	12	6, 14
0.76		12	———
1.37		———	———
2.06		4, 8, 12, 16	———
0.30	7.6/1.27cm	4, 8, 12, 16	6, 8, 16
0.76	15.2/3.81cm	12	10
1.37	15.2/3.81cm	———	6
2.06	7,6/1.27cm	4, 8, 12, 16	6
2.06	15.2/3.81cm	4, 8, 12, 16	6, 8, 10, 12, 14, 16

TABLE 3.1 Directory of mean velocity profile measurements; no grid and square mesh, square bar, biplane turbulence grid.
x(metres) = 0.152 × (station number).

PLATE POSITION $X_{LE(m)}$	GENERATOR BAR SPACING/ BAR SIZE	PROFILE MEASUREMENTS AT STATIONS; NO HEATING WIRES AT LEADING EDGE	UNHEATED WIRES AT LEADING EDGE
0.30	7.6/1.27cm	12	———
2.06	7.6/1.27cm	12	———
2.06	15.2/3.81cm	12	———

TABLE 3.2 Directory of mean velocity profile measurements; single-row-of-square-bars turbulence generator.
x(metres) = 0.152 × (station number).

STN	u'/U_e	L_e^u/δ_{995}	δ_{995}	δ^*	θ	U_e	Re_θ	$\frac{u_\tau \delta_{995}}{\nu}$	$C_f(1)$	$C_f(2)$	H	$\frac{k\Delta U}{2u_\tau}$	$y_{\Delta U}/\delta_{995}$	PROFILE NUMBER
NO GRID			X_{LE}=0.30m			NO HEATING WIRES AT LEADING EDGE								
12		-	29.7	4.67	3.37	16.46	3670	1270	.00310		1.384	0.54	0.97	22
NO GRID			X_{LE}=0.76m			NO HEATING WIRES AT LEADING EDGE								
12		-	28.4	4.60	3.31	16.43	3620	1200	.00310	.00307	1.389	0.56	0.98	25
NO GRID			X_{LE}=2.06m			NO HEATING WIRES AT LEADING EDGE								
4		-	13.0	2.16	1.49	16.20	1600	603	.00375	.00371	1.442	0.45	0.94	1
4		-	12.8	2.15	1.49	16.20	1590	591	.00375		1.443			17
8		-	21.5	3.57	2.52	16.22	2700	928	.00326	.00326	1.414	0.56	0.96	4
12		-	29.9	4.74	3.41	16.32	3660	1260	.00307	.00306	1.390	0.56	0.95	8
16		-	38.8	5.91	4.31	16.11	4710	1630	.00294	.00293	1.371	0.56	0.96	10
NO GRID			X_{LE}=0.30m			UNHEATED WIRES AT LEADING EDGE								
6		-	22.7	3.87	2.72	16.17	2870	953	.00316		1.424	0.64	0.98	39
14		-	38.7	5.89	4.30	16.60	4680	1620	.00296		1.368	0.55	0.98	40
7.6cm GRID			X_{LE}=0.30m			NO HEATING WIRES AT LEADING EDGE								

TABLE 3.3 Boundary layer mean flow and free-stream turbulence parameters; no-grid and square mesh, square bar biplane grids

TABLE 3.3 cont'd

STN	u'/U_e	L_e^u/δ_{995}	δ_{995}	δ^*	θ	U_e	Re_θ	$\frac{u_\tau \delta_{995}}{\nu}$	$C_f(1)$	$C_f(2)$	H	$\frac{k\Delta U}{2u_\tau}$	$y_{\Delta U}/\delta_{995}$	PROFILE NUMBER
4	.0597	1.16	27.4	2.19	1.68	16.12	1810	1380	.00434	.00436	1.300	0	0.15	19
8	.0399	1.03	39.2	3.51	2.72	16.21	2930	1830	.00377	.00377	1.291	0.04	0.34	20
12	.0307	0.93	50.9	4.71	3.66	16.45	3990	2310	.00347	.00346	1.285	0.08	0.47	21
16	.0255	0.90	58.9	5.86	4.54	16.68	4940	2580	.00323	.00321	1.291	0.16	0.58	24
7.6cm GRID			X_{LE}=0.30m			UNHEATED WIRES AT LEADING EDGE								
6	.0482	0.77	46.7	3.71	2.95	16.16	3140	2190	.00388		1.260	0	0.10	34
8	.0399	0.71	56.9	4.38	3.48	16.26	3710	2600	.00368		1.260	0.02	0.20	35
16	.0255	0.67	78.4	6.62	5.23	16.75	5760	3480	.00325		1.264	0.08	0.42	36
7.6cm GRID			X_{LE}=2.06m			NO HEATING WIRES AT LEADING EDGE								
4	.0262	3.51	14.8	2.18	1.54	16.29	1640	688	.00382	.00384	1.418	0.34	0.88	2
8	.0224	2.31	24.7	3.55	2.57	16.30	2740	1080	.00339	.00340	1.382	0.41	0.90	5
12	.0197	1.75	35.2	4.74	3.48	16.41	3710	1500	.00319	.00320	1.361	0.41	0.85	9
16	.0181	1.48	43.8	5.83	4.34	16.23	4721	1870	.00307	.00308	1.342	0.39	0.87	11
7.6cm GRID			X_{LE}= 2.06m			UNHEATED WIRES AT LEADING EDGE								
6	.0240	1.88	29.1	3.81	2.81	16.19	2980	1280	.00344		1.357	0.30	0.84	33

TABLE 3.3 cont'd

STN	u'/U_e	L_e^u/δ_{995}	δ_{995}	δ^*	θ	U_e	Re_θ	$\frac{u_\tau \delta_{995}}{\nu}$	$C_f(i)$	$C_f(2)$	H	$\frac{k\Delta U}{2u_\tau}$	$y_{\Delta U}/\delta_{995}$	PROFILE NUMBER
15.2cm	GRID		X_{LE}=0.76m			NO HEATING WIRES AT LEADING EDGE								
12	.0525	1.48	59.0	4.38	3.48	16.93	3780	2740	.00365		1.261	0.02	0.25	26
15.2cm	GRID		X_{LE}=0.76m			UNHEATED WIRES AT LEADING EDGE								
10	.0575	1.34	66.0	4.54	3.66	16.12	3860	3390	.00376		1.240	0	0.10	38
15.2cm	GRID		X_{LE}=1.37m			UNHEATED WIRES AT LEADING EDGE								
6	.0575	1.83	48.1	3.74	2.94	16.12	3100	2220	.00382		1.273	0	0.10	37
15.2cm	GRID		X_{LE}=2.06m			NO HEATING WIRES AT LEADING EDGE								
4	.0514	4.89	19.3	2.19	1.59	16.49	1640	895	.00404		1.378	0.17	0.68	3
4	.0514	4.94	19.1	2.22	1.63	16.57	1730	910	.00403		1.366			15
8	.0442	3.28	31.5	3.49	2.62	16.55	2770	1410	.00360		1.334	0.18	0.62	6
12	.0387	2.53	44.3	4.73	3.62	16.78	3850	1940	.00340		1.307	0.17	0.65	7
16	.0345	2.15	55.9	5.55	4.30	16.40	4650	2460	.00330		1.291	0.13	0.61	12
15.2cm	GRID		X_{LE}=2.06m			UNHEATED WIRES AT LEADING EDGE								
6	.0468	2.72	36.7	3.77	2.88	15.92	3030	1650	.00364		1.310	0.14	0.56	27
8	.0442	2.23	46.4	4.55	3.54	15.95	3750	2060	.00352		1.286	0.10	0.54	28
10	.0410	1.90	56.8	5.27	4.09	16.02	4320	2470	.00339		1.286	0.10	0.53	29

TABLE 3.3 cont'd

STN	u'/U_e	L_e^u/δ_{995}	δ_{995}	δ^*	θ	U_e	Re_θ	$\frac{u_\tau \delta_{995}}{\nu}$	$C_f^{(1)}$	$C_f^{(2)}$	H	$\frac{k\Delta U}{2u_\tau}$	$y_{\Delta U}/\delta_{995}$	PROFILE NUMBER
12	.0387	1.70	65.7	5.83	4.57	16.09	4790	2820	.00334		1.278	0.09	0.47	30
14	.0362	1.69	68.9	6.23	4.88	16.01	5240	2990	.00326		1.276	0.10	0.52	31
16	.0345	1.55	77.5	6.98	5.48	16.13	5850	3300	.00318		1.274	0.13	0.47	32

$C_f^{(1)}$ FROM LOG-LAW FIT

$C_f^{(2)}$ FROM PRESTON TUBE

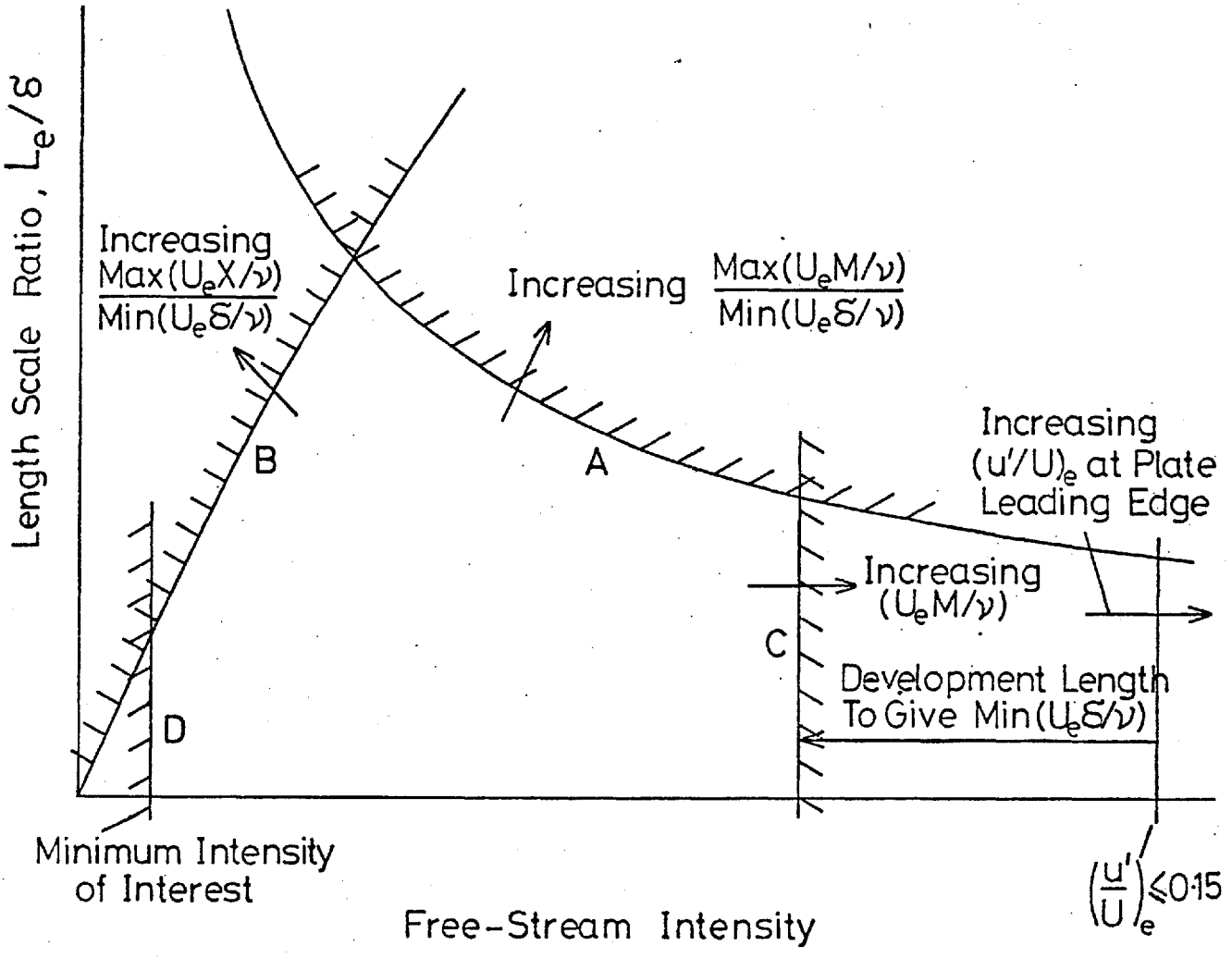

Fig. 3.1 Illustration of the constraints of wind tunnel and boundary layer Reynolds numbers, and free-stream intensity, on the usable range of free-stream intensity and length scale ratio.

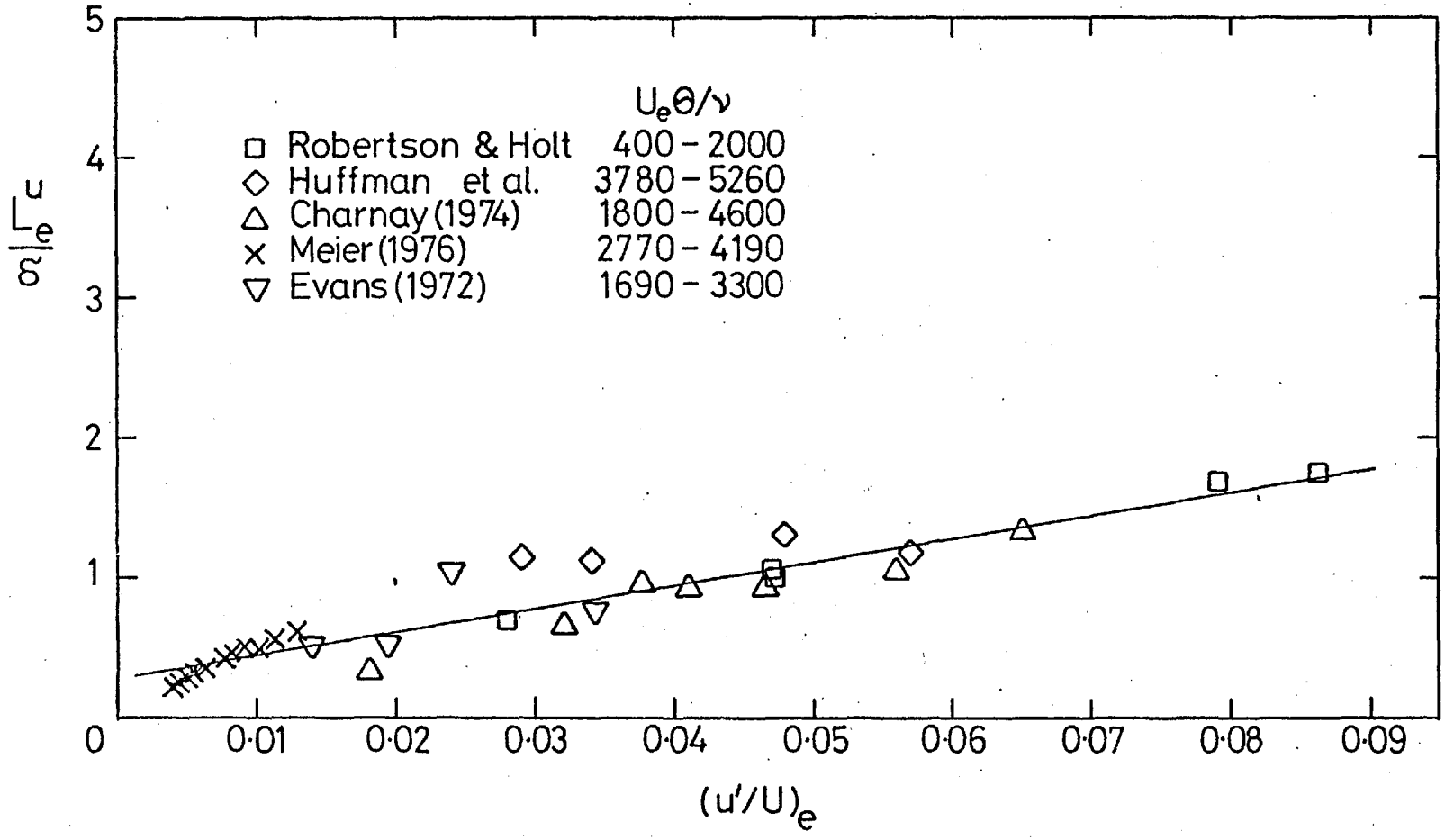

Fig. 3.2 Free-stream intensities and length-scale ratios used by some previous workers.

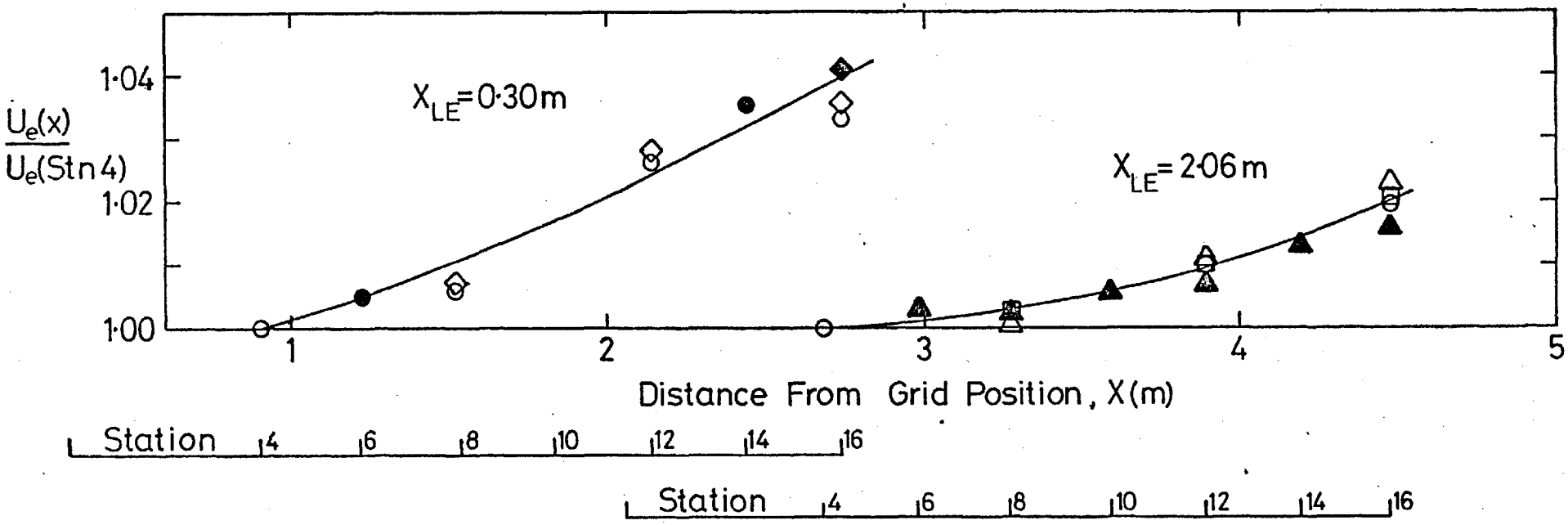

o No Grid ; ◇,□ 7·6cm Grid ; △ 15·2cm Grid. Open Symbols – No Heating Wires At Leading Edge. Closed Symbols – (Unheated) Heating Wires At Leading Edge.

Fig. 3.3 Variation of free-stream mean velocity along the plate for the plate in two positions in working section.

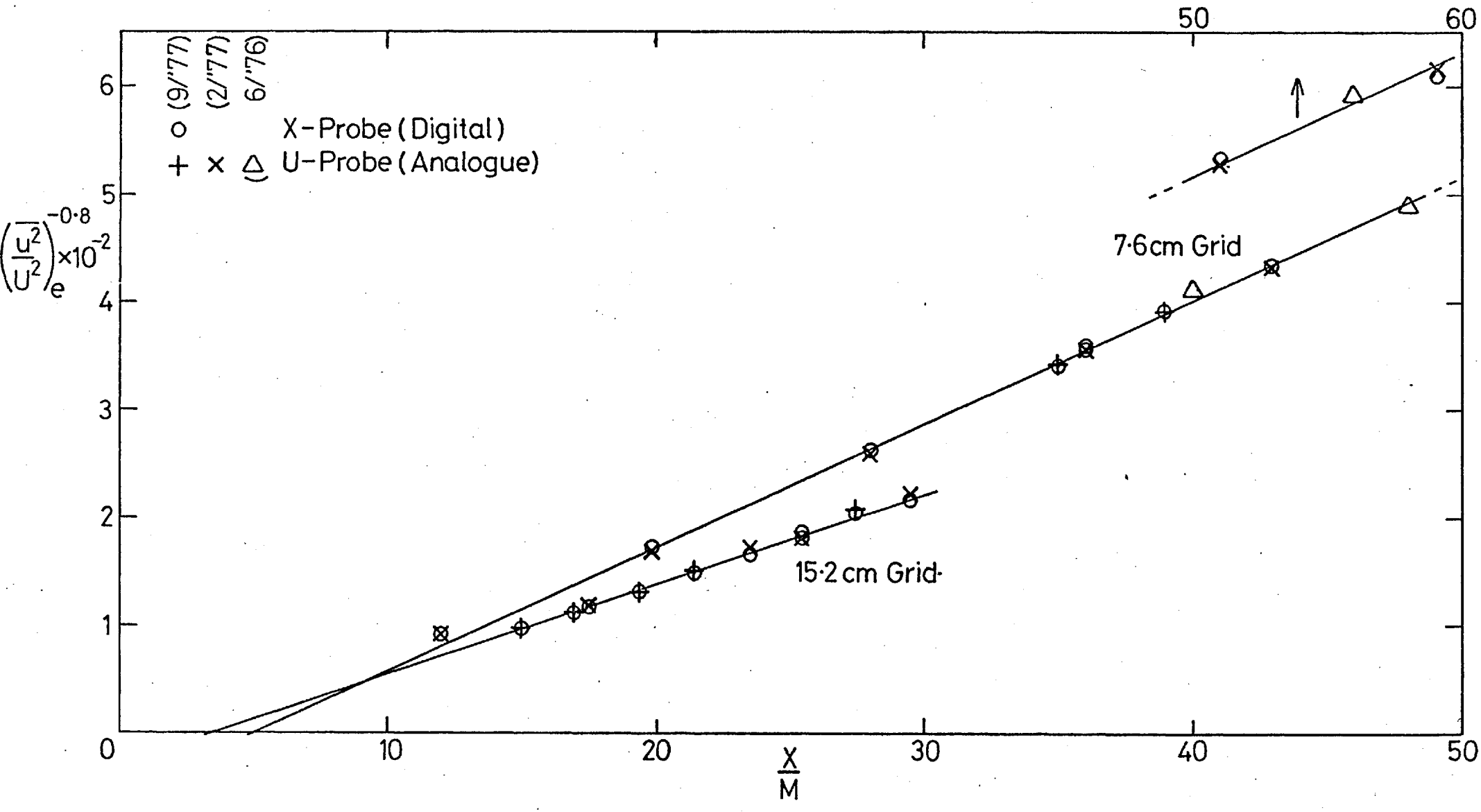

Fig. 3.4 Decay laws for the 7.6 cm and 15.2 cm turbulence grids.

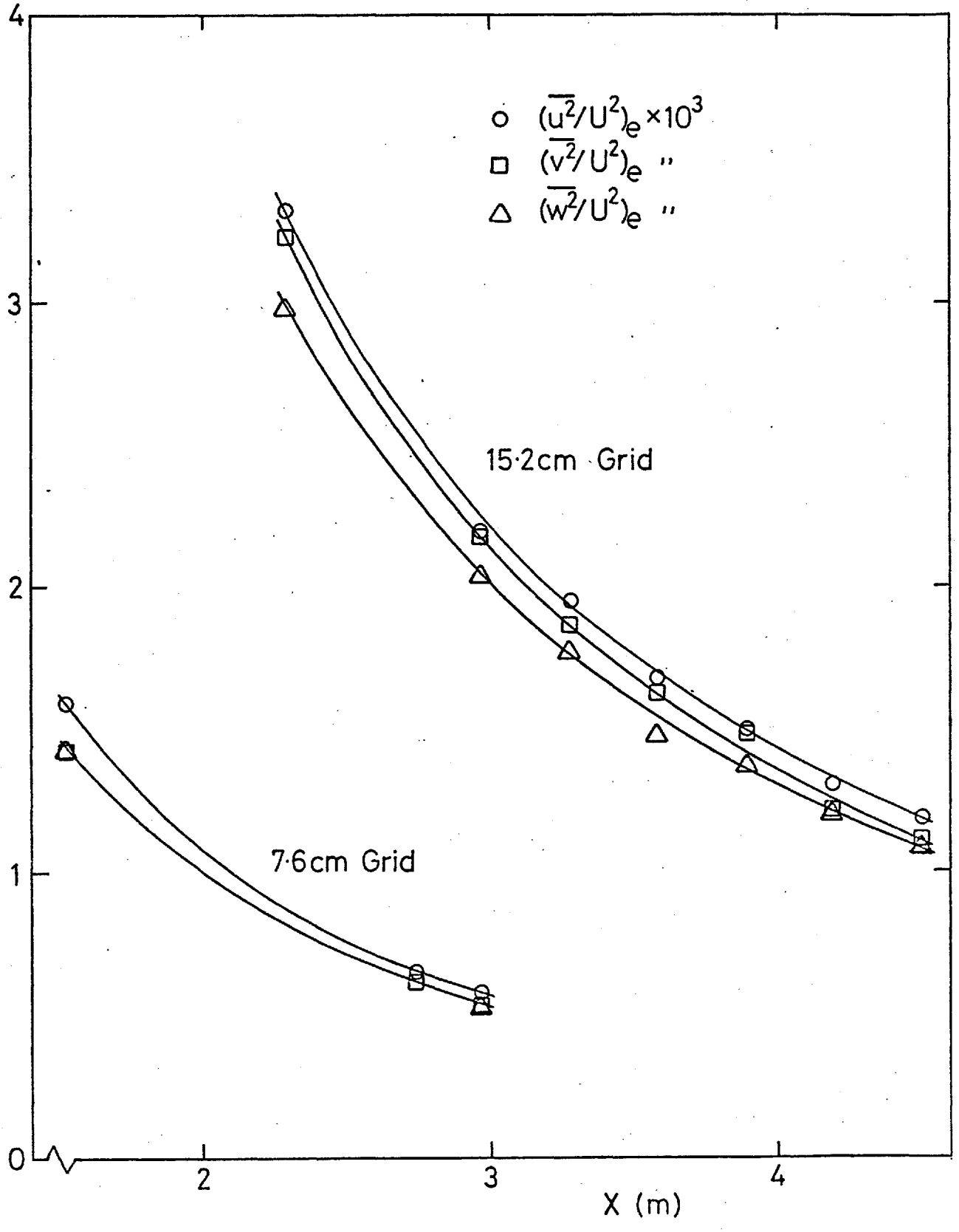

Fig. 3.5 Contributions to $\overline{q_e^2}$ from $\overline{u_e^2}$, $\overline{v_e^2}$ and $\overline{w_e^2}$.

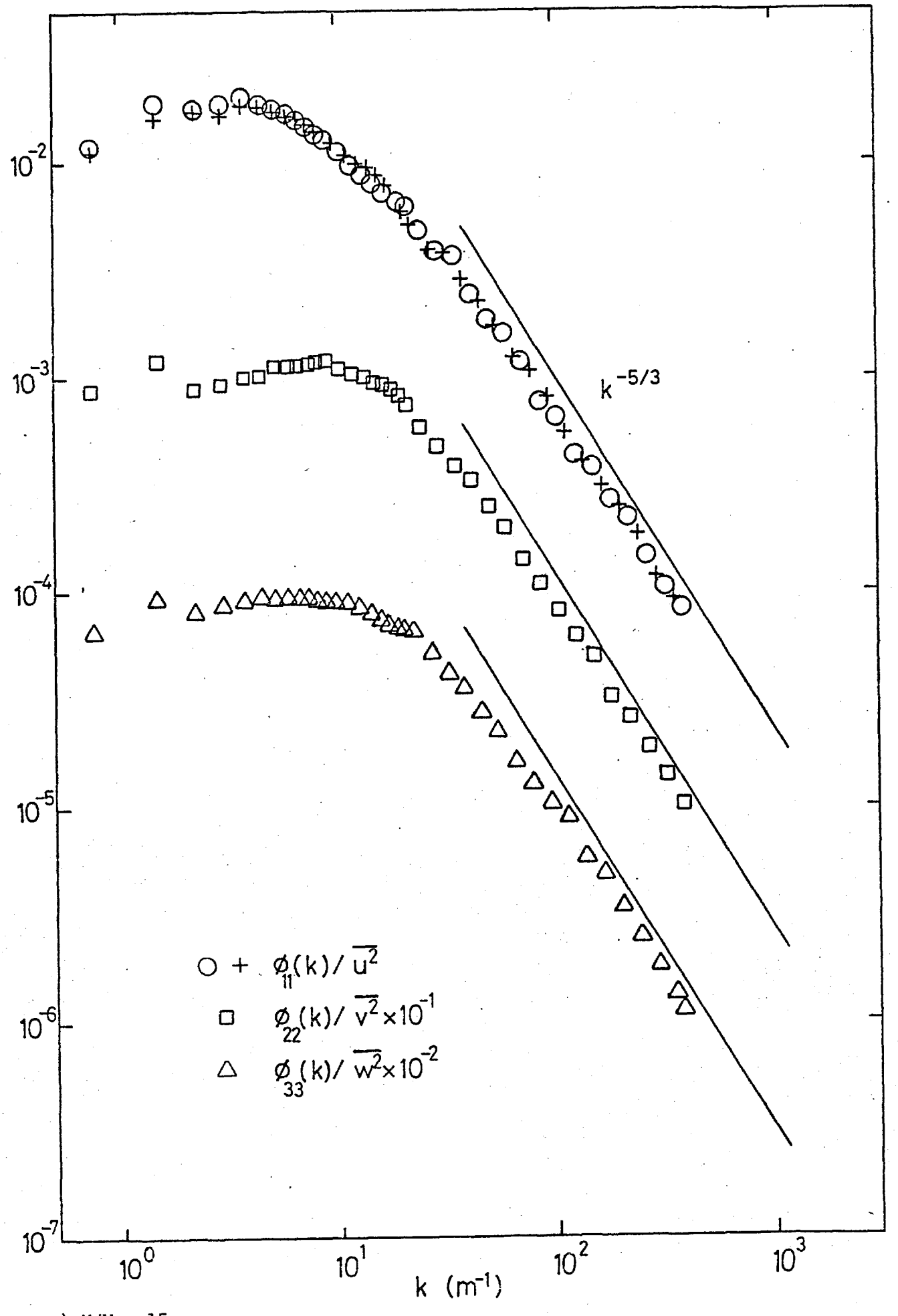

a) X/M = 15.

Fig. 3.6 Free-stream spectra, M = 15.2 cm:

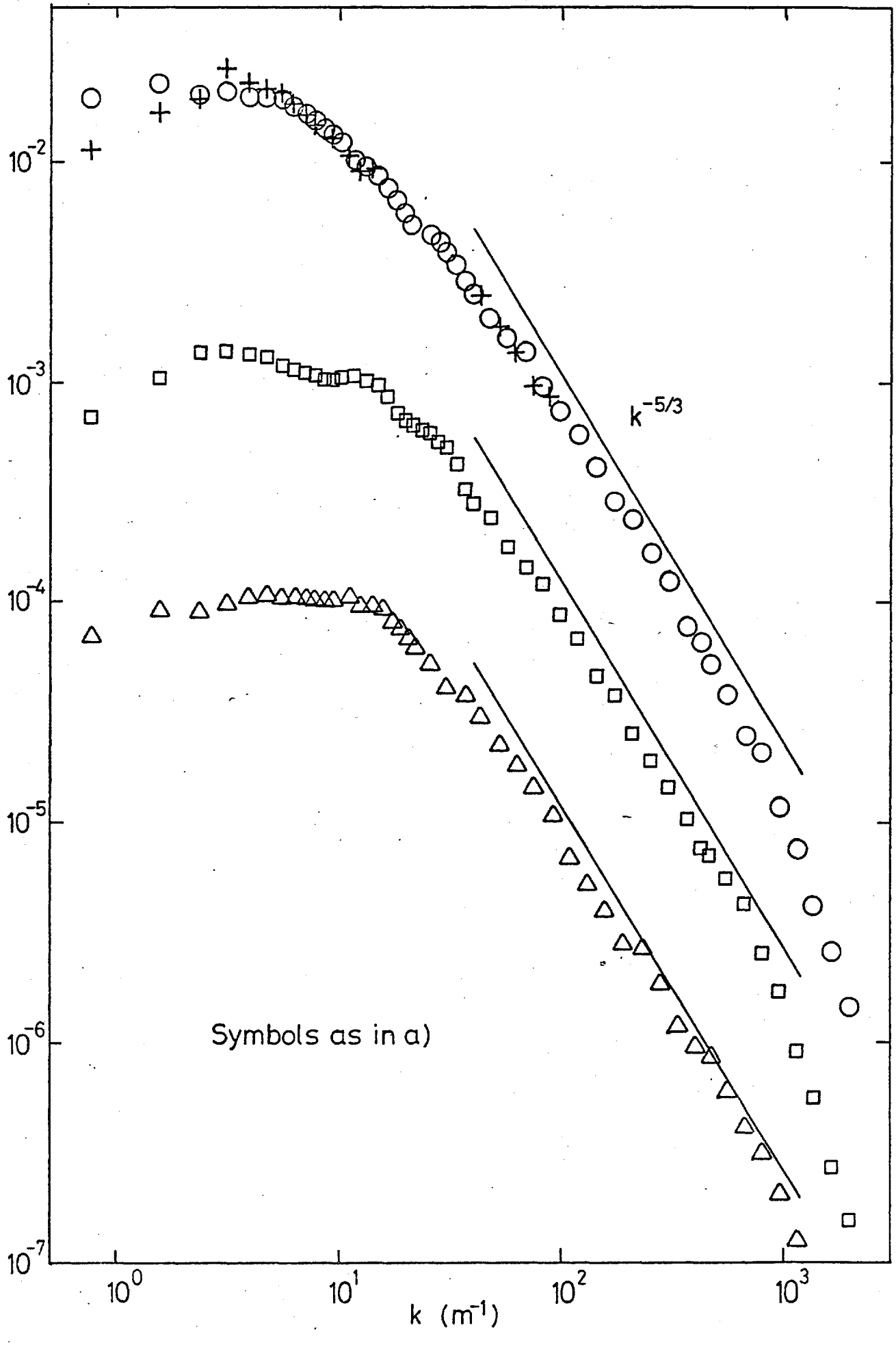

Fig. 3.6b, X/M = 19.5.

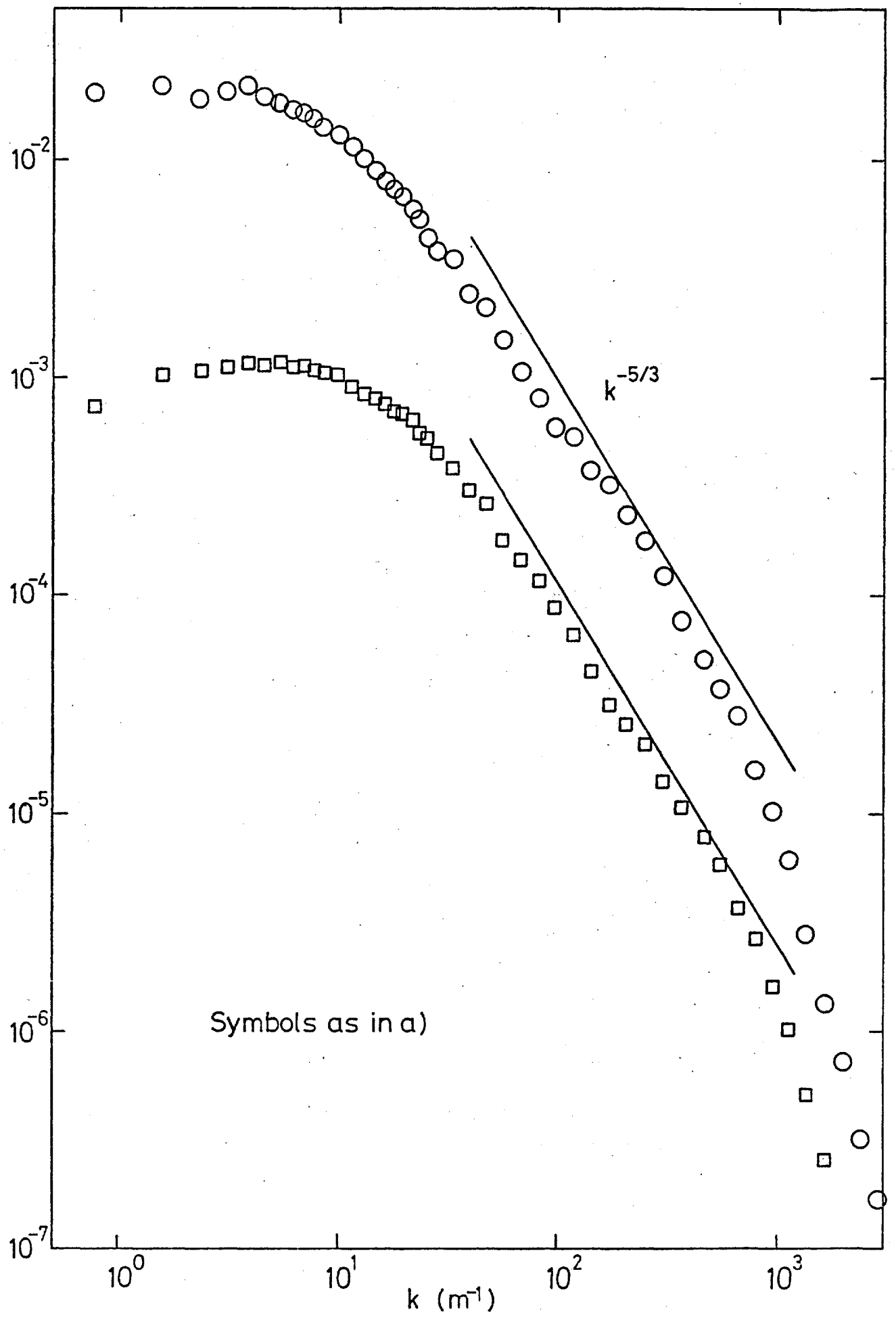

Fig. 3.6c, X/M = 21.5.

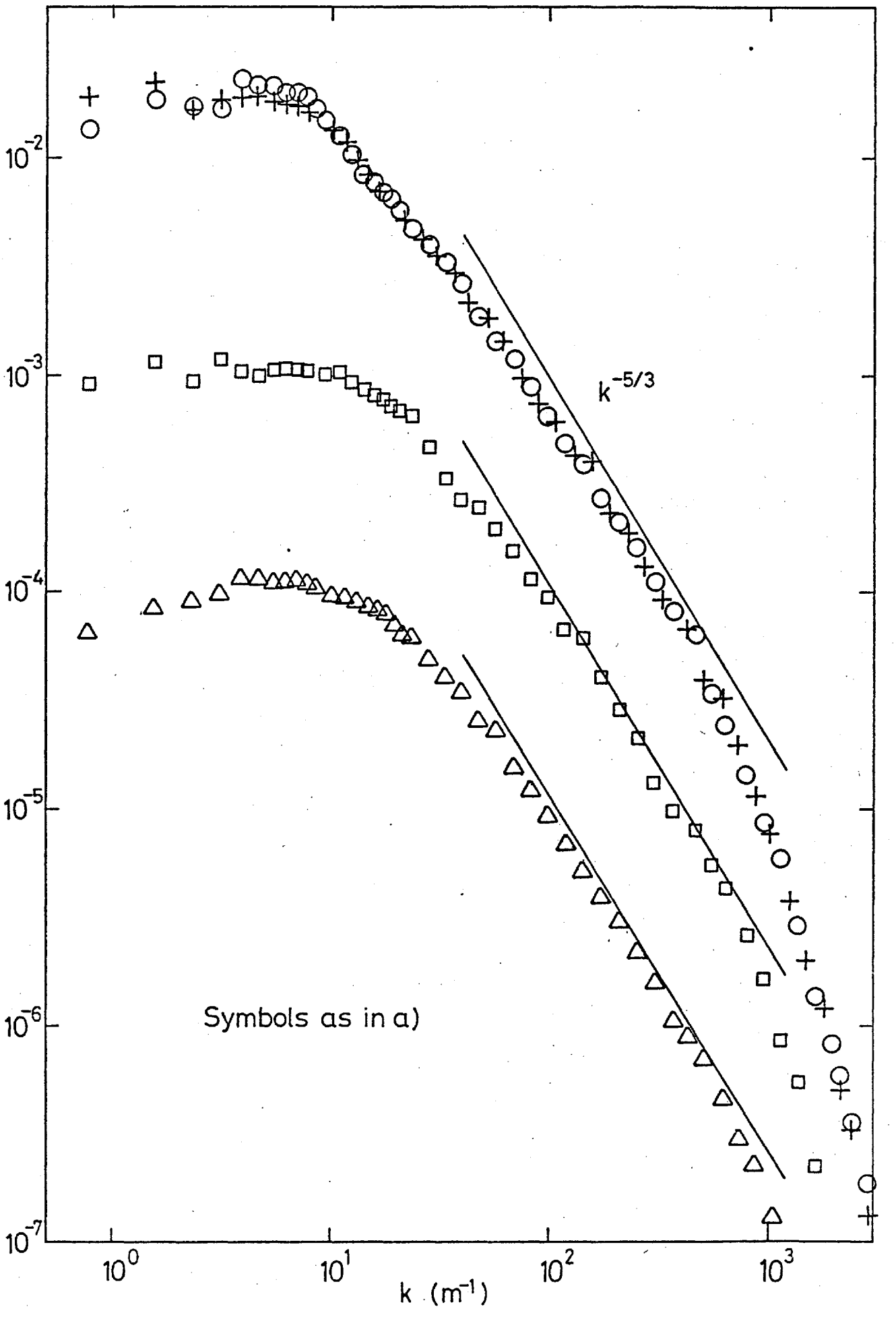

Fig. 3.6d, X/M = 23.5.

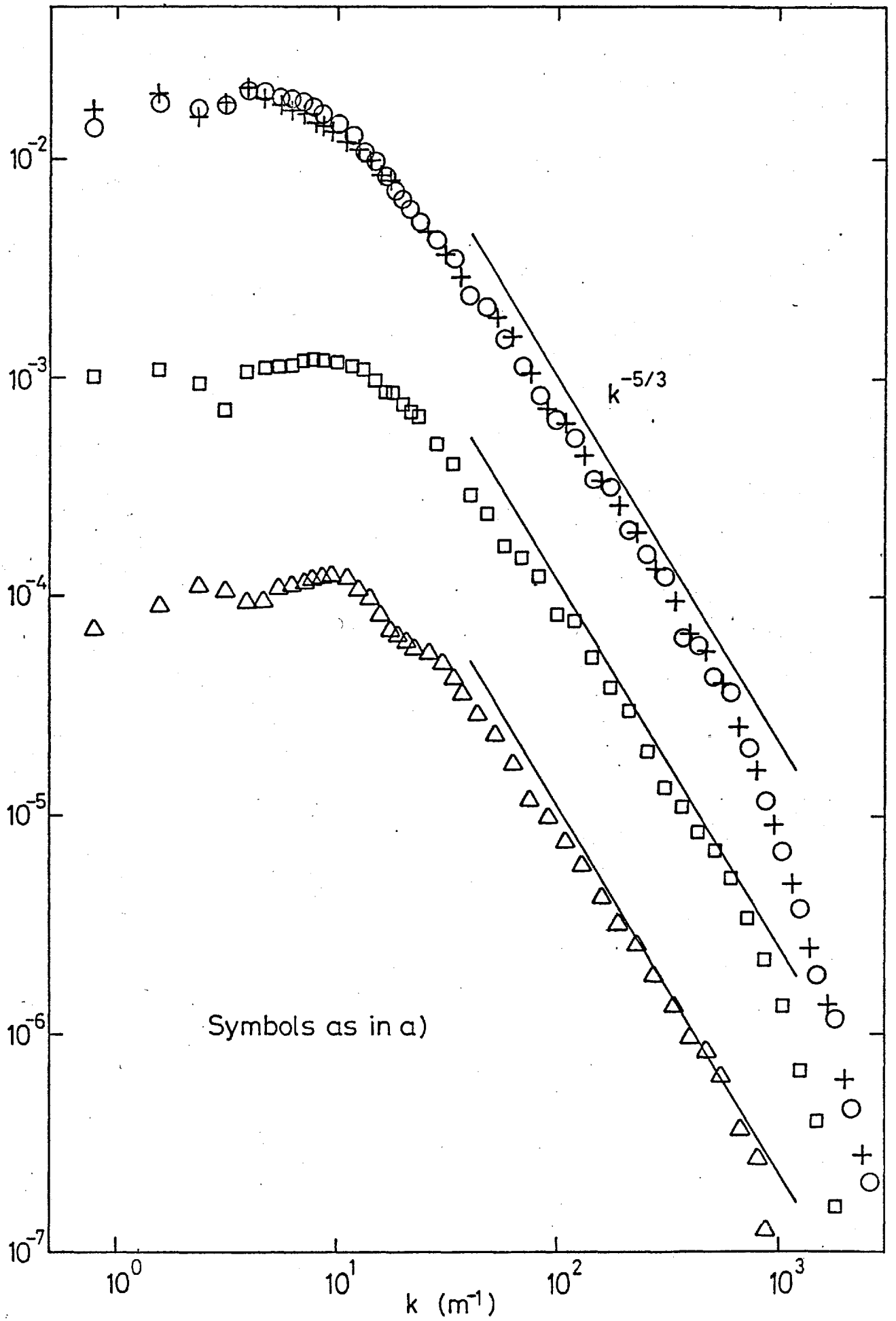

Fig. 3.6e, X/M = 25.5.

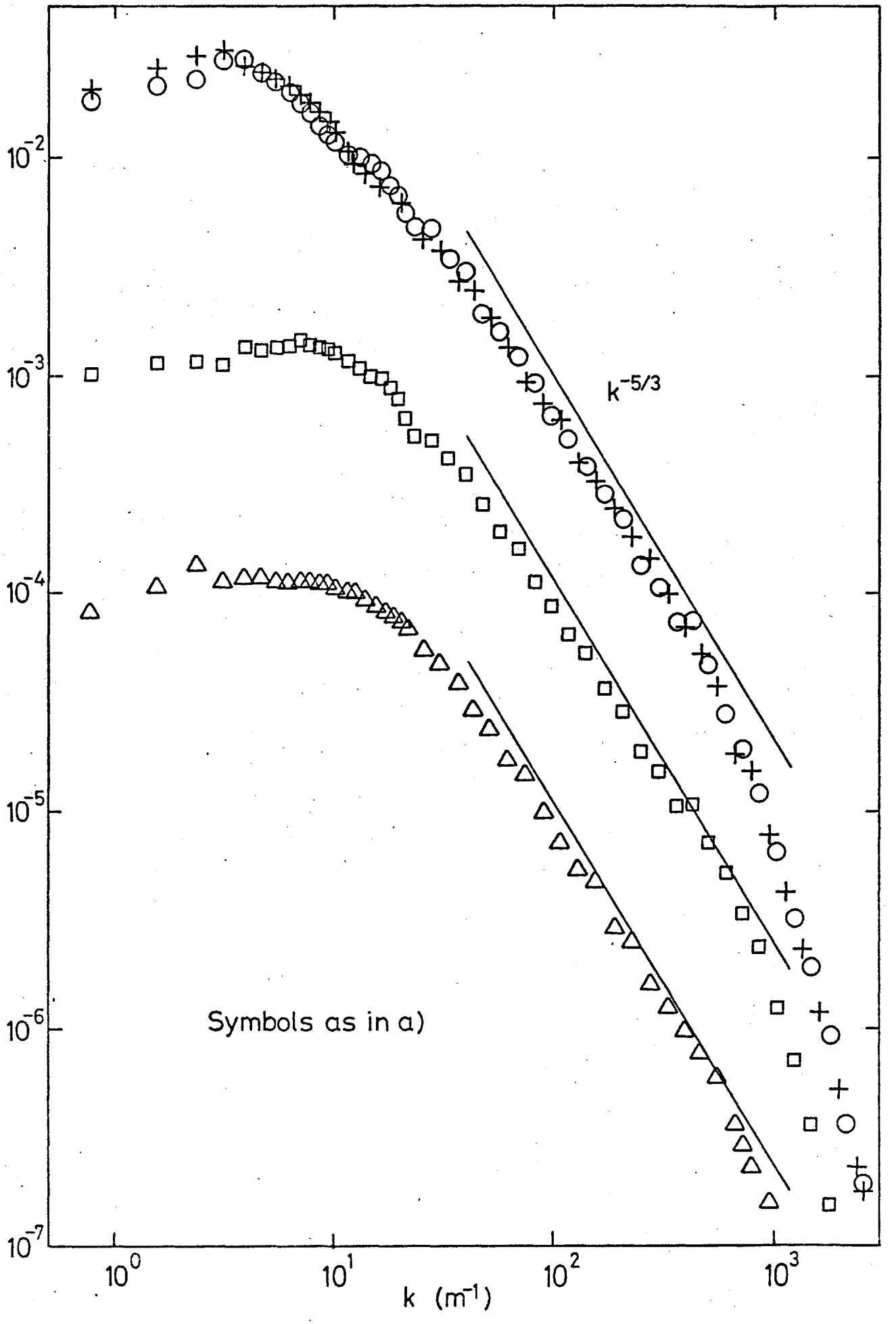

Fig. 3.6f, X/M = 27.5.

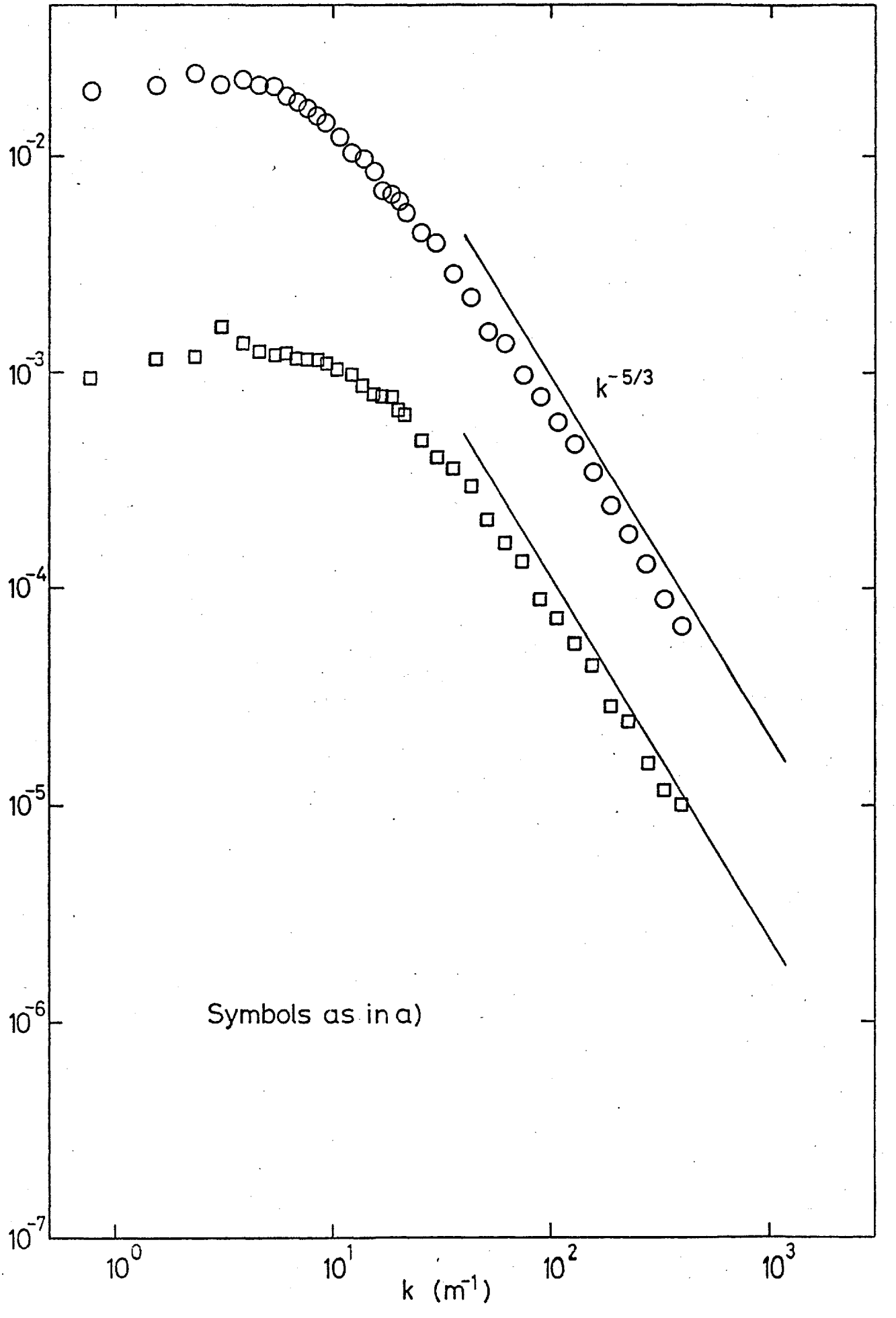

Fig. 3.6g, X/M = 29.5.

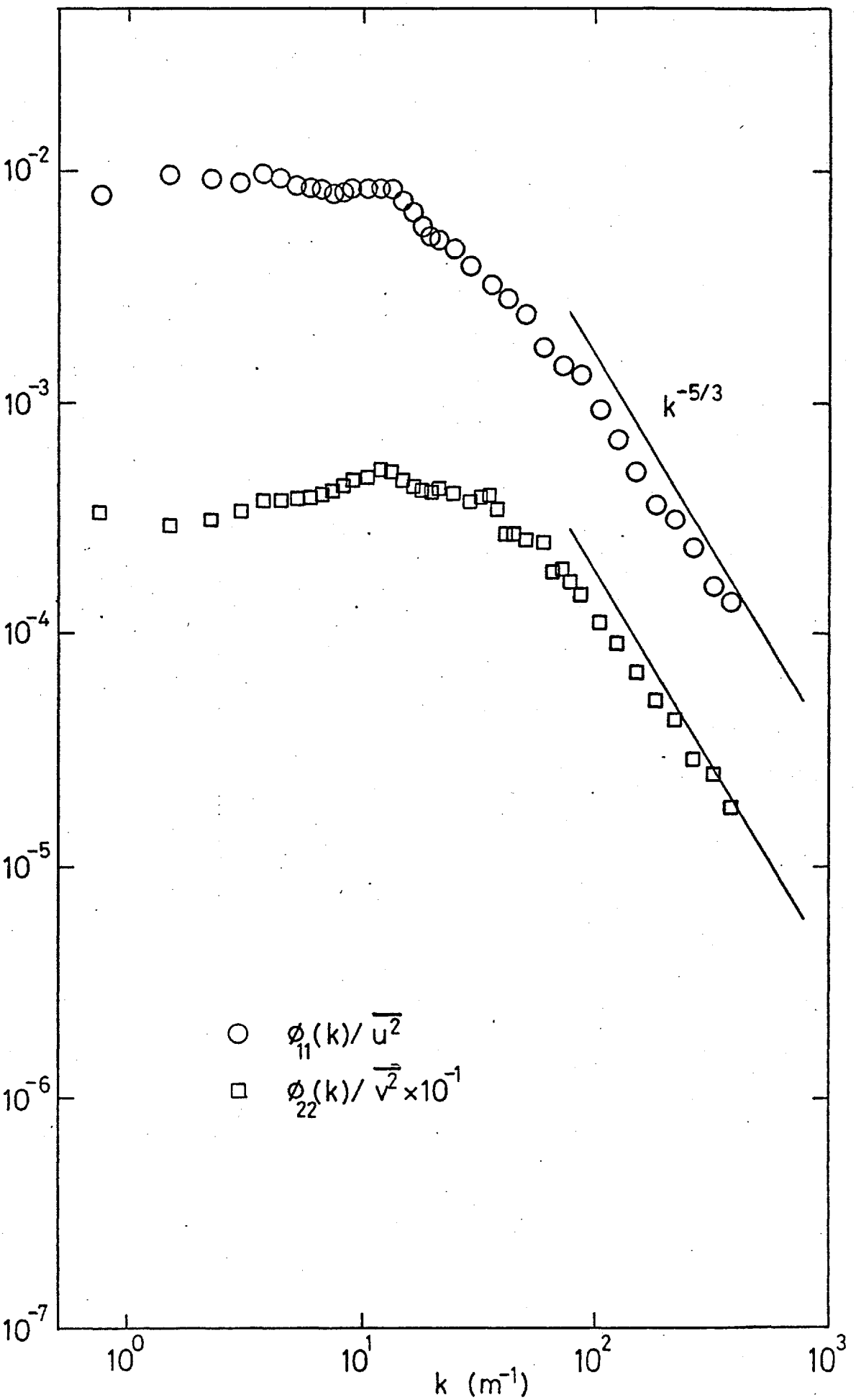

a) X/M = 20.

Fig. 3.7 Free-stream spectra, M = 7.6 cm:

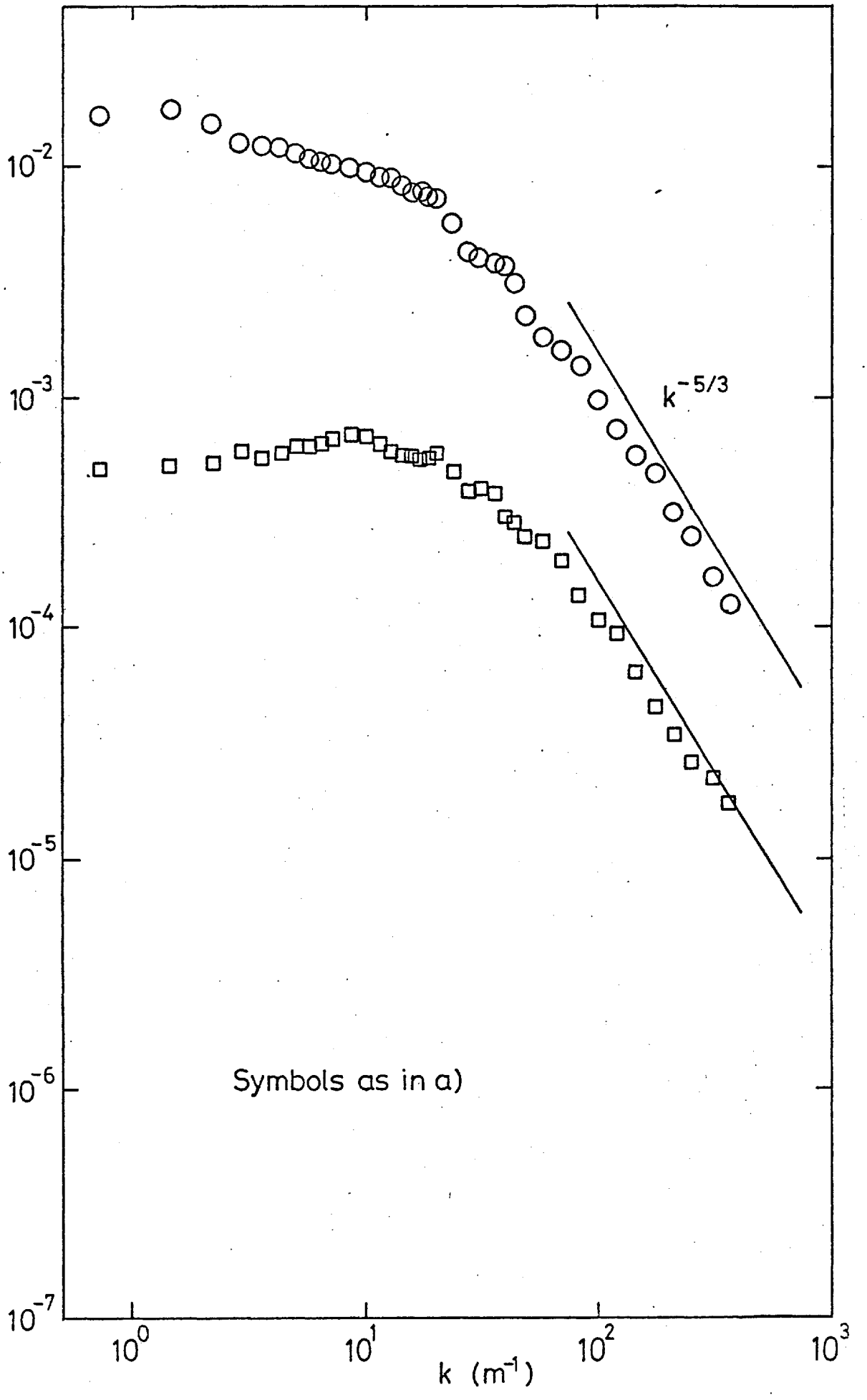

Fig. 3.7b, X/M = 36.

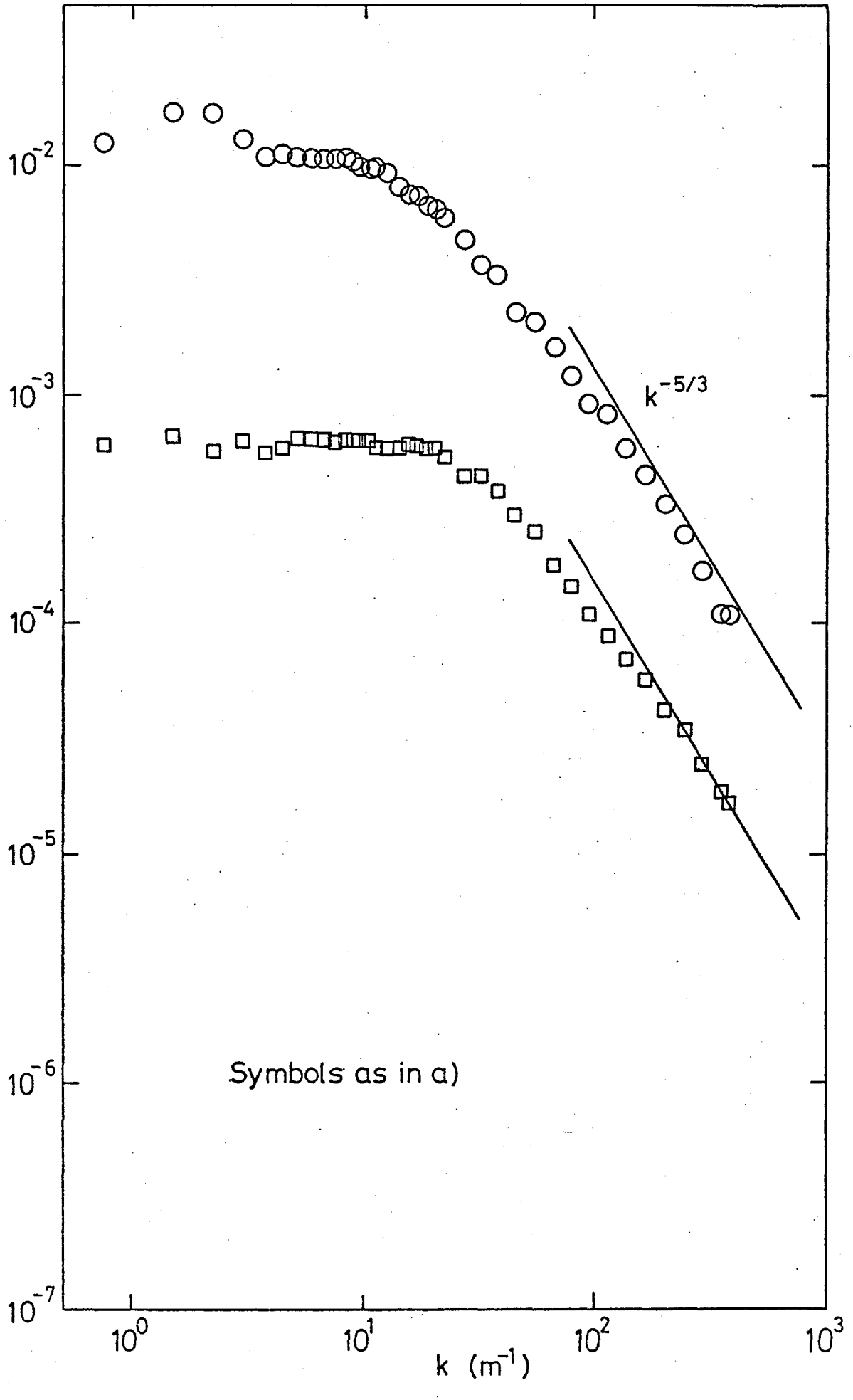

Fig. 3.7c, X/M = 39.0.

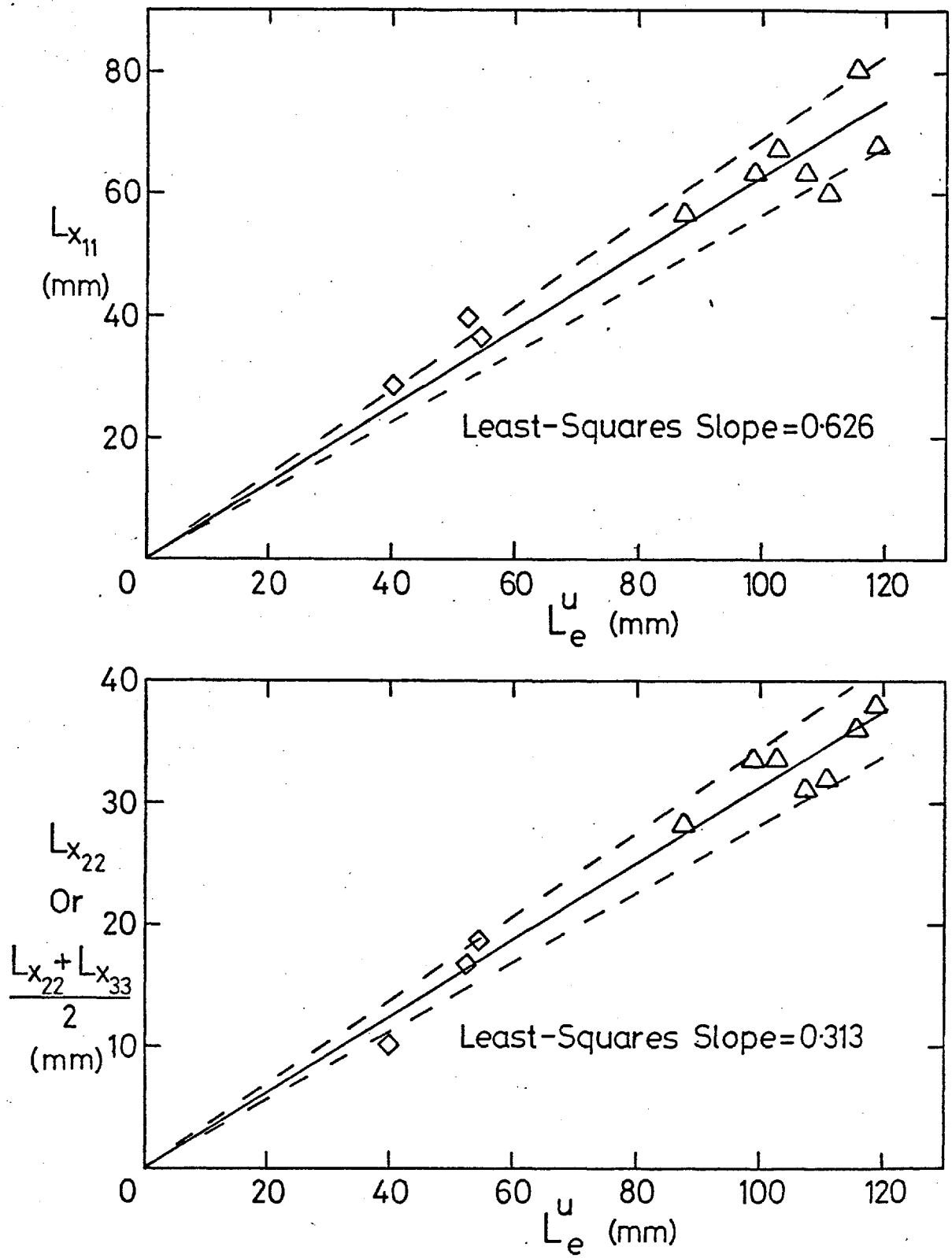

Fig. 3.8 Integral length scales $L_{x_{11}}$, $L_{x_{22}}$ and $L_{x_{33}}$ plotted against the dissipation length scale L_e^u.

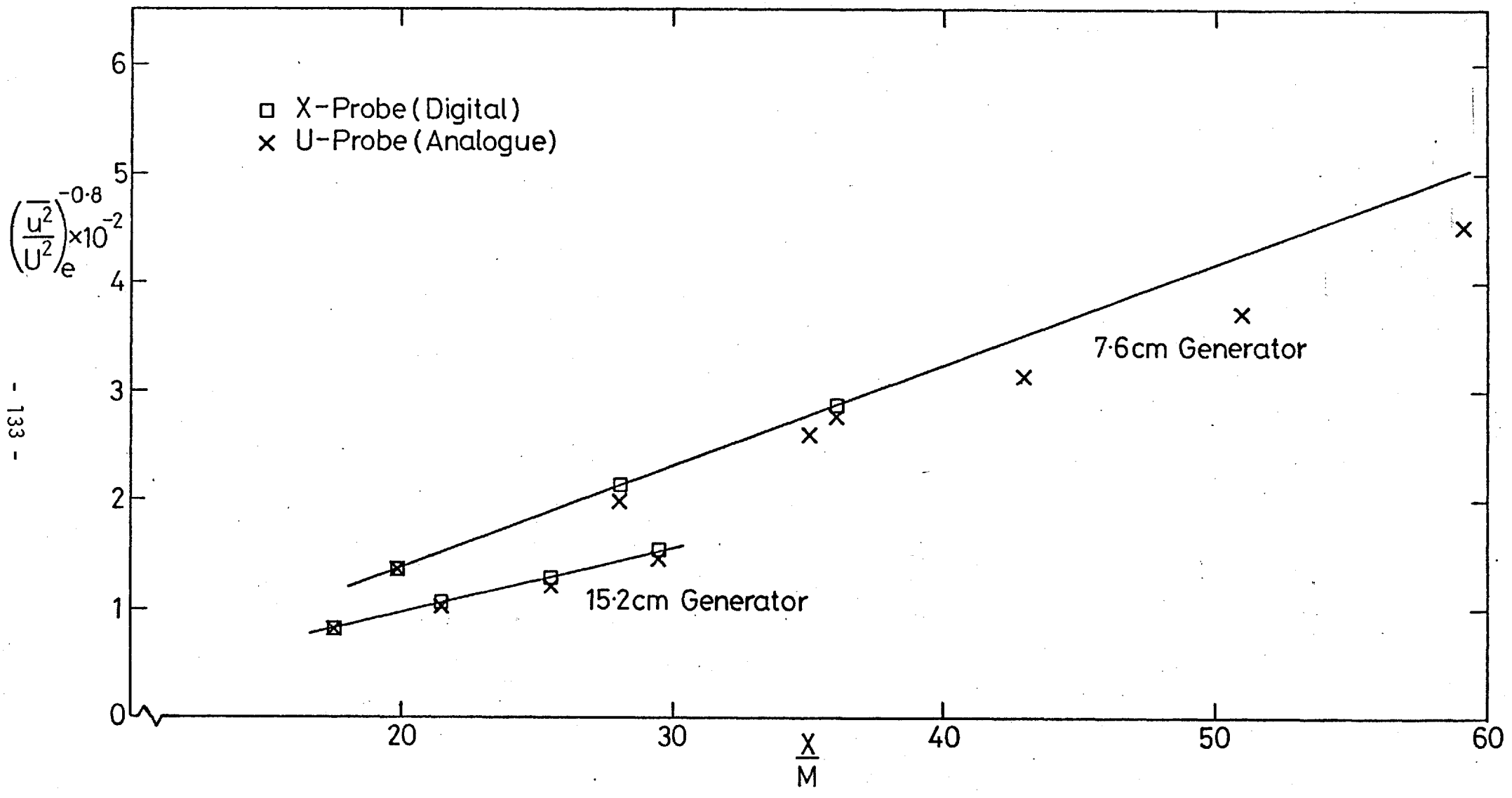

Fig. 3.9 Decay laws for the 7.6 cm and 15.2 cm turbulence generators (single rows of square bars).

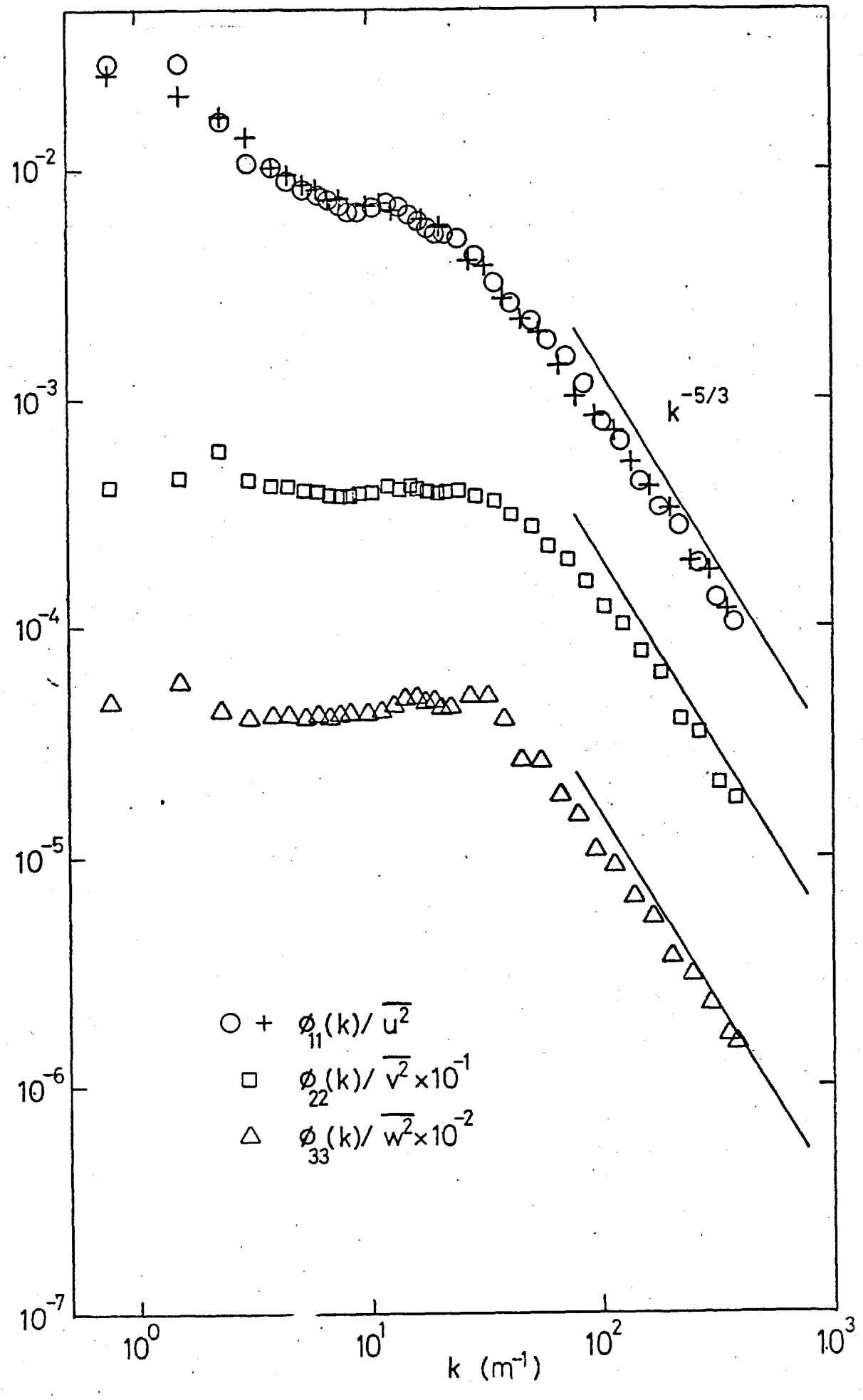

Fig. 3.10 Free-stream spectra, single row of square bars spaced 7.6 cm, X/M = 19.

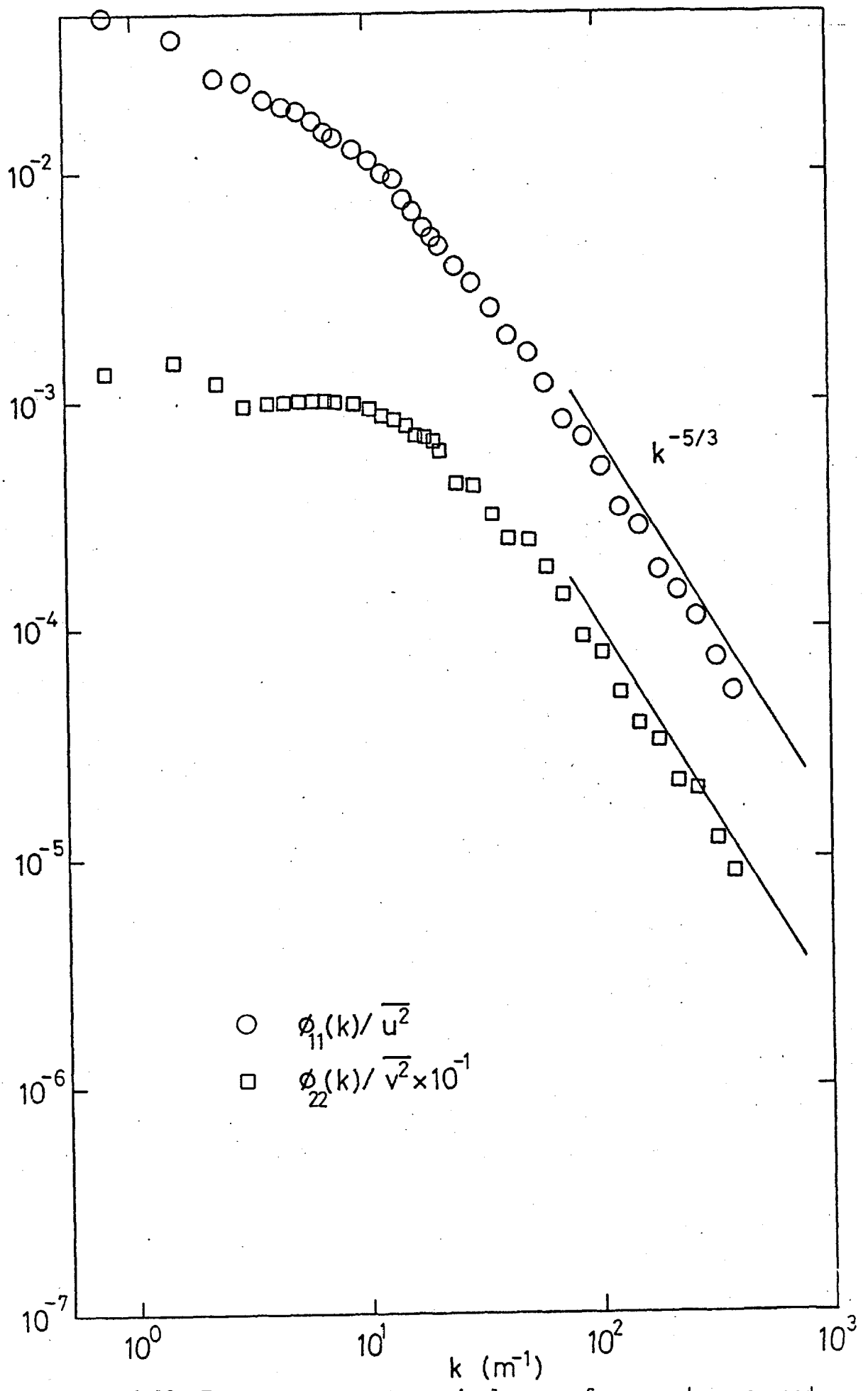

Fig. 3.11 Free-stream spectra, single row of square bars spaced 15.2 cm, X/M = 29.5.

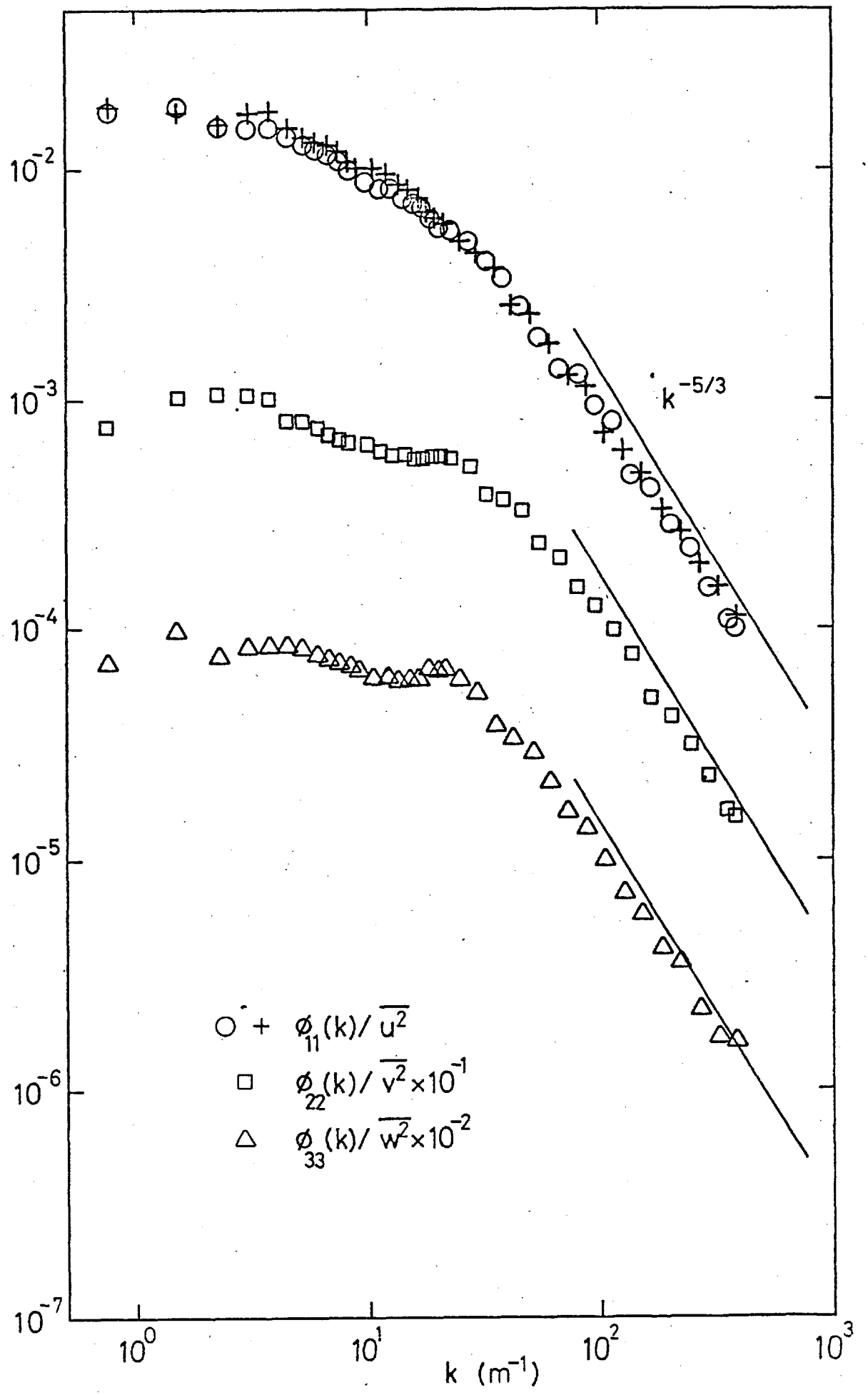

Fig. 3.12 Free-stream spectra, single row of round bars spaced 11.4 cm, X/M = 20.

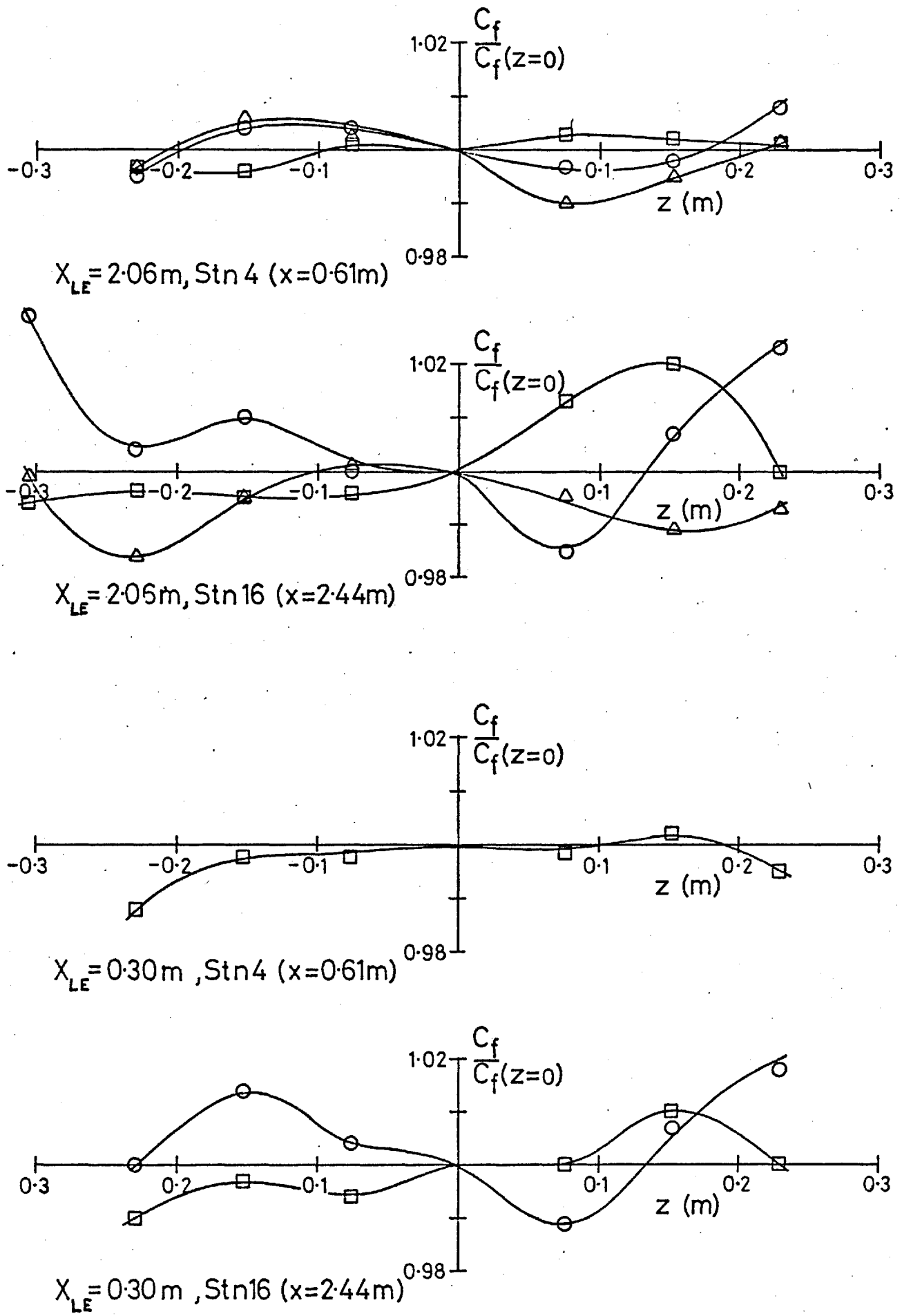

○, No Grid ; □, 7·6cm Grid; △, 15·2cm Grid. (Side Walls at ± 0·46)

Fig. 3.13 Variation of C_f with distance from plate centre line.

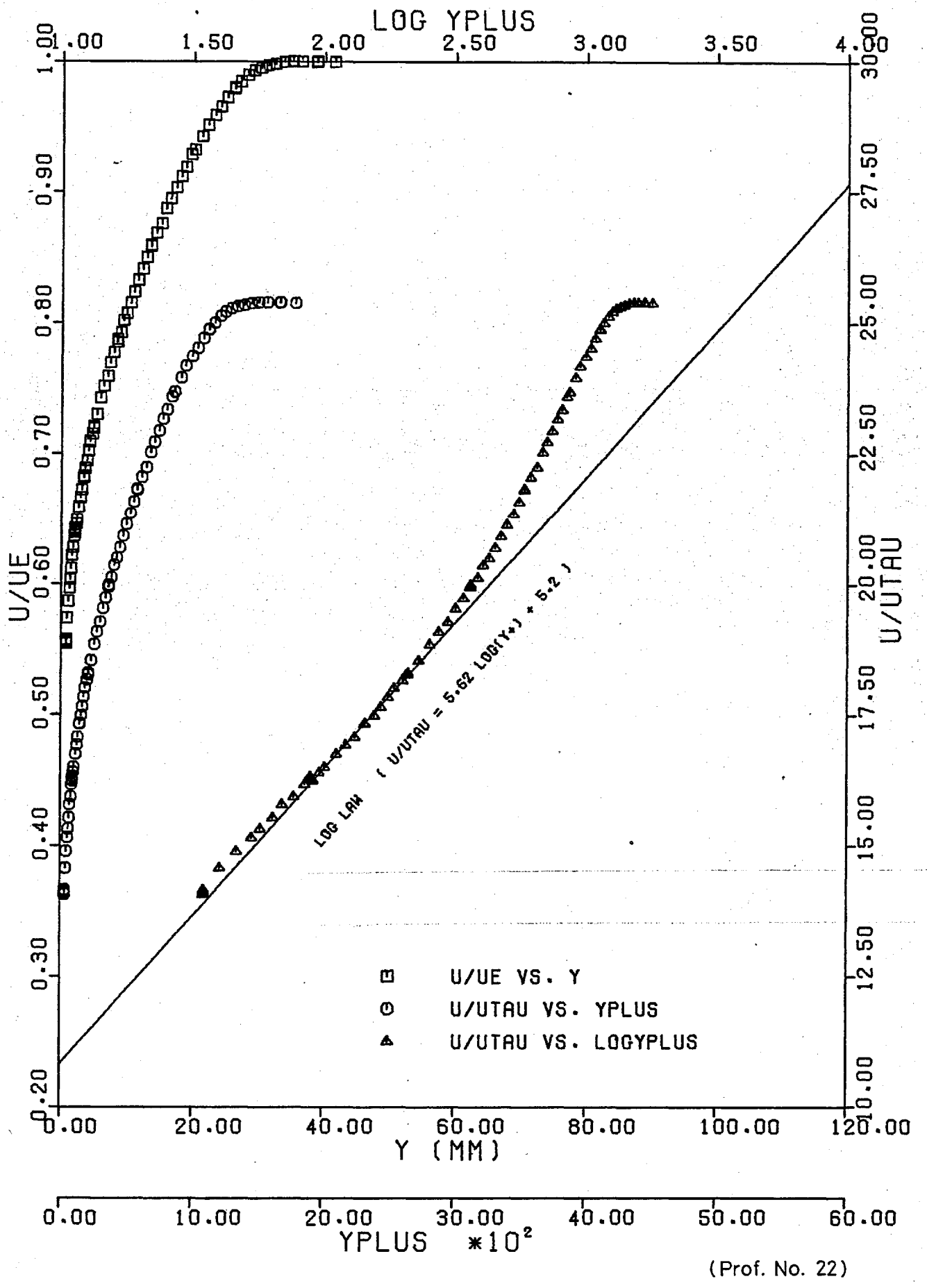

Fig. 3.14. Velocity Profile. No Grid, X_{LE} = 0·30m, Stn 12.

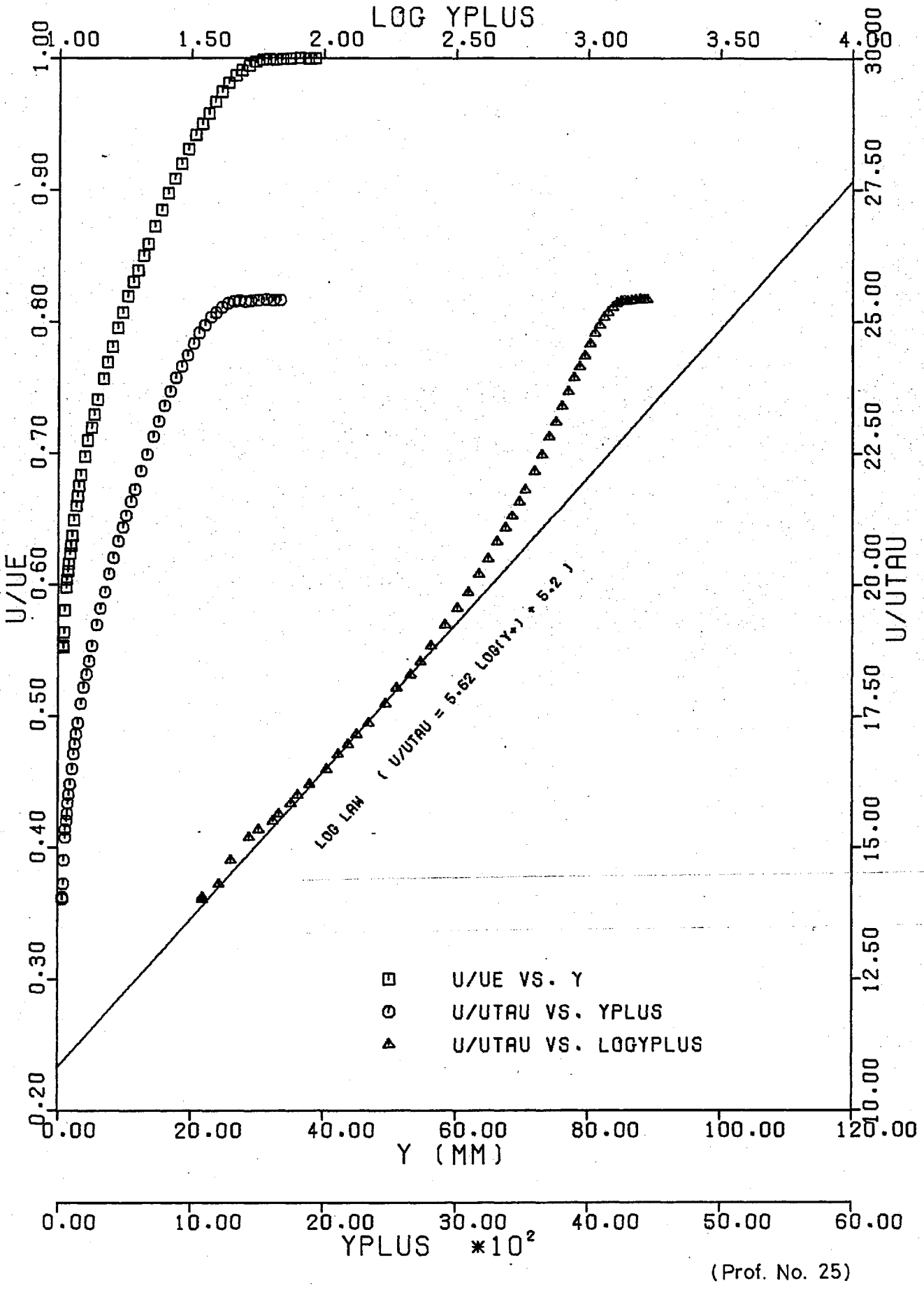

Fig. 3.15. Velocity Profile. No Grid, X_{LE} = 0·76 m, Stn 12.

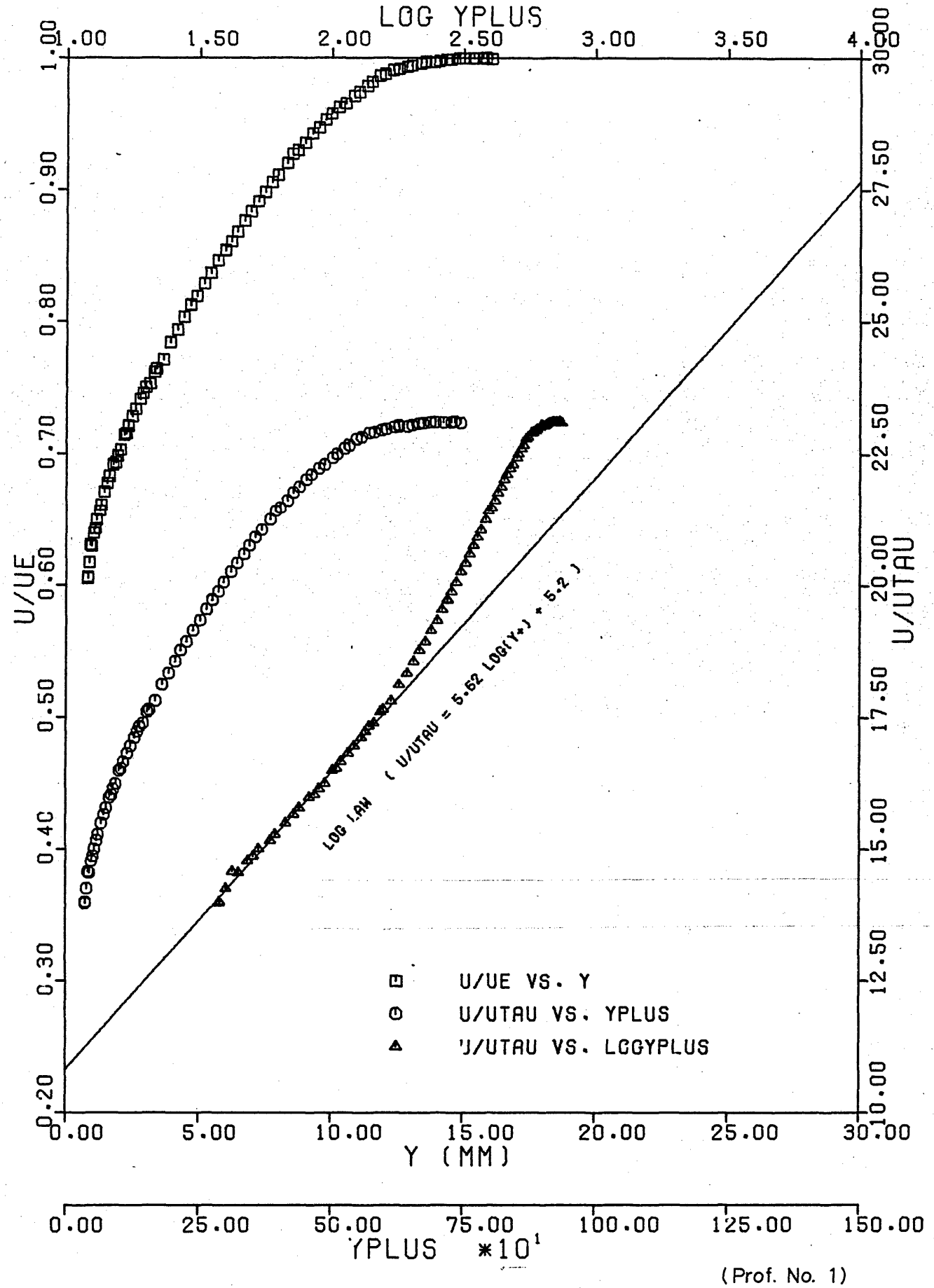

(Prof. No. 1)

a) Stn 4

Fig. 3.16. Velocity Profiles. No Grid, $X_{LE} = 2{\cdot}06\,m$;

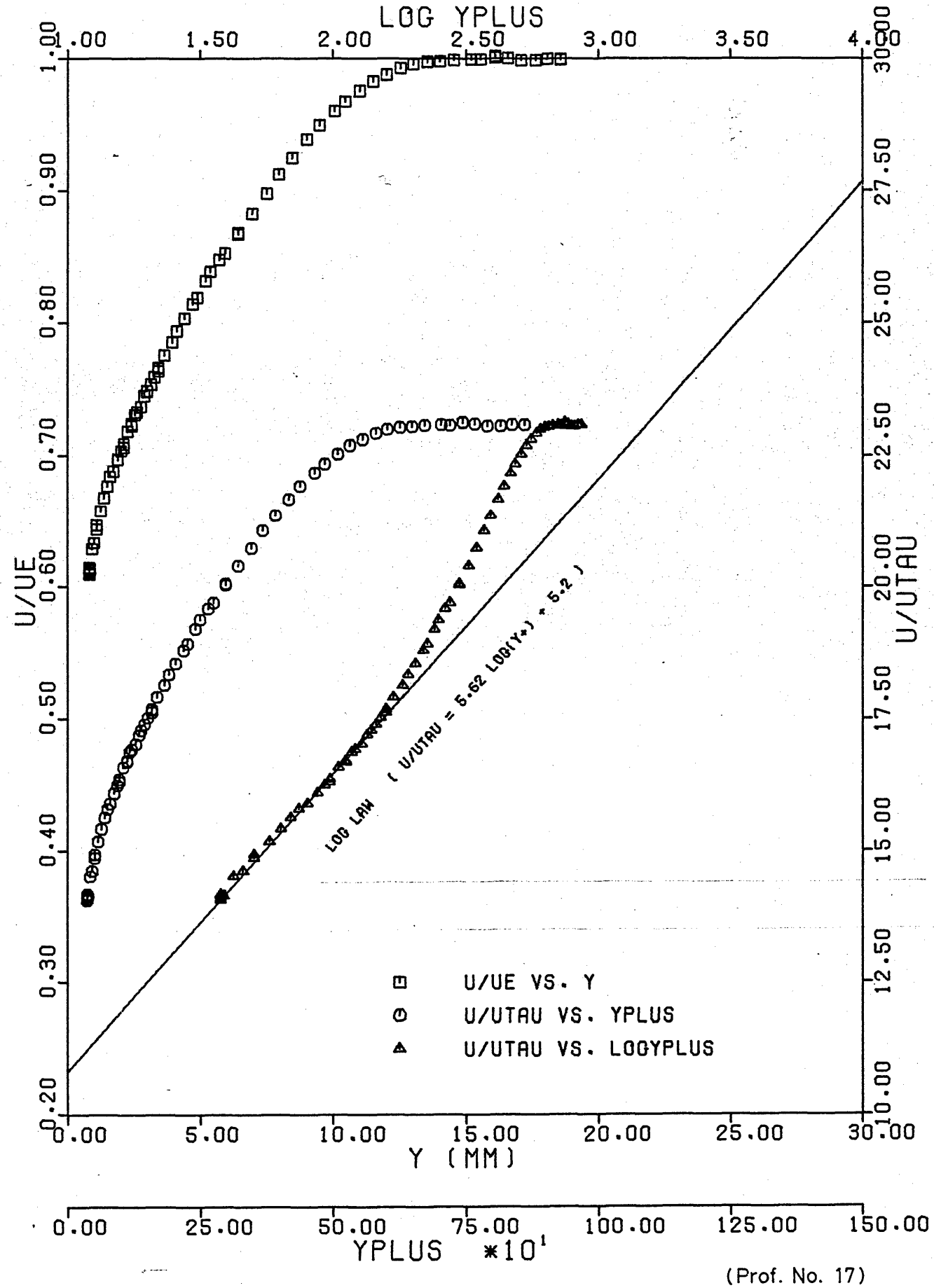

(Prof. No. 17)

b) Stn 4

Fig. 3.16.

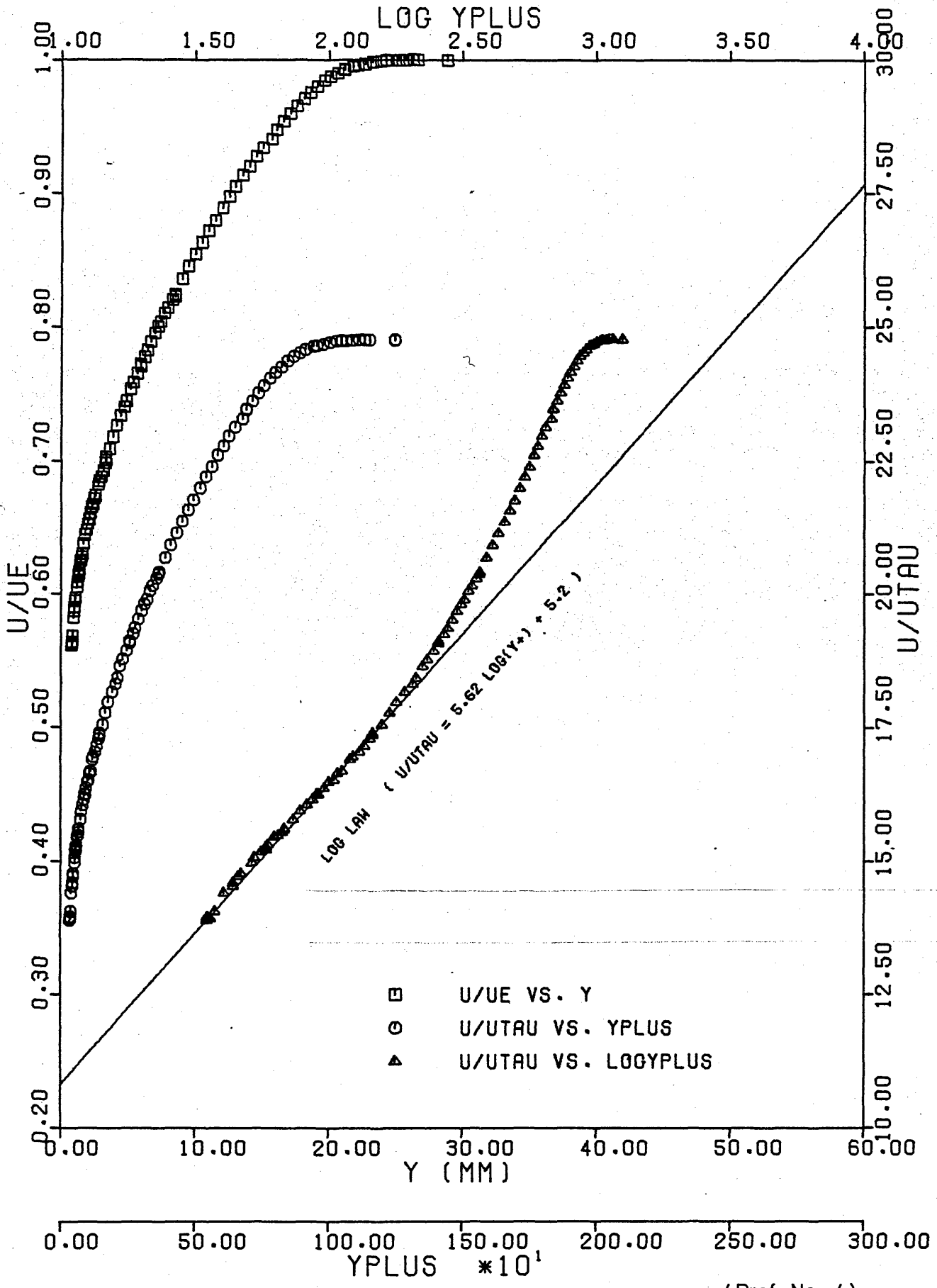

(Prof. No. 4)

c) Stn 8

Fig. 3.16

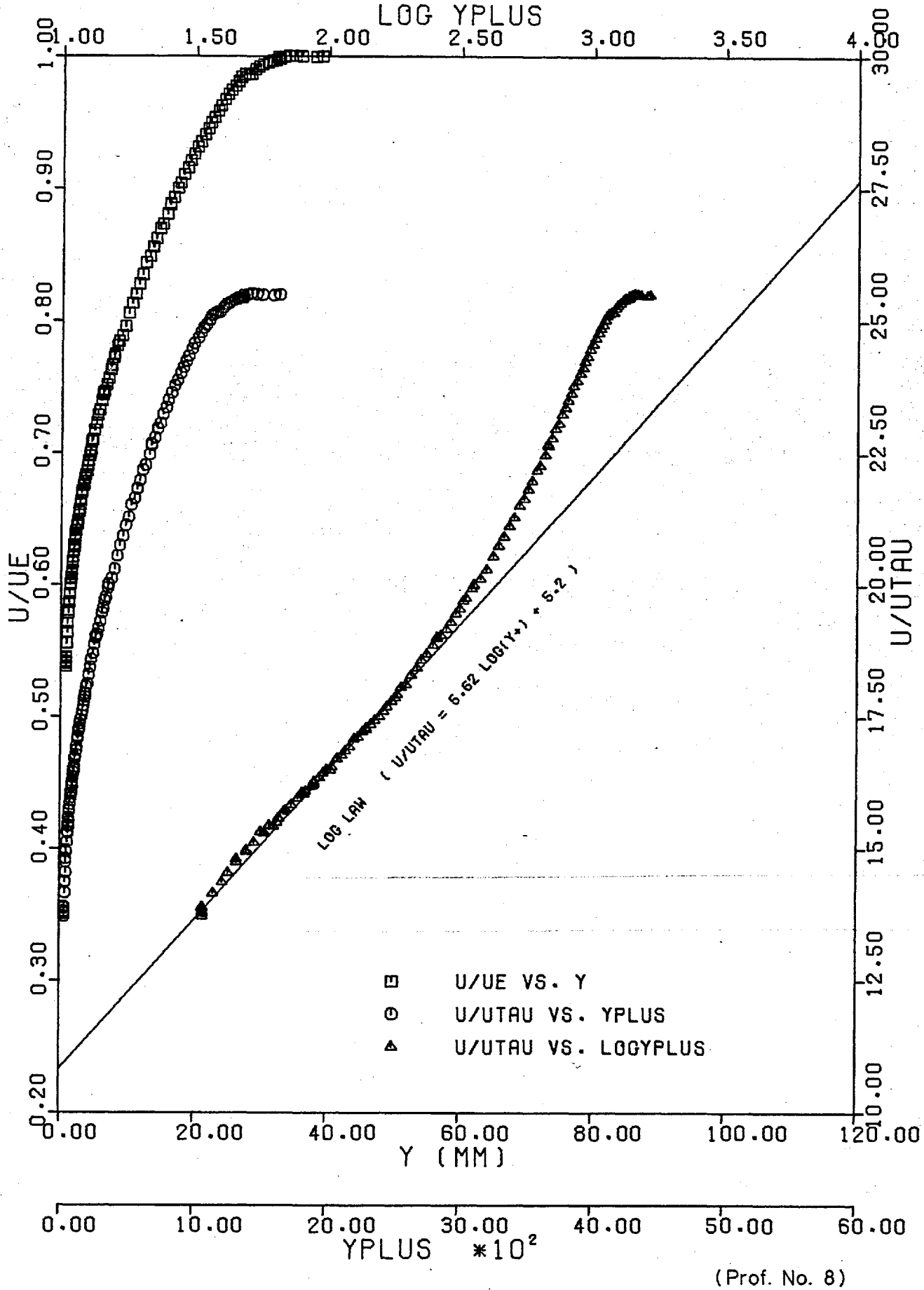

(Prof. No. 8)

d) Stn 12

Fig. 3.16.

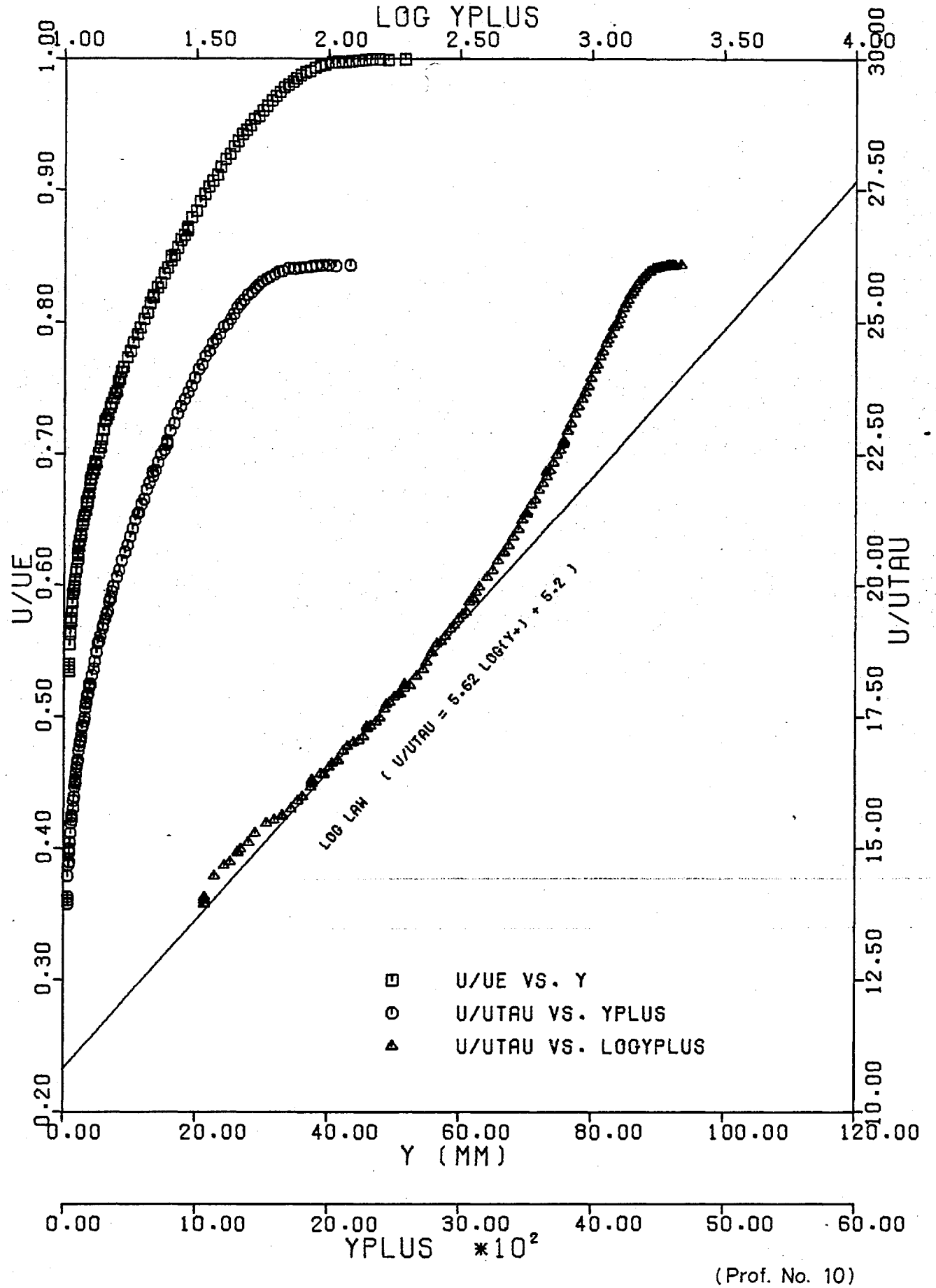

(Prof. No. 10)

e) Stn 16

Fig. 3.16.

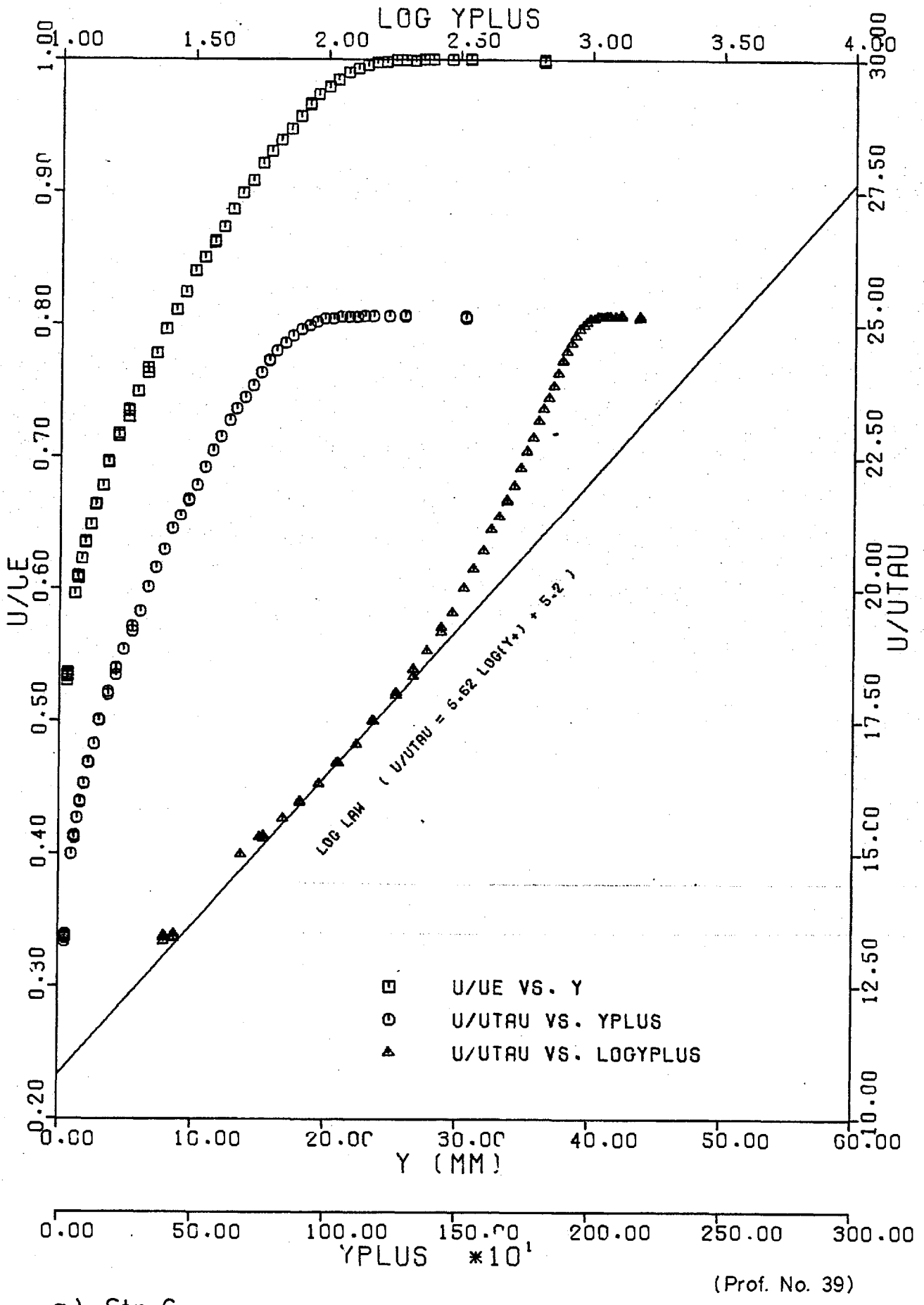

(Prof. No. 39)

a) Stn 6

Fig. 3.17. Velocity Profiles. No Grid, X_{LE} = 0·30m;

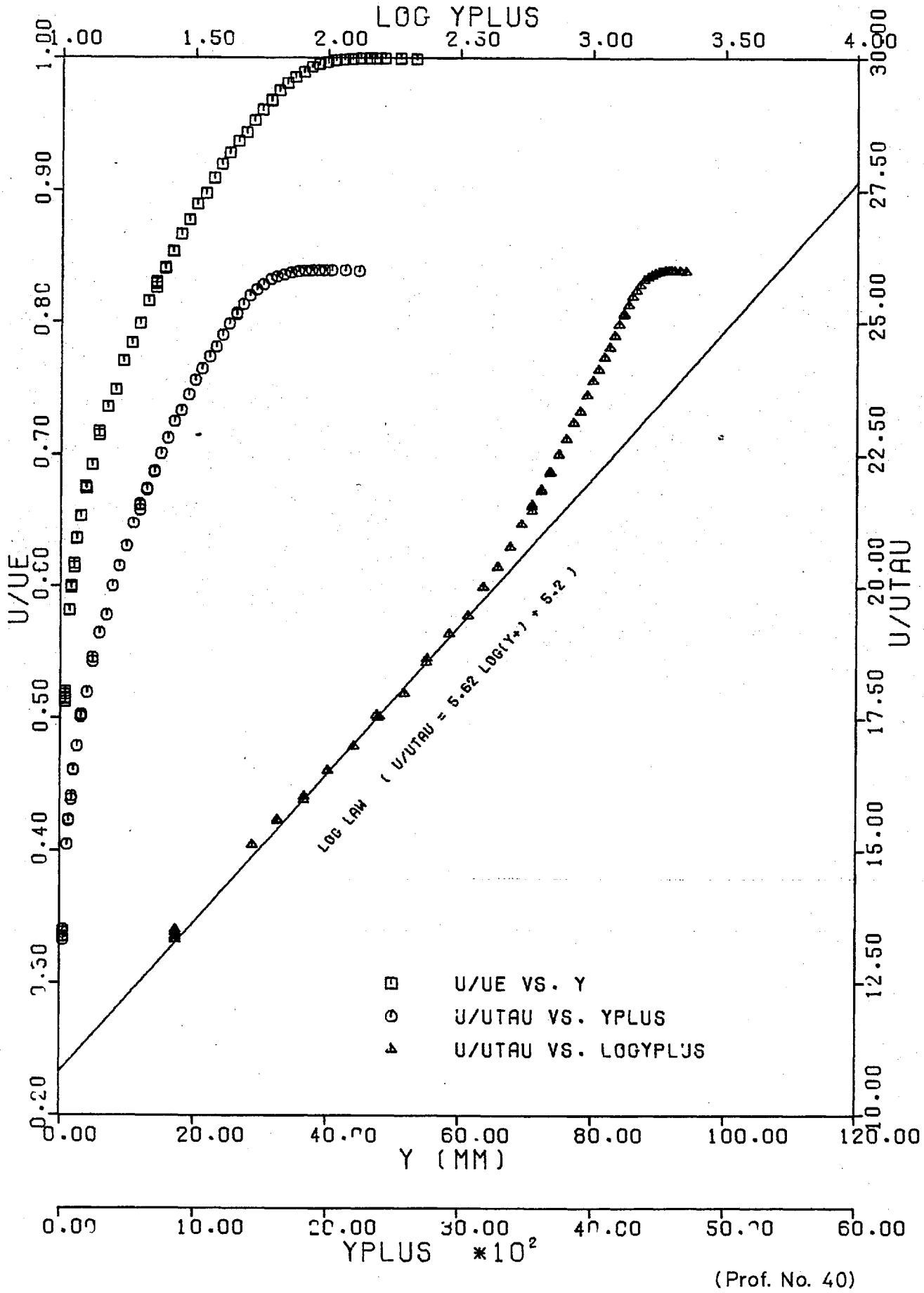

(Prof. No. 40)

b) Stn 14

Fig. 3.17.

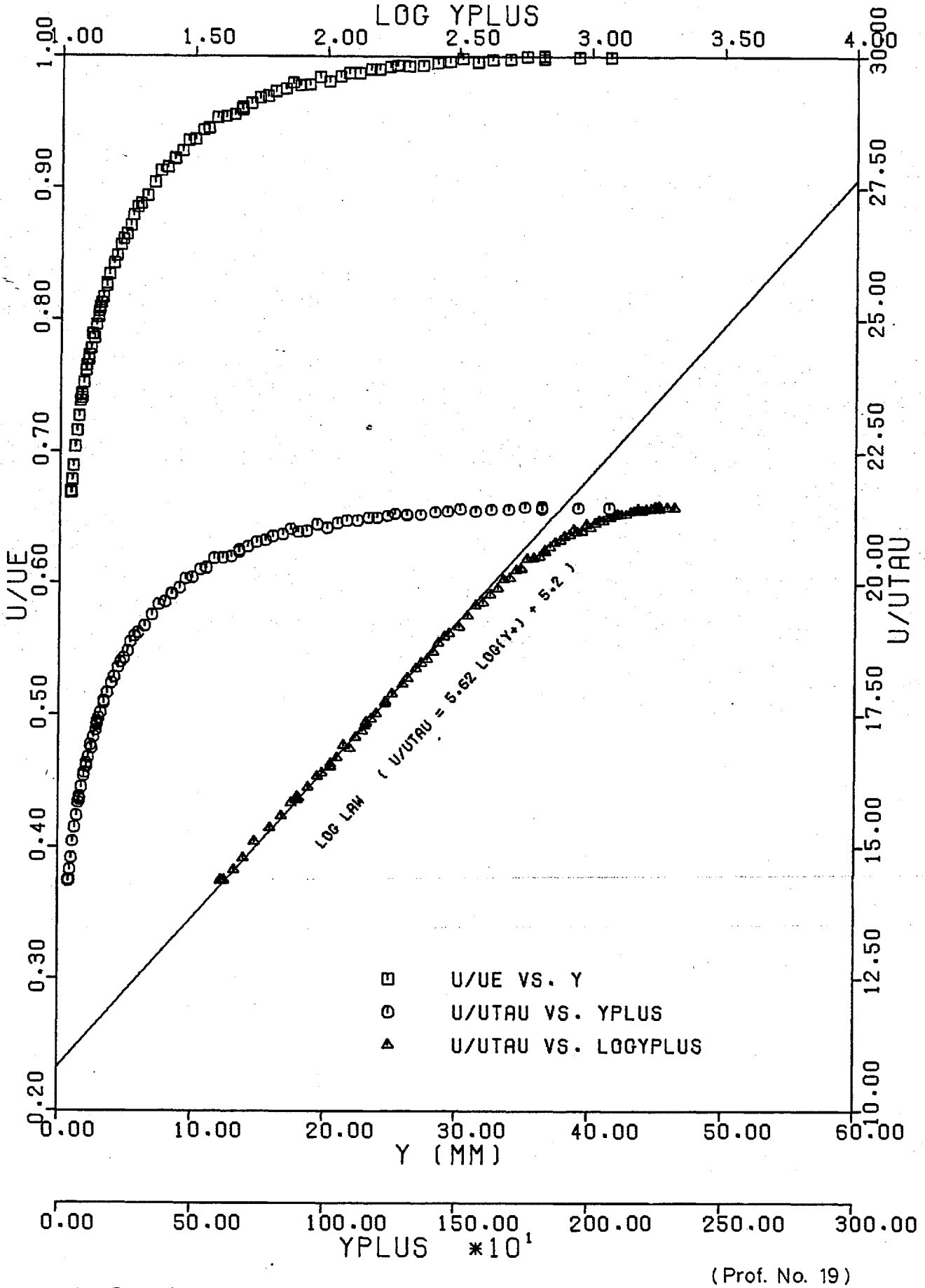

(Prof. No. 19)

a) Stn 4

Fig. 3.18. Velocity Profiles. 7·6cm Grid, X_{LE}=0·30m;

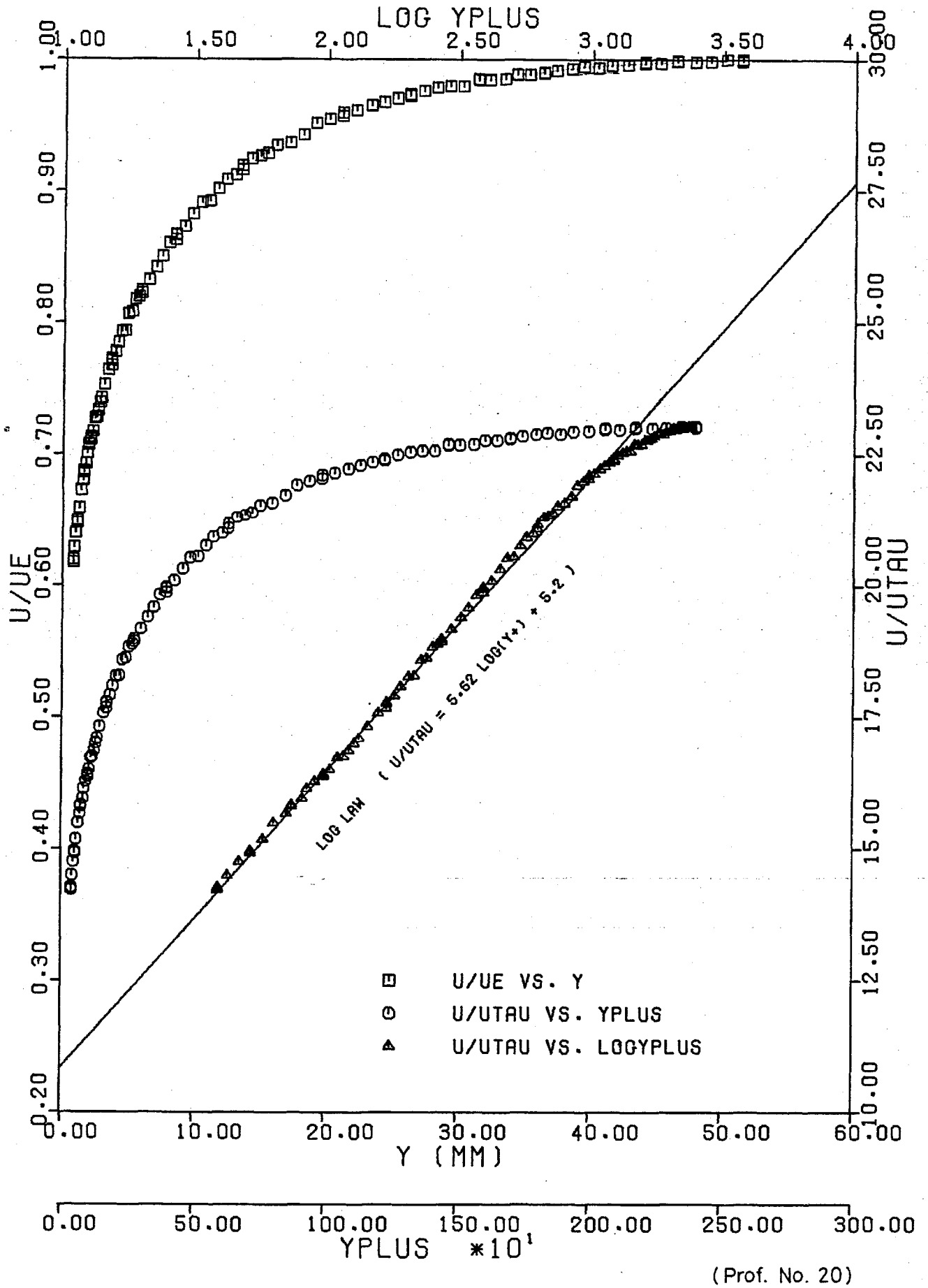

(Prof. No. 20)

b) Stn 8

Fig. 3.18.

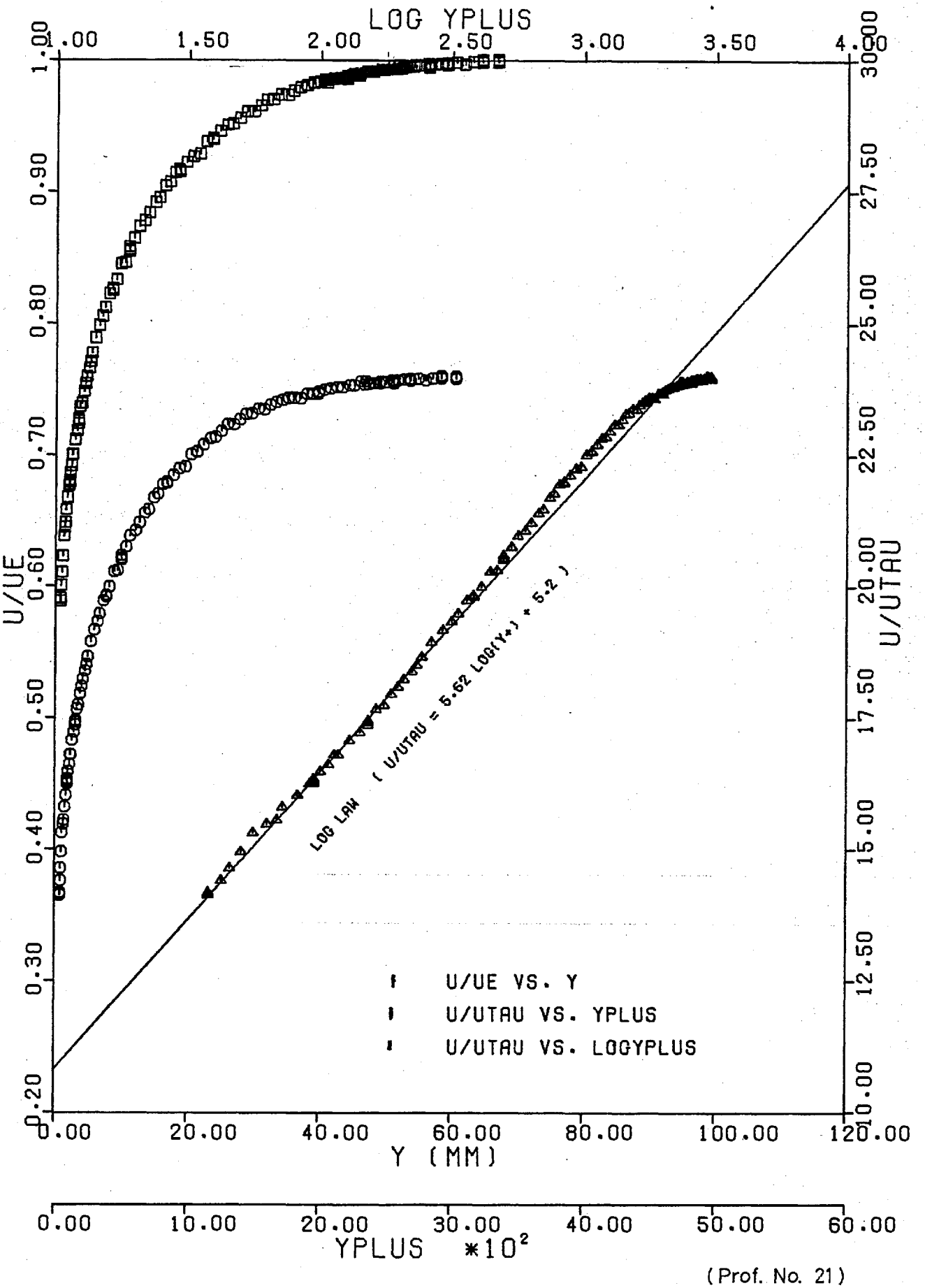

(Prof. No. 21)

c) Stn 12

Fig. 3.18.

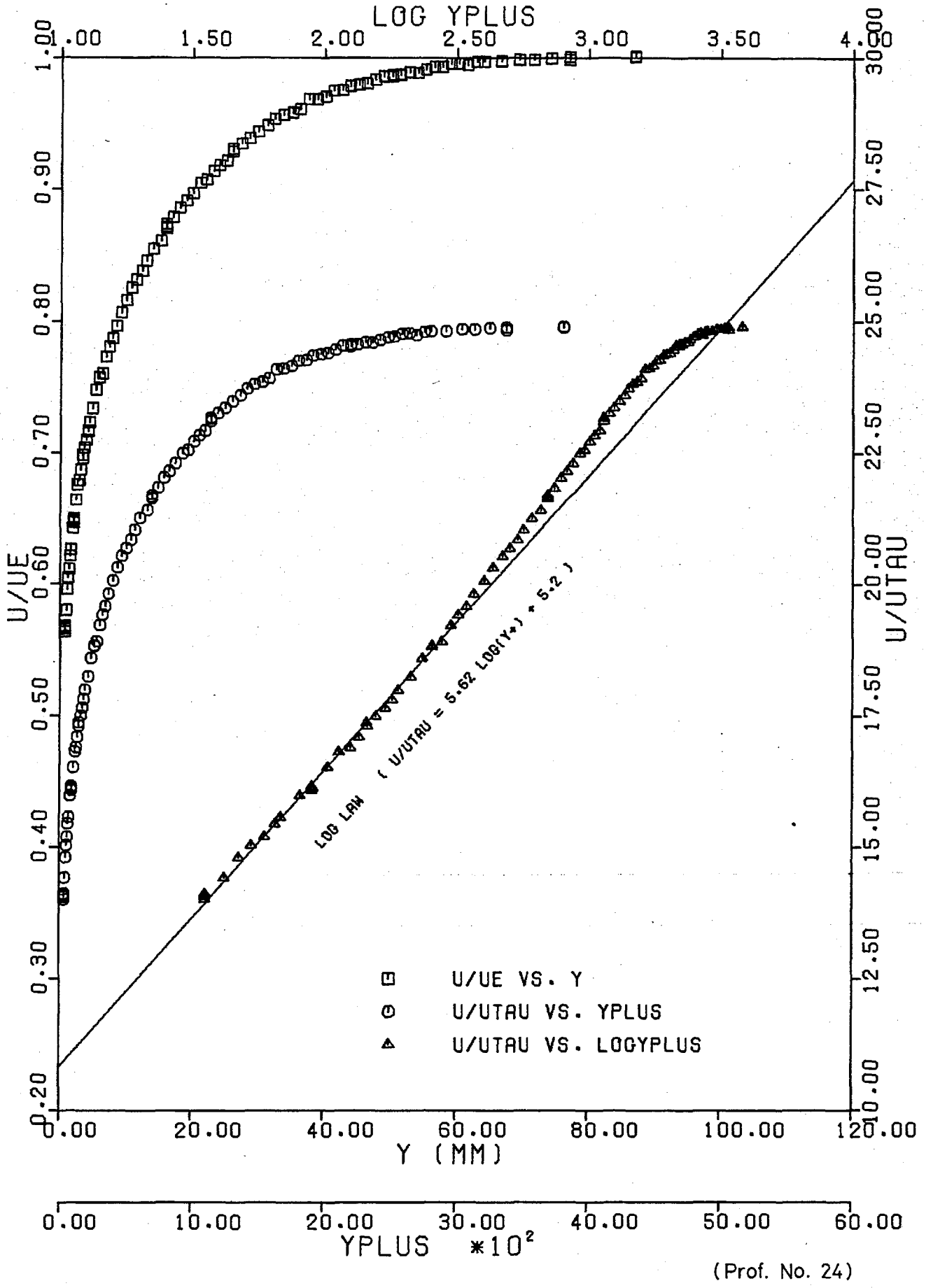

(Prof. No. 24)

d) Stn 16

Fig. 3.18.

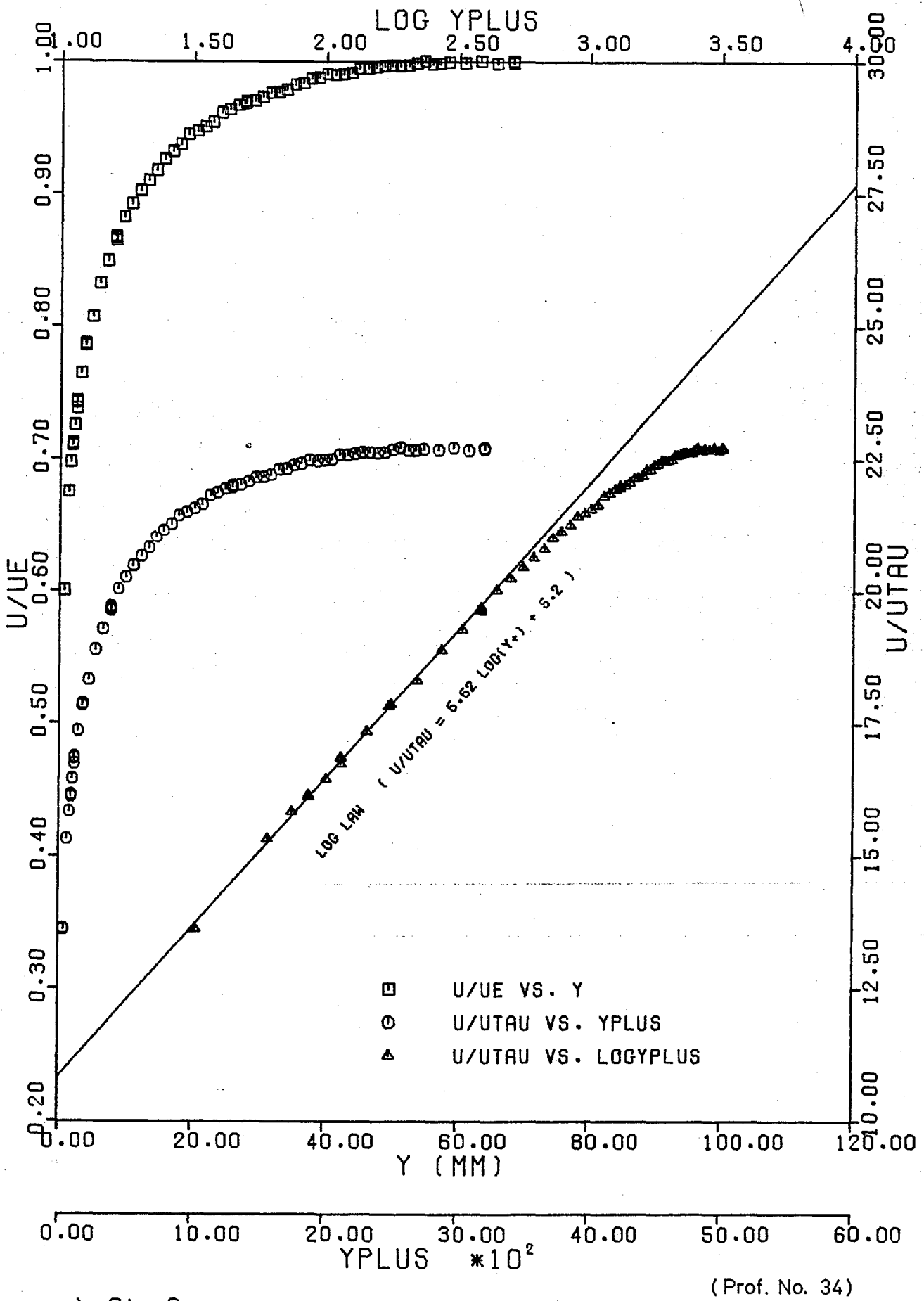

(Prof. No. 34)

a) Stn 6

Fig. 3.19. Velocity Profiles. 7·6cm Grid, X_{LE} = 0·30 m;

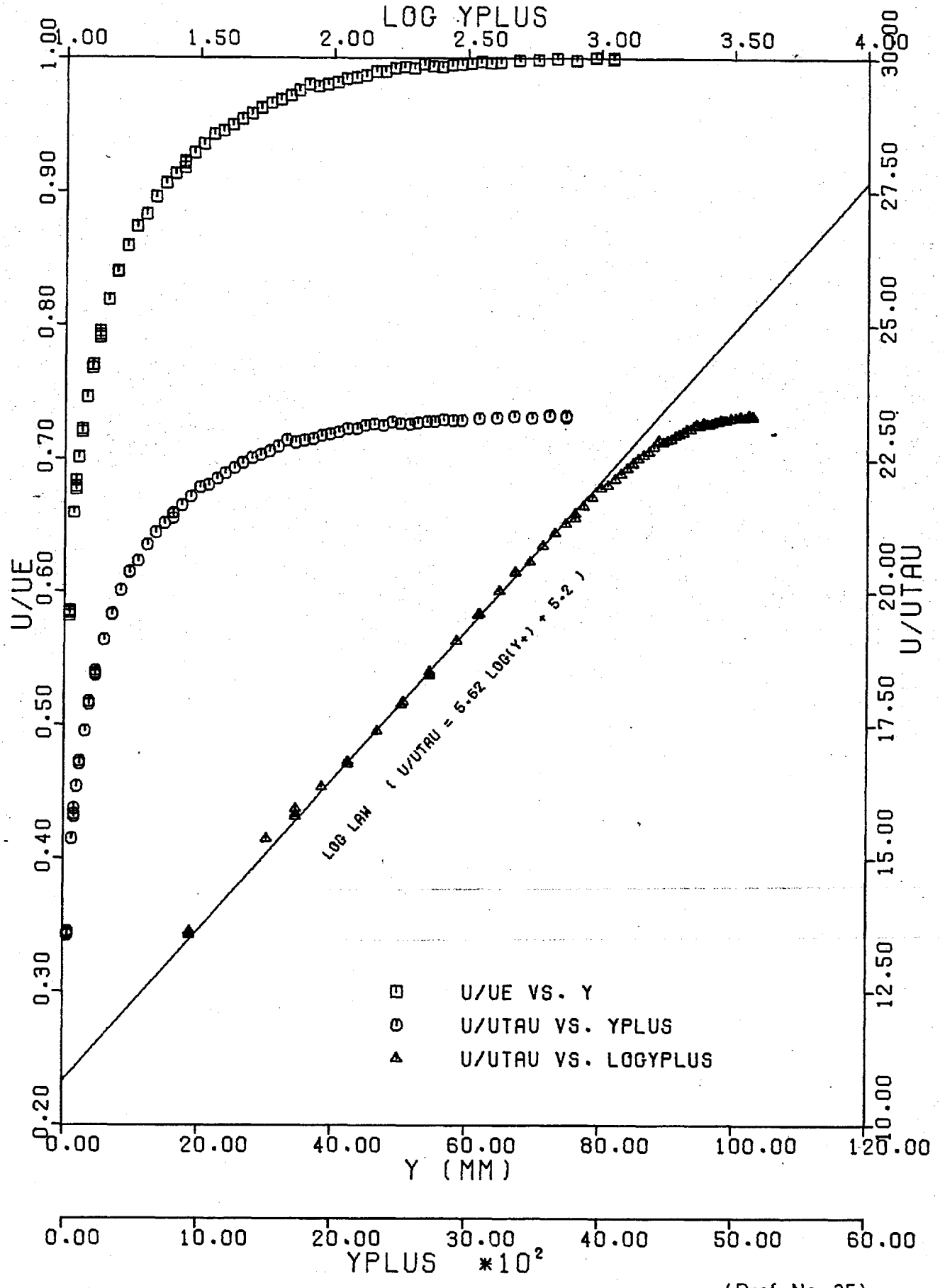

(Prof. No. 35)

b) Stn 8

Fig. 3.19.

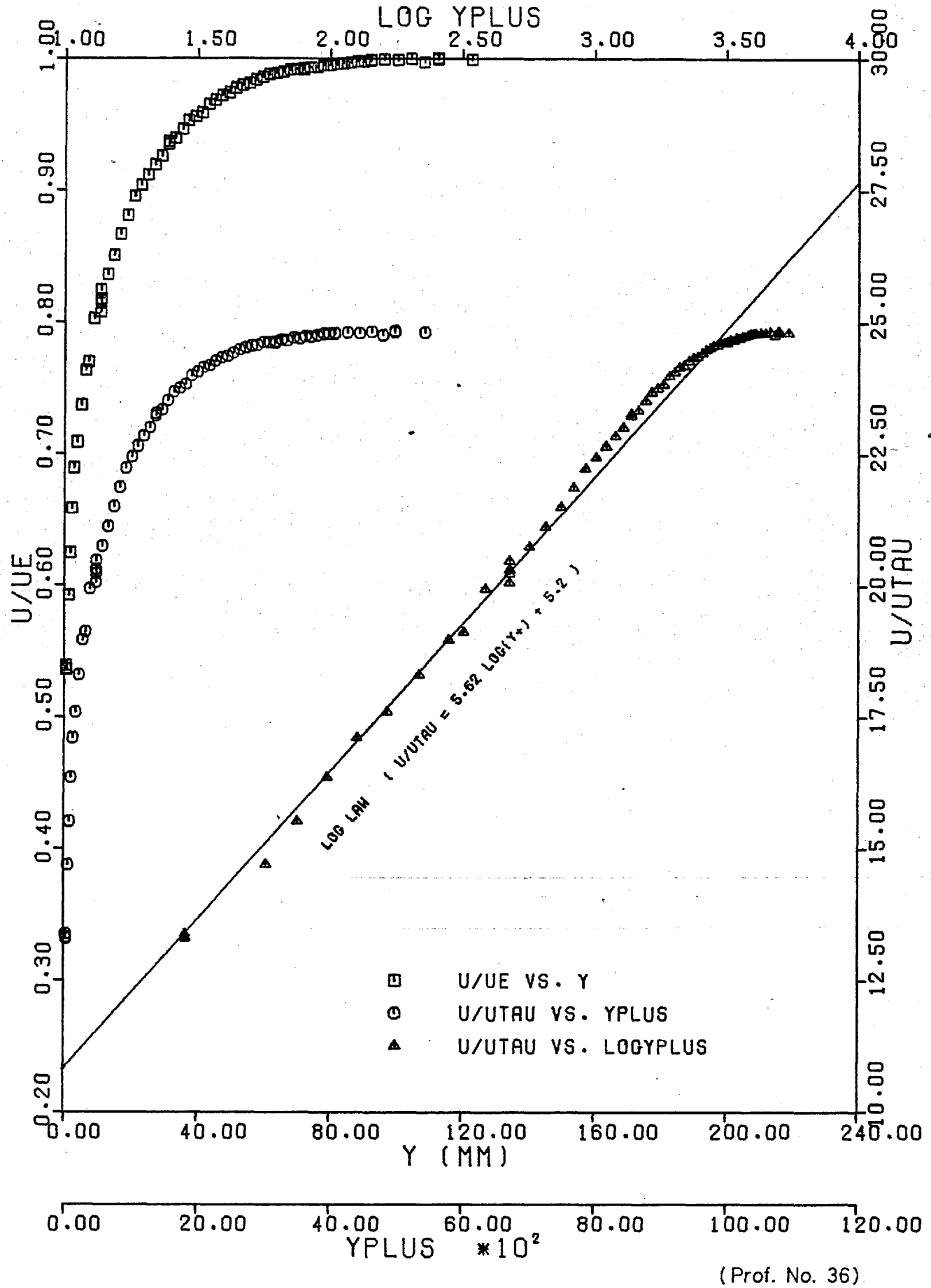

(Prof. No. 36)

c) Stn 16

Fig. 3.19.

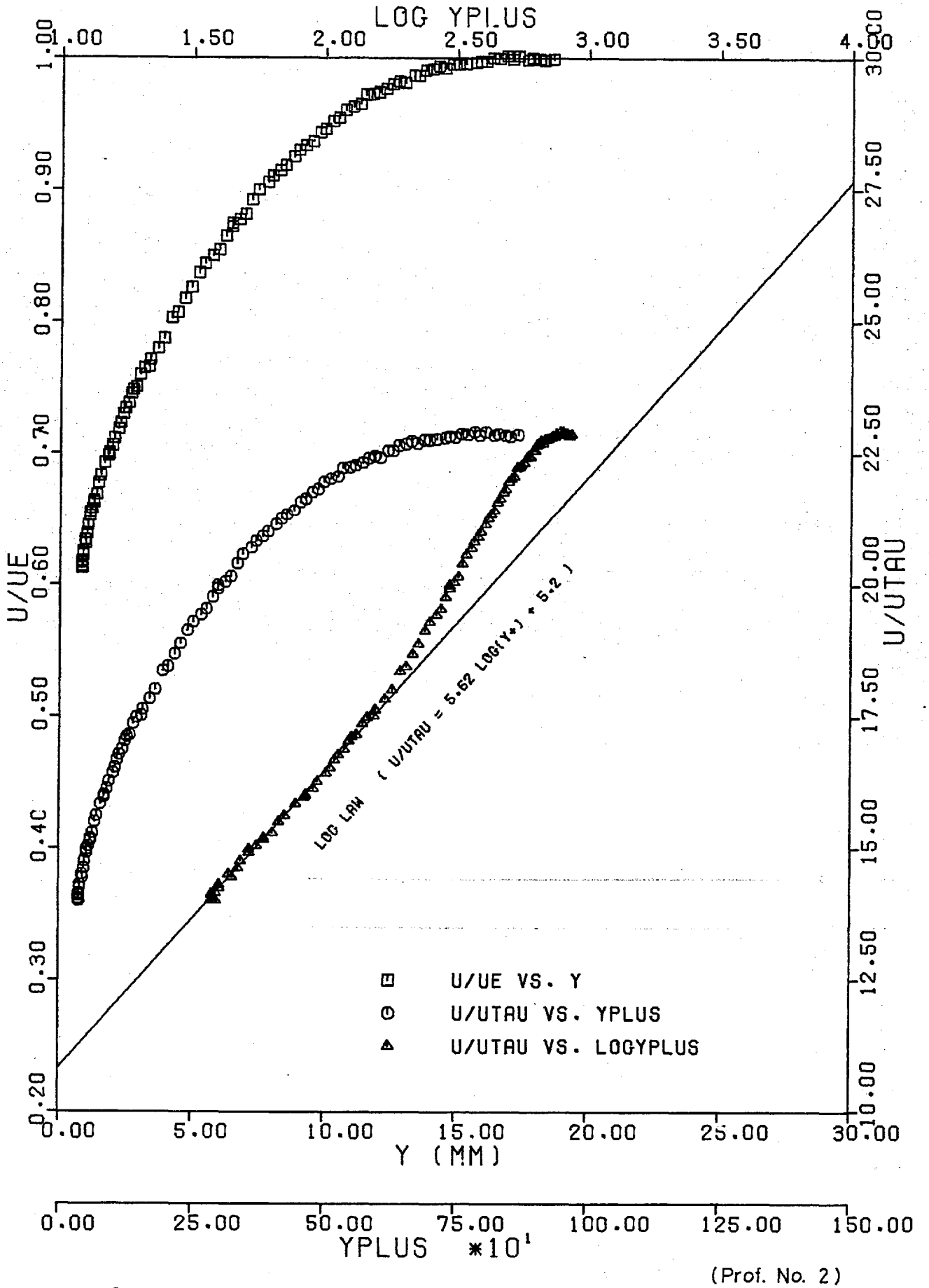

(Prof. No. 2)

a) Stn 4

Fig. 3.20. Velocity Profiles. 7·6 cm Grid, X_{LE} = 2·06m;

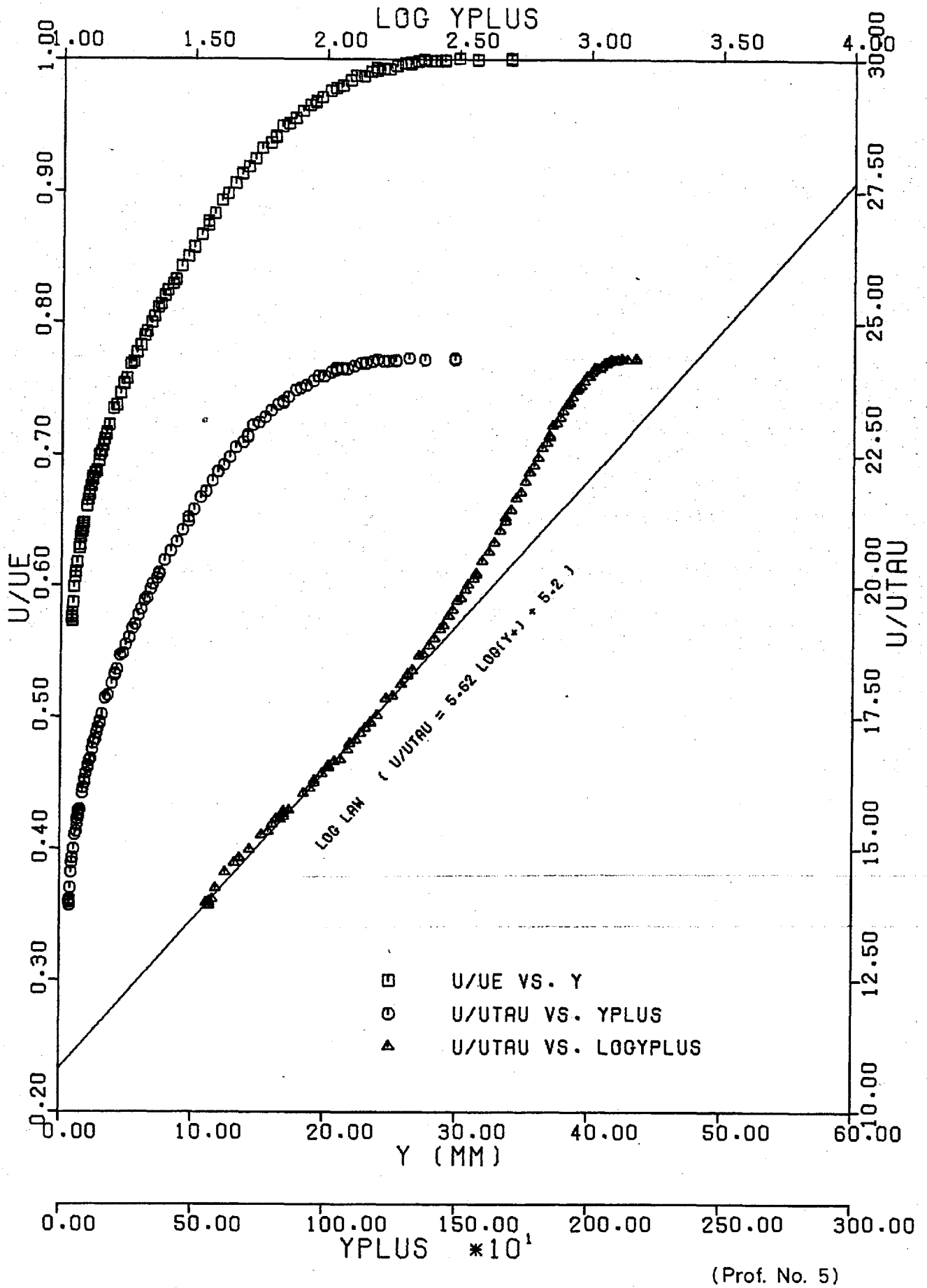

(Prof. No. 5)

b) Stn 8

Fig. 3.20.

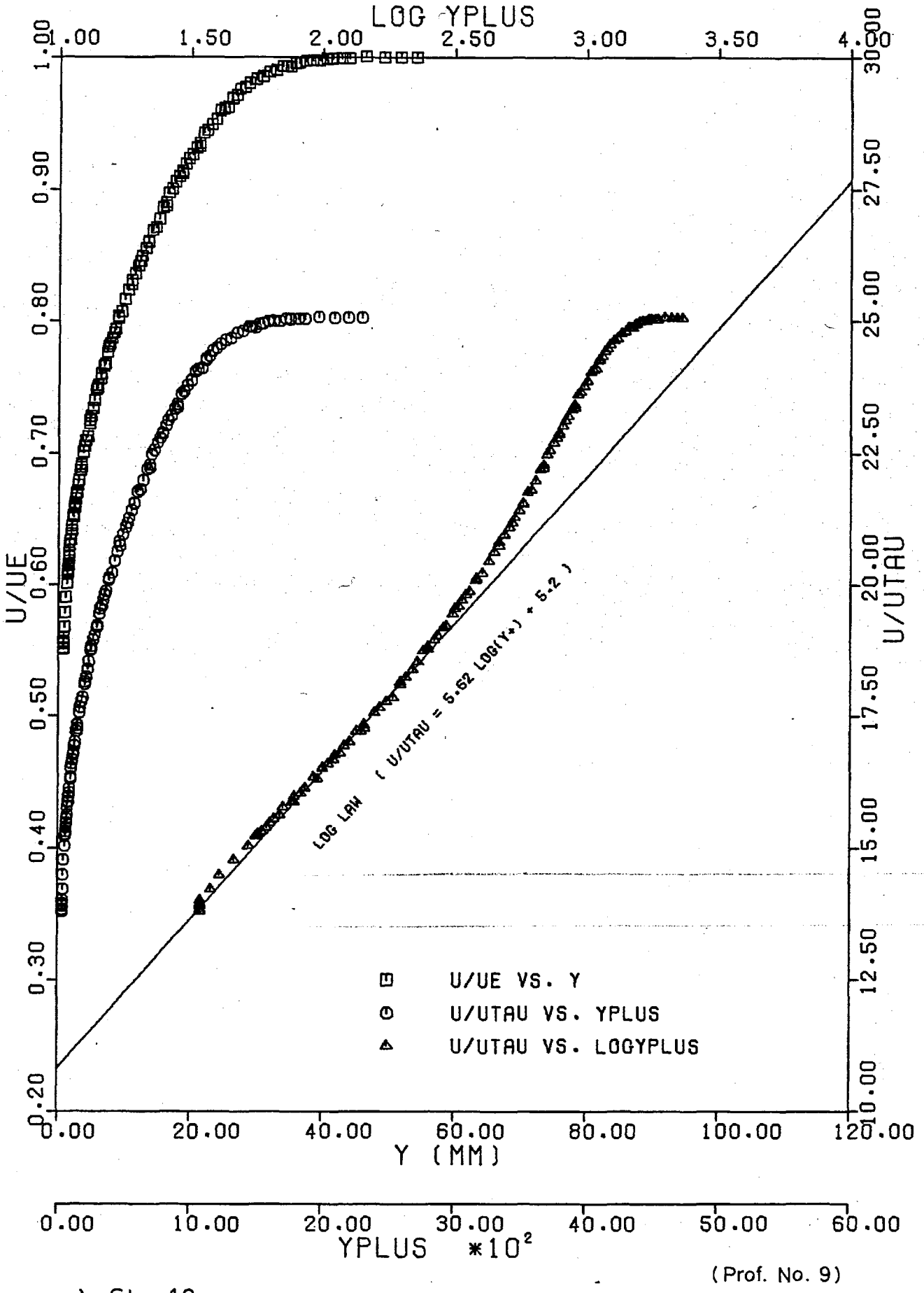

(Prof. No. 9)

c) Stn 12

Fig. 3.20.

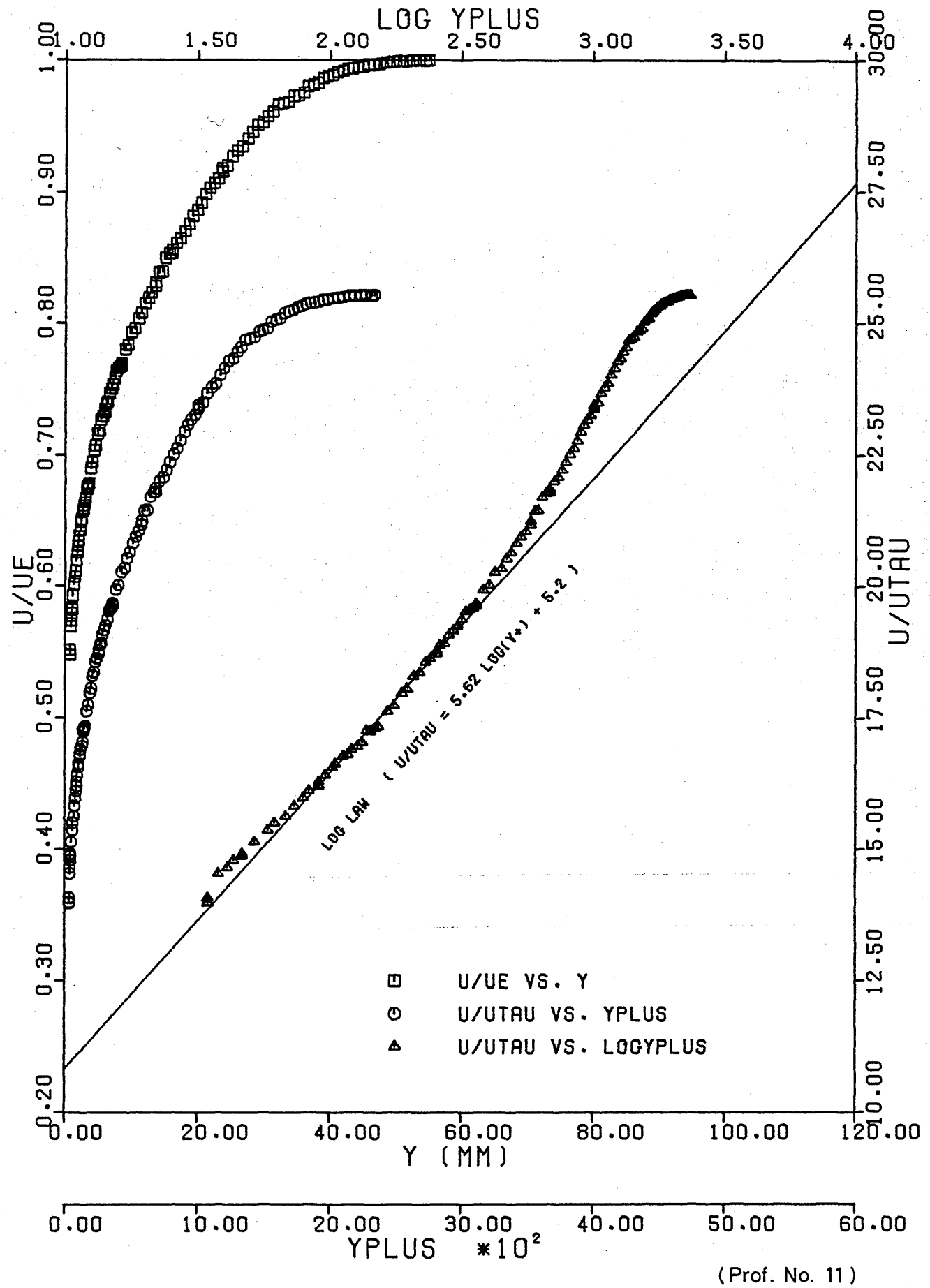

(Prof. No. 11)

d) Stn 16

Fig. 3.20.

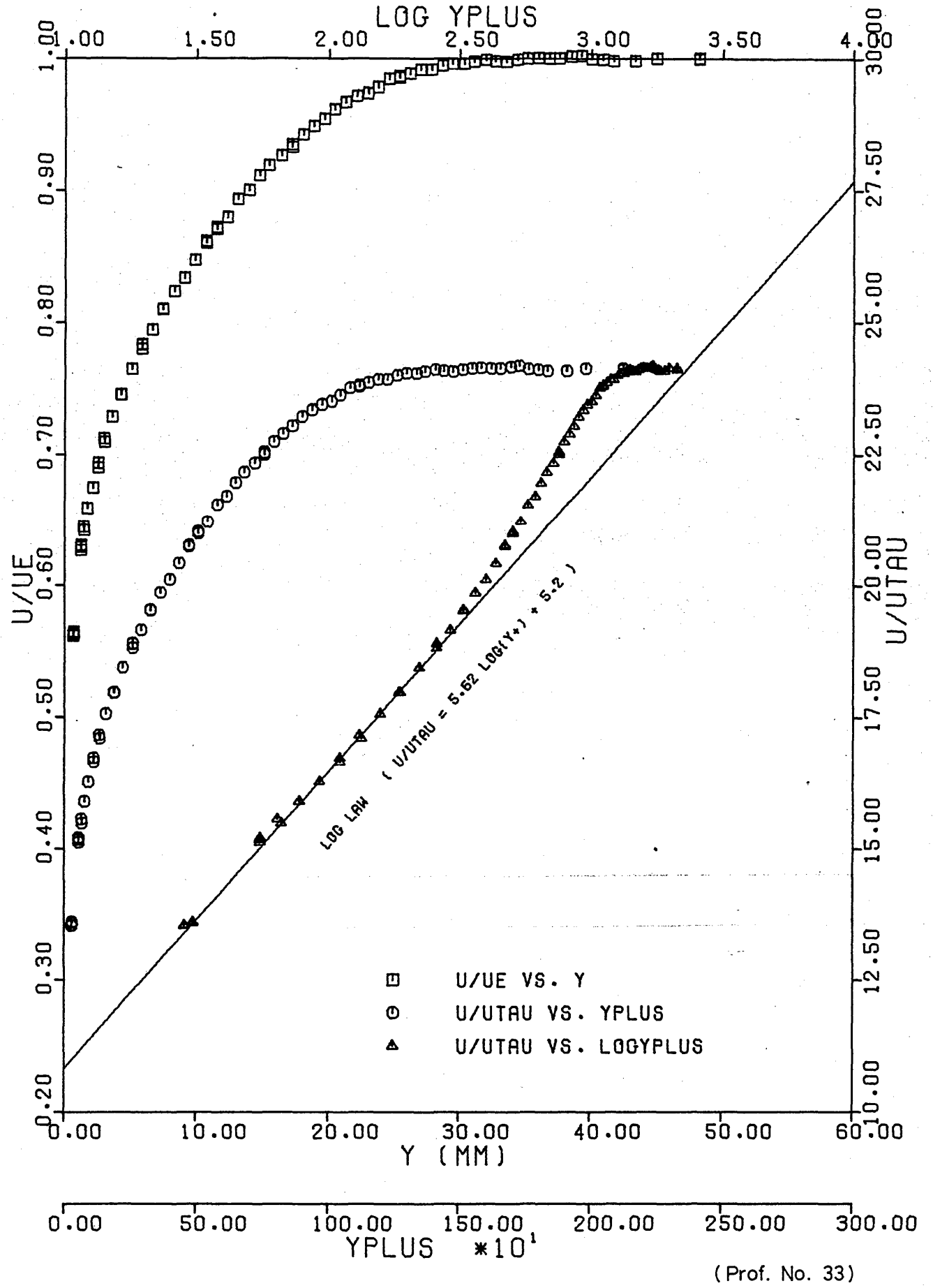

Fig. 3.21 Velocity Profile 7·6cm Grid, X_{LE} = 2·06m, Stn 6.

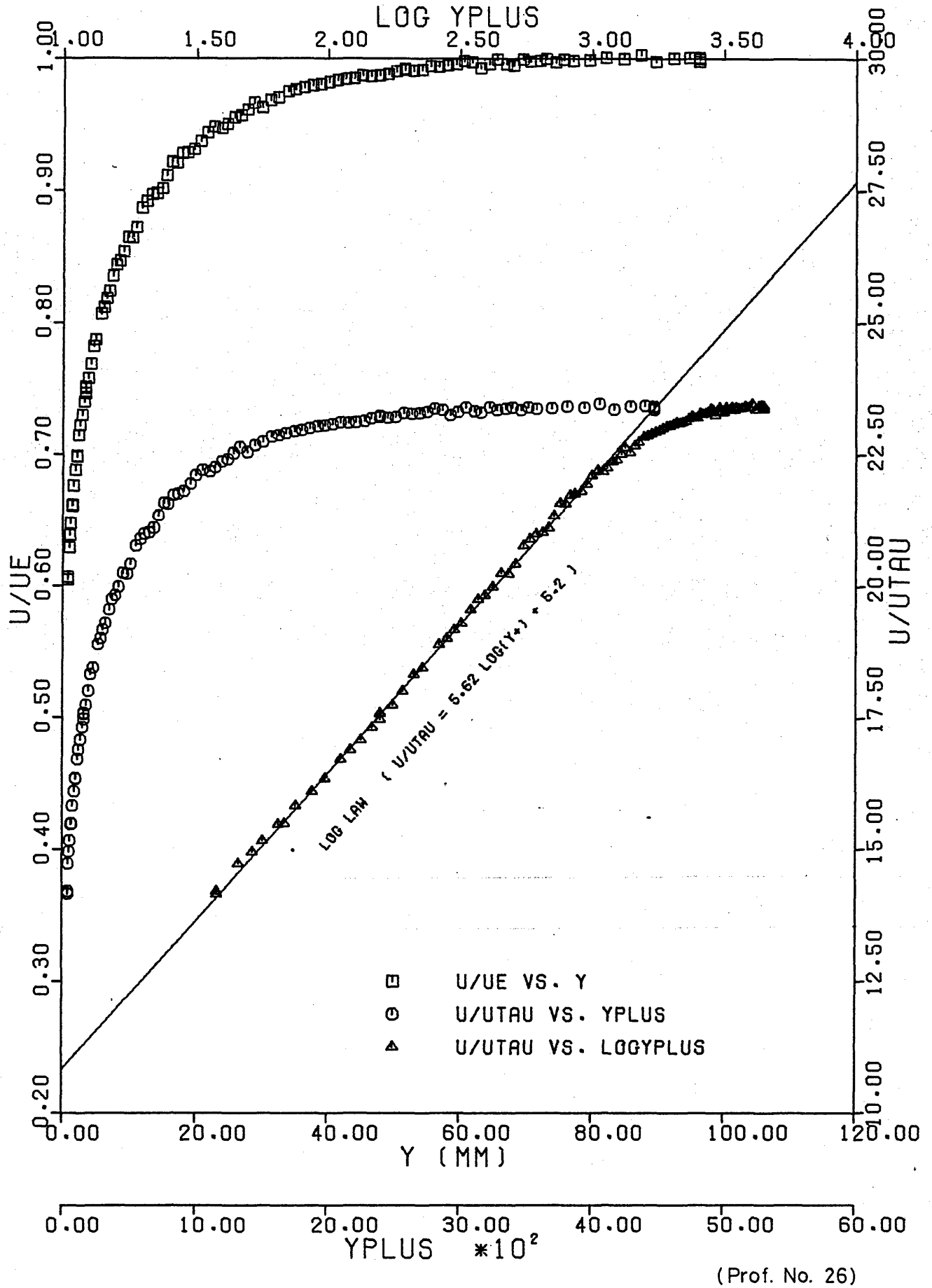

Fig. 3.22. Velocity Profile. 15·2cm Grid, X_{LE}=0·76m, Stn 12.

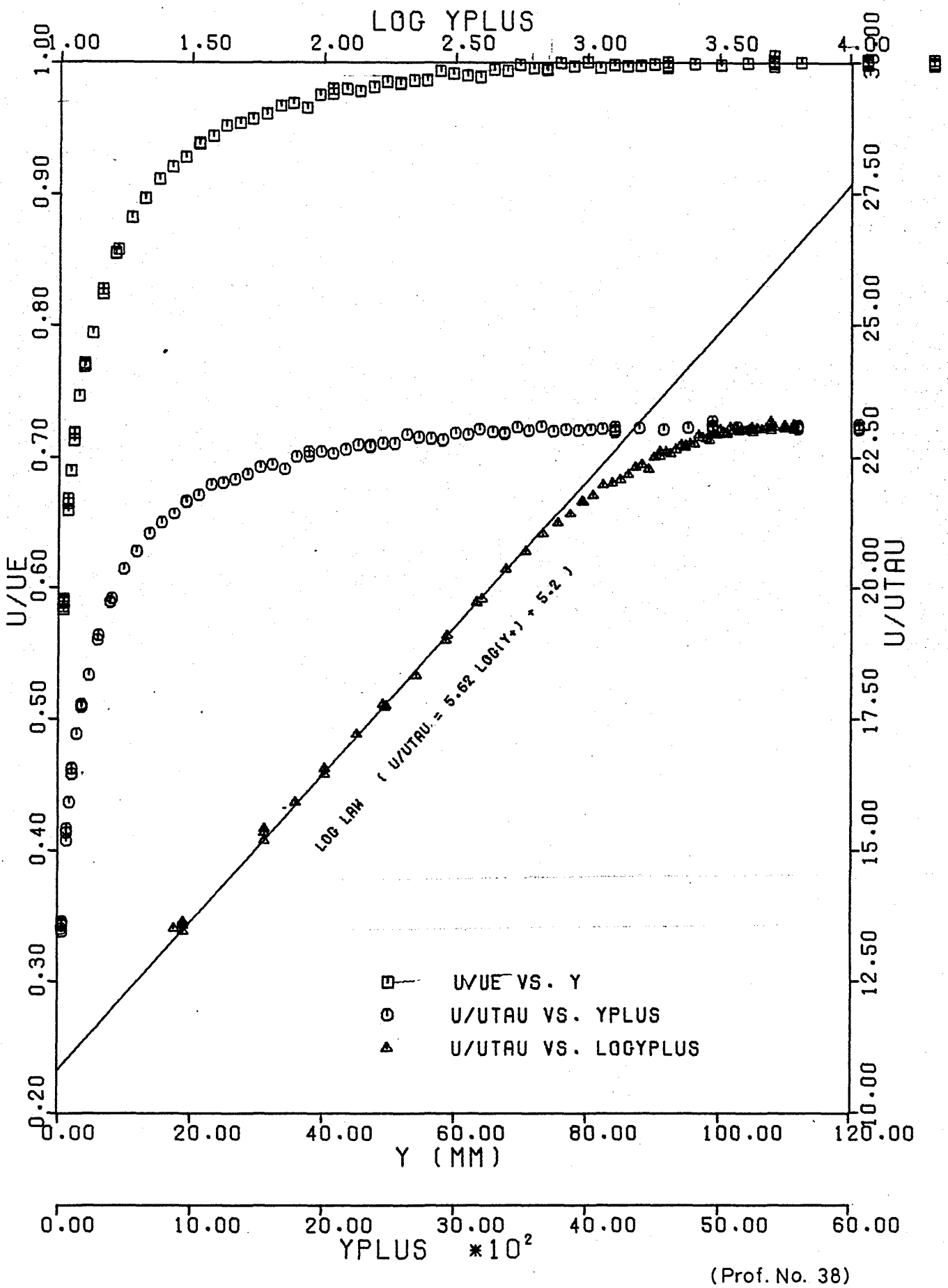

Fig. 3.23. Velocity Profile. 15·2cm Grid, X_{LE}=0·76m, Stn 10.

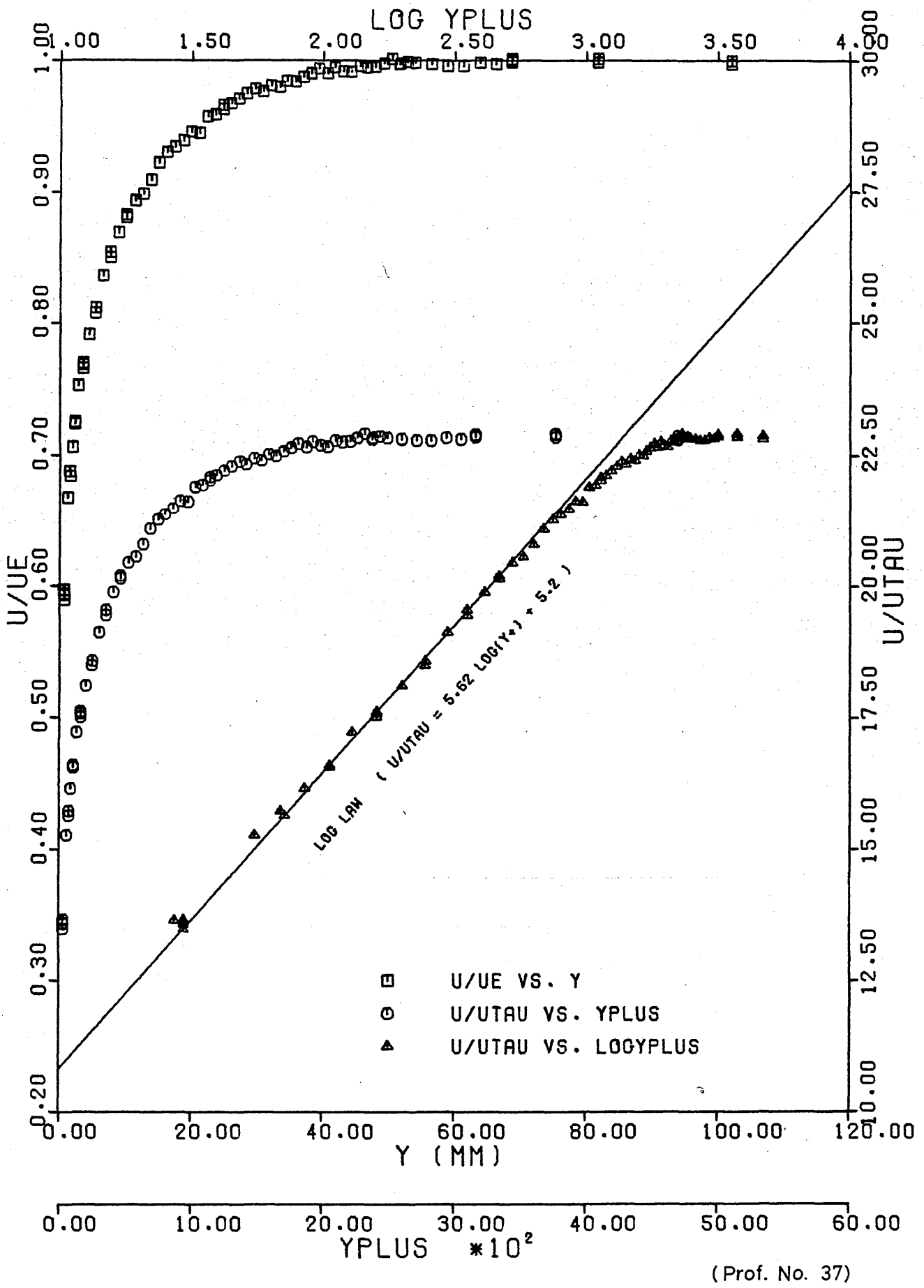

Fig. 3.24. Velocity Profile. 15·2cm Grid, X_{LE}= 1·37m, Stn 6.

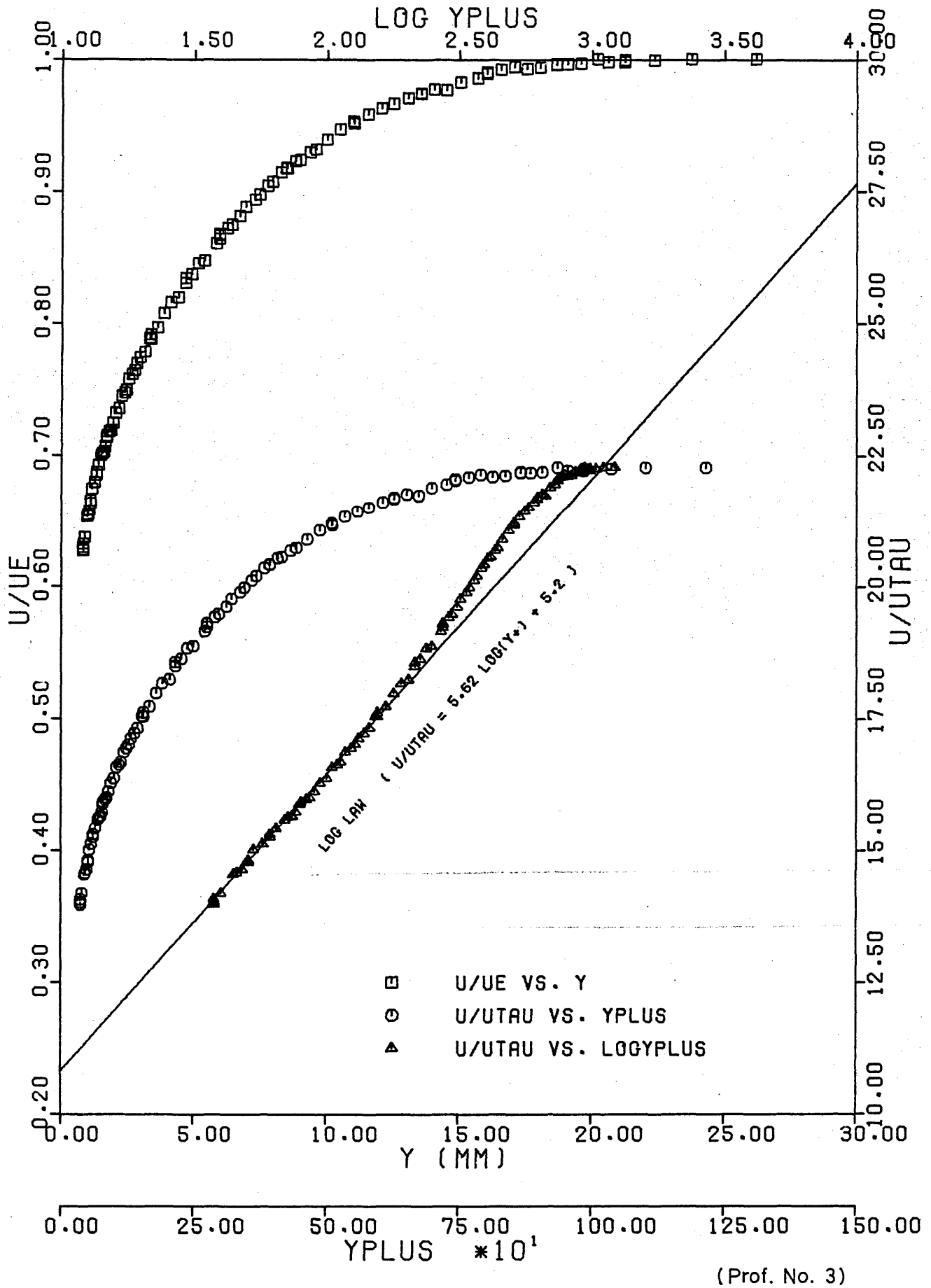

(Prof. No. 3)

a) Stn 4

Fig. 3.25. Velocity Profiles. 15·2cm Grid, X_{LE}= 2·06m;

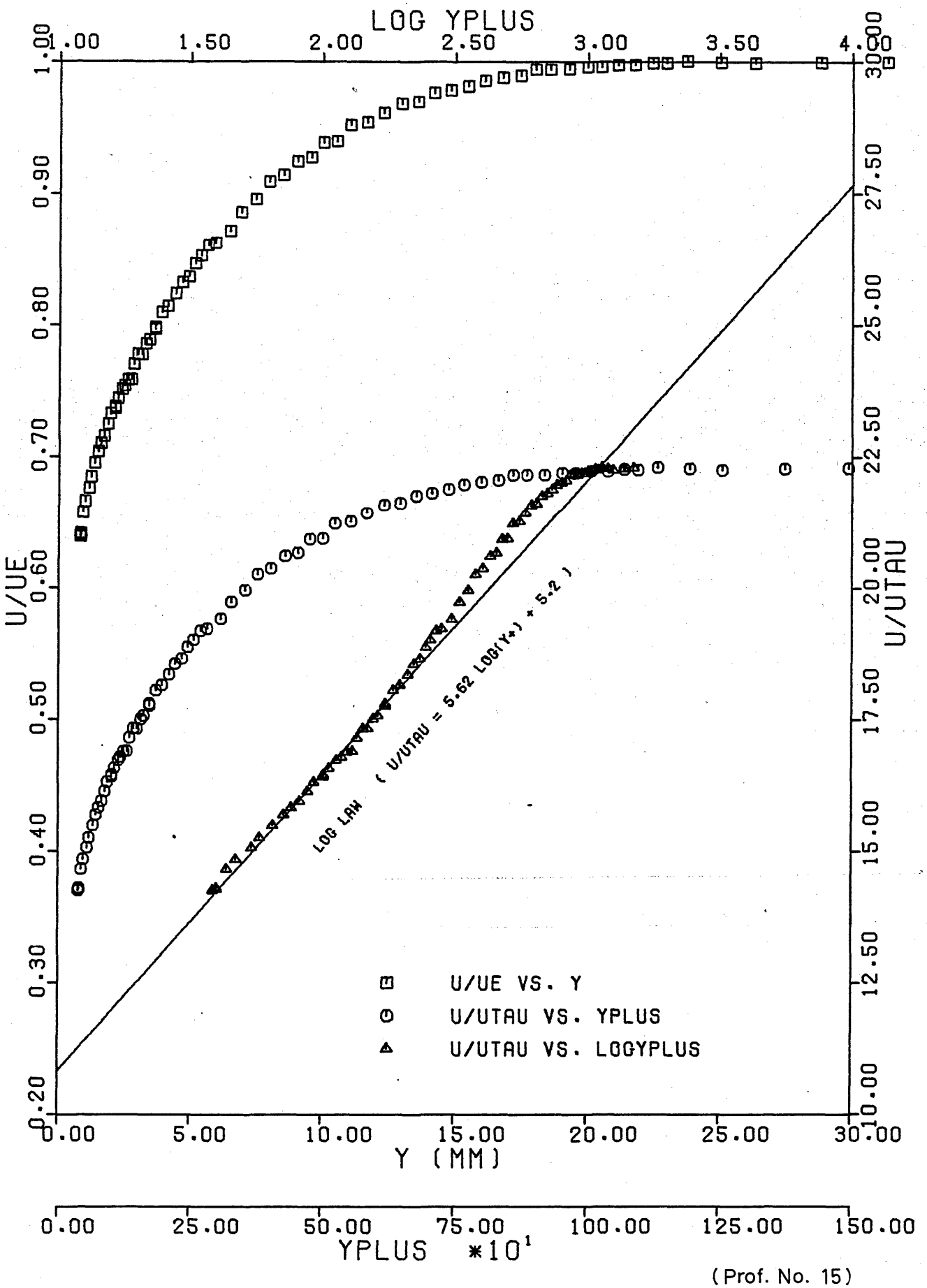

(Prof. No. 15)

b) Stn 4

Fig. 3.25.

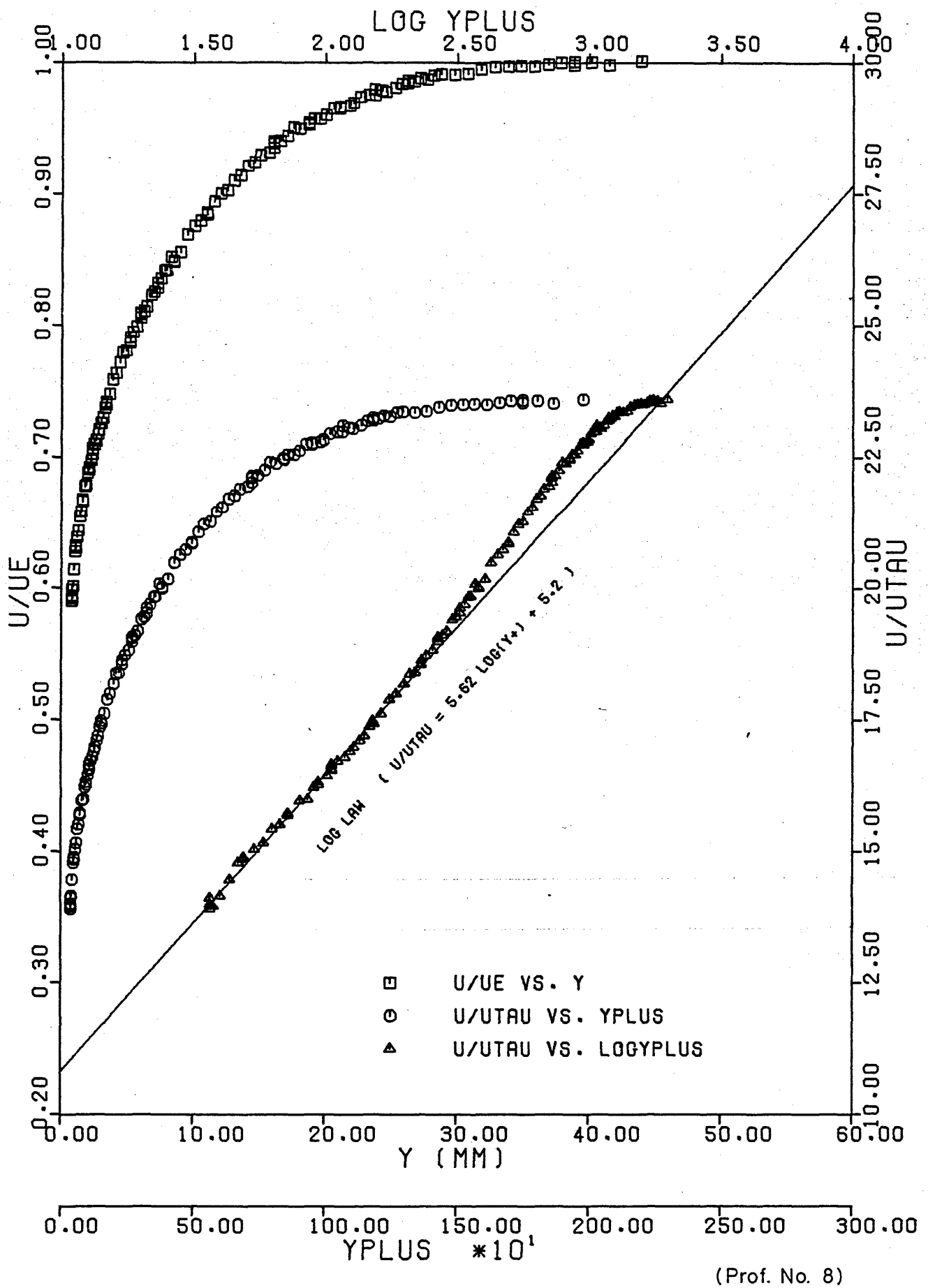

(Prof. No. 8)

c) Stn 8

Fig. 3.25.

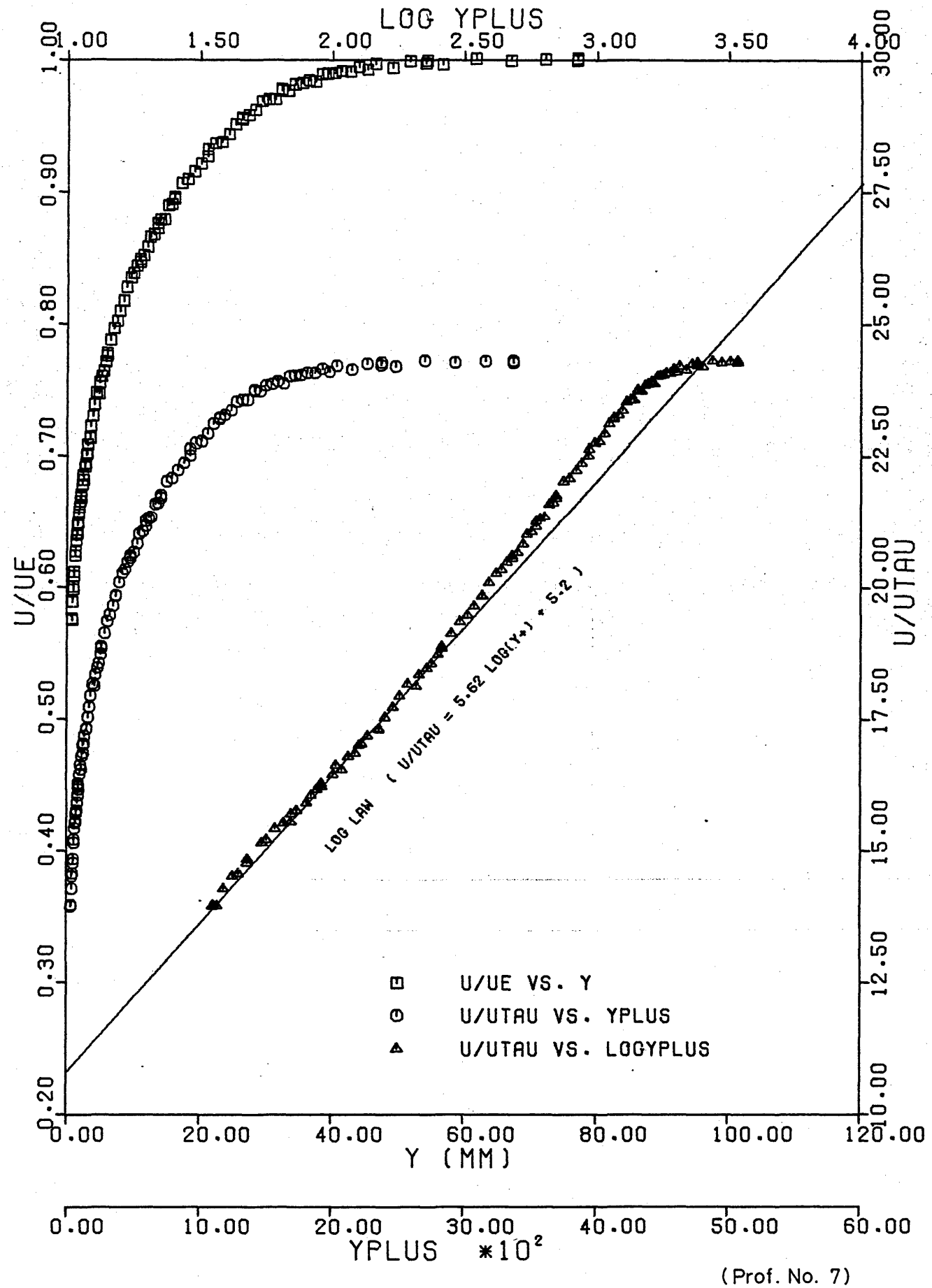

(Prof. No. 7)

d) Stn 12

Fig. 3.25.

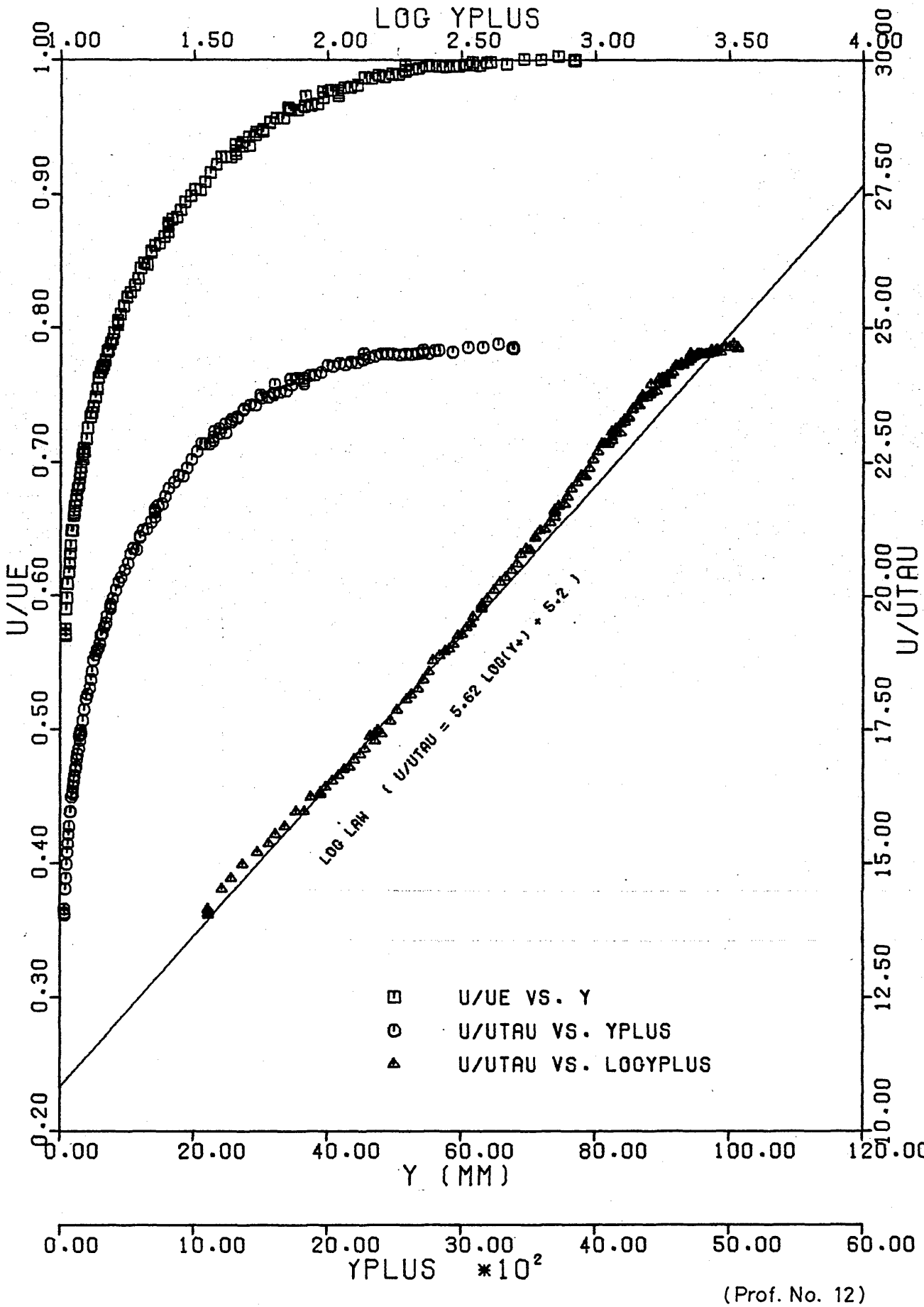

e) Stn 16

Fig. 3.25.

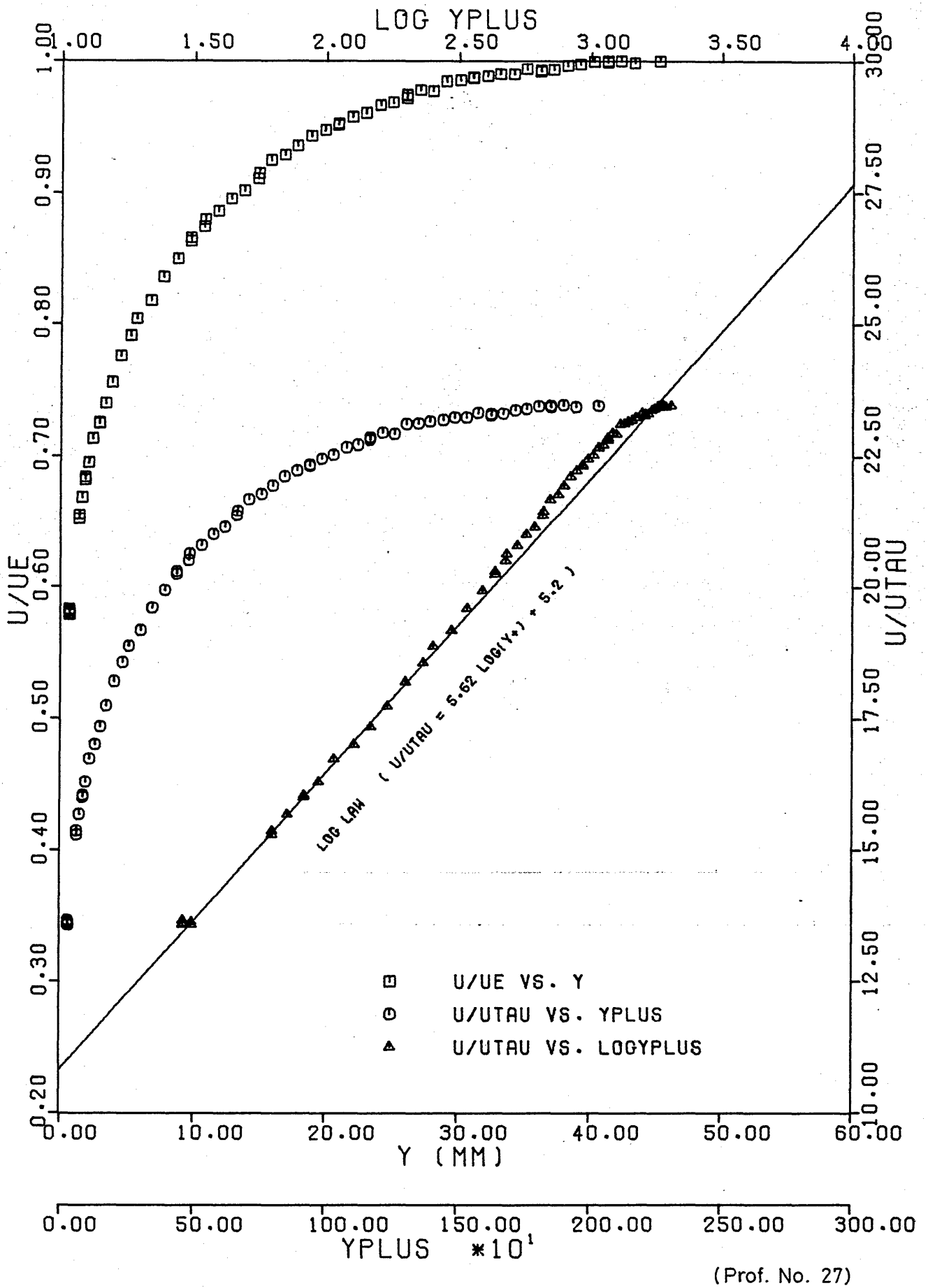

(Prof. No. 27)

a) Stn 6

Fig. 3.26. Velocity Profiles. 15·2cm Grid, X_{LE}= 2·06m;

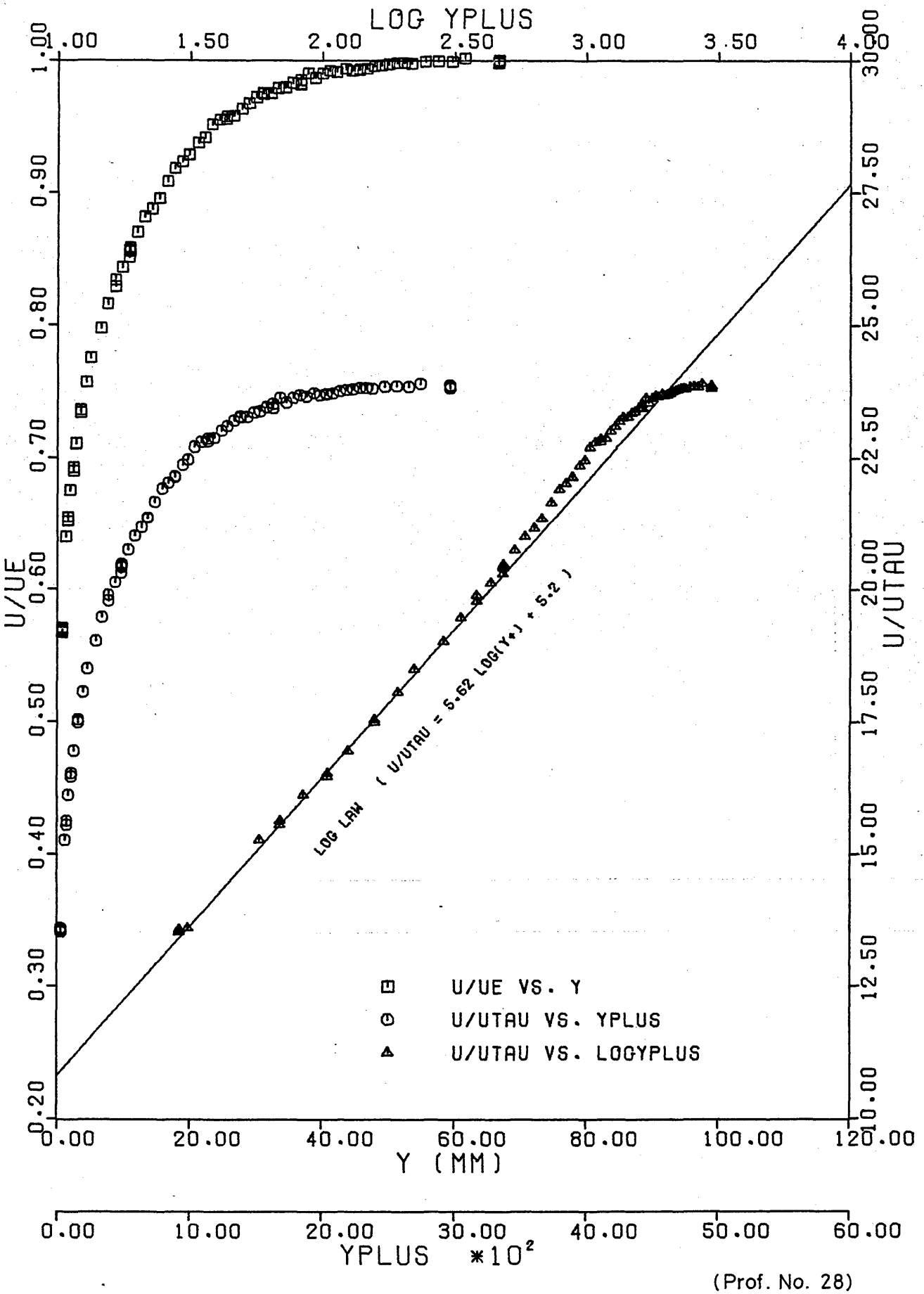

(Prof. No. 28)

b) Stn 8

Fig. 3.26.

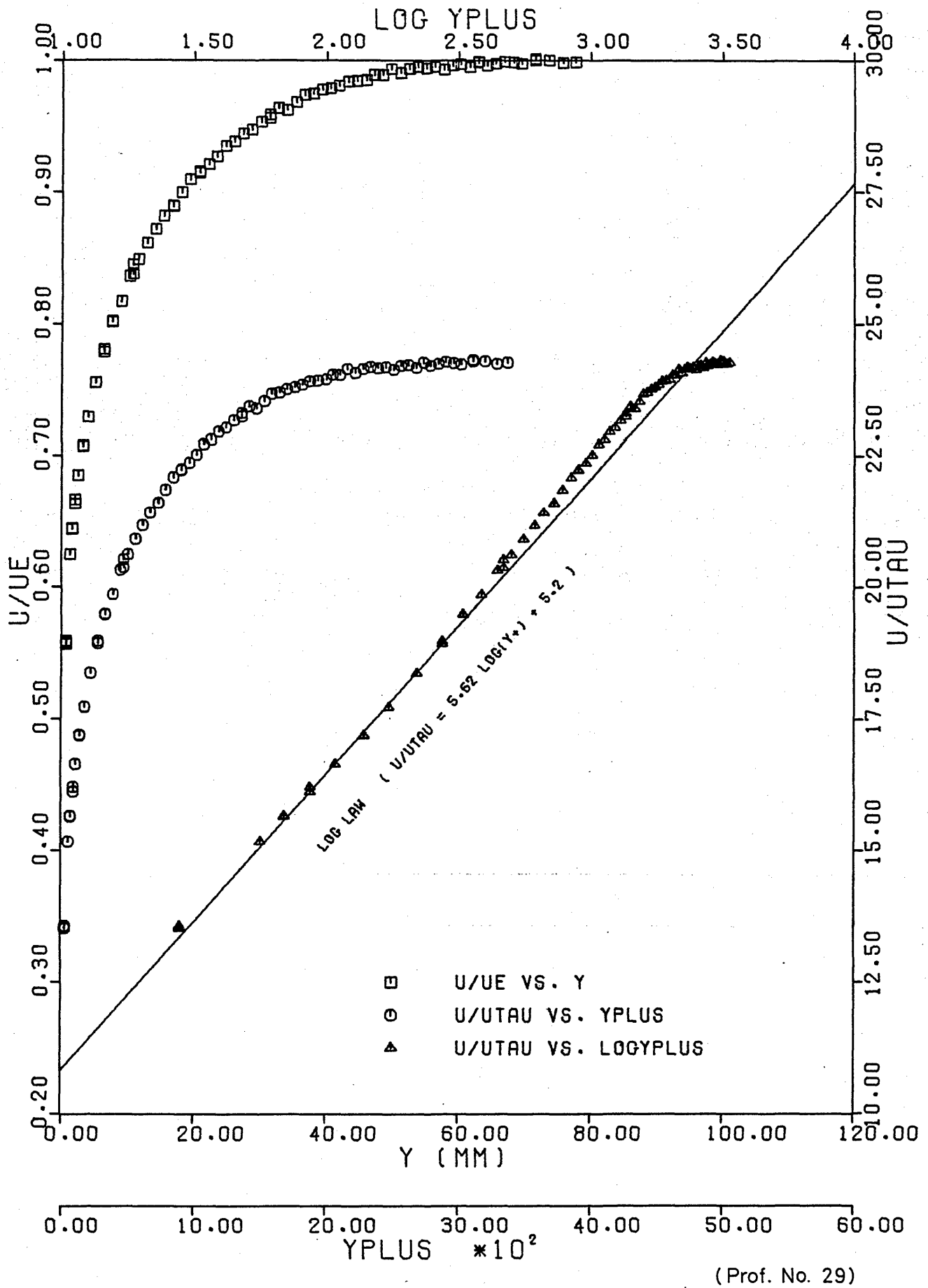

(Prof. No. 29)

c). Stn 10

Fig. 3.26.

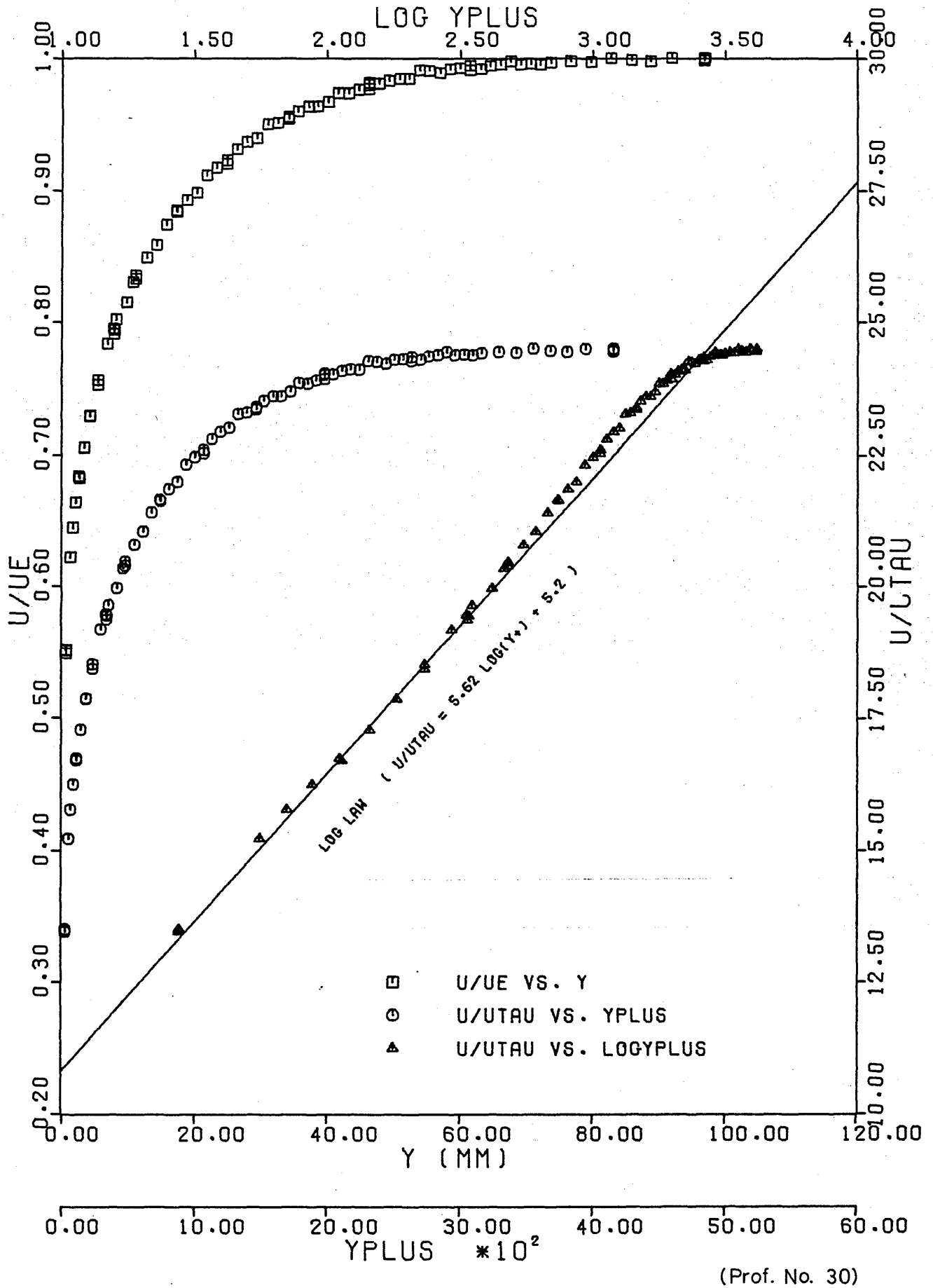

(Prof. No. 30)

d) Stn 12

Fig. 3.26.

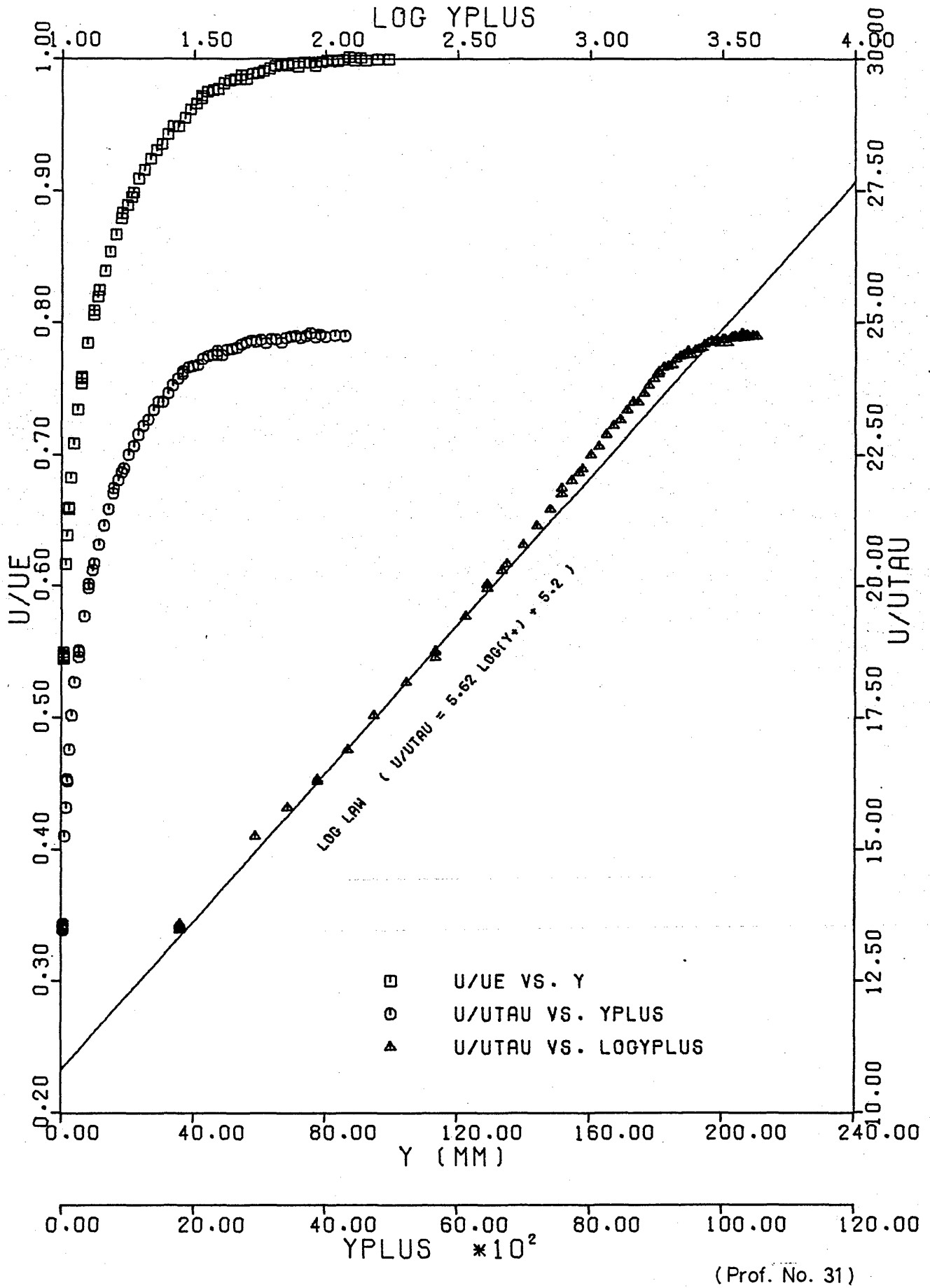

(Prof. No. 31)

e) Stn 14

Fig. 3.26.

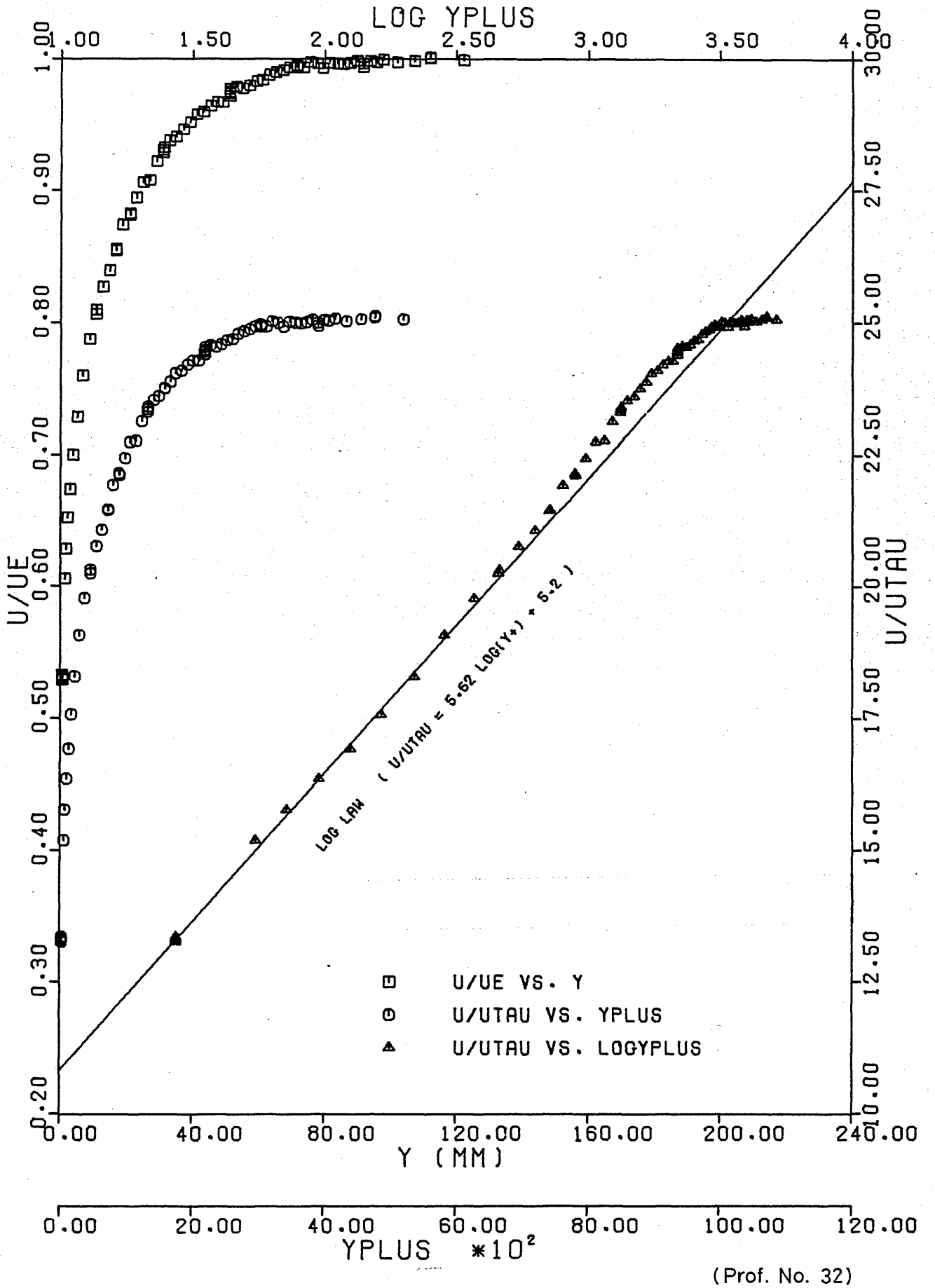

(Prof. No. 32)

f) Stn 16

Fig. 3.26.

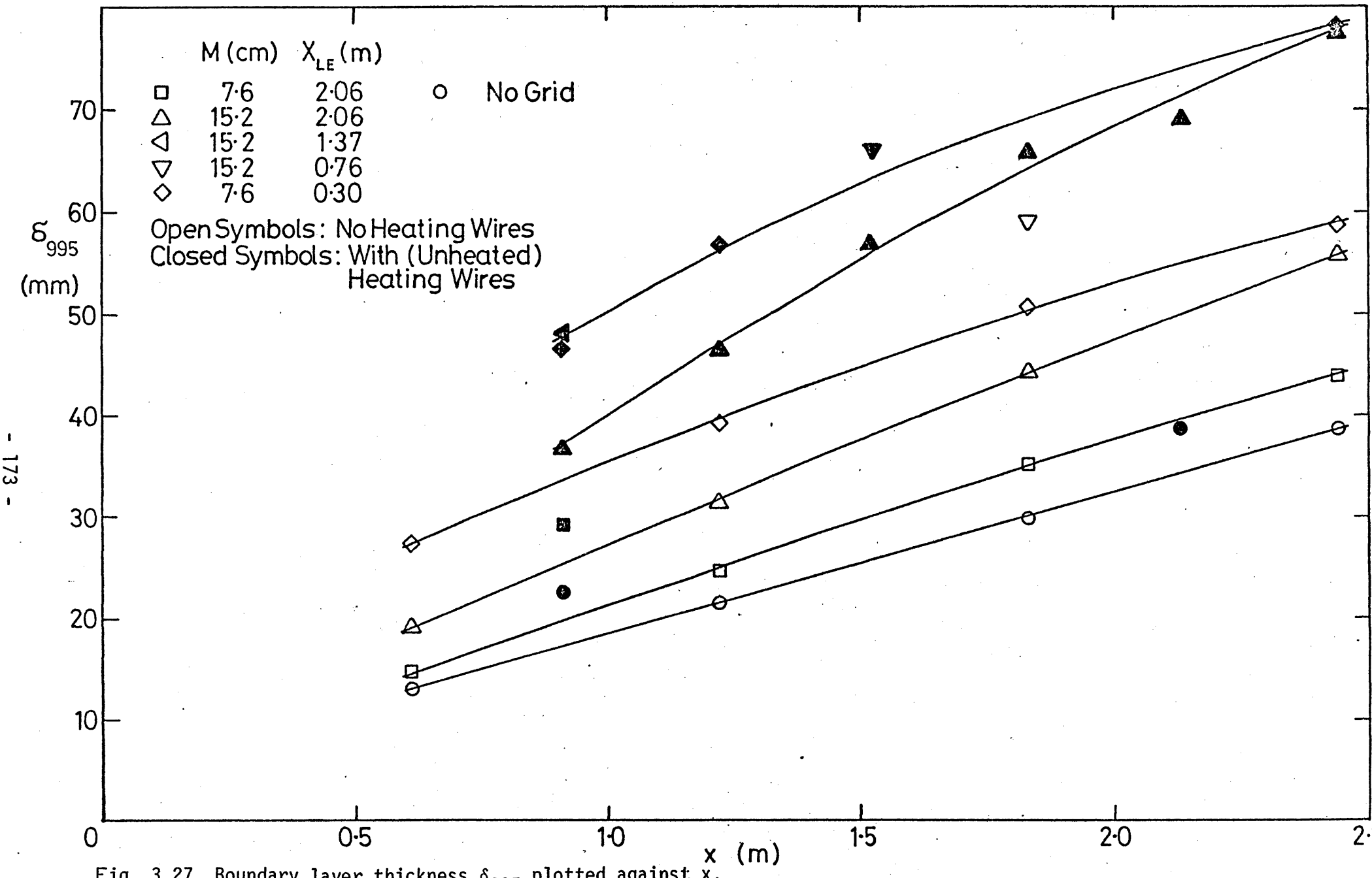

Fig. 3.27 Boundary layer thickness δ_{995} plotted against x.

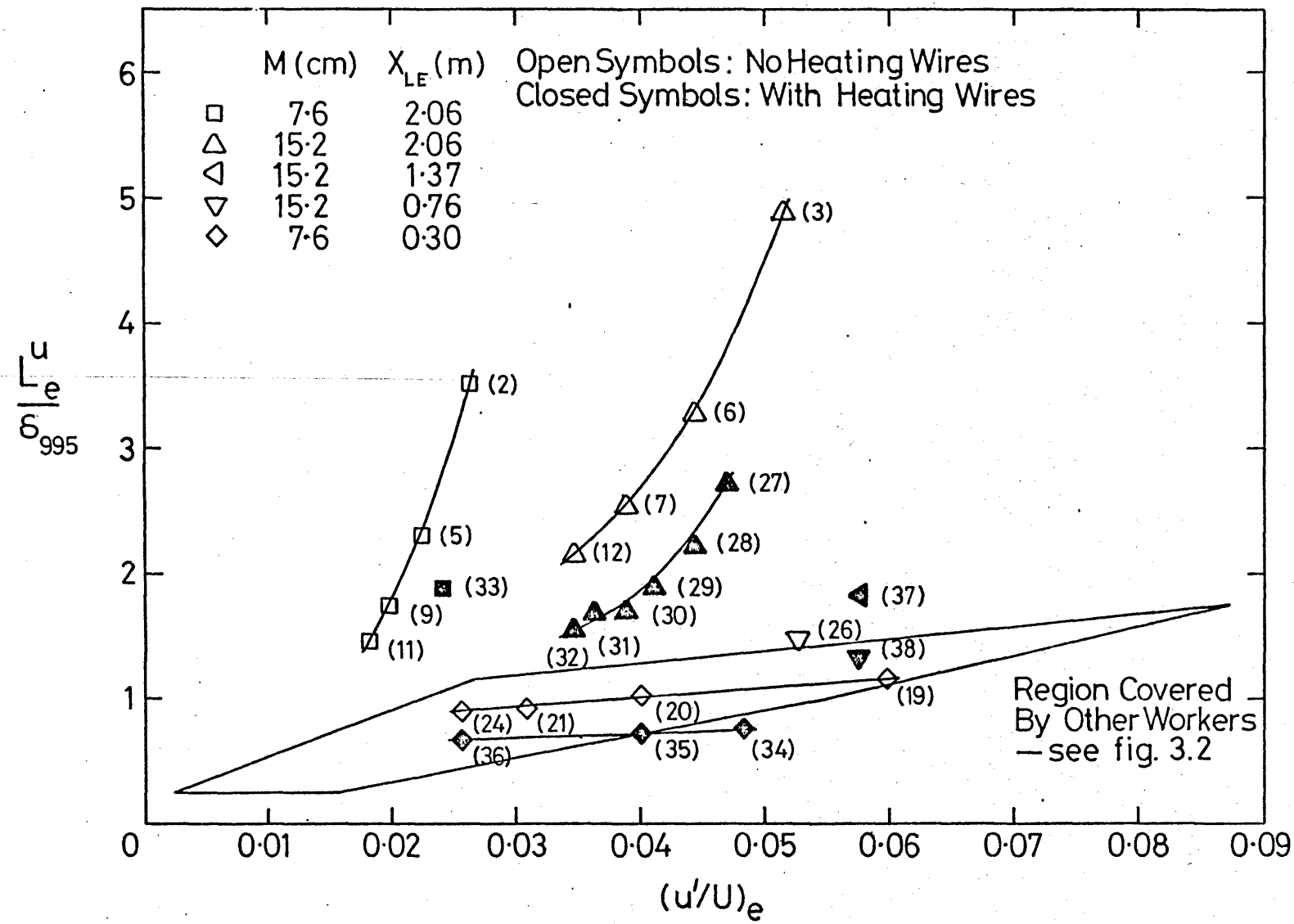

Fig. 3.28 Free-stream intensities and length scale ratios of present and previous measurements.

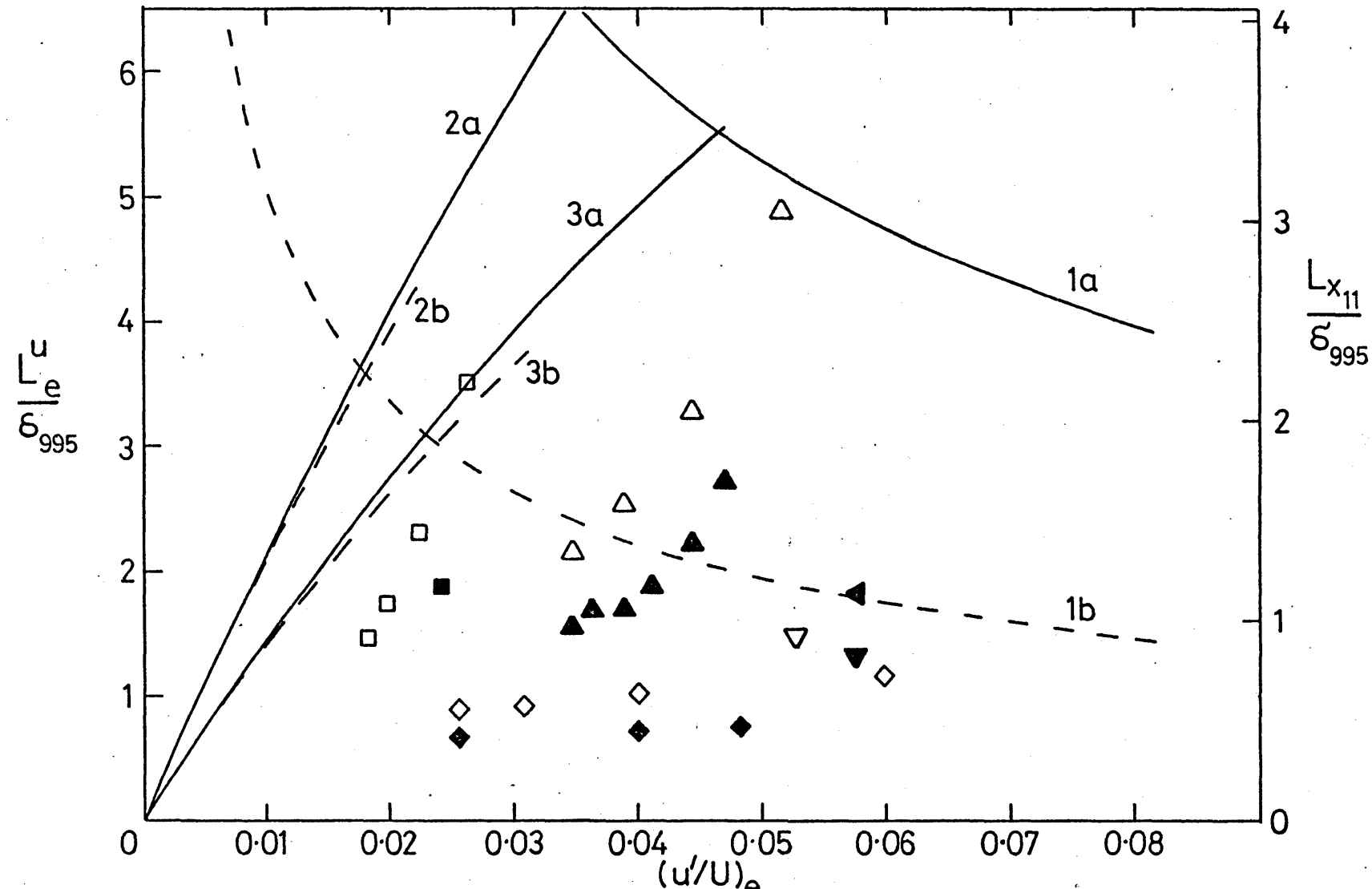

Fig. 3.29 Limits on the range of free-stream intensity and length scale ratio of the present measurements imposed by boundary layer Reynolds number constraints.
1 a,b Max.$(U_eM/\nu)/(U_e\delta/\nu)$; 2 a,b Max. $(U_e\ell/\nu)/(U_e\delta/\nu)$ where ℓ = working section length; 3 a,b Max $(U_e\ell/\nu)/(U_e\delta/\nu)$ where ℓ is an effective reduced working section length, see subsection 3.1.3. a : 15.2 cm Grid; b : 7.6 cm Grid.

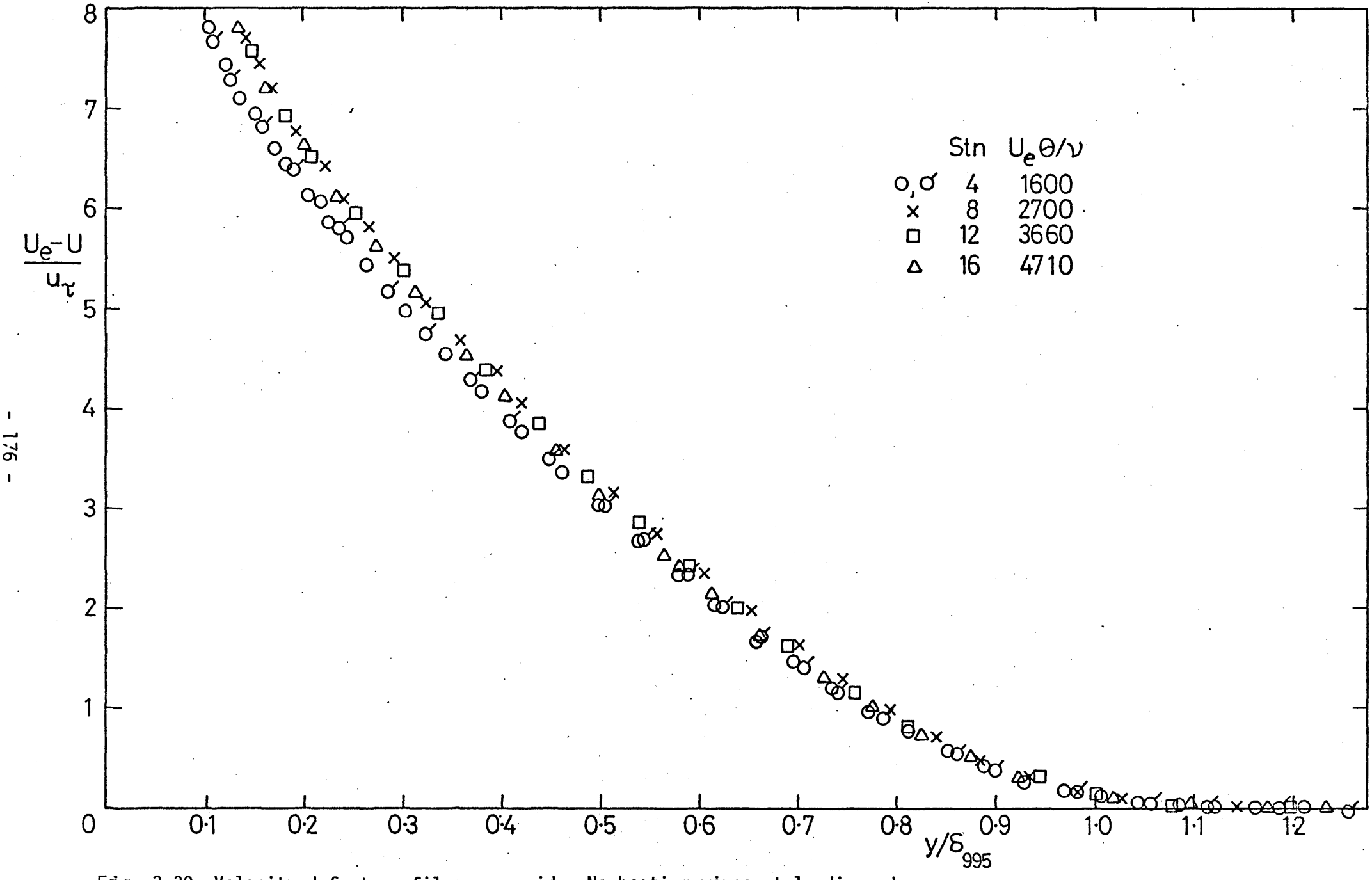

Fig. 3.30 Velocity-defect profiles, no grid. No heating wires at leading edge.

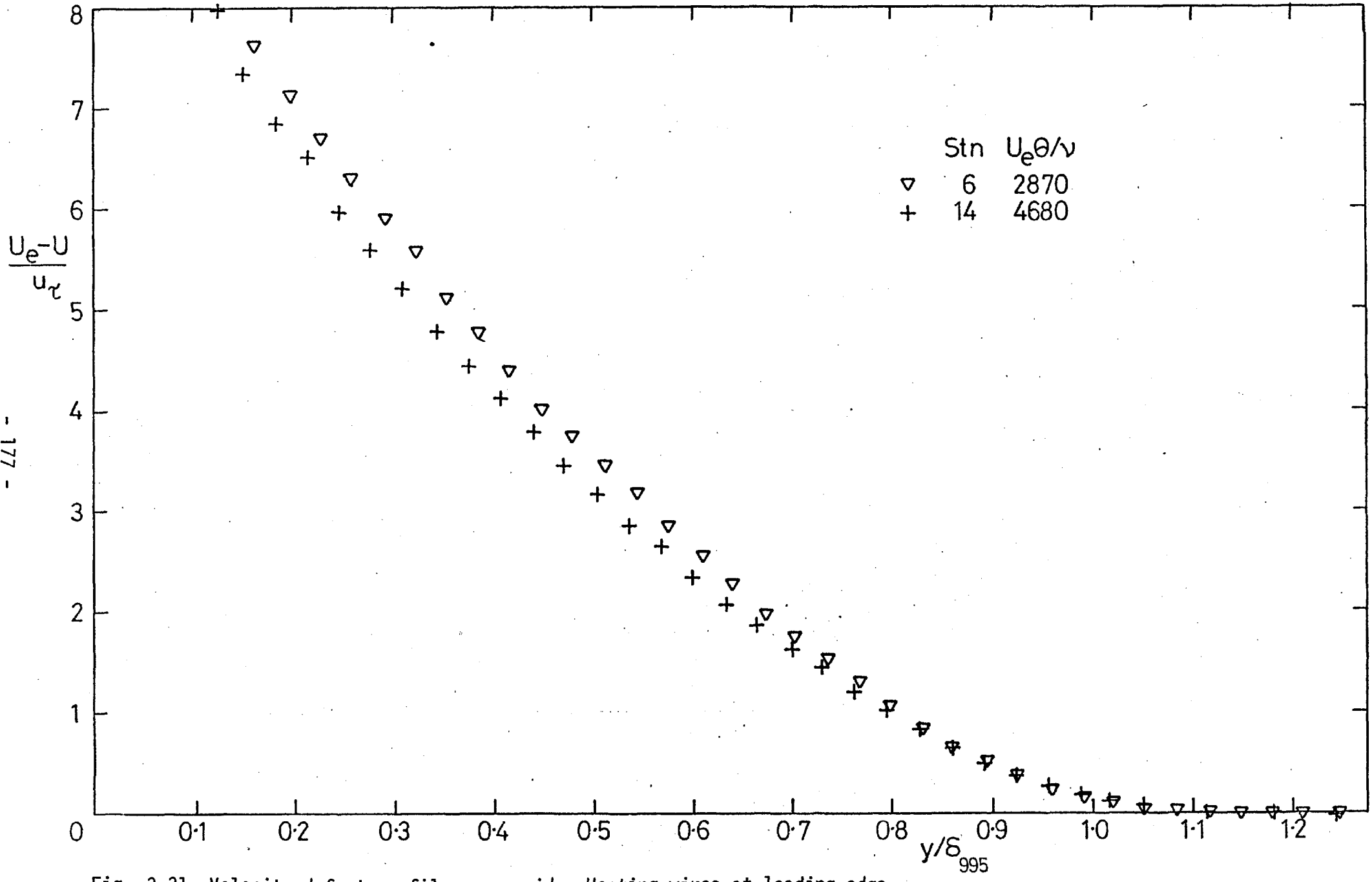

Fig. 3.31 Velocity-defect profiles, no grid. Heating wires at leading edge.

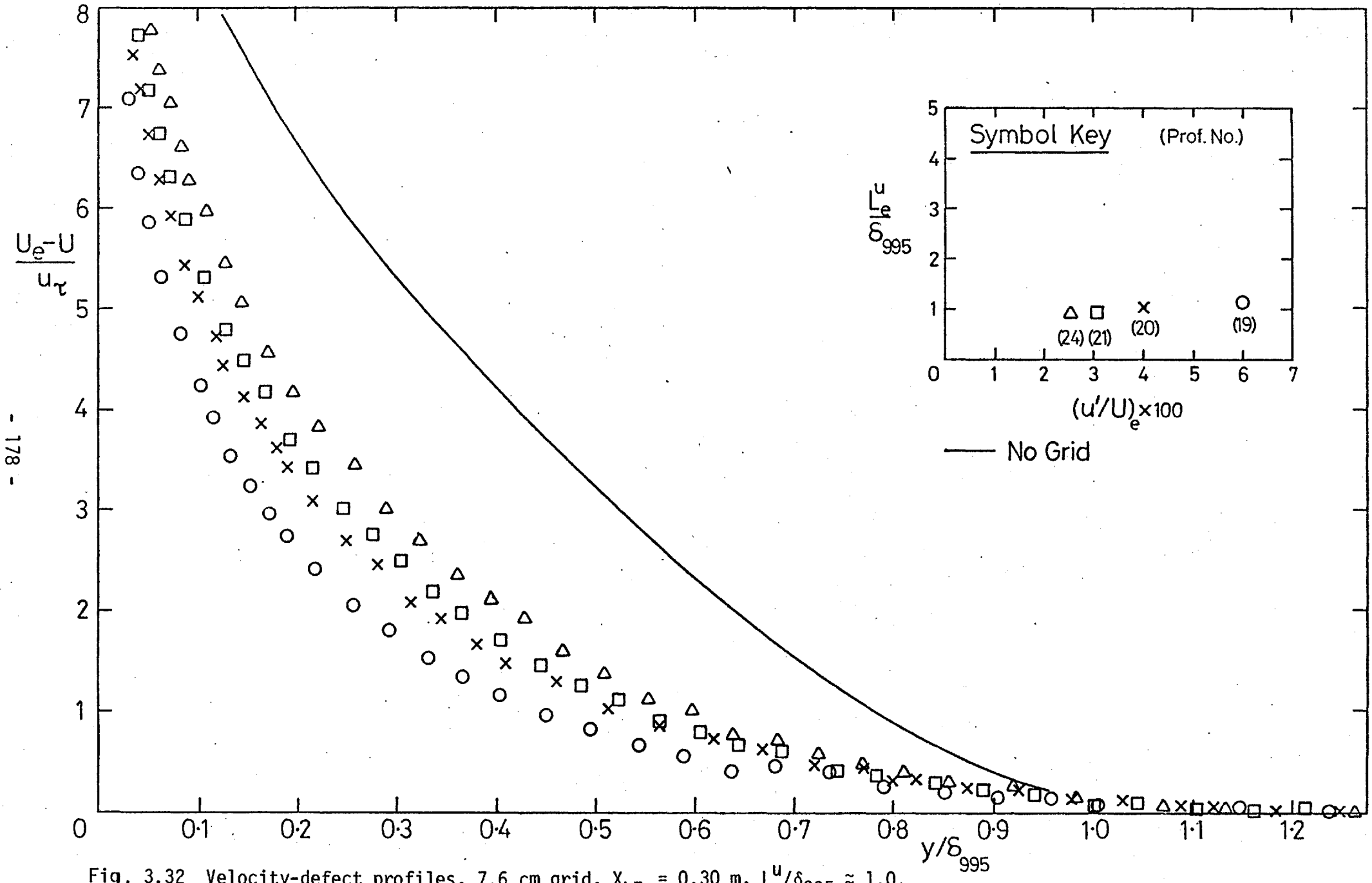

Fig. 3.32 Velocity-defect profiles, 7.6 cm grid, X_{LE} = 0.30 m, $L_e^u/\delta_{995} \approx 1.0$.

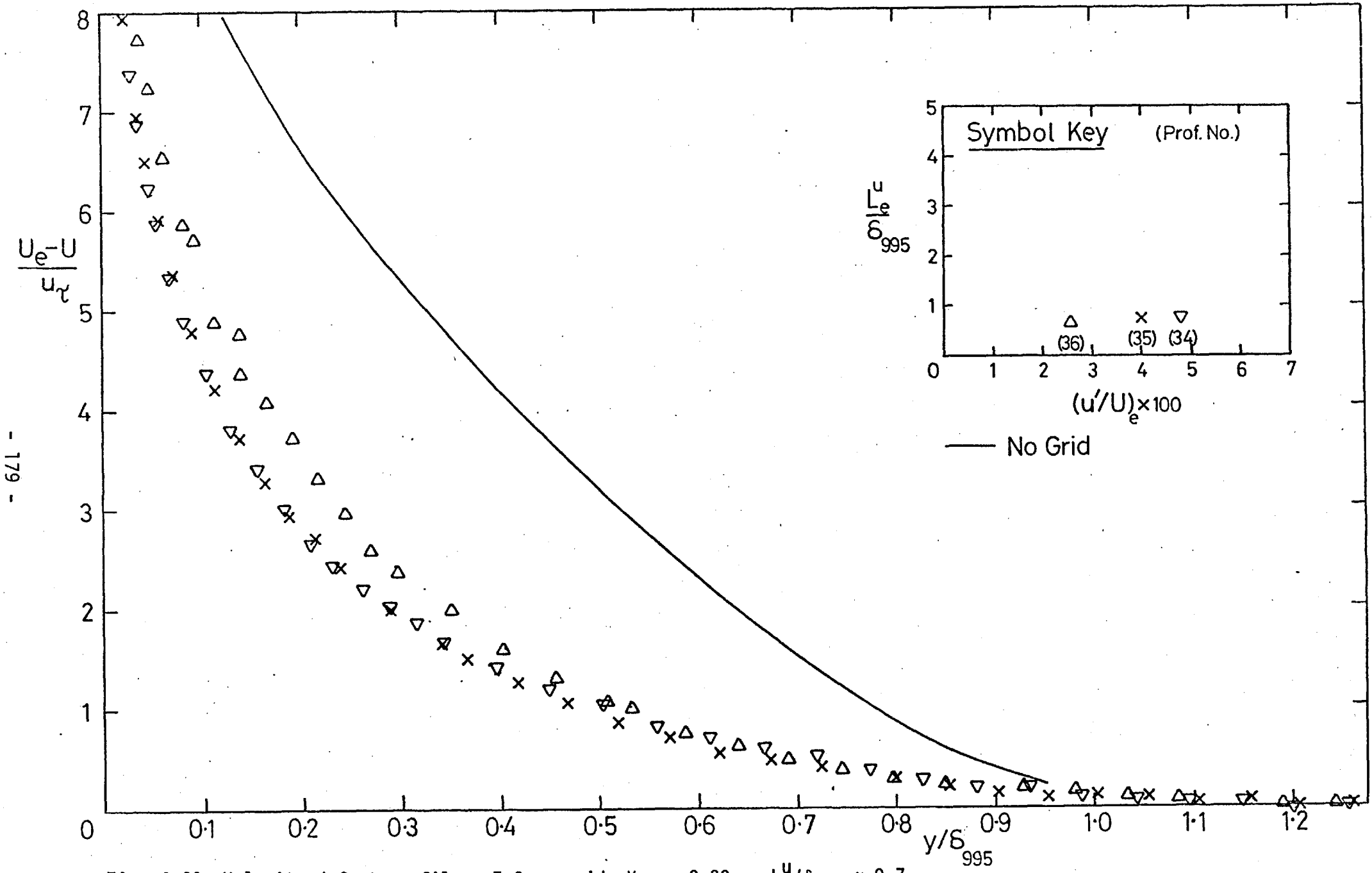

Fig. 3.33 Velocity-defect profiles, 7.6 cm grid, X_{LE} = 0.30 m, $L_e^u/\delta_{995} \approx 0.7$.

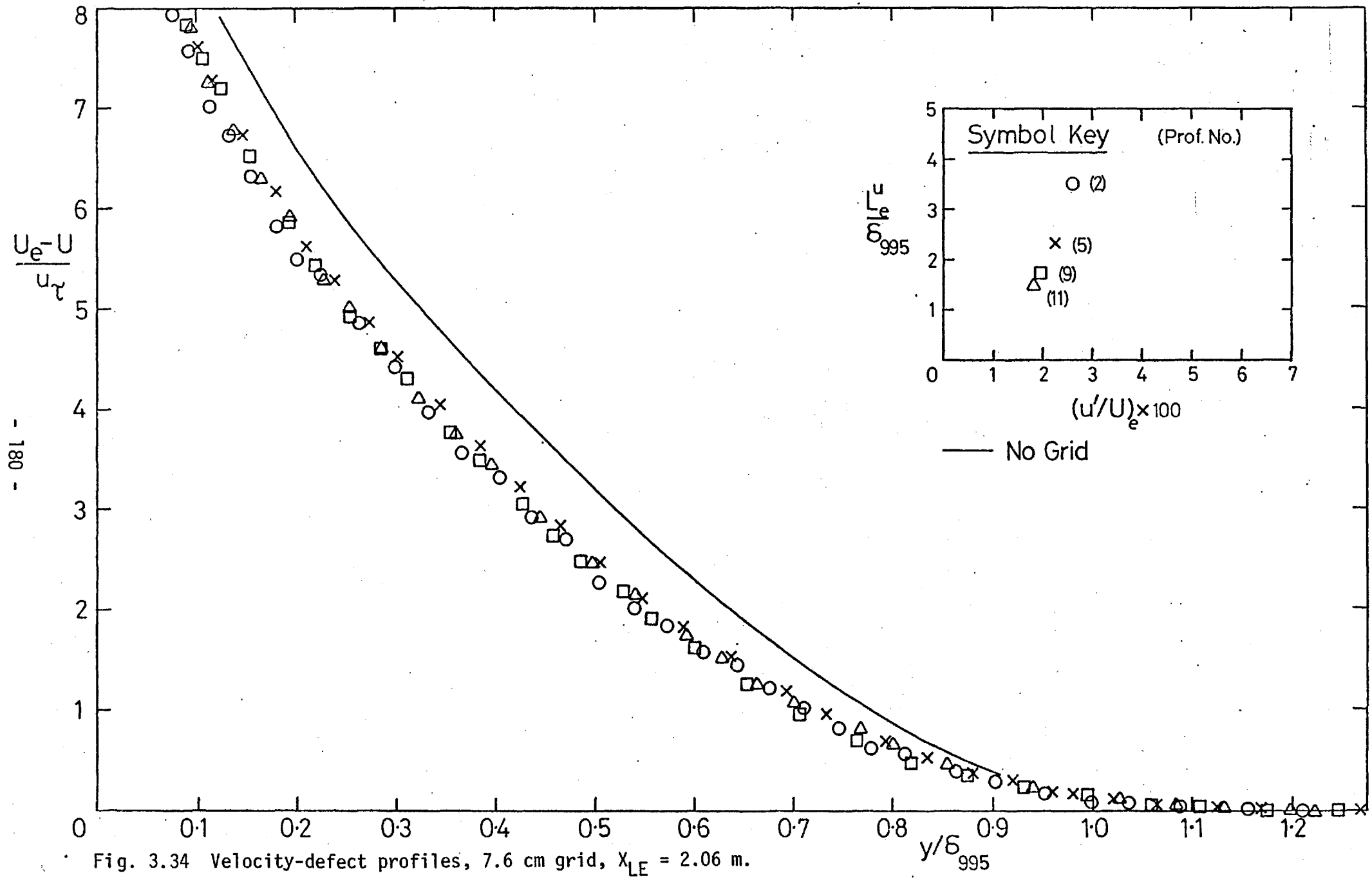

Fig. 3.34 Velocity-defect profiles, 7.6 cm grid, X_{LE} = 2.06 m.

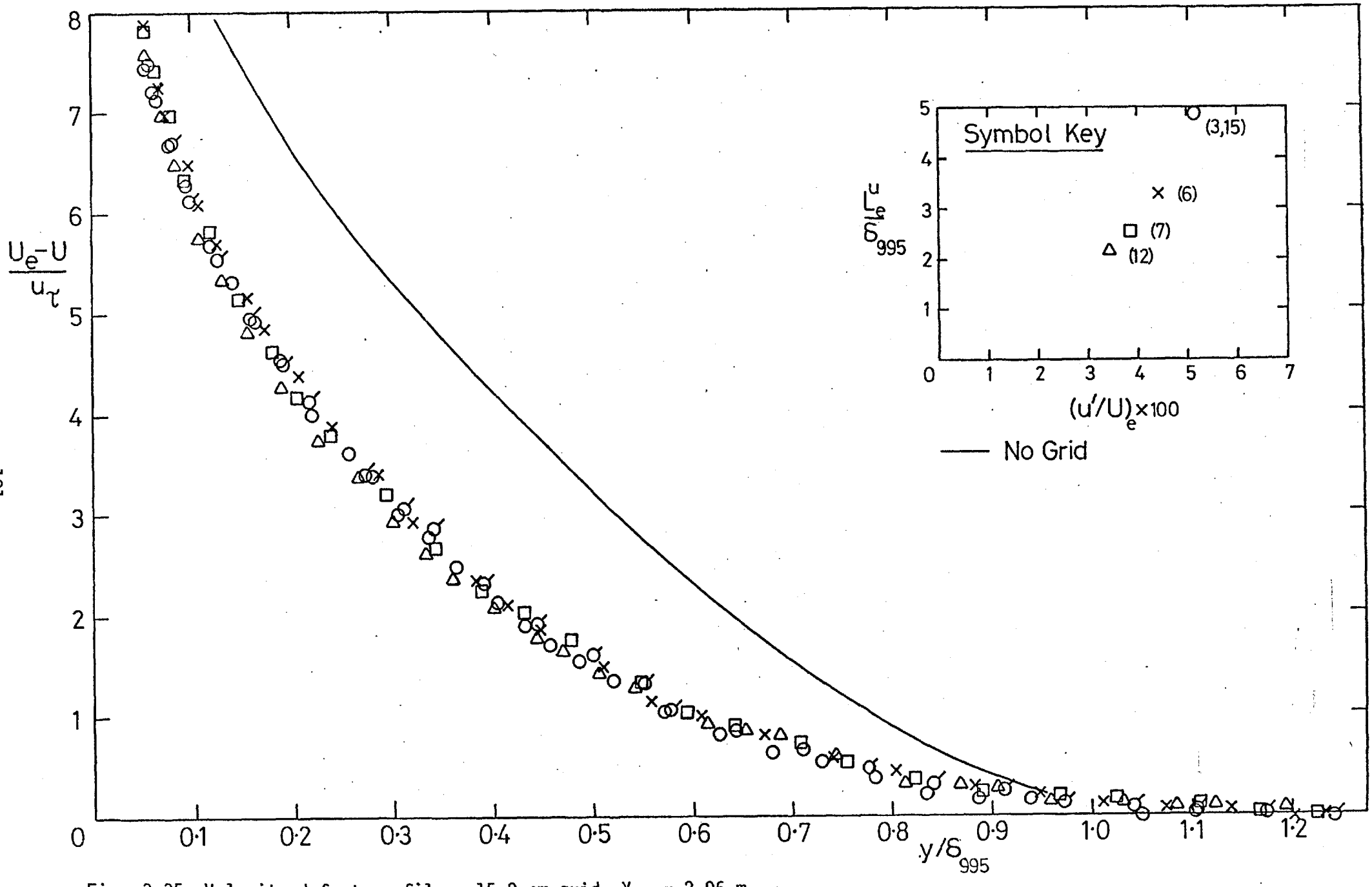

Fig. 3.35 Velocity-defect profiles, 15.2 cm grid, X_{LE} = 2.06 m.

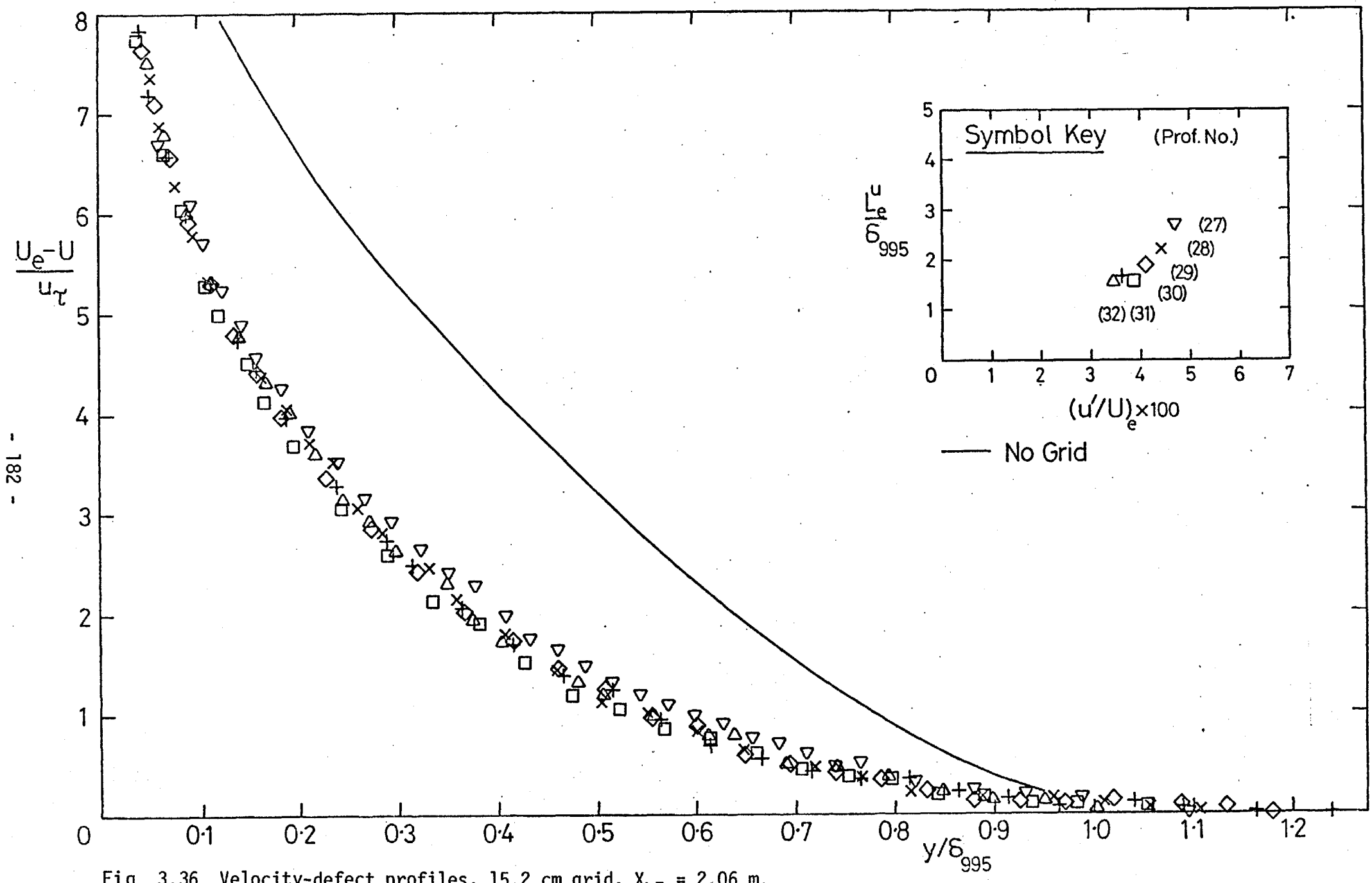

Fig. 3.36 Velocity-defect profiles, 15.2 cm grid, X_{LE} = 2.06 m.

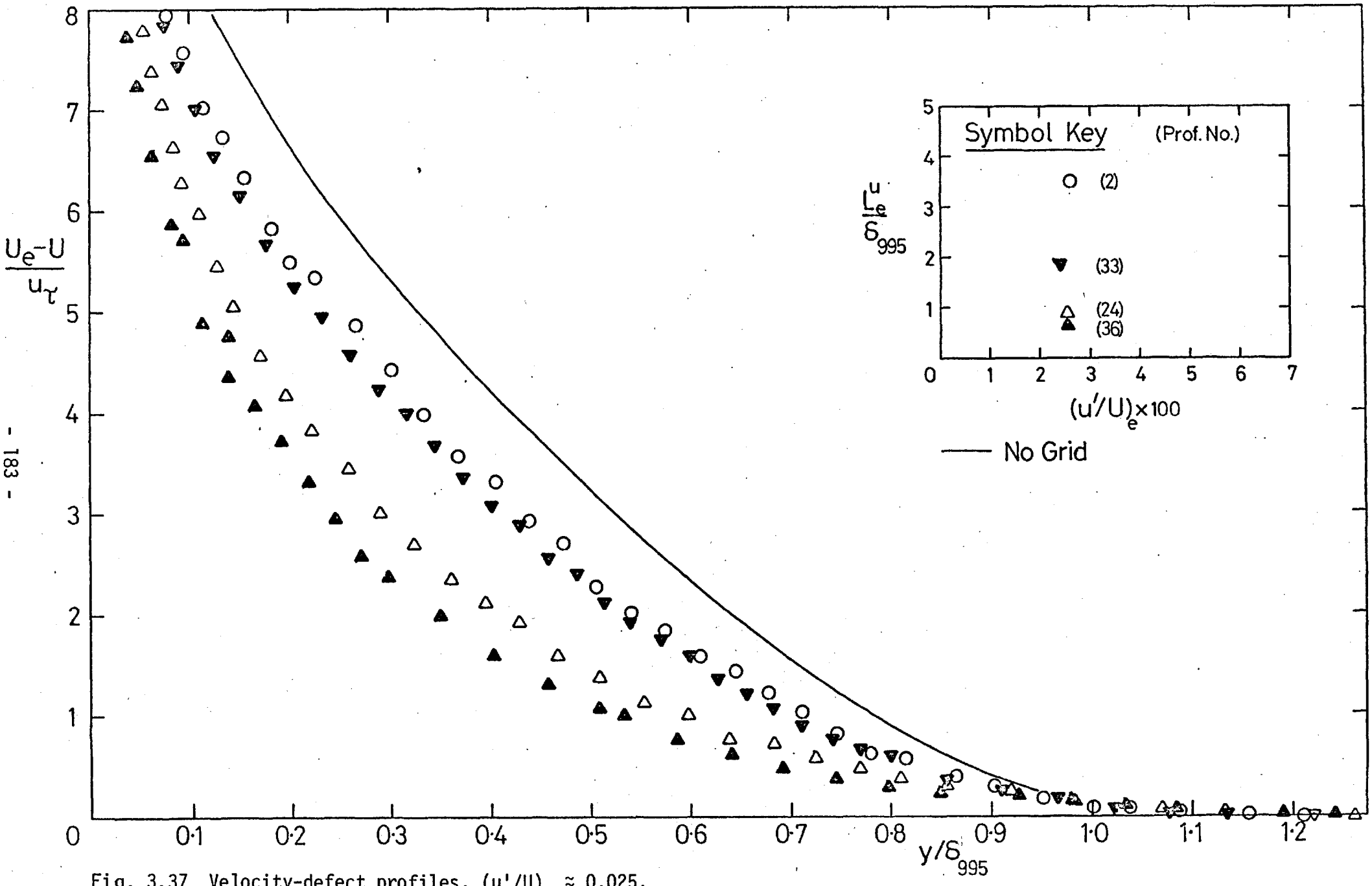

Fig. 3.37 Velocity-defect profiles, $(u'/U)_e \approx 0.025$.

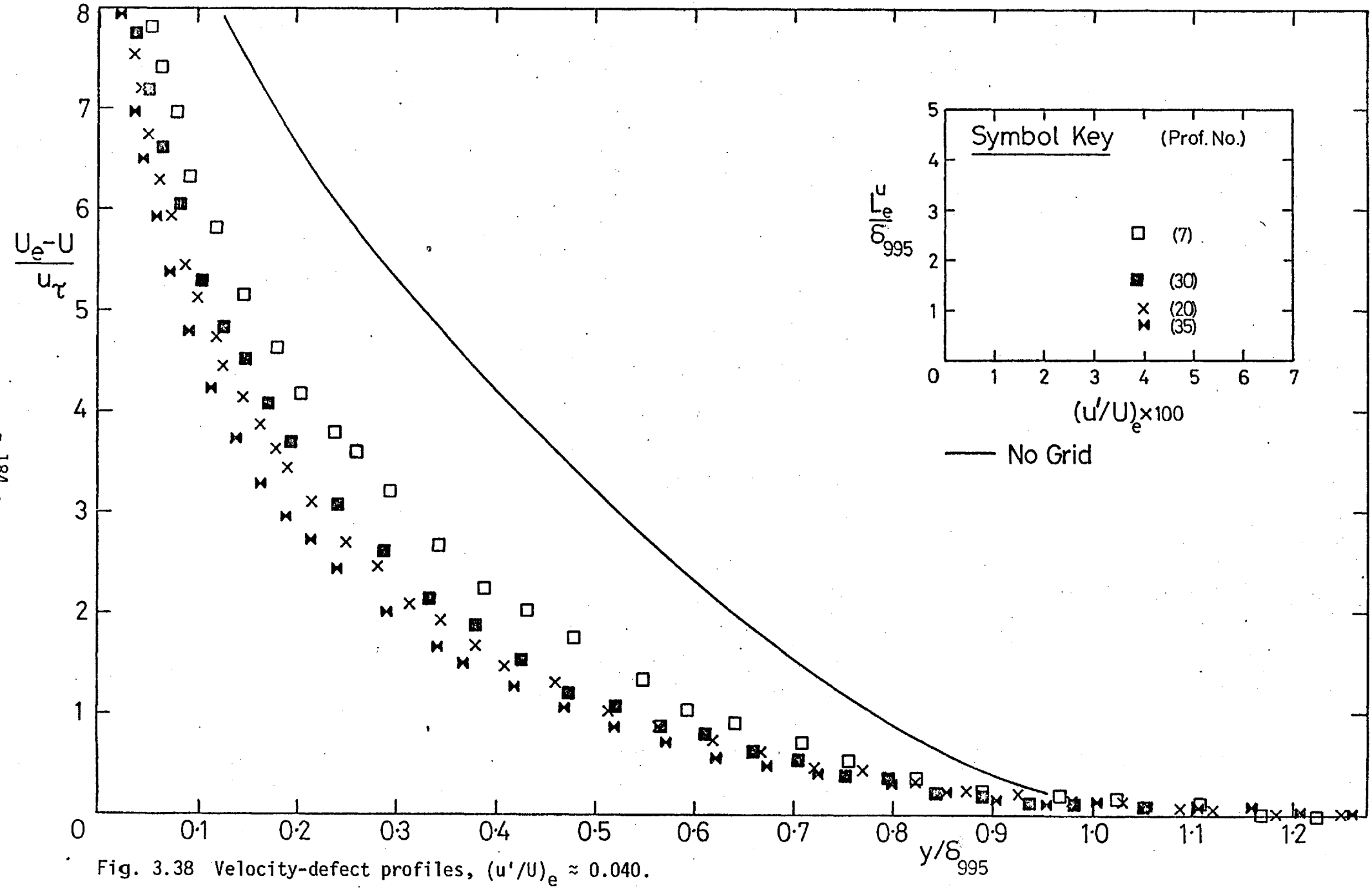

Fig. 3.38 Velocity-defect profiles, $(u'/U)_e \approx 0.040$.

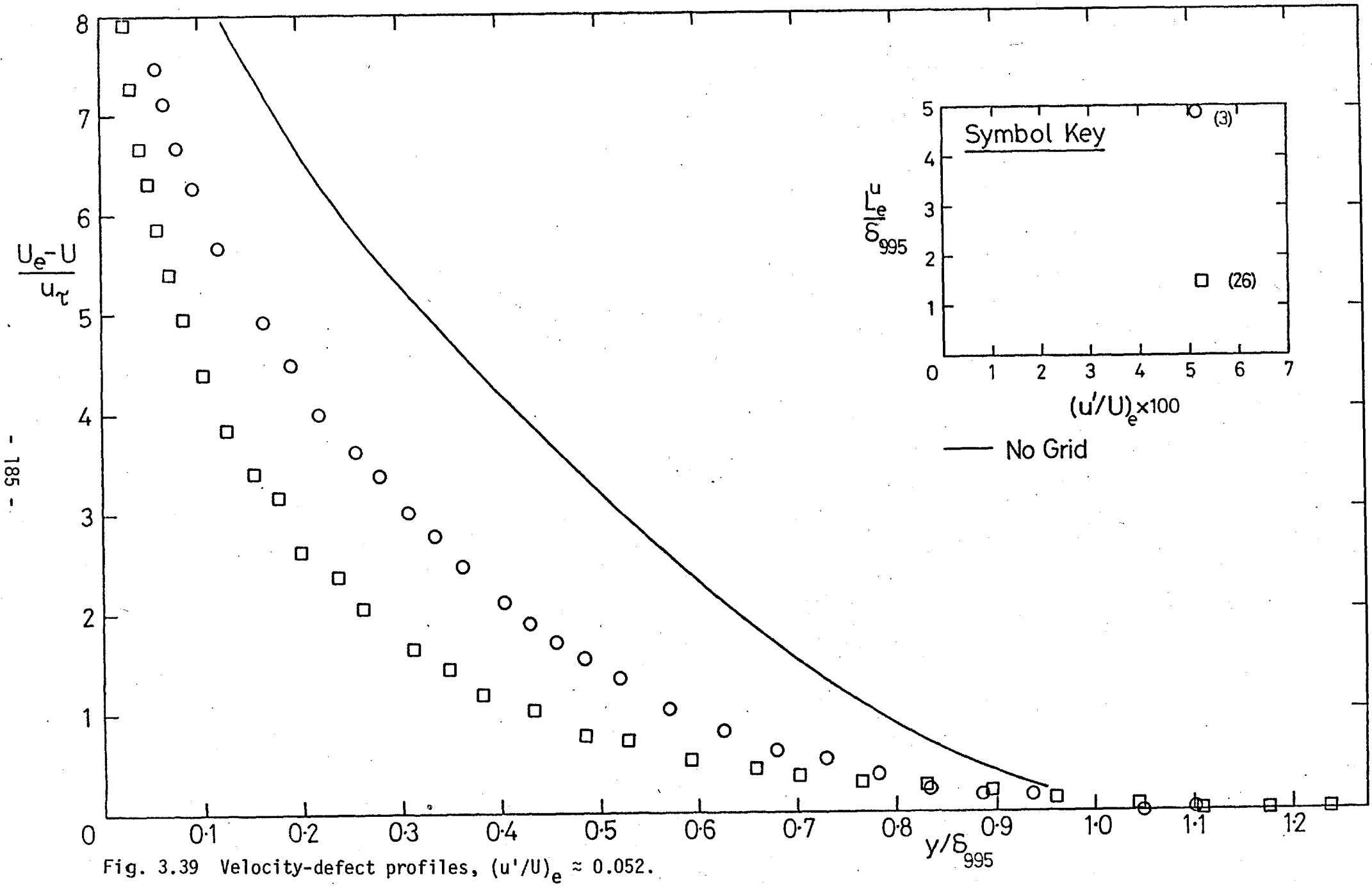

Fig. 3.39 Velocity-defect profiles, $(u'/U)_e \approx 0.052$.

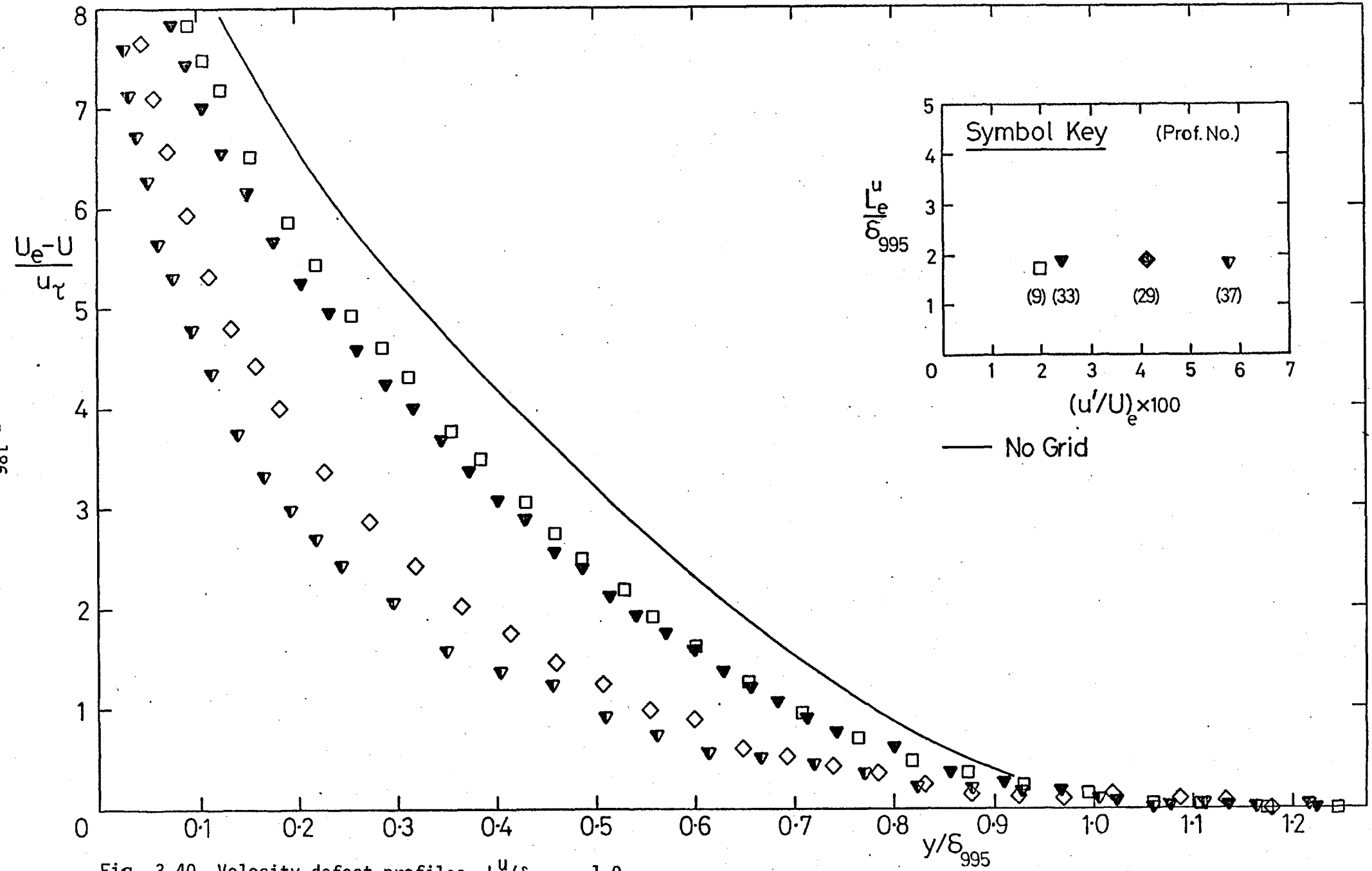

Fig. 3.40 Velocity-defect profiles, $L_e^u/\delta_{995} \approx 1.9$.

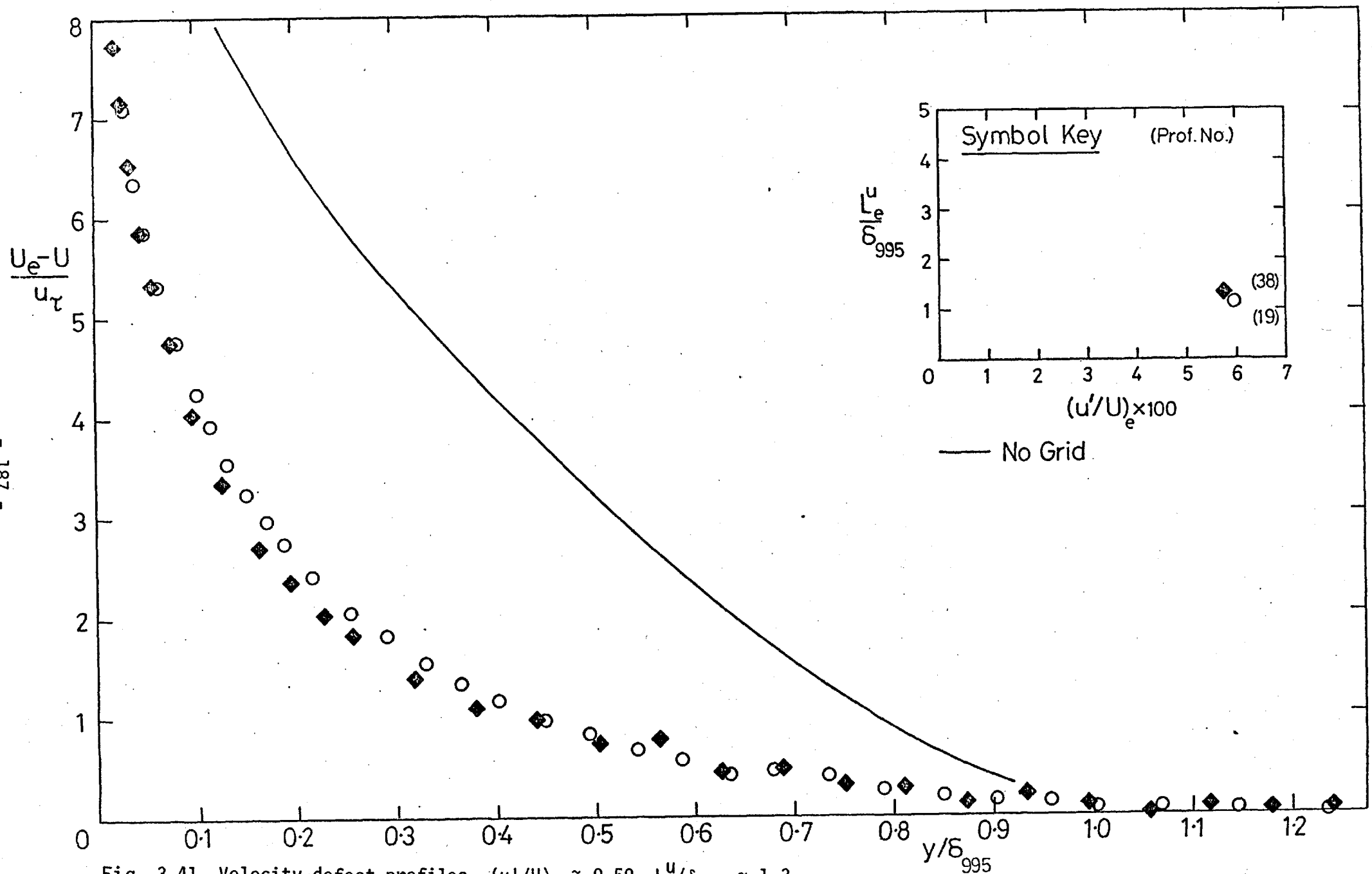

Fig. 3.41 Velocity-defect profiles, $(u'/U)_e \approx 0.59$, $L^u_e/\delta_{995} \approx 1.3$.

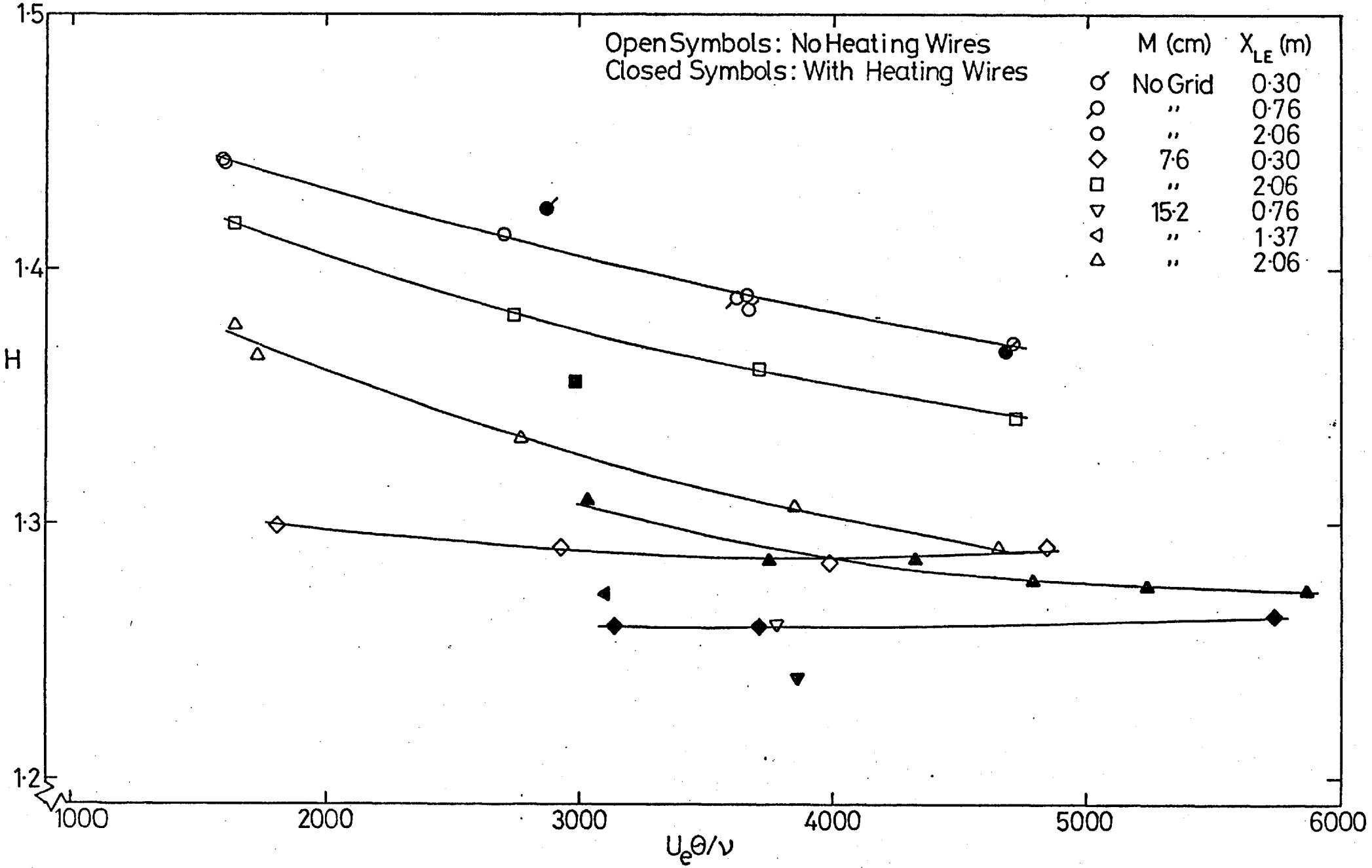

Fig. 3.42 Shape factor H plotted against Reynolds number $U_e\theta/\nu$.

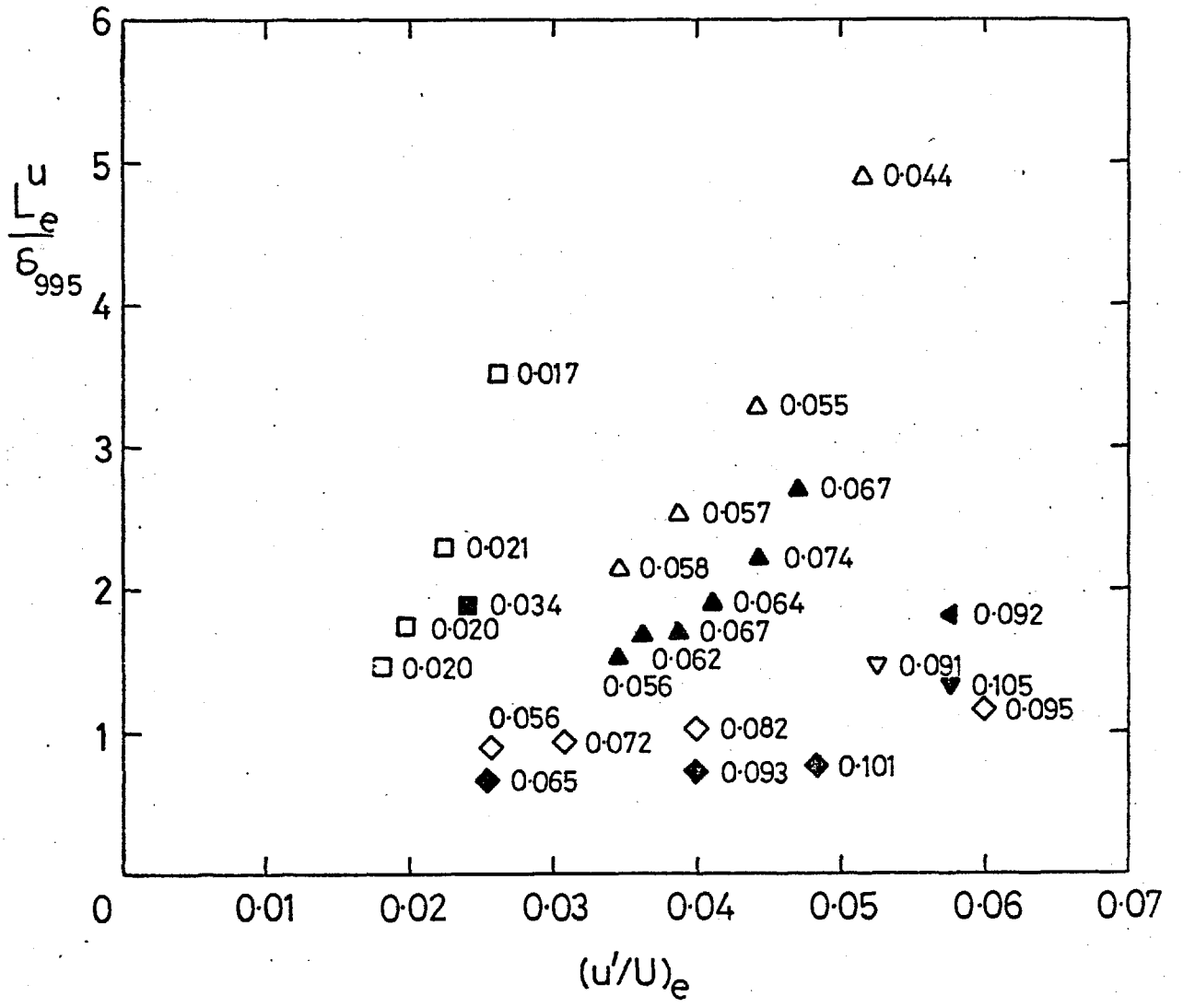

Fig. 3.43 Values of $-\Delta H/H_o$ tabulated at appropriate $(u'/U)_e$ and L_e^u/δ_{995}.

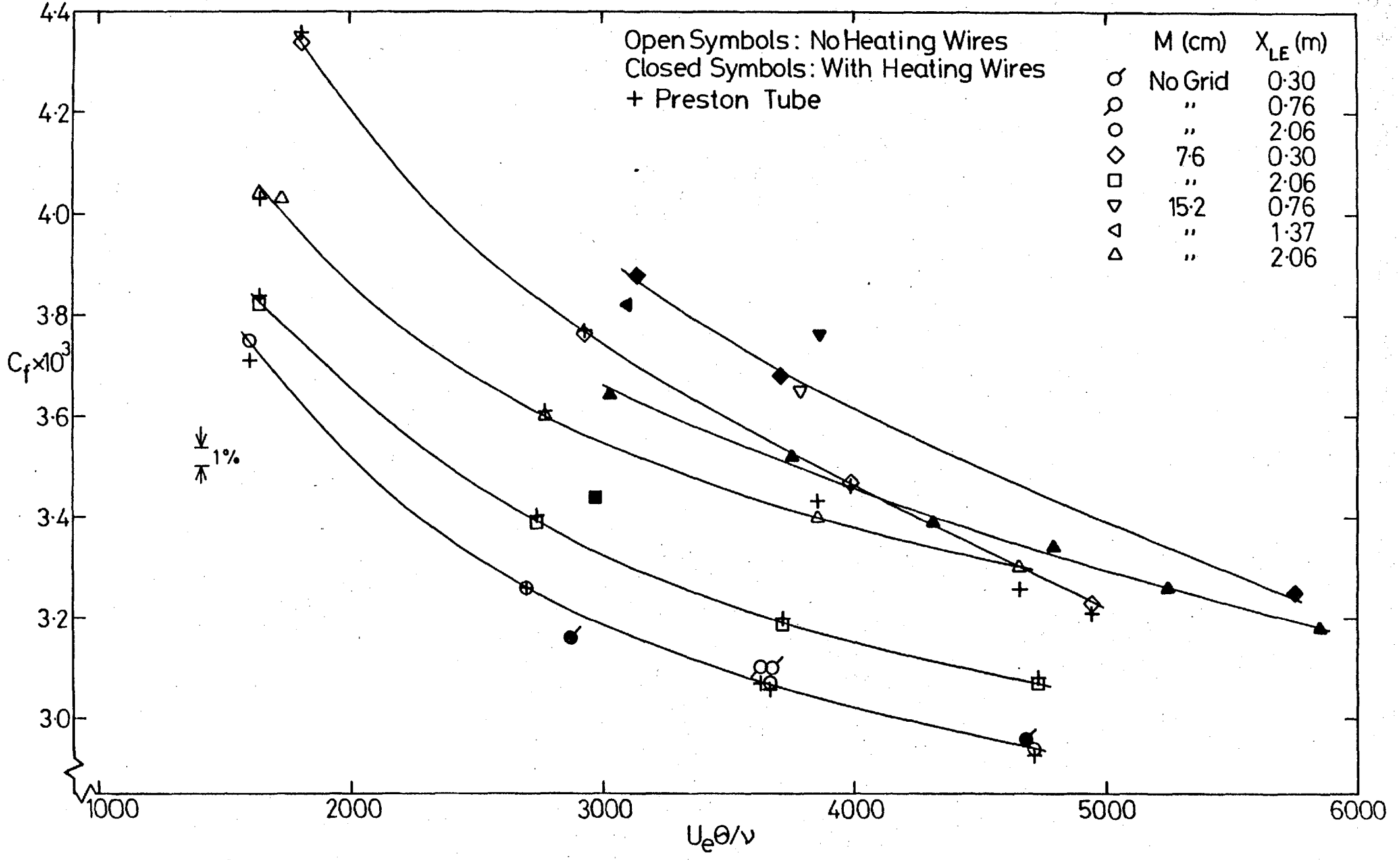

Fig. 3.44 Skin-friction coefficient plotted against Reynolds number $U_e\theta/\nu$

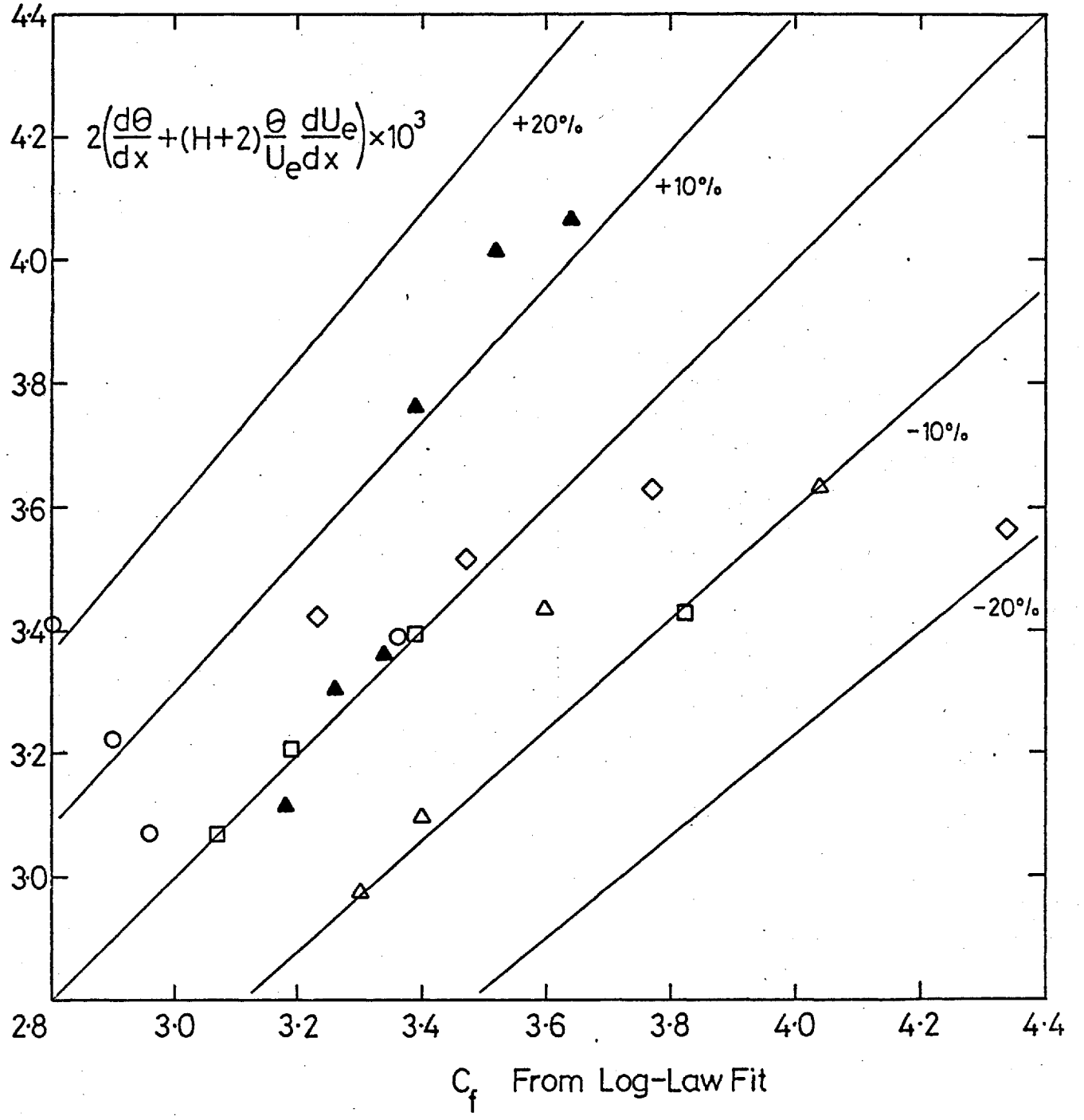

Fig. 3.45 Comparison of C_f from the (two-dimensional) momentum integral equation with values from log-law fit.

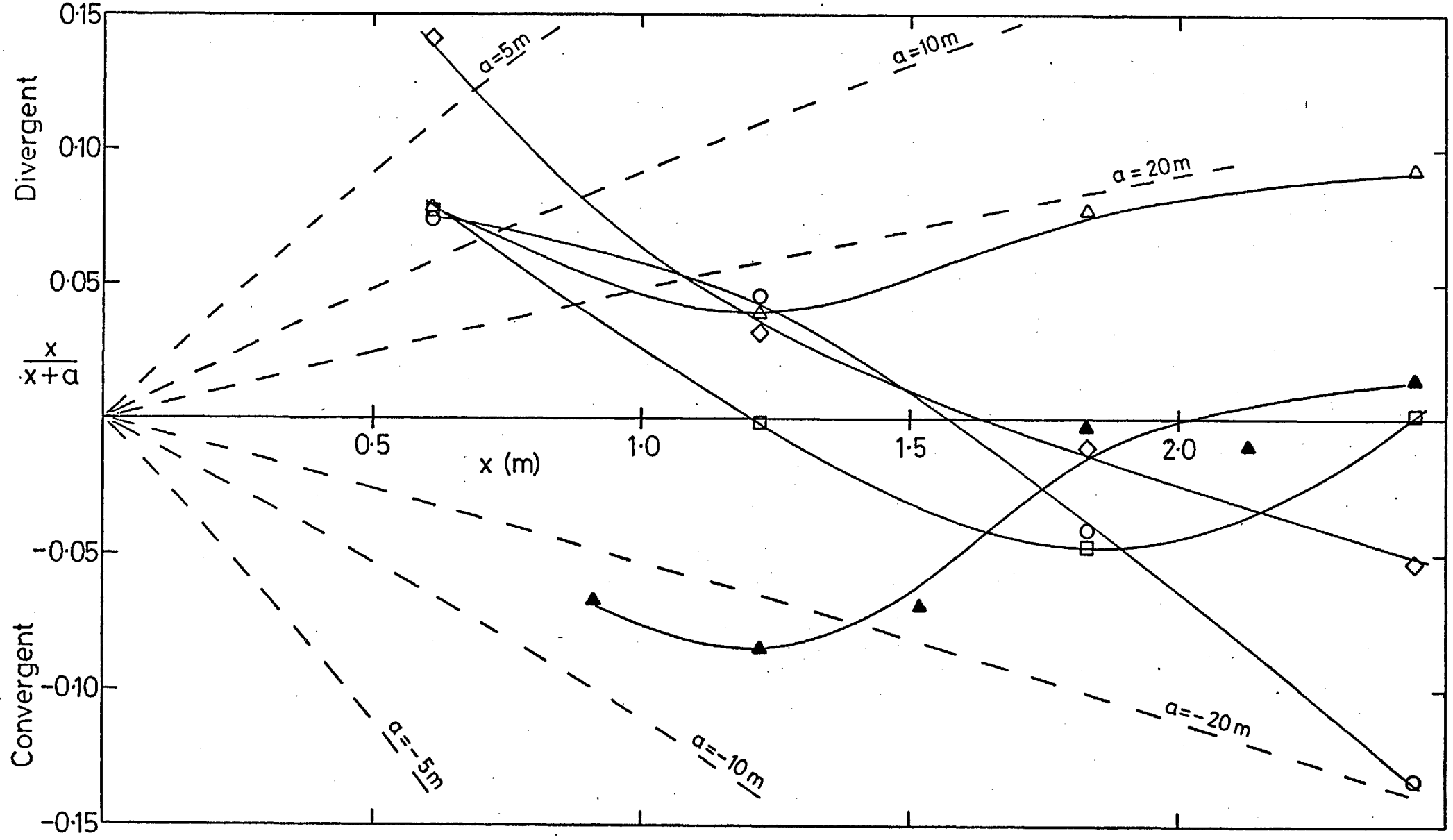

Fig. 3.46 Convergence/divergence implied by momentum integral equation.

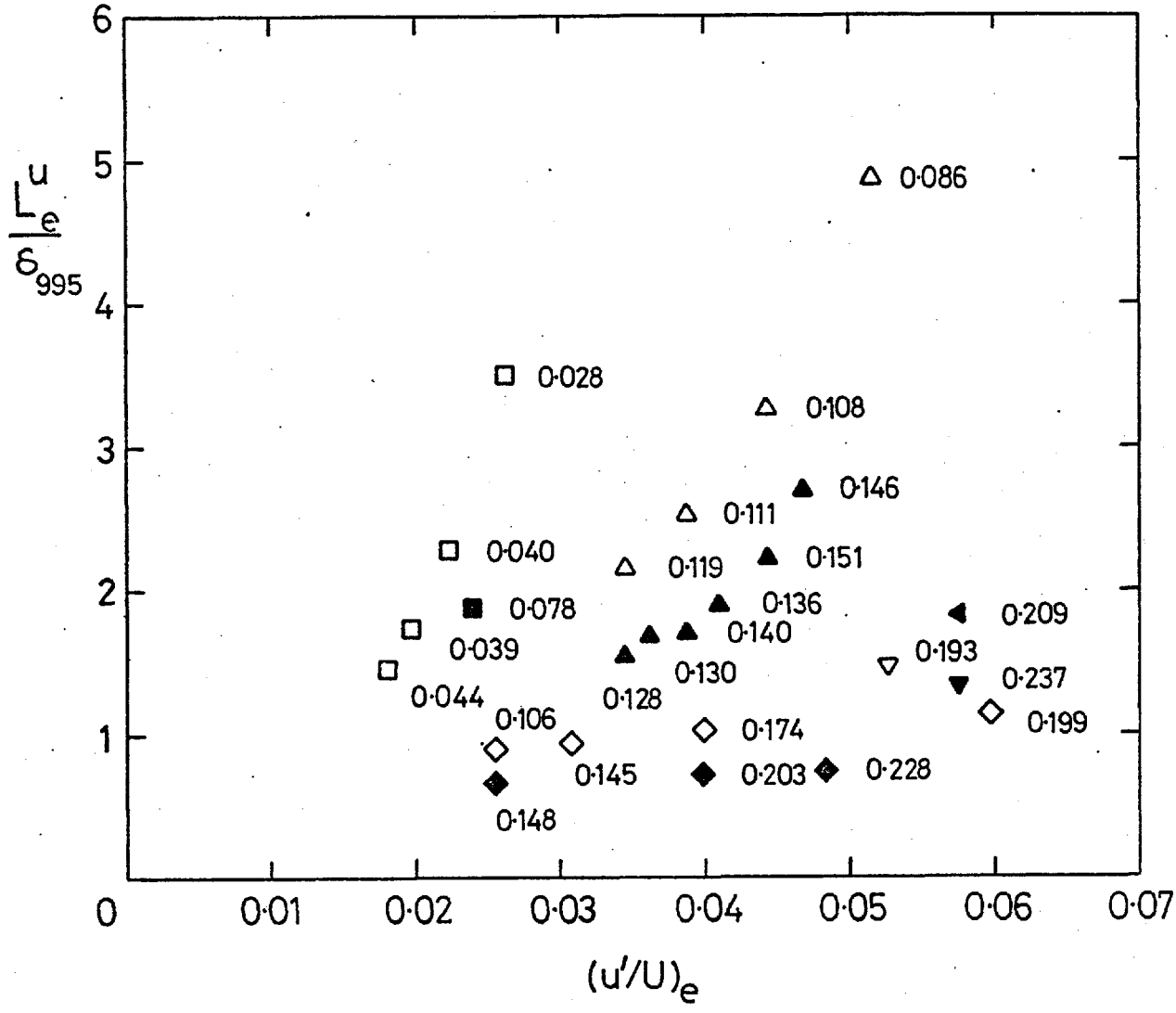

Fig. 3.47 Values of $\Delta C_f/C_{f_o}$ tabulated at appropriate $(u'/U)_e$ and L_e^u/δ_{995}.

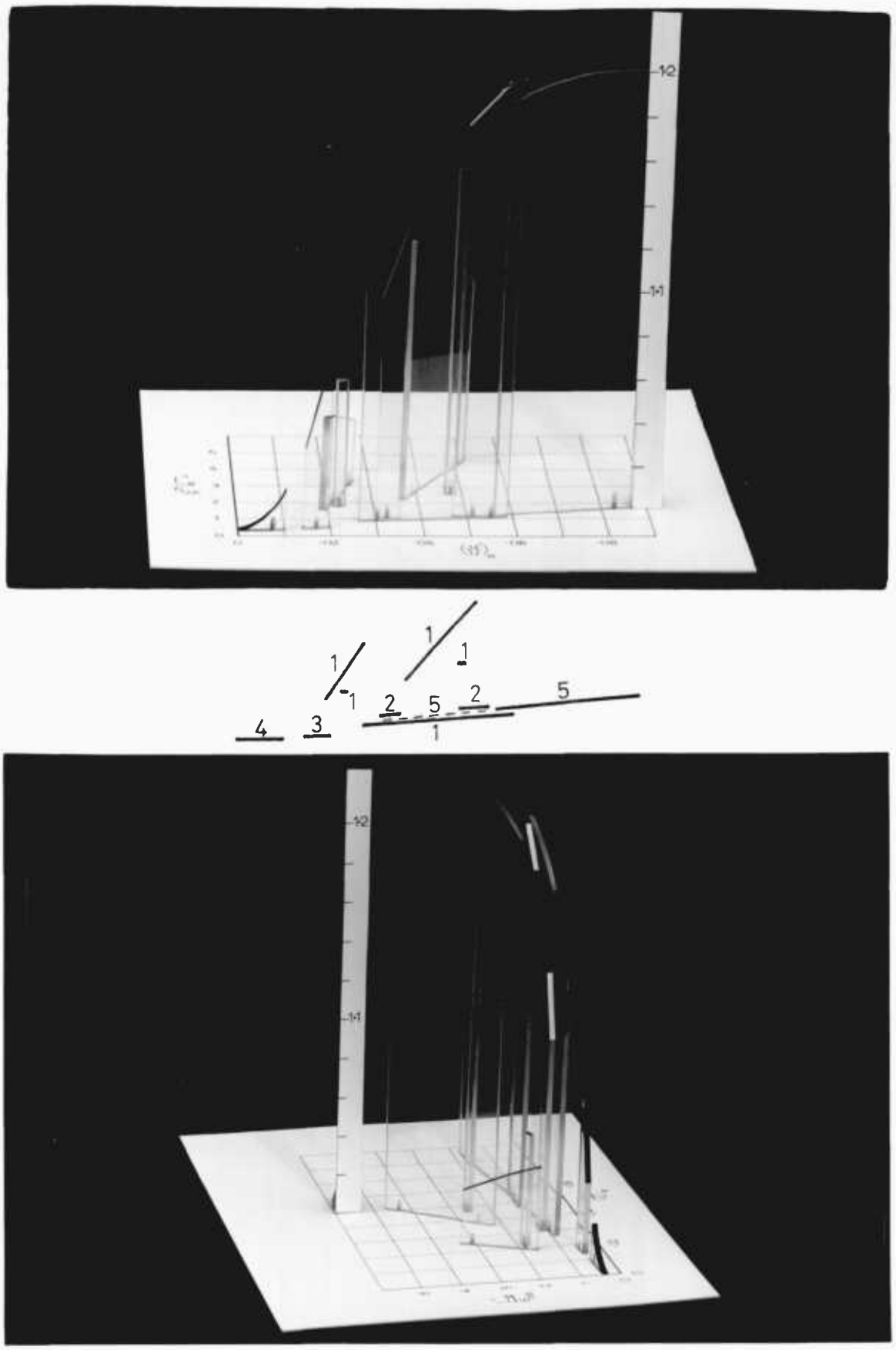

Fig. 3.48 C_f/C_{f_o} as a function of $(u'/U)_e$ and L^u_e/δ_{995} (Perspex model).
1, Present; 2, Huffman et al.; 3, Evans (1972); 4, Meier;
5, Robertson & Holt.

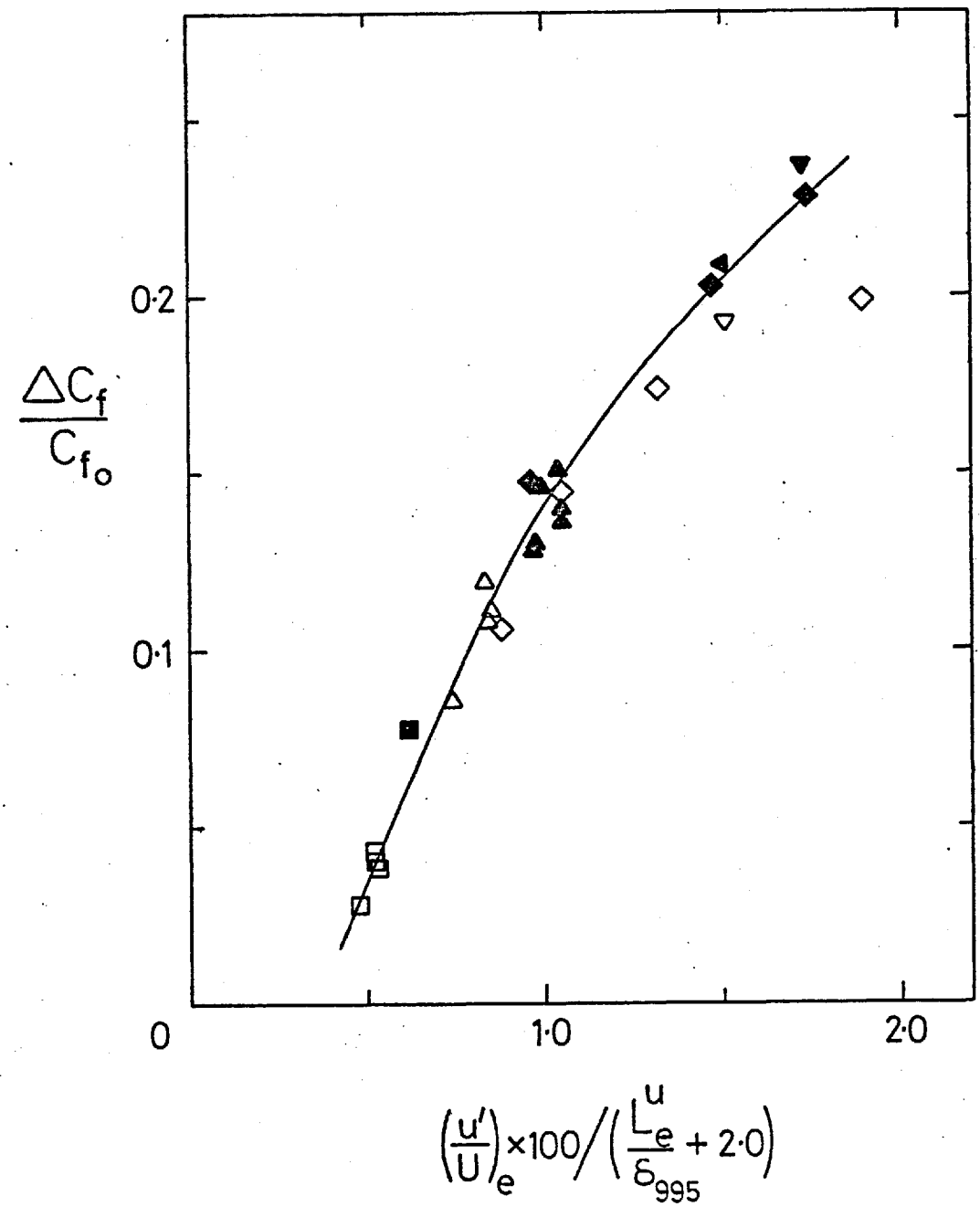

Fig. 3.49 Correlation of $\Delta C_f/C_{f_o}$ with $(u'/U)_e$ and L_e^u/δ_{995}.

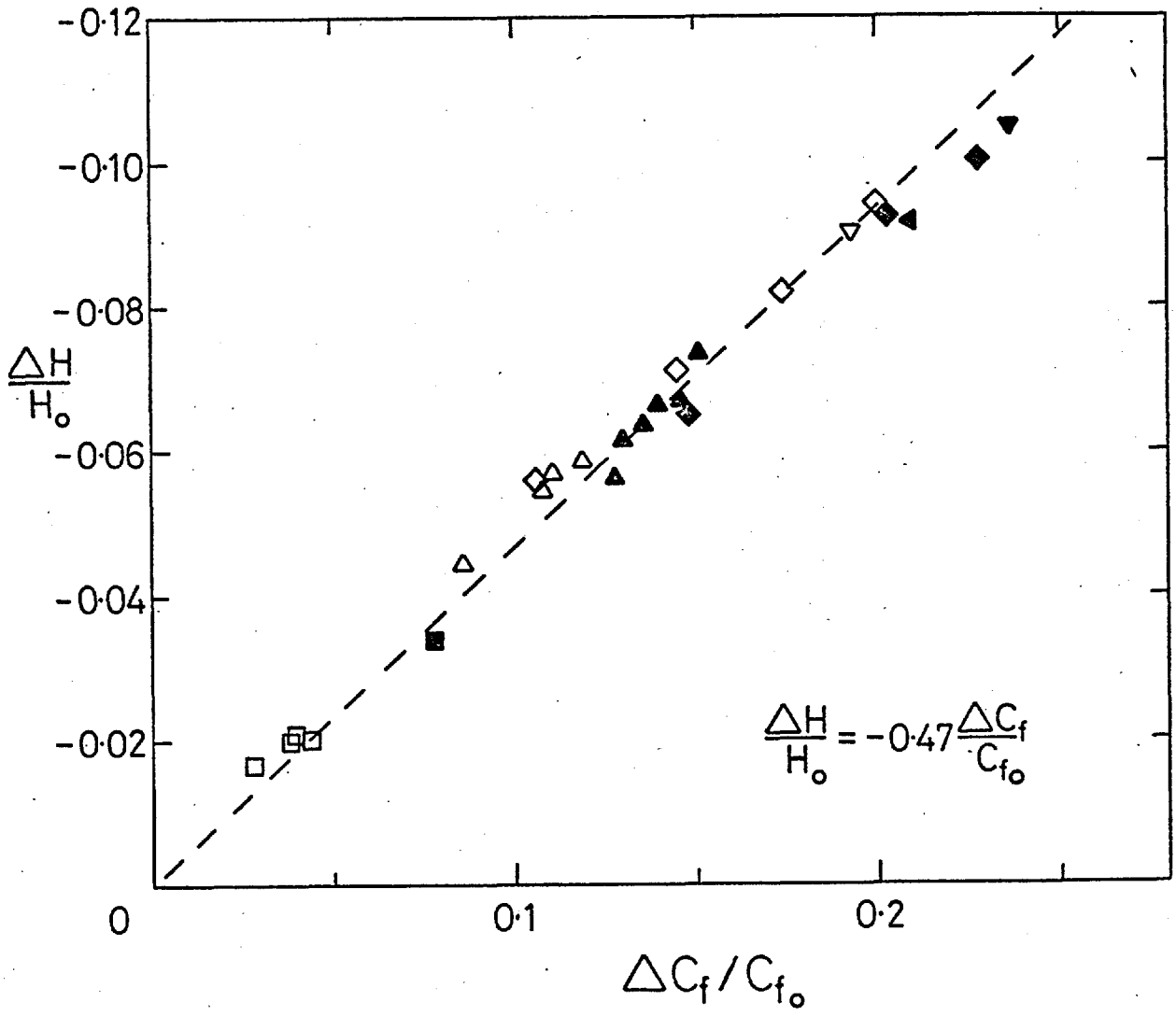

Fig. 3.50 Correlation between $\Delta H/H_o$ and $\Delta C_f/C_{f_o}$.

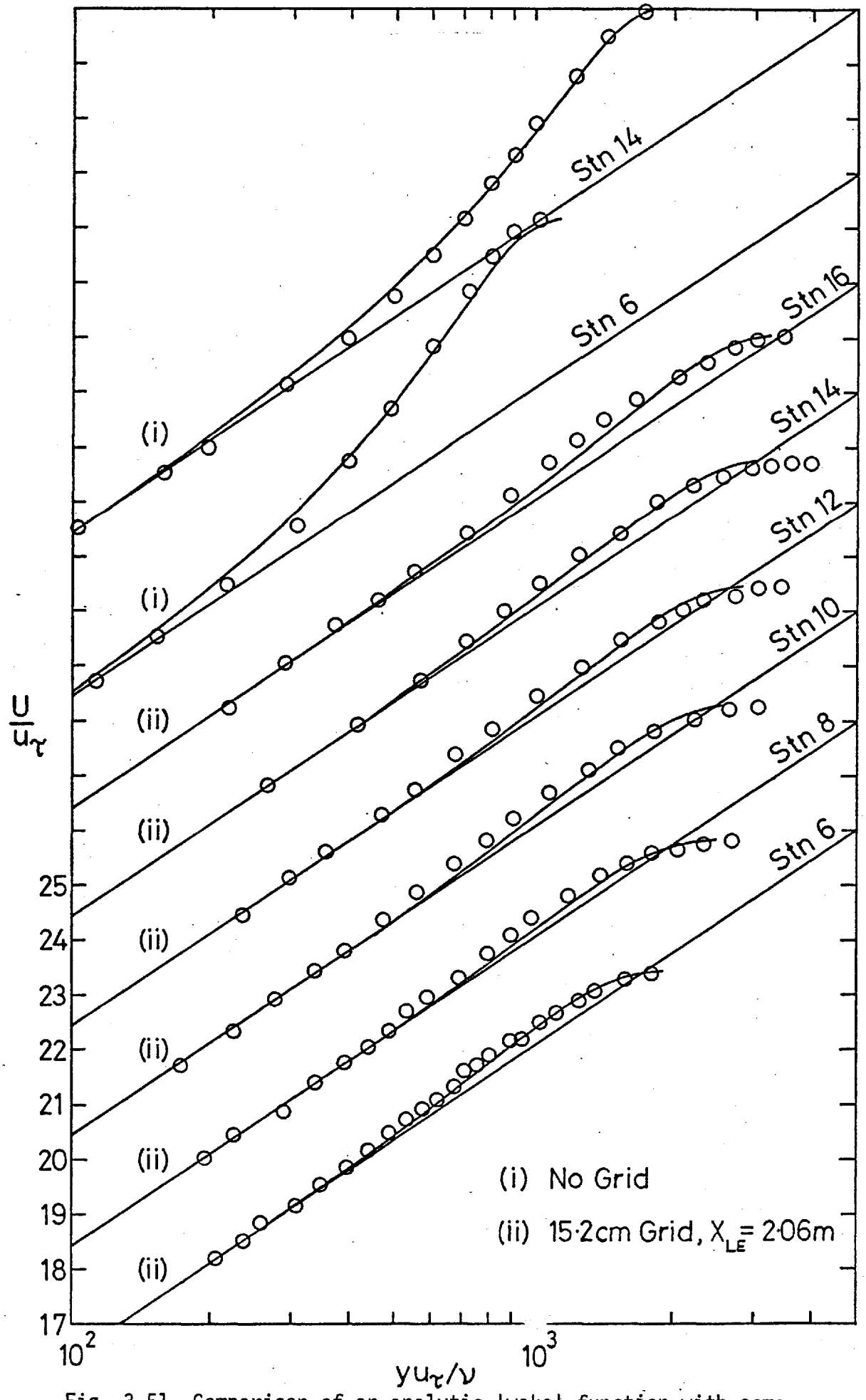

Fig. 3.51 Comparison of an analytic 'wake' function with some wake profiles. $g(\Pi, y/\delta)$ given by equation 3.3.12.

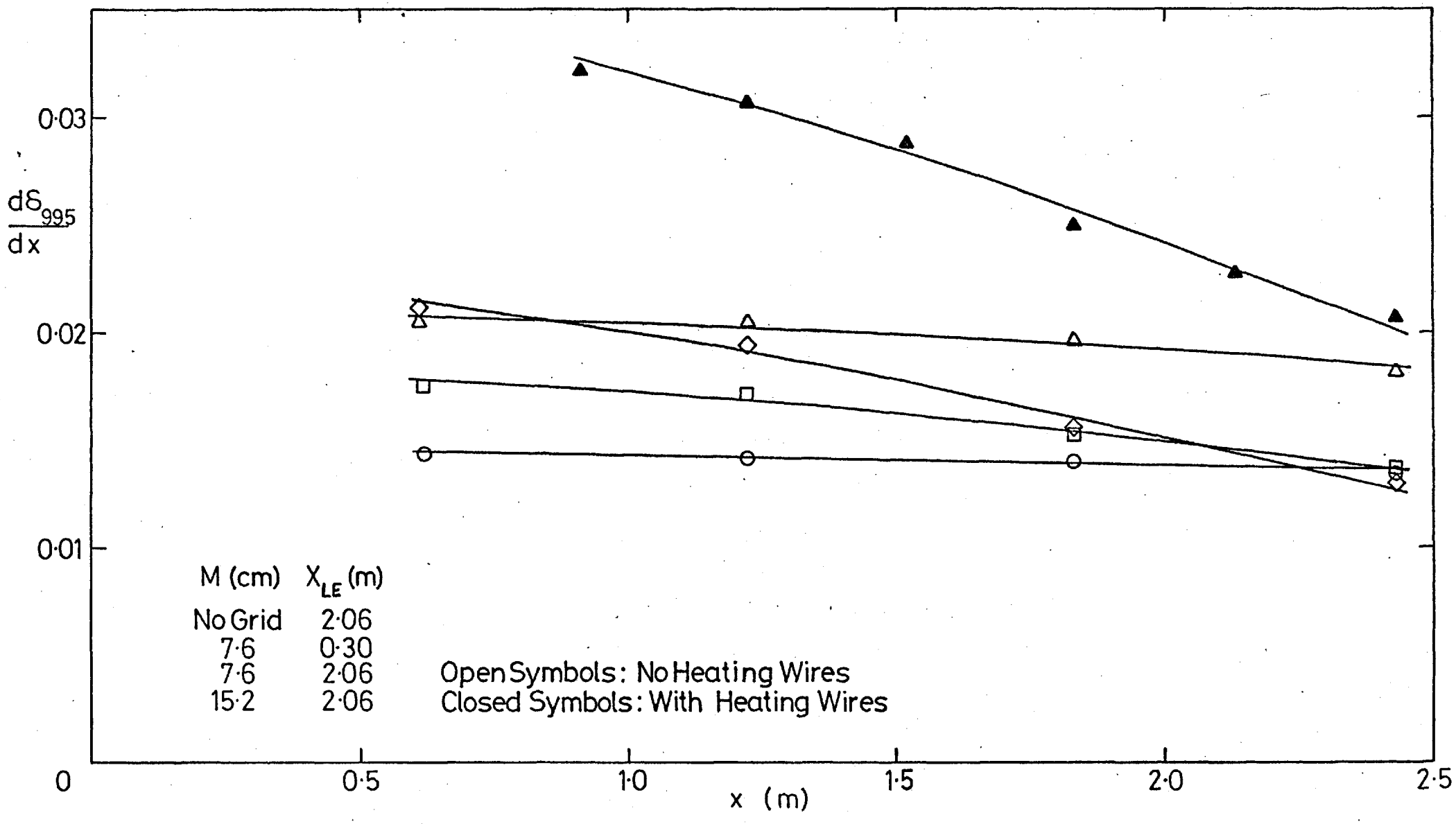

Fig. 3.52 Boundary layer growth rate, $d\delta_{995}/dx$, plotted against x.

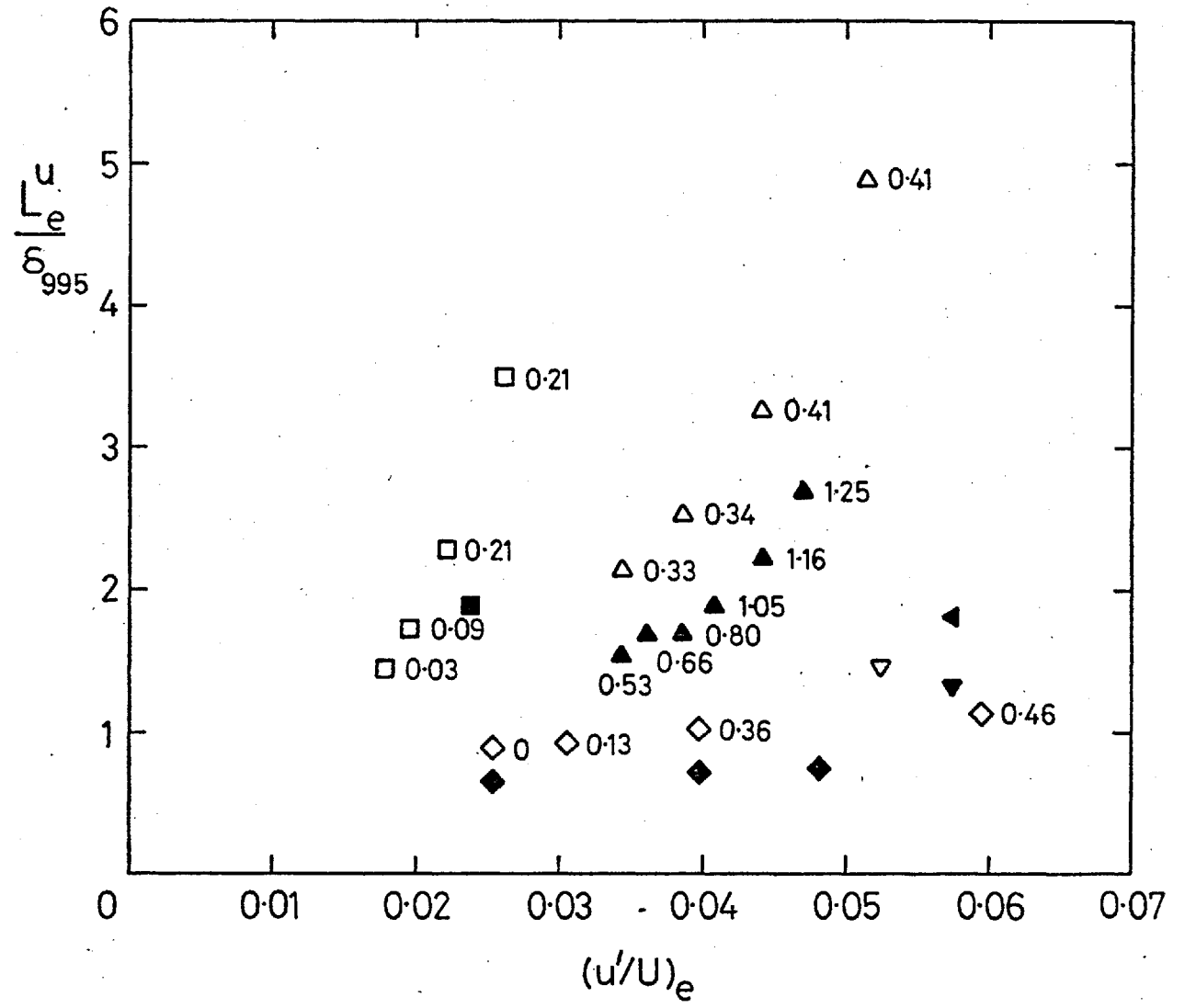

Fig. 3.53 Values of $\Delta(d\delta_{995}/dx)/(d\delta_{995}/dx)_o$ displayed at appropriate $(u'/U)_e$ and L_e^u/δ_{995}.

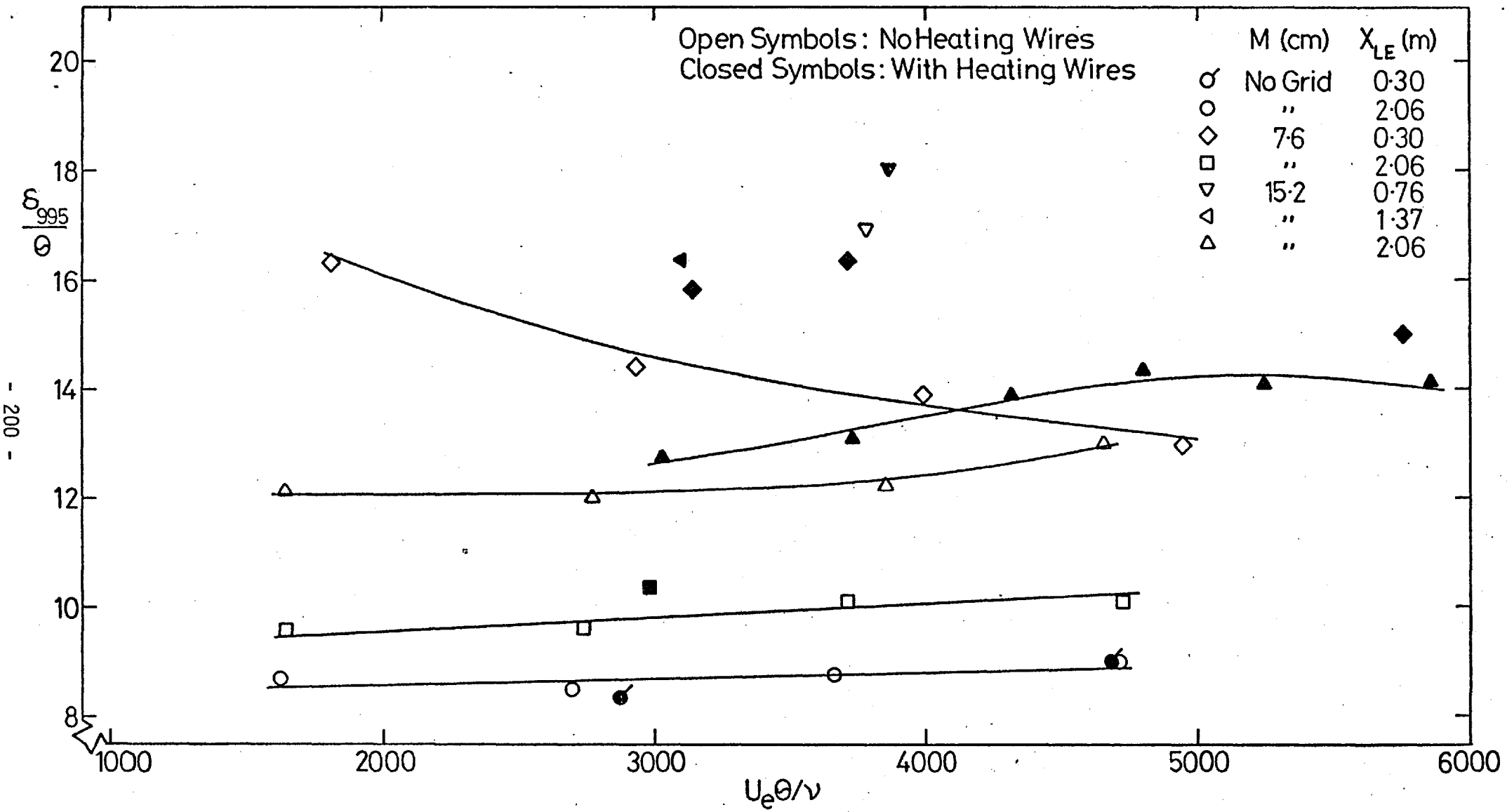

Fig. 3.54 Shape parameter δ_{995}/θ plotted against Reynolds number $U_e\theta/\nu$.

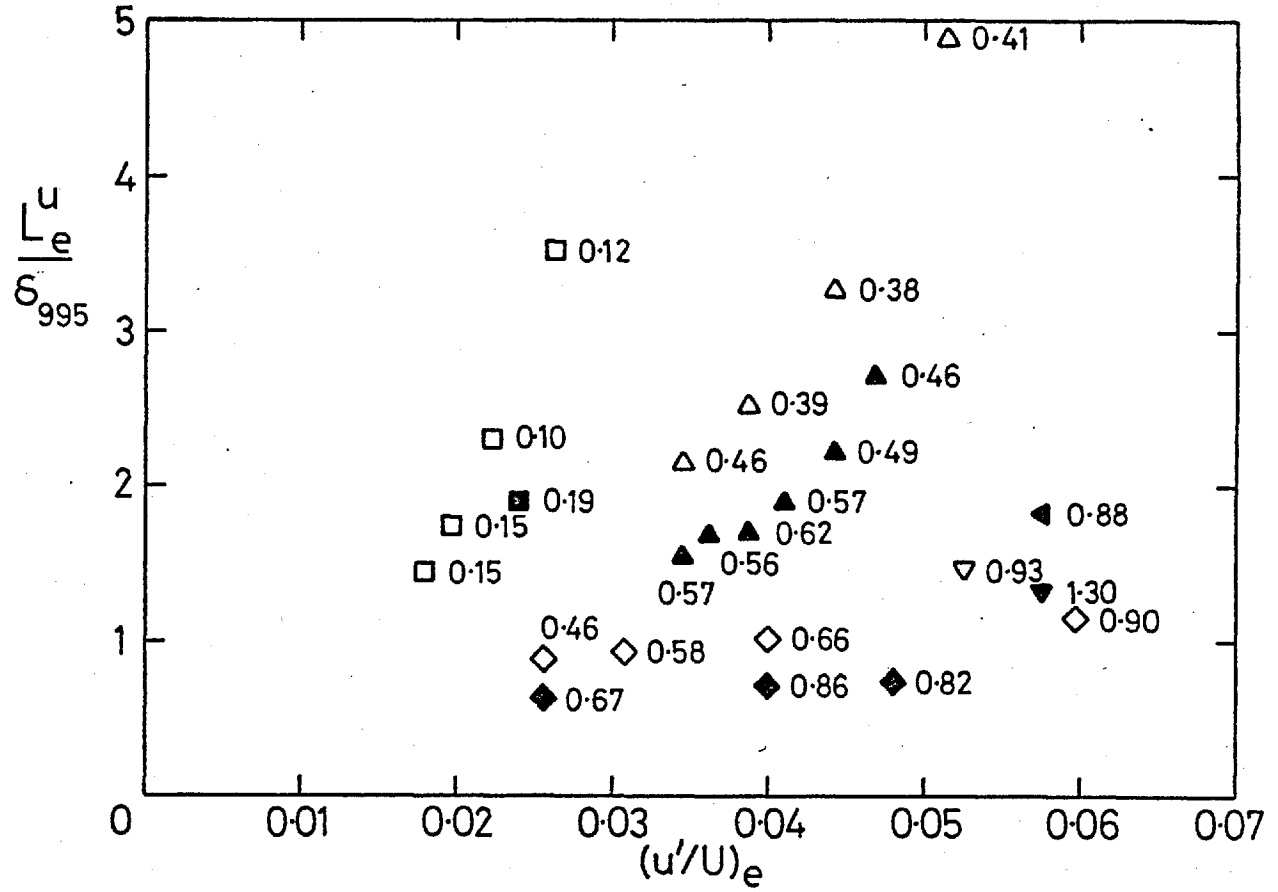

Fig. 3.55. Values of $\Delta(\delta_{995}/\theta)/(\delta_{995}/\theta)_o$ displayed at appropriate $(u'/U)_e$ and L_e^u/δ_{995}.

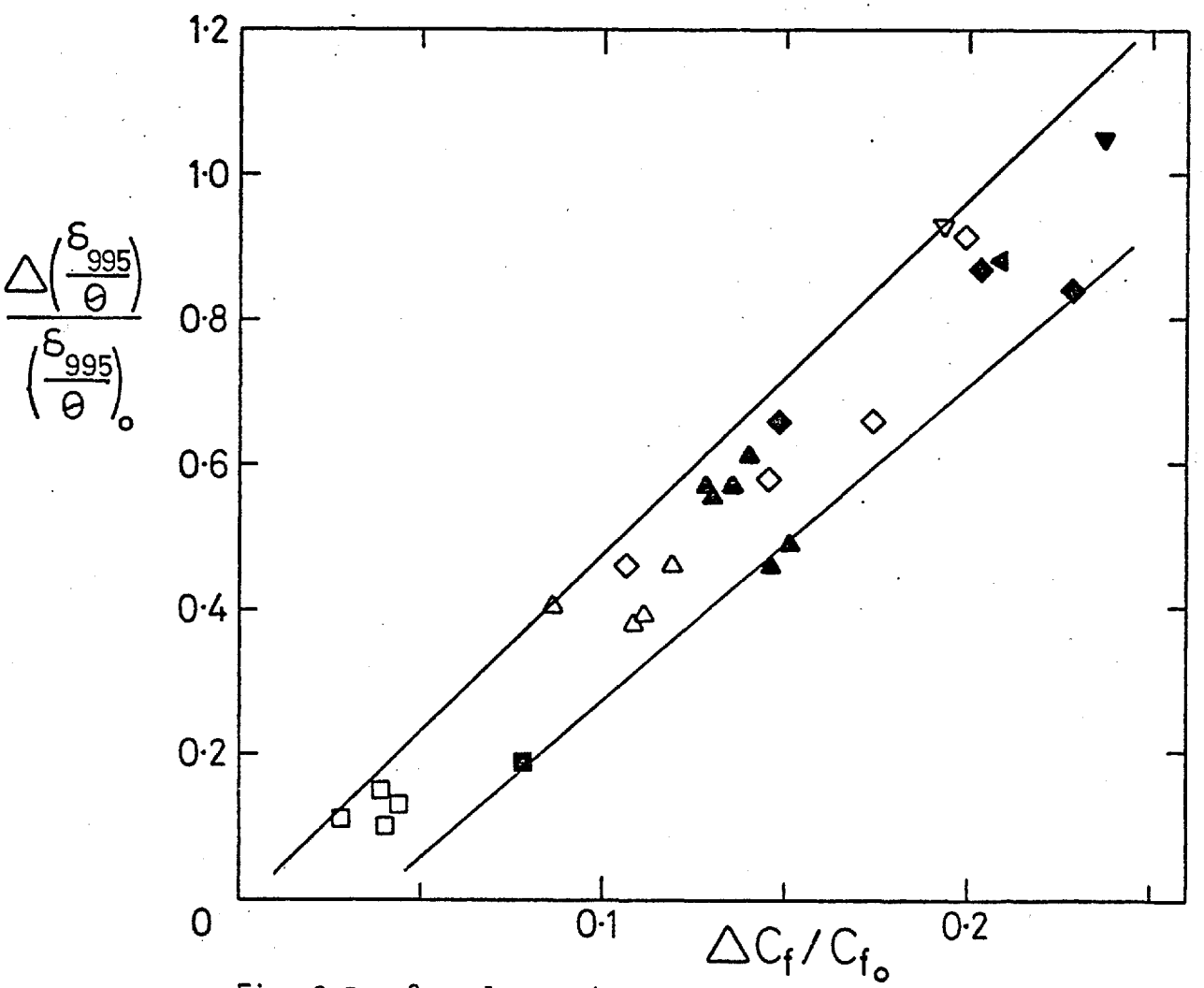

Fig. 3.56 Correlation between $\Delta(\delta_{995}/\theta)/(\delta_{995}/\theta)_o$ and $\Delta C_f/C_{f_o}$

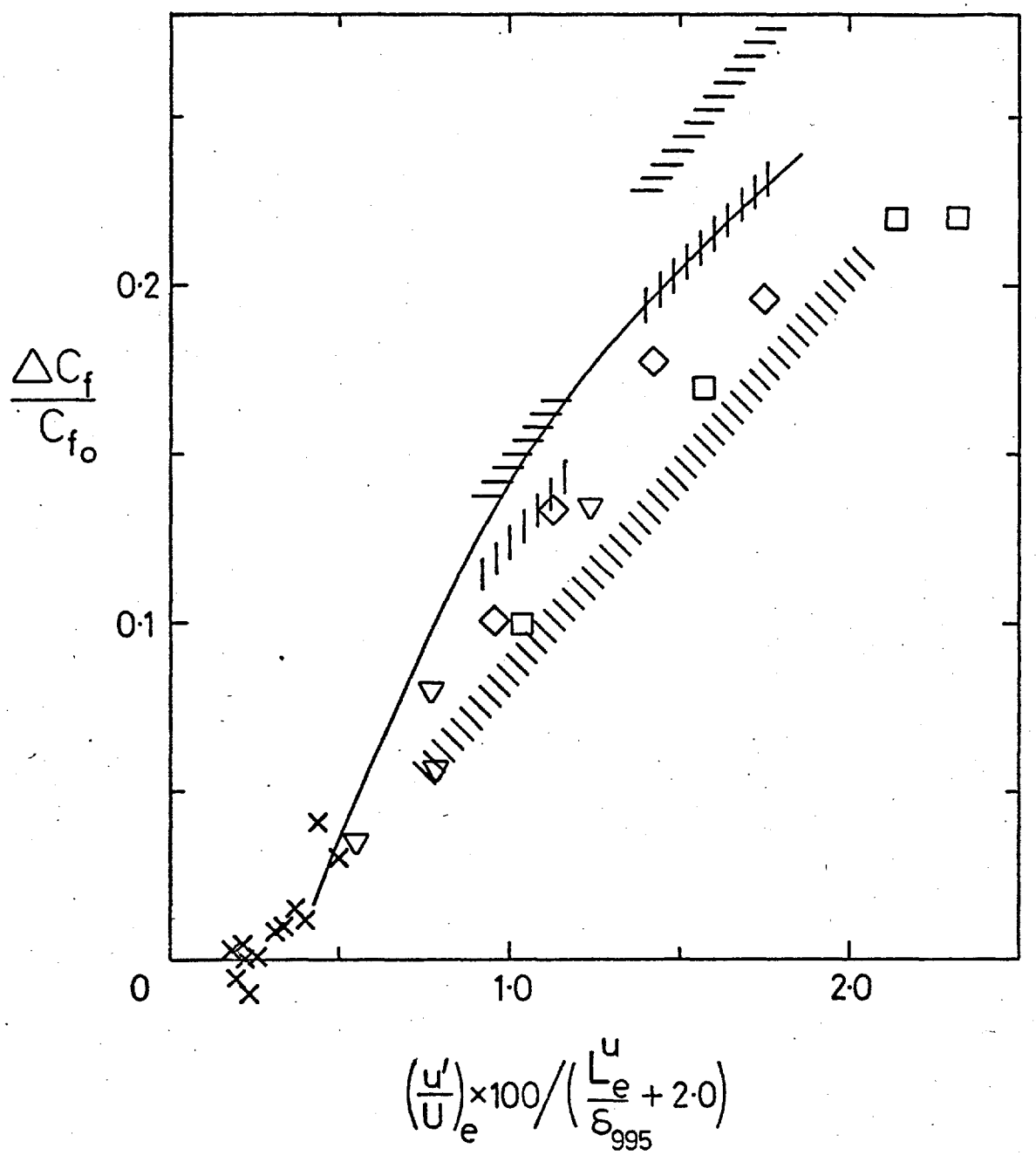

Fig. 3.57 Comparison of present $\Delta C_f/C_{f_o}$ with those of other workers.

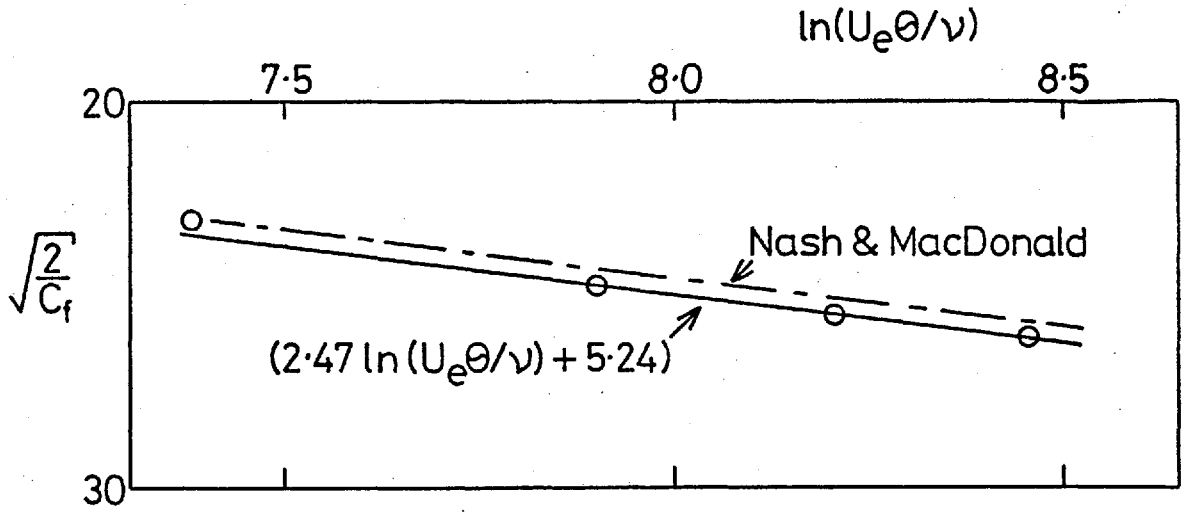

a) Present 'No Grid' Measurements

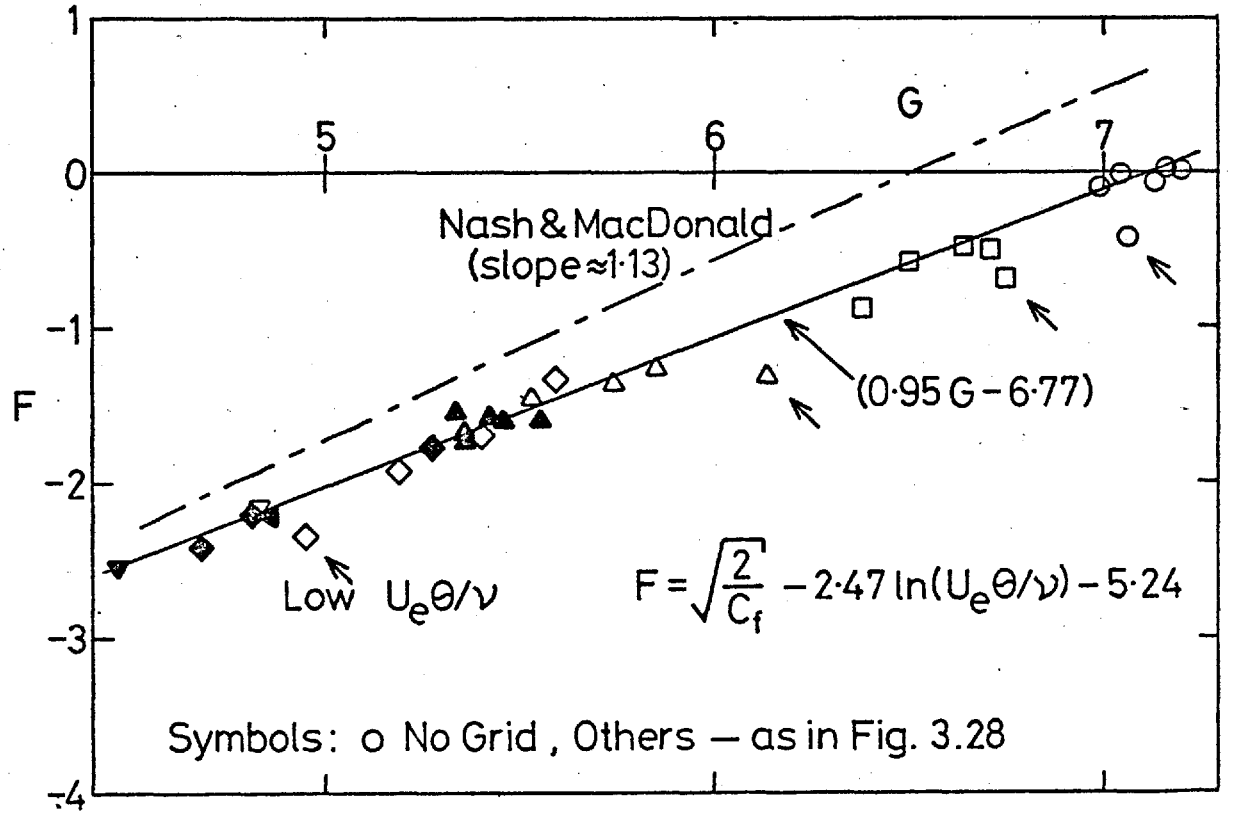

b) Present Measurements

Fig. 3.58 Skin-friction formula following Nash & MacDonald.

CHAPTER 4

TURBULENCE MEASUREMENTS

4.1 INTRODUCTION

Measurements of the mean flow presented in chapter 3 clearly show that the boundary layer is sensitive to both the free-stream turbulence intensity and the length scale ratio, L_e/δ, at least for $u'_e = O[u_\tau]$ and $L_e = O[\delta]$. Measurements of turbulence quantities inside the boundary layer (δ_{995}) edge and beneath the free-stream were obtained for eleven combinations of $(u'/U)_e$ and L_e^u/δ_{995}, as given in figure 4.1, using a three-wire probe. Of these combinations, six correspond to the development of the boundary layer with distance x for one grid and one plate position (15.2 cm grid and X_{LE} = 2.06 m, respectively). One combination of the six (station 10) plus the five others are used to show the effect of length scale ratio at three values of free-stream intensity. Measurements of u, v and θ, and u, w and θ were made for each of the eleven combinations except one, where only u, v and θ were measured. Some analogue check measurements were also obtained with a U-probe. Since the Reynolds numbers were fairly low ($2900 \lesssim Re_\theta \lesssim 5900$) for all these measurements reference boundary-layer turbulence measurements (of u, v and θ, and u, w and θ) in the absence of free-stream grid-generated turbulence were obtained at two Reynolds numbers near the maximum and minimum.

A directory of the turbulence measurements presented and the associated mean-flow and free-stream turbulence parameters is given in table 4.1. For the three-wire-probe measurements heating was applied to the boundary layer via the heating wires positioned at the plate leading edge. No current was passed through the heating wires for the analogue measurements.

4.2 CONDITIONAL SAMPLING TECHNIQUES

In this thesis, unless otherwise stated, "intermittency" refers to the intermittency associated with the interface that separates fluid that is considered to be primarily shear layer fluid from that which is considered to be primarily free-stream fluid. (More generally, it is the interface that separates two shear layers.) Of course, the presence of an interface does not imply that the fluid motion one side is independent of the fluid motion on the other side.

When the fluid on one side of the interface is non-turbulent the shear layer is characterized by rotational velocity fluctuations. Consequently the presence of turbulence or particular events within the turbulence may be detected by appropriate discrimination applied to one or more fluctuating velocity signals. The velocity fluctuation that is most easily measured is that obtained from a single straight hot wire, u. However, the derivative $\partial u/\partial t$ or a simple function of $\partial u/\partial t$, for example $(\partial u/\partial t)^2$ or $(\partial u/\partial t)$, are more commonly used because they emphasise the difference between the frequency of velocity fluctuation within the turbulent part of the flow and the frequency of velocity fluctuations in the non-turbulent part of the flow. Detection of turbulence by using the streamwise velocity fluctuation has been employed by Bradbury (1964), Fiedler & Head (1966), Kaplan & Laufer (1968), Wygnanski & Fiedler (1970), Antonia & Bradshaw (1970), Sunyach (1971), Thomas (1973). Since a shear layer is generally characterized by a large Reynolds shear stress, say $-\overline{uv}$, a function of the instantaneous velocity product uv may be fairly safely used, as for example by Antonia (1972), Castro (1973), Murlis (1975). Hedley & Keffer (1974) favoured the use of the functions $(\partial u/\partial t)^2 + (\partial v/\partial t)^2$ and $(\partial^2 u/\partial t^2)^2 + (\partial^2 v/\partial t^2)^2$ in preference to functions of u alone or functions of the instantaneous product uv. The esteemed intermittency measurements of Corrsin & Kistler (1955) employed a four-wire probe sensitive to the

streamwise component of fluctuating vorticity. Kovasznay et al. (1970) have used a two-wire probe to obtain $\partial^2 u/\partial y \partial t$.

When, as in the present case, turbulent fluid is present on both sides of the interface the fluctuating velocity cannot be used as a discriminator. A neat technique that is increasingly being used in the quantitative measurement of adjacent turbulent flows is that of marking or "tagging" one of the shear layers with a passive contaminant (precisely as for flow visualization). In the present case a small amount of heat is supplied to the boundary layer fluid. The temperature difference either side of the interface must be large enough to provide satisfactory detection of the tagged fluid but small enough to give negligible buoyancy effects. In ideal conditions the determination of the intermittency function requires only the detection of the instantaneous temperature rise above the constant temperature of the unheated part of the flow. Electronic noise and the presence of small temperature fluctuations within the unheated fluid require the use of a temperature threshold; only temperatures greater than the threshold are called "hot". Slow, unpredictable temperature variation of the unheated fluid (due to heat dissipation in the tunnel) presents an additional and not insignificant problem which is commonly overcome by using a time-derivative or slope criterion in addition to, or possibly instead of, a level criterion. Obviously, the temperature derivative can of course be zero in a fully turbulent tagged region, so a 'slope-alone' test can be dangerous. Detection of temperature-tagged fluid by using only a level criterion has been used by Johnson (1959), Antonia et al. (1975), Antonia et al. (1977), Chen & Blackwelder (1978). A level criterion backed up by a secondary slope criterion has been used by Weir & Bradshaw (1977) and Andreopoulos (1978). Charnay (1974) has used a level criterion and a slope criterion either of which, when satisfied, asserted the presence of tagged fluid. Dean & Bradshaw (1976) have used a slope

criterion backed up by a secondary level criterion; this order was used partly because their signal to noise ratio was not large. Weir & Bradshaw and Andreopoulos used an intermittency algorithm developed by Weir (1976). A slightly modified form of Weir's algorithm is used here.

In the present work the conditionally-sampled turbulence quantities have been evaluated by measuring the fluctuations with respect to conventionally-averaged mean velocities, permitting the addition law

$$\overline{Q}_{TOTAL} = \gamma \overline{Q}_{HOT} + (1 - \gamma) \overline{Q}_{COLD}, \qquad (4.2.1)$$

where Q is an arbitrary turbulence quantity. $\gamma \overline{Q}_{HOT}$ and $(1 - \gamma)Q_{COLD}$ are the respective contributions from the "hot" and "cold" zones to the total. $\overline{Q}_{HOT}$ and $\overline{Q}_{COLD}$ are the zone averages in the hot and cold zones, respectively. Other workers, for example, Hedley & Keffer (1974), Kovasznay et al. (1970), Charnay (1974) have measured the conditionally-discriminated velocity fluctuations with respect to the conditionally-averaged mean velocities, thus ignoring the large-eddy contribution to the conditional averages. In their cases the zone averages obey a more complicated form of equation 4.2.1.

4.2.1 An intermittency algorithm

For the present flow an intermittency algorithm discriminating primarily by temperature level and secondarily by (bulk) slope was found to be adequate. This assessment is based upon the inspection of a large number of Calcomp plots showing both the temperature signal and the intermittency function provided by the algorithm. Some examples are discussed in section 4.5. Clear disagreement between the intermittency function so determined and a visual interpretation of the temperature fluctuations was rare. Although the human eye is very good at pattern recognition it operates qualitatively. Digital analysis on the other hand is quantitatively consistent and avoids

subjective interpretation of the signal from which the intermittency function is to be determined - except insofar as the thresholds are chosen by eye. Difficulty of 'correct' intermittency discrimination increased with increased free-stream intensity because of increased free-stream temperature fluctuations.

The intermittency algorithm 'LAGTHR' used in the present work is essentially that constructed by Weir (1976) but with some slight modifications considered necessary for its present application. A listing of the Fortran subroutine 'LAGTHR' is provided in appendix 6, and a flow diagram and a table describing the associated variables is given in figure 4.2. The digital analysis was carried out in records each consisting of about 267 points or samples of data. (See chapter 2 for more details.) Necessary initialisation of some parameters is excluded from figure 4.2 for clarity. Only the first few records or so of typically 800 analysed for each probe position and each ϕ are affected by the initial values of the thresholds.

Referring to figures 4.2 and 4.3, the current temperature sample T(J) is first compared with the level threshold temperature $\theta_A = \theta_2 + TMIN2$, where θ_2 is the level-above-cold threshold and TMIN2 is the minimum temperature of the last-but-one cold burst. Whenever a hot point is detected the 'bulk slope' test is applied in which T(J-NLAG) - T(J) is compared with θ_{3D} provided that NLAG is greater than or equal to the number of points in the current hot burst. This proviso is included because the slope test can give errors if there exists a short cold burst between the digitized points (J-NLAG) and J. If $T(J-NLAG) - T(J) > \theta_{3D}$ the temperature level is compared with a second threshold $\theta_B = \theta_4 + TBOT5$, where θ_4 is another level-above-cold threshold parameter and TBOT5 is the minimum temperature encountered in the previous NB5 records (not necessarily the current record unless NB5 set to zero). When $T(J-NLAG) - T(J) > \theta_{3D}$ and $T(J) < \theta_B$ the point is called cold and the thresholds TMIN0, TMIN2 and

θ_A reset. A point called cold by the slope and second level tests is indicated by setting ID(J) = -2 for that point. If, though, T(J-NLAG) - T(J) < θ_{3D} the point is still declared hot. θ_2, θ_4, θ_{3D}, NLAG and NB5 are input parameters. $\theta_4 > \theta_2$. At the first point of a hot burst the variables TMIN1 and TMIN2 are moved-up one cold burst and the threshold θ_A (= θ_2 + TMIN2) re-evaluated. However, if the value to be ascribed to TMIN2 is greater than the minimum temperature TMINO of the cold burst just ended then the threshold θ_A is evaluated as θ_2 + TMINO. This latter facility speeds up the ability of the algorithm level thresholds to follow falls in the ambient cold temperature, although it takes no account of a possible fall in the temperature of the subsequent cold burst below the current reference level $\theta_A - \theta_2$. Allownace is made for this by resetting θ_A to $\theta_A = T + \theta_2$ whenever T(J) falls below $\theta_A - \theta_2$. A fall in the cold temperature level is shown exaggerated in the sketch in figure 4.3. In the event that the detection of a cold burst results in the hot burst just ended containing only one point, the single hot point is rejected and called cold. A rejected single-point hot burst is indicated by setting ID(J) = -1 for that point. Calcomp plots confirmed that single-point hot bursts were generally not due to unambiguous hot burst of one point in length but mostly the result of the updating of the threshold θ_A on detection of the first point of a (possible) hot burst. Changing the event that triggered the updating of the threshold θ_A would have merely changed the time at which single-point burst would have appeared. Thus, assuming that the new and old values of θ_A are equally valid, single-point hot bursts are justifiably ignored in the context of the present algorithm. Note though, that rejecting a single point for a signal digitized at a low sampling rate (with respect to the time scales of the smaller scales of the temperature signal) would result in genuine short hot

bursts being incorrectly identified. Strictly, on rejecting a single-point hot burst the newly reset threshold θ_A should have been reset to its old value. Omitting back-setting of the threshold was not found to be particularly deleterious and on occasions was found to be an advantage in regions of low intermittency in the event of a slow rise in the level of a long cold burst which occurred before NL was exceeded. In the event of the length of a hot or cold burst exceeding respective maxima, NU and NL, the hot or cold is terminated and the temperatures TMIN2, TMIN1, TMIN0, θ_A reset. NU and NL are input parameters. Apart from the intermittency function ID(J) the remainder of the algorithm given in figure 4.2 consists of counters.

4.2.2 Intermittency algorithm thresholds

It is likely that intermittency measurements will be most credible if the algorithm parameters, where possible, are independent of y/δ and change consistently with the length, velocity and temperature scales of each profile. For each profile the threshold value θ_2 was selected by repeated analysis of a sample of data at a position for which it was expected that $\gamma \approx 0.5$, the other parameters θ_4, θ_{3D}, NLAG, NB5, NU and NL being kept constant. Typically, six values of θ_2 in the range $0 < \theta_2 \leq 2\times$ "expected θ_2" were tried. The selected value was then checked for probe positions either side of $\gamma \approx 0.5$. θ_2 was then kept constant for the whole profile. The slope parameters θ_4, θ_{3D}, NLAG and NB5, were set to be sensitive to the short cold bursts that exist in regions of high intermittency factor, some of which would not have been detected by the level threshold alone without increasing θ_2. The slope parameters selected were also required to ensure that the slope test was well behaved at lower values of the intermittency factor. θ_2, θ_4 and NLAG were also kept constant for the whole profile and satisfactory intermittency discrimination was obtained with

$$\theta_2/\theta_4 = 0.5,$$

$$\theta_{3D}/(T_w - T_e) = 0.5,$$

and $$NLAG \times \delta/(sxU_e) \approx 0.15,$$

where s is the sampling rate. NB5 was kept constant at 5 except close to the wall where it was increased to 10; θ_4 was not adjusted. Figure 4.4 shows the level threshold θ_2 plotted with respect to the temperature scale of the boundary layer fluid, $T_w - T_e$. The increase in θ_2 at constant $(T_w - T_e)$ with grid size is consistent with an observed increase in the free-stream temperature fluctuations. In all, about ½% of the data used to evaluate the conventional and conditional averages was used to establish the intermittency thresholds.

At $\gamma \approx 0.5$ a reduction of NLAG by half changed both the intermittency factor and the interface crossing frequency by less than 1%. Halving the effective digitizing rate by analysing only every other digitized point showed about a 1% change in the intermittency factor and about a 10% reduction in the interface average crossing frequency, where the effect of rejecting single-point hot bursts has been neglected in this comparison.

4.3 BUOYANCY EFFECTS

The boundary layer mean temperature profiles are shown in figure 4.5. For each combination of grid size and plate position the power supplied to the heating wires was kept constant at a value large enough to give satisfactory temperature intermittency discrimination at the downstream most station at which measurements were obtained. The convected heat flux implied by these temperature profiles $\rho Cp\int_0^\infty U(T - T_e)dy$ is roughly 15% less than the heat supplied (per unit width) by the heating wires, showing no consistent trend with distance along the (heat resistant) plate. Presumably, the heat loss was due to radiation from the heating wires and from conduction near the leading edge. The plate was always allowed to

warm up before measurements were taken.

For a buoyant layer of height h, velocity U perpendicular to the gravitational vector, and density difference $\Delta\rho$ the ratio of the buoyancy to inertia forces is of the order of

$$\frac{\Delta\rho\, hg}{\rho U^2} \quad .$$

For the present slightly heated boundary layer this may be re-written

$$\frac{-\Delta T\, hg}{TU^2}$$

which is of the order of the gradient Richardson number

$$R_i = -\frac{g}{T}\frac{\partial T/\partial y}{(\partial U/\partial y)^2} \quad . \tag{4.3.1}$$

Negligible buoyancy effects require $|\Delta T hg/(TU^2)| << 1$. Taking as the temperature scale, ΔT, the average excess temperature across the boundary layer

$$\Delta\overline{T} = \int_o^\infty (T(y) - T_e)\, d\,(y/\delta_{995}), \tag{4.3.2}$$

and as the length scale, h, the boundary layer thickness δ_{995}, then

$$\frac{\Delta\overline{T}\,\delta_{995} g}{TU^2} \lesssim 1.3 \times 10^{-5} \quad .$$

Therefore, buoyancy effects should have been quite negligible, except perhaps very close to the heating wires.

4.4 CONVENTIONALLY-AVERAGED MEASUREMENTS

4.4.1 Reynolds stresses

Direct-stress profiles measured in the absence of (grid-generated) free-stream turbulence are shown in figures 4.6a and 4.6b. Klebanoff's (1955) measurements, which have been scaled for the present values of u_τ/U_e and corrected for the different definitions of boundary layer thickness, are also shown. The present measurements of $\overline{u^2}$ obtained with the x-wire probe sensitive to the u and w

fluctuations ($\phi = \pi/2$) are seen to be consistently higher than those obtained with the x-wire probe sensitive to the u and v fluctuations ($\phi = 0$). There is only one other profile (figure 4.6j) which shows a similarly large and consistent discrepancy. It is difficult to reconcile the magnitude of these discrepancies with the errors to be expected as a result of the finite probe resolution volume. One x-wire probe was used for both of the no-grid cases for which the calibrations were consistent throughout. The consistent discrepancy at these two stations tends to discount equipment errors other than probe-related errors, or unnoticed experimental procedure errors. Unfortunately no U-probe measurements of $\overline{u^2}$ were obtained for the no-grid cases. Klebanoff's measurements show closer agreement with the measurements at station 14. It was pointed out in chapter 3 that at station 6 there is a small residual effect of the heating wires at the leading edge.

Direct-stress profiles for the cases when (grid-generated) free-stream turbulence is present are shown in figures 4.6c to 4.6m. Unfortunately, $\overline{w^2}$ was not measured for the case given in figure 4.6d. Comparison of figures 4.6c and 4.6d reveals a surprising length-scale effect. At the lower length scale ratio, $\overline{u^2}$ and $\overline{v^2}$ are larger than the respective free-stream values over a considerably smaller portion of the boundary layer than for the larger length scale ratio. Indeed, for the most part, $\overline{u^2}$ and $\overline{v^2}$ in figure 4.6d fall well below the no-grid measurements of $\overline{u^2}$ and $\overline{v^2}$ (figures 4.6a and 4.6b). A similar effect can also be seen in figures 4.6g and 4.6k at $(u'/U)_e \approx 0.040$ and in figures 4.6ℓ and 4.6m at $(u'/U)_e \approx 0.058$. This is consistent with the mean flow measurements if the decrease in $\partial U/\partial(y/\delta_{995})$ with decreasing L_e/δ_{995} (chapter 3, section 3.3) is accompanied by a not-so- rge increase in the shear stress $-\overline{uv}$, resulting in a reduced production of turbulent kinetic energy.

The effect of the presence of the wall on the normal velocity component, as observed by Thomas & Hancock (1977, appendix 1), is evident in all of the figures except figure 4.6d. For $(u'/U)_e \lesssim 0.040$; $\overline{v^2} < \overline{v_e^2}$ is more noticeable at the higher length scale ratios. At $(u'/U)_e = 0.058$ $\overline{v^2}$ is everywhere less than $\overline{v_e^2}$.

Figures 4.7a to 4.7n show the shear stress $-\overline{uv}$ for all thirteen cases, and the shear stress $-\overline{uw}$, which by symmetry should be zero, for twelve cases. Extrapolation of the $-\overline{uv}$ profiles to $y = 0$ gives, without exception, wall shear stress values well below those determined from the mean-flow measurements. The magnitudes of the discrepancies lie in the range 10% to 25% and on average the error is 16%. No consistent trend with Reynolds number is evident. A considerable amount of time was expended examining the experimental and digital analysis techniques with the exception of a detailed study of the probe itself, but no source of error was revealed. In all, five x-wire probes were used for the measurements presented in this chapter, as shown in table 4.1. The effect of the slightly heated boundary layer on the hot-wire probe calibration can be discounted as the correction to the velocity is only about 1%/^{o}C. Hot-wire temperature correction errors and the effects of temperature on the turbulence, the latter already discounted in section 4.3, are further discounted by a single x-wire measurement close to the wall but without any heating to the boundary layer (primarily intended as a record of the velocity sensitivity of the temperature wire). Repeated analysis of the same digital records of some of the x-wire probe signals but with each wire (of the x-wire probe) treated as an independent slant wire gave the same values of $\overline{u^2}$, $\overline{v^2}$ and $-\overline{uv}$ as previously. Unlike $\overline{u^2}$, $\overline{v^2}$ and $\overline{w^2}$, $-\overline{uv}$ is the mean of positive and negative contributions. The existence of a positive correlation between the sum and difference signals of the x-wire probe thus reducing positive values of $-\overline{uv}$ is discounted by the measurements of $\overline{uw}$.

It was considered that evaluation of the shear stress profiles by integration of the momentum equations would have demanded too much of the mean velocity profile measurements. Low values of $-\overline{uv}$ have also been measured by other workers, although other workers in the Aeronautics Department using virtually identical techniques have not found such large errors. The measurements of Charnay (1974) show a short-fall of about 10%, and the smooth wall x-wire probe measurements of Antonia & Luxton (1971) show a short-fall of about 20%. Antonia & Luxton's measurements of $-\overline{uv}$ using a single slant wire are stated to give much better agreement. They also found that the magnitude of the measured shear stress depended upon the type of x-wire probe, that the error was proportional to the shear stress and that the error decreased with increased Reynolds number. Some preliminary measurements not presented here, using a standard Disa gold plated p55 x-wire probe showed about a 7% underestimate of the wall value. Initially, no discrepancy was observed for these measurements owing to a yaw-saddle calibration error that had passed unnoticed by several users. The error amounted to a 7% error in v. Although the present Reynolds shear stress measurements are not very satisfactory, rather than make any assumption about the nature of the error they are presented as measured. Nevertheless, it will be seen that in the absence of free-stream turbulence, the correlation coefficient $-\overline{uv}/\sqrt{(\overline{u^2}.\overline{v^2})}$ and the structural parameter $-\overline{uv}/\overline{q^2}$ are more easily comparable with those measured by other workers.

In all cases the shear stress measured in the free-stream is negligible by comparison with the wall shear stress. As the effect of the free-stream turbulence increases, the shear stress profile edge, δ_{05} say, extends further beyond the mean velocity profile edge defined by δ_{995}. Figure 4.7n shows a large overlap but this is most likely due to the rather poor accuracy of δ_{995} arising from the very

small $\partial U/\partial y$ at $y = \delta_{995}$ for this case. In contrast, Huffman et al. (1972), for a free-stream intensity and length scale ratio comparable with those for figure 4.7n, measured a shear stress of about 60% of the wall value of $y = \delta$. However, they did not check that the measured shear stress was in fact zero well away from the plate. The present results are therefore believed to be quantitatively more credible. The shear stress profiles at six consecutive stations are shown in figure 4.7k and are seen to follow a closely self-preserving behaviour as also observed for the corresponding mean velocity profiles but not for the direct stress profiles. Note, the sufficient conditions for self-preserving flow, u'_e/u_τ = constant and L_e/δ = constant, are not satisfied. For a self-preserving constant-pressure flow the shear stress near the mean velocity edge is given by

$$-\overline{uv} = V_E\,(U_e - U), \qquad (4.4.1)$$

where V_E is the entrainment velocity defined by

$$V_E \equiv \frac{d}{dx}\,(U_e(\delta - \delta^*)). \qquad (4.4.2)$$

The shear stress at the boundary layer edge inferred from equation 4.4.1 is shown in figures 4.7a, 4.7b and 4.7e to 4.7j inclusive and adds support to the self-consistency of the present measurements. Figure 4.8 displays tabulated values of δ_{05}/δ_{995} as a function of $(u'/U)_e$ and L^u_e/δ_{995}, where δ_{05} is based upon the wall shear stress inferred from the x-wire measurements. The uncertainty in $-\overline{uv}$ arising from the discrepancy with the mean flow measurements of wall shear stress leads to a likely error in δ_{05} of less than 5%.

Figures 4.9a to 4.9d show more succinctly the separate effects of free-stream intensity and length scale ratio on $\overline{u^2}$, $\overline{v^2}$, and $\overline{w^2}$, each normalised by u_τ^2 obtained from the logarithmic law. Corresponding to these profiles, figures 4.10a to 4.10d show the shear-stress correlation coefficient $-\overline{uv}/\sqrt{(\overline{u^2}.\overline{v^2})}$ and the structural parameter

$-\overline{uv}/\overline{q^2}$. In the outer layer $-\overline{uv}/\sqrt{(\overline{u^2}.\overline{v^2})}$ and $-\overline{uv}/\overline{q^2}$ both decrease as the free-stream intensity increases and the length scale ratio decreases. However, in the inner layer $-\overline{uv}/\sqrt{(\overline{u^2}.\overline{v^2})}$ and $-\overline{uv}/\overline{q^2}$ (and $\overline{u^2}$, $\overline{v^2}$ and $\overline{w^2}$ in figure 4.9) appear to be mostly affected by free-stream intensity and only weakly affected by the length scale ratio. This apparently weak dependence on length scale ratio is most probably due to "inactive" motion(Townsend, 1961; Bradshaw, 1967) driven by the free-stream turbulence tending to cancel the length-scale effect seen in the outer layer.

Figure 4.10e shows profiles of $-\overline{uv}/\sqrt{(\overline{u^2}.\overline{v^2})}$ and $-\overline{uv}/\overline{q^2}$ at the six consecutive stations (15.2 cm grid, X_{LE} = 2.06 m). In the outer layer they display a larger amount of scatter than the shear stress profiles themselves (figure 4.7k).

4.4.2 Third-order products

The triple products of fluctuating velocity representing the turbulent transport of Reynolds stresses for the thirteen cases are shown in figures 4.11 and 4.12; figures 4.11a to 4.11m show the measurements of $\overline{u^3}$, $\overline{u^2w}$ and $\overline{w^3}$ and figures 4.12a to 4.12m show the measurements of $\overline{u^2v}$, $\overline{v^3}$, $\overline{uv^2}$ and $\overline{uw^2}$. Since the flow is closely two-dimensional and symmetric about the measurement plane $\overline{w^3}$ and $\overline{u^2w}$ should be zero for all y/δ_{995}. In the free-stream $\overline{v^3}$ and $\overline{u^2v}$ should also be zero. Departure from homogeneity in the streamwise direction due to the decay of the turbulence prevents the same argument being applied to the free-stream values of $\overline{u^3}$, $\overline{uv^2}$ and $\overline{uw^2}$; it is not obvious that (instantaneous) v^2, for instance, should, on average, be the same for $u < 0$ as for $u > 0$.

The present measurements of the skewness $S_u \equiv \overline{u^3}/(\overline{u^2})^{3/2}$ (figure 4.33) in the free-stream show a roughly linear decrease with x/m from +0.1 to +0.01 for $15 < x/m < 40$. $(\overline{uv^2})_e$ and $(\overline{uw^2})_e$ are less than $(\overline{u^3})_e$ and more scattered. For a free-stream subject to negligible

mean strain the present values of S_u are considerably larger than the constant-pressure measurements of Comte-Bellot & Corrsin (1966) who obtained $|S_u| < 0.002$ in the range $20 < X/M < 400$. However, they note Klebanoff & Frenkel's unpublished value of approximately 0.03. There is no firm reason for believing the present measurements of S_u to be seriously in error. Further discussion of skewness is deferred until subsection 4.6.4.

Surprisingly, in view of the corresponding measurements of $\overline{u^2}$, $\overline{u^3}$ (for the same data samples) shows no consistent sensitivity to probe rotation for the no-grid cases. $\overline{w^3}$ is approximately zero for $y/\delta_{995} \gtrsim 0.5$ but increases dramatically (and indeed embarrassingly so) near the wall. In fact the extent over which $\overline{w^3}$ is large depends almost entirely upon the distance of the probe from the wall and not upon the boundary layer thickness, which suggests either a wall effect or an absolute mean shear effect, or both. The effect of the velocity gradient $\partial U/\partial y$ on an x-wire probe sensitive to u and w fluctuations gives rise to an erroneous non-zero mean velocity, W, because the two wires are at different distances from the wall. In the present case $W^3 \ll \overline{w^3}$. (Consequences of probe asymmetry caused, for instance, by the temperature probe being mounted on one side of the x-wire probe body were not investigated). The negative values of $\overline{v^3}$ are possibly incorrect since in several cases $\overline{v^3}$ is not zero well into the free stream, although, in as much as $\partial\overline{v^2}/\partial y > 0$, the implied inward transport of $\overline{v^2}$ is consistent with the frequent observation that $\overline{vq^2}$ has the opposite sign to $\partial\overline{q^2}/\partial y$. Unfortunately, Thomas & Hancock (1977, appendix 1) did not measure any of the triple products. The measurements of $\overline{w^3}$ in the same region are much closer to zero and so tend to discount measurement errors; incorrect x-wire effective-angles should not have caused non-zero values of $\overline{v^3}$ or $\overline{w^3}$ - see appendix 3.

Possibly, the effect of $v = 0$ at $y = 0$ extends further from the wall for $\overline{v^3}$ than for $\overline{v^2}$. Alternatively, the free stream turbulence may not have been perfectly homogeneous in the y-direction. A rise in $\overline{v^3}$ near the wall occurs at most stations implying, if it is to be believed, an increase in the rate of outward transport of $\overline{v^2}$. In some cases $\overline{uv^2}$ and $\overline{u^2v}$ also exhibit rises near the wall. Similar results have been noted by, among others, Bradshaw (1967) and Andreopoulos (1978) who have also considered them to be physically unreasonable. Nevertheless, the measurements of $\overline{u^3}$, $\overline{u^2v}$, $\overline{uv^2}$ and $\overline{v^3}$ not too close to the wall and in the absence of free-stream turbulence are in good agreement with other recent measurements, for example, Andreopoulos and Smits et al. (1979 a,b).

When $\overline{u^3}$ is negative u^2 is larger on average for $u < 0$ than for $u > 0$ and vice versa when $\overline{u^3}$ is positive. For most of the boundary layer $\overline{u^3}$ is negative implying a net transport of $\overline{u^2}$ in the x direction by negative fluctuations. Negative $\overline{u^3}$ is to be expected if the fluid containing most of the turbulent kinetic energy moves at a velocity less than the mean velocity. Near the wall $\overline{u^3}$ is positive implying a net transport of $\overline{u^2}$ by positive fluctuations. Despite the rapid changes in $\overline{u^3}$ near the wall, the skewness S_u is small, as can be seen in figure 4.33 (to be discussed in subsection 4.6.4).

At small values of the free-stream intensity the magnitude of the negative peak in $\overline{u^3}$ is increased. At higher values the subsequent decrease in the size of the peak is accompanied by an increase of similar magnitude in the free-stream value of $\overline{u^3}$ (> 0). The effect of decreasing length scale ratio is to push the negative peak of $\overline{u^3}$ to smaller y/δ_{995}. Within the boundary layer the overall level of $\overline{v^3}$ is not so strongly affected by free-stream intensity but the peak of $\overline{v^3}$, like that of $\overline{u^3}$, moves to smaller y/δ_{995} with decreasing length scale ratio. Although the peak of $\overline{u^2v}$ appears to increase significantly the increase is in fact less marked if $\overline{u^2v}$

is scaled on u_τ^3 instead of U_e^3. It is noticeable that for each case the peaks of $\overline{u^3}$, $\overline{v^3}$, $\overline{u^2v}$, $\overline{uv^2}$ and $\overline{uw^2}$ occur at closely equal values of y/δ_{995}. Since u and w are fluctuations tangential to the wall $\overline{uw^2}$ and $\overline{u^3}$ may be expected to behave in the same way. Also, in the outer part of the boundary layer, where $\overline{v^2} \approx \overline{w^2}$, $\overline{uv^2} \approx \overline{uw^2}$ would be expected. Both of these assertions are supported by the measurements presented in figures 4.11 and 4.12.

Transport velocities defined by

$$V_q \equiv \frac{\overline{v(u^2 + v^2)}}{\overline{u^2} + \overline{v^2}} \quad \text{and} \quad V_\tau \equiv \frac{\overline{uv^2}}{\overline{uv}} \qquad (4.4.3,\ 4.4.4)$$

are presented in figures 4.13a to 4.13e. (No correction has been made to V_q and V_τ for the probably erroneous measurements of some triple products obtained near the wall.) V_q is expected to be close to $\overline{vq^2}/\overline{q^2}$; $\overline{vw^2}$ was not measured. Since the shear stress and the turbulent kinetic energy are mainly contained by the large-scale motion V_τ and V_q pertain to the large scales of the motion.

The two sets of transport-velocity measurements obtained in the absence of free-stream turbulence agree well, as shown in figure 4.13a. For a non-turbulent free-stream, the balance of the turbulent kinetic transport energy equation, discussed formally in section 4.7, reduces to "advection = diffusion" near the boundary layer edge. That is, at $y \approx \delta$,

$$(U\frac{\partial}{\partial x} + V\frac{\partial}{\partial y})\ \frac{1}{2}\overline{q^2} \approx \frac{\partial}{\partial y}\ (\frac{\overline{pv}}{\rho} + \frac{1}{2}\overline{vq^2}) \approx \frac{\partial}{\partial y}\ (\frac{1}{2}\overline{q^2}\ V_q). \qquad (4.4.5)$$

Now, for a self-preserving flow $\partial/\partial x = -d\delta/dx.\partial/\partial y$, so that at $y \approx \delta$,

$$(-U\frac{d\delta}{dx} + V)\ \frac{\partial}{\partial y}\ \frac{1}{2}\overline{q^2} \approx \frac{\partial}{\partial y}\ (\frac{1}{2}\overline{q^2}\ V_q). \qquad (4.4.6)$$

When $\overline{q^2}$ goes rapidly to zero this equation can be integrated to give, near $y = \delta$,

$$(-U\frac{d\delta}{dx} + V)\ \frac{1}{2}\overline{q^2} \approx \frac{1}{2}\overline{q^2}\ V_q. \qquad (4.4.7)$$

Since $(-Ud\delta/dx + V)_{y=\delta} = V_E$, where V_E is the entrainment velocity also given by equation 4.4.2, $V_q \approx V_E$. V_E is indicated in figure 4.13a. Near the boundary layer edge, the pressure-strain term in the shear stress transport equation is of the same order of magnitude as the convection and turbulent transport terms and precludes an equation analogous to equation 4.4.5.

The effect of free-stream turbulence is to increase V_q and V_τ for the flow near the wall and to decrease V_q further out. As might be expected since the free-stream contains no shear stress V_τ is less affected than V_q in the outer flow. Clearly, the convection velocities do not exhibit a simple dependence upon the free-stream intensity and length scale ratio. Near the boundary layer edge the dissipation is no longer insignificant so that "advection ≠ diffusion" and therefore V_q is no longer equal to the entrainment velocity, V_E. (For figure 4.13e, $V_E/V_q(y = \delta_{995}) \approx 3$ at station 6 and $V_E/V_q(y = \delta_{995}) \approx 2$ at station 16.)

4.5 INTERMITTENCY MEASUREMENTS

Prior to quantitative measurements the effect of free-stream turbulence on a smoke-filled boundary layer was investigated. The observations were made on the floor of the Department's 1.2 m × 0.6 m low speed flow visualization wind tunnel. The "background" turbulence intensity in the working section (measured by another user) was about 0.2%. Figure 4.14 shows two instances of a smoke-filled boundary layer with low free-stream turbulence, and two instances for which $(u'/U)_e \approx 0.03$ and $L^u_e/\delta \approx 0.4$. Illumination is by a thin vertical plane of light. The turbulence grid was approximately 25 mesh lengths upstream of the field of vision shown in figure 4.14b. Just upstream of the grid the boundary layer was laminar and thin when compared with the grid mesh size. For all the photographs $Re_\theta \approx 700$. Approximate boundary layer thicknesses are shown against

the photographs. In the absence of grid-generated free-stream turbulence the interface has features similar to those observed by Fiedler & Head (1966) at about the same Reynolds number. The effect of free-stream turbulence on the interface is clearly quite dramatic. The interface defined by the smoke has become ragged and wispy, extending well beyond the mean velocity edge. Further, the rolling motion of the larger eddies, evident for low free-stream intensity, is far less obvious at the high free-stream intensity, and the stream direction is not so easily inferred. The more highly contorted interface due to free-stream turbulence provides a mechanism for the increased boundary layer growth rates observed from the mean flow measurements. Increased mixing in the neighbourhood of the boundary layer edge is consistent with the observed reduction in the mean velocity gradient.

The effect of the grid on the boundary layer immediately downstream of it was to produce a rapid thickening associated with the high velocity fluctuation intensity in this region. This is discussed in more detail in chapter 2. A thinner smoke-filled boundary layer on a flat plate with its leading edge about 12 mesh lengths downstream of the same grid was also investigated. Qualitatively, the effect of the free-stream turbulence on the interface was as observed of the floor boundary layer shown in figure 4.14. Photographs of the plate boundary layer were of poor quality mainly because of its smaller size; they are not presented here.

A turbulent/turbulent interface cannot be a vorticity front or "superlayer" precisely in the sense deduced by Corrsin & Kistler (1955) for a turbulent/non-turbulent interface unless the scales of the turbulent motion either side of the interface are widely separated, which in the pr ent case they are not. Measurements by Andreopoulos (1978) of the near wake of a two-dimensional aerofoil,

with one boundary layer heated, showed significant fine-grained mixing in the region of the interface separating the two parts of the shear layer. The fine-grained mixing in his case was due mainly to the small-scale high intensity turbulence originating in the flow close to the aerofoil surface. Dean & Bradshaw's (1976) investigation of two merging boundary layers in a two-dimensional duct exhibited only a small amount of fine-grained mixing. In the present case the scale of the mixing will depend upon the length scale ratio, L_e/δ; the amount of fine-grained mixing will be negligible when L_e/δ is large and will increase with decreasing L_e/δ.

Figure 4.15 shows some samples of Calcomp plots of velocity (u and v) and temperature fluctuations and the output of the intermittency algorithm. (ID = +1 if fluid is declared 'hot' and ID $\leq$ 0 if fluid is declared 'cold'. All hot bursts containing only one point are rejected and these are indicated by setting ID = -1. ID = -2 if a point is called cold via the slope and second level tests.) The samples show typical features seen in the remainder of the plots (not presented here). There is a significantly greater tendency for fairly slow changes in temperature at one or both ends of some hot bursts when free-stream turbulence is present, and the temperature within a substantial part if not the whole of these bursts sometimes remains near to, though definitely above, the cold level. These bursts, or parts of bursts, are probably at least part of the wispy motion seen in the photographs of figure 4.14. (The absence of a sharp temperature rise at the beginning of a hot burst enabled the first level threshold in the original version of the intermittency algorithm to climb up the hot burst. The modified algorithm used here reduced this problem to an acceptable level although still better results might have been obtained had the level threshold been referred to a minimum temperature over a fixed time delay rather than to the last-but-one cold burst.)

Measurements of the intermittency factor, γ, are shown in figure 4.16. Figures 4.16a and 4.16b show the intermittency factor in the absence of grid-generated free-stream turbulence. The difference between Andreopoulos' measurements (obtained in the same wind tunnel) and the present measurements is partly attributable to a difference of opinion of the most appropriate threshold levels. He also used Weir's intermittency algorithm but without the minor changes the present author found necessary for the algorithm to cope with temperature signals affected by free-stream turbulence. The no-grid intermittency factor measurements of Charnay et al. (1976), which were obtained with an uncompensated temperature wire, fall below the present results in the centre of the layer. Low-pass filtering effected by an uncompensated temperature wire would, all else constant, tend to indicate a higher γ if ignoring the finer indentations of the interface outweighed the failure to register the full length of short hot bursts. The intermittency factor measurements of Klebanoff (1955), Kovasznay et al. (1970) and Hedley & Keffer (1974, b) are also shown. These, as with those of Charnay et al., have been adjusted to account for the different definitions of boundary layer thickness. The present measurements of γ agree quite well with those of Klebanoff. Following the last named and other workers an error function curve,

$$\gamma = \frac{1}{2}\left(1 - \mathrm{erf}\left(\frac{y - \bar{y}}{\sqrt{2}\,\sigma}\right)\right), \qquad (4.5.1)$$

has been fitted to the data of figure 4.16a. $\bar{y}$ is the position where $\gamma = 0.5$, and σ is the standard deviation of the fitted curve;

$$\frac{\sigma}{\delta_{995}} = 0.13\,, \qquad \frac{\bar{y}}{\delta_{995}} = 0.90.$$

Figures 4.16c to 4.16e show the effect of free-stream intensity and length scale ratio on the intermittency factor. The

present no-grid distribution is also shown. At $(u'/U)_e = 0.025$ and $L^u_e/\delta_{995} \approx 2$ γ is significantly affected only inside $y/\delta_{995} \approx 1$ where it is reduced, implying a deeper relative penetration of the free-stream fluid. At the same free-stream intensity but with $L^u_e/\delta_{995} \approx 0.7$, the penetration by the free-stream fluid is further increased and, in addition, a large amount of boundary layer fluid is present well outside the boundary layer edge defined by δ_{995}, as observed of the smoke-filled boundary layer. Increased penetration of free-stream fluid towards the wall is difficult to discern from the photographs. Still with $L^u_e/\delta_{995} \approx 0.7$, the intermittency factor profile, to the likely accuracy of its measurement, changes very little when $(u'/U)_e$ is increased from 0.025 to 0.040 but there is a larger change at $L^u_e/\delta_{995} \approx 2$ for the same change in intensity. Increasing $(u'/U)_e$ from 0.040 to 0.058 results in only a further small change in the intermittency factor profiles when $L^u_e/\delta_{995} \approx 2$. The seemingly large length-scale effect at $(u'/U)_e = 0.058$ is due to a poor estimate of δ_{995}; γ is also shown plotted against y/δ_{05} at this intensity, showing a much smaller length-scale effect. Outside $y/\delta_{995} = 1$, say, the increase in γ with decreasing length scale ratio is what would be expected if the normal component of fluctuating velocity was principally responsible for large-scale mixing of the boundary layer and free-stream fluid. Near the wall, increased mixing of boundary layer and free-stream fluid must reduce γ. If the above simple explanation for the behaviour outside $y \approx \delta_{995}$ was also true near the wall, the profiles of γ would have to cross over. The intermittency factor profiles for the six consecutive stations (6 to 16 inclusive) are shown in figure 4.16f and are seen to be all nearly the same shape. The corresponding profiles of shear stress and mean velocity were noted to be closely self preserving but the direct-stress profiles were not. As will be seen, the corresponding profiles of average burst frequency,

scaled on U_e/δ_{995}, and average burst length, scaled on δ_{995}, also do not collapse onto single curves. The intermittency factor profiles of Charnay et al. show the same qualitative trend with increasing free-stream intensity as the present results, but the absolute values are different and the change is less marked. Figure 4.17 tabulates $\overline{y}/\delta_{995}$ and $\overline{y}/\delta_{05}$ at appropriate values of $(u'/U)_e$ and, respectively, L_e^u/δ_{995} and L_e^u/δ_{05}. Since the profiles of γ are generally not antisymmetrical about $y = \overline{y}$ when free-stream turbulence is present, curves of the form given in equation 4.5.1 cannot be fitted closely except over a narrow range, near $y = \overline{y}$ say. Figure 4.17 also tabulates (in brackets) values of σ'/δ_{995} and σ'/δ_{05} where σ' has been determined graphically from

$$\sigma' = \frac{1}{\sqrt{2\pi}} \left[\frac{d\gamma}{dy}\right]^{-1}_{y=\overline{y}} . \qquad (4.5.2)$$

In practice, the average burst frequency, and hence the average burst length, is more difficult to determine reliably than the intermittency factor because all the bursts have to be correctly interpreted. For instance, a spurious short cold burst near the middle of each hot burst will halve the average hot-burst length. There is no simple answer to this sort of problem and quantities based on measurements of the interface crossing rate should always be viewed cautiously. Note, however, that the interface crossing rate is relatively easier to determine reliably from temperature signals than from velocity signals in so far as the latter have to be treated much more carefully in order to avoid spurious dropouts in the intermittency function.

Measurements of the average burst frequency, f_γ, and average hot-burst lengths,

$$L_\gamma = \frac{\gamma\, U(y)}{f_\gamma} , \qquad (4.5.3)$$

are shown in figure 4.18. f_γ is equal to one half of the interface average crossing frequency. The average cold-burst length,

$$L_{(1-\gamma)} = \frac{(1-\gamma)\,U(y)}{f_\gamma} = \frac{(1-\gamma)}{\gamma} L_\gamma \,, \qquad (4.5.4)$$

is also shown but only as a faired curve. (For the average burst lengths a convection velocity equal to the local mean velocity has been assumed.) f_γ was not found to be very sensitive to threshold settings, although this in itself does not ensure reliability. Nevertheless, the present no-grid measurements of average burst frequency, shown in figure 4.18a, are in reasonable agreement with those of Kovasznay et al., which were obtained at a similar Reynolds number. At Reynolds numbers much below Re_θ= 5000 the interface becomes progressively less contorted and hence the interface average crossing frequency also decreases (Fiedler & Head; Murlis 1975). The average burst frequency measurements of Charnay et al. show, for their no-grid case, a much broader distribution than do the present measurements or those of Kovasznay et al. and are more easily comparable with the measurements of Hedley & Keffer (see figure 4.18a). As would be expected from the smoke pictures the effect of free-stream turbulence is to increase the magnitude and breadth of the average burst frequency profile. The effect of the length scale ratio is most dramatic at $(u'/U)_e \approx 0.025$. (At $(u'/U)_e$ = 0.058 the average burst frequency is also shown plotted against y/δ_{05}.) Irrespective of the magnitude of free-stream intensity or the length scale ratio the distribution of the average burst frequency remains asymmetric about the average interface position, $\overline{y}$. Except outside a position roughly coincident with the boundary layer edge the average hot-burst length is considerably reduced by free-stream turbulence, and is consistent with the wispy motion seen in the smoke pictures.

In the absence of free-stream turbulence, low Reynolds

number effects are associated with the superlayer becoming thicker and less contorted (Fiedler & Head; Murlis). Free-stream turbulence on the other hand has the opposite effect (even at low Reynolds numbers, as evidenced in the first place by the photographs in figure 4.14). It is, therefore, tentatively suggested that the low-Reynolds-number effects on C_f/C_{fo}, discussed in chapter 3 (subsection 3.3.4) arise because the decrease in the degree of folding of the interface at low Reynolds numbers tends to be inhibited by free-stream turbulence. It follows that the low Reynolds number effects in C_f/C_{fo} would be more evident when the effect of free-stream turbulence on the interface is large.

4.6 CONDITIONALLY-AVERAGED MEASUREMENTS

Averages in the hot zone will be denoted by a suffix 'H' and averages in the cold zone by a suffix 'C'. Conventional averages will be denoted by no suffix. Where both hot and cold-zone quantities are presented in the same figure the following convention will be used: the hot-zone quantity will be denoted by '∇' (mnemonic, a plume); the cold-zone quantity will be denoted by '$\triangle$' (mnemonic, an iceberg); and the total will be denoted by '$\circ$'. When either hot or cold-zone quantities are presented separately the convention will be that used in the preceding part of this chapter. Any departure from either of these conventions should be evident from the context.

4.6.1 Mean velocities

Conditionally-averaged mean velocities U_H, U_C, $(V_H - V)$, and $(V_C - V)$, not weighted by the intermittency factor, are shown in figures 4.19a to 4.19g. The conventionally-averaged mean velocity, U, as measured with a Pitot tube, is also shown. Although the x-wire measurements of U are within about 1% of the Pitot tube measurements they are more scattered, so that U_H - for instance - has been derived as the sum of U from the Pitot tube and $(U_H - U)$ from the x-wire probe.

U_C has been similarly derived. The normal component of mean velocity, V, is also difficult to measure accurately with an x-wire probe. Here, V has been evaluated from the streamwise mean velocity U and the continuity equation. $V < 0.004\ U_e$. There is no reason why V_C should tend to V in regions of high γ (other than that V_C, V_H and V must be zero at the wall). Even tiny errors in detecting cold bursts in these regions will most likely cause V_C to approach V_H. Profiles of V_C for $\gamma > 0.95$ are shown as broken lines.

Qualitatively, the conditionally-averaged mean velocities are in agreement with the well established results of other workers, for example, those of Kovasznay et al. (1970) and Hedley & Keffer (1974, b) in the absence of free-stream turbulence; on average, the boundary layer fluid moves slower than the local mean and moves outwards while the free-stream fluid moves faster than the local mean and moves inwards. In the absence of free-stream turbulence $(U_C - U)$ and $(V_C - V)$ are close to the measurements of Kovasznay et al. Charnay's (1974) no-grid measurements of $(U_C - U)$ and $(V_C - V)$ are smaller than the present measurements by about half. $(U - U_H)$ and $(V - V_H)$ are smaller than measured by Kovasznay et al. but $(U - U_H)$ is in better agreement with Hedley & Keffer's results. Charnay's measurements of $(U - U_H)$ are larger than those of Kovasznay et al. but his $(V - V_H)$ are closer to the present ones.

The effect of free-stream turbulence is to reduce $(U_C - U)$ consistent with the decrease in the mean velocity gradient $\partial U/\partial y$ in the outer part of the boundary layer. Charnay's measurements show an increase of $(U_C - U)$ with free-stream intensity. The present results show that $(U - U_H)$ would appear to be more consistently affected by, and decreasing with, decreasing length scale ratio, than by free-stream intensity. $(V_H - V)$ is increased across the whole layer with increased free-stream intensity, qualitatively consistent with Charnay's

measurements. In the proximity of the boundary layer edge $(V_C - V)$ becomes more negative with increasing free-stream intensity, again as also observed by Charnay.

4.6.2 Reynolds stresses

The weighted conditionally-averaged direct stresses $\gamma\overline{u_H^2}$, $(1 - \gamma)\overline{u_C^2}$, $\gamma\overline{w_H^2}$, $(1 - \gamma)\overline{w_C^2}$, $\gamma\overline{U_H^2}$, and $(1 - \gamma)\overline{U_C^2}$ are given in figures 4.20a to 4.20m, and the weighted conditionally-averaged shear stresses $-\gamma\overline{uv}_H$ and $-(1 - \gamma)\overline{uv}_C$ in figures 4.21a to 4.21i. Note again that the weighted averages are the hot- and cold-zone contributions to the conventional average; see equation 4.2.1. The conventional averages, previously presented in figures 4.6 and 4.7, are shown as faired curves. It is more convenient to discuss the shear stresses first.

The extent by which the hot-zone shear stress, $\gamma\overline{uv}_H$, overlaps the mean velocity profile edge, δ_{995}, increases with free-stream turbulence intensity. The overlap is less than that observed of the intermittency factor or of the hot-zone contributions to the direct stresses. Thus, the boundary layer fluid that is "torn out" by the free-stream turbulence, as shown qualitatively by the smoke pictures in figure 4.14 and quantitatively by the intermittency factor measurements, is torn out in such a way that the shear stress it may have had is smeared out, presumably by the action of the pressure-strain "redistribution" term. The same result might be deduced from the smoke pictures since the smoke entrained into the free-stream does not appear on average to exhibit a pattern that can be associated with the stream direction. Closer to the wall, or of course when free-stream turbulence is absent, the smoke pattern can be more strongly associated with the stream direction. Had the boundary layer fluid been torn out in large roughly spherical lumps rather than in wisps, it is likely that the lumps would have retained

their shear stress much longer than the wisps, forcing increased overlap. The fact that the wispy motion outside the boundary layer does not contain very much shear stress tends to suggest that the wispy motion inside the boundary layer may not locally contain much more shear stress than occurs in the cold-zone.

In the absence of free-stream turbulence the cold-zone shear stress, $-(1-\gamma)\overline{uv}_c$, has the same sign as the total shear stress, $-\overline{uv}$, but is much smaller in magnitude. (The Navier-Stokes equations do not demand that irrotational fluctuations should have a zero shear stress.) Since the irrotational fluctuations in the cold-zone are due to turbulent fluctuations in the hot-zone it is reasonable that the cold-zone fluctuations should be correlated with the same sign as the hot-zone fluctuations. When free-stream turbulence is present the magnitude of the shear stress ratio $-(1-\gamma)\overline{uv}_c/-\overline{uv}$ is larger. Qualitatively, the behaviour of the cold-zone shear stress is as expected if it were produced by the already existing gradient of conventionally-averaged mean velocity, $\partial U/\partial y$. (It is not intended in this thesis to consider in detail transport equations for the conditionally-averaged Reynolds stresses.) It follows that, because the effect of free-stream turbulence is to reduce $\partial U/\partial y$, generation of the cold-zone shear stress, $-(1-\gamma)\overline{uv}_c$, will not increase in proportion to the turbulent kinetic energy in the cold-zone. Further, in a region roughly coinciding with the outer layer the decrease in the magnitude of $-(1-\gamma)\overline{uv}_c$ with decreasing length-scale ratio can, at least in part, be associated with the decrease in $\partial U/\partial y$ that also occurs in the same region. For some of the profiles, some measurements of $(1-\gamma)\overline{uv}_c$ in the region of the boundary layer edge and outside are positive. They may be attributed to scatter and small errors (of less than 1^o) in probe alignment for these profiles. It is difficult from the present measurements to find substantial support for the

linearized rapid-distortion prediction of Durbin (1976) that there should be a region of positive $\overline{uv}$ outside the boundary layer edge.

Outside $y/\delta_{995} \gtrsim 1$, $\gamma\overline{u_H^2}$, $(1-\gamma)\overline{u_C^2}$, $\gamma\overline{w_H^2}$, and $(1-\gamma)\overline{w_C^2}$, are seen in most of the figures to change more rapidly with y/δ_{995} than the respective conventional averages $\overline{u^2}$ and $\overline{w^2}$. $\overline{v^2}$ is discussed later. Now, the contaminated proportion, γ, of a randomly (passively) contaminated field of turbulence has statistical characteristics no different from the whole. It follows that in this case the net contribution from the contaminated fluid to any statistical average of the whole is proportional to γ. The quantities $\gamma\overline{u_e^2}$, $(1-\gamma)\overline{u_e^2}$, $\gamma\overline{w_e^2}$, and $(1-\gamma)\overline{w_e^2}$ are shown by broken lines in figures 4.20c, d, g, k, ℓ and m. Surprisingly, outside $y/\delta_{995} \approx 1$, $(1-\gamma)\overline{u_C^2}$ is accurately described by $(1-\gamma)\overline{u_e^2}$, and $(1-\gamma)\overline{w_C^2}$ is accurately described by $(1-\gamma)\overline{w_e^2}$ everywhere. Inside $y/\delta_{995} \approx 1$, $(1-\gamma)\overline{u_C^2}$ is larger than $(1-\gamma)\overline{u_e^2}$ and the extent over which the difference occurs decreases with decreasing length scale ratio. This length-scale dependence is qualitatively consistent with the amplification of $\overline{u^2}$ measured by Thomas & Hancock (1977, appendix 1). $\overline{v^2}$, however, is reduced slightly more by the presence of the wall than measured by Thomas & Hancock or predicted by Hunt & Graham (1978), preventing a similar simple comparison.

The shear-stress correlation coefficient $-\overline{uv}_H/\sqrt{(\overline{u_H^2}\,\overline{v_H^2})}$ and the ratio $-\overline{uv}_H/\overline{q_H^2}$ are shown in figure 4.22. $-\overline{uv}_C/\sqrt{(\overline{u_C^2}\,\overline{v_C^2})}$ and $-\overline{uv}_C/\overline{q_C^2}$ are shown in figure 4.23. In the absence of free-stream turbulence $=\overline{uv}_H/\sqrt{(\overline{u_H^2}.\overline{v_H^2})}$ and $-\overline{uv}_H/\overline{q_H^2}$ differ from the analogous ratio formed from conventional averages only for $y/\delta_{995} \gtrsim 0.8$. The effect of free-stream turbulence is to reduce the amount of shear-stress-containing motion in the hot zone. The ratios $-\overline{uv}_C/\sqrt{(\overline{u_C^2}.\overline{v_C^2})}$ and $-\overline{uv}_C/\overline{q_C^2}$ for the cases when free-stream turbulence is absent are included primarily for consistency. However, they are particularly interesting in that the peak values of these ratios are considerably

larger than normally measured for turbulent fluctuations. The decrease of both $-\overline{uv}_C/\sqrt{(\overline{u_C^2}.\overline{v_C^2})}$ and $-\overline{uv}_C/\overline{q_C^2}$ inside $y/\delta_{995} \approx 0.4$ could easily be due to incorrect discrimination simply because the intermittency factor is close to unity. (The fact that the measurements show the cold fluid, on average, to move towards the wall (figure 4.19) tends to discount a large amount of incorrect discrimination.) A similarly large correlation coefficient at $y/\delta_{995} \approx 0.4$ can be deduced from the measurements of Hedley & Keffer (1974, b) and Charnay (1974) after referring the external fluctuations to the conventionally-averaged mean velocities rather than the conditionally-averaged mean velocities. Free-stream turbulence has the effect of reducing $-\overline{uv}_C/\sqrt{(\overline{u_C^2}\ \overline{v_C^2})}$ and $-\overline{uv}_C/\overline{q_C^2}$, but the reduction is rather slow, and the two quantities reach, respectively, about 0.45 and 0.15 near the wall only when $(u'/U)_e \approx 0.058$.

4.6.3 Third-order products

The conditionally-averaged triple products represent the transport of the conditionally-averaged Reynolds stresses by the velocity fluctuations occurring in the conditionally-averaged zone. Results for the six cases emphasising the separate effects of free-stream intensity and length scale ratio are presented, but in a different order from preceding results. Figures 4.25 to 4.28 show respectively $\gamma\overline{u_H^3}$ & $(1-\gamma)\overline{u_C^3}$, $\gamma\overline{v_H^3}$ & $(1-\gamma)\overline{v_C^3}$, $\gamma\overline{u^2v}_H$ & $(1-\gamma)\overline{u^2v}_C$, and $\gamma\overline{uv_H^2}$ & $(1-\gamma)\overline{uv_C^2}$ as well as the conventional averages. In the absence of free-stream turbulence the cold-zone triple products, shown in figure 4.24, are small, and so the corresponding hot-zone products are not presented since they are close to the conventional averages which are discussed in subsection 4.4.2. Also, only the conditionally-averaged measurements of $\overline{u^3}$ obtained with the x-wire probe sensitive to u and v ($\phi = 0$) are provided. Only the triple products that contain v appear in the thin-shear-layer approximation to the Reynolds-stress transport equations.

The measurements of $\gamma\overline{u_H^3}$ and $(1-\gamma)\overline{u_C^3}$ show that in the boundary layer the net transport of $\overline{u_H^2}$ is by negative u-fluctuations and the net transport of $\overline{u_C^2}$ is by positive u-fluctuations. Indeed, this is suggested by the mean velocity measurements of figure 4.19. $\gamma\overline{u_H^3}$ and $(1-\gamma)\overline{u_C^3}$ increase in magnitude with free-stream intensity, more so for the higher values of the length scale ratio. The latter behaviour is presumably due to the effect the wall has on the free-stream turbulence (i.e. the amplification of $\overline{u^2}$) although it is not obvious that the hot- and cold-zone contributions should both increase in magnitude due to this effect.

The measurements of $\gamma\overline{u^2v}_H$, $\gamma\overline{v_H^3}$ and $\gamma\overline{uv_H^2}$ show that there is a net outward transport of, respectively, $\gamma\overline{u_H^2}$, $\gamma\overline{v_H^2}$ and $\gamma\overline{uv}_H$ throughout the boundary layer. Conversely, the measurements of $(1-\gamma)\overline{u^2v}_C$, $(1-\gamma)\overline{v_C^3}$ and $(1-\gamma)\overline{uv_C^2}$ show that there is a net inward transport of, respectively, $(1-\gamma)\overline{u_C^2}$, $(1-\gamma)\overline{v_C^2}$ and $(1-\gamma)\overline{uv}_C$. Compared with the conventional averages the response of all these zone contributions is clearly quite dramatic. A striking feature is that the profiles of the hot-zone quantities, particularly $\gamma\overline{u^2v}_H$ and $\gamma\overline{v_H^3}$, overlap well beyond the boundary layer edge as defined by, say, δ_{995} or δ_{05}, before finally falling to zero. Outside $y/\delta_{995} \approx 1$, $\gamma\overline{v_H^3}$ and $(1-\gamma)\overline{v_C^3}$ are approximately equal and opposite, as are also $\gamma\overline{u^2v}_H$ and $(1-\gamma)\overline{u^2v}_H$. The magnitudes of these four increase roughly as $(\overline{v^2})^{3/2}$, and their behaviour is probably a direct result of the 'turnover-time' of the free-stream energy-containing eddies, L_e/u_e, being of the order of the boundary layer life time, x/u.

The order of increasing overlap of the hot-zone profiles, including the hot-zone contributions to the Reynolds stresses, is

$$\gamma\overline{uv}_H\ ,\ \gamma\overline{u_H^3}\ ,\ \gamma\overline{uv_H^2}\ ,\ \gamma\overline{u_H^2}\ ,\ \gamma\overline{u^2v}_H\ ,\ \gamma\overline{v_H^2}\ ,\ \gamma\overline{v_H^3}\ ,\ \gamma\overline{w_H^2}$$

where the characteristic overlap distances have been taken to be the positions at which each profile has fallen to 50% of its value at $y = \delta_{995}$. (The usual definition of a profile edge, that is, the position at which a profile has fallen to some specified fraction of its maximum, is arguably an inappropriate measure for the comparison of the overlap, particularly where different turbulence quantities are concerned). The overlap of $\gamma\overline{u^3_H}$ is only marginally larger than that of $\gamma\overline{uv}_H$, and the overlaps of $\gamma\overline{u^2_H}$ and $\gamma\overline{w^2_H}$ are closely equal. Except for $\overline{u^2}$ †, this is the same order as for boundary layers merging in a two-dimensional duct (Dean & Bradshaw, 1976). In that case the overlap of $\gamma\overline{u^2_H}$ was larger than the overlap of $\gamma\overline{v^3_H}$.

Shear stress and turbulent kinetic energy transport velocities, defined for the hot-zone as

$$V_{\tau,H} \equiv \frac{\overline{uv^2_H}}{\overline{uv}_H} \quad \text{and} \quad V_{q,H} \equiv \frac{\overline{v(u^2 + v^2)_H}}{(\overline{u^2} + \overline{v^2})_H} \quad , \qquad (4.6.1,\ 4.6.2)$$

are presented in figures 4.29a to 4.29d. For the two no-grid cases, $V_{\tau,H}$ and $V_{q,H}$ are close to the transport velocities formed from conventional averages, respectively V_τ and V_q, except near the boundary layer edge where the latter are smaller. Both $V_{\tau,H}$ and $V_{q,H}$ are affected by free-stream turbulence but not as much as V_τ and V_q. Note that $V_{q,H}$ is in fact far less affected than V_q which, as was seen in subsection 4.4.2, is substantially reduced for a considerable part of the outer layer principally because $\overline{q^2}$ is increased. $V_{\tau,H}$ and $V_{q,H}$ are significantly increased inside y/δ_{995} of roughly 0.5 except for the case in which the interaction is weakest (figure 4.29b) when they are fairly close to those in the no-grid cases. The ratio of transport velocities $V_{\tau,H}/V_{q,H}$ is shown in figure 4.30, and is seen to be at most only weakly dependent on the interaction. The ratio is also approximately constant at about 2.3 for most of the boundary layer.

†Dean & Bradshaw do not quote the overlap of $\overline{w^2}$.

Smits et al. (1979) obtained for V_τ/V_q a value of about 2.5 in a constant-pressure layer. Figure 4.31 shows the profiles of $V_{q,H}$ for the cases given in figure 4.29 but scaled on the average position of the interface, $\overline{y}$, rather than δ_{995}. Outside $y/\overline{y} \approx 0.8$ $V_{q,H}(y/\overline{y})$ is unaltered for $(u'/U)_e \lesssim 0.025$, and at higher values there appears to be only a weak length-scale dependence.

Shear stress and turbulent kinetic energy transport velocities, defined for the cold-zone as

$$V_{\tau,C} \equiv \frac{\overline{uv_C^2}}{\overline{uv}_C} \qquad \text{and} \quad V_{q,C} \equiv \frac{\overline{v(u^2 + v^2)_C}}{(\overline{u^2} + \overline{v^2})_C}, \qquad (4.6.3,\ 4.6.4)$$

are shown in figures 4.32a to 4.32d. Clearly, both $V_{\tau,C}$ and $V_{q,C}$ are affected by free-stream turbulence, although it is not surprising that transport velocities for irrotational motion should be different from those for rotational motion, i.e. external turbulence. Note that $V_{\tau,C}$ and $V_{q,C}$, like $V_{\tau,H}$ and $V_{q,H}$ are shown normalised by u_τ which obviously cannot be a generally suitable velocity scale of the cold-zone except perhaps in the near-wall region, or of course when there is no appreciable free-stream turbulence. In fact, $V_{\tau,C}/u_\tau$ and $V_{q,C}/u_\tau$ do appear to be approximately constant near the wall when free-stream turbulence is present. Although quantities evaluated in the cold-zone are not particularly reliable where γ is close to unity, near the wall the cold-zone transport velocities are still substantially different from the hot-zone transport velocities, implying that any error in the discrimination is not overwhelmingly large. Very roughly the cold-zone transport velocities near the boundary layer edge increase as $\sqrt{(\overline{v^2})}$.

4.6.4 Skewness and flatness factors

Skewness and flatness factors of u and v, formed from conventional and conditional averages, are presented in figures 4.33 to 4.36 for one no-grid case and the six cases showing the separate

effects of free-stream intensity and length scale ratio. Where conditional averages have been used they have not been multiplied by γ or $(1 - \gamma)$. In any case the skewness and flatness factors would not, of course, conform to the addition law of equation 4.1.1. It is worth noting at the outset that unless the third- and fourth-order products change sufficiently rapidly the effect of free-stream turbulence will reduce the skewness and the flatness factors simply because $\overline{u^2}$ and $\overline{v^2}$ increase.

Except at $(u'/U)_e \approx 0.025$, the skewness of the unconditional u-fluctuations, S_u, shows negligible dependence on the length scale ratio. On the other hand, the skewness of the unconditioned v-fluctuations, S_v, shows a small but perceptible dependence on the length scale ratio at all three nominal values of $(u'/U)_e$, but otherwise behaves much as S_u. The magnitudes of S_u and S_v decrease as the free-stream intensity is increased, and at $(u'/U)_e \approx 0.058$ they are almost zero. The decrease is more rapid in the outer part of the boundary layer. $S_{u,H}$, the skewness of the hot-zone u-fluctuations, follows the same trend as S_u but does not decrease as rapidly. $S_{u,C}$, $S_{v,H}$ and $S_{v,C}$ exhibit plateau regions in nearly all their profiles, and the magnitudes of the skewnesses within them are not changed very greatly by free-stream turbulence. Although the significance of the plateaux is not altogether clear, their existence is partly due to the use of conventionally-averaged base lines. If the hot-zone velocity, say, was constant but different from the conventional-average velocity the skewness as evaluated here would be ± 1. A fluctuation that first increases linearly from zero and then decreases linearly to zero - i.e., a triangular-shaped fluctuation - has a skewness of $3\sqrt{3}/4 = 1.30$; the present plateau regions have magnitudes of about 1.2 to 1.4. Small values of S_u and $S_{u,H}$ near the boundary layer edge and outside concur with the observation of the smoke-filled boundary layer that

the stream direction cannot be inferred from the wispy motion. In contrast, the strong inhomogeneity in the y-direction is evident from the non-zero values of $S_{v,H}$ and $S_{v,C}$.

Flatness factors of both u- and v-fluctuations are also significantly affected by free-stream turbulence. As the effect of the free-stream turbulence increases the large flatness factors in the region of $y/\delta_{995} \approx 1$ are progressively reduced to the closely Gaussian values measured in the free-stream. (See, for example, Batchelor, 1953, chapter 8, for a discussion on the velocity probability distribution in grid-generated turbulence.) The flatness of the v-fluctuations do not approach the Gaussian value of 3 as quickly as the flatnesses of the u-fluctuations, again probably because of the obviously much stronger inhomogeneity in the y-direction. Inside the boundary layer the cold-zone flatness factors $F_{u,C}$ and $F_{v,C}$ exhibit particularly low values when free-stream turbulence is absent or not too strong, being well below the Gaussian value and well below the other flatness factors. The triangular-shaped velocity fluctuation discussed above has a flatness factor of 9/5 = 1.8 which is close to these low values. The rise in $F_{u,C}$ and $F_{v,C}$ as the wall is approached could easily be due to poor discrimination of the cold-zone proper, since the intermittency factor is close to unity. The same is true of the skewnesses $S_{u,C}$ and $S_{v,C}$. The low values of $F_{u,C}$ are, however, undoubtedly genuine and most likely exist for the same reason that $-\overline{uv}_C/\sqrt{(\overline{u_C^2}\ \overline{v_C^2})}$ is large. As the free-stream intensity increases the minima in $F_{u,C}$ and $F_{v,C}$ move towards the wall and become less prominent, presumably as a result of the increased penetration by free-stream fluid.

4.7 BALANCES OF THE TURBULENT KINETIC ENERGY AND TURBULENT SHEAR STRESS TRANSPORT EQUATIONS

The equations of motion for a constant-property, Newtonian fluid are given in appendix 7.

The forms commonly quoted for the turbulent kinetic energy and turbulent shear stress transport equations for a thin, closely two-dimensional shear layer are, respectively,

$$\frac{D}{Dt}\left(\frac{1}{2}\overline{q^2}\right) = -\overline{uv}\frac{\partial U}{\partial y} - \frac{\partial}{\partial y}\left(\frac{1}{2}\overline{vq^2} + \overline{p'v}\right) - \varepsilon, \qquad (4.7.1)$$

Advection (or Mean Transport) = Production - Diffusion - Dissipation

and

$$\frac{D}{Dt}\left(\overline{uv}\right) = -\overline{v^2}\frac{\partial U}{\partial y} - \frac{\partial}{\partial y}\left(\overline{uv^2} + \overline{p'u}\right) - \overline{p'\left(\frac{\partial u}{\partial y} + \frac{\partial v}{\partial x}\right)}, \qquad (4.7.2)$$

Convection (or Mean Transport) = Generation - Turbulent Transport - Destruction

where $$\frac{D}{Dt} \equiv \frac{\partial}{\partial t} + U\frac{\partial}{\partial x} + V\frac{\partial}{\partial y}. \qquad (4.7.3)$$

These equations also assume that the Reynolds number is large enough so that the viscous transport of turbulent kinetic energy is negligible by comparison with the dissipation and that the viscous terms in the shear stress transport equation are negligible by comparison with the destruction term. A necessary condition for a shear layer to be thin is that the Reynolds number must be large.

For the present flow the thin shear layer approximation can be expected to be valid in so far as $0.014 \lesssim d\delta_{995}/dx \lesssim 0.05$. The production of turbulent kinetic energy by direct stresses, which in a two-dimensional flow is given by $-(\overline{u^2} - \overline{v^2})\partial U/\partial x$, was found to be negligible by comparison with $-\overline{uv}\partial U/\partial y$. Similarly, the generation of shear stress by the shear stress itself, $-\overline{uv}(\partial U/\partial x + \partial V/\partial y)$ is clearly negligible by comparison with $-\overline{v^2}\partial U/\partial y$. Evaluation of the terms representing the turbulent transport of kinetic energy and shear stress by streamwise velocity fluctuations, respectively $\partial(\overline{uq^2})/\partial x$ and $\partial(\overline{u^2v})/\partial x$, would show them to be small by comparison with the cross-

stream transport terms. $\overline{vq^2}$ has been approximated by 3/2 $\overline{v(u^2 + v^2)}$. (Measurements of $\overline{vw^2}$ were obtained at station 8 but are not entirely satisfactory, partly because $\overline{w^3}$ is erroneously non-zero near the wall and partly because of scatter. The measurements of $\overline{vw^2}$ are not presented.) At worst, the approximated diffusion, 3/4 $\partial(\overline{v(u^2 + v^2)})/\partial y$, can only be locally in error since the net contribution over the whole flow should be zero; in the absence of errors arising from graphical differentiation of $\overline{vu^2}$ and $\overline{v^3}$ it would be exactly zero. Further, if the (probably erroneous) high values close to the wall are ignored, the curves of $\overline{vu^2}$ and $\overline{v^3}$ do not differ greatly in shape, only in magnitude, suggesting that $\overline{vw^2}$ is probably also similar in shape. Turbulent diffusion and turbulent transport by pressure fluctuations have been neglected. These terms are discussed later. The mean transport terms have been measured directly. The mean velocity V was determined in the inner layer by use of the law of the wall and the measured du_τ/dx, and in the outer layer by numerical integration of the mean velocity profiles. Although insignificant here, the effects of the sub-layer and buffer layer were included, using the description given by Coles (1968). Dissipation and destruction have been determined by difference. No adjustment has been applied to the shear stress to force better agreement with the mean flow measurements of wall shear stress. Where permitted by the measurements, use has been made of similarity assumptions to obtain V, $\partial\overline{q^2}/\partial x$ and $\partial\overline{uv}/\partial x$.

Balances of the turbulent kinetic energy and shear stress transport equations are shown in figures 4.37 and 4.38 for three cases. Note, the points presented in each figure correspond to faired interpolations of the measurements and not to the measurements proper. The various contributions to the balances have been presented so that their sum is zero (i.e. t terms on the r.h. sides of equations 4.7.1 and 4.7.2 have been transferred to the l.h. sides).

When free-stream turbulence is absent the balance of the turbulent kinetic energy equation in the region $y/\delta_{99.5} \gtrsim 1$ reduces to "advection ≈ diffusion by velocity fluctuations", as shown in figure 4.37a. The approximate equality implies that the diffusion by pressure fluctuations is not a large part of the whole diffusion in that region. From figures 4.37b and 4.37c it is seen that the effect of free-stream turbulence is to change the sign of the advection, at least in the outer part of the boundary layer, and to adjust the distribution of the diffusion. The slight rise (gain) in advection near the wall is consistent in both figures 4.37b and 4.37c. The existence of a minimum in the advection implies that the gain near the wall is not a direct result of the negative advection in the free-stream but rather an indirect effect that must be associated with the presence of the wall. That is, the gain by advection near the wall is an increase in 'inactive' motion brought about by the free-stream turbulence. Increased loss by diffusion near the wall follows from the peaks of $\overline{vu^2}$ and $\overline{v^3}$ being pushed closer to the wall. A small gain by diffusion well outside the boundary layer edge is indicated by some measurements of $\overline{v^3}$. These small contributions have not been included in figures 4.37b and 4.37c. When free-stream turbulence is present there is no region where "advection ≈ diffusion". Production is reduced in the whole of the outer layer.

The convection of shear stress, in contrast to the advection of turbulent kinetic energy, is not greatly affected by free-stream turbulence, which is partly to be expected because $D\overline{uv}/Dt$ is zero in the free-stream. On the other hand, the turbulent transport of shear stress, $\partial\overline{uv^2}/\partial y$, is qualitatively affected by free-stream turbulence much as the diffusion of turbulent kinetic energy, $\partial\overline{vq^2}/\partial y$, is affected. The generation of shear stress, $-\overline{v^2}\partial U/\partial y$, is increased near the boundary layer edge, but further in it is reduced. Irrespective of the presence or absence of free-stream turbulence there is no region where the

generation and destruction of shear stress are small enough to permit "convection ≈ turbulent transport".

The dissipation length scale L_τ, defined as

$$L_\tau \equiv \frac{(-\overline{uv})^{3/2}}{\varepsilon} , \qquad (4.7.3)$$

is presented in figure 4.39 for the three cases. Discrepancy between the three profiles is small and the profiles themselves are close to the 'theoretical' algebraic distribution used by Bradshaw et al. (1967). Although the algebraic length scale works well in several flows it is difficult to accept the present adherence on the basis of that success. For, near the boundary layer edge $\sqrt{(-\overline{uv})}$ cannot by itself be an adequate velocity scale of the energy dissipation when appreciable free-stream turbulence is present. In the inner layer, universality of L_τ is more or less guaranteed if both the logarithmic law and "production ≈ dissipation" are obeyed. Clearly though, the fact that the distribution of the dissipation length scale, L_τ, appears to be unaffected by free-stream turbulence has useful implications for calculation methods. The dissipation length scale $L_q \equiv (\overline{q^2})^{3/2}/\varepsilon$, used in several calculation methods, cannot be independent of free-stream turbulence because, of course, in the outer layer it must depend upon the free-stream length scale. L_q is presented in figure 4.40 for the three cases.

4.9 SOME IMPLICATIONS FOR CALCULATION METHODS

The measurements presented in chapter 3 clearly show that the presence of free-stream turbulence affects the mean flow and that the effect is dependent upon both the free-stream intensity and the length scale ratio L_e/δ. The conditionally-averaged measurements have shown that the interaction affects the turbulence structure in both the hot and cold zones. Consequently, the first-order-accurate superposition or time-sharing approach, permitted when the interaction has negligible or only a small effect on the turbulence structure,

cannot be employed in the present case. Superposition has been shown by Dean & Bradshaw (1976) to be applicable to the merging boundary layers in a developing duct flow, and has been proposed by Andreopoulos for calculating the near wake of a thin aerofoil. (When the interaction affects the turbulence structure of either or both turbulence fields, it is not possible to write separate transport equations for each zone without including some sort of transfer term in each equation representing the interaction. The nature of these transfer terms is not considered in the present thesis.)

Many simple calculation methods use an eddy viscosity or a mixing length hypothesis. These two quantities, defined by

$$\nu_T \equiv -\overline{uv}/(\partial U/\partial y) \quad \text{and} \quad \ell \equiv \sqrt{(-\overline{uv})}/(\partial U/\partial y), \qquad (4.8.1,\ 4.8.2)$$

are shown in figures 4.41 and 4.42, respectively. The figures also show eddy viscosities and mixing lengths, defined by

$$\nu_{T,H} \equiv -\gamma\overline{uv}_H/(\partial U/\partial y)\ , \quad \ell_H \equiv \sqrt{(-\gamma\overline{uv}_H)}/(\partial U/\partial y), \qquad (4.8.3,\ 4.8.4)$$

$$\nu_{T,C} \equiv -(1-\gamma)\overline{uv}_C/(\partial U/\partial y) \text{ and } \ell_C \equiv \sqrt{(-(1-\gamma)\overline{uv}_C)}/(\partial U/\partial y) \qquad (4.8.5,\ 4.8.6)$$

Any change in the mean-velocity or shear-stress profiles necessarily implies a change in either the eddy viscosity or the mixing length, or both. Figures 4.41 and 4.42 show that they are both affected but that the mixing length is affected the most. Notably, the eddy viscosity $\nu_{T,C}$ shows a consistent increase with free-stream intensity but no consistent trend with length scale ratio. Variation of both ν_T and ℓ with free-stream turbulence can be seen to be necessary from the mean flow measurements and the thin-shear-layer momentum equation

$$U\frac{\partial U}{\partial x} + V\frac{\partial U}{\partial y} = -\frac{1}{\rho}\frac{dp}{dx} - \frac{\partial\overline{uv}}{\partial y} - \frac{\partial\overline{u^2}}{\partial x} \qquad (4.8.7)$$

if $\partial\overline{u^2}/\partial x$ is neglected and dp/dx assumed unaffected. Near the boundary layer edge $\partial\overline{u^2}/\partial x \approx d\overline{u_e^2}/dx = (\overline{u_e^2})^{3/2}/(U_e L_e^u)$, and over most

of the boundary layer $\partial\overline{uv}/\partial y = o\left[-u_\tau^2/\delta_{995}\right]$. Therefore

$$\frac{d\overline{u_e^2}/dx}{\partial\overline{uv}/\partial y} = o\left[-\left(\frac{\overline{u_e^2}}{U_e^2}\right)^{3/2}\left(\frac{U_e}{u_\tau}\right)^2 \Big/ \frac{L_e^u}{\delta_{995}}\right] \quad , \tag{4.8.8}$$

and for the present measurements $(\overline{u_e^2}/U_e^2)^{3/2}(U_e/u_\tau)^2 \approx 0.009$ at $(u'/U)_e = 0.025$, 0.036 at $(u'/U)_e = 0.04$, and 0.097 at $(u'/U)_e = 0.058$.

Calculation methods using algebraic eddy viscosity or mixing length are known to give poor results in strongly non-equilibrium flows. More sophisticated methods relate the eddy viscosity or mixing length to turbulence quantities or abandon these hypotheses altogether. The remaining discussion pertains mainly to the calculation method of Bradshaw et al. (1967). These authors employed three closure equations, namely

$$a_1 = -\overline{uv}/\overline{q^2} \quad , \tag{4.8.9}$$

$$G = (\overline{p'v} + \frac{1}{2}\overline{vq^2})/((-\overline{uv}_{MAX})^{1/2}(-\overline{uv})) \tag{4.8.10}$$

and

$$L_\tau = (-\overline{uv})^{3/2}/\varepsilon \quad , \tag{4.9.11}$$

permitting the thin-shear-layer turbulent kinetic energy transport equation to be transformed into a thin-shear-layer shear-stress transport equation. $-\overline{uv}_{MAX}$ is the maximum shear stress in the region $0.25 \lesssim y/\delta_{995} \lesssim 1$, and a_1 is taken to be constant at 0.15. In the previous section $L_\tau(y/\delta_{995})$ was found not to be significantly affected by free-stream turbulence. This being so, free-stream turbulence effects are confined to effects on a_1 and G. Measurements of $-\overline{uv}/\overline{q^2}$ have already been presented in figure 4.10 and discussed in subsection 4.4.1. The diffusion function, G, has been approximated as

$$G' = \frac{3}{4}\overline{v(u^2 + v^2)}/((-\overline{uv}_{MAX})^{1/2}(-\overline{uv})) \quad . \tag{4.8.12}$$

In the absence of free-stream turbulence the empirical result that the entrainment velocity $V_E \approx 10U_e(-\overline{uv}_{MAX}/U_e^2)^{1.0}$ implies that

$G \propto (-\overline{uv}_{MAX})^{0.5}/U_e$. Figure 4.43 shows the separate free-stream intensity and length-scale effects on $G'/(-\overline{uv}_{MAX}/U_e^2)^{0.5}$. At $(u'/U_e) \approx 0.025$ the diffusion function is quite different for the two values of L_e^u/δ_{995}. At the larger value of L_e^u/δ_{995} in figure 4.43b the interaction is fairly weak and the diffusion function is not very different from that which exists in the absence of free-stream turbulence. At the smaller value of L_e^u/δ_{995} in figure 4.43b the diffusion function profile has established a shape that persists at higher free-stream intensity; the diffusion function increases rapidly near the wall and then outside $y/\delta_{995} \approx 0.4$ remains level. Credible errors in the measurement of $-\overline{uv}$ would explain, at least in part, the scatter of the diffusion function near the boundary layer edge, most evident in figure 4.43d. The level of the diffusion function outside $y/\delta_{995} \approx 0.4$ decreases slowly with increasing free-stream intensity. Figure 4.43e shows profiles of $G'/(-\overline{uv}_{MAX}/U_e^2)^{0.5}$ at the six consecutive stations (15.2 cm grid, X_{LE} = 2.06 m).

4.9 CONCLUSION TO THE CHAPTER

Despite what was believed to be fairly careful attention to experimental detail the accuracy of the present set of measurements is not entirely satisfactory. In particular, the shear stress, $-\overline{uv}$, is roughly 16% too small when compared with the mean flow skin-friction measurements and $\overline{w^3}$ is embarrassingly large near the wall. Nevertheless, in the absence of free-stream turbulence, the ratios of turbulence quantities (except those involving $\overline{w^3}$) agree satisfactorily with those of other workers. Overall, the present measurements otherwise show themselves to be self-consistent. Furthermore, the discrepancies are unlikely to be serious when the effects of free-stream turbulence are considered comparatively.

The effect of free-stream turbulence on the turbulence structure, as inferred from the conventionally-averaged Reynolds

stresses, is greatest in the outer layer. In the inner layer the effect is manifested as "inactive" motion; the inactive contributions to $\overline{u^2}/u_\tau^2$ and $\overline{w^2}/u_\tau^2$ are roughly 0.3 $\overline{u_e^2}/u_\tau^2$ for the present cases (figure 4.9). The apparently weak dependence on length scale ratio in the inner layer is consistent with the inactive motion driven by the free-stream turbulence tending to cancel the length-scale effect seen in the outer layer. The effect of the presence of the wall on the free-stream turbulence is clearly evident in the profiles of $\overline{v^2}$, and much of the dependence of the boundary layer on the length scale ratio, L_e/δ, can be qualitatively reconciled with the dependence of $\overline{v^2}$ on the free-stream length scale, L_e. The shear-stress profile edge δ_{05} does not move very far from the mean velocity profile edge δ_{995} (with one exception where δ_{995} is of poor accuracy anyway). Near the boundary layer edge the shear stress measurements are consistent with those inferred from mean flow measurements through $-\overline{uv} = V_E(U_E - U)$, where V_E, the entrainment velocity, is given by equation 4.4.2.

Illumination of a smoke-filled boundary layer by a thin (perpendicular) plane of light (figure 4.14) shows the turbulent/turbulent interface to be much more highly contorted, with wisps of smoke extending well outside the mean-velocity profile edge. The "rolling motion", clearly evident for a turbulent/non-turbulent interface, is still discernible within the boundary layer proper. The wispy motion is randomly orientated with respect to the stream direction, a fact further supported by measurement.

Visual observations of the interface are supported quantitatively by the temperature-intermittency measurements of a passively-heated boundary layer. The intermittency-factor profile is broadened by free-stream turbulence, the average burst frequency profile is increased in magnitude and breadth, and the average hot-burst length is considerably reduced inside $y \approx \delta_{995}$. Compared with,

say δ_{05}, the length scale of the boundary layer eddy motion as inferred from the average position of the interface, $\overline{y}$, varies with free-stream intensity and length scale ratio, L_e^u/δ_{05} say, but not by a large amount (figure 4.17); both δ_{05} and δ_{995} remain pertinent scales of the boundary layer turbulence proper. It is suggested that the effect of free-stream turbulence in maintaining a highly contorted interface at low Reynolds numbers, as shown by figure 4.14, tends to reduce low-Reynolds-number effects, and is responsible for the low-Reynolds-number dependence of C_f/C_{fo} discussed in chapter 3.

Conditionally-averaged Reynolds stress measurements show the cold-zone shear stress, $-(1 - \gamma)\overline{uv}_C$, (figure 4.21) to be significantly non-zero only within the boundary layer. There, $-(1 - \gamma)\overline{uv}_C$ increases with free-stream intensity but, over the present range of measurements, decreases with decreasing length scale ratio. The latter behaviour is roughly commensurate with the reduction of $\partial U/\partial y$ that also occurs in so far as the production of turbulent kinetic energy is also reduced. The wispy motion of the turbulent/turbulent interface outside the boundary layer edge, δ_{995} say, contains very little shear stress. Also, it is tentatively suggested that the wispy motion inside the boundary layer may not contain much more shear stress than the cold-zone. An almost certainly genuine and interesting incidental result is that in the absence of free-stream turbulence the ratios $-\overline{uv}_C/\overline{q_C^2}$ and $-\overline{uv}_C/\sqrt{(\overline{u_C^2}.\overline{v_C^2})}$ (figure 4.23) are considerably larger than normally measured for turbulent motion for a substantial part of the boundary layer. Furthermore, these ratios decrease only slowly as the free-stream intensity is increased. Similarly large ratios can be deduced from the measurements of Hedley & Keffer (1974) and Charnay (1974) once their use of conditionally-averaged base lines has been removed. The cold-zone flatness factors $F_{u,C}$ and $F_{v,C}$ (figures 4.35 and 4.36) exhibit particularly low values in the part of the boundary

layer where $-\overline{uv}_C/\overline{q_C^2}$ and $-uv_C/\sqrt{(\overline{u_C^2}.\overline{v_C^2})}$ are large, quite likely for the same reason. $-\overline{uv}_H/\overline{q_H^2}$ and $-\overline{uv}_H/\sqrt{(\overline{u_H^2}.\overline{v_H^2})}$ are affected by free-stream turbulence but not as much as $-\overline{uv}/\overline{q^2}$ and $-\overline{uv}/\sqrt{(\overline{u^2}.\overline{v^2})}$.

The profiles of the hot-zone contributions to the various double and triple products overlap the edge of the boundary layer by differing amounts; the order of increasing overlap is

$$\gamma\overline{uv}_H \ , \ \gamma\overline{u_H^3} \ , \ \gamma\overline{uv_H^2} \ , \ \gamma\overline{u_H^2} \ , \ \gamma\overline{u^2v}_H \ , \ \gamma\overline{v_H^2} \ , \ \gamma\overline{v_H^3}$$

$$\gamma\overline{w_H^2}$$

Except for $\overline{u^2}$ †, this is the same order as for merging boundary layers in a two-dimensional duct (Dean & Bradshaw, 1976), for which the overlap of $\overline{u^2}$ is larger than that of $\overline{v^3}$. The turbulent shear stress and turbulent kinetic energy hot-zone transport velocities $V_{\tau,H}$ and $V_{q,H}$ are affected by free-stream turbulence (figure 4.29) but not as much as V_τ and V_q (figure 4.13). A certain amount of structural similarity exists within the hot-zone in that, within the scatter, the ratio $V_{\tau,H}/V_{q,H}$ is at most only weakly dependent upon the interaction (figure 4.30). $V_{\tau,C}$ and $V_{q,C}$ (figure 4.32) are also affected by free-stream turbulence, but this is to be expected if only because there is no reason to suppose that transport velocities for irrotational fluctuations (i.e. the cold-zone fluctuations in the absence of free-stream turbulence) should be the same as those for rotational fluctuations (i.e. external turbulence). Near the wall $V_{\tau,C}$ and $V_{q,C}$ - which are substantially different from $V_{\tau,H}$ and $V_{q,H}$, implying that any errors in discrimination are not overwhelmingly large even though γ is close to unity - appear to scale fairly well on u_τ when free-stream turbulence is present. Near the boundary layer edge $V_{\tau,C}$ and $V_{q,C}$ vary roughly as $\sqrt{(\overline{v^2})}$.

---

†See footnote on page 235.

Balances of the turbulent kinetic energy and turbulent shear-stress transport equations are presented for three cases including one no-grid case (figures 4.37 and 4.38). The advection changes sign in at least the outer-most part of the layer, and increased 'inactive' motion is evident by a small rise (gain) near the wall. Loss by diffusion in the inner layer is also increased and the gain in the outer part of the layer extends over a larger range of y/δ. Production in the outer layer is reduced. The dissipation length scale base on $-\overline{uv}$ (equation 4.7.3) is apparently insensitive to free-stream turbulence while the dissipation length scale based on $\overline{q^2}$ behaves rather oddly (figures 4.39 and 4.40). However, complete insensitivity of L_τ near the boundary layer edge is difficult to believe.

Since the interaction as inferred from the conditionally-sampled turbulence measurements is generally not weak separate transport equations cannot be written for the hot and cold zones without including some sort of transfer term in each. This complexity is not considered in detail in this thesis; only the transport equations for the conventionally-averaged Reynolds stresses are discussed. Brief consideration is given to the calculation methods of Bradshaw et al. (1967). Although the stress ratio $-\overline{uv}/\overline{q^2}$ (figure 4.10) and the diffusion function G (approximated by equation 4.9.9 and given in figure 4.43) are fairly complicated functions of u'_e/u_τ and L_e/δ and will probably need careful treatment they are reasonably well behaved.

GRID	$X_{LE(m)}$	STATION	$x_{(m)}$	Re_θ	$(u'/U)_e$	L^u_e/δ_{995}	$\Delta C_f/C_{f_o}$	DIGITIZED MEASUREMENTS	x-WIRE PROBE	ANALOGUE MEASUREMENTS	PROFILE NUMBER
NONE	0.30	6	.91	2870	≈0.0003	-	-	u, v, θ; u, w, θ	E	U, $\overline{T}$	39
		14	2.13	4680	≈0.0003	-	-	u, v, θ; u, w, θ	E	U, $\overline{T}$	40
7.6cm	2.06	6	.91	2980	0.0240	1.88	0.078	u, v, θ; u, w, θ	C	u, U, $\overline{T}$	33
15.2cm	2.06	6	.91	3030	0.0468	2.72	0.146	u, v, θ; u, w, θ	A	u, U, $\overline{T}$	27
		8	1.22	3750	0.0442	2.23	0.151	u, v, θ; u, w, θ	B	u, U, $\overline{T}$	28
		10	1.52	4320	0.0410	1.90	0.136	u, v, θ; u, w, θ	B	u, U, $\overline{T}$	29
		12	1.83	4790	0.0387	1.70	0.140	u, v, θ; u, w, θ	B	u, U, $\overline{T}$	30
		14	2.13	5240	0.0362	1.69	0.130	u, v, θ; u, w, θ	B	u, U, $\overline{T}$	31
		16	2.44	5850	0.0345	1.55	0.128	u, v, θ; u, w, θ	C	u, U, $\overline{T}$	32
7.6cm	0.30	8	1.22	3710	0.0399	0.71	0.203	u, v, θ; u, w, θ	D	U, $\overline{T}$	35
		16	2.44	5760	0.0255	0.67	0.148	u, v, θ	D	U, $\overline{T}$	36
15.2cm	1.37	6	.91	3100	0.0575	1.83	0.209	u, v, θ; u, w, θ	D,E	u, U, $\overline{T}$	37
15.2cm	0.76	10	1.52	3860	0.0575	1.34	0.237	u, v, θ; u, w, θ	E	U, $\overline{T}$	38

TABLE 4.1 Directory of Turbulence Measurements, Mean Flow and Free-Stream Turbulence Parameters.

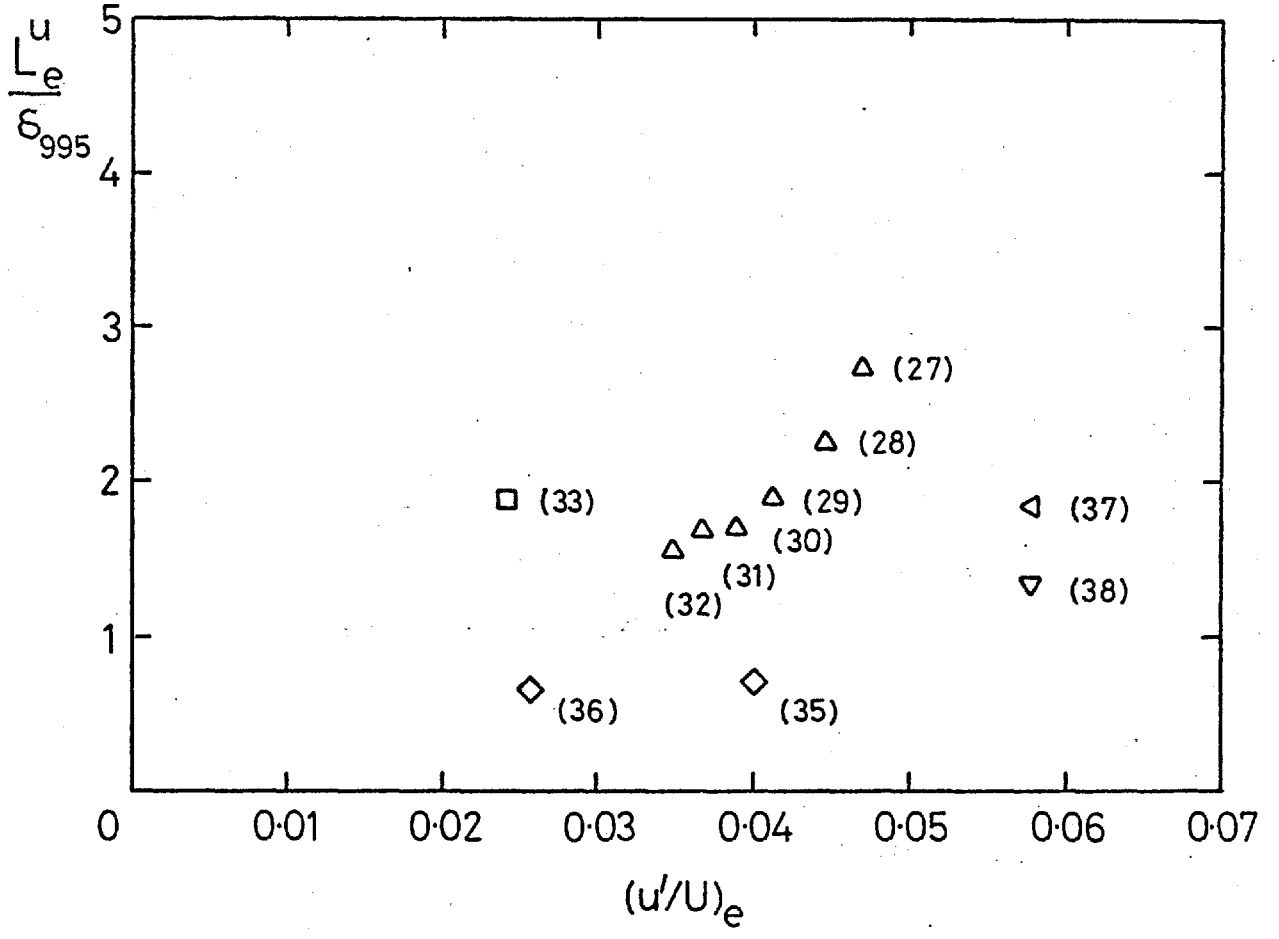

Fig. 4.1 Free-stream intensity, $(u'/U)_e$, and length scale ratio, L^u_e/δ_{995}, for the boundary layer turbulence measurements. Numbers in brackets are profile numbers listed in table 4.1 (and also table 3.3).

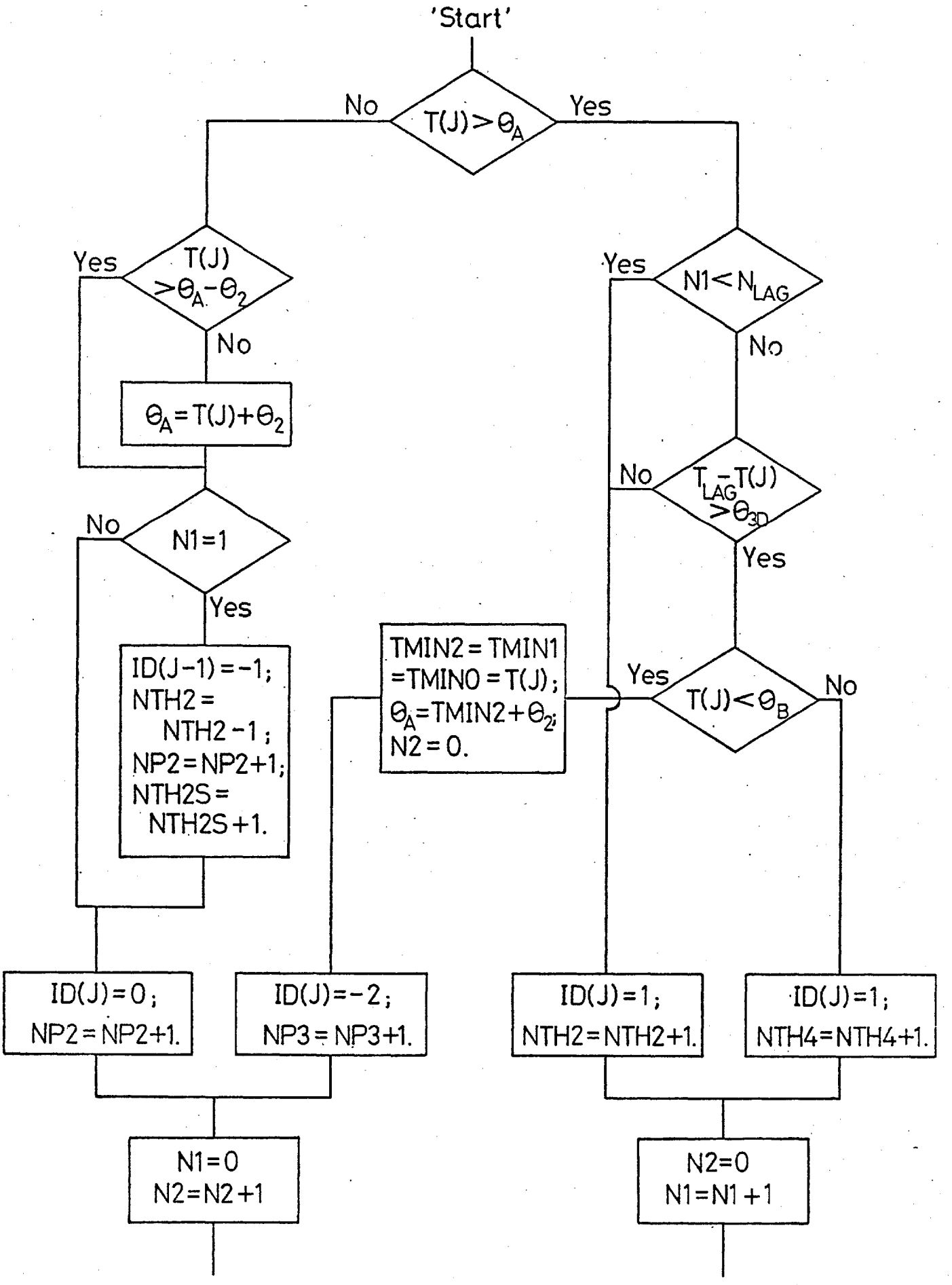

a) Flow diagram (continued on next page)

Fig. 4.2 Flow diagram for intermittency algorithm LAGTHR.

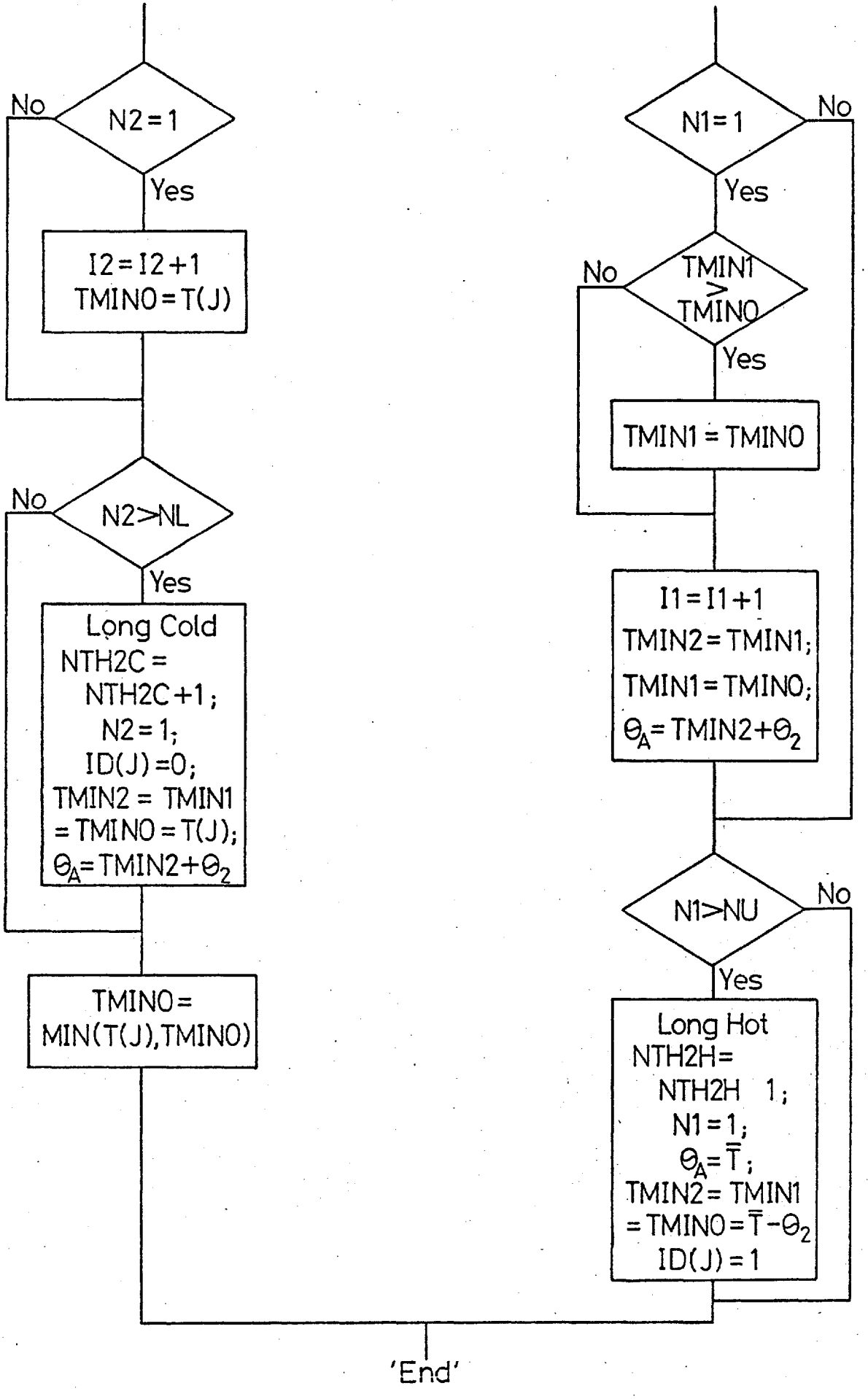

Fig. 4.2 a) cont'd.

FLOW DIAGRAM	APPENDIX 6	VARIABLE FUNCTION
Θ_2	TH2	†Temperature level-threshold above cold level TMIN2
Θ_A	THA	Temperature level-threshold = Θ_2 + TMIN2
(Θ_4)	TH4	†Temperature level-threshold above cold level TBOT5
Θ_B		Temperature level-threshold of fall-to-cold slope test = Θ_4 + TBOT5
Θ_{3D}	TH3D	†Slope-check threshold temperature drop
N_{LAG}	NLAG	†Slope-check threshold time delay (NLAG $\lesssim$ 19)
T(J)	IZJ	Temperature of J^{th} point in current record
T_{LAG}	TLAG =	T(J-NLAG) Temperature of $(J-NLAG)^{th}$ point in current record
TMIN0	TMIN0	Minimum temperature of the current cold burst
TMIN1	TMIN1	Minimum temperature of the last cold burst
TMIN2	TMIN2	Minimum temperature of the last but one cold burst
ID(J)	ID(J)	Value of the intermittency function at the j^{th} point ID(J)=1 J^{th} point declared hot by level test or slope test ID(J)=0 J^{th} point declared cold by level test ID(J)=-2 J^{th} point declared cold by slope test ID(J-1)=-1 previous point declared cold by single-hot-point rejection test
N1	N1	Number of points in current hot burst
N2	N2	Number of points in current cold burst
I1	I1	Total number of hot points
I2	I2	Total number of cold points

Fig. 4.2b) Algorithm variables

FLOW DIAGRAM	APPENDIX 6	VARIABLE FUNCTION
NTH2	NTH2	Total number of points declared hot by level test alone
NTH4	NTH4	Total number of points declared hot by slope test
NP2	NP2	Total number of points declared cold by level test alone
NP3	NP3	Total number of points declared cold by slope test
NU	NU	†Maximum permitted number of points in any single hot burst
NL	NL	†Maximum permitted number of points in any single cold burst
NTH2H	NTH2H	Number of long hot bursts
NTH2C	NTH2C	Number of long cold bursts
NTH2S	NTH2S	Number of points declared cold by single hot point rejection test
	TBOT0	Minimum temperature of current record
	TBOT5	Minimum temperature of last NB5 records
NB5	NB5	†Number of previous records used for slope-test reference minimum temperature

†Input parameters

Fig. 4.2b) cont'd.

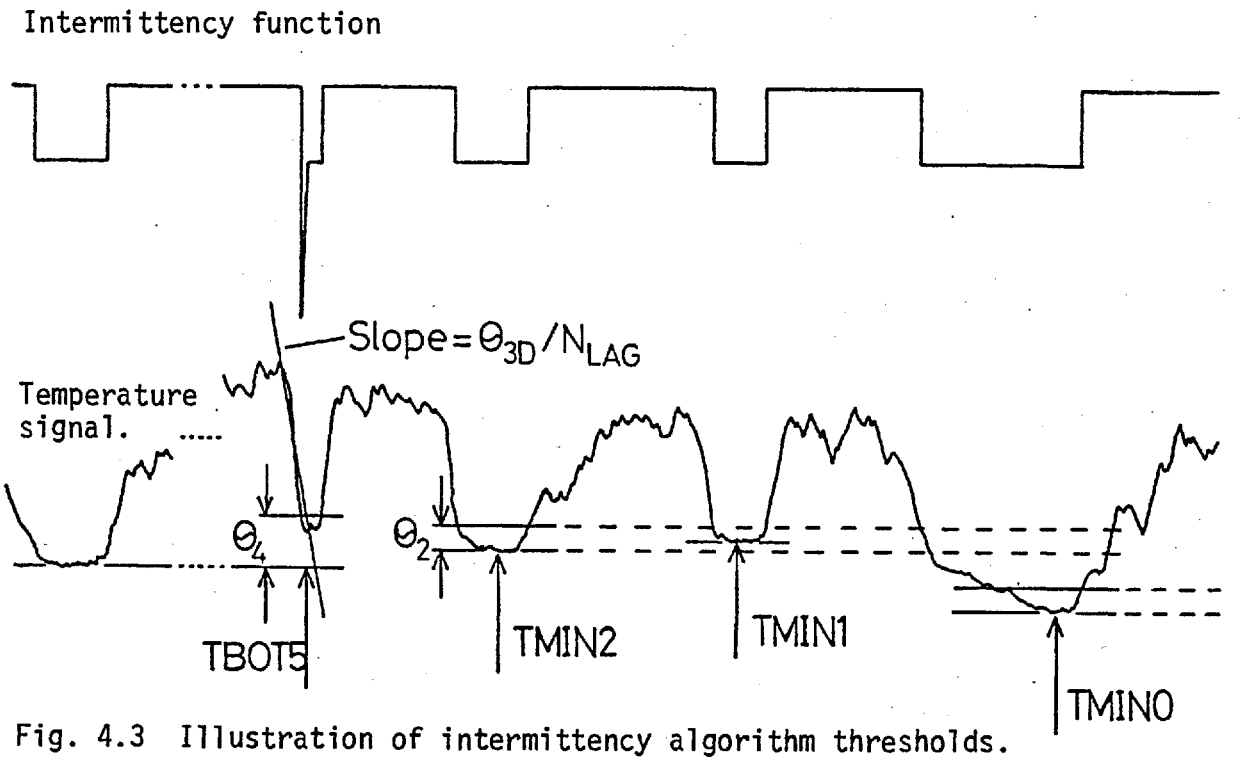

Fig. 4.3 Illustration of intermittency algorithm thresholds.

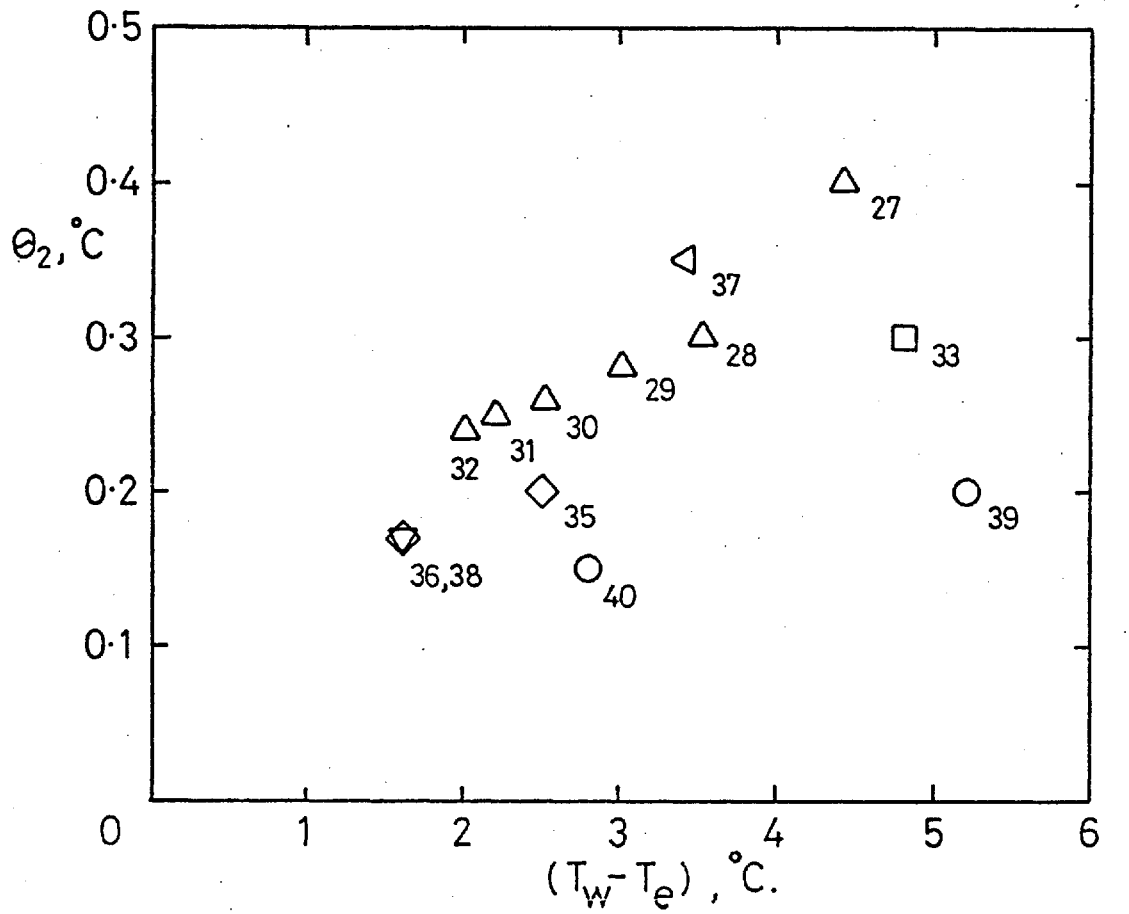

Fig. 4.4 Threshold θ_2 values. Profile numbers adjacent to symbols.

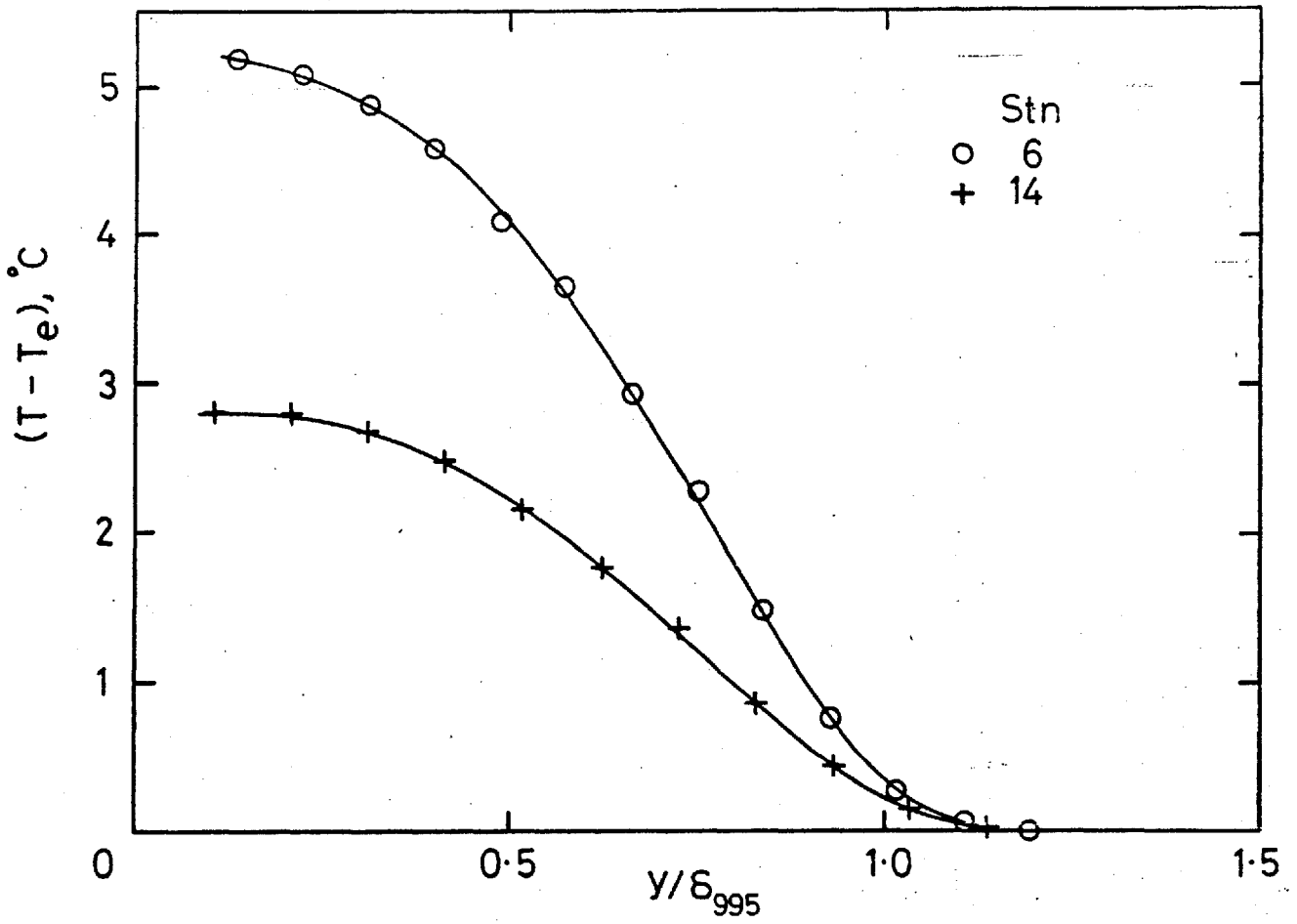

a) No grid

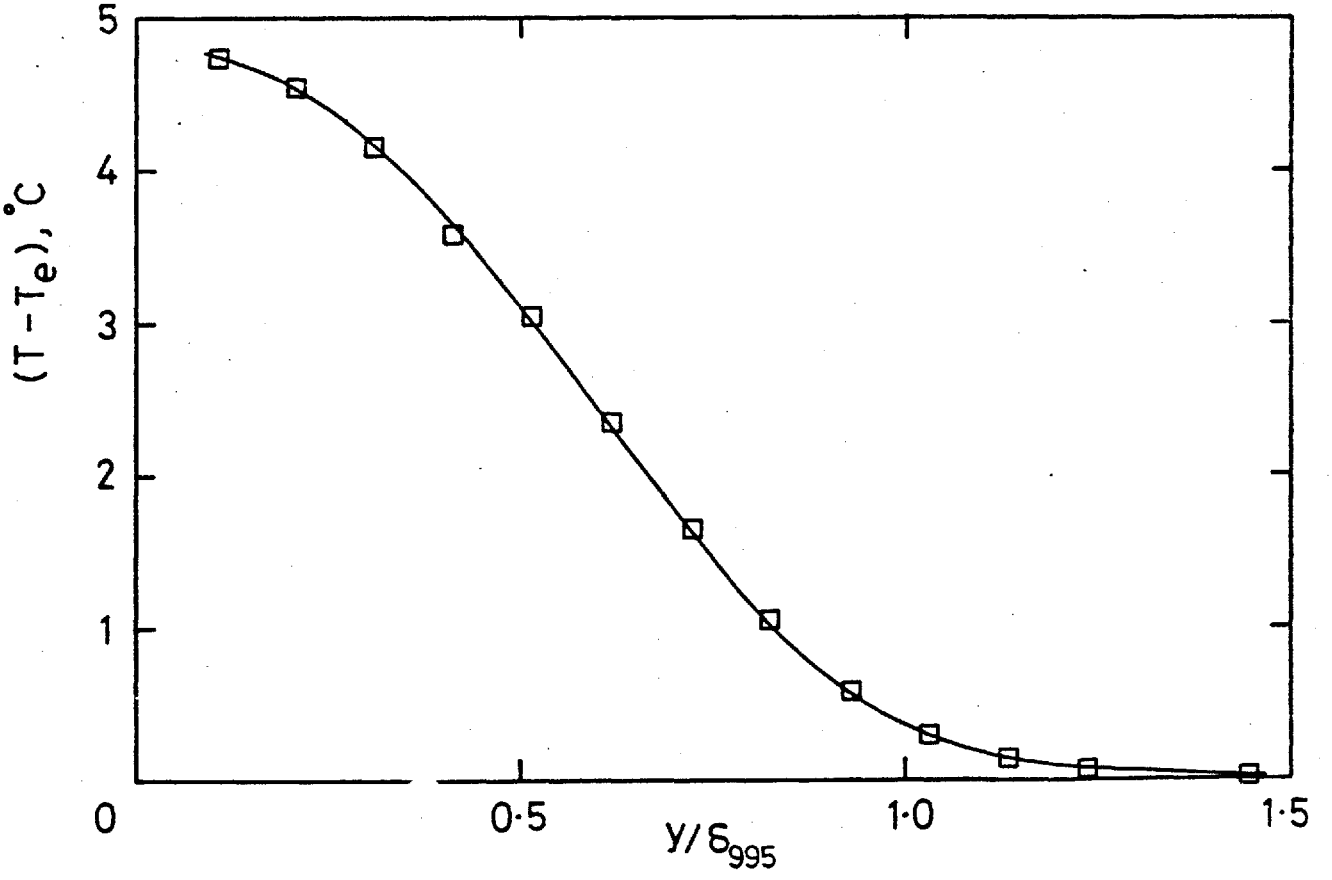

b) 7.6 cm grid, X_{LE} = 2.06 m, stn 6

Fig. 4.5 Mean temperature profiles:

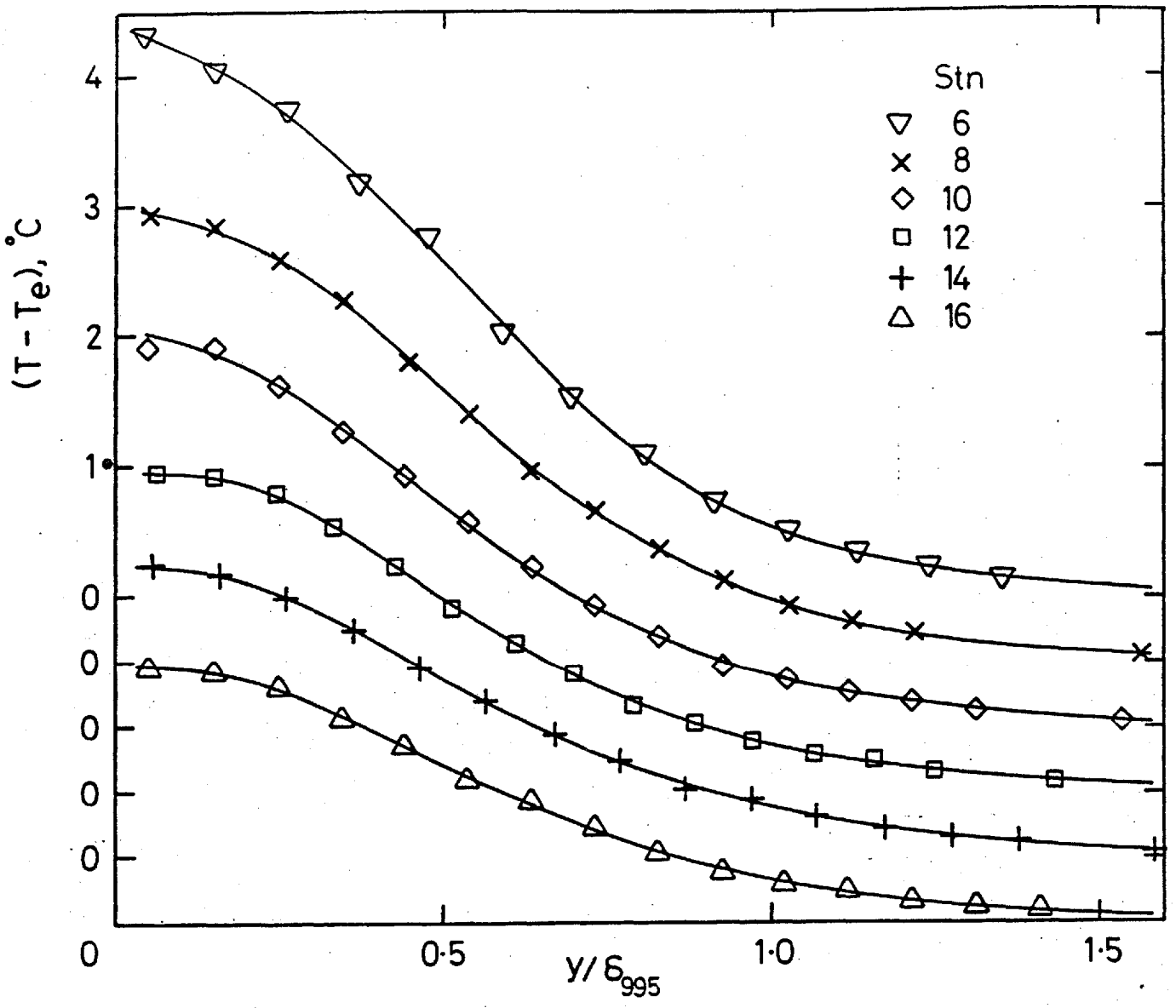

Fig. 4.5c, 15.2 cm grid, X_{LE} = 2.06 m, stns 6, 8, 10, 12, 14, 16

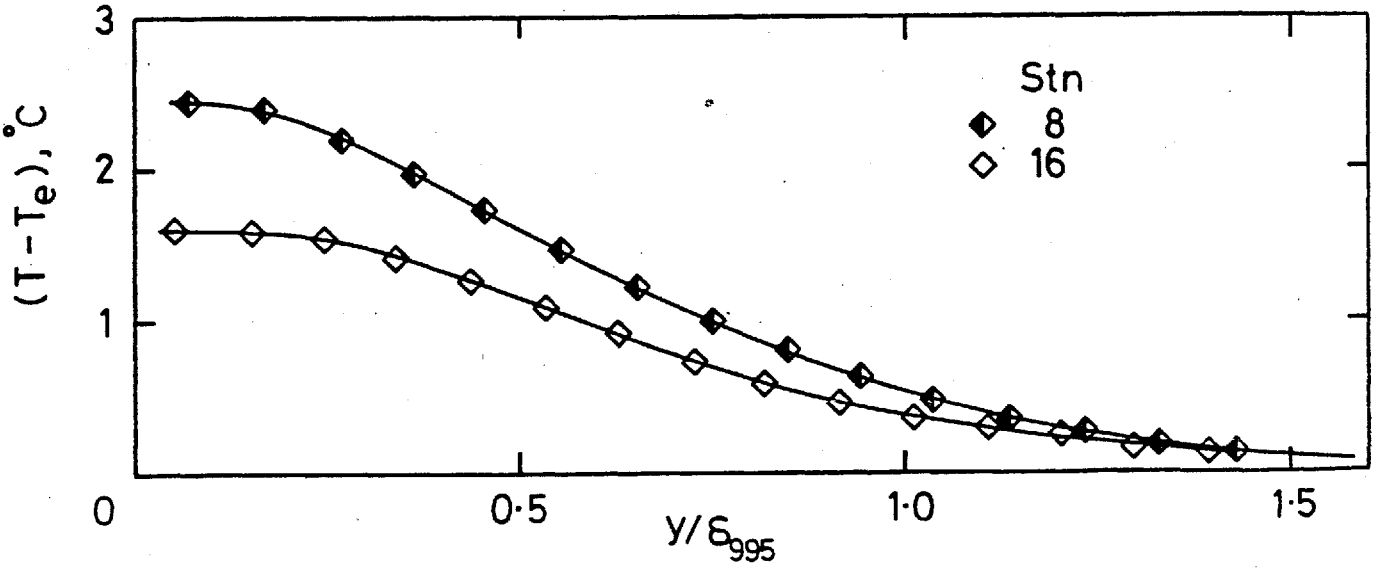

Fig. 4.5d, 7.6 cm grid, X_{LE} = 0.30 m, stns 8, 16

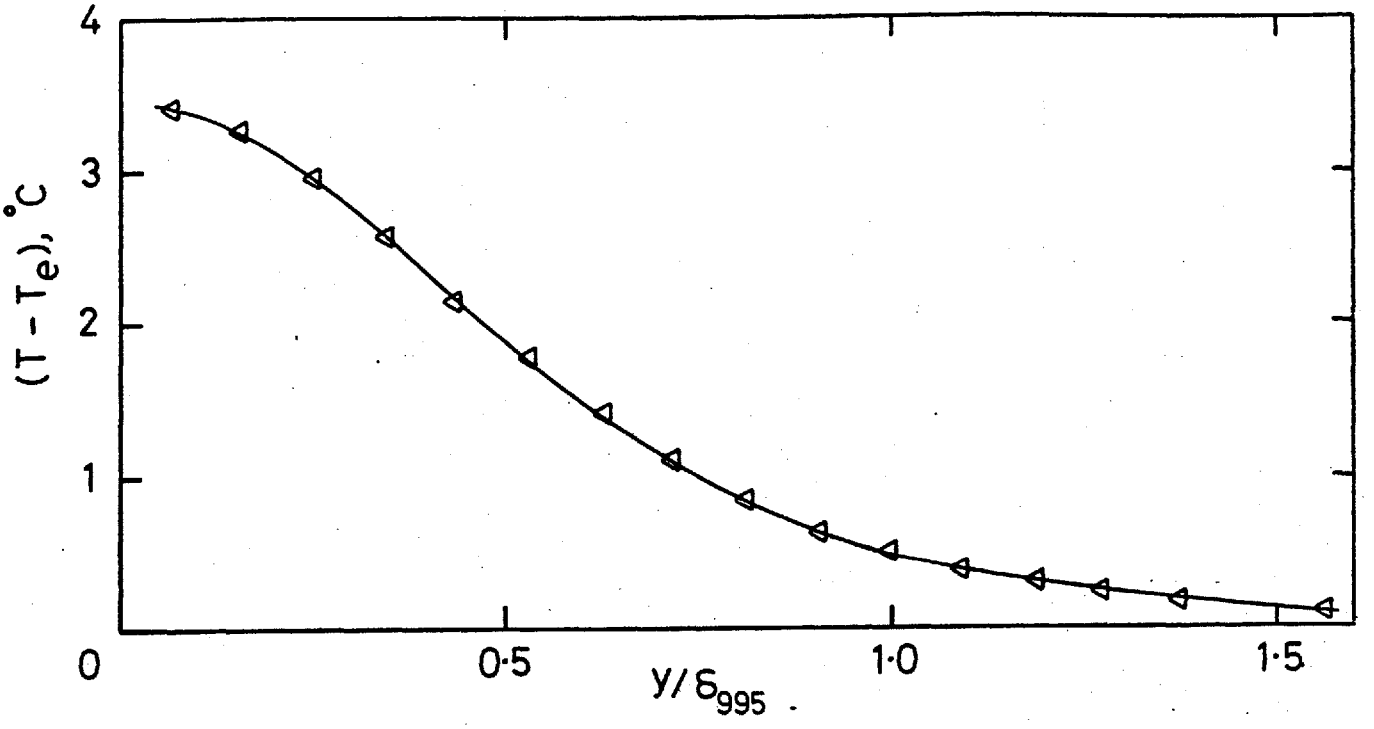

Fig. 4.5e, 15.2 cm grid, X_{LE} = 1.37 m, stn 6

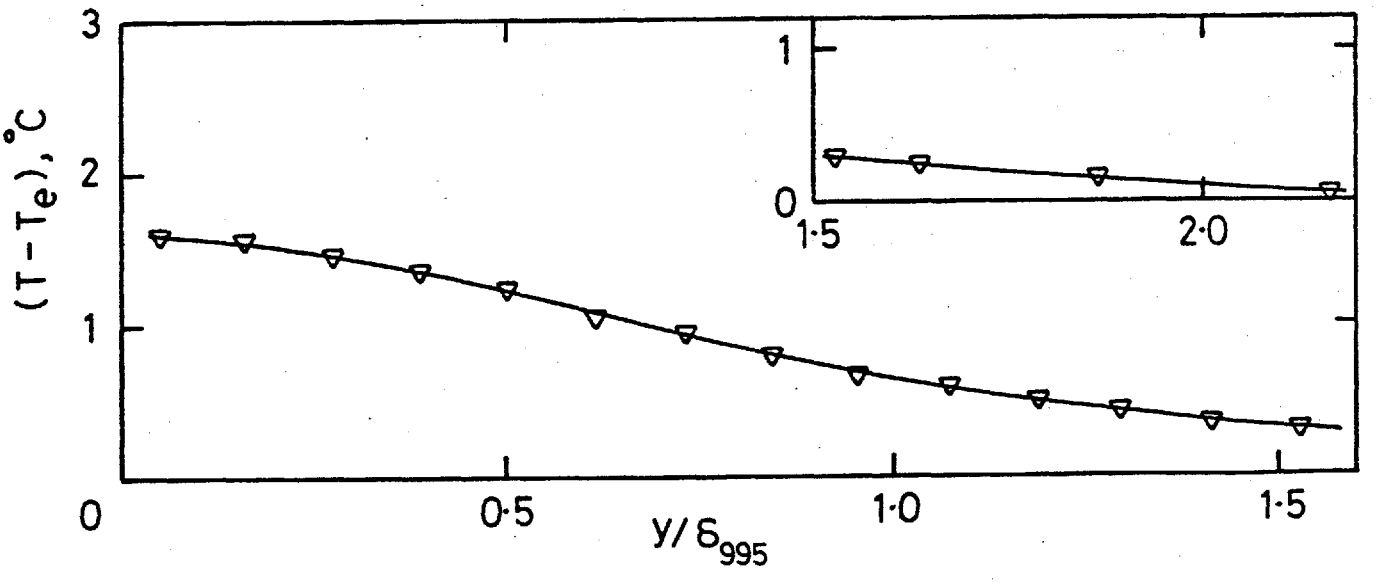

Fig. 4.5f, 15.2 cm grid, X_{LE} = 0.76 m, stn 10

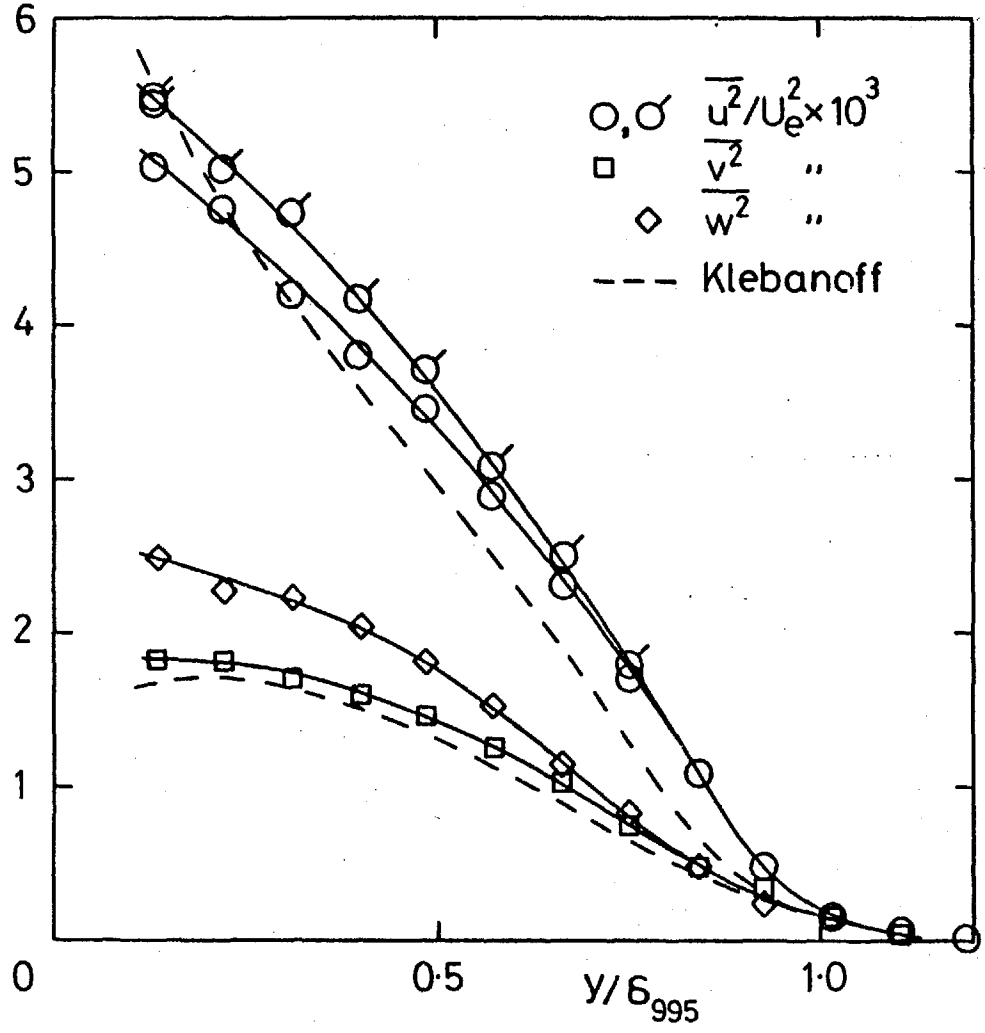

a) No grid, stn 6

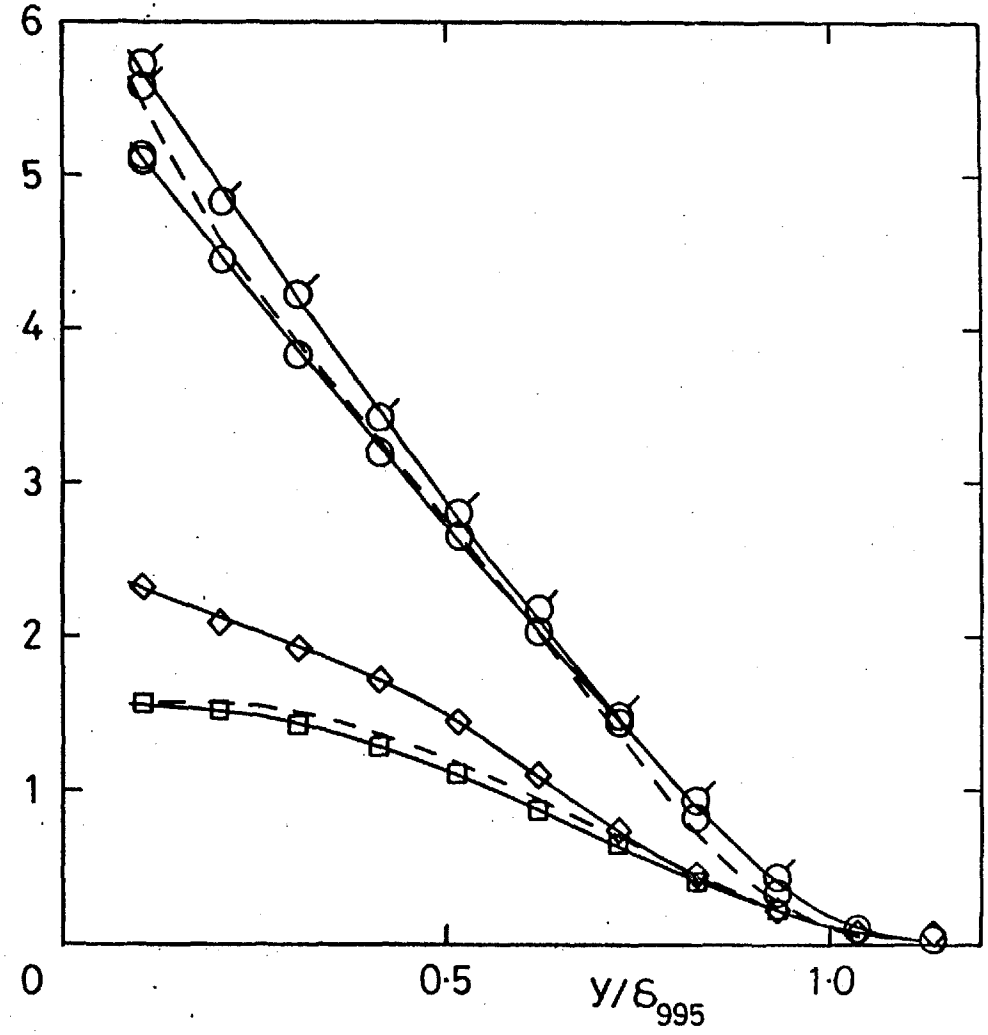

b) No grid, stn 14. Symbols as in a)

Fig. 4.6 Direct-stress profiles. (, $\phi = 0$; , $\phi = \pi/2$)

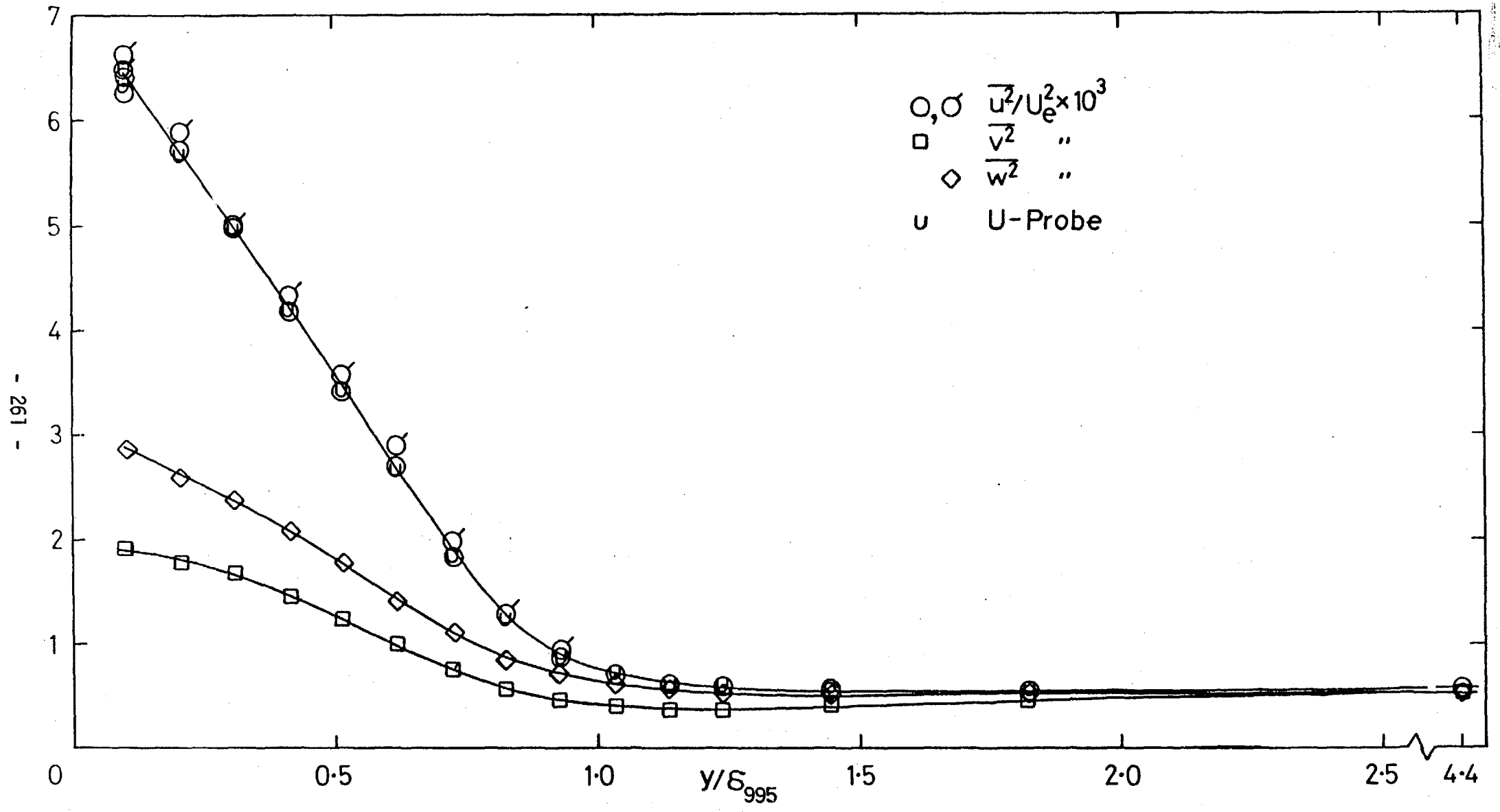

Fig. 4.6c, 7.6 cm grid, X_{LE} = 2.06 m, stn 6. $(u'/U)_e$ = 0.0240, L_e^u/δ_{995} = 1.88

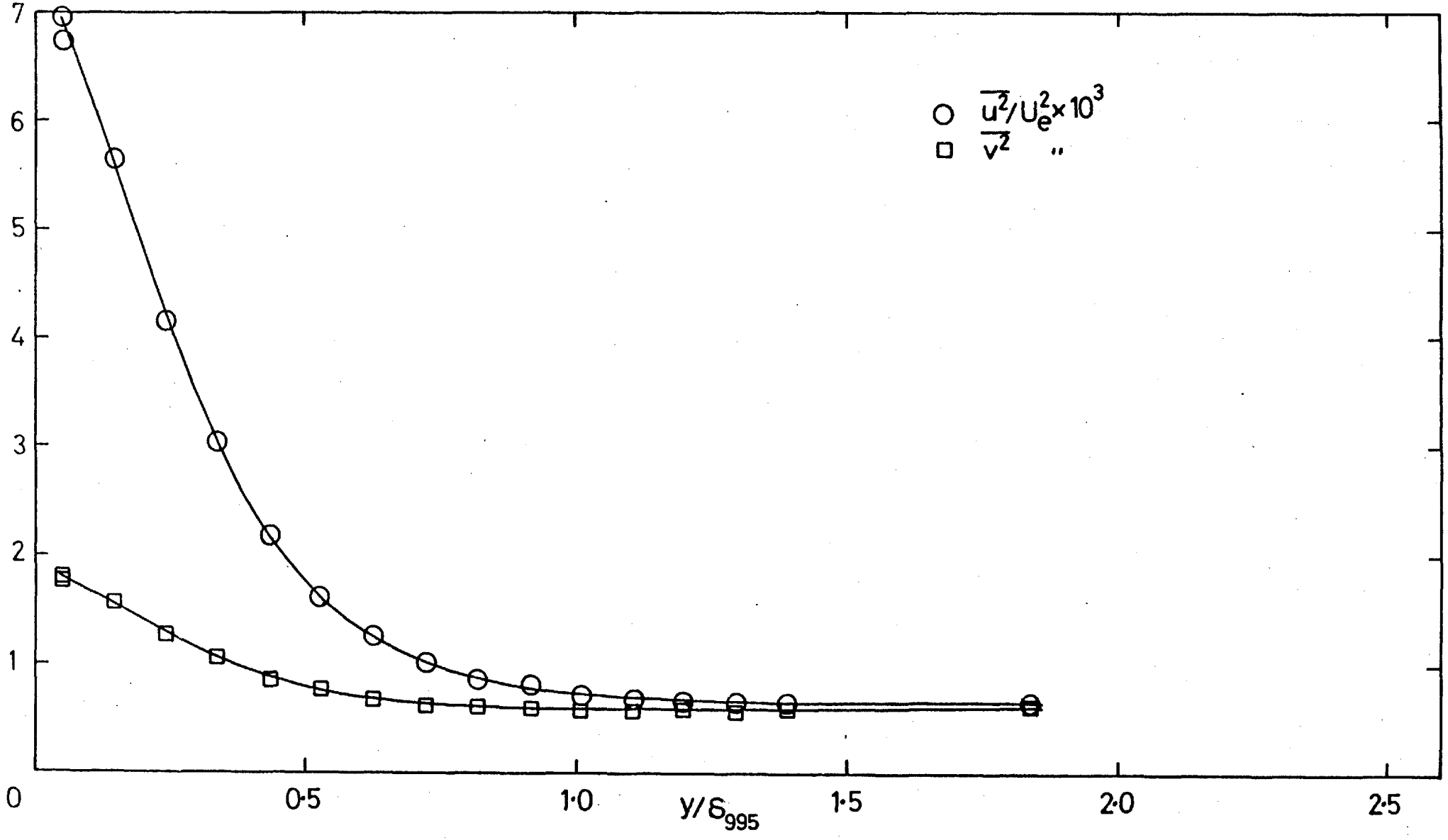

Fig. 4.6d, 7.6 cm grid, X_{LE} = 0.30 m, stn 16. $(u'/U)_e$ = 0.0255, L^u_e/δ_{995} = 0.67

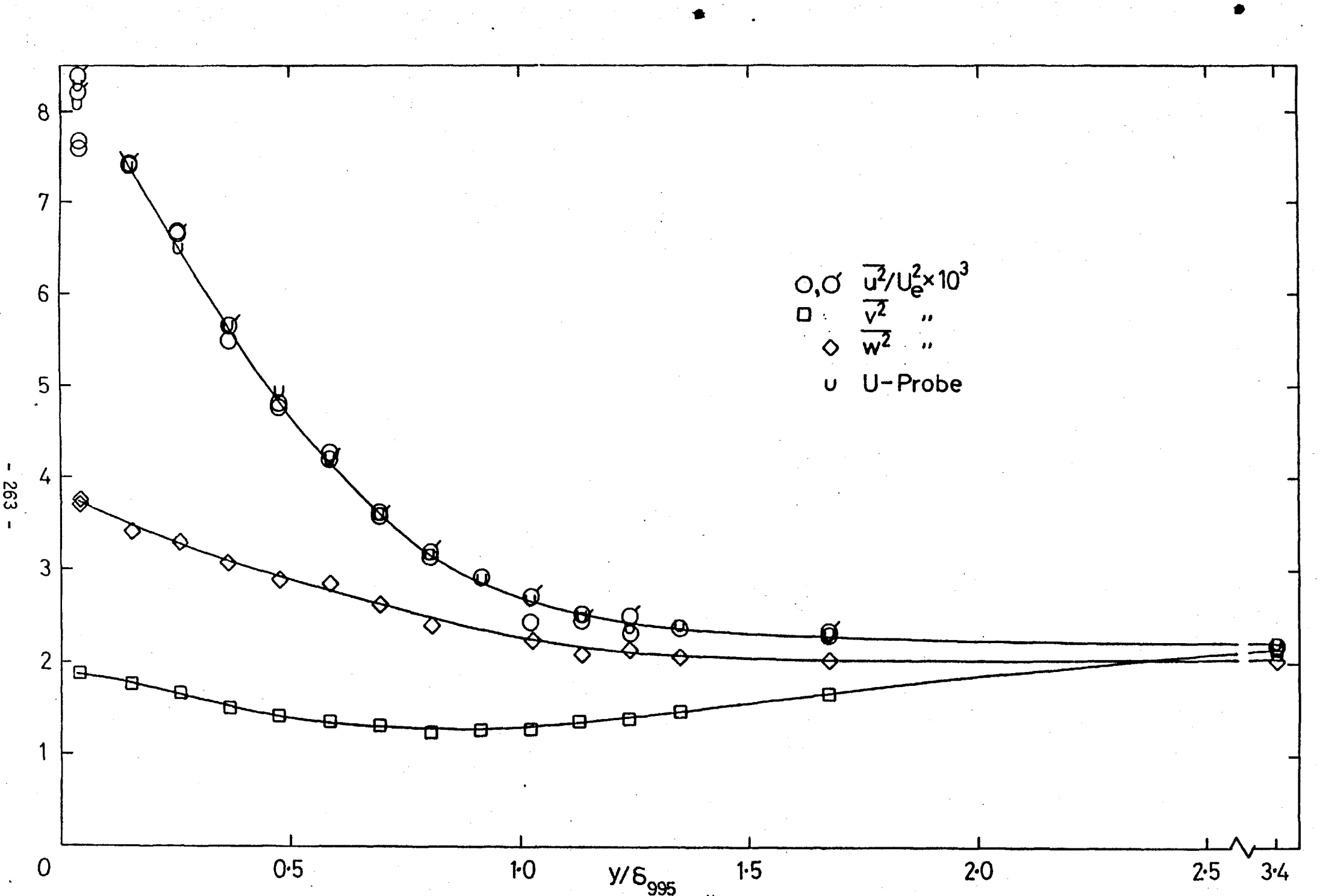

Fig. 4.6e, 15.2 cm grid, X_{LE} = 2.06 m, stn 6. $(u'/U)_e$ = 0.0468, L^u_e/δ_{995} = 2.72

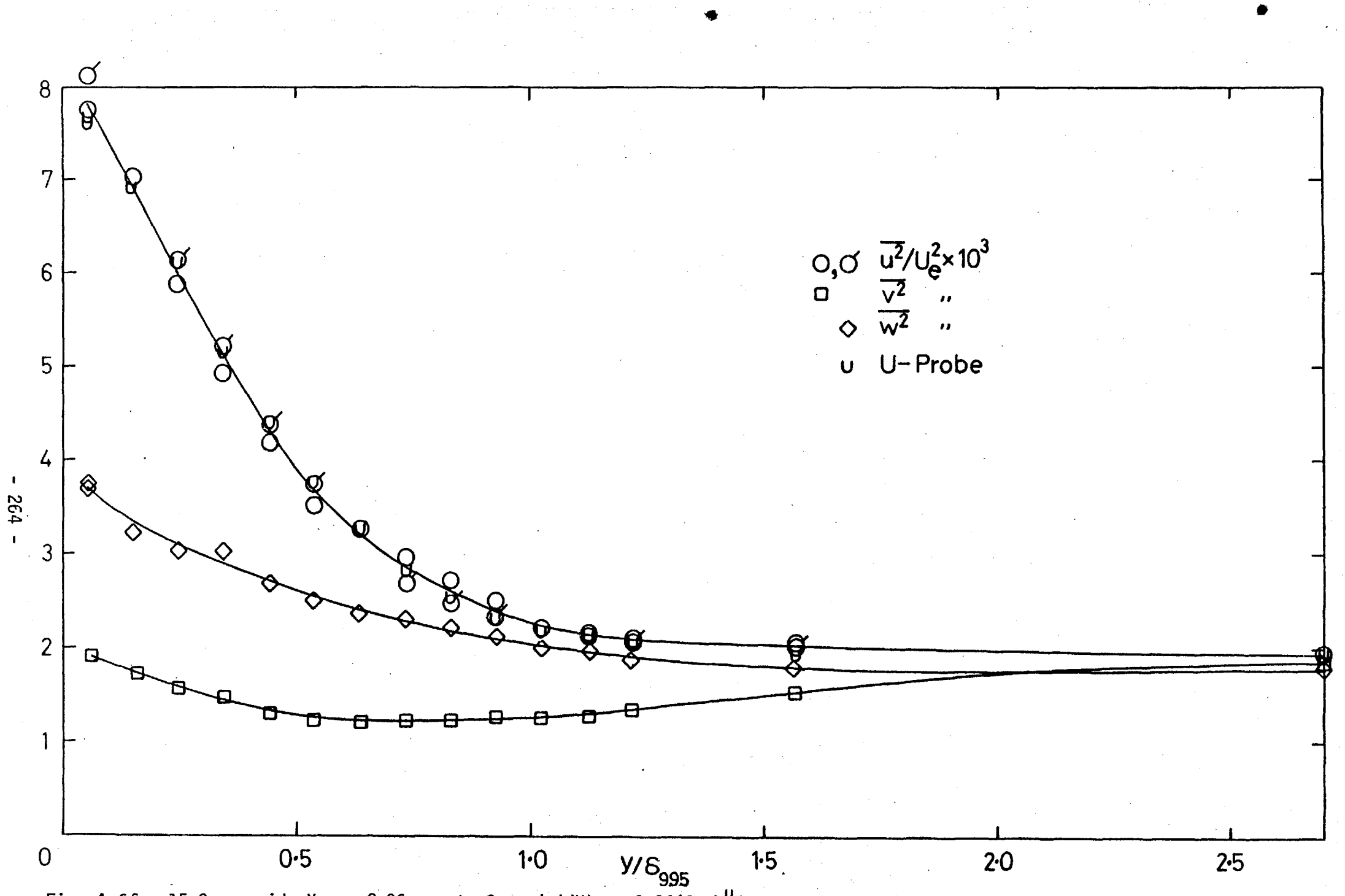

Fig. 4.6f, 15.2 cm grid, X_{LE} = 2.06 m, stn 8. $(u'/U)_e$ = 0.0442, L^u_e/δ_{995} = 2.23

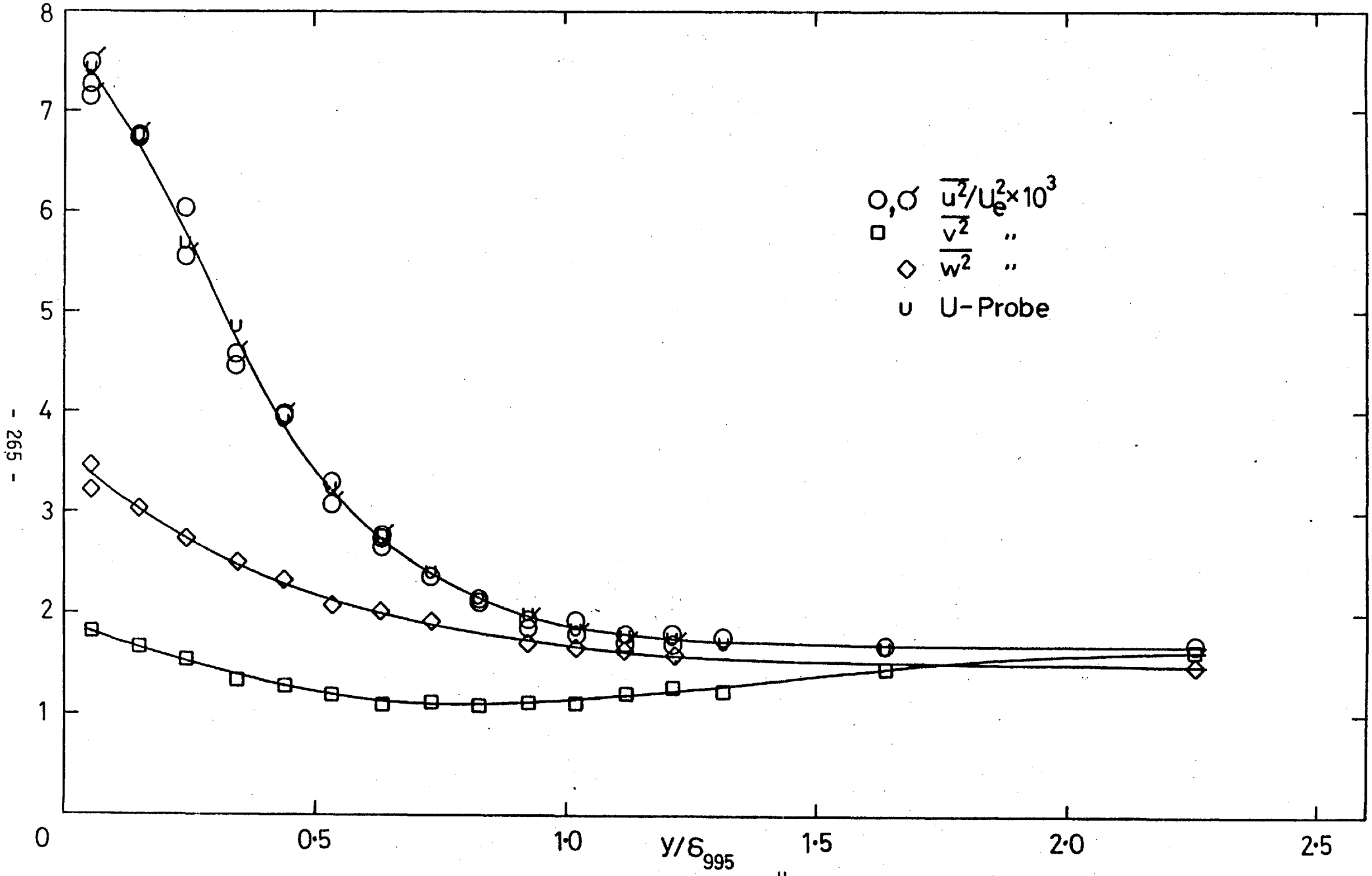

Fig. 4.6g, 15.2 cm grid, X_{LE} = 2.06 m, stn 10. $(u'/U)_e$ = 0.0410, L_e^u/δ_{995} = 1.90

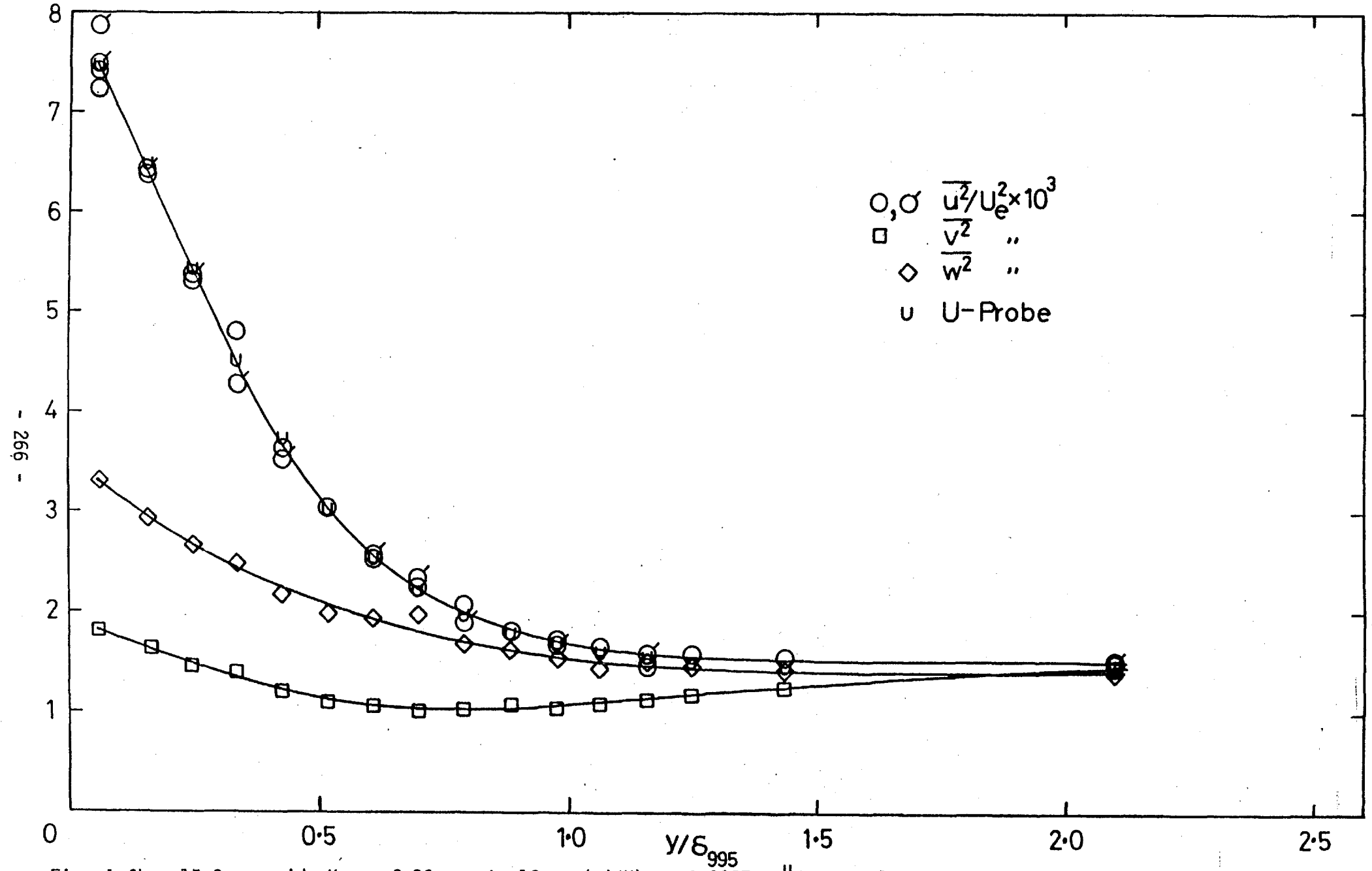

Fig. 4.6h, 15.2 cm grid, X_{LE} = 2.06 m, stn 12. $(u'/U)_e$ = 0.0387, L^u_e/δ_{995} = 1.70

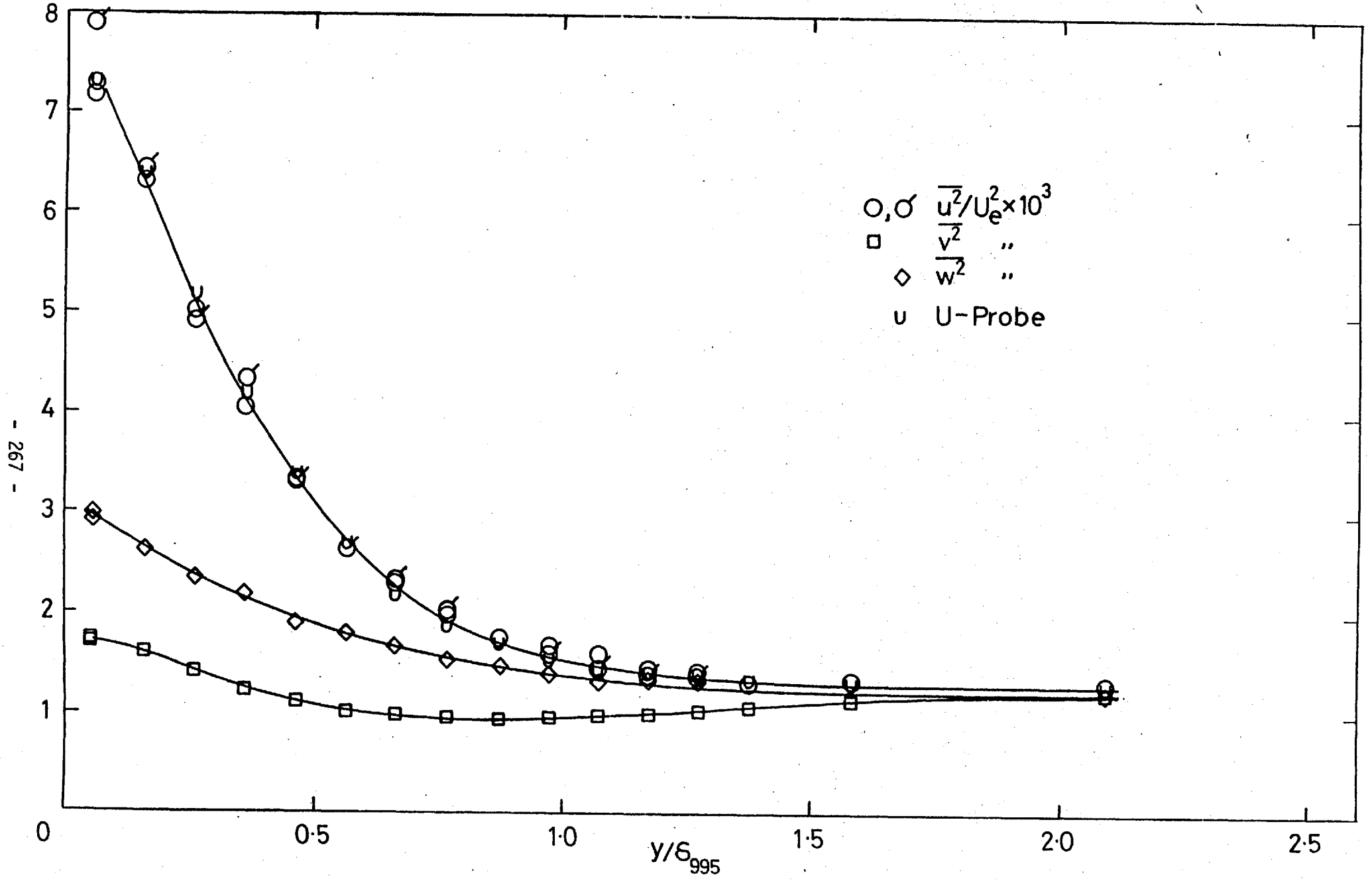

Fig. 4.6i, 15.2 cm grid, X_{LE} = 2.06 m, stn 14. $(u'/U)_e$ = 0.0362, L^u_e/δ_{995} = 1.69

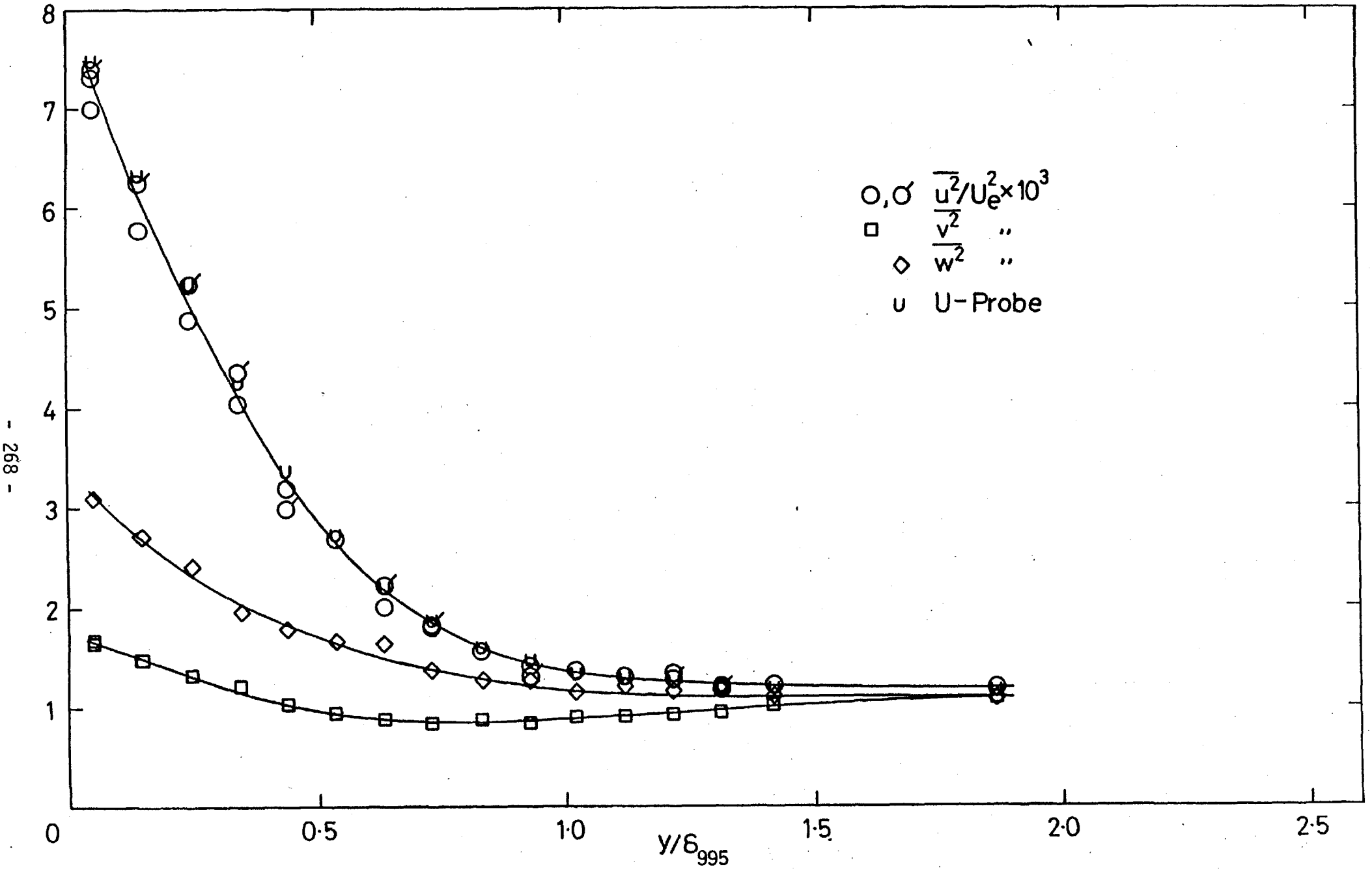

Fig. 4.6j, 15.2 cm grid, X_{LE} = 2.06 m, stn 16. $(u'/U)_e$ = 0.0345, L_e^u/δ_{995} = 1.55

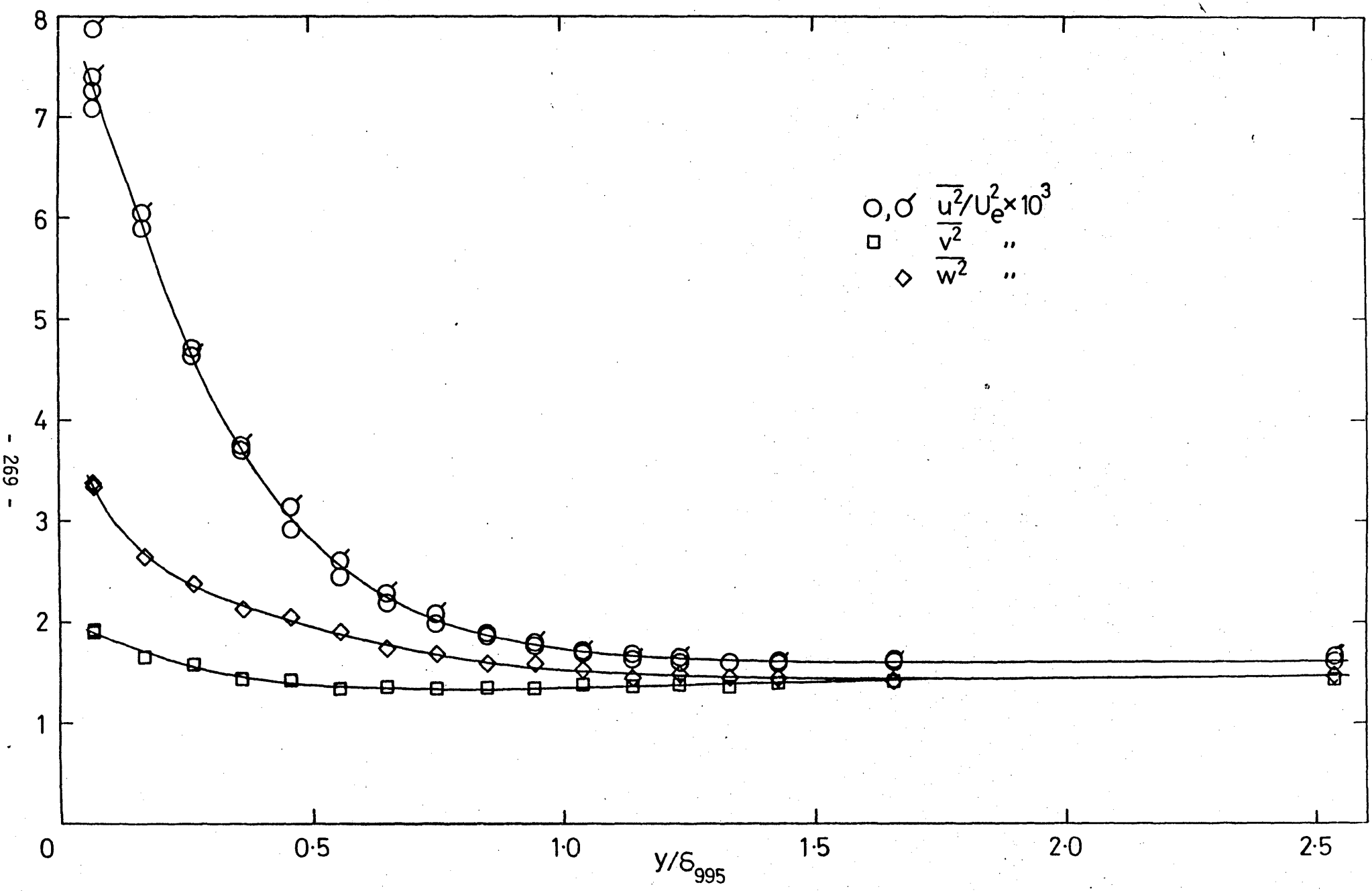

Fig. 4.6k, 7.6 cm grid, X_{LE} = 0.305 m, stn 8. $(u'/U)_e$ = 0.0399, L_e^u/δ_{995} = 0.71

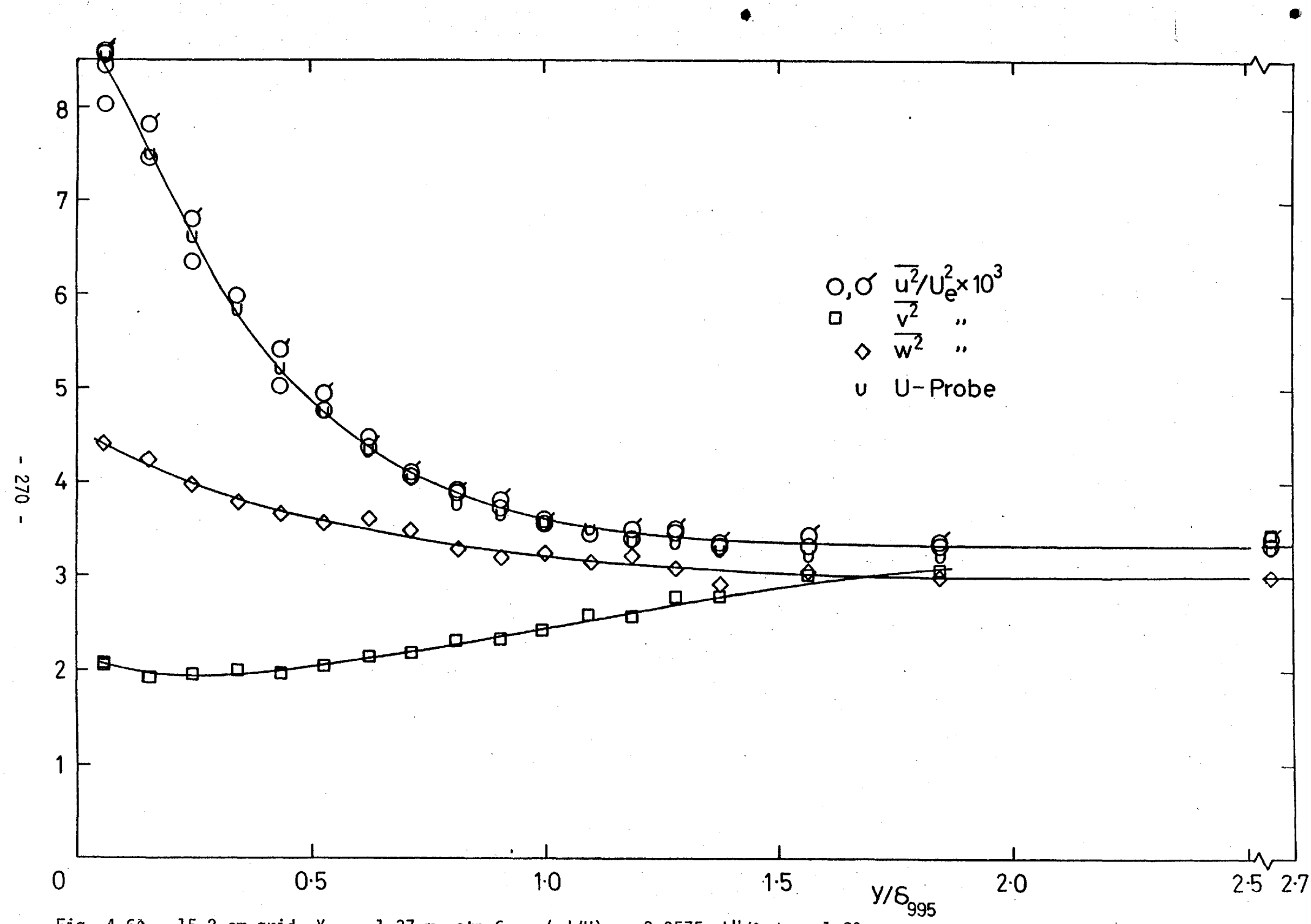

Fig. 4.6ℓ, 15.2 cm grid, X_{LE} = 1.37 m, stn 6. $(u'/U)_e$ = 0.0575, L^u_e/δ_{995} = 1.83

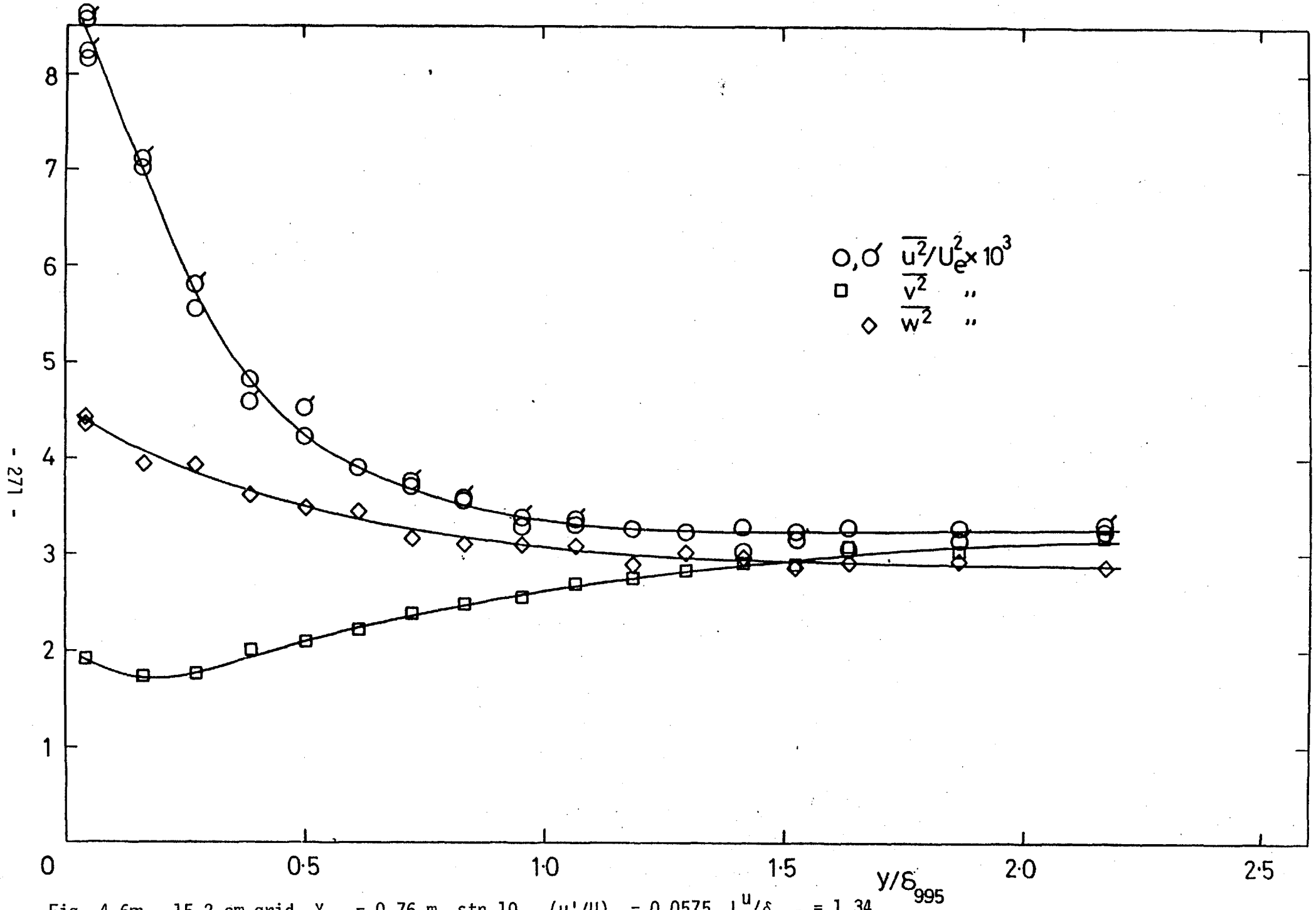

Fig. 4.6m, 15.2 cm grid, X_{LE} = 0.76 m, stn 10. $(u'/U)_e$ = 0.0575, L^u/δ_{995} = 1.34

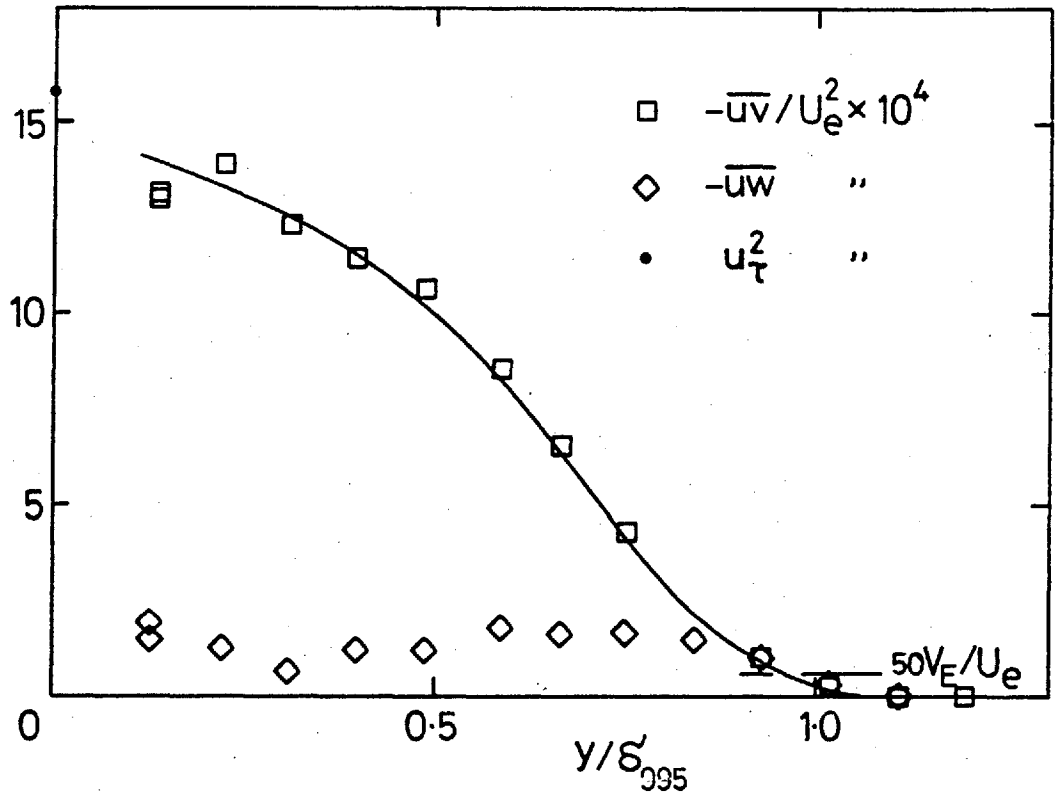

a) No grid, stn 6.

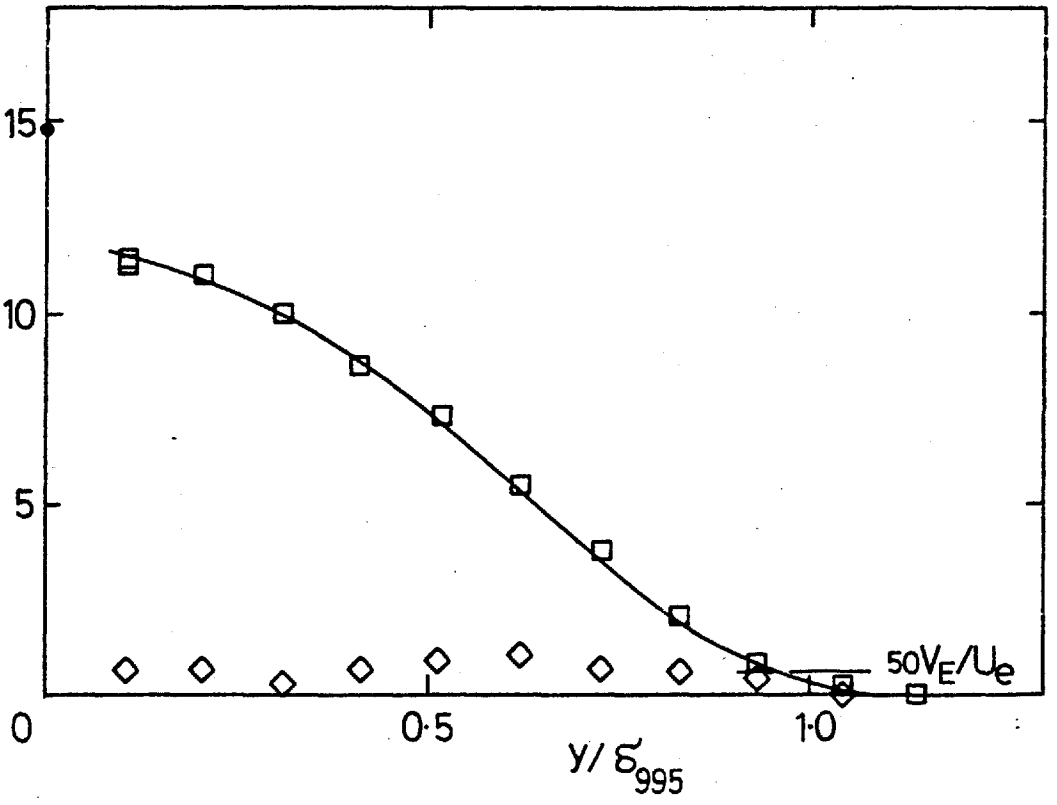

b) No grid, stn 14. Symbols as in a).

Fig. 4.7 Shear-stress profiles

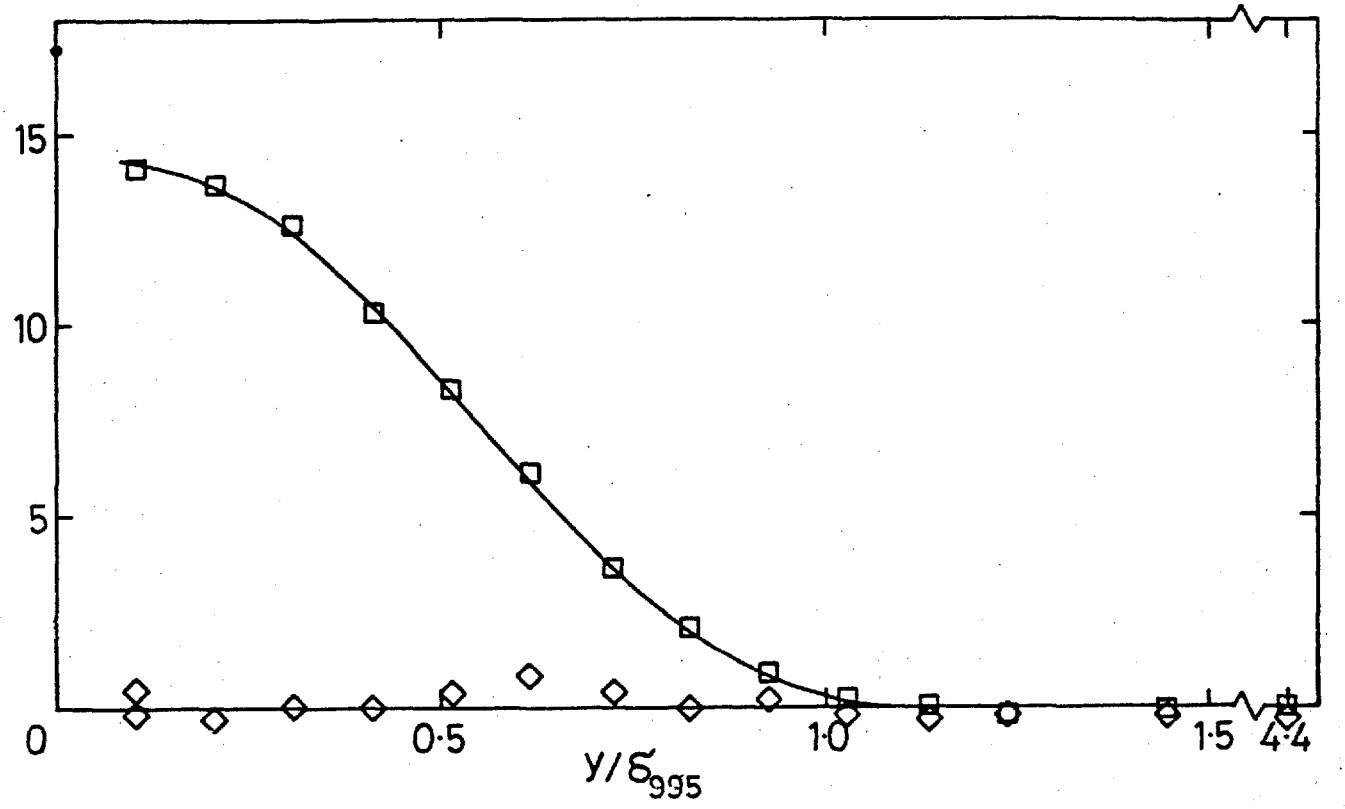

Fig. 4.7c, Shear-stress profiles; 7.6 cm grid, X_{LE} = 2.06 m, stn 6.
$(u'/U)_e$ = 0.0240, L^u_e/δ_{995} = 1.88. Symbols as in a).

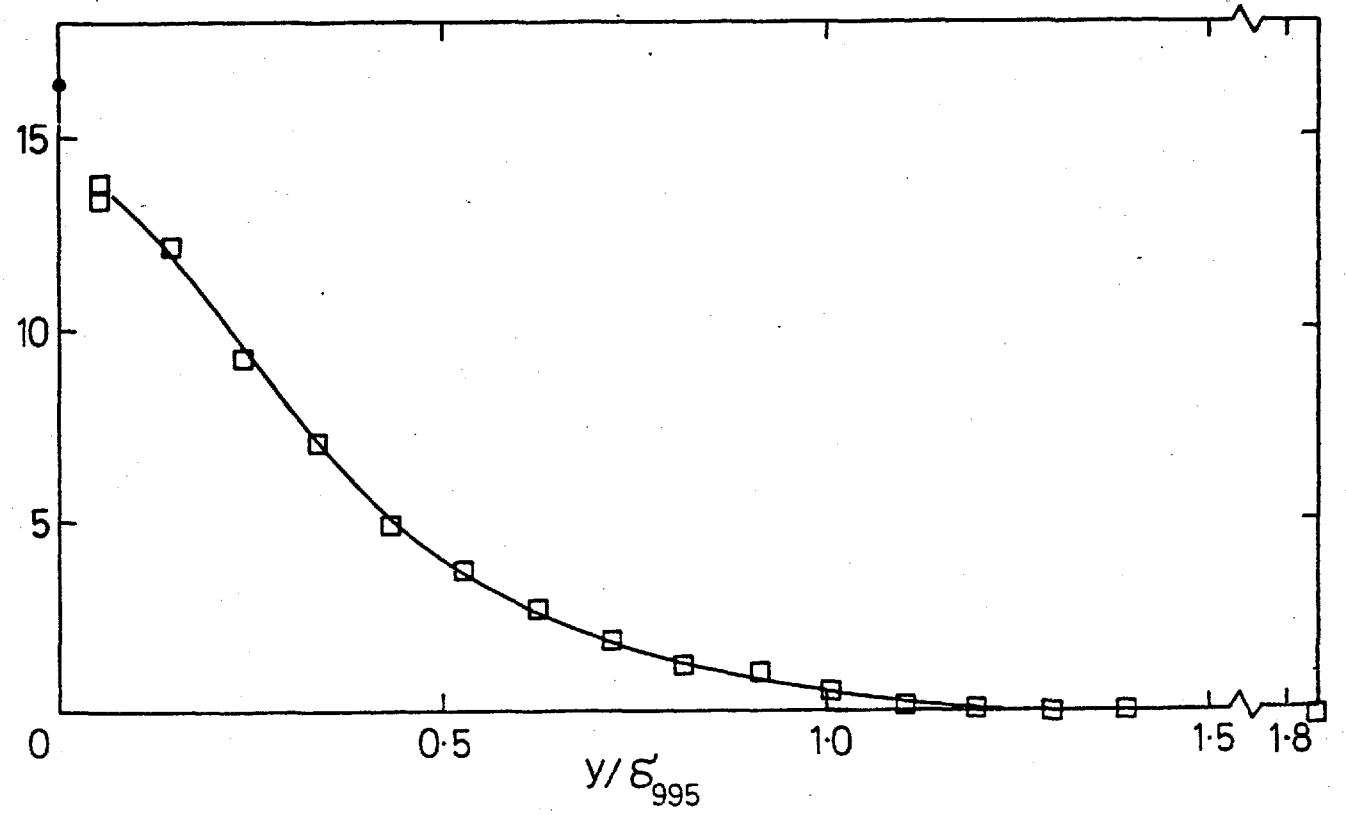

Fig. 4.7d, Shear-stress profile; 7.6 cm grid, X_{LE} = 0.30 m, stn 16.
$(u'/U)_e$ = 0.0255, L^u_e/δ_{995} = 0.67. Symbols as in a).

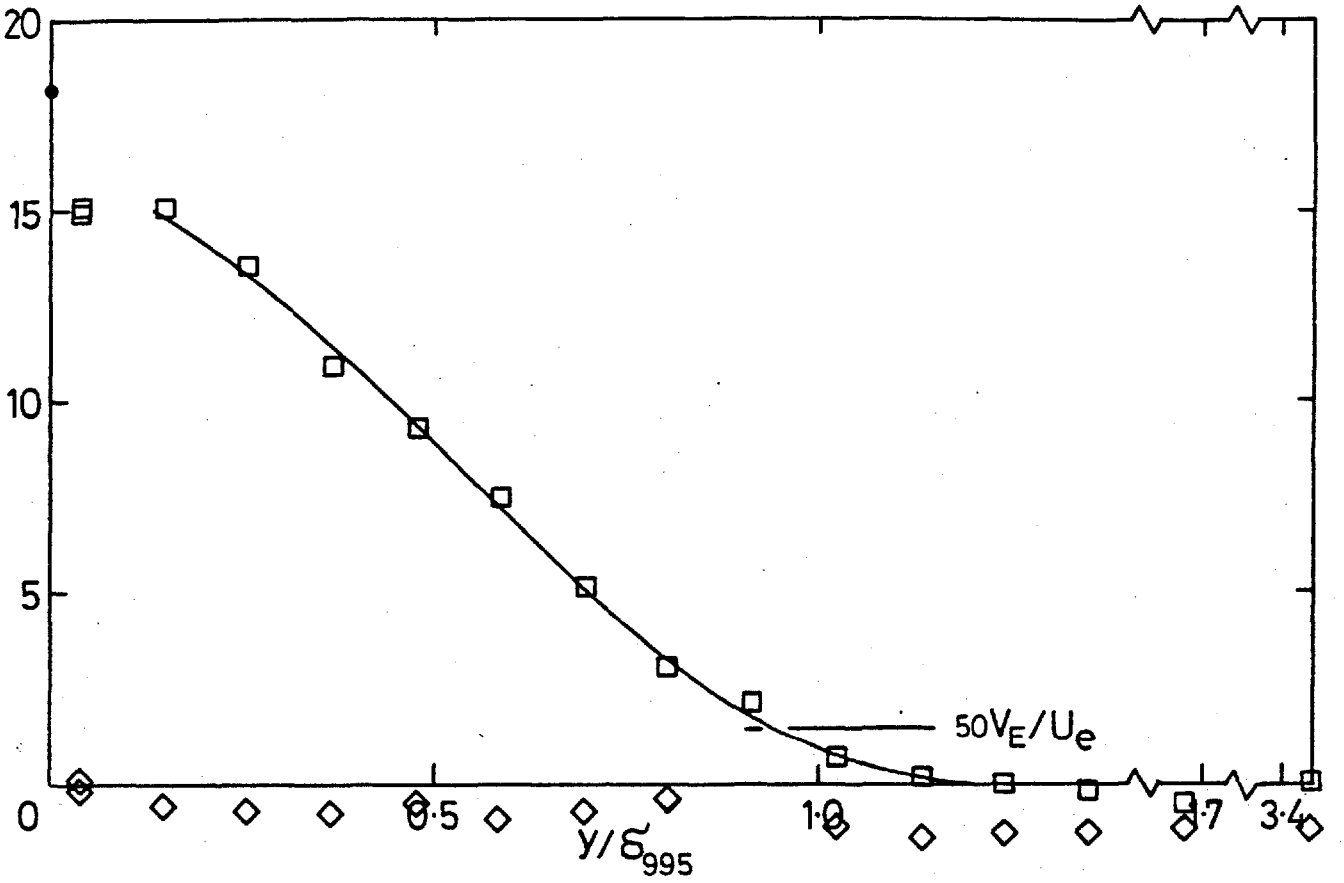

Fig. 4.7e, Shear-stress profiles; 15.2 cm grid, X_{LE} = 2.06 m, stn 6.
$(u'/U)_e$ = 0.0468, L^u_e/δ_{995} = 2.72. Symbols as in a).

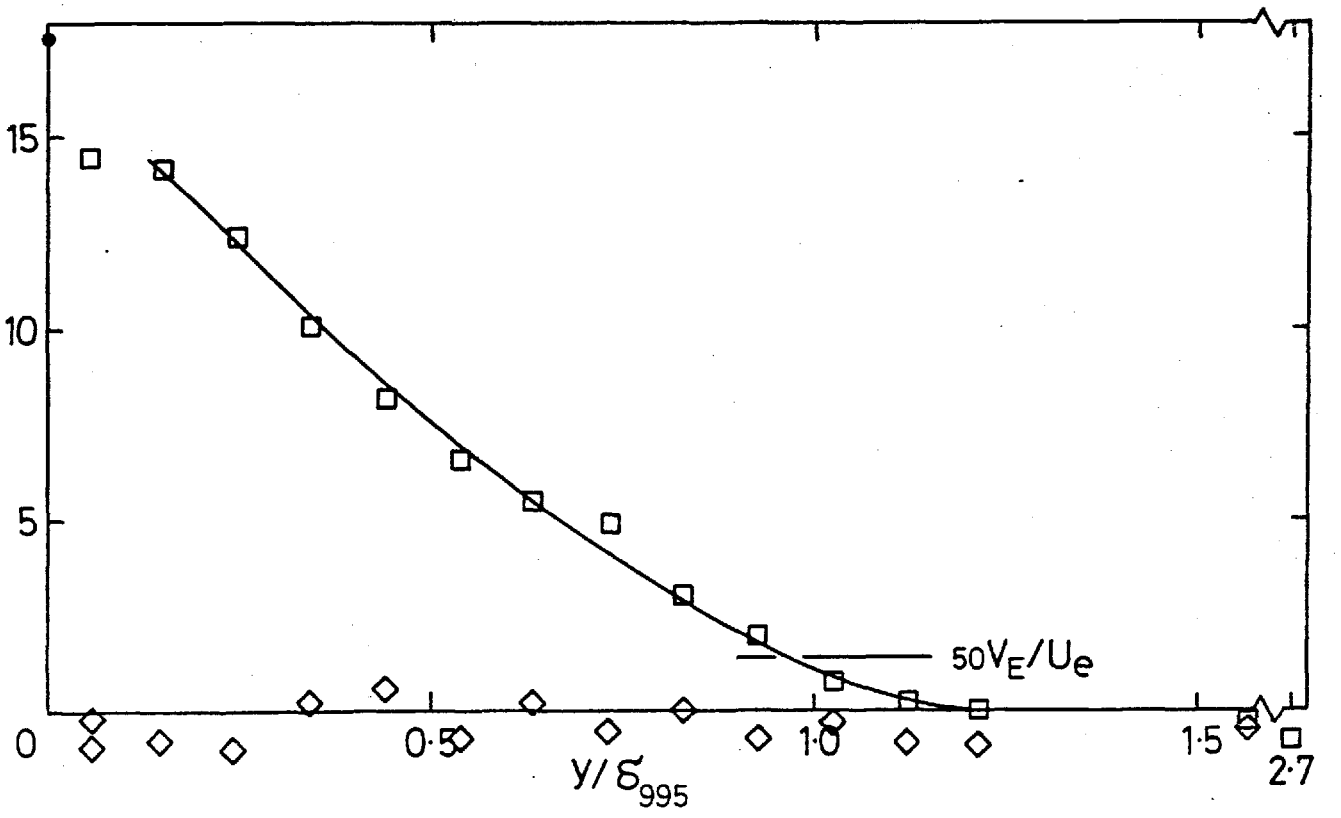

Fig. 4.7f, Shear-stress profiles; 15.2 cm grid, X_{LE} = 2.06 m, stn 8.
$(u'/U)_e$ = 0.0442, L^u_e/δ_{995} = 2.23. Symbols as in a).

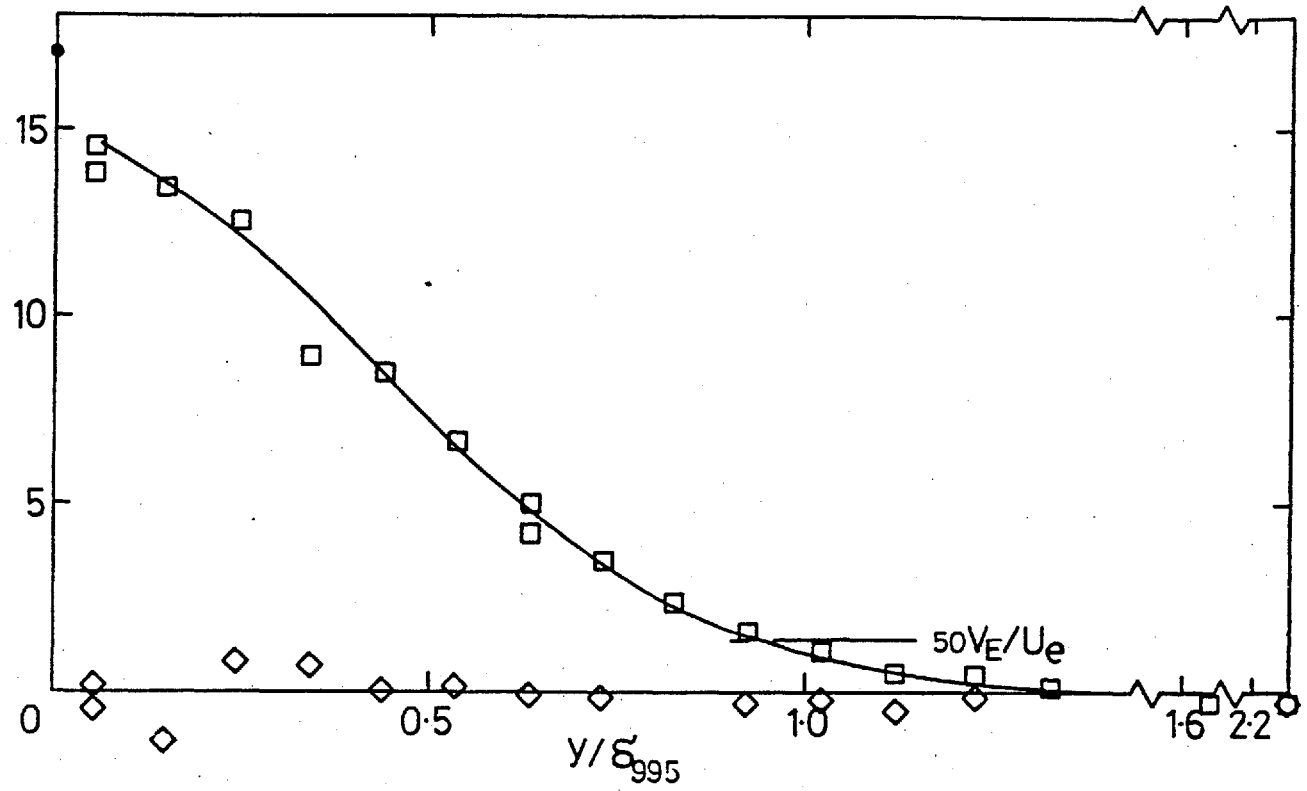

Fig. 4.7g, Shear-stress profiles; 15.2 cm grid, X_{LE} = 2.06 m, stn 10.
$(u'/U)_e$ = 0.0410, L^u_e/δ_{995} = 1.90. Symbols as in a).

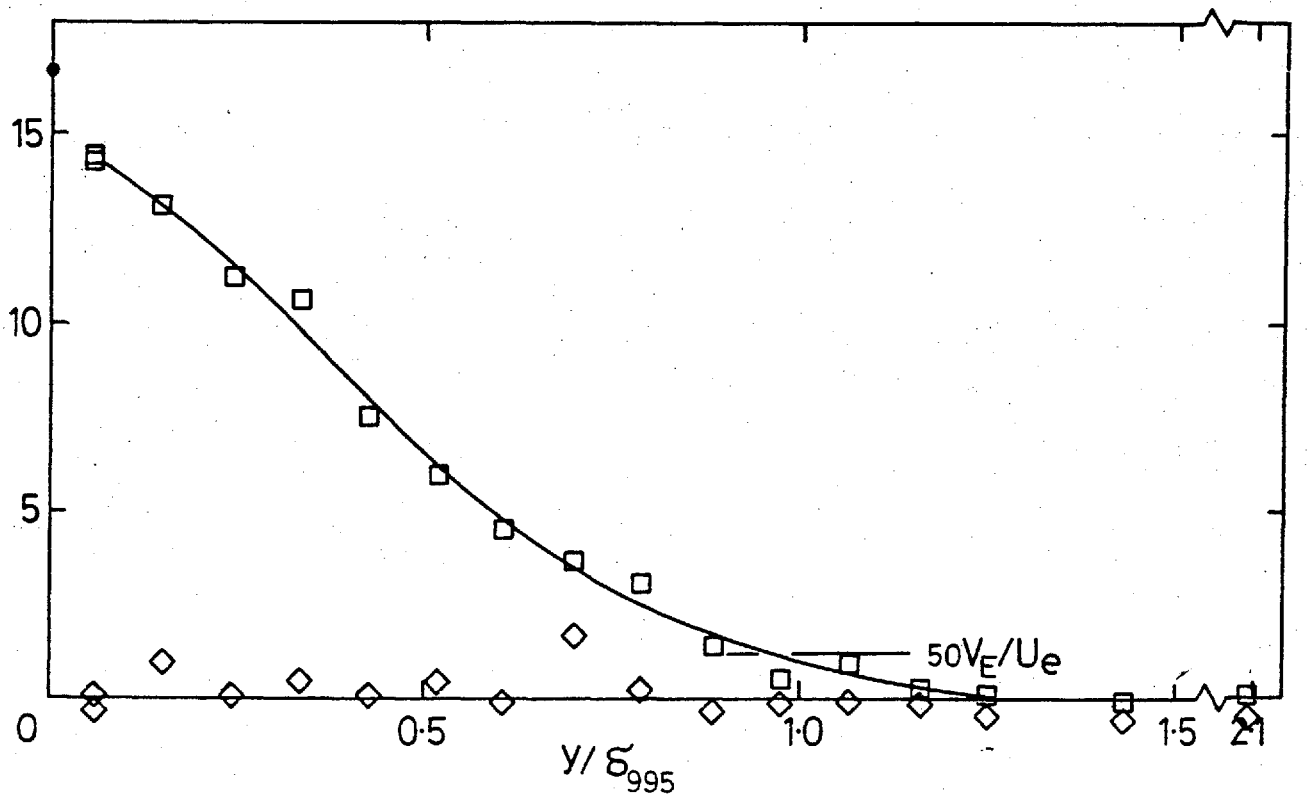

Fig. 4.7h, Shear-stress profiles; 15.2 cm grid, X_{LE} = 2.06 m, stn 12.
$(u'/U)_e$ = 0.0387, L^u_e/δ_{995} = 1.70. Symbols as in a).

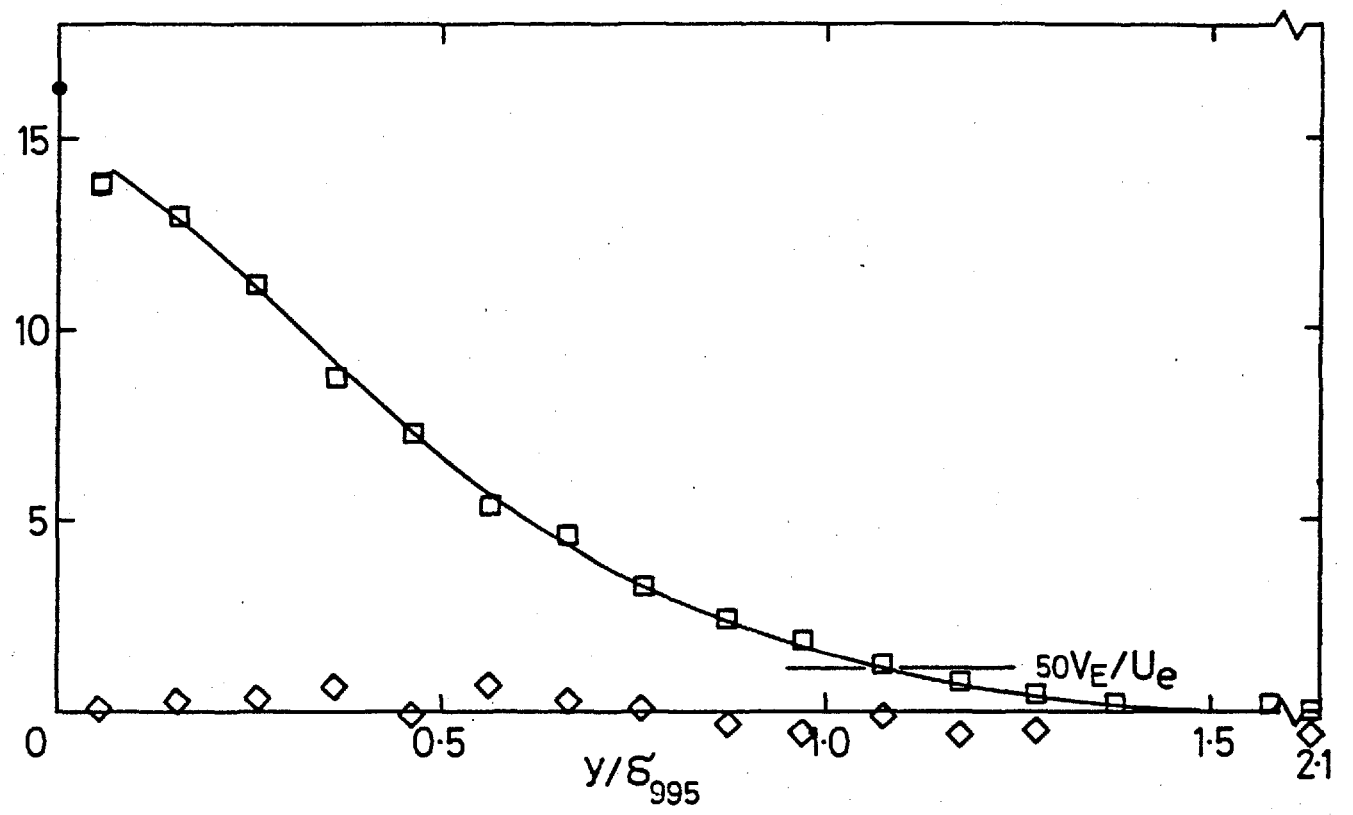

Fig. 4.7i, Shear-stress profiles; 15.2 cm grid, X_{LE} = 2.06 m, stn 14.
$(u'/U)_e$ = 0.0362, L^u_e/δ_{995} = 1.69. Symbols as in a).

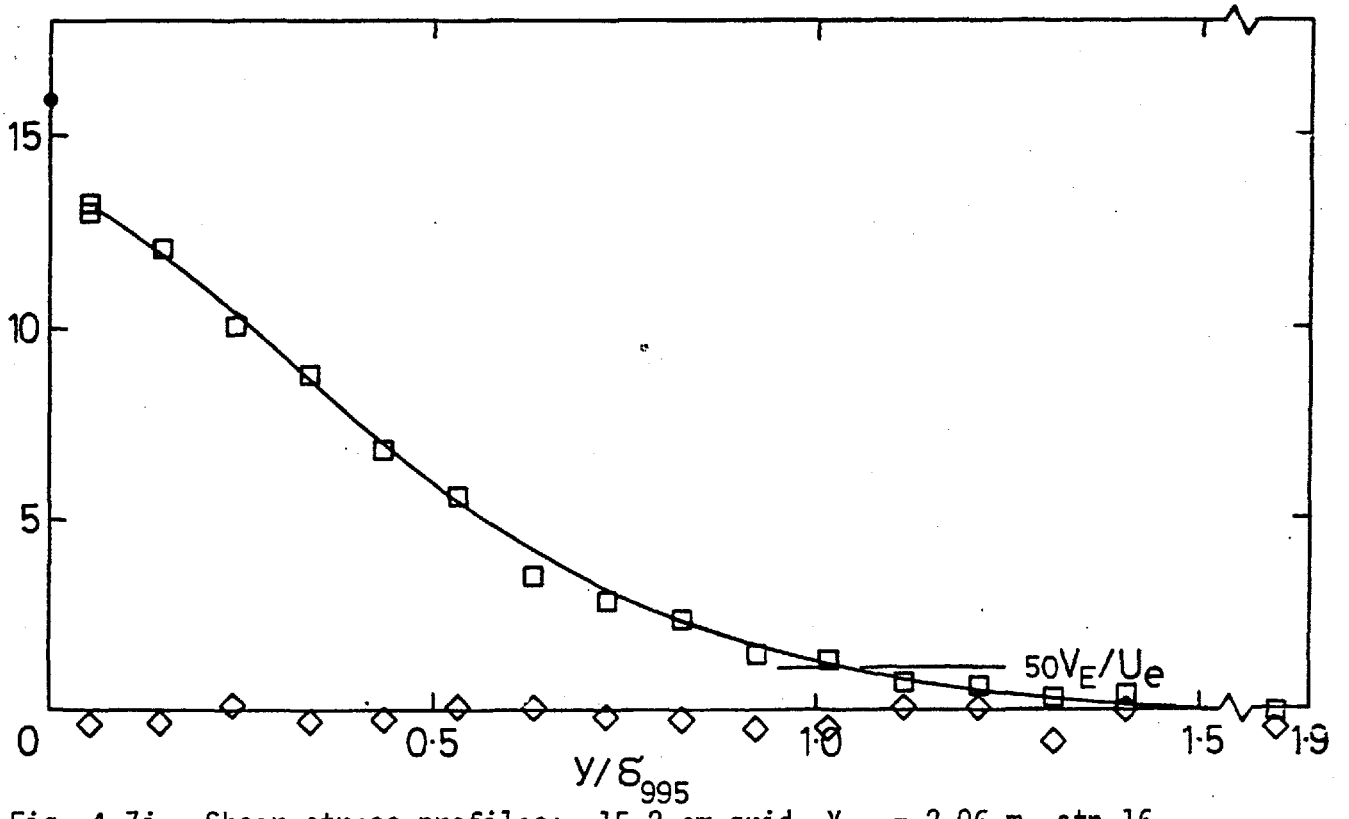

Fig. 4.7j, Shear-stress profiles; 15.2 cm grid, X_{LE} = 2.06 m, stn 16.
$(u'/U)_e$ = 0.0345, L^u_e/δ_{995} = 1.55. Symbols as in a).

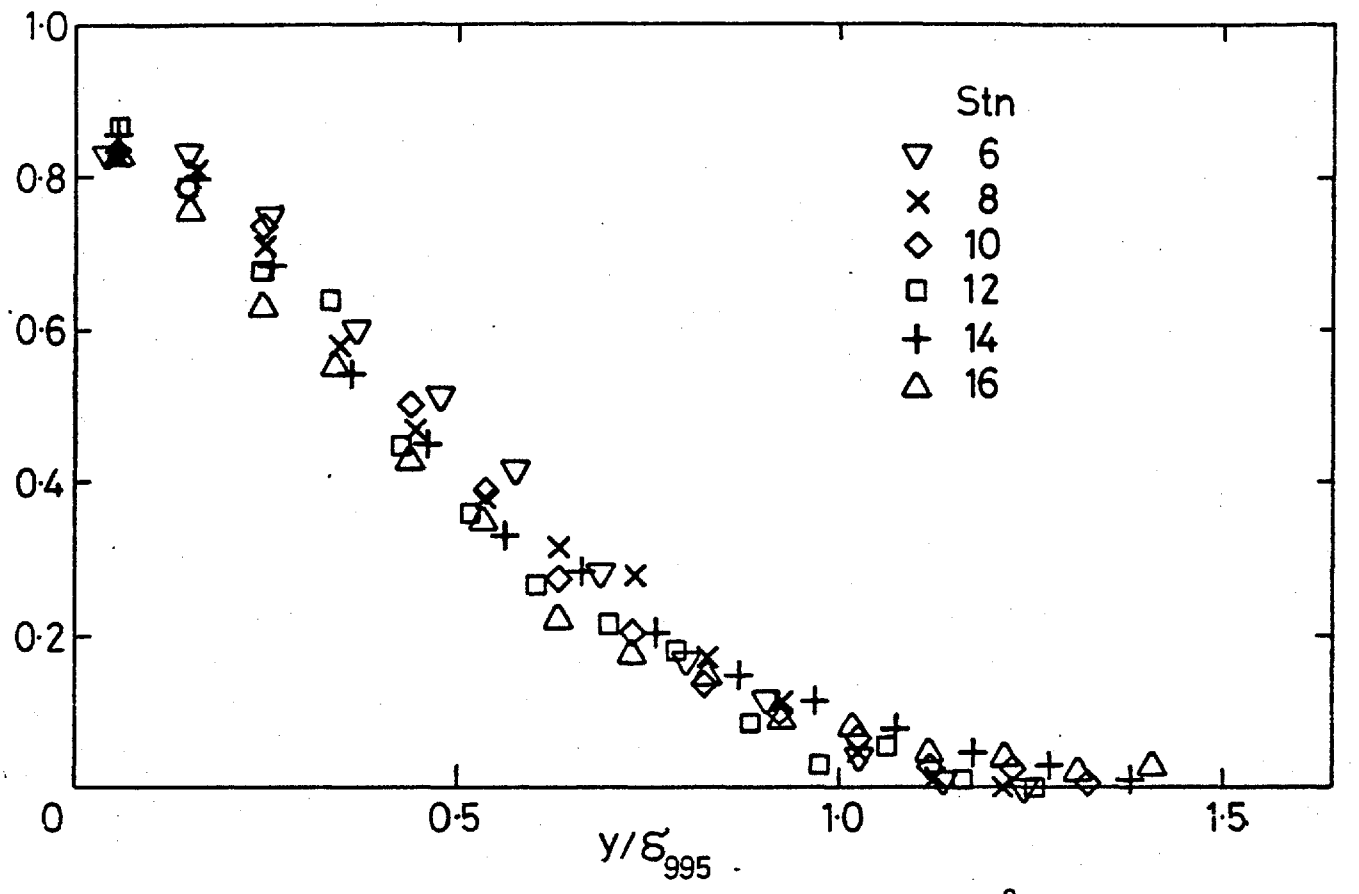

Fig. 4.7k, $-\overline{uv}$ profiles of figures e) to j) normalized on u_τ^2.

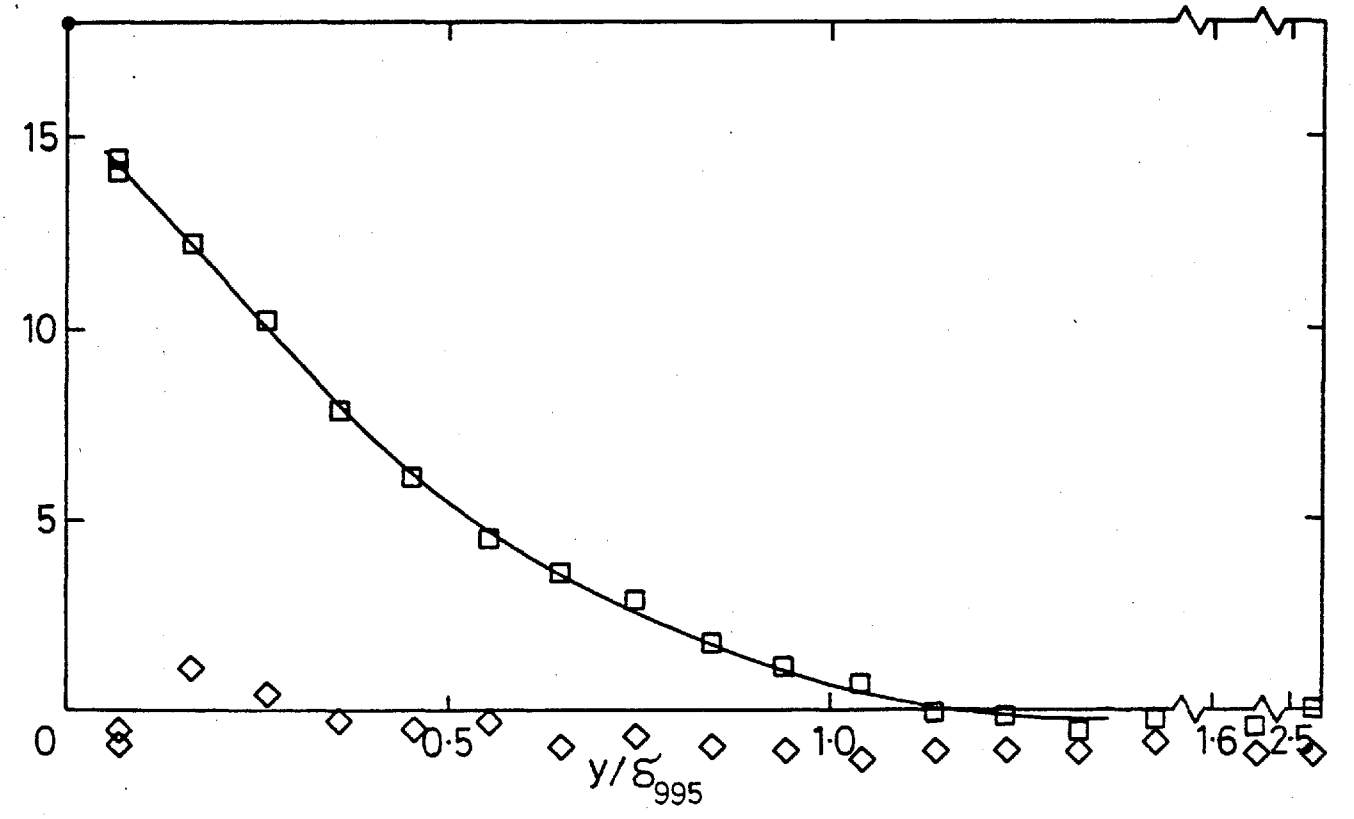

Fig. 4.7ℓ, Shear-stress profiles; 7.6 cm grid, X_{LE} = 0.30 m, stn 8. $(u'/U)_e$ = 0.0399, L_e^u/δ_{995} = 0.71. Symbols as in a).

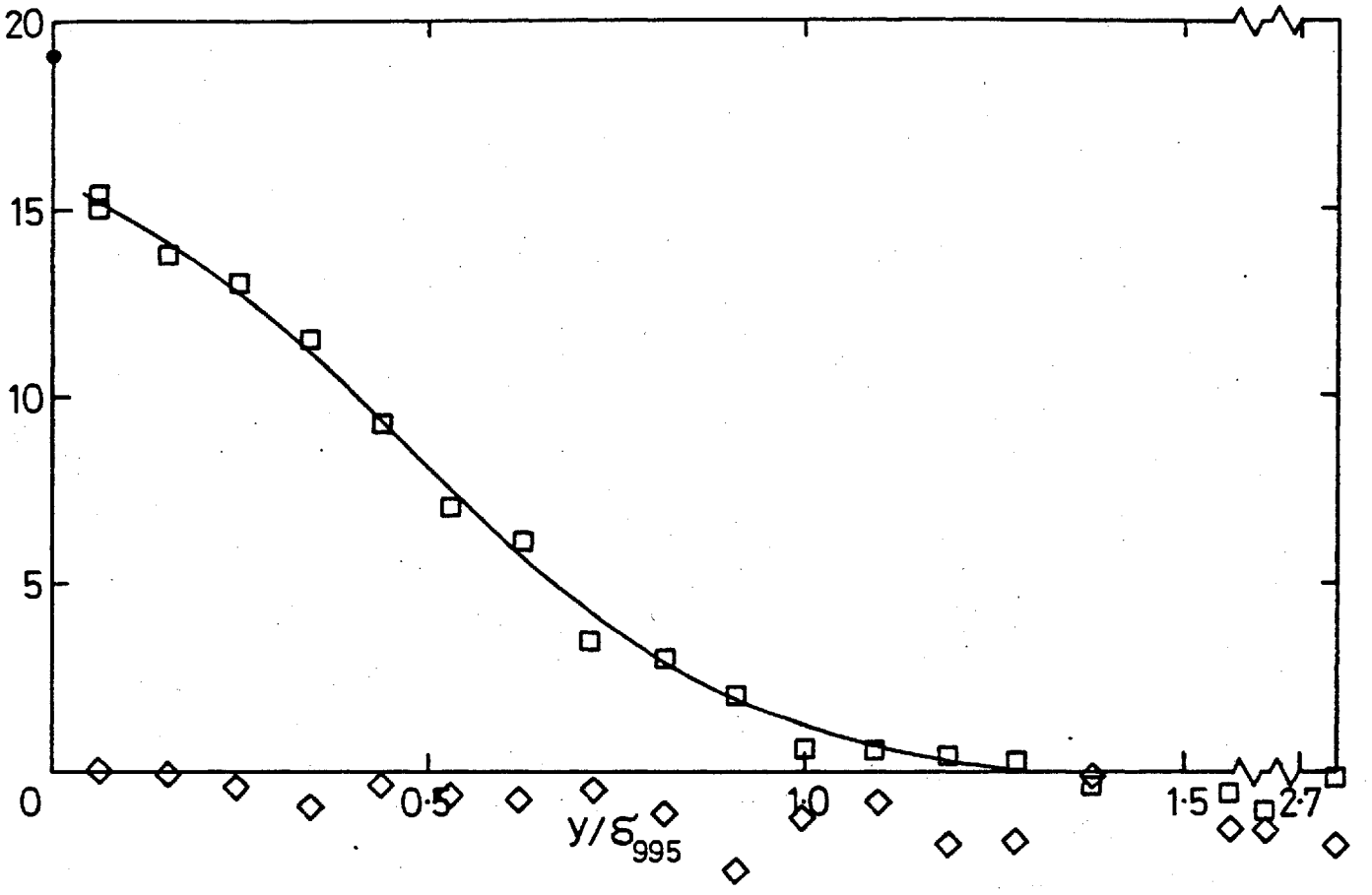

Fig. 4.7m, Shear-stress profiles; 15.2 cm grid, X_{LE} = 1.37 m, stn 6. $(u'/U)_e$ = 0.0575, L^u_e/δ_{995} = 1.83. Symbols as in a).

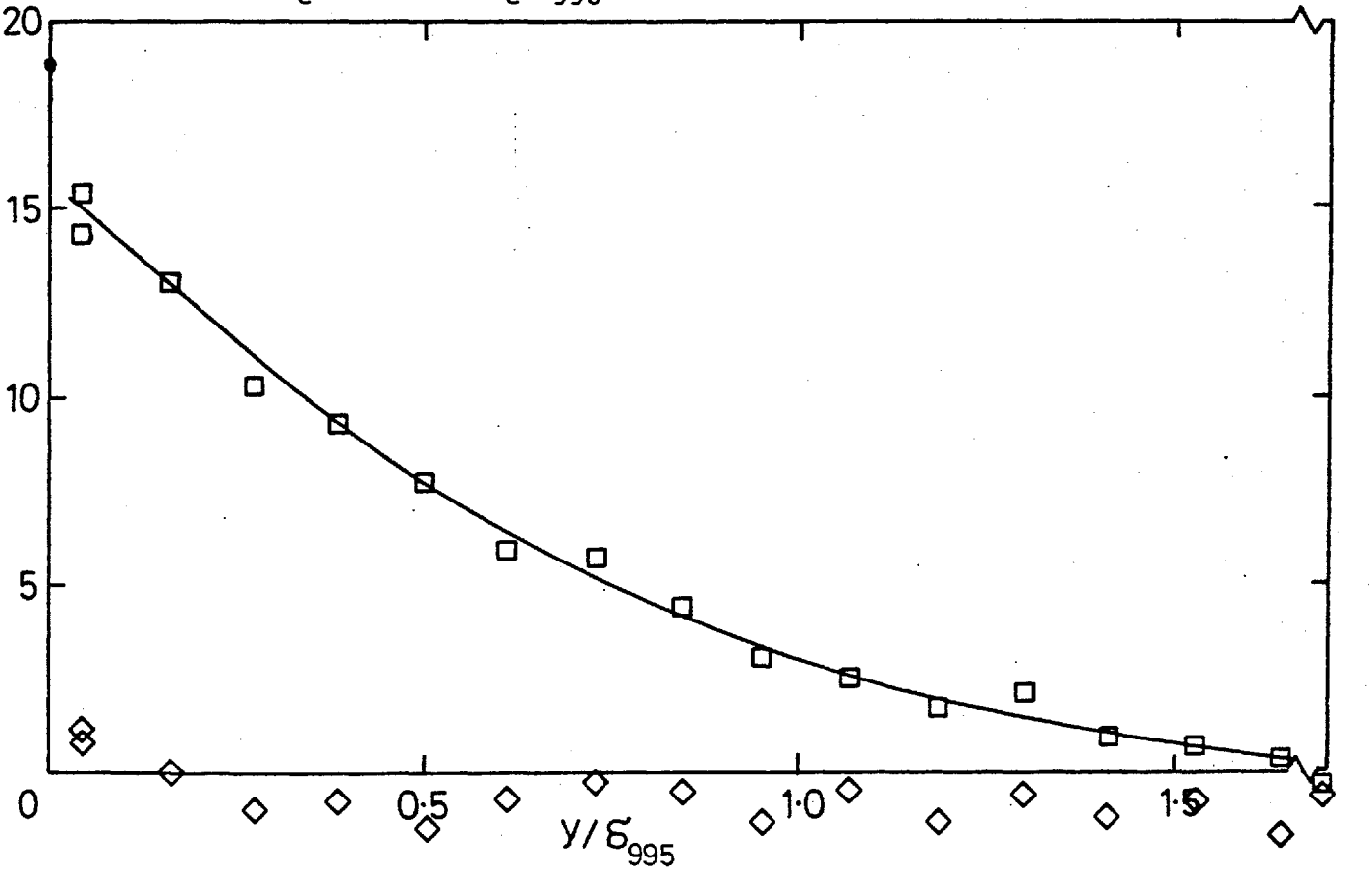

Fig. 4.7n, Shear-stress profiles; 15.2 cm grid, X_{LE} = 0.76 m, stn 10. $(u'/U)_e$ = 0.0575, L^u_e/δ_{995} = 1.34. Symbols as in a).

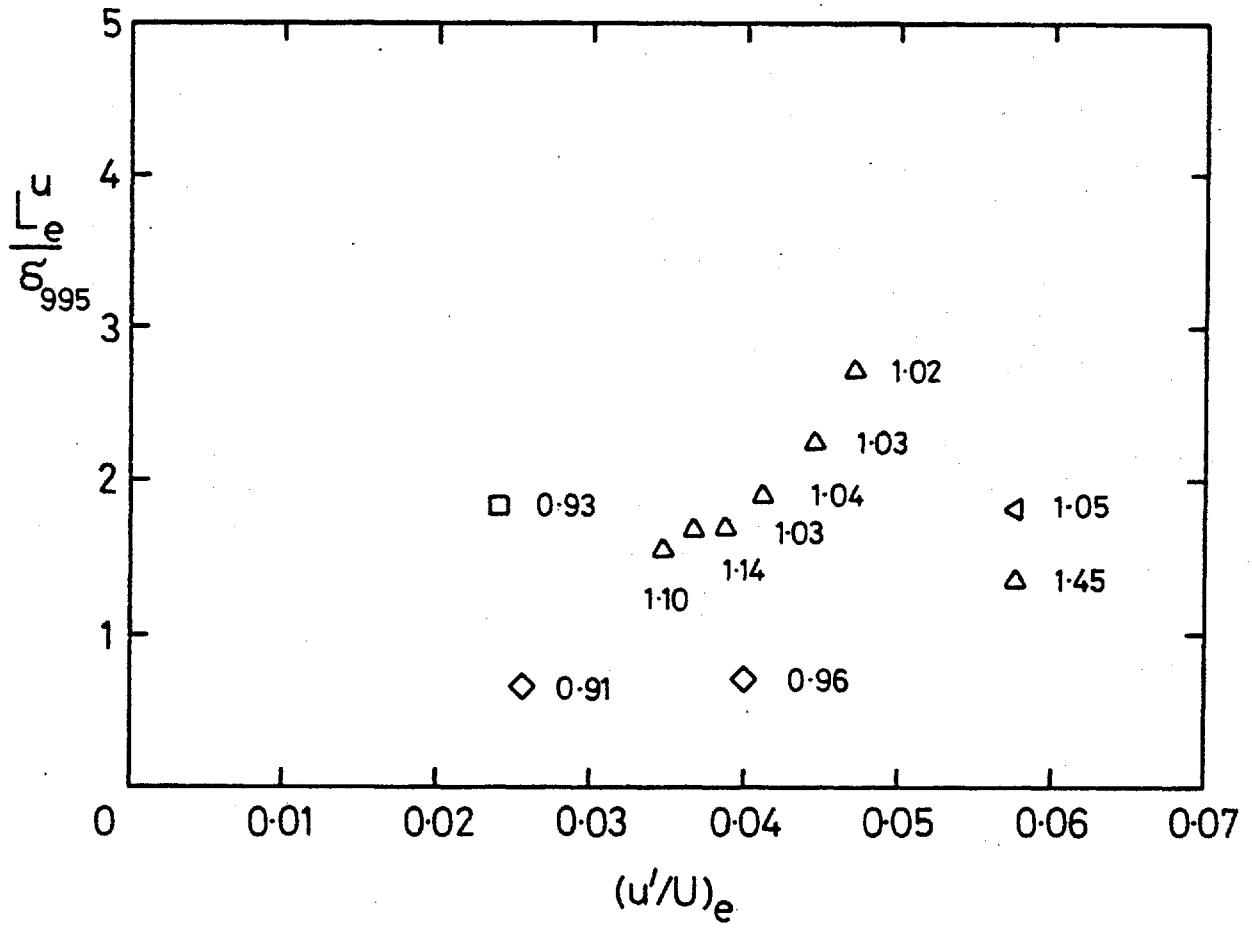

Fig. 4.8 Values of δ_{05}/δ_{995} displayed at appropriate $(u'/U)_e$ and L_e^u/δ_{995}.

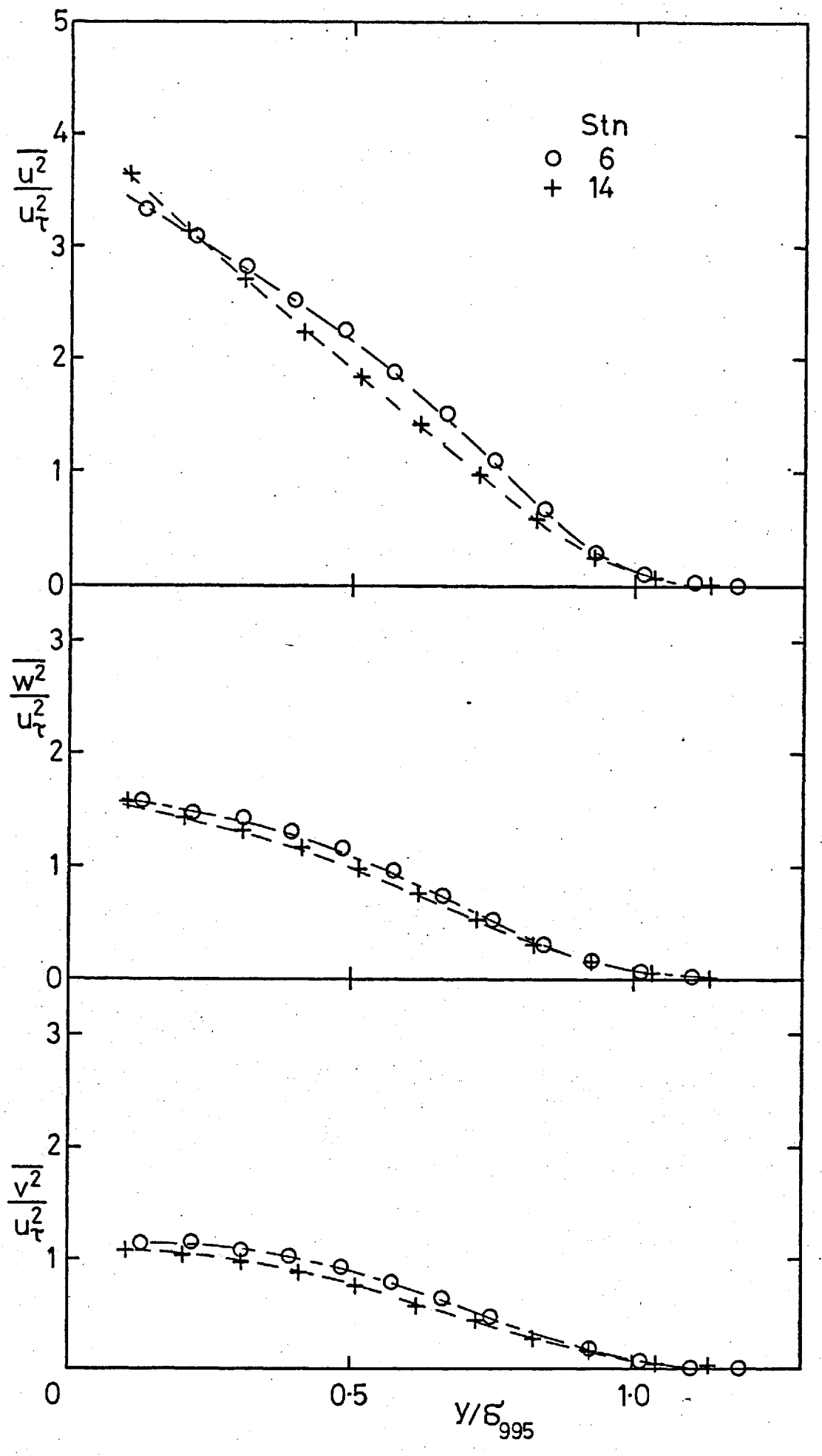

a) No grid

Fig. 4.9 Direct-stress profiles at $(u'/U)_e \approx 0$, 0.025, 0.040, 0.058

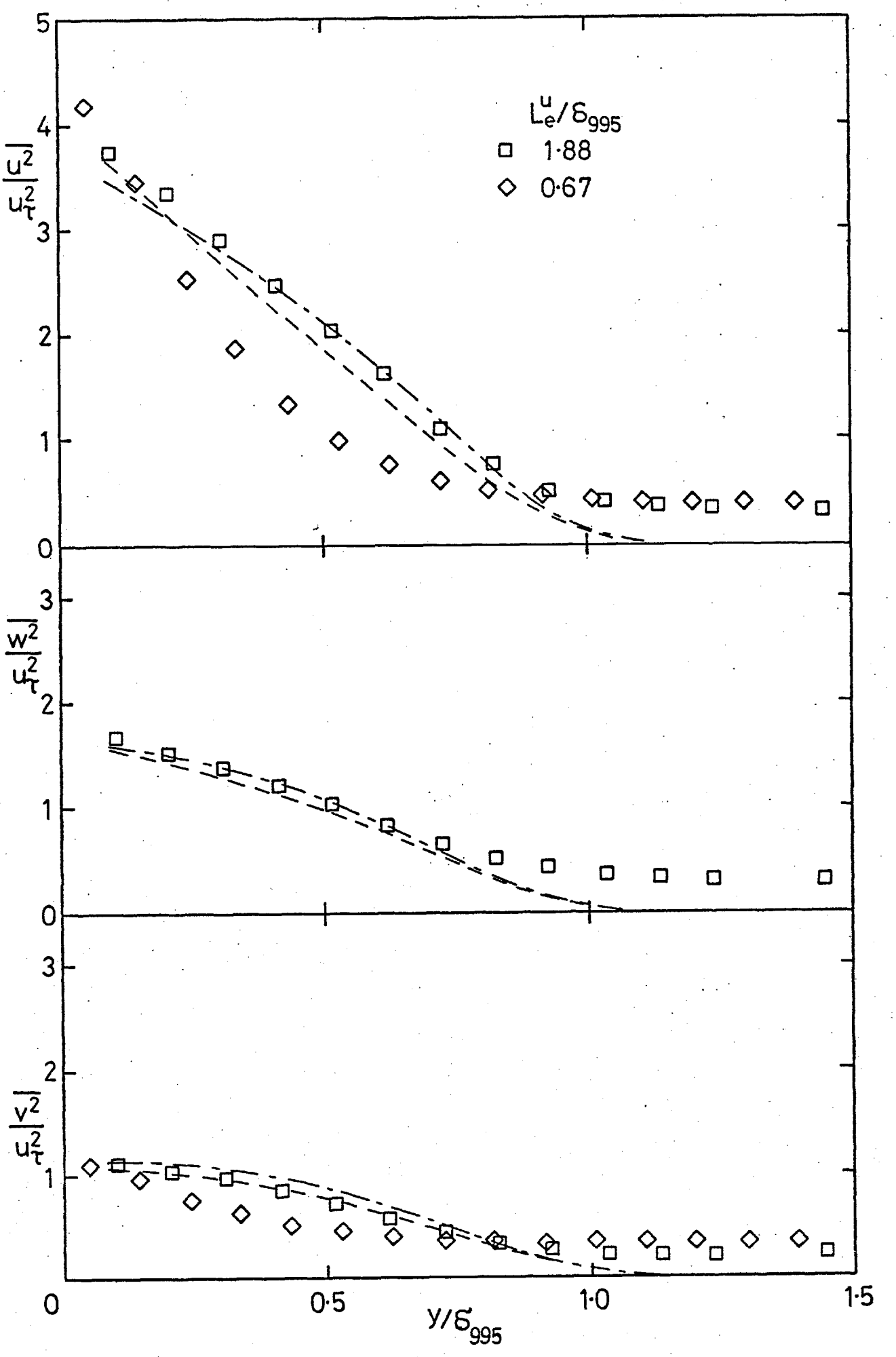

Fig. 4.9b, $(u'/U)_e \approx 0.025$. Broken lines as in a).

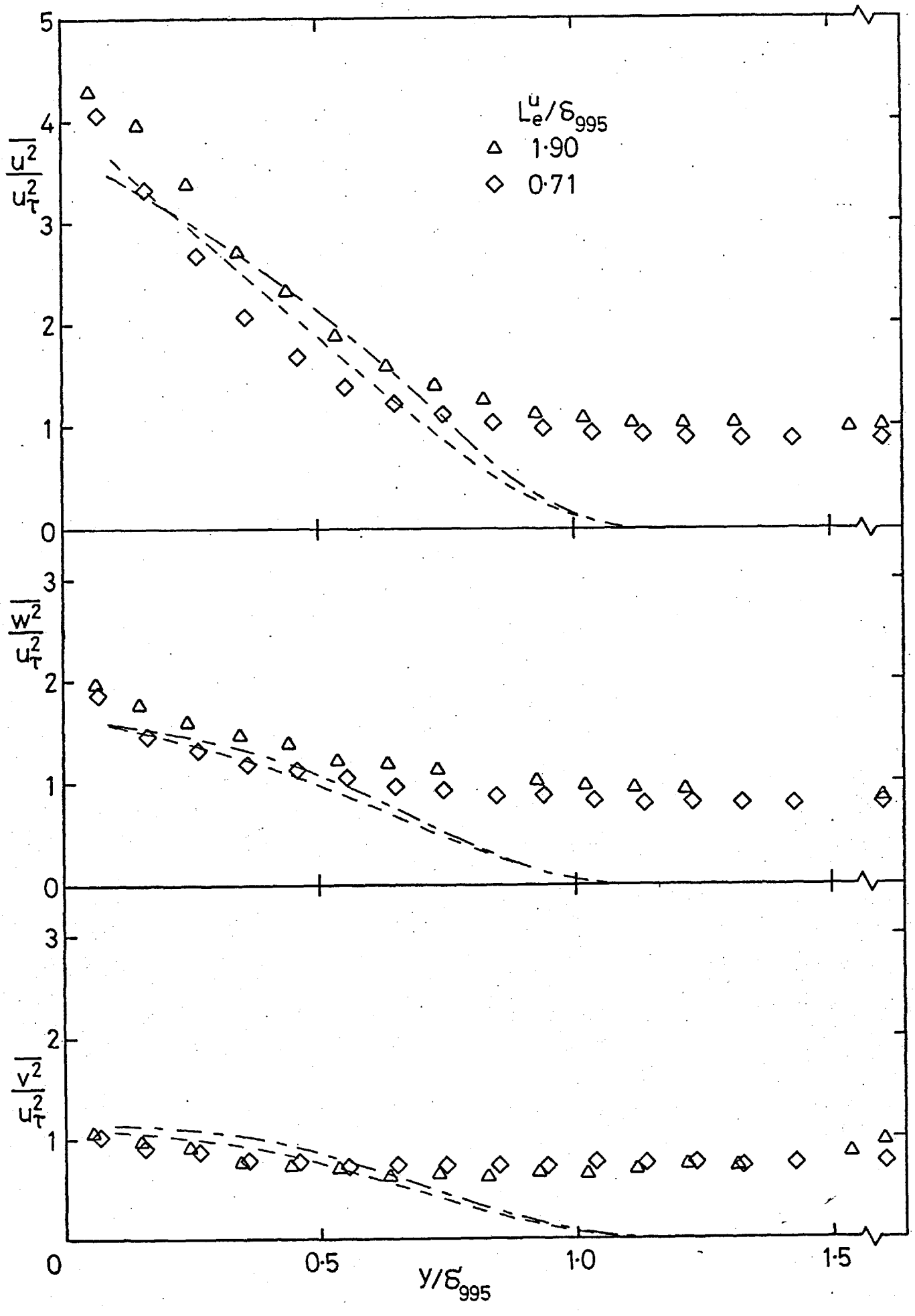

Fig. 4.9c, $(u'/U)_e \approx 0.040$. Broken lines as in a).

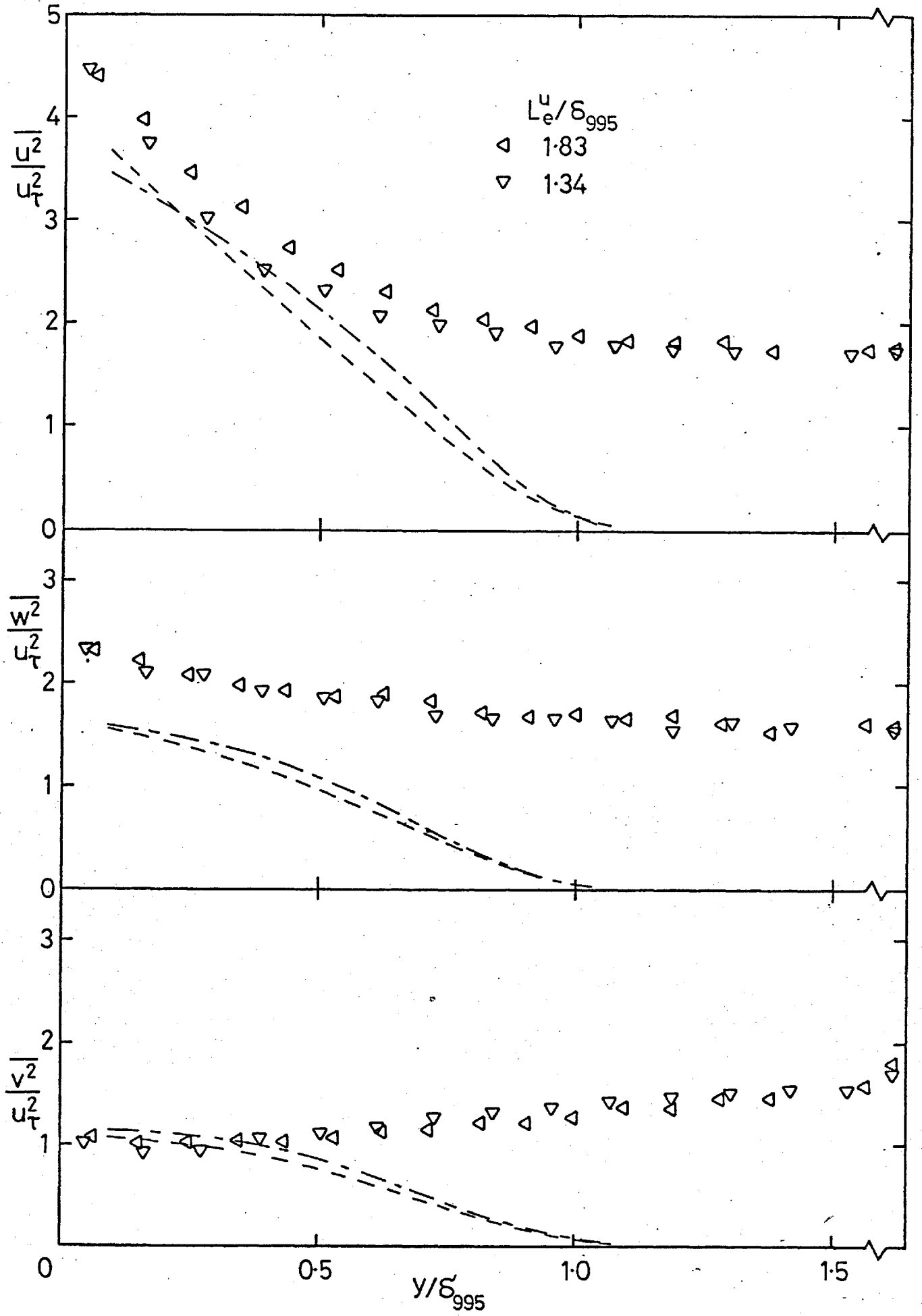

Fig. 4.9d, $(u'/U)_e = 0.0575$. Broken lines as in a).

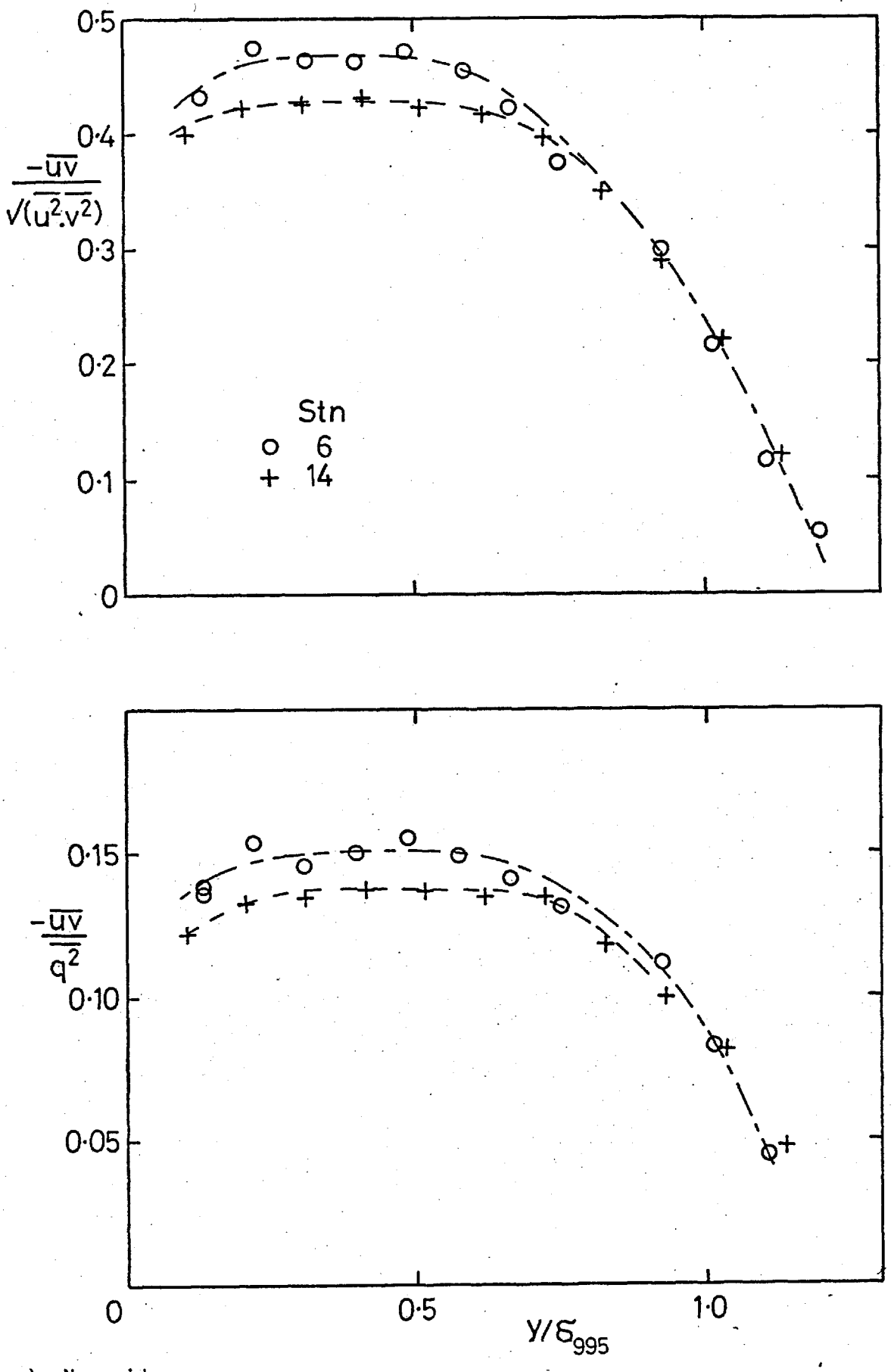

a) No grid

Fig. 4.10 Shear-stress correlation coefficient and the ratio $-\overline{uv}/\overline{q^2}$;

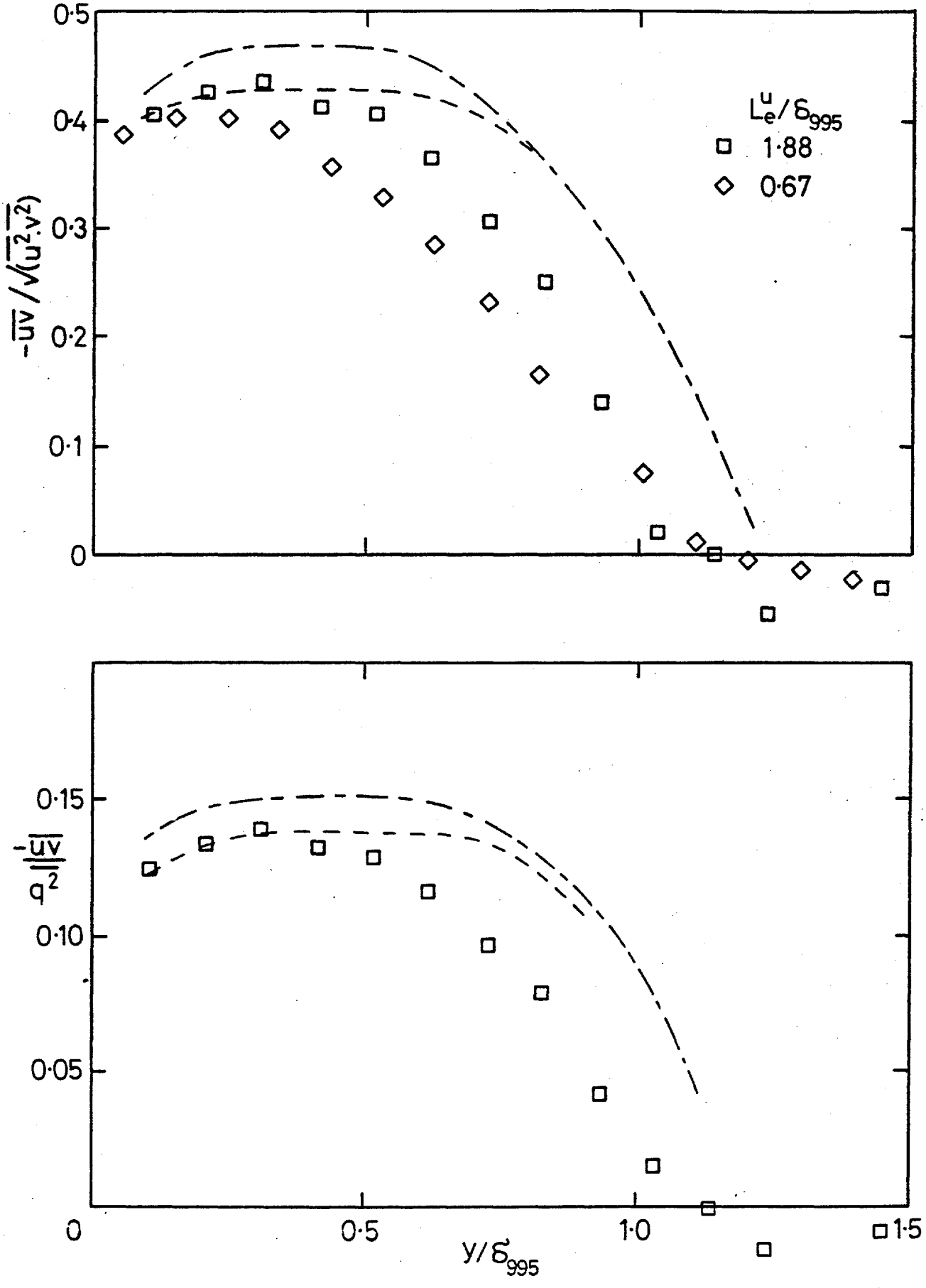

Fig. 4.10b, $(u'/U)_e \approx 0.025$. Broken lines as in a).

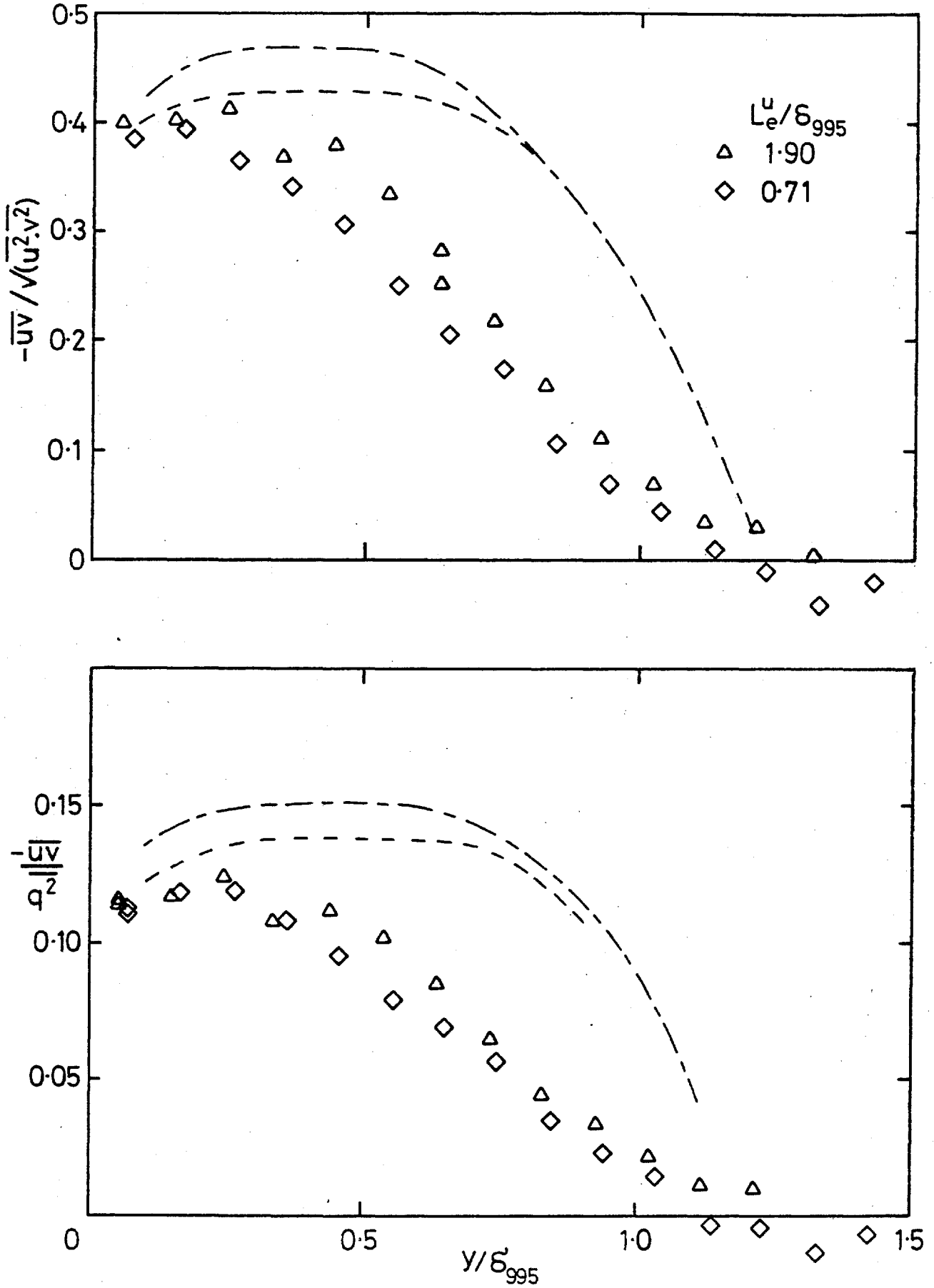

Fig. 4.10c, $(u'/U)_e \approx 0.040$. Broken lines as in a).

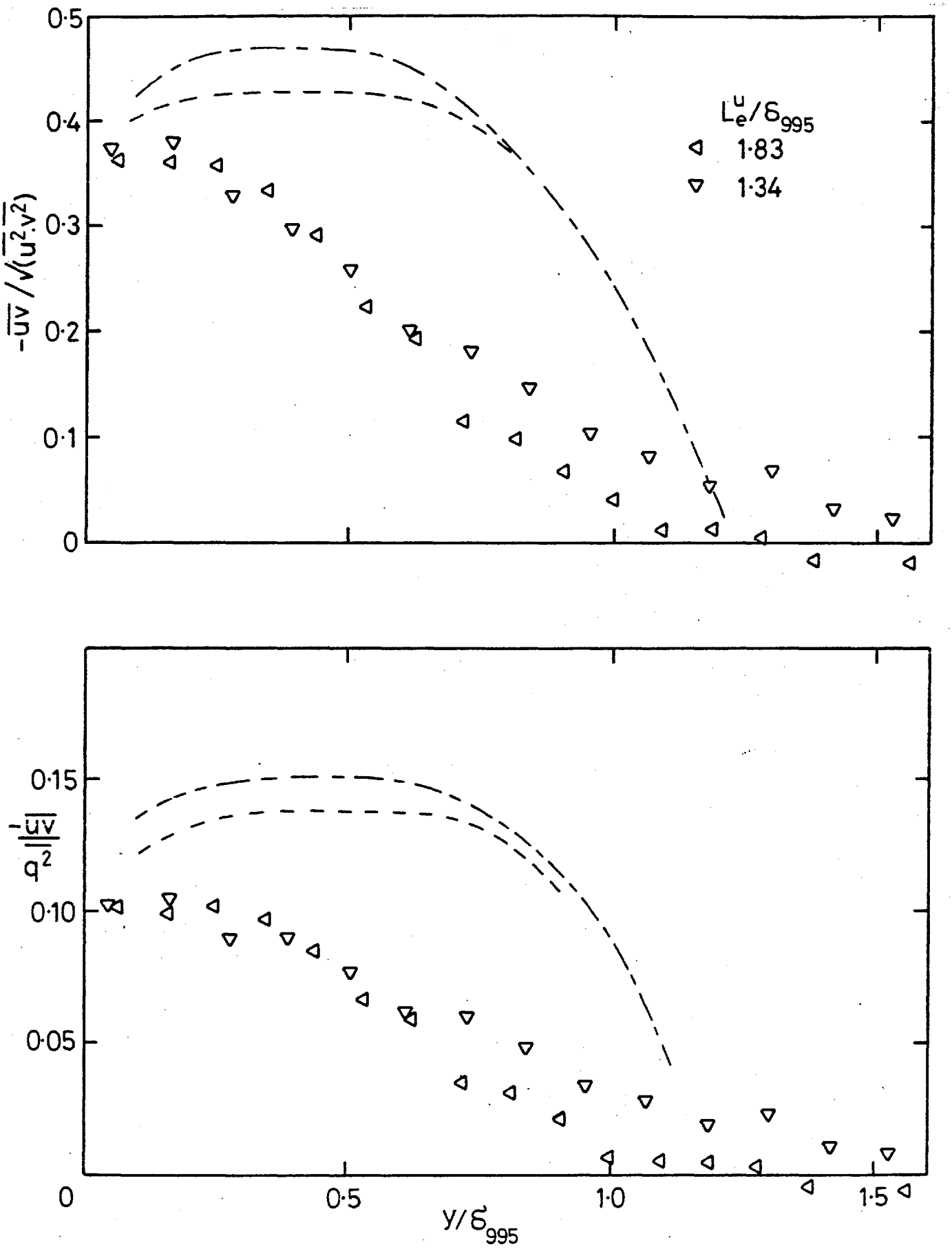

Fig. 4.10d, $(u'/U)_e$ = 0.0575. Broken lines as in a).

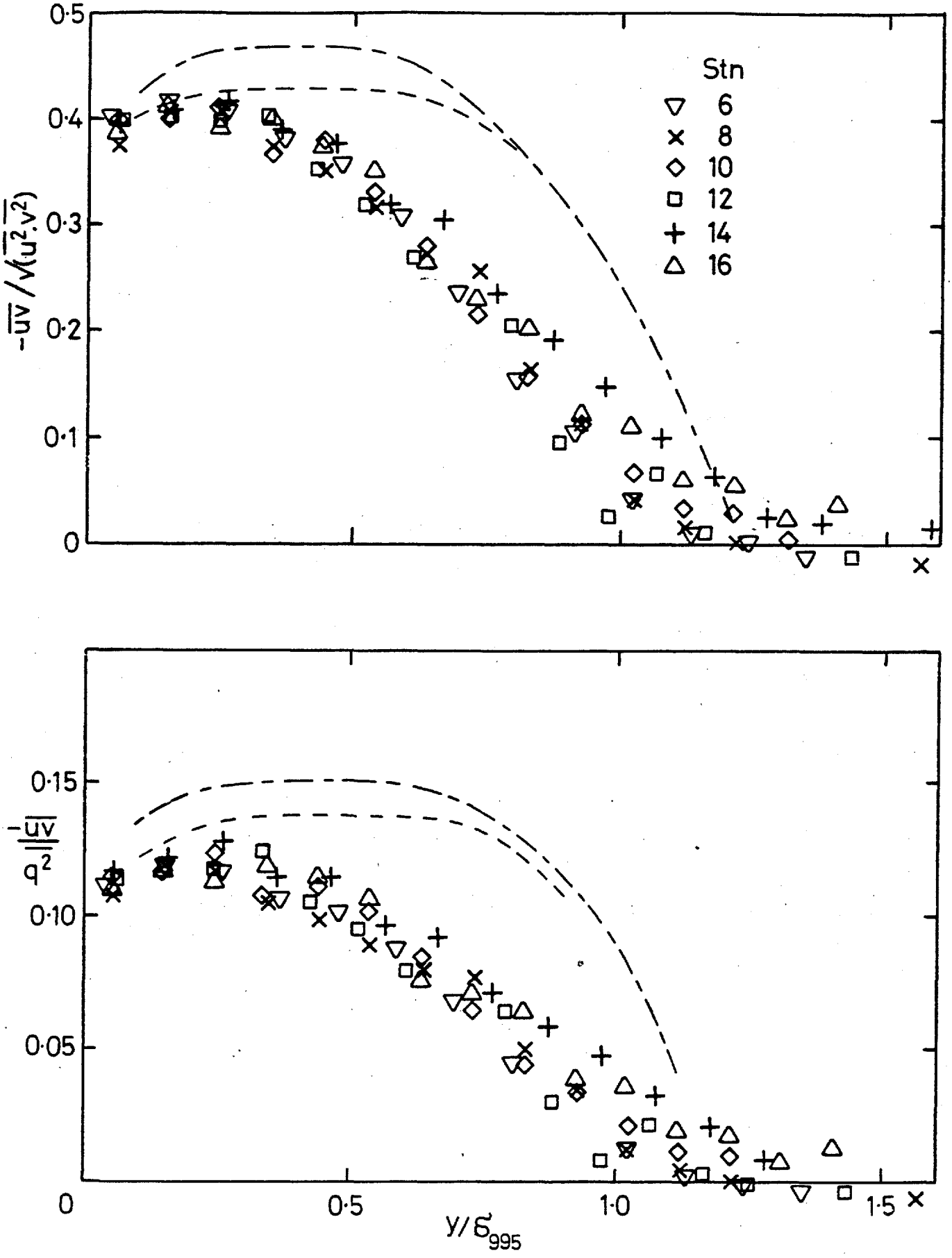

Fig. 4.10e, 15.2 cm grid, X_{LE} = 2.06 m, stns 6, 8, 10, 12, 14, 16.
Broken lines as in a).

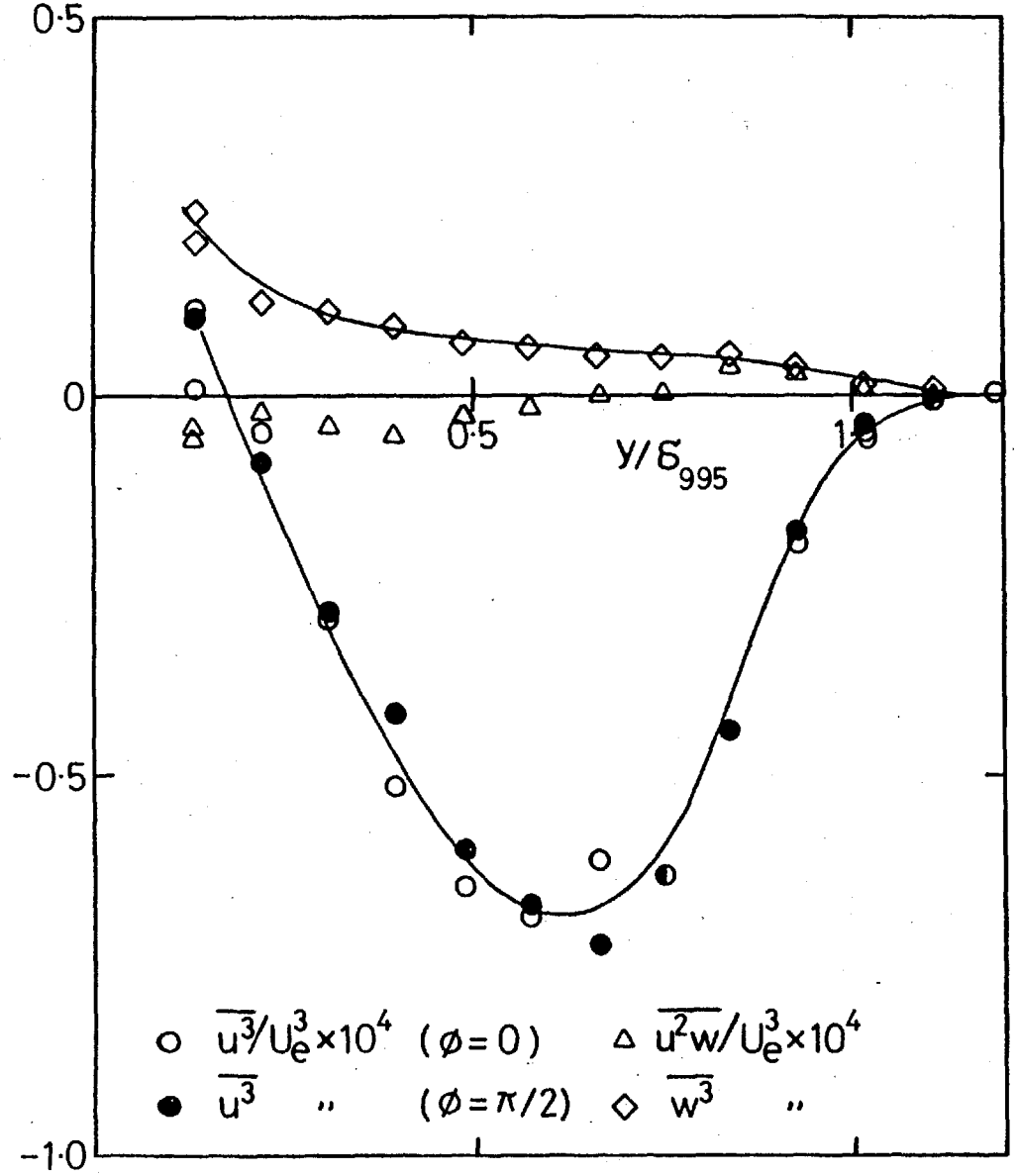

a) No grid, stn 6.

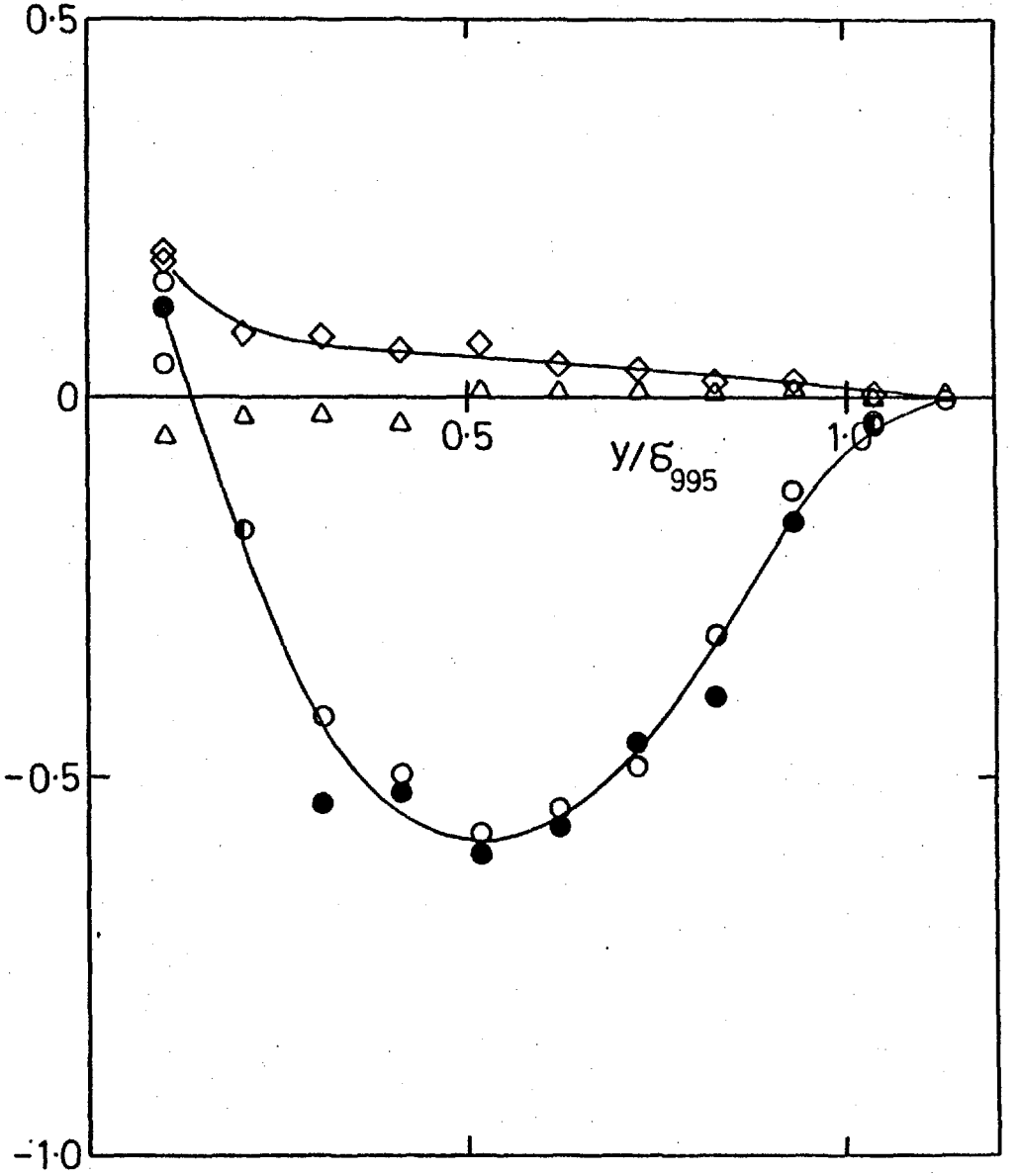

b) No grid, stn 14. Symbols as in a).

Fig. 4.11 Third-order products, $\overline{u^3}$, $\overline{u^2w}$, $\overline{w^3}$;

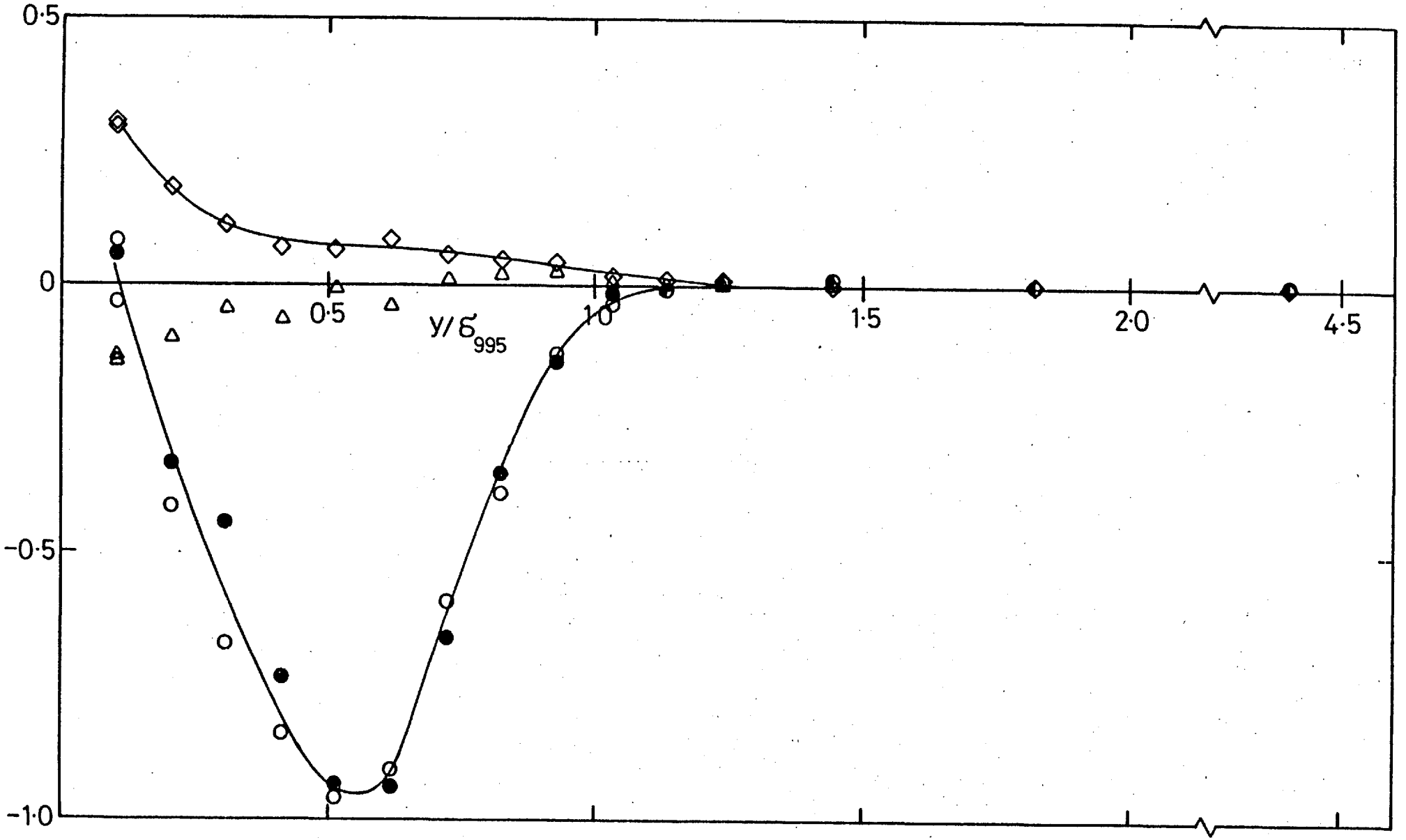

Fig. 4.11c, $\overline{u^3}$, $\overline{u^2w}$, $\overline{w^3}$; 7.6 cm grid, X_{LE} = 2.06 m, stn 6. $(u'/U)_e$ = 0.0240, L^u_e/δ_{995} = 1.88. Symbols as in a).

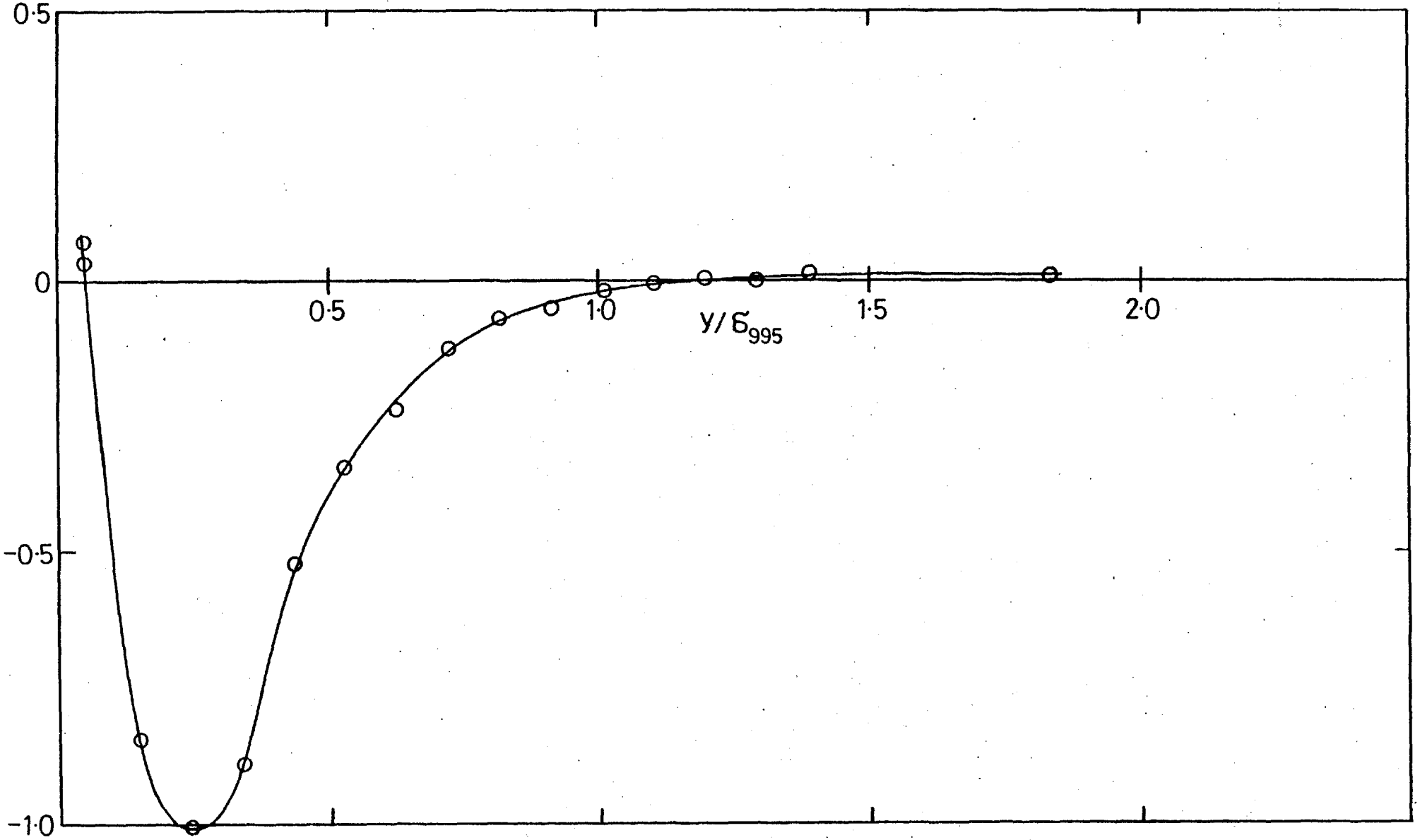

Fig. 4.11d, $\overline{u^3}$; 7.6 cm grid, X_{LE} = 0.30 m, stn 16. $(u'/U)_e$ = 0.0255, L^u_e/δ_{995} = 0.67. Symbols as in a).

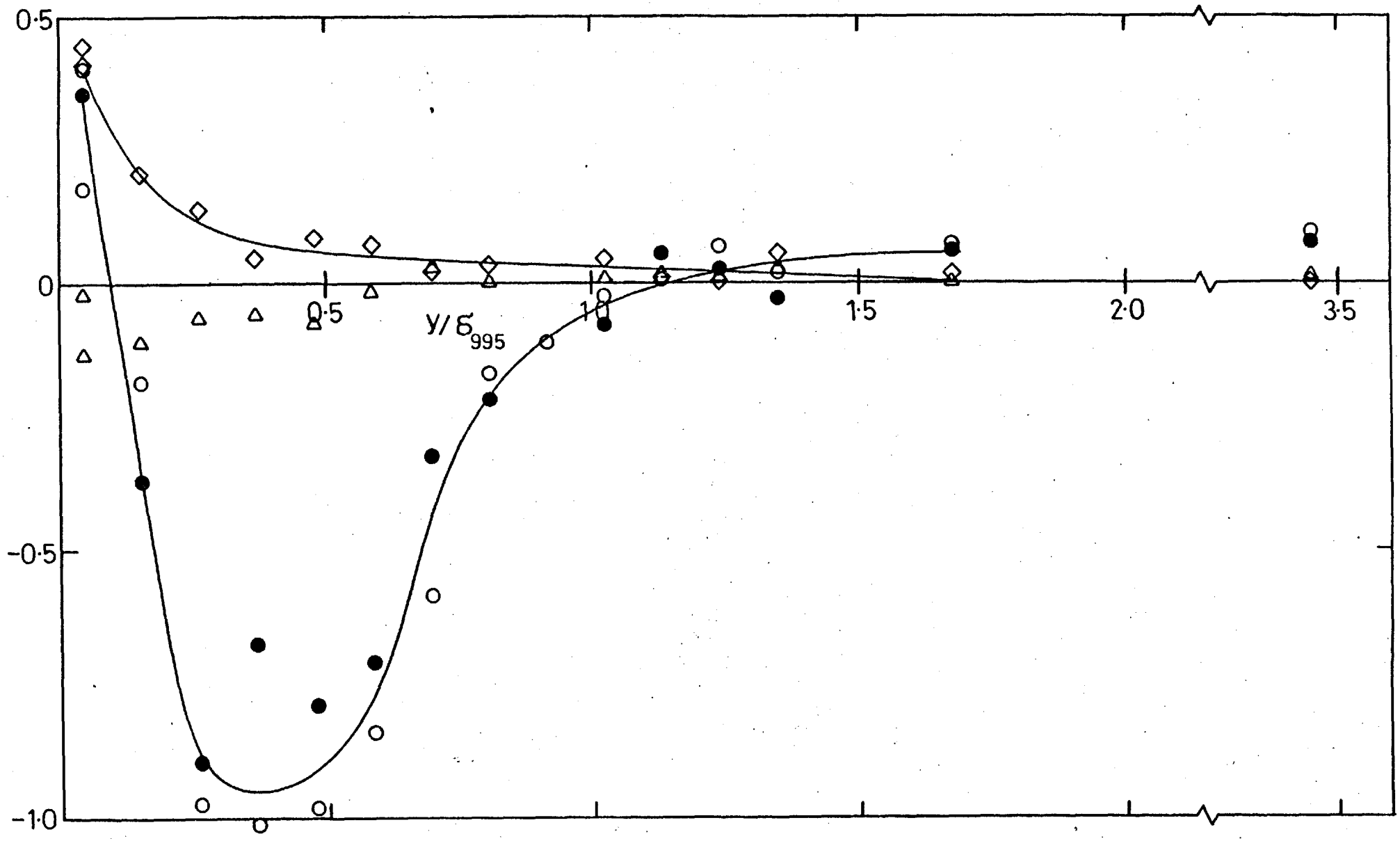

Fig. 4.11e, $\overline{u^3}$, $\overline{u^2w}$, $\overline{w^3}$; 15.2 cm grid, X_{LE} = 2.06 m, stn 6. $(u'/U)_e$ = 0.0468, L^u_e/δ_{995} = 2.72. Symbols as in a).

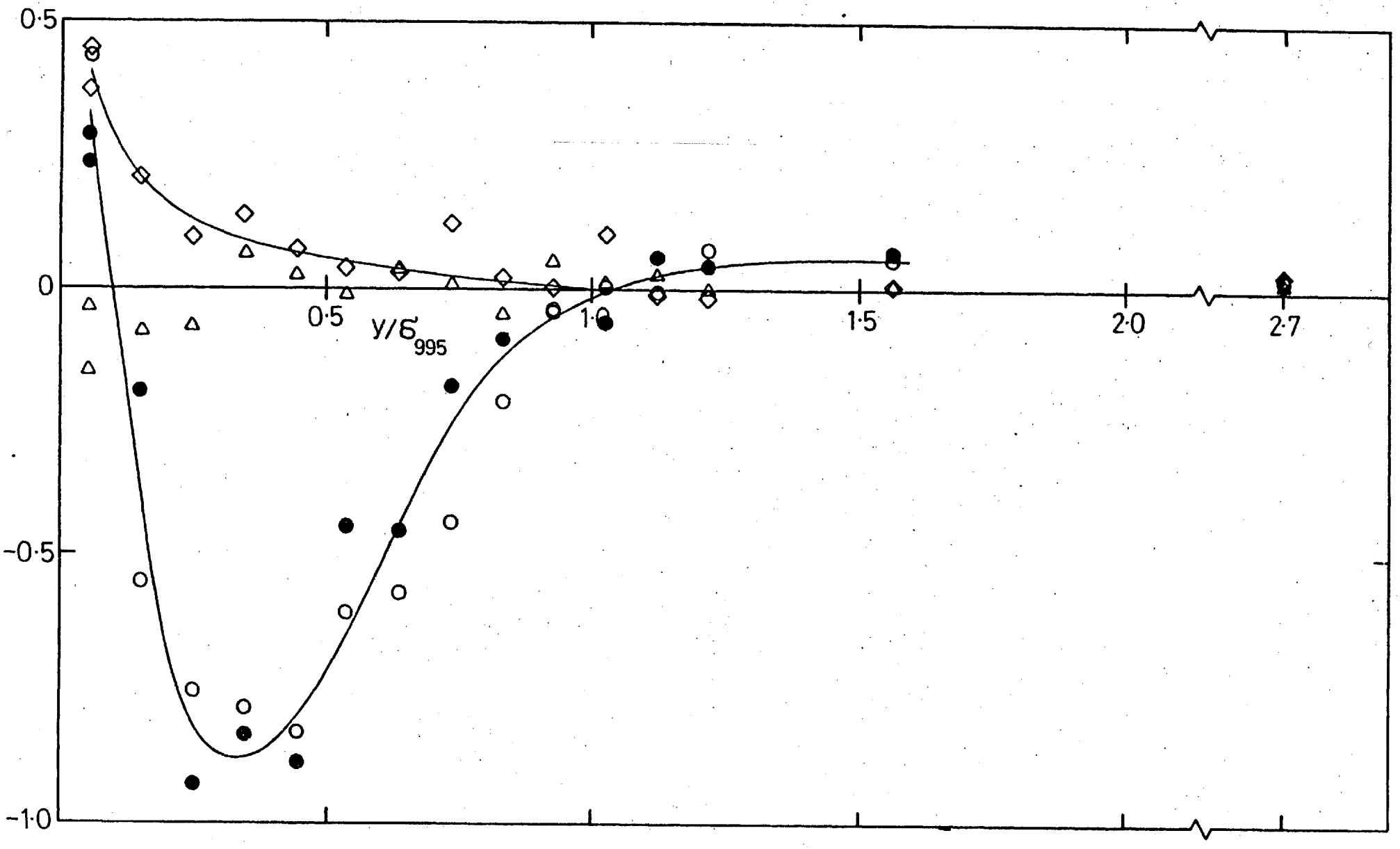

Fig. 4.11f, $\overline{u^3}$, $\overline{u^2w}$, $\overline{w^3}$; 15.2 cm grid, X_{LE} = 2.06 m, stn 8. $(u'/U)_e$ = 0.0442, L^u_e/δ_{995} = 2.23. Symbols as in a).

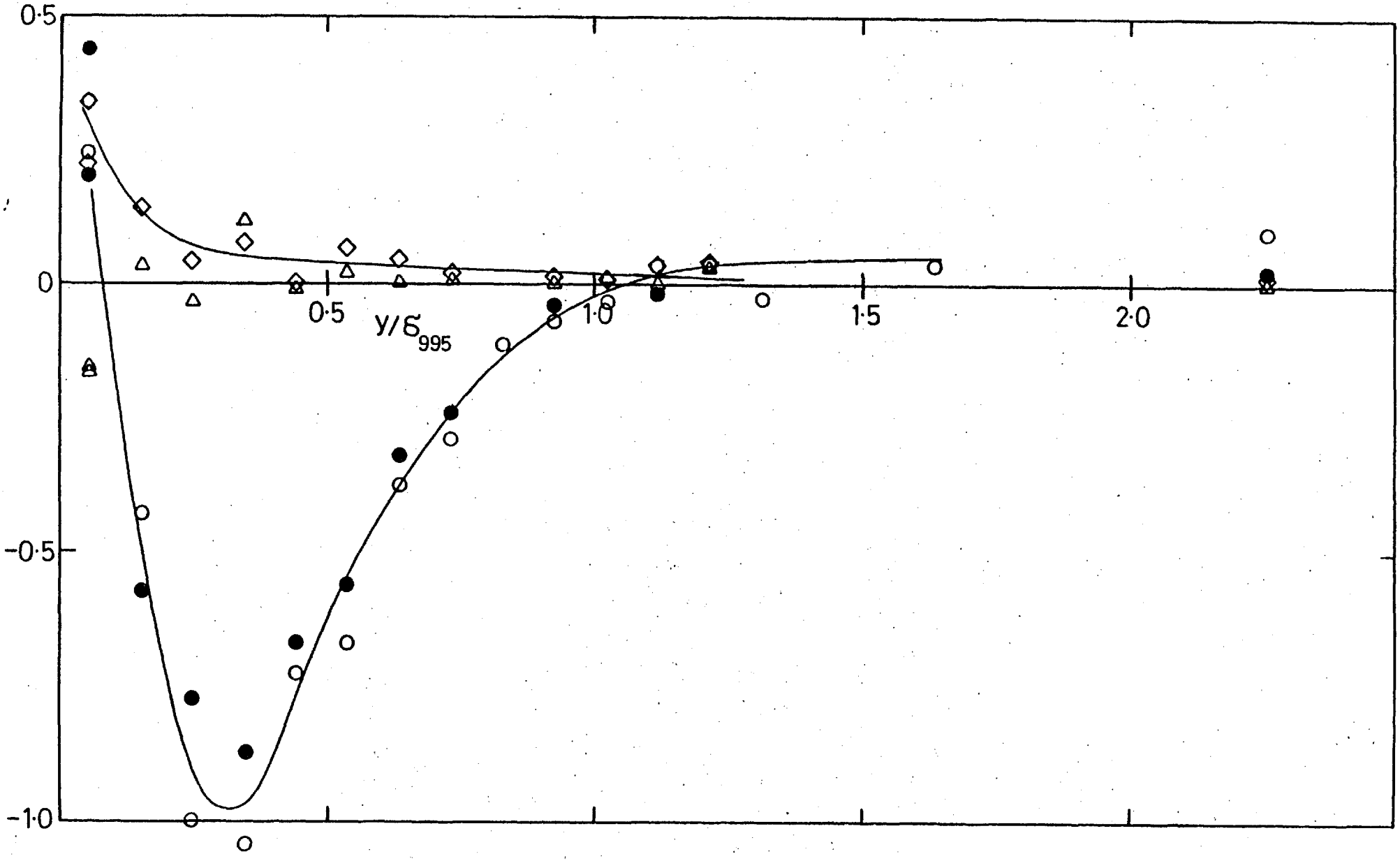

Fig. 4.11g, $\overline{u^3}$, $\overline{u^2w}$, $\overline{w^3}$; 15.2 cm grid, X_{LE} = 2.06 m, stn 10. $(u'/U)_e$ = 0.0410, L^u_e/δ_{995} = 1.90. Symbols as in a).

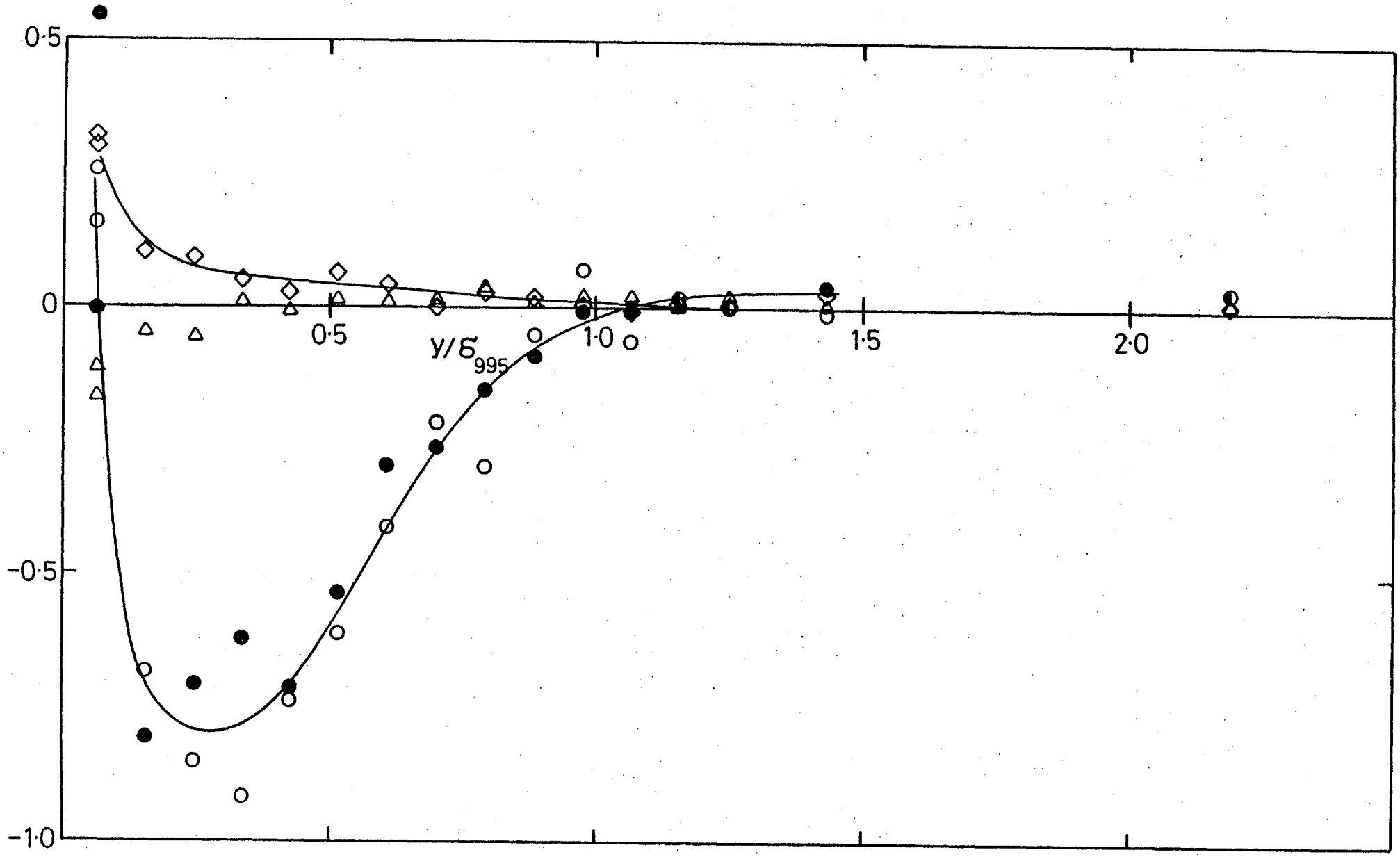

Fig. 4.11h, $\overline{u^3}$, $\overline{u^2w}$, $\overline{w^3}$; 15.2 cm grid, X_{LE} = 2.06 m, stn 12. $(u'/U)_e$ = 0.0387, L^u_e/δ_{995} = 1.70. Symbols as in a).

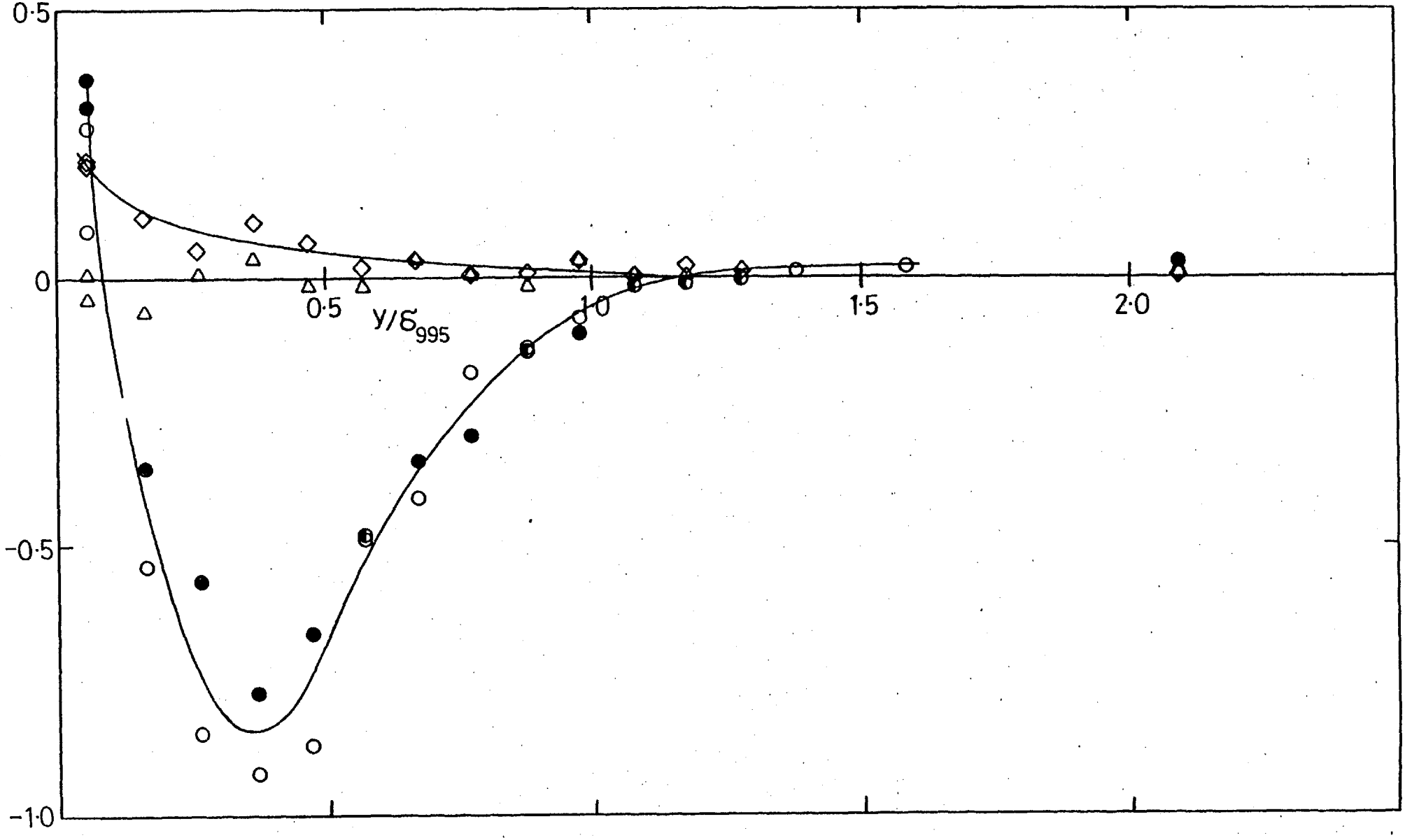

Fig. 4.11i, $\overline{u^3}$, $\overline{u^2w}$, $\overline{w^3}$; 15.2 cm grid, X_{LE} = 2.06 m, stn 14. $(u'/U)_e$ = 0.0362, L^u_e/δ_{995} = 1.69. Symbols as in a).

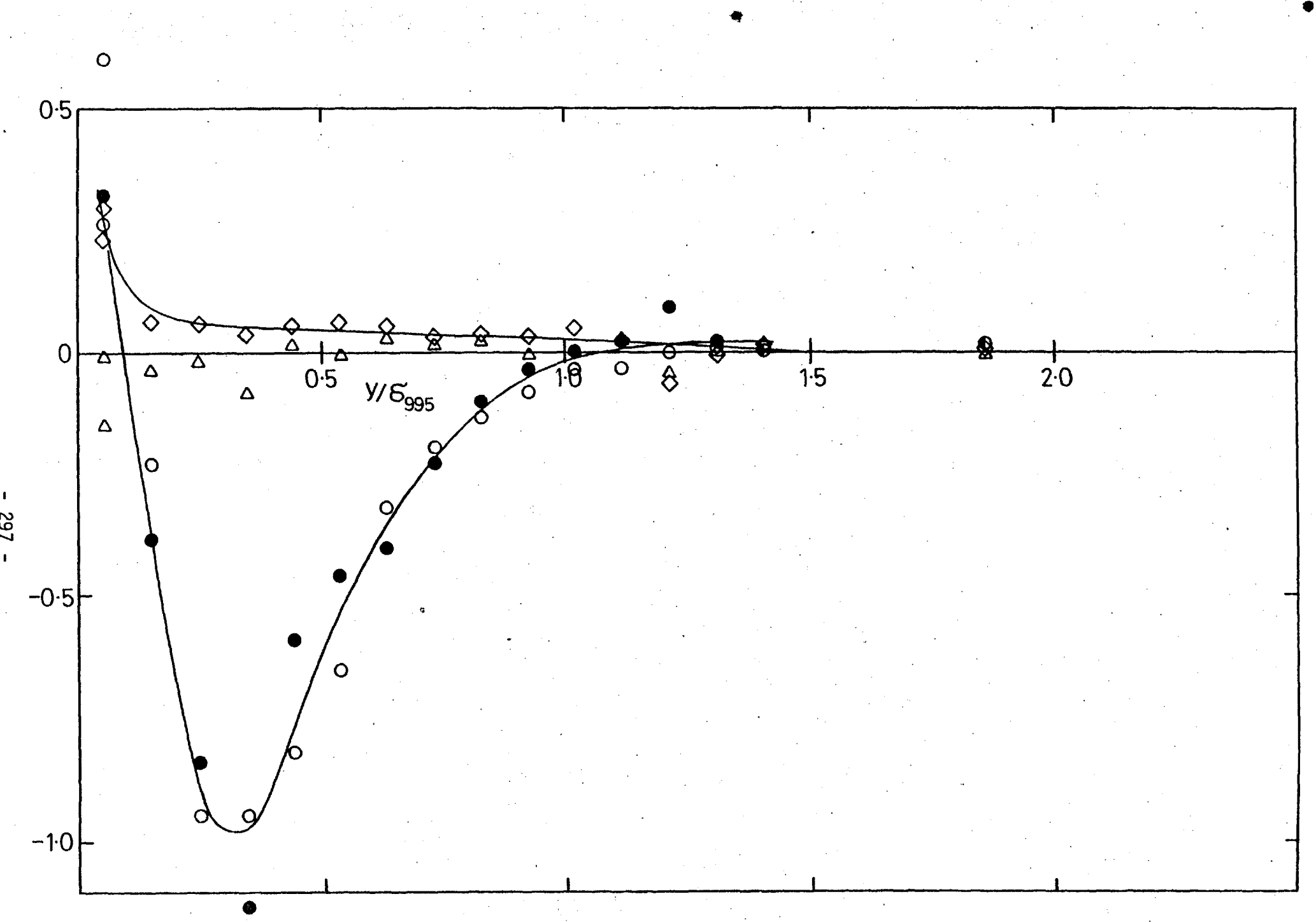

Fig. 4.11j, $\overline{u^3}$, $\overline{u^2w}$, $\overline{w^3}$; 15.2 cm grid, X_{LE} = 2.06 m, stn 16. $(u'/U)_e$ = 0.0345, L_e^u/δ_{995} = 2.72. Symbols as in a).

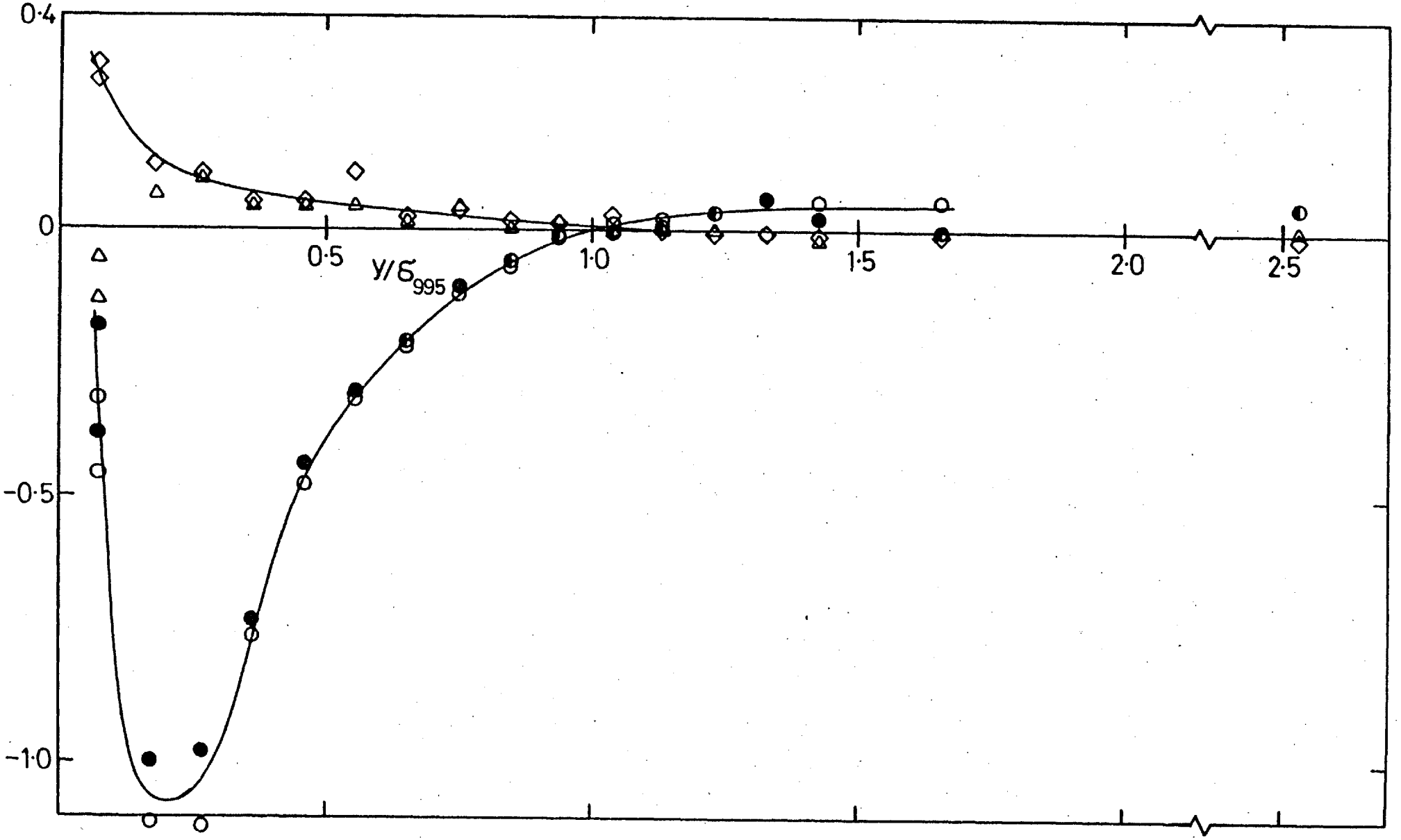

Fig. 4.11k, $\overline{u^3}$, $\overline{u^2w}$, $\overline{w^3}$; 7.6 cm grid, X_{LE} = 0.30 m, stn 8. $(u'/U)_e$ = 0.0399, L^u_e/δ_{995} = 0.71. Symbols as in a).

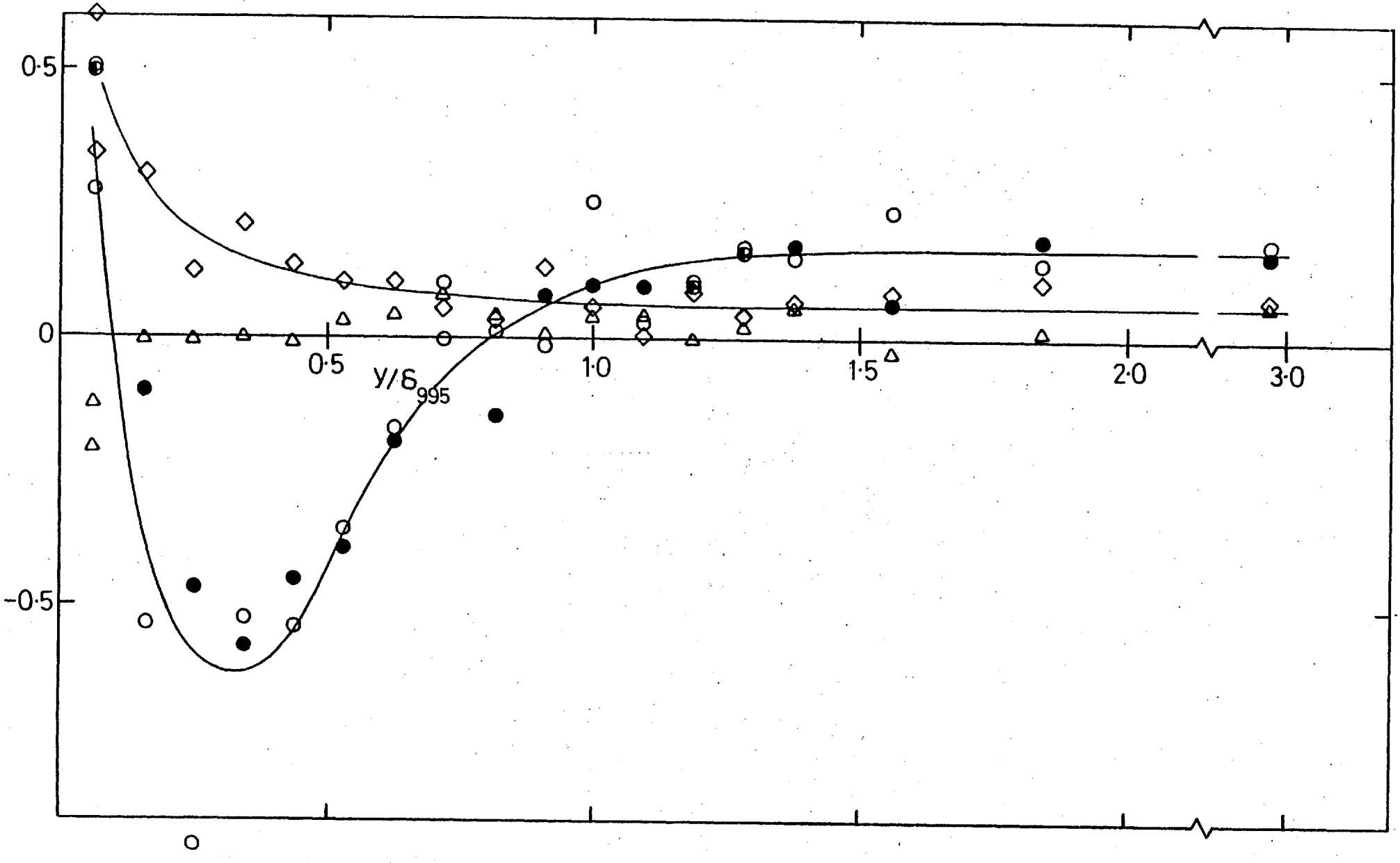

Fig. 4.11ℓ, $\overline{u^3}$, $\overline{u^2w}$, $\overline{w^3}$; 15.2 cm grid, X_{LE} = 1.37 m, stn 6. $(u'/U)_e$ = 0.0575, L^u_e/δ_{995} = 1.83. Symbols as in a).

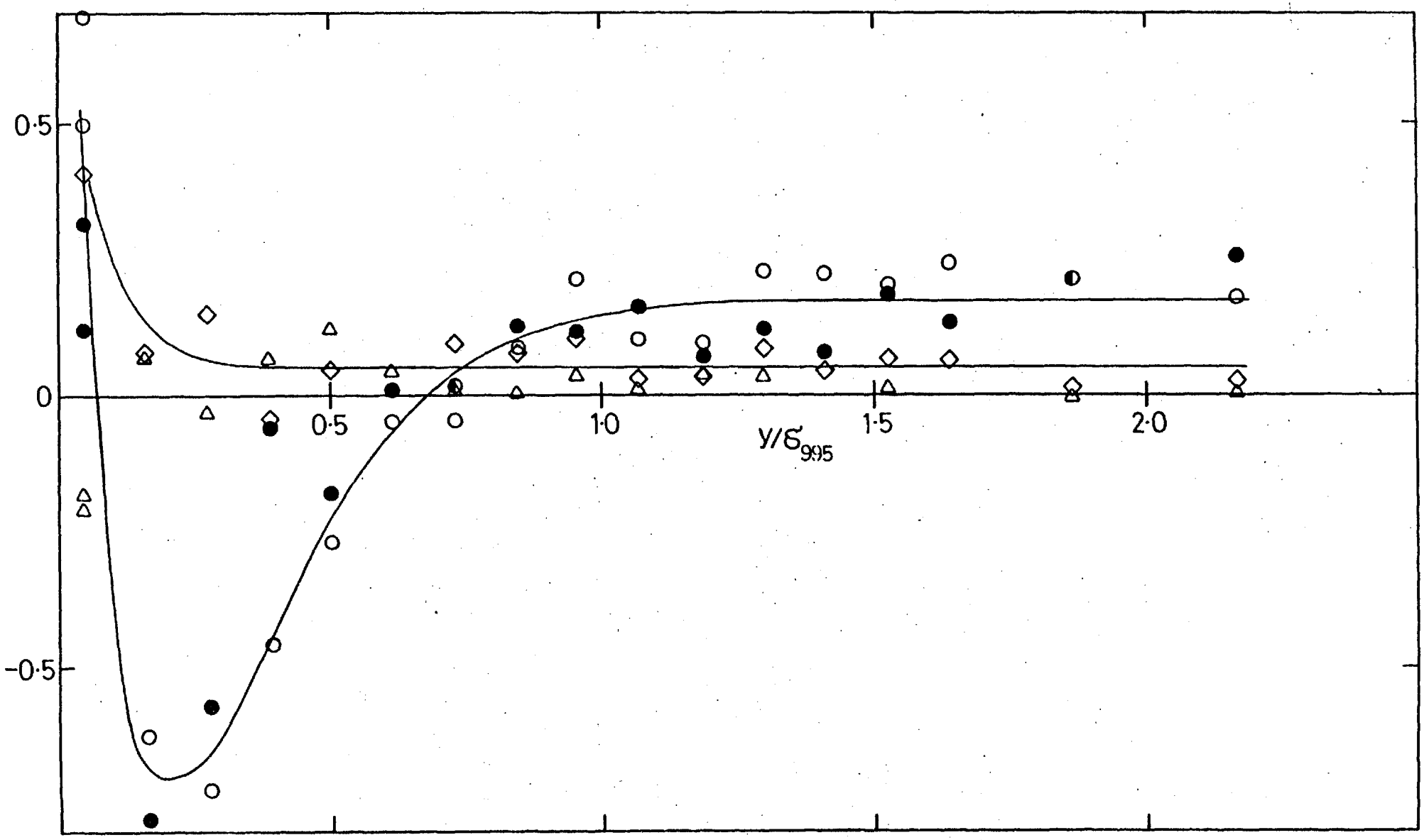

Fig. 4.11m, $\overline{u^3}$, $\overline{u^2w}$, $\overline{w^3}$; 15.2 cm grid, X_{LE} = 0.76 m, stn 10. $(u'/U)_e$ = 0.0575, L_e^u/δ_{995} = 1.34. Symbols as in a).

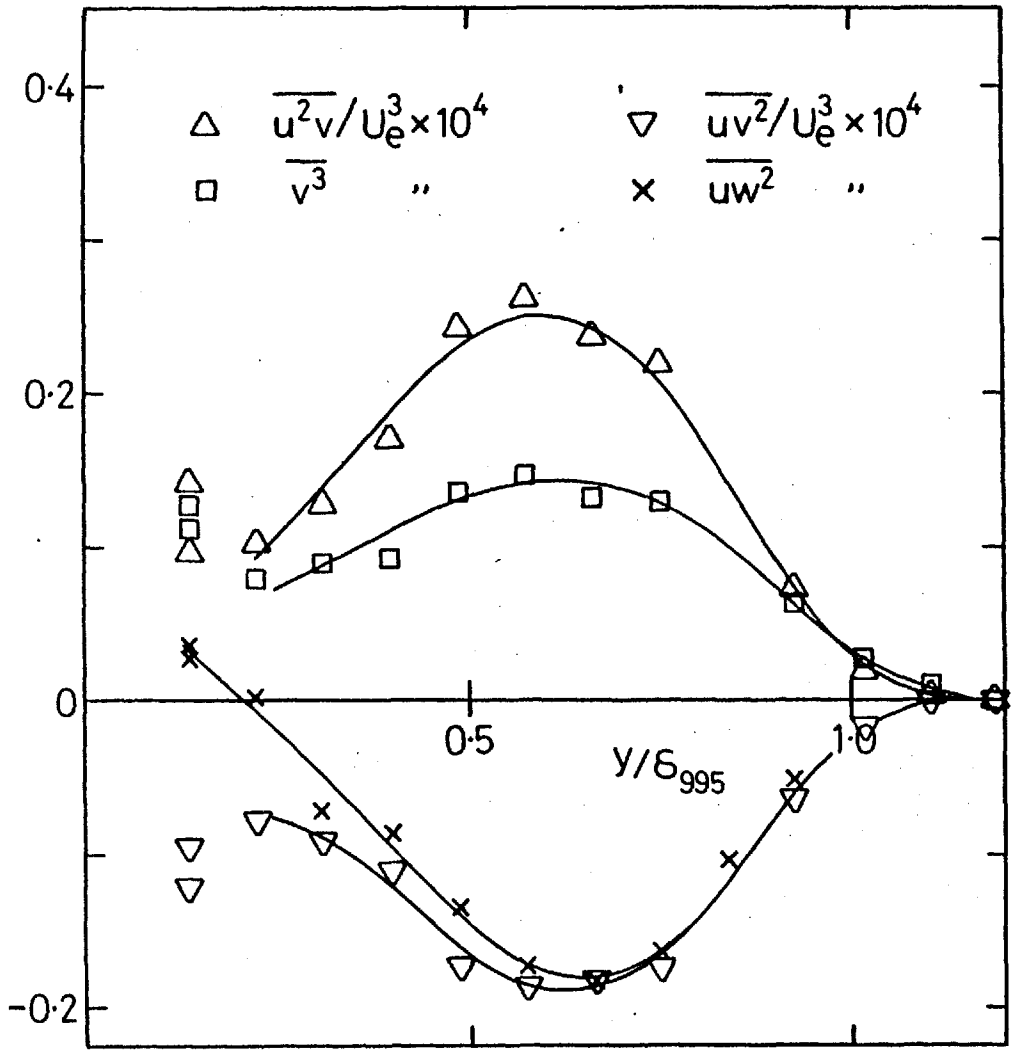

a) No grid, stn 6.

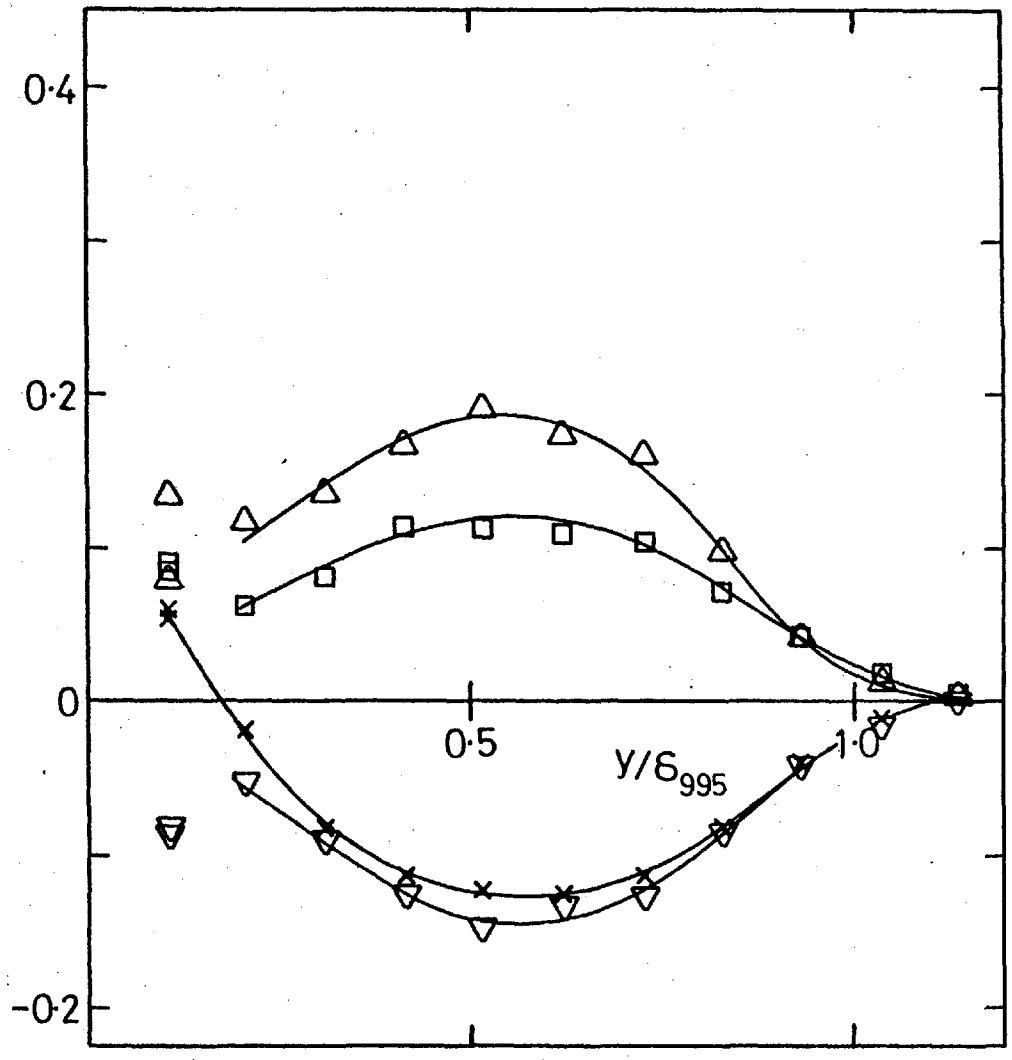

b) No grid, stn 14. Symbols as in a).

Fig. 4.12 Third-order products $\overline{v^3}$, $\overline{u^2v}$, $\overline{uv^2}$, $\overline{uw^2}$;

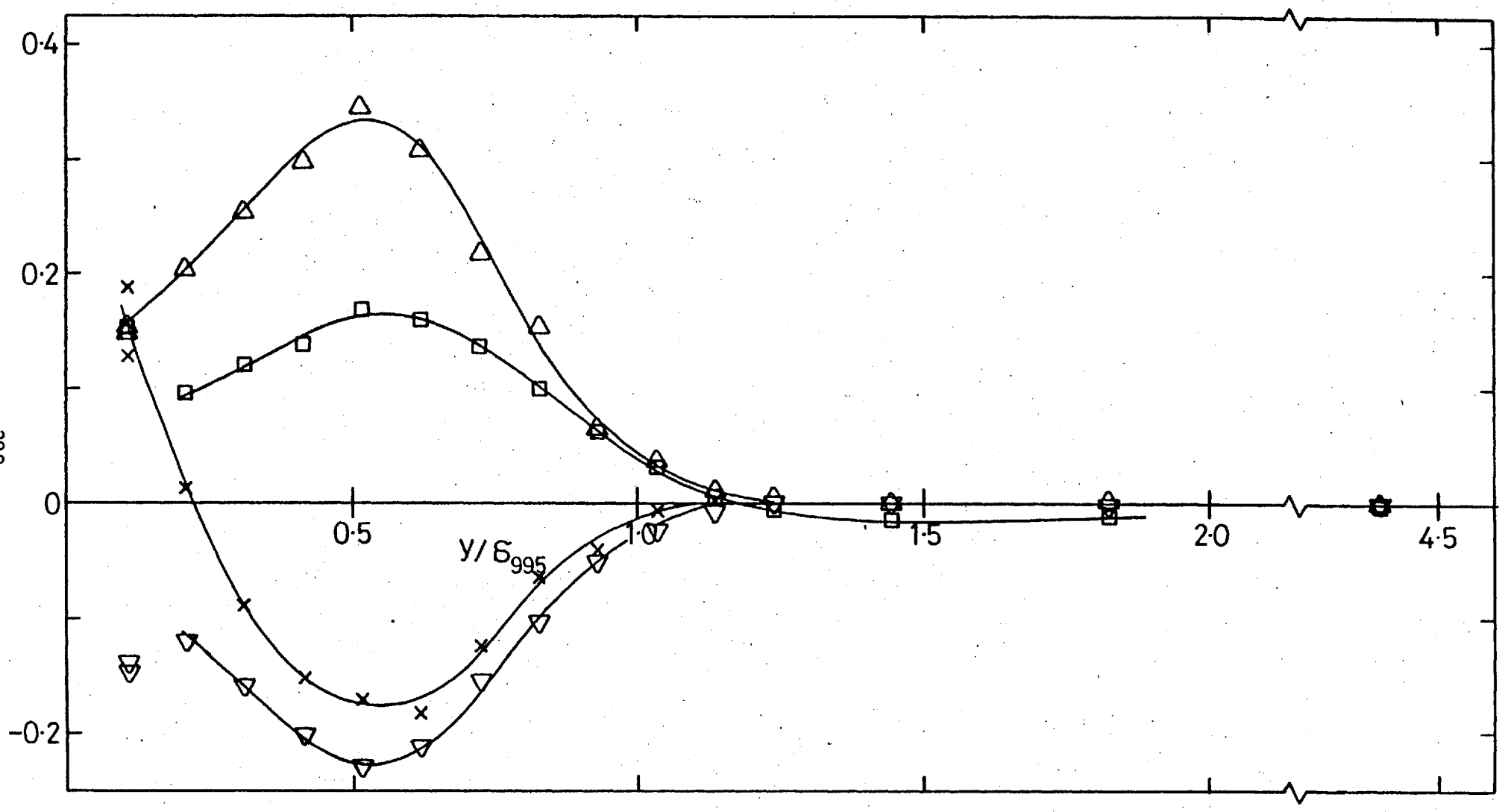

Fig. 4.12c, $\overline{v^3}$, $\overline{u^2v}$, $\overline{uv^2}$, $\overline{vw^3}$; 7.6 cm grid, X_{LE} = 2.06 m, stn 6. $(u'/U)_e$ = 0.0240, L^u_e/δ_{995} = 1.88. Symbols as in a).

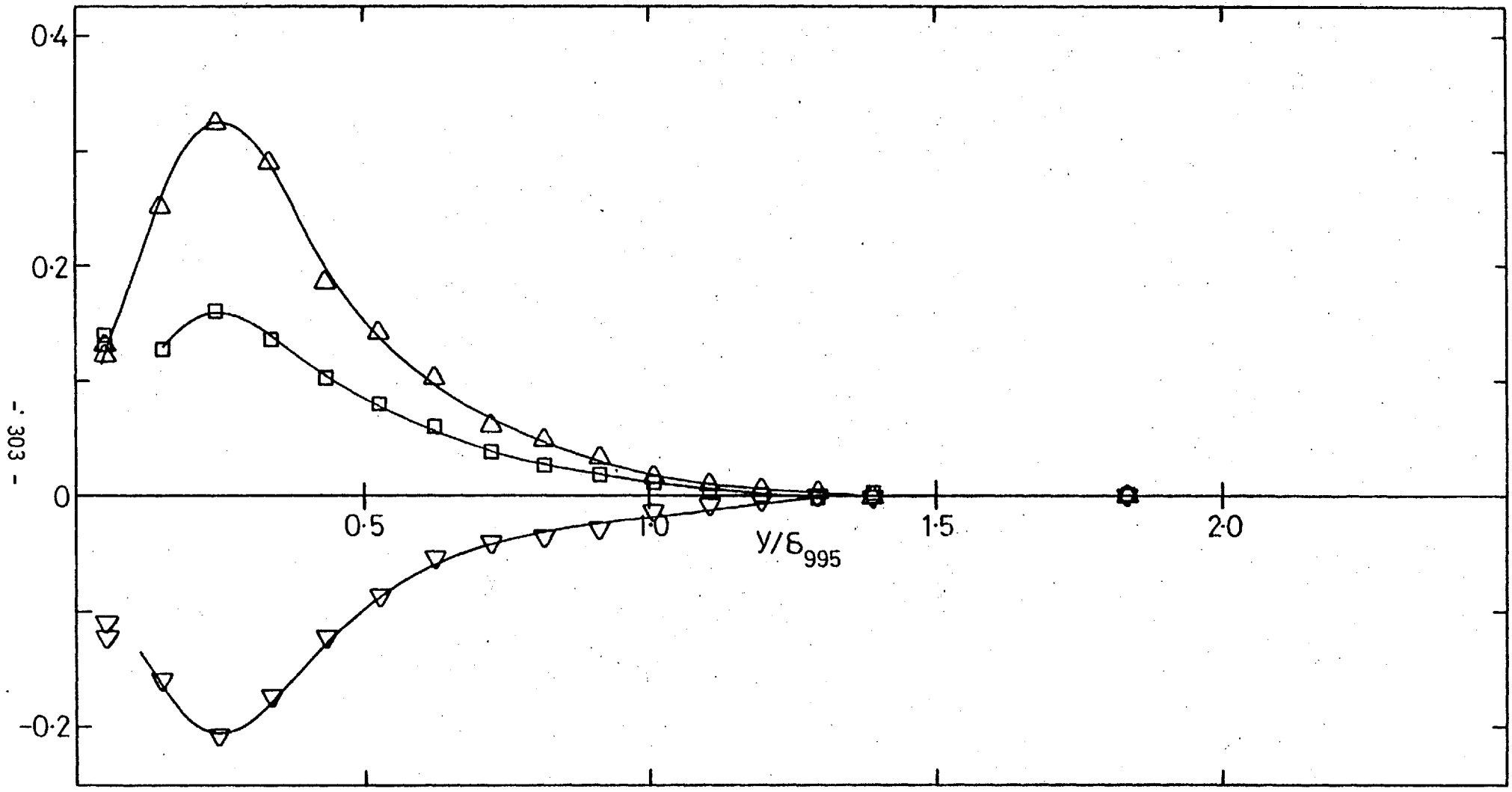

Fig. 4.12d, $\overline{v^3}$, $\overline{u^2v}$, $\overline{uv^2}$; 7.6 cm grid, X_{LE} = 0.30 m, stn 16. $(u'/U)_e$ = 0.0255, L^u_e/δ_{995} = 0.67. Symbols as in a).

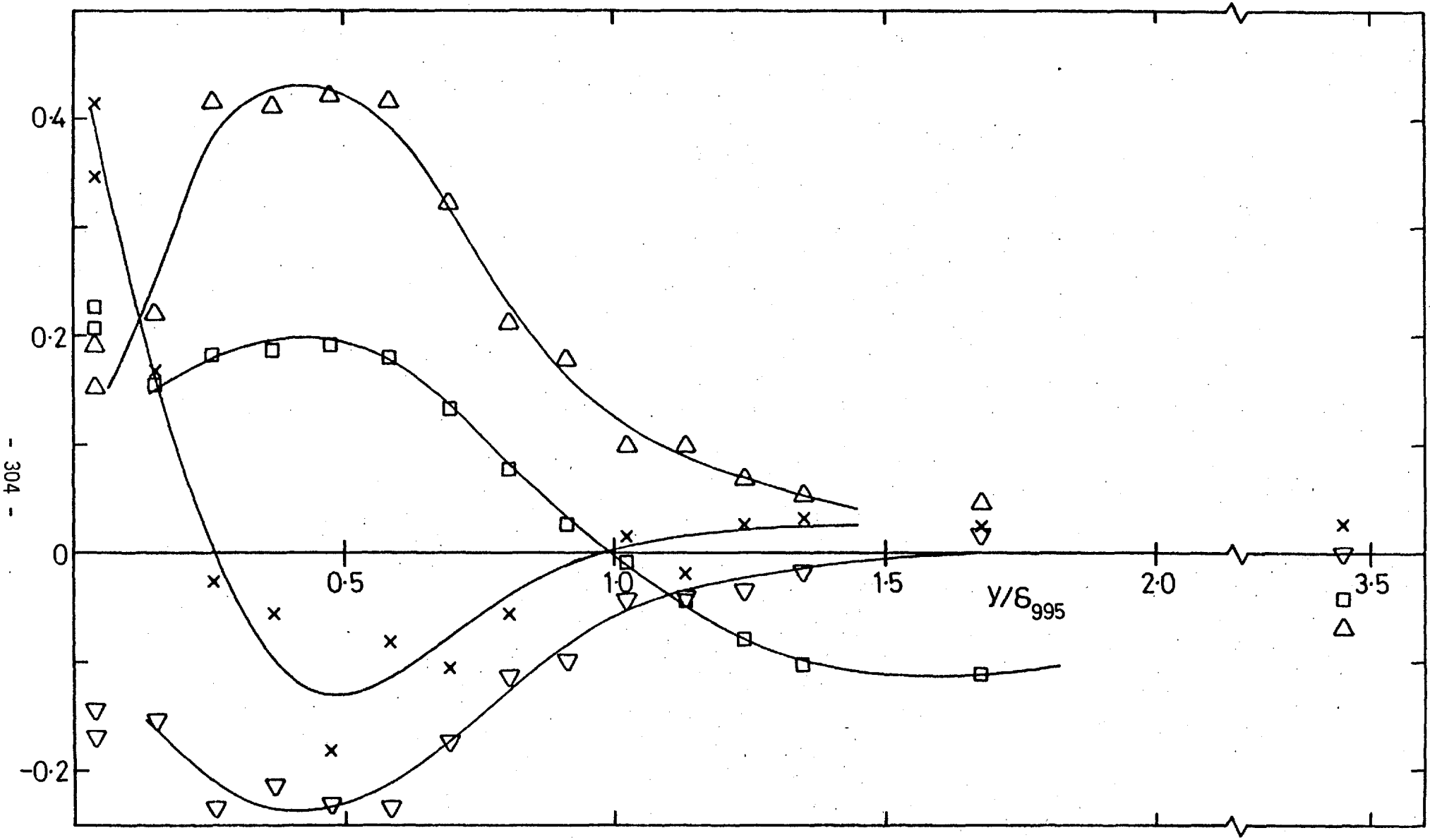

Fig. 4.12e, $\overline{v^3}$, $\overline{u^2v}$, $\overline{uv^2}$, $\overline{uw^2}$; 15.2 cm grid, X_{LE} = 2.06 m, stn 6. $(u'/U)_e$ = 0.0468, L_e^u/δ_{995} = 2.72. Symbols as in a).

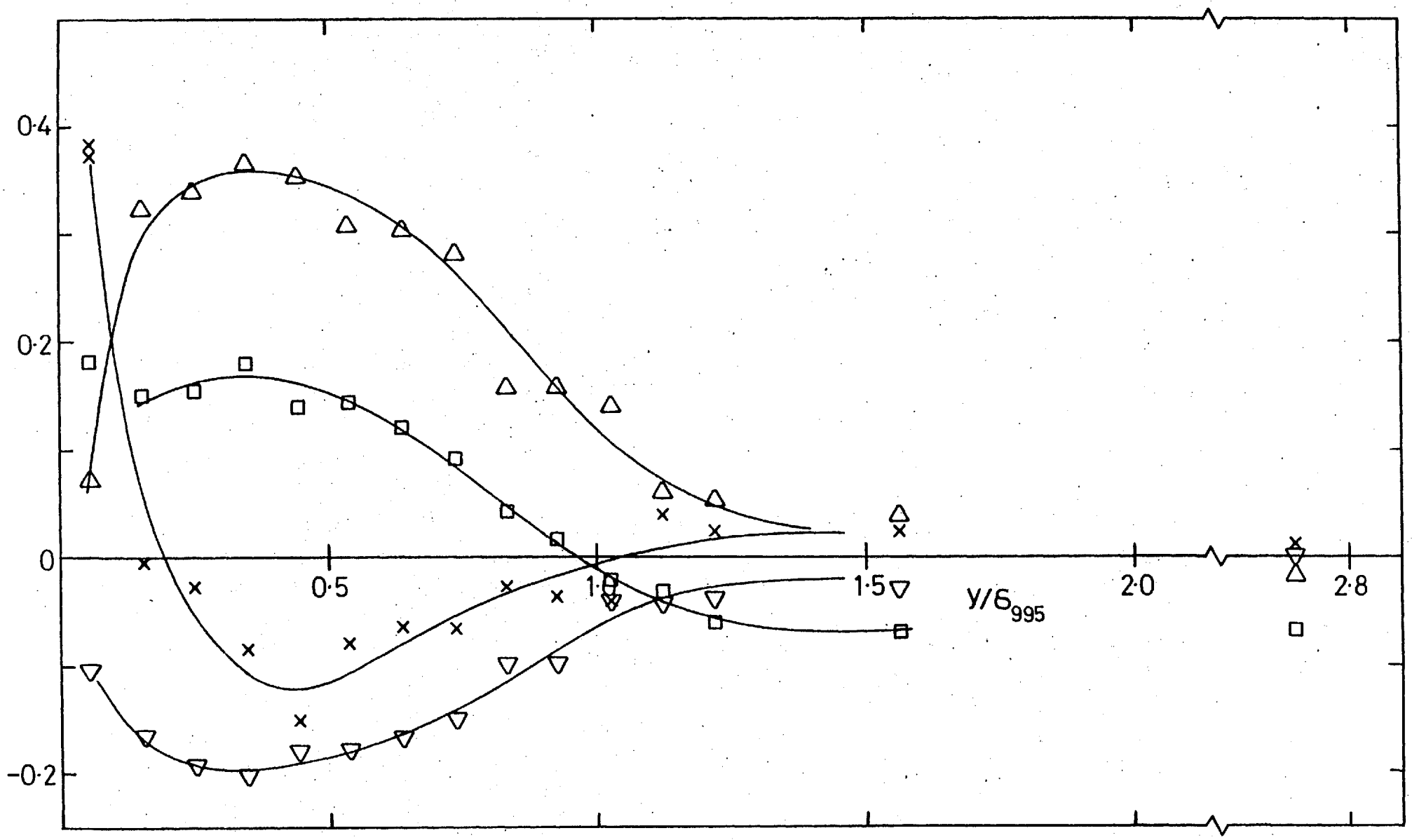

Fig. 4.12f, $\overline{v^3}$, $\overline{u^2v}$, $\overline{uv^2}$, $\overline{uw^2}$; 15.2 cm grid, X_{LE} = 2.06 m, stn 8. $(u'/U)_e$ = 0.0442, L^u_e/δ_{995} = 2.23. Symbols as in a).

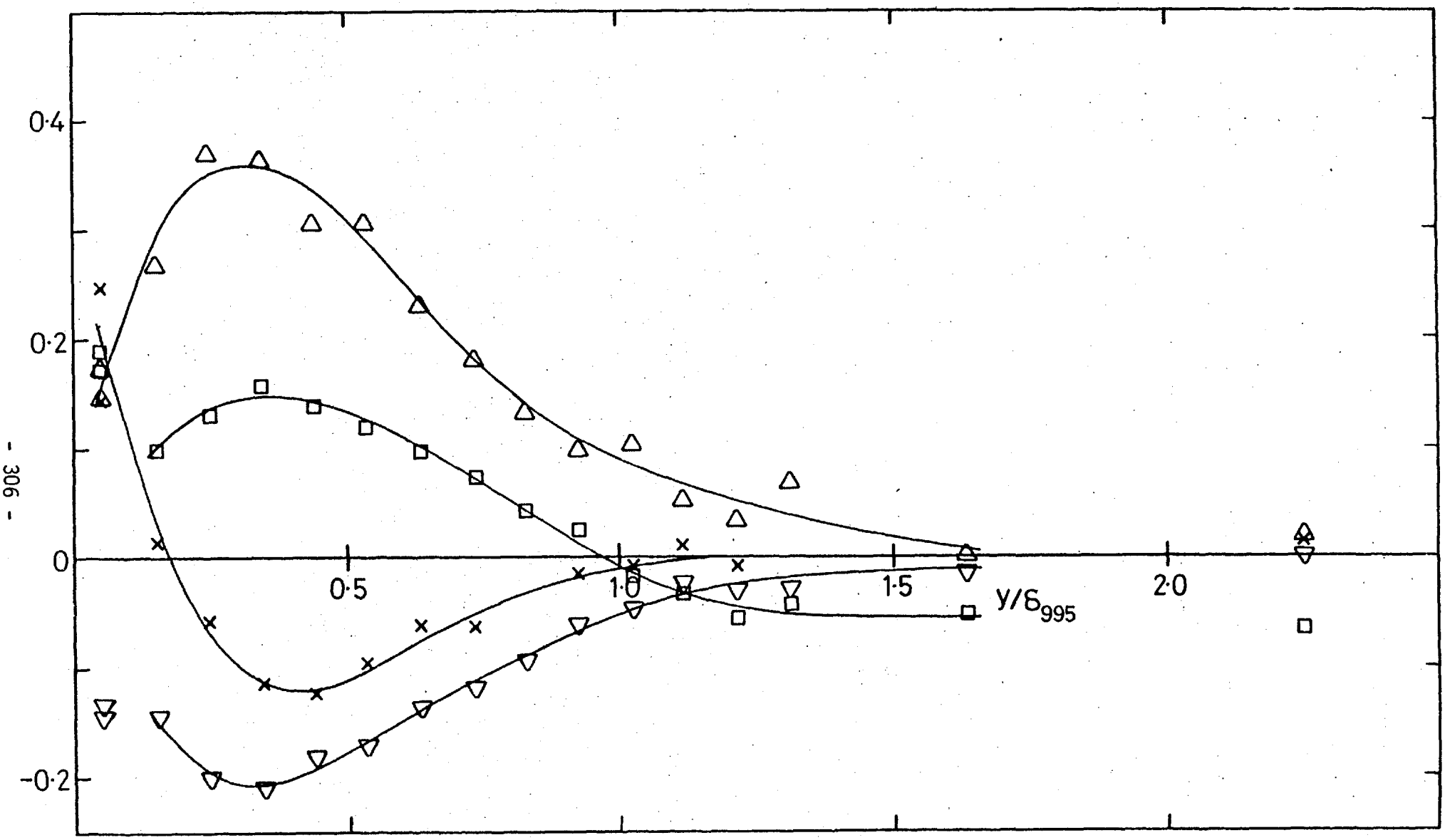

Fig. 4.12g, $\overline{v^3}$, $\overline{u^2v}$, $\overline{uv^2}$, $\overline{uw^2}$; 15.2 cm grid, X_{LE} = 2.06 m, stn 10. $(u'/U)_e$ = 0.0410, L^u_e/δ_{995} = 1.90. Symbols as in a).

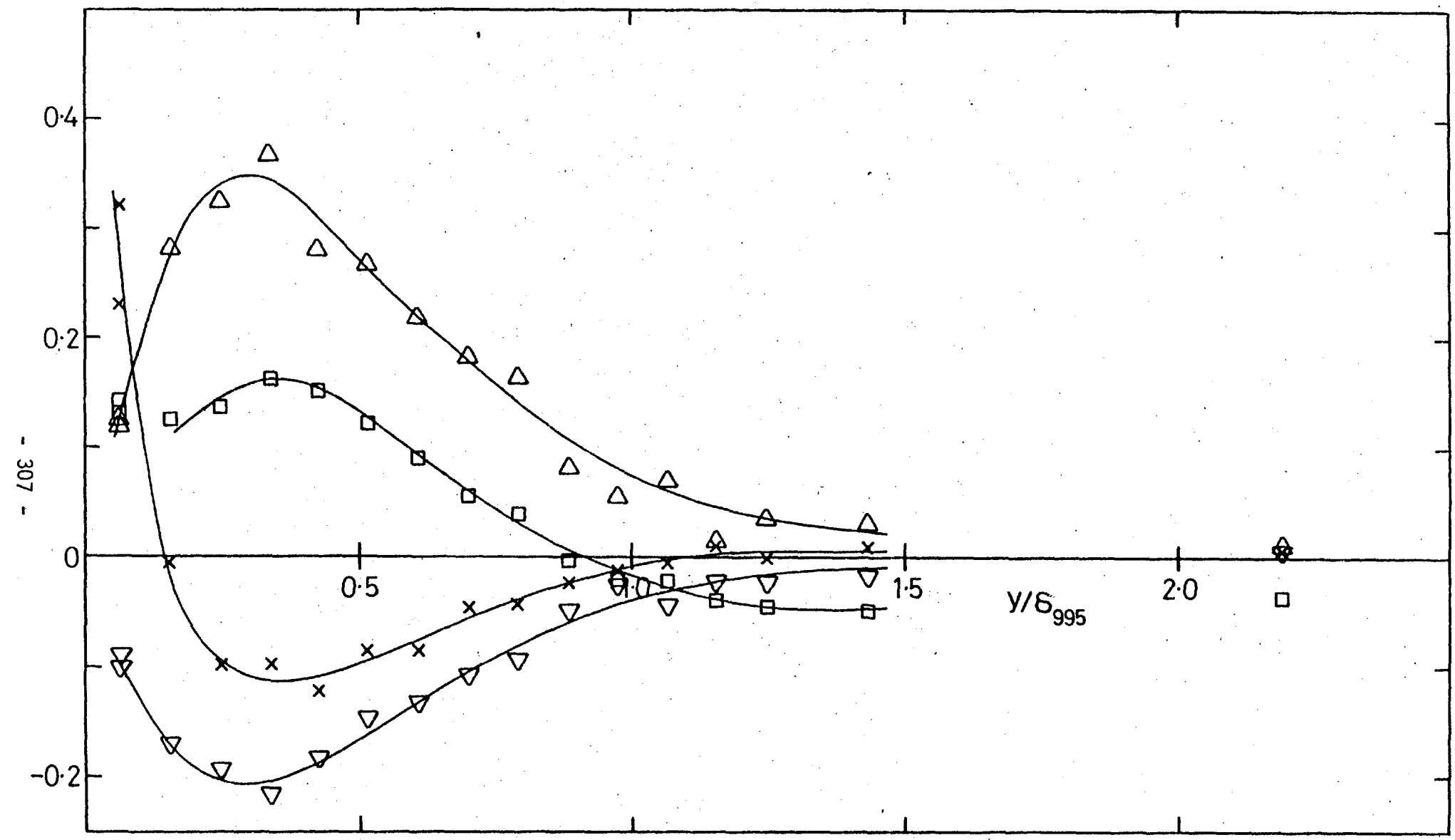

Fig. 4.12h, $\overline{v^3}$, $\overline{u^2v}$, $\overline{uv^2}$, $\overline{uw^2}$; 15.2 cm grid, X_{LE} = 2.06 m, stn 12. $(u'/U)_e$ = 0.0387, L^u_e/δ_{995} = 1.70. Symbols as in a).

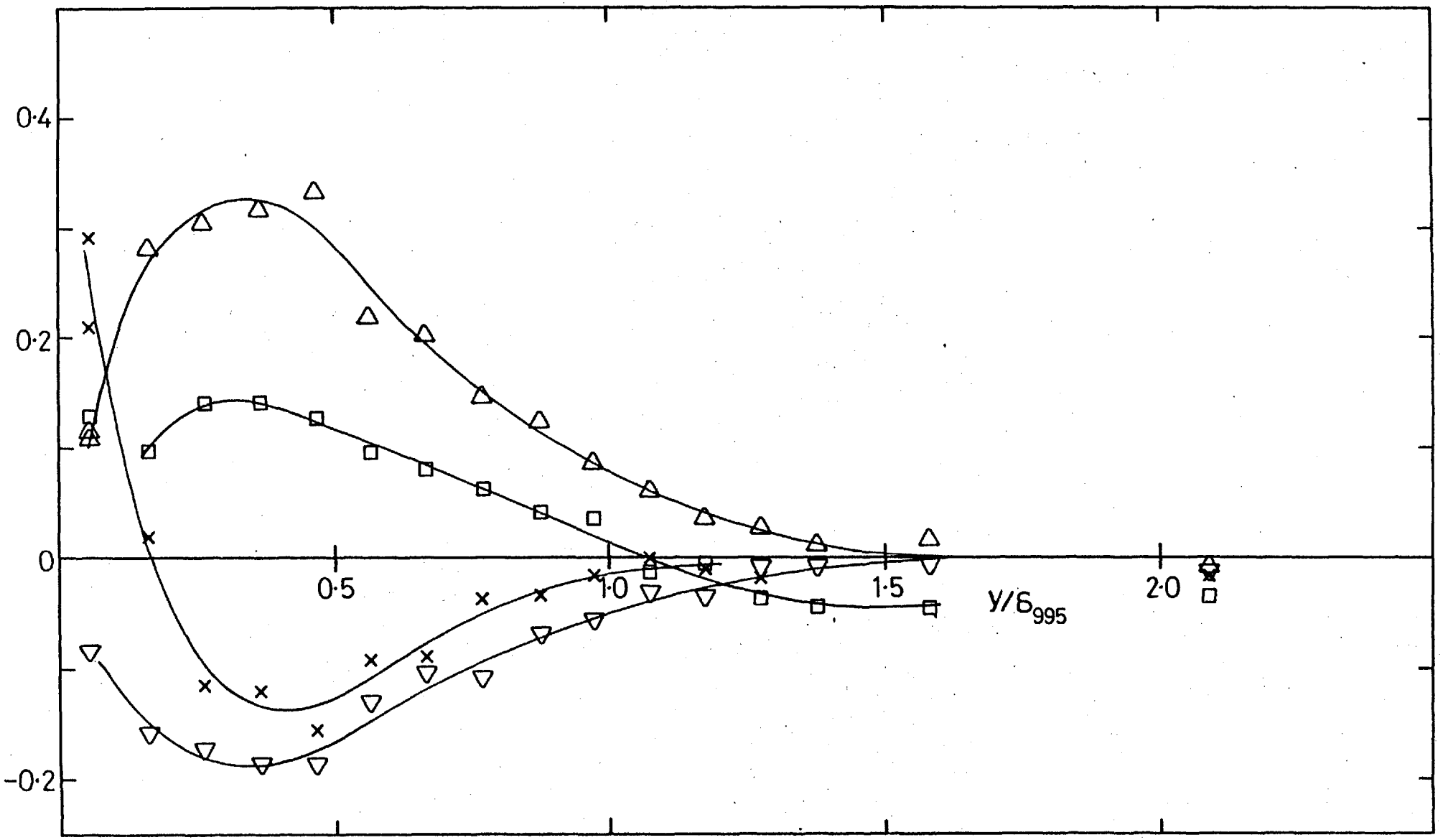

Fig. 4.12i, $\overline{v^3}$, $\overline{u^2v}$, $\overline{uv^2}$, $\overline{uw^2}$; 15.2 cm grid, X_{LE} = 2.06 m, stn 14. $(u'/U)_e$ = 0.0362, L^u_e/δ_{995} = 1.69. Symbols as in a).

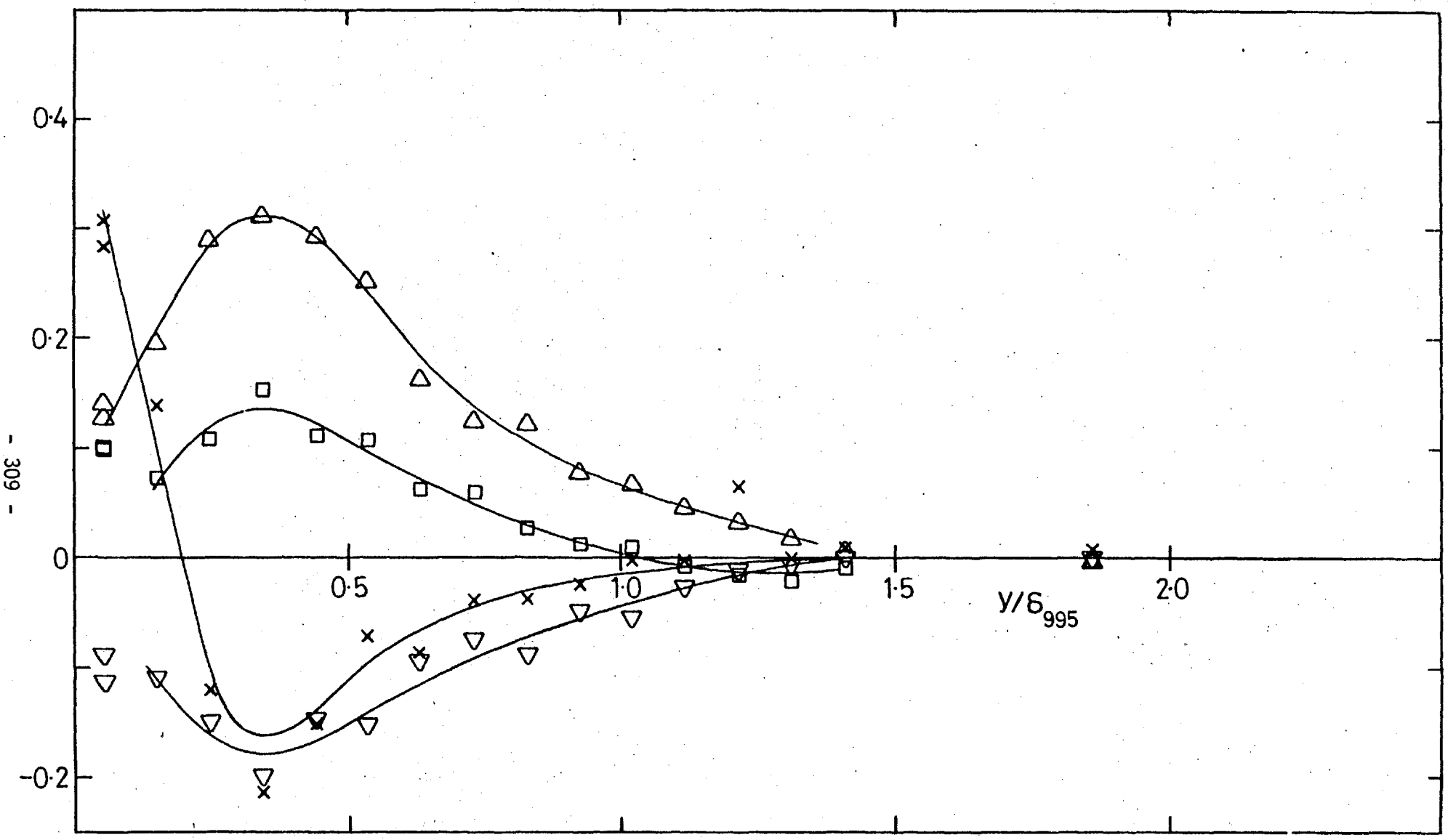

Fig. 4.12j, $\overline{v^3}$, $\overline{u^2v}$, $\overline{uv^2}$, $\overline{uw^2}$; 15.2 cm grid, X_{LE} = 2.06 m, stn 16. $(u'/U)_e$ = 0.0345, L^u_e/δ_{995} = 1.55. Symbols as in a).

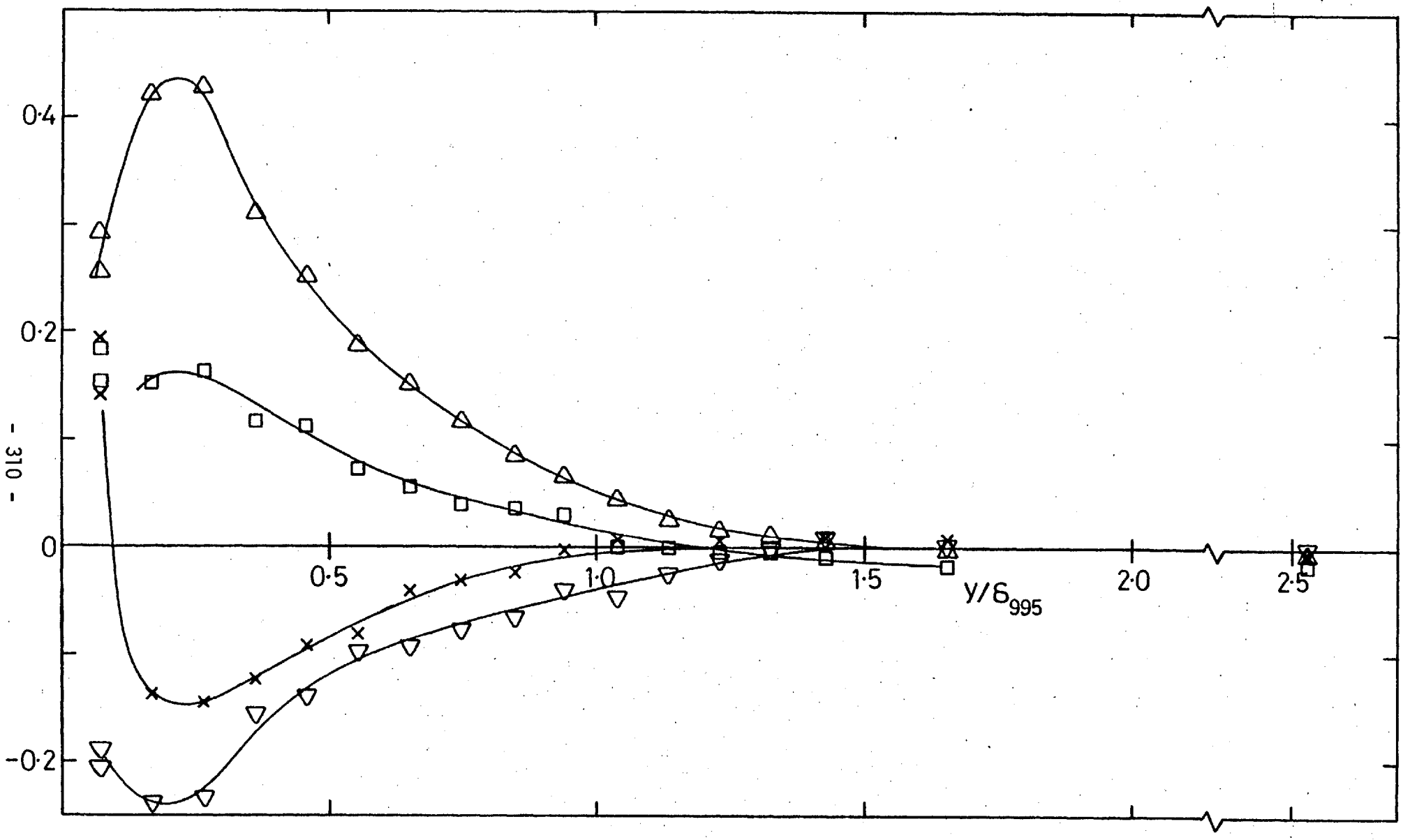

Fig. 4.12k, $\overline{v^3}$, $\overline{u^2v}$, $\overline{uv^2}$, $\overline{uw^3}$; 7.6 cm grid, X_{LE} = 0.30 m, stn 8. $(u'/U)_e$ = 0.0399, L^u_e/δ_{995} = 0.71. Symbols as in a).

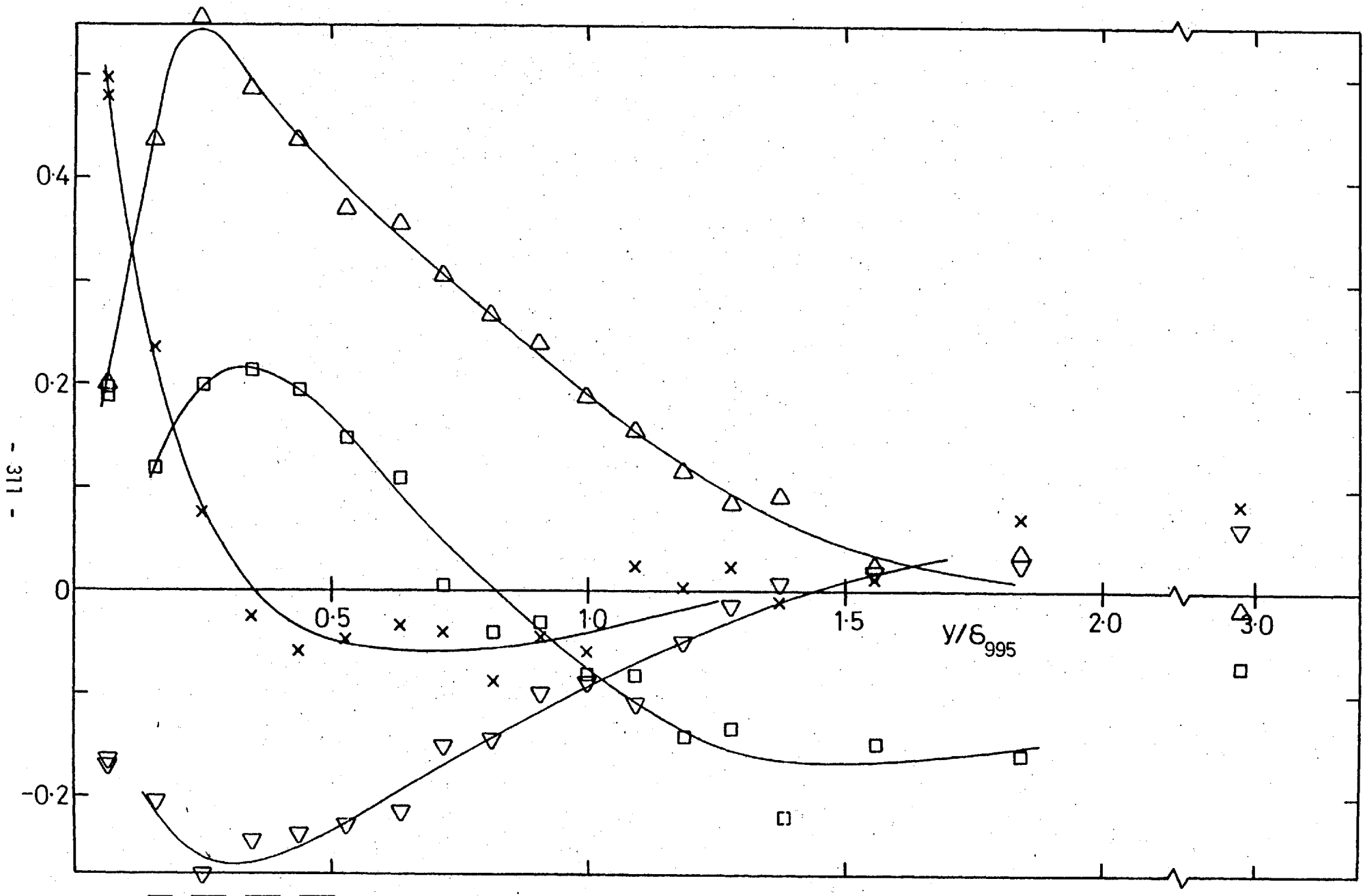

Fig. 4.12ℓ, $\overline{v^3}$, $\overline{u^2v}$, $\overline{uv^2}$, $\overline{uw^2}$; 15.2 cm grid, X_{LE} = 1.37 m, stn 6. $(u'/U)_e$ = 0.0575, L^u_e/δ_{995} = 1.83, Symbols as in a).

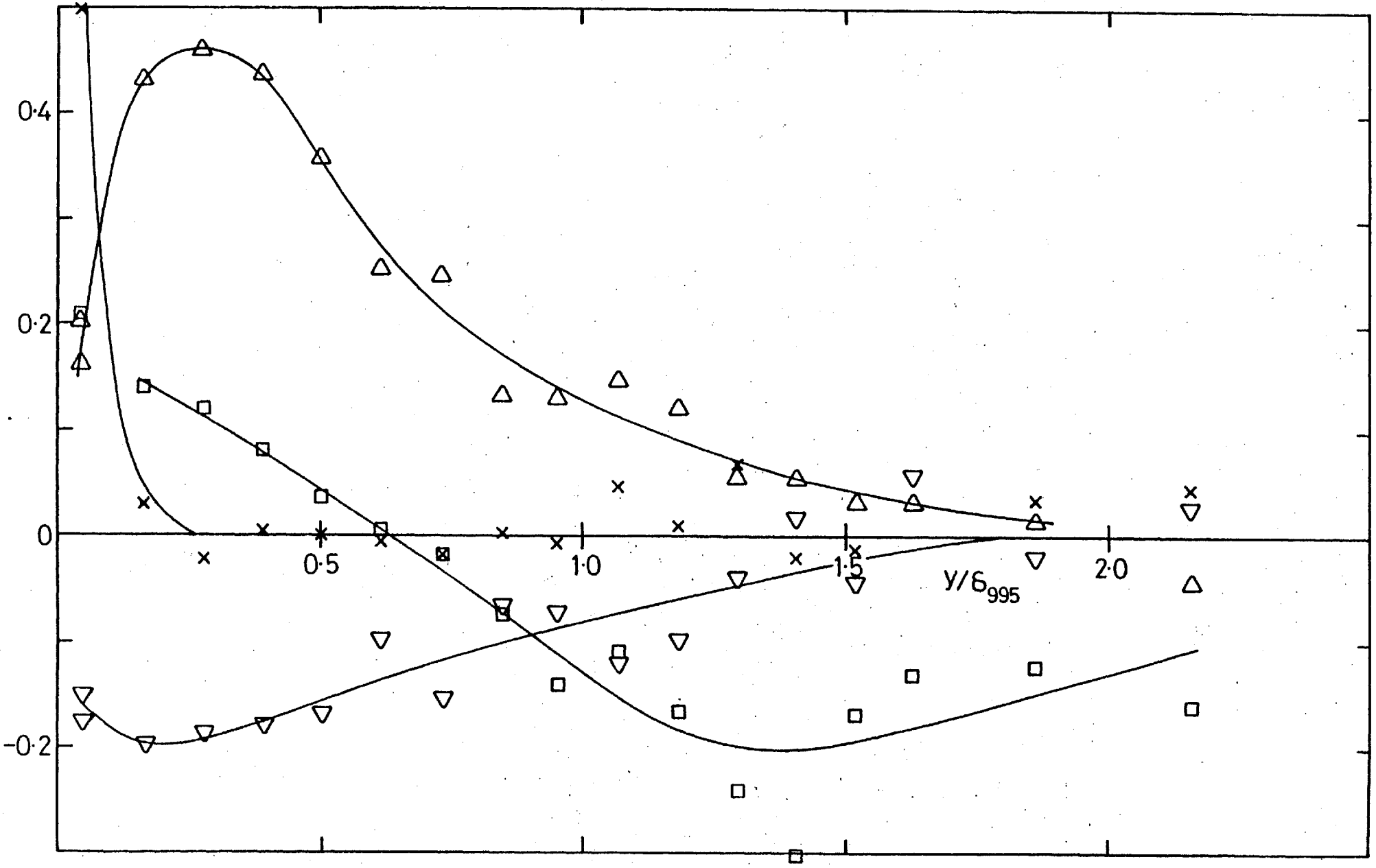

Fig. 4.12m, $\overline{v^3}$, $\overline{u^2v}$, $\overline{uv^2}$, $\overline{uw^2}$; 15.2 cm grid, X_{LE} = 0.76 m, stn 10. $(u'/U)_e$ = 0.0575, L^u_e/δ_{995} = 1.34. Symbols as in a).

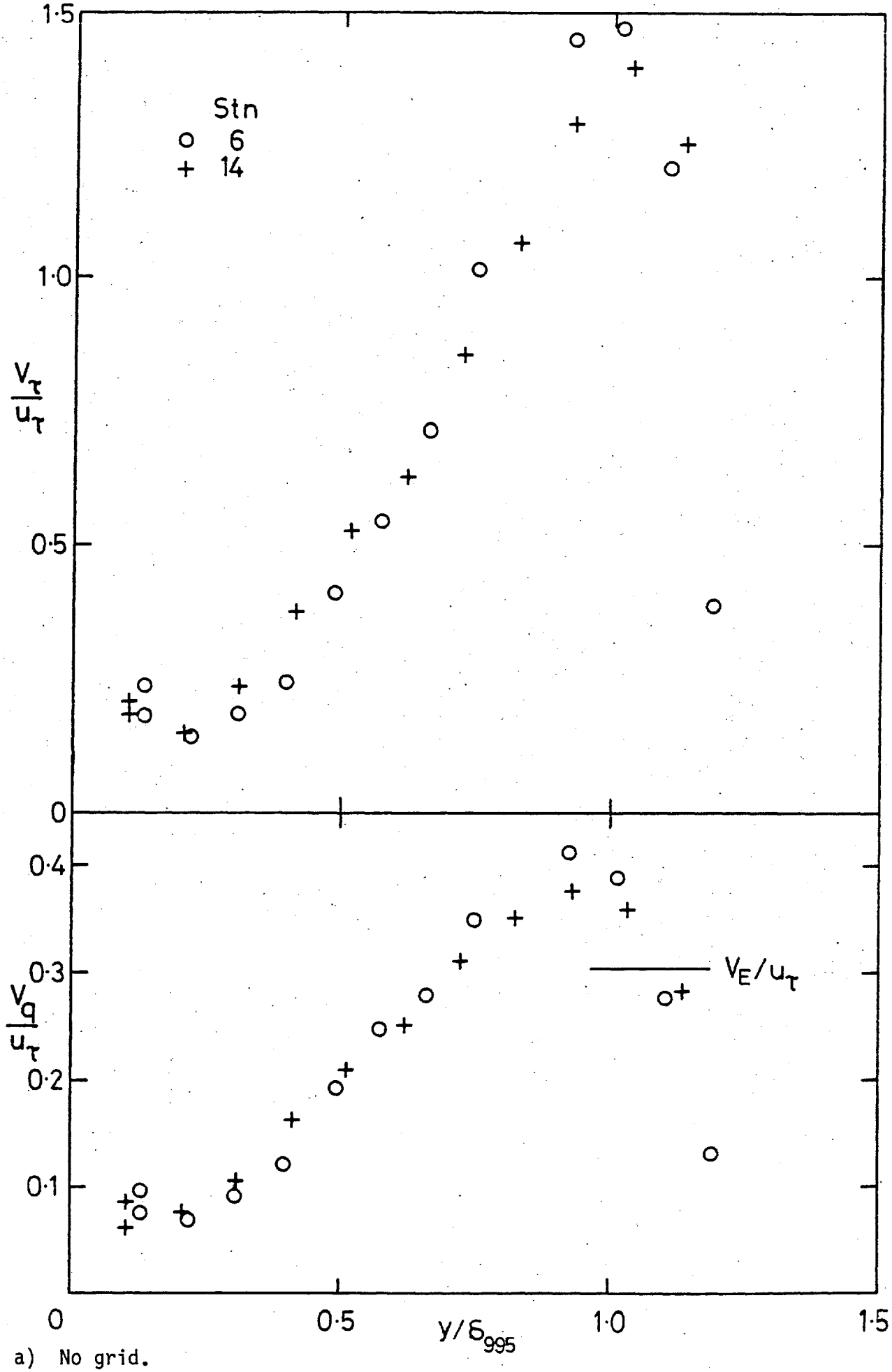

a) No grid.

Fig. 4.13 Transport velocities V_τ and V_q;

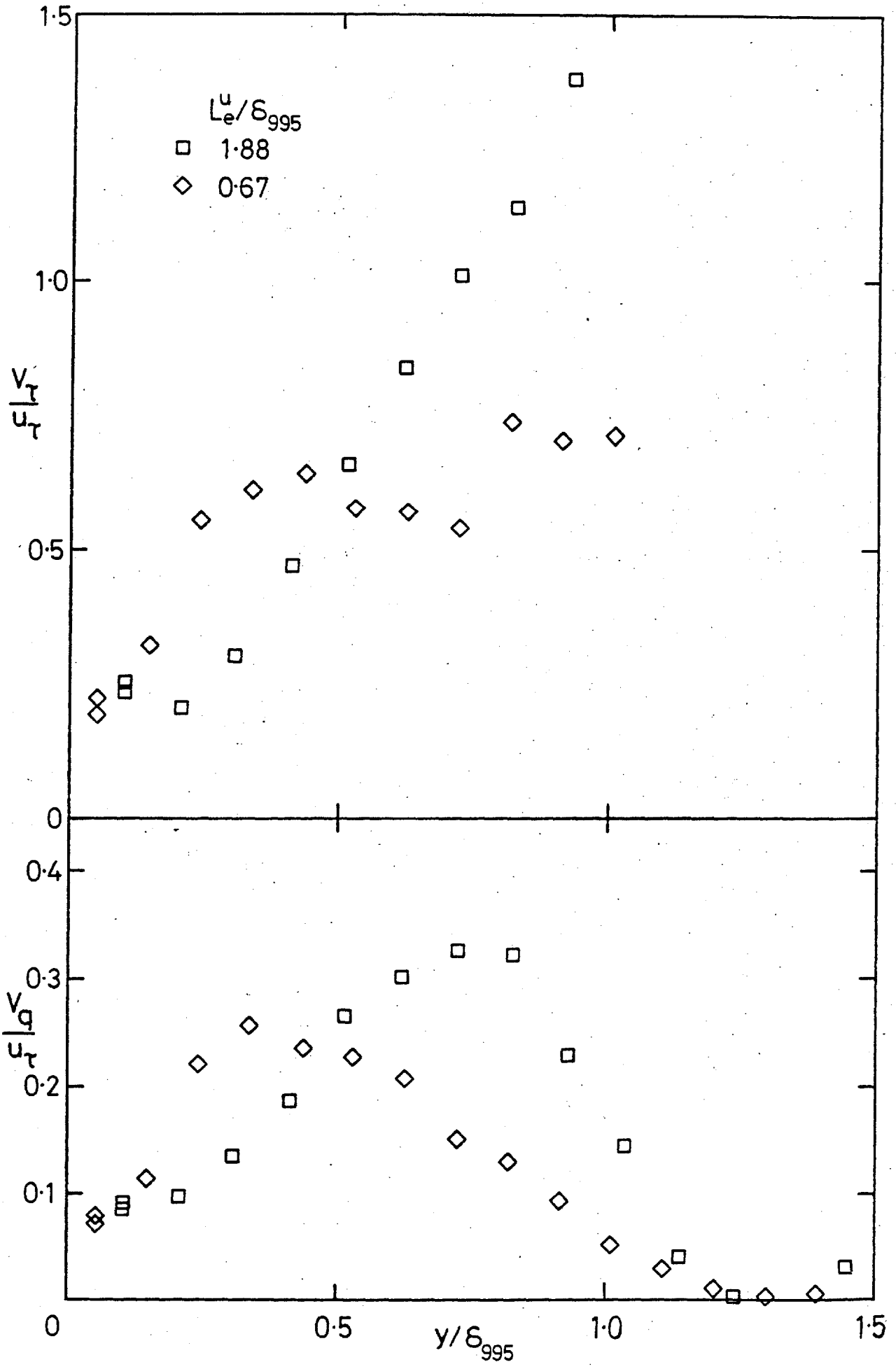

Fig. 4.13b, $(u'/U)_e \approx 0.025$.

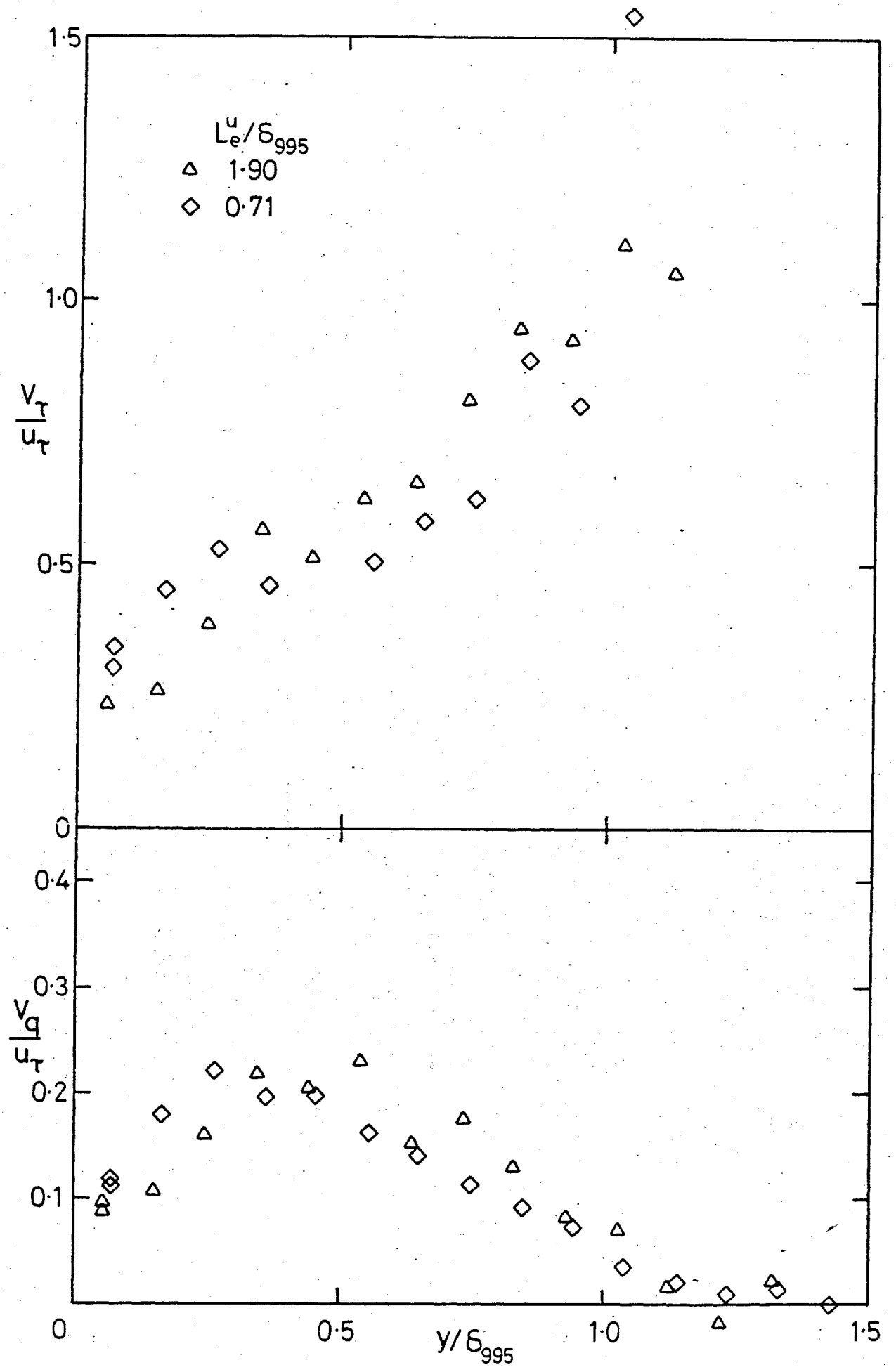

Fig. 4.13c, $(u'/U)_e \approx 0.040$.

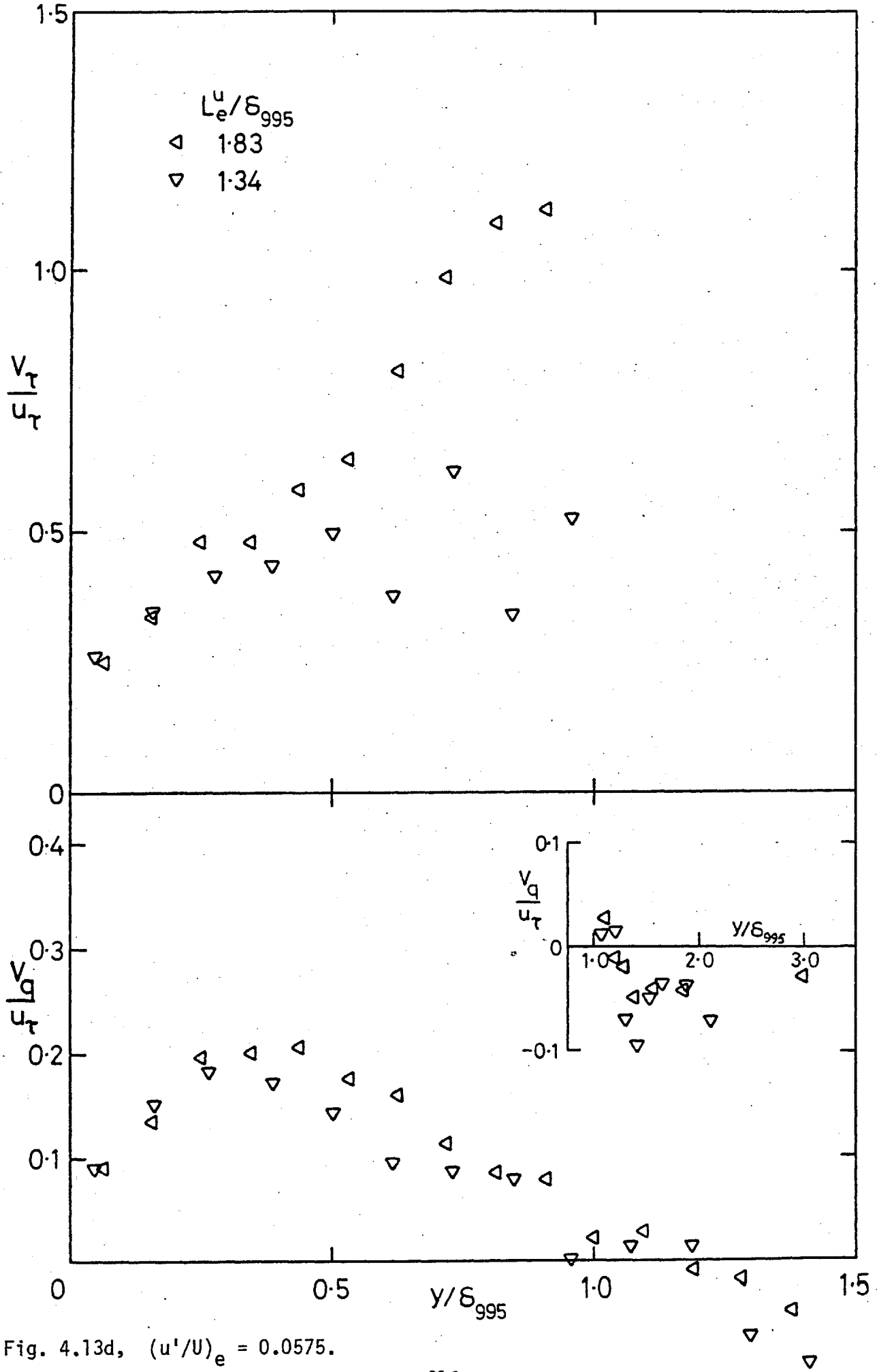

Fig. 4.13d, $(u'/U)_e = 0.0575$.

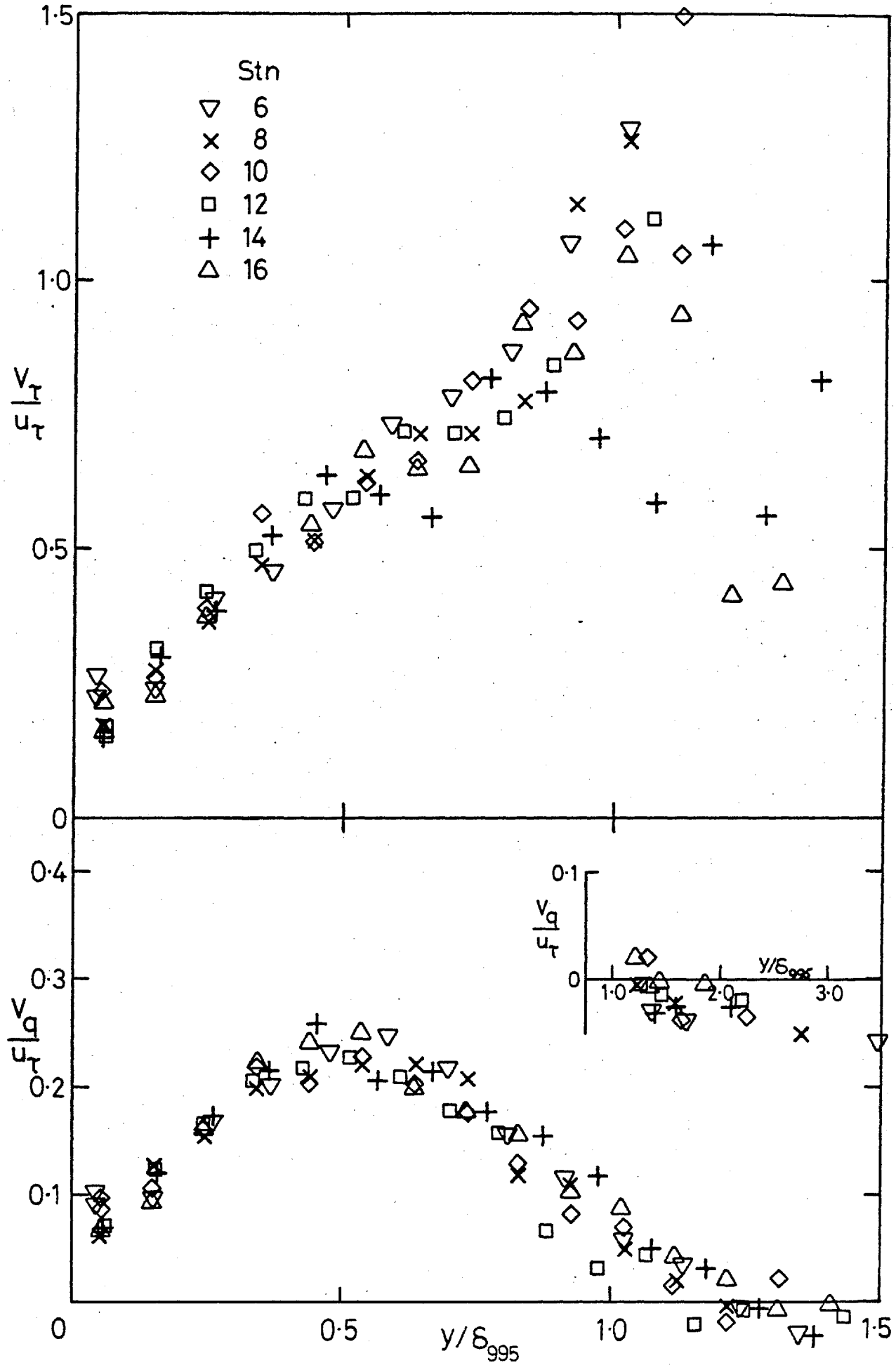

Fig. 4.13e, 15.2 cm grid, X_{LE} = 2.06 m, stns 6, 8, 10, 12, 14, 16.

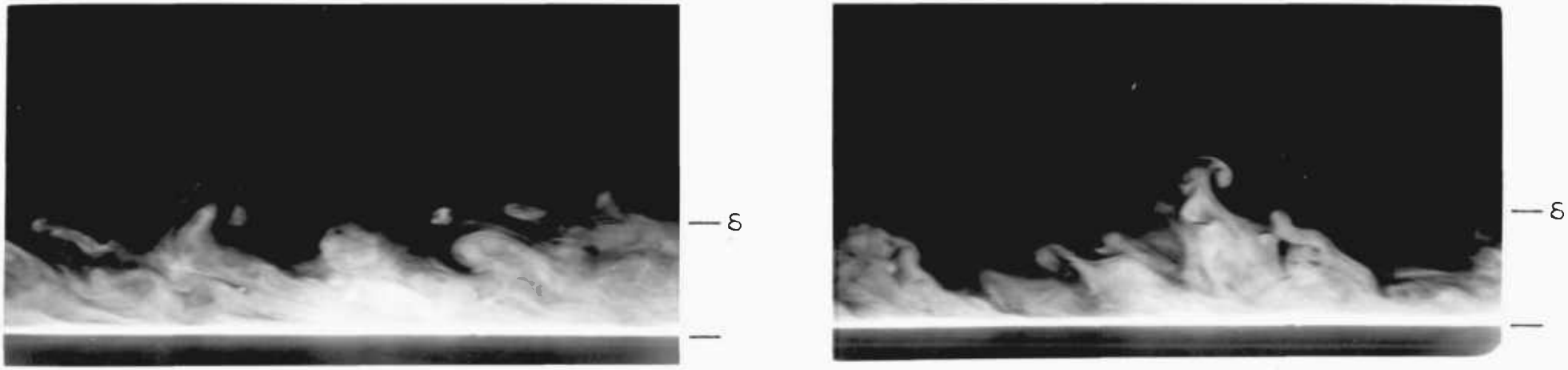

a) No grid. $(u'/U)_e \approx 0.002$.

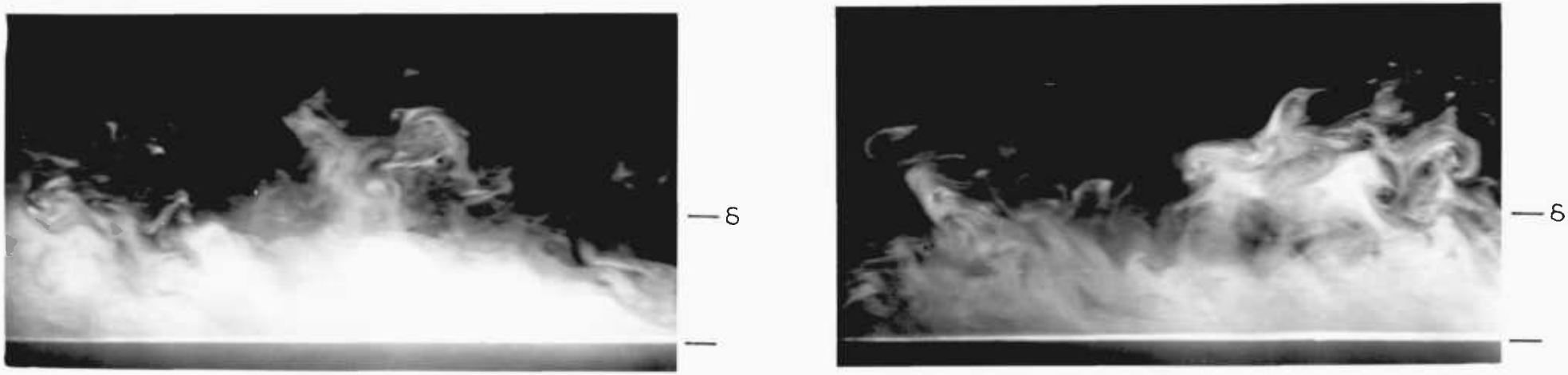

b) $(u'/U)_e \approx 0.03$, $L_e^u/\delta \approx 0.4$.

Fig. 4.14 Smoke-filled boundary layer. $Re_\theta \approx 700$. Flow right to left. Illumination by thin plane of light.

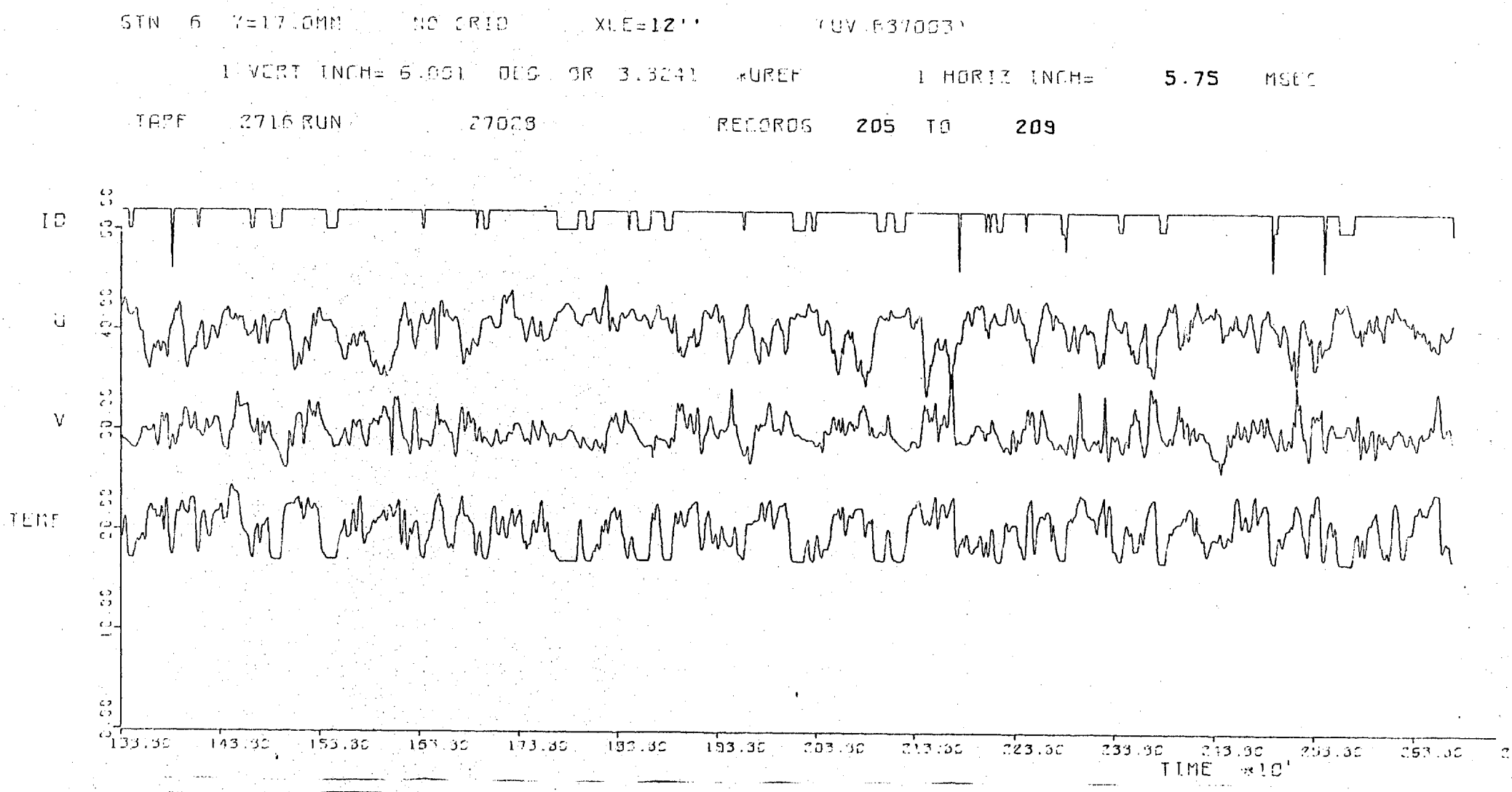

a) No Grid, stn 6

Fig. 4.15 Calcomp-plot samples:

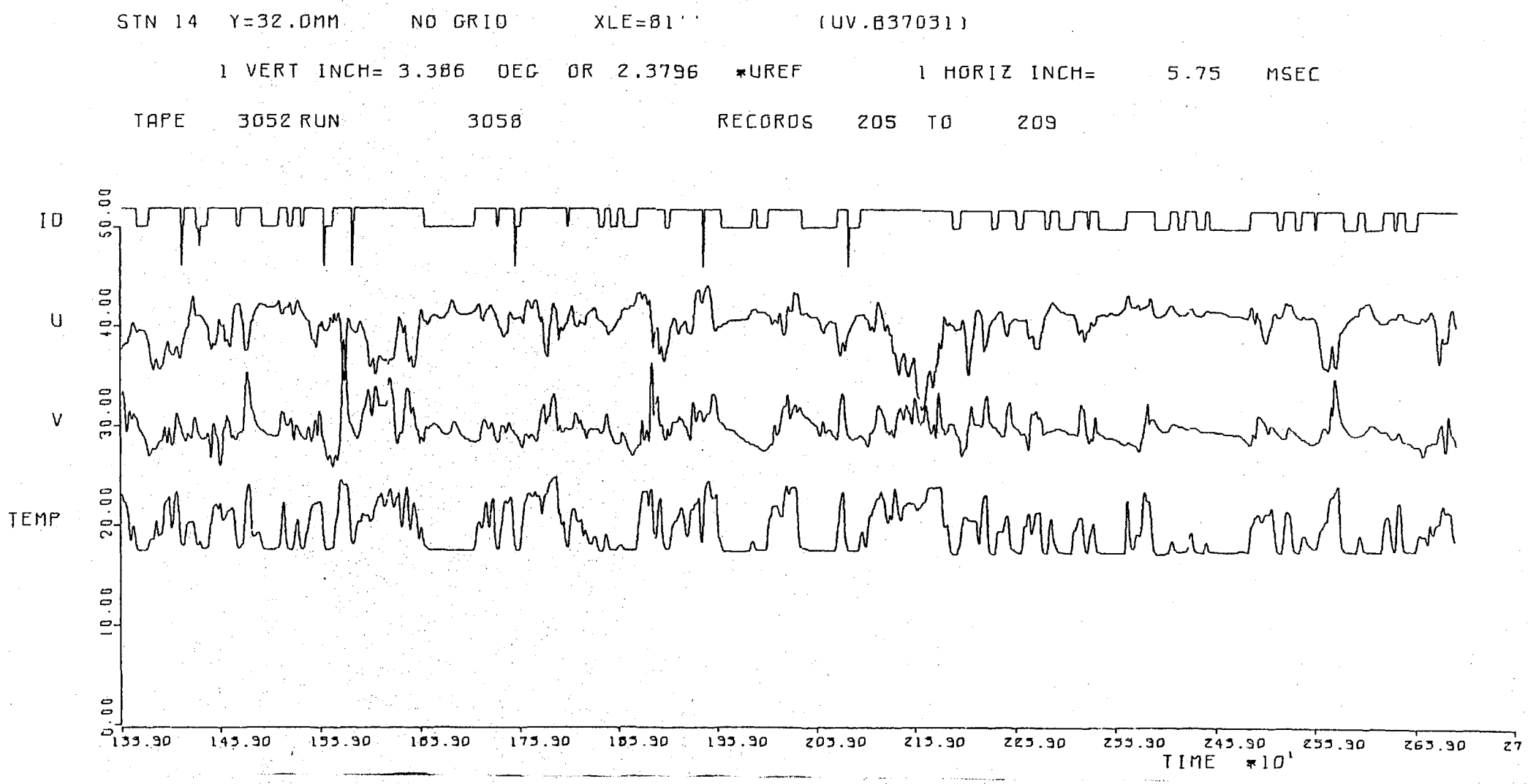

Fig. 4.15b, No Grid, stn 14

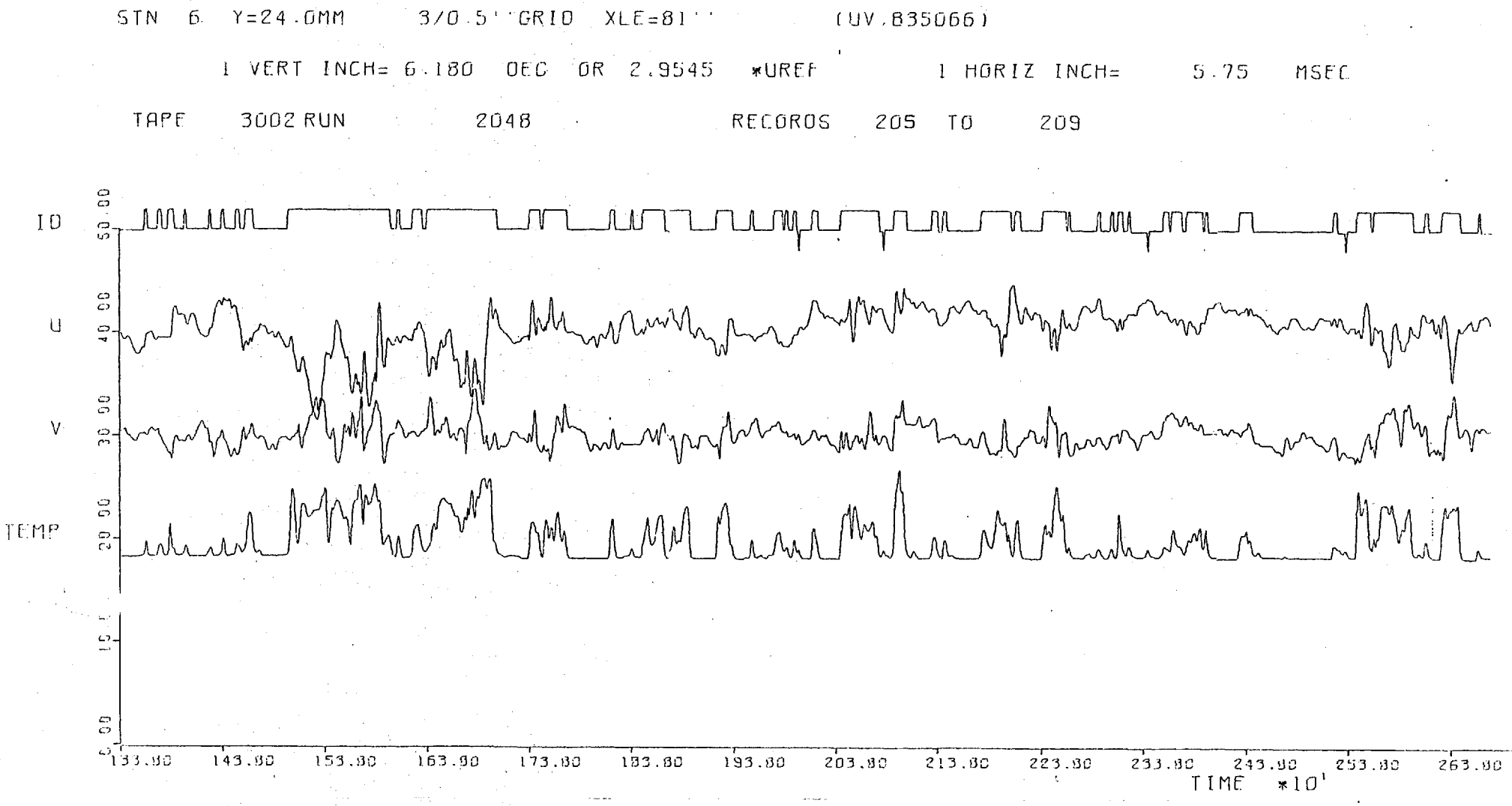

Fig. 4.15c, $(u'/U)_e = 0{\cdot}0240$, $L^u_e/\delta_{995} = 1{\cdot}88$

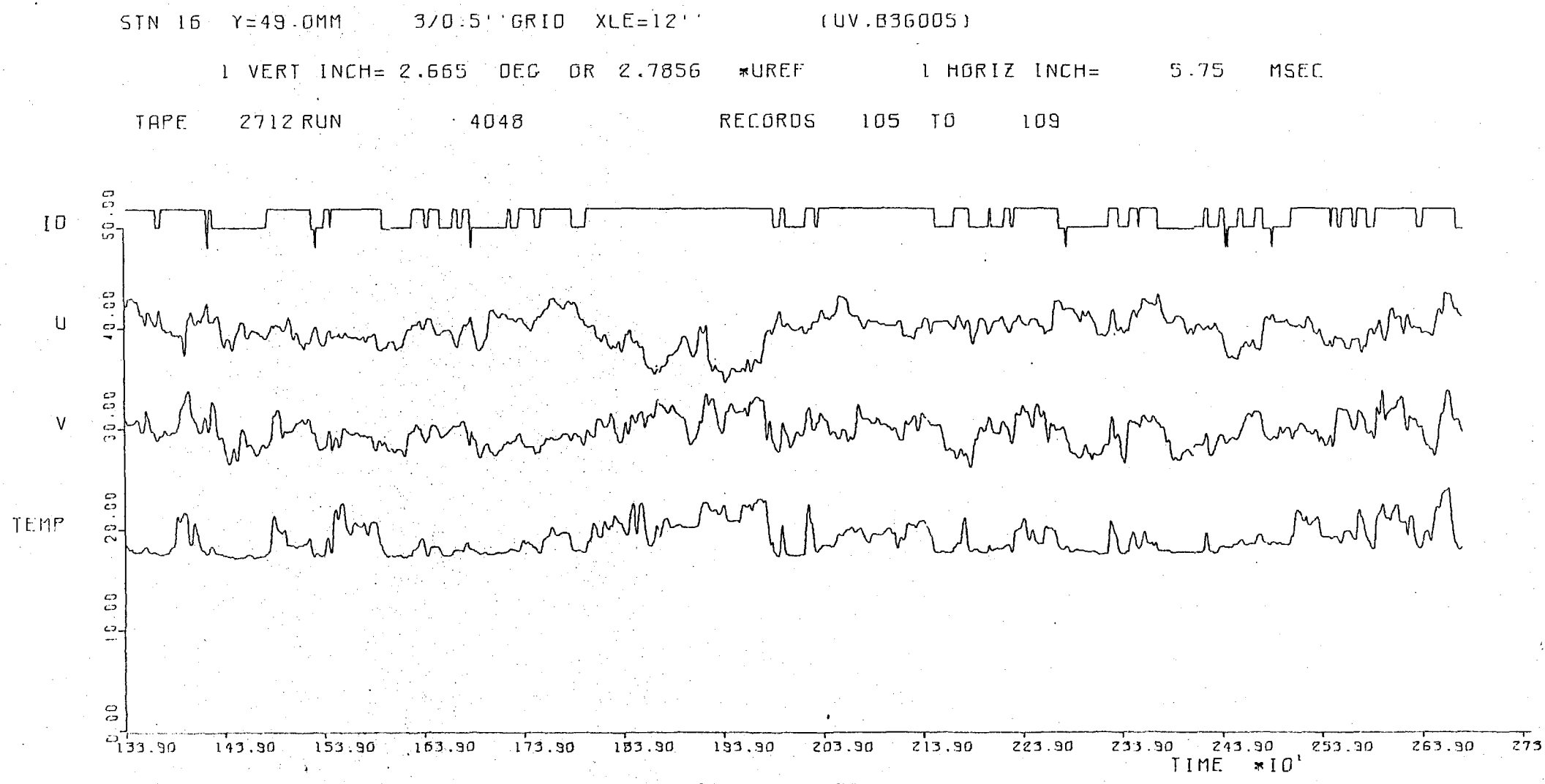

Fig. 4.15d, $(u'/U)_e = 0{\cdot}0255$, $L_e^u/\delta_{995} = 0{\cdot}67$

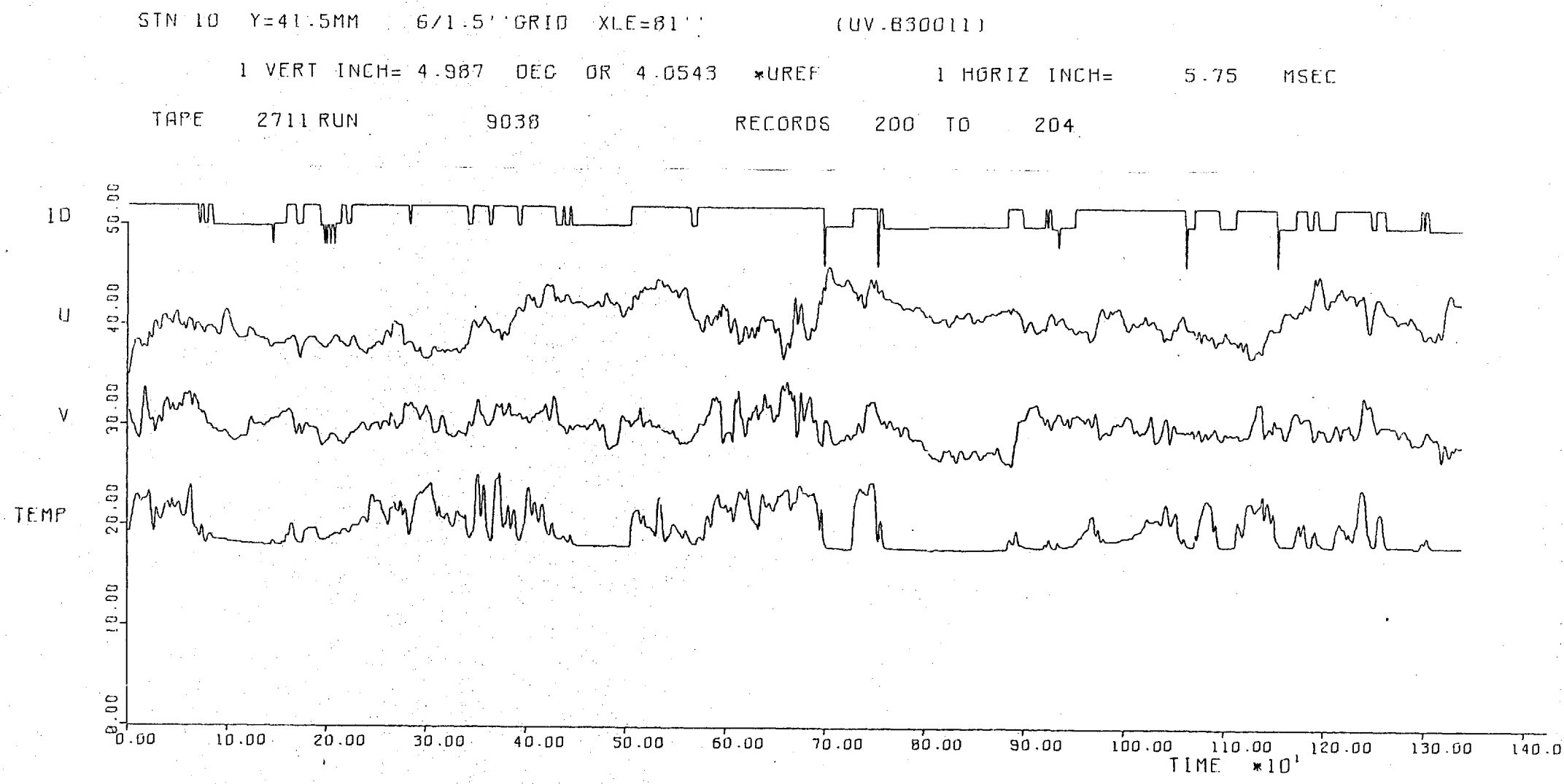

Fig. 4.15e, $(u'/U)_e = 0{\cdot}0410$, $L_e^u/\delta_{995} = 1{\cdot}90$

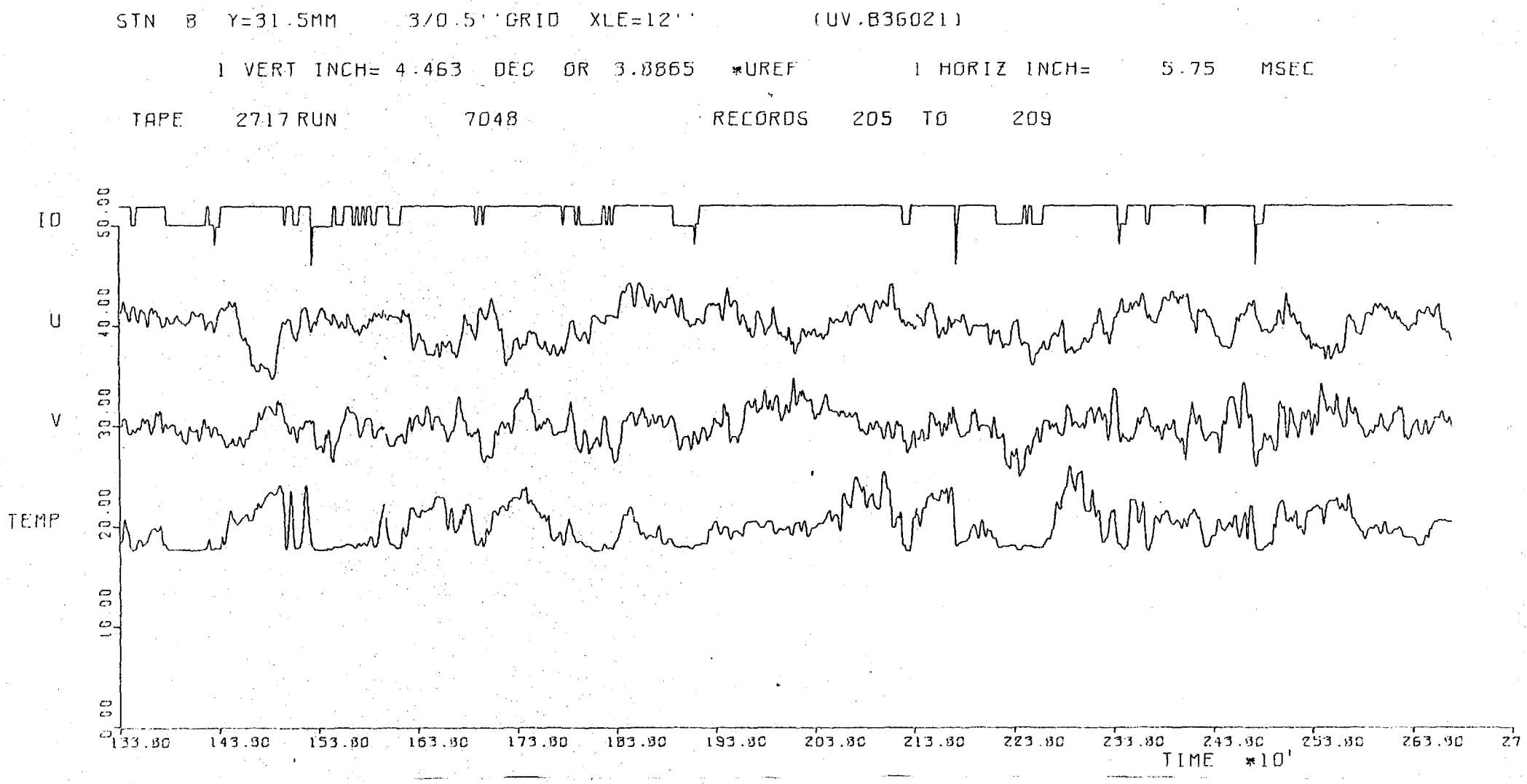

Fig. 4.15f, $(u'/U)_e = 0{\cdot}0399$, $L_e^u/\delta_{995} = 0{\cdot}71$

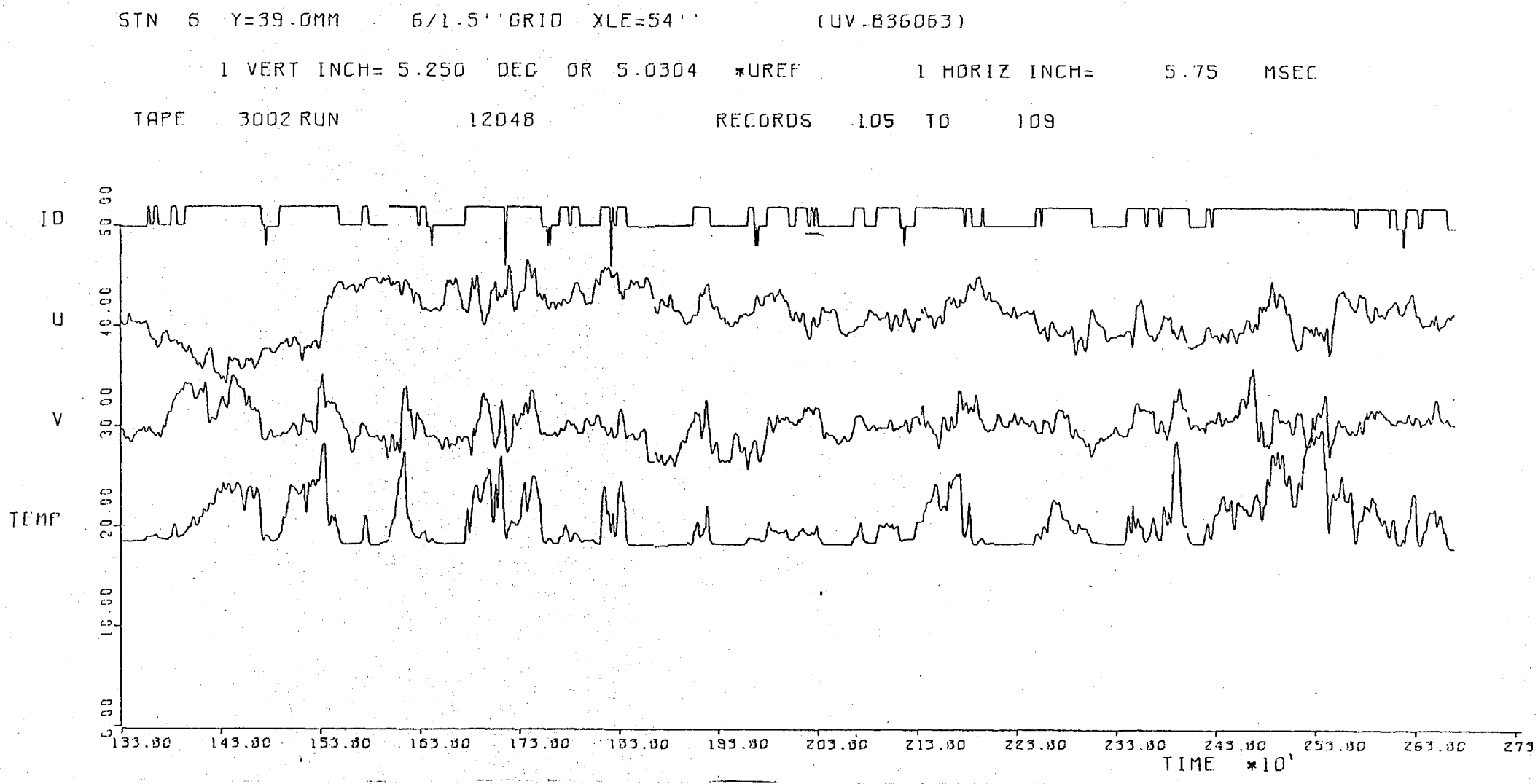

Fig. 4.15g, $(u'/U)_e = 0.0575$, $L_e^u/\delta_{995} = 1.83$

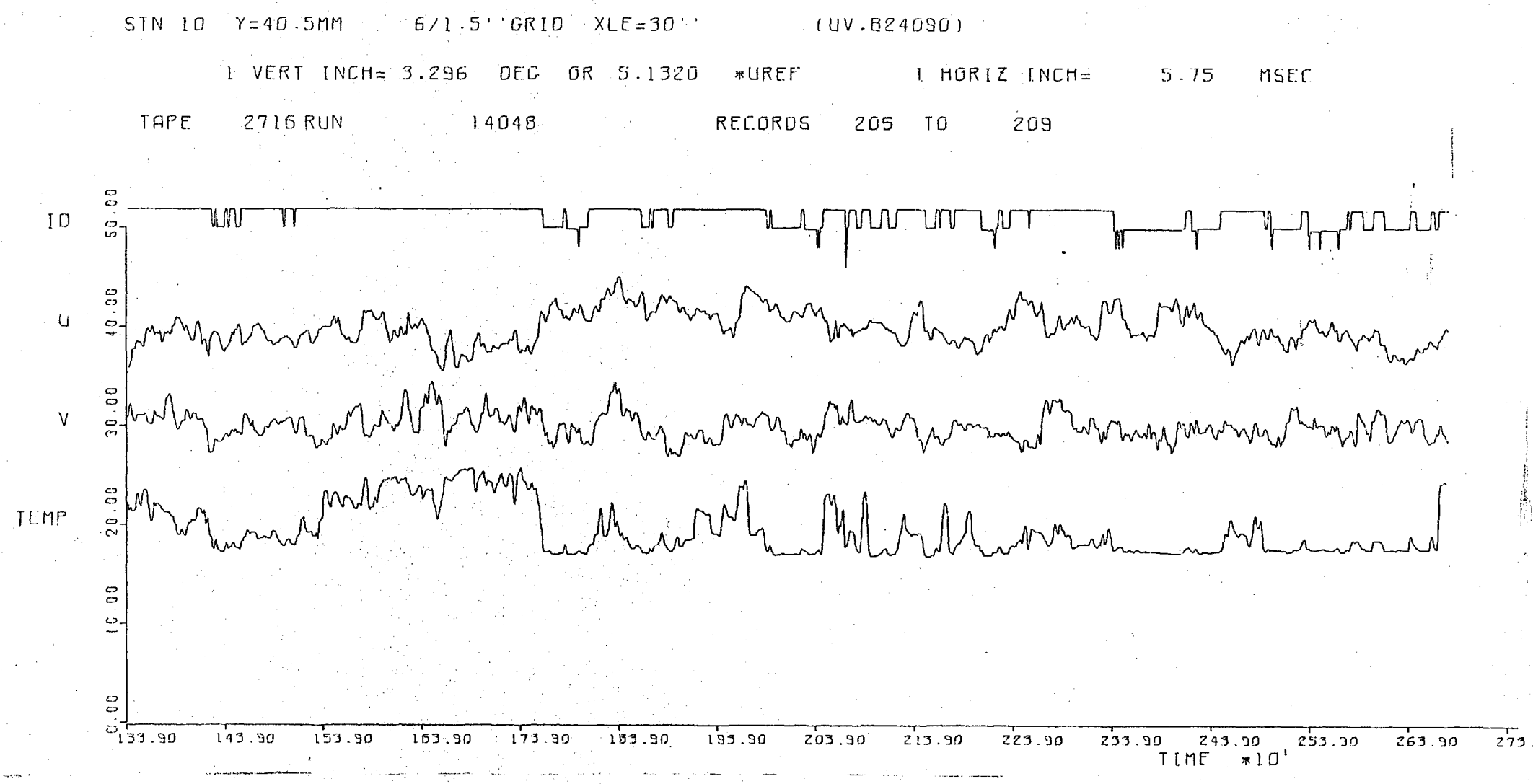

Fig. 4.15h, $(u'/U)_e = 0{\cdot}0575$, $L_e^u/\delta_{995} = 1{\cdot}34$

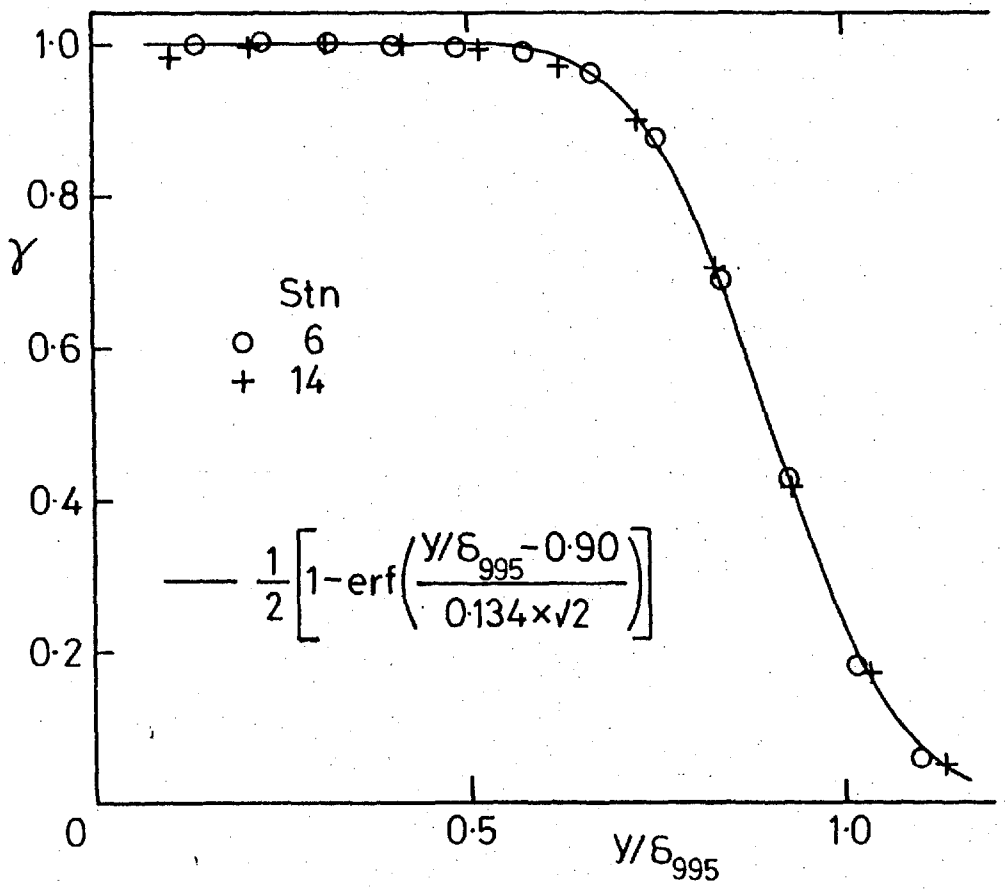

a) No grid.

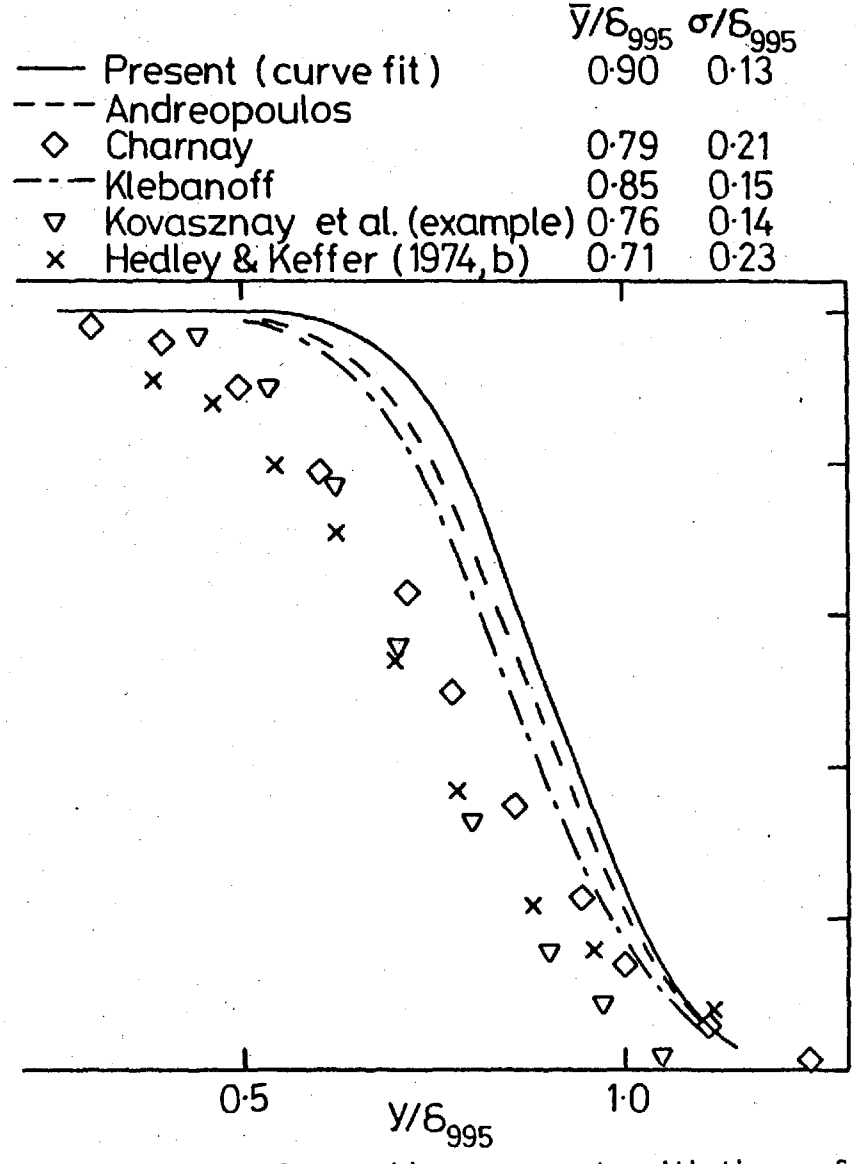

b) Comparison of no-grid measurements with those of other workers.

Fig. 4.16 Intermittency factor profiles;

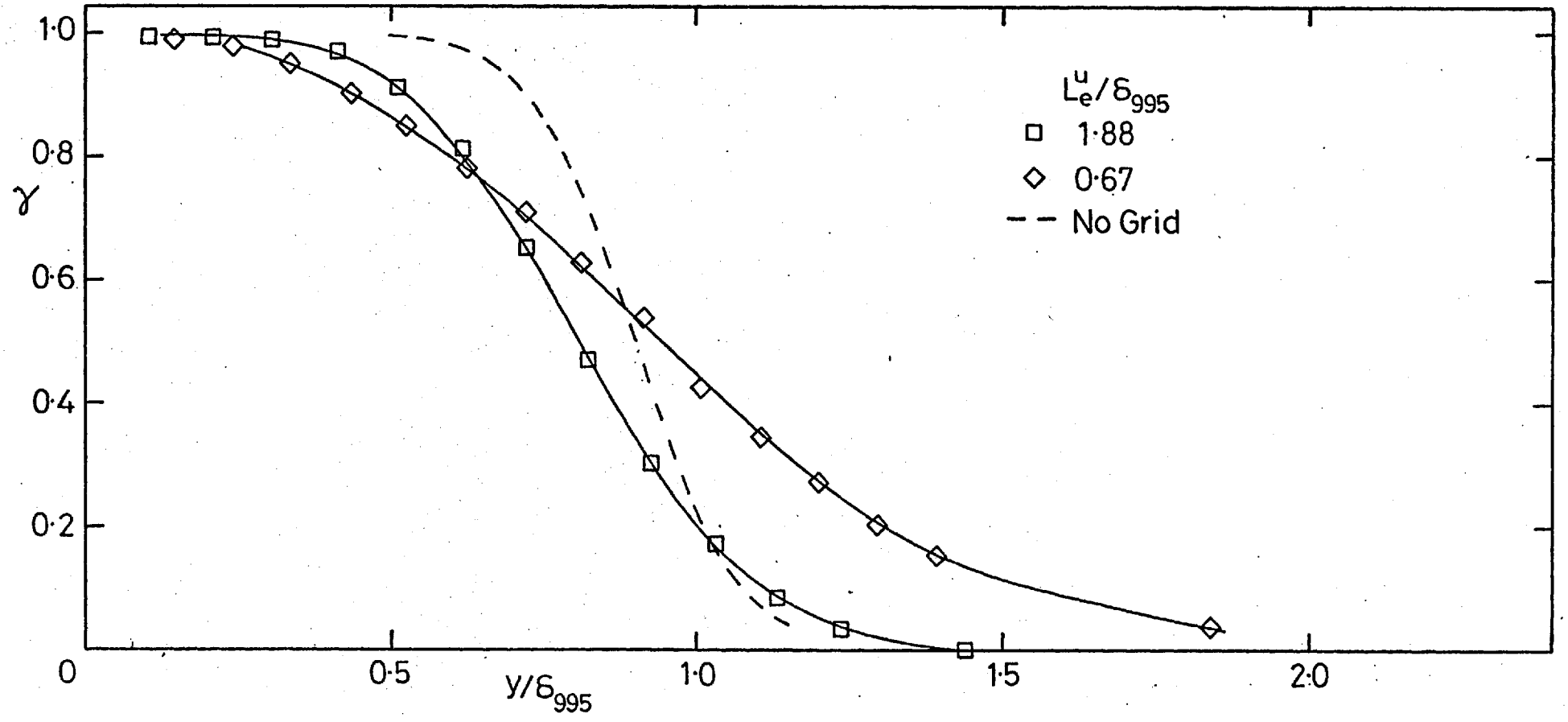

Fig. 4.16c, $(u'/U)_e \approx 0.025$.

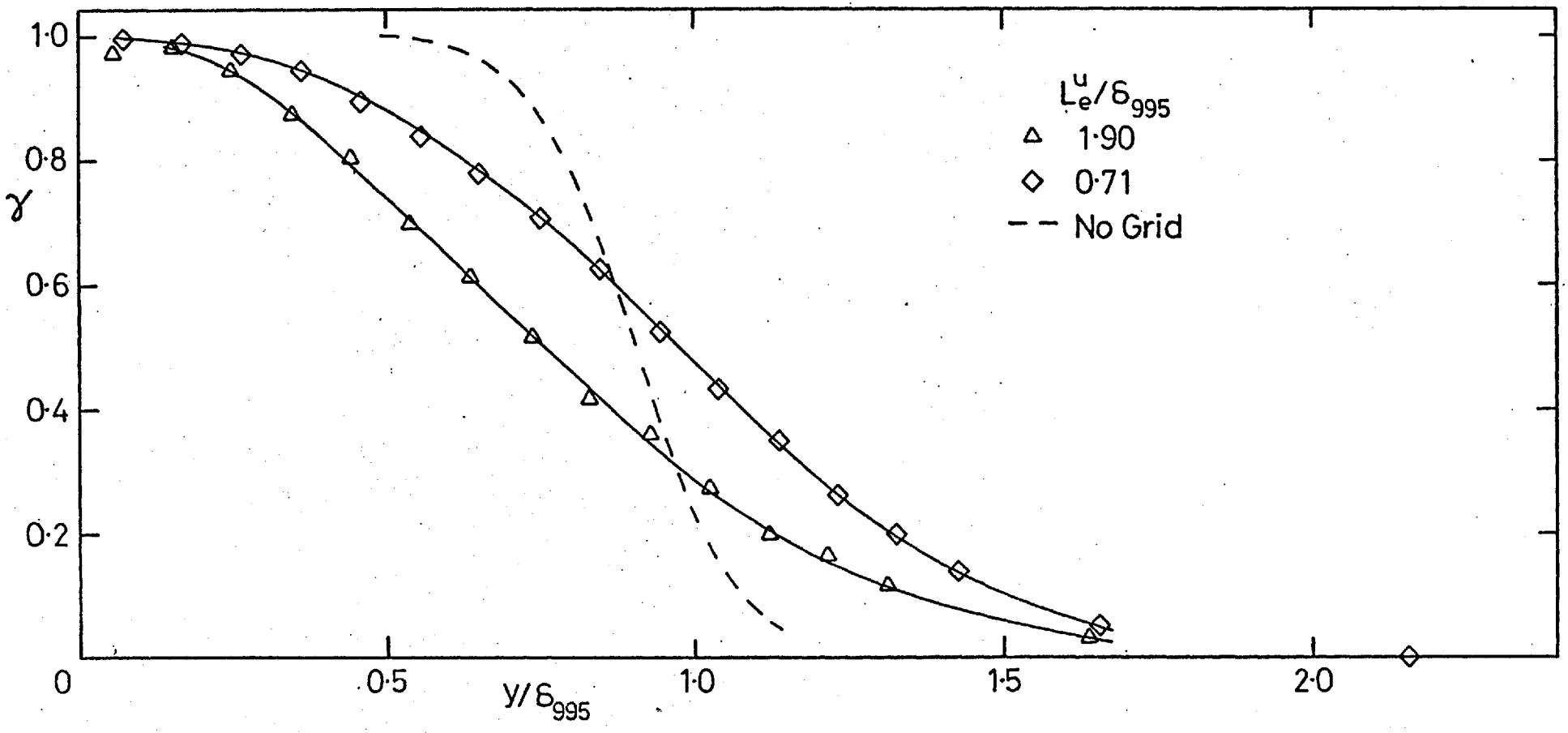

Fig. 4.16d, $(u'/U)_e \approx 0.040$.

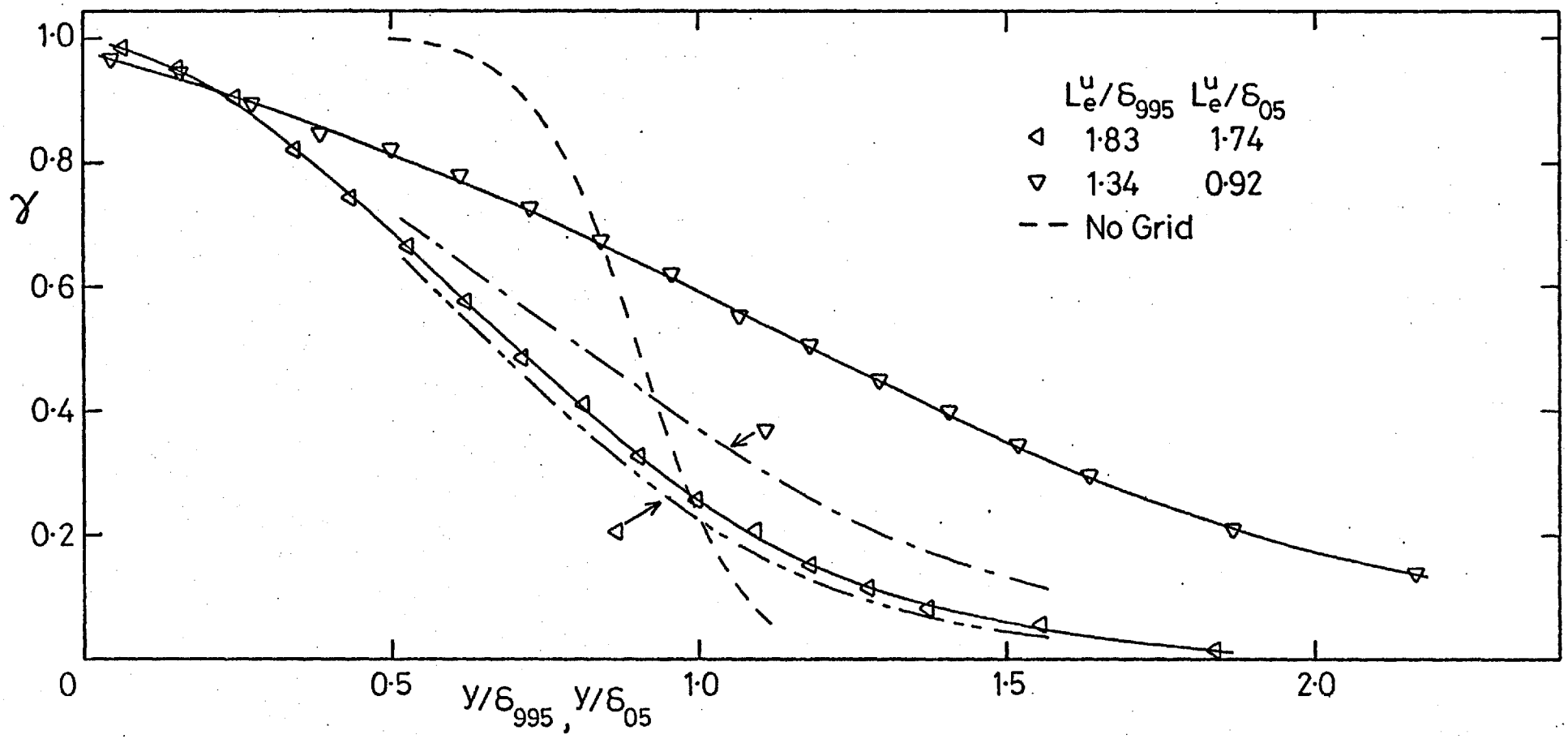

Fig. 4.16e, $(u'/U)_e = 0.0575$.

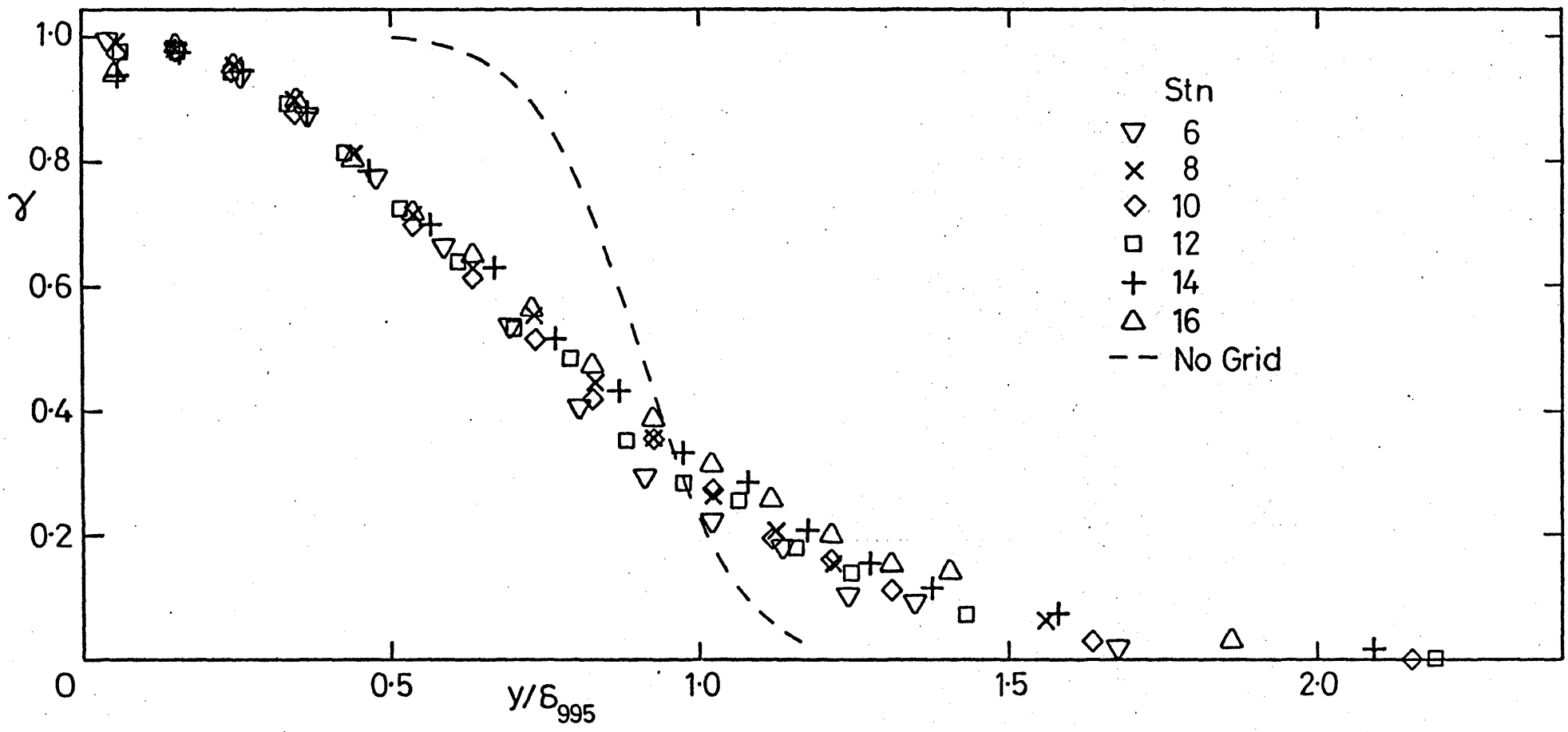

Fig. 4.16f, 15.2 cm grid, X_{LE} = 2.06 m, stns 6, 8, 10, 12, 14, 16.

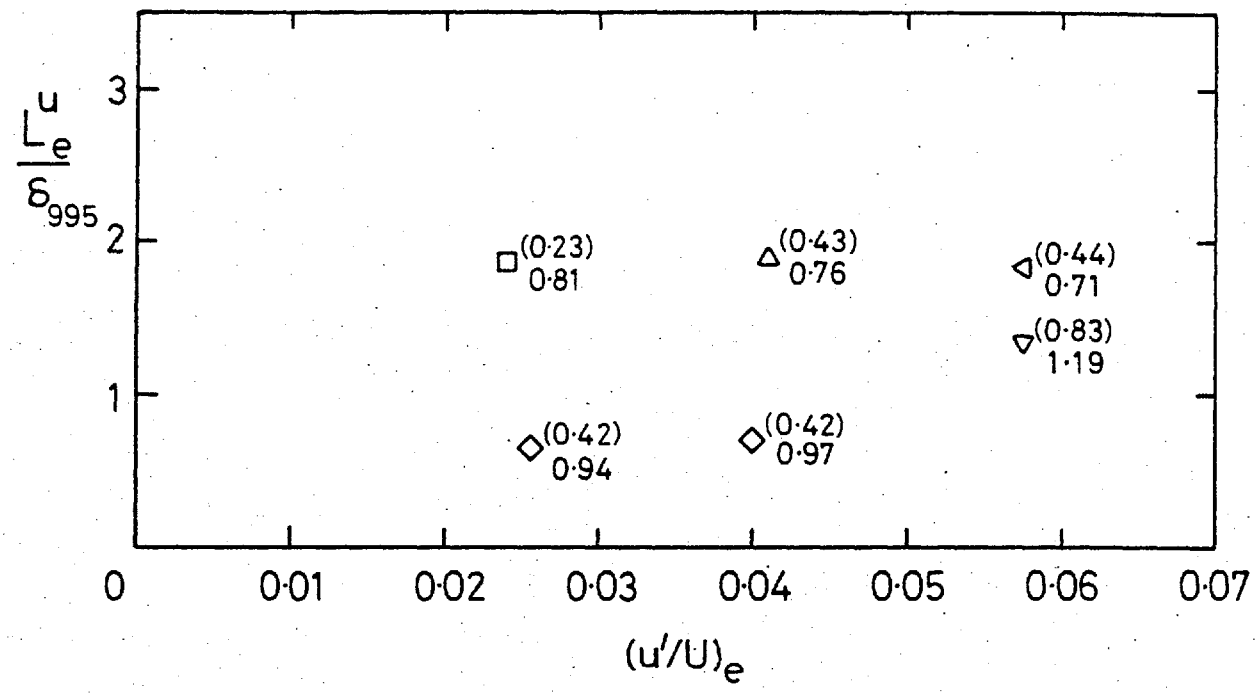

a) Values of $\overline{y}/\delta_{995}$ displayed at appropriate $(u'/U)_e$ and L_e^u/δ_{995}

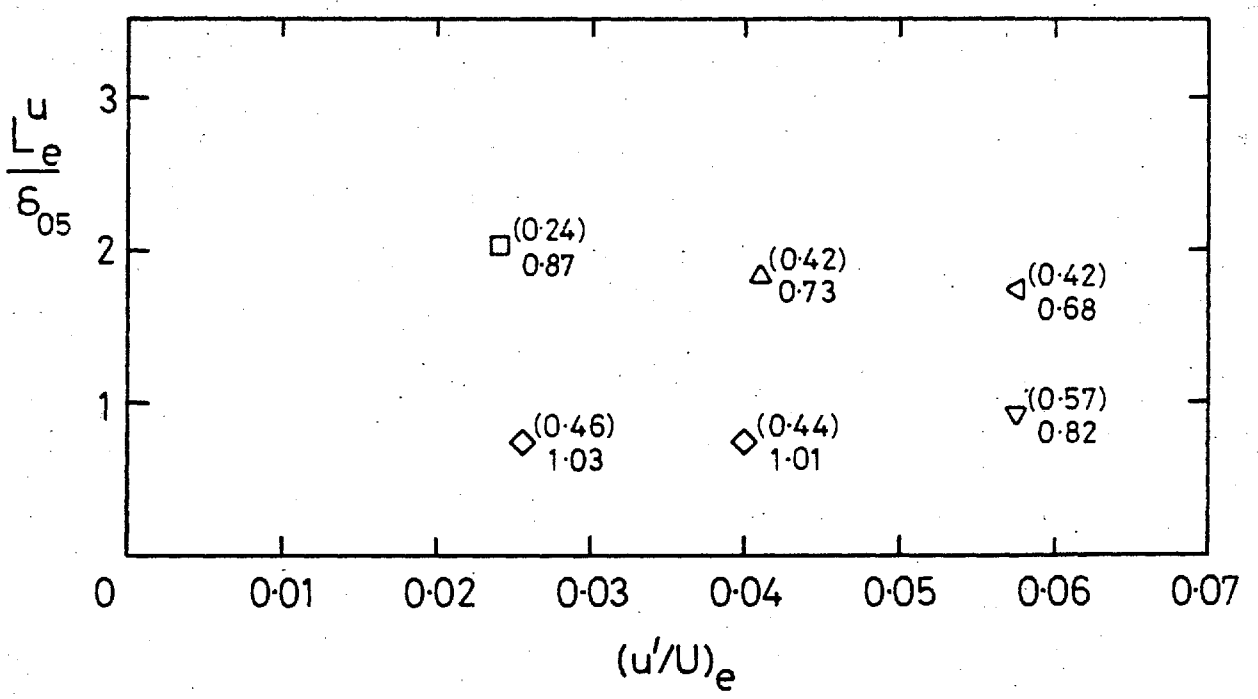

b) Values of $\overline{y}/\delta_{05}$ displayed at appropriate $(u'/U)_e$ and L_e^u/δ_{05}

Fig. 4.17 Average position $\overline{y}$ of the interface

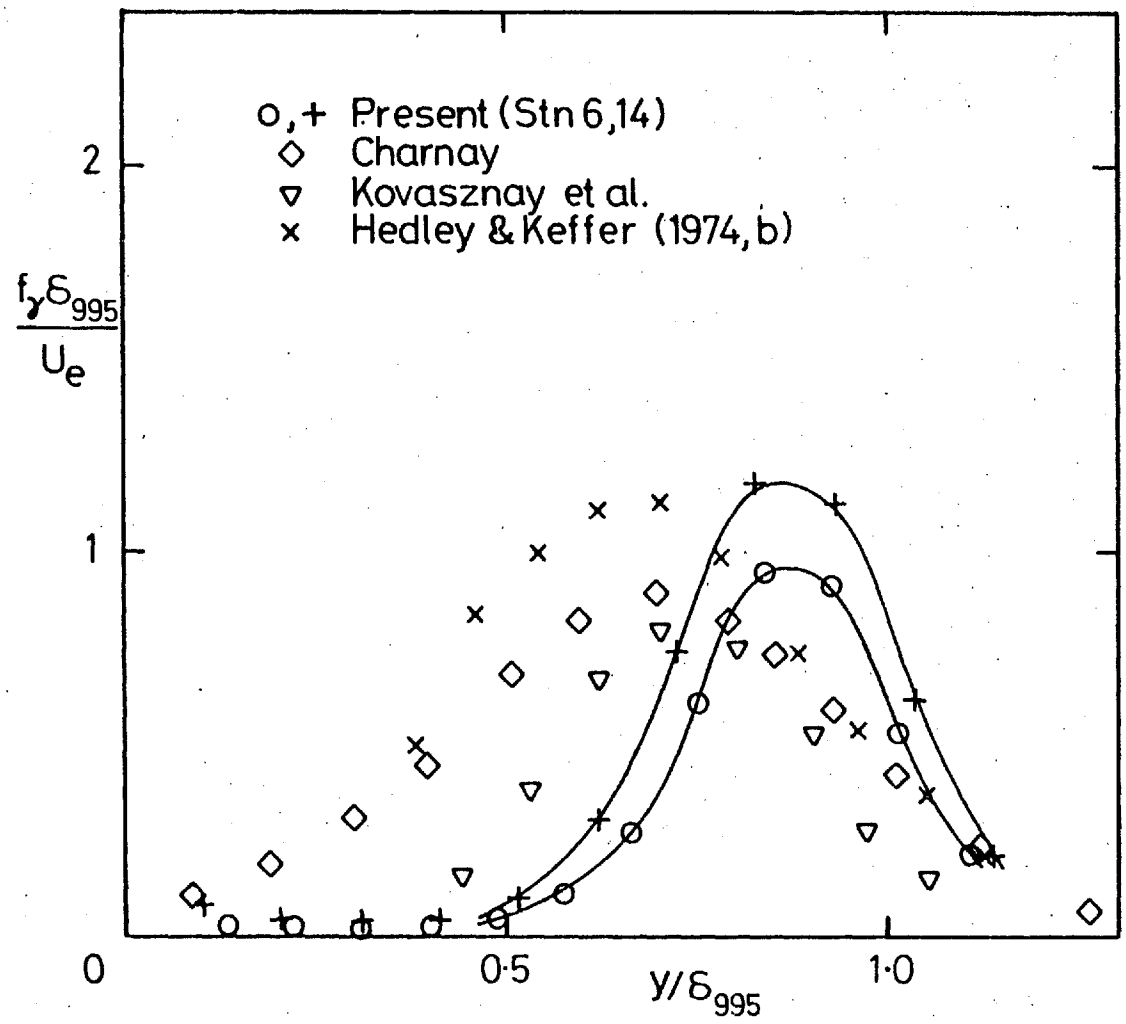

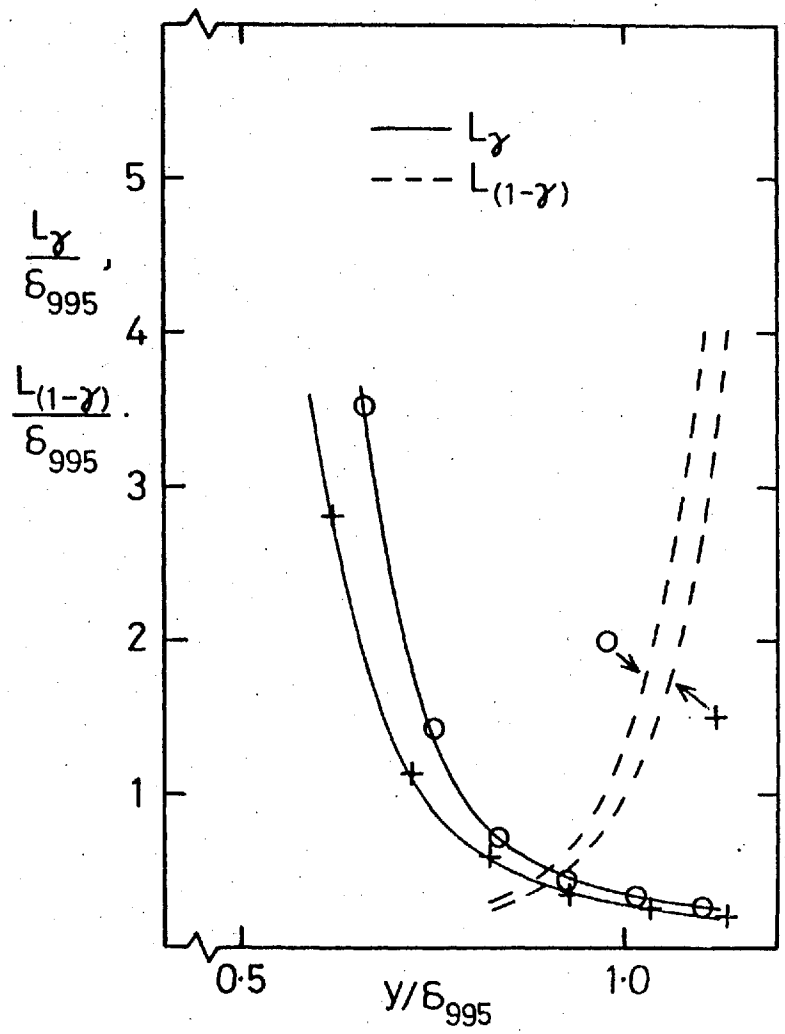

a) No grid.

Fig. 4.18 Average burst frequency and average burst lengths

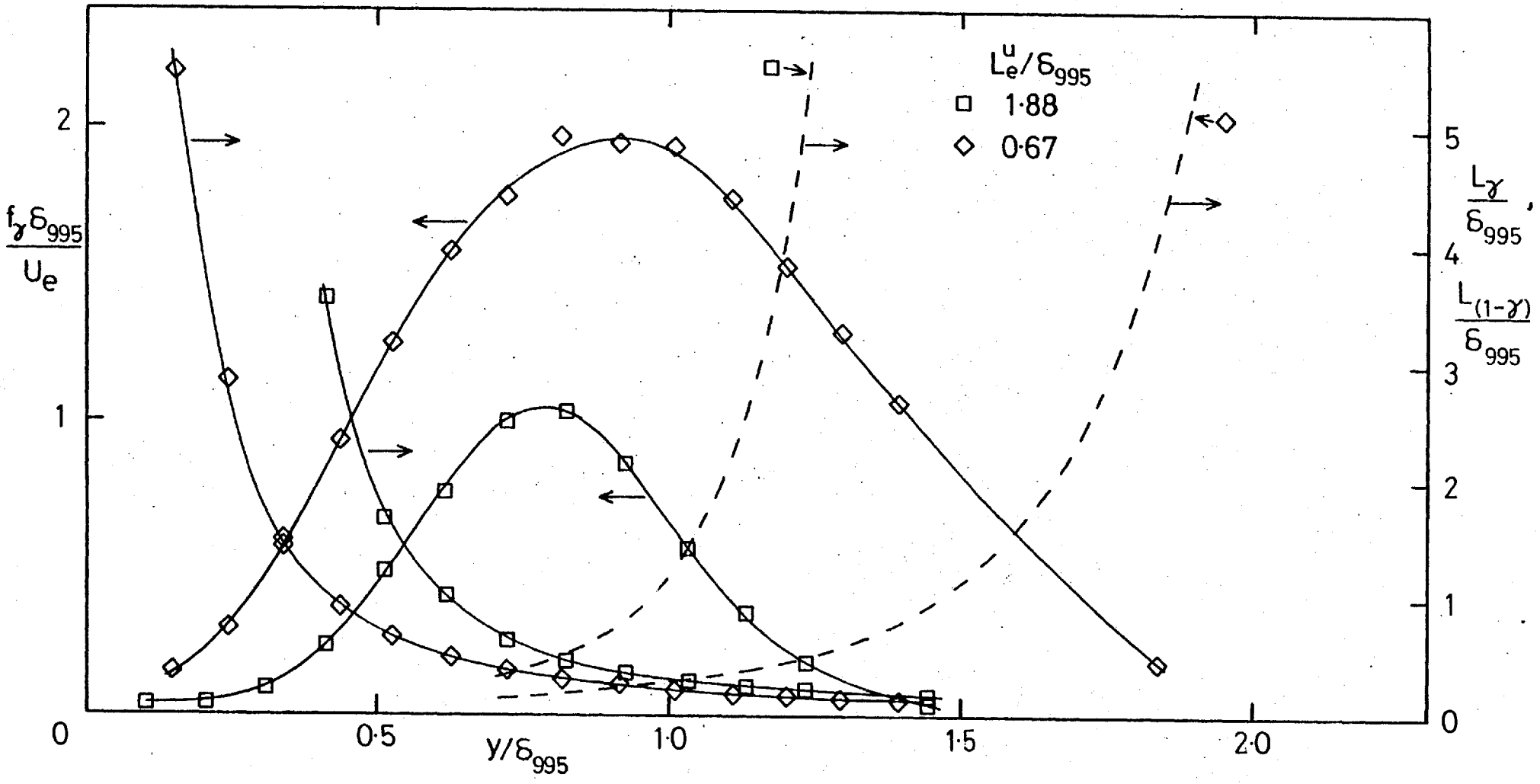

Fig. 4.18b, $(u'/U)_e \approx 0.025$.

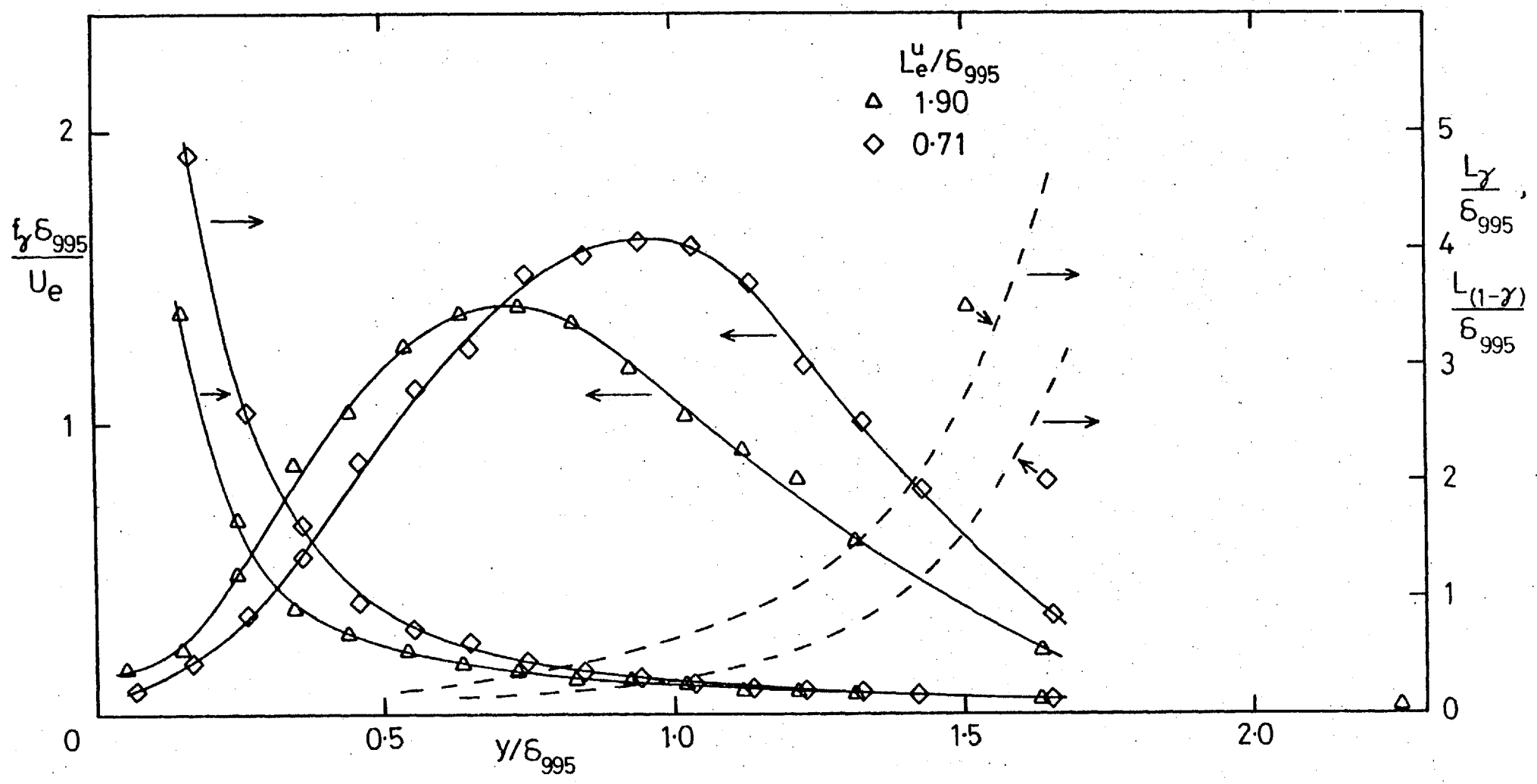

Fig. 4.18c, $(u'/U)_e \approx 0.040$.

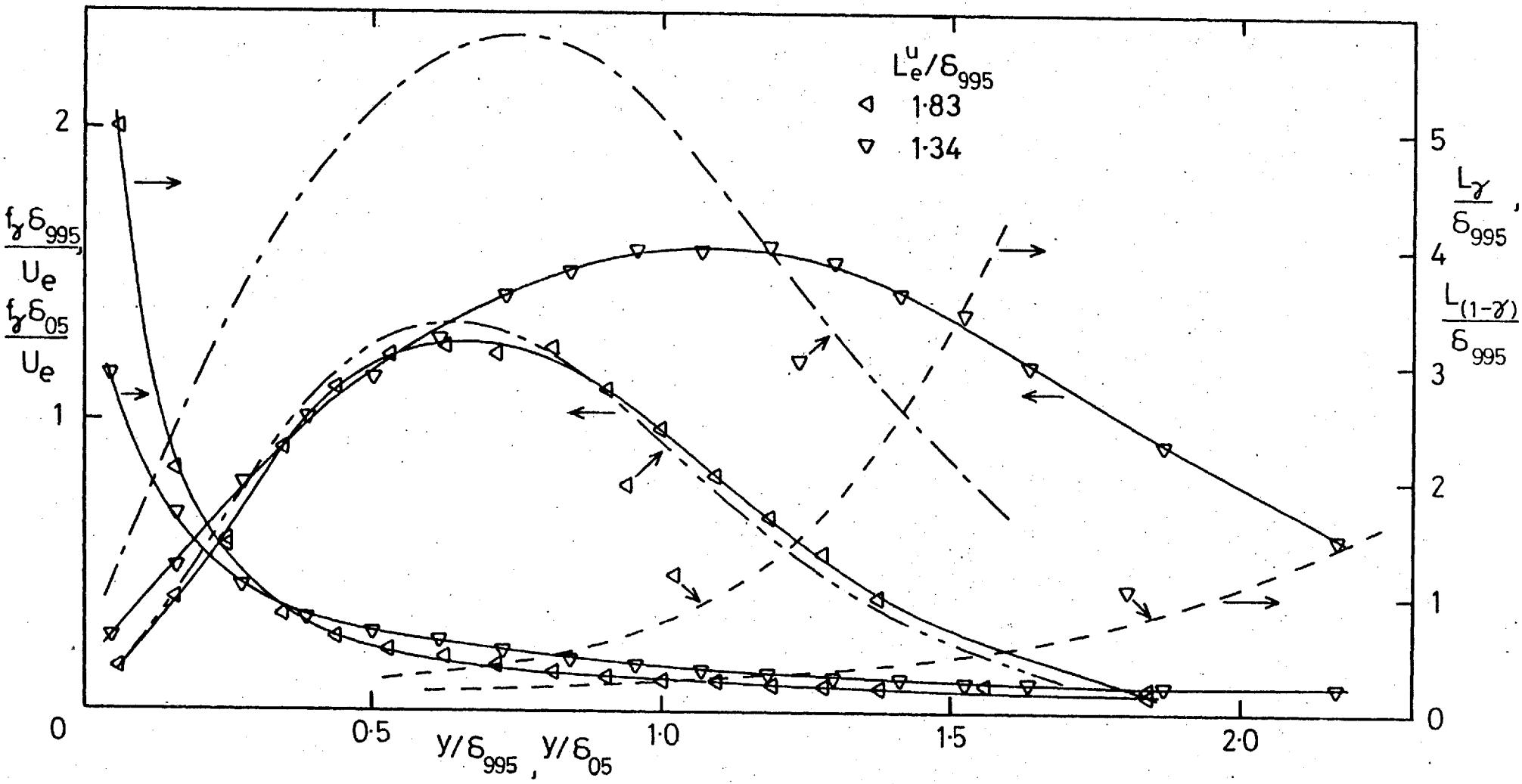

Fig. 4.18d, $(u'/U)_e = 0.0575$.

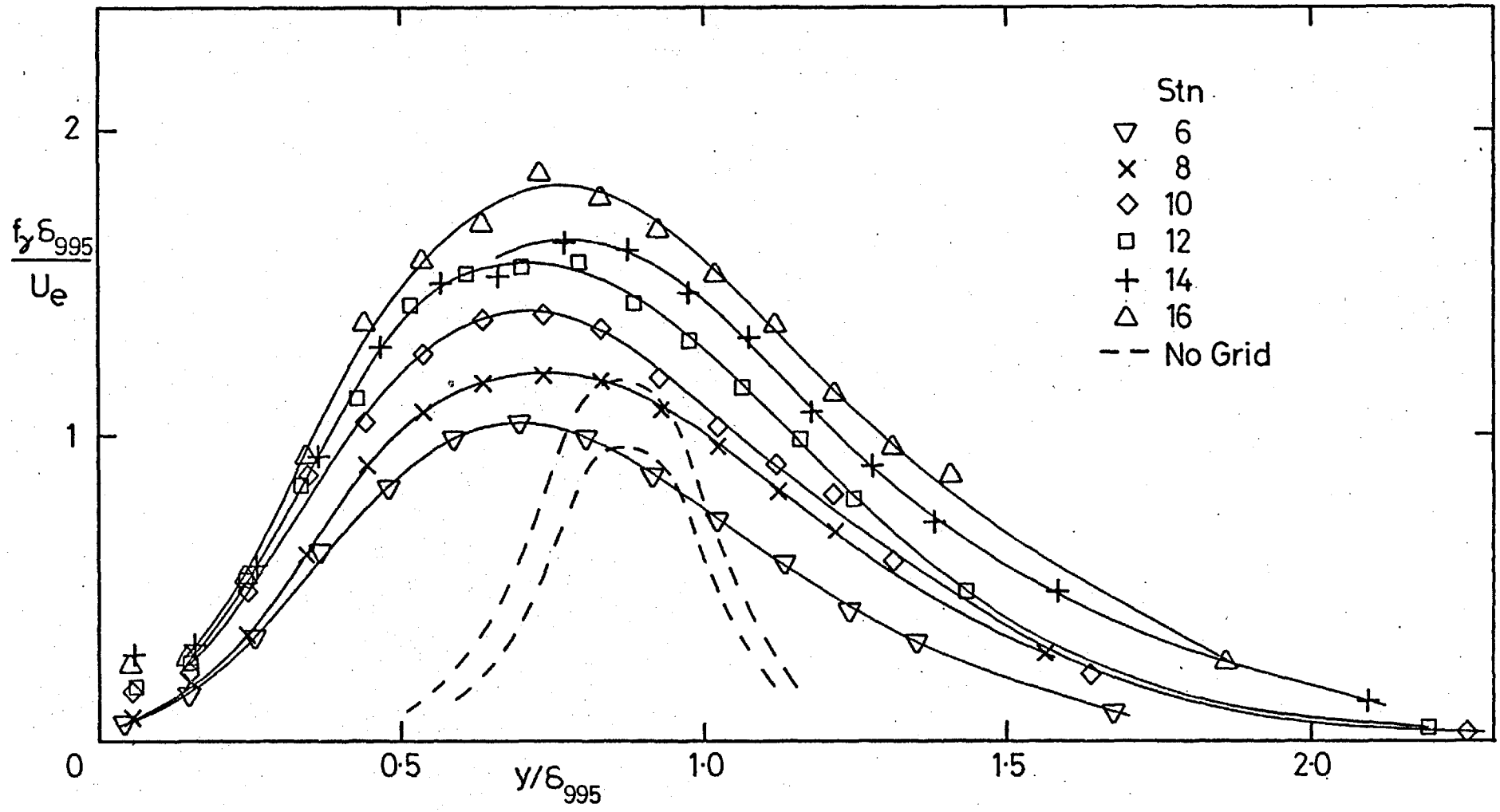

Fig. 4.18e, Average burst frequency, 15.2 cm grid, X_{LE} = 2.06 m.

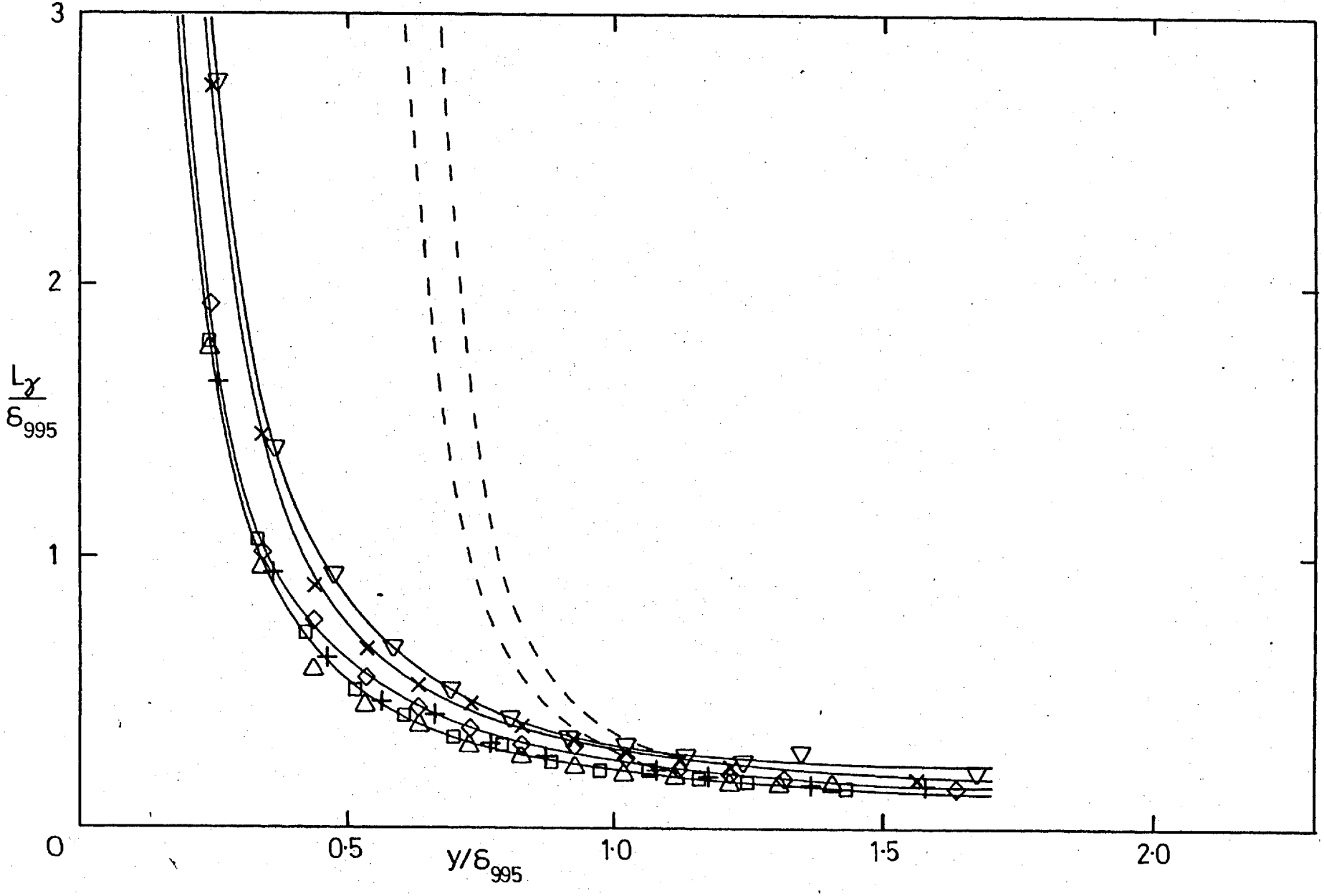

Fig. 4.18f, Average burst length, 15.2 cm grid, X_{LE} = 2.06 m. Symbols as in e).

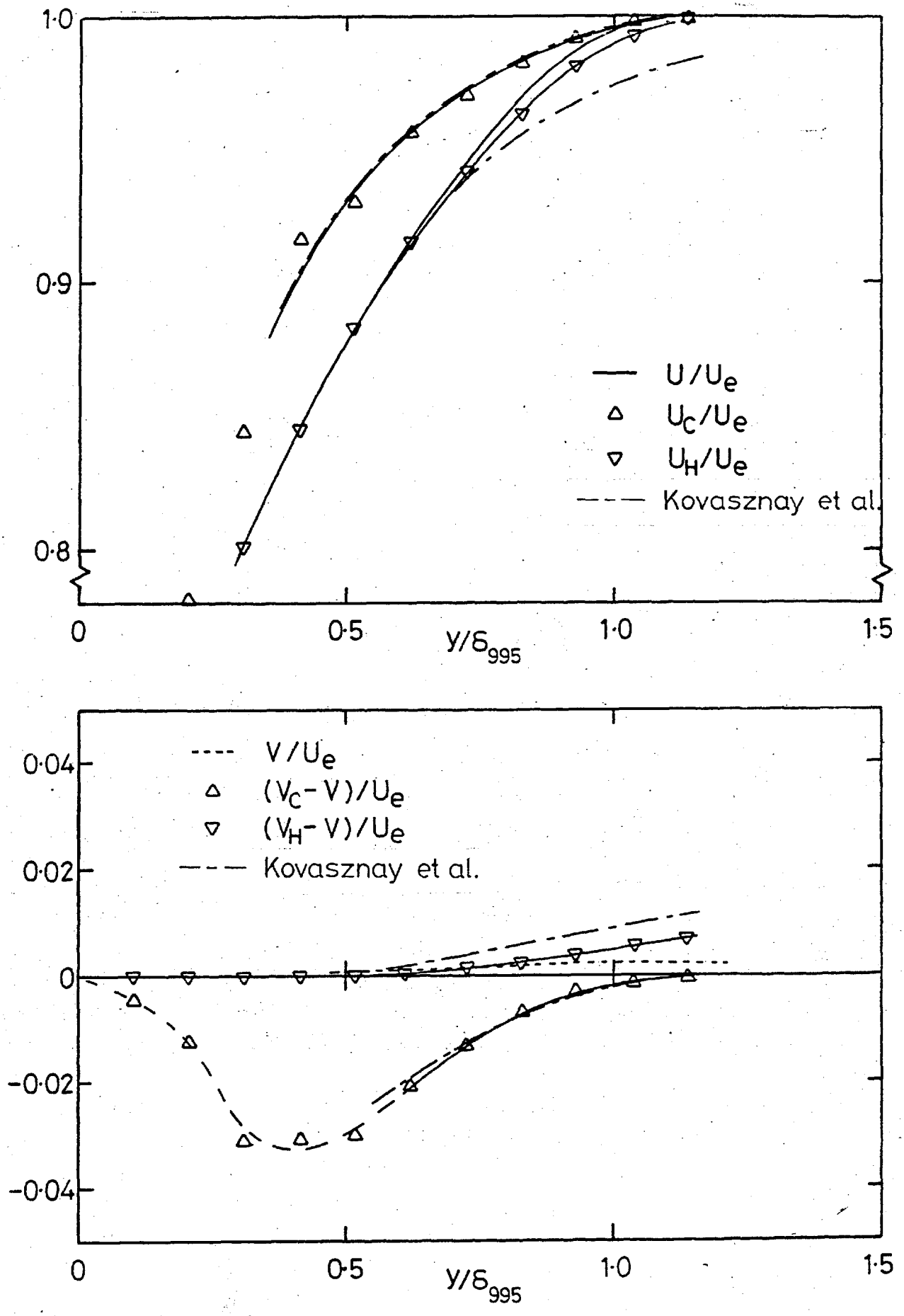

a) No grid, stn 14.

Fig. 4.19 Conditionally-averaged mean velocities

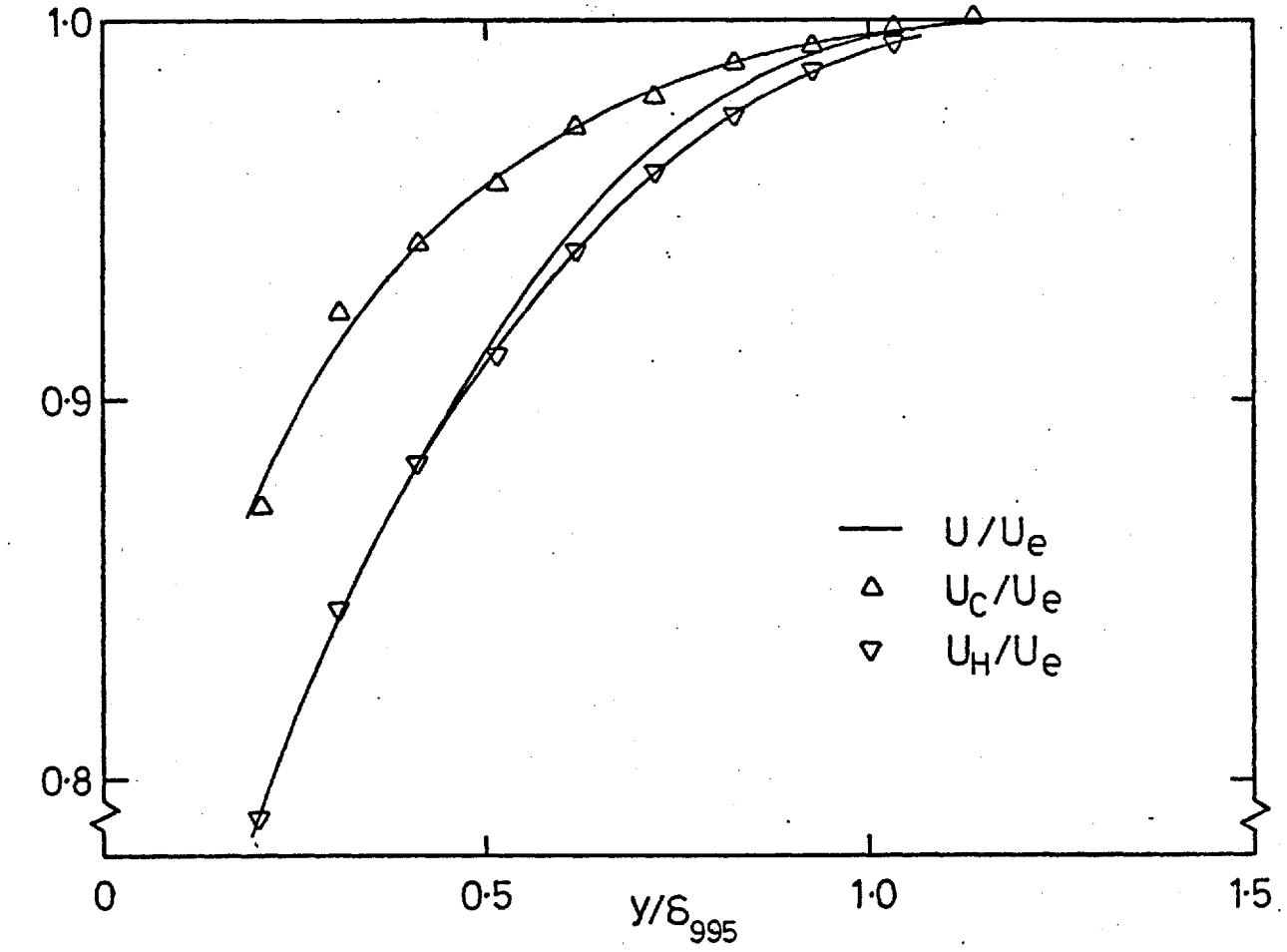

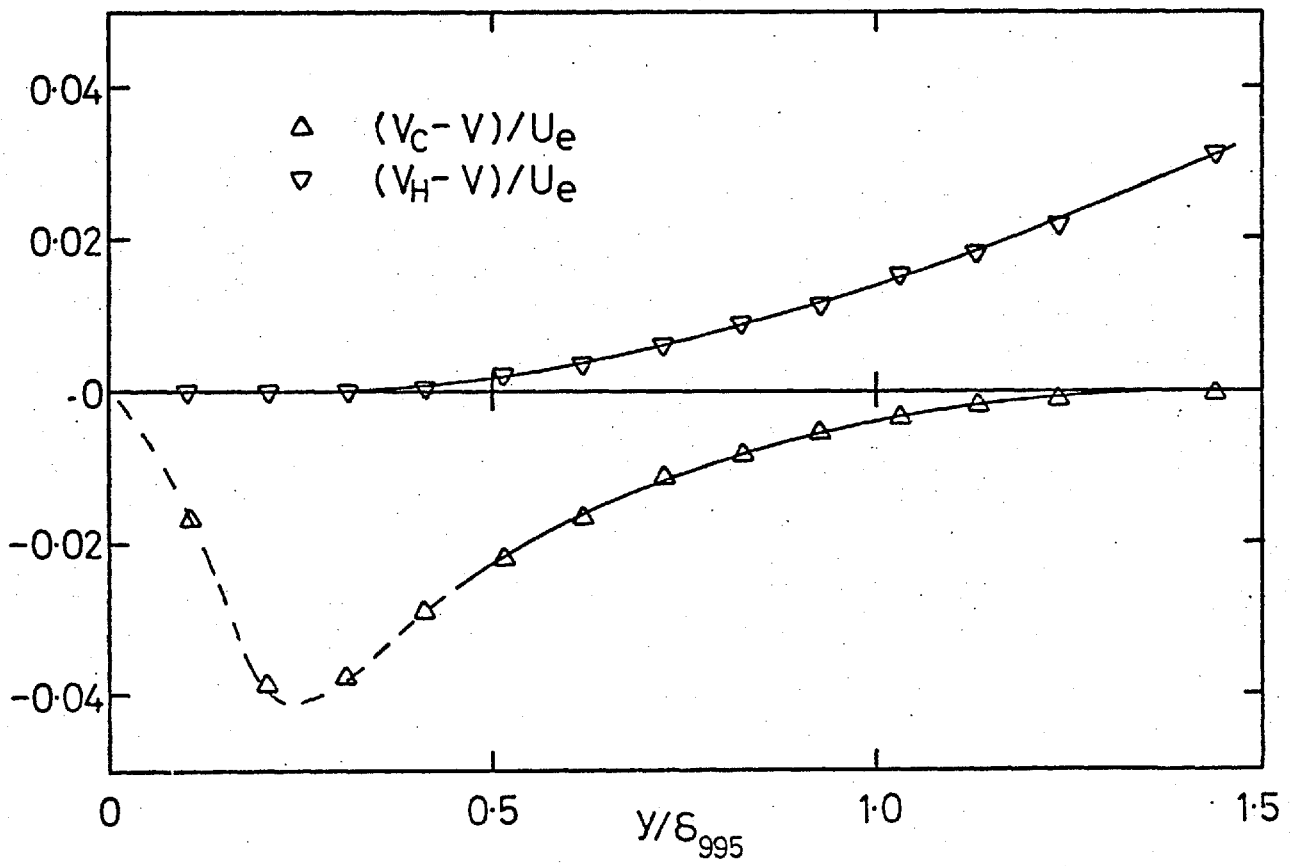

Fig. 4.19b, 7.6 cm grid, X_{LE} = 2.06 m, stn 6. $(u'/U)_e$ = 0.0240, L_e^u/δ_{995} = 1.88

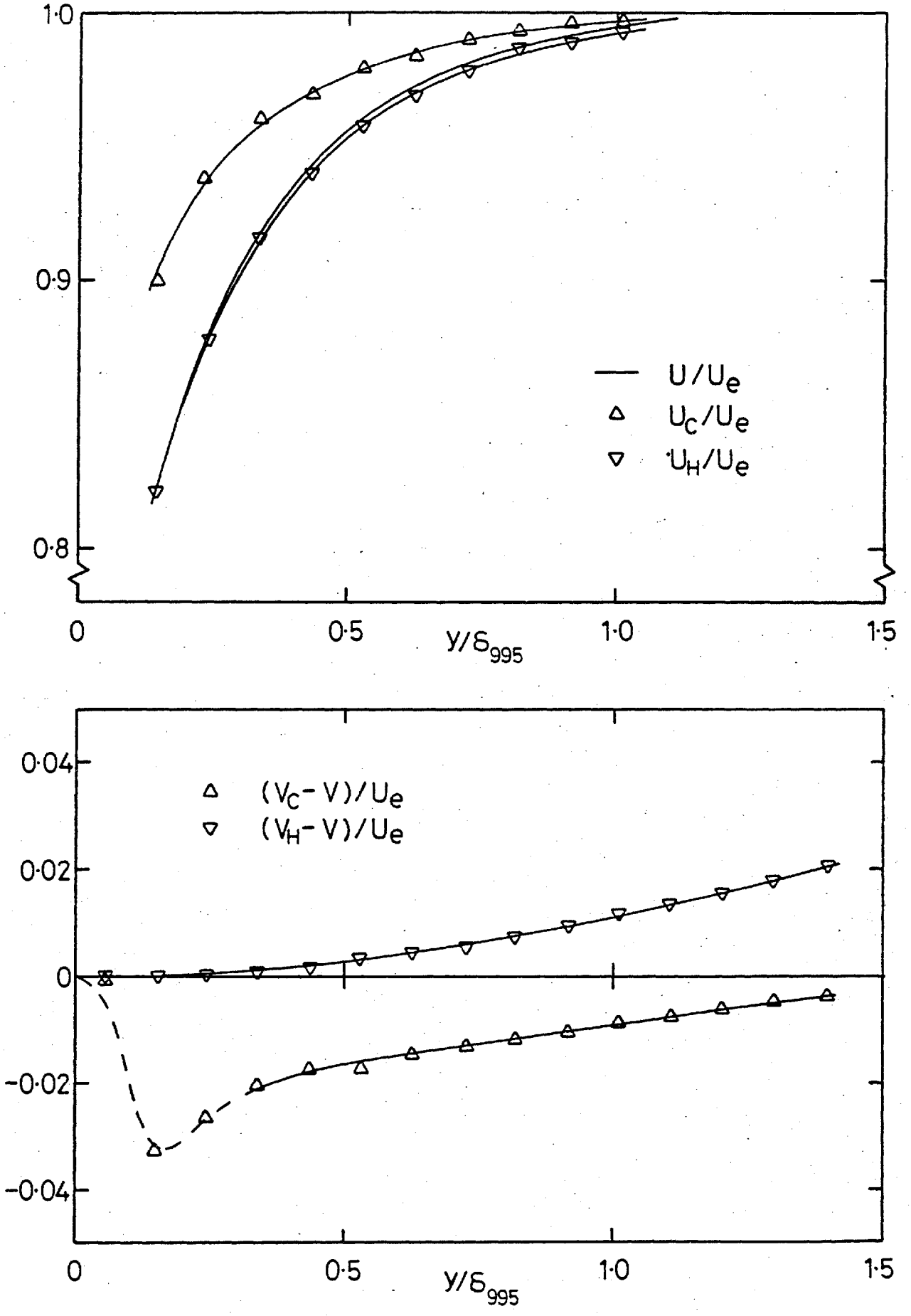

Fig. 4.19c, 7.6 cm grid, X_{LE} = 0.30 m, stn 16. $(u'/U)_e$ = 0.0255, L^u_e/δ_{995} = 0.67

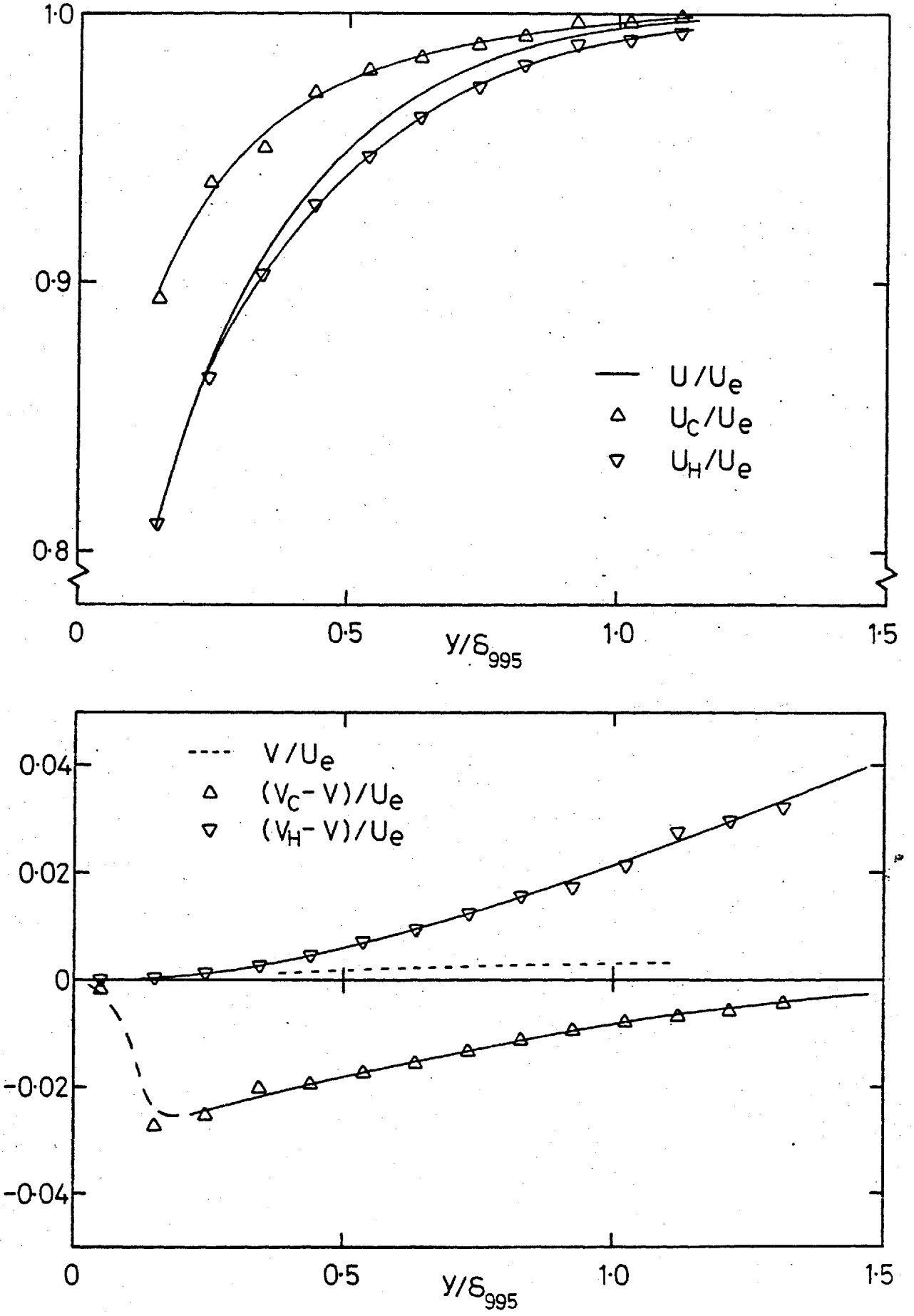

Fig. 4.19d, 15.2 cm grid, X_{LE} = 2.06 m, stn 10. $(u'/U)_e$ = 0.0410, L^u_e/δ_{995} = 1.90

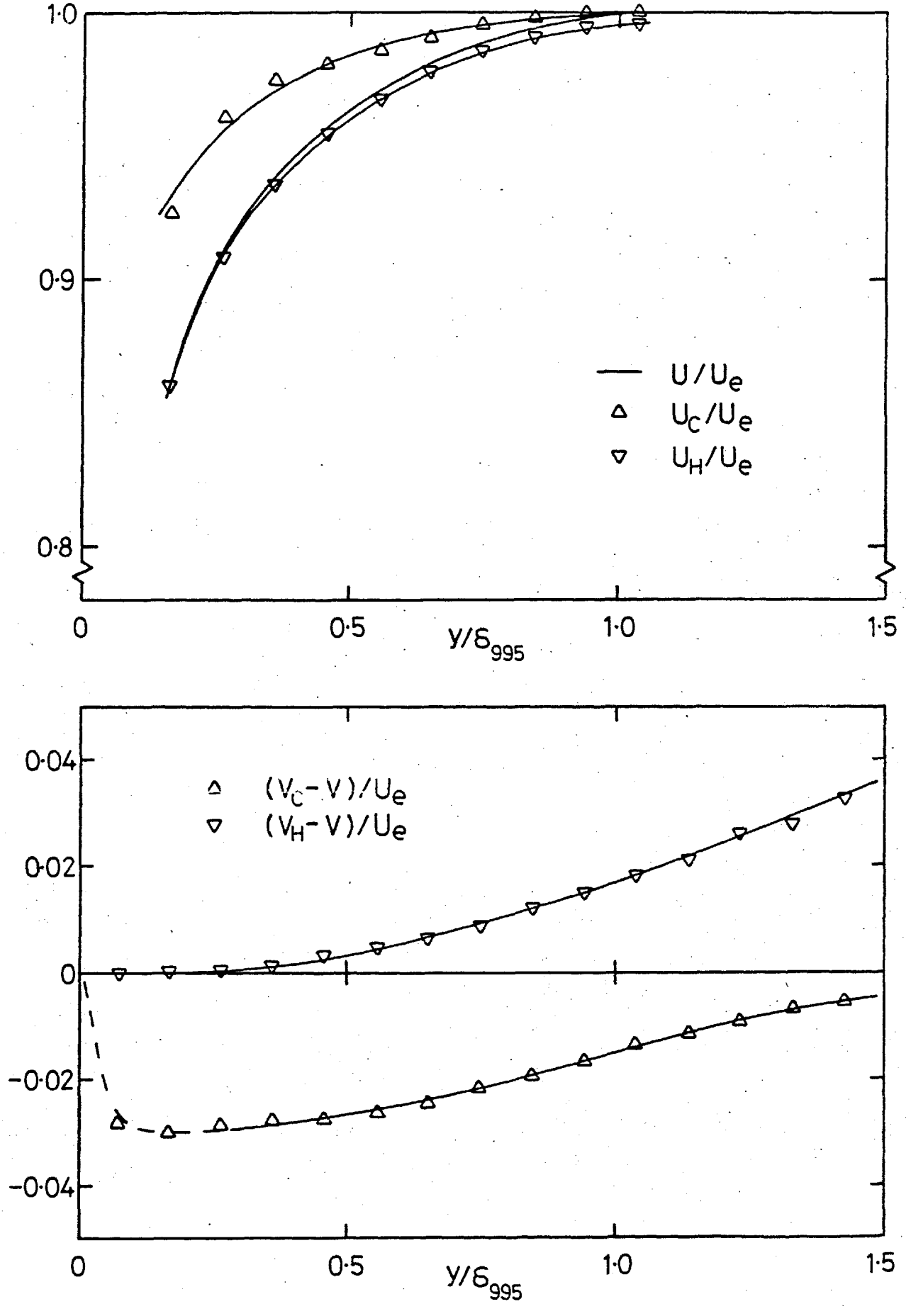

Fig. 4.19e, 7.6 cm grid, X_{LE} = 0.30 m, stn 8. $(u'/U)_e$ = 0.0399, L^u_e/δ_{995} = 0.71

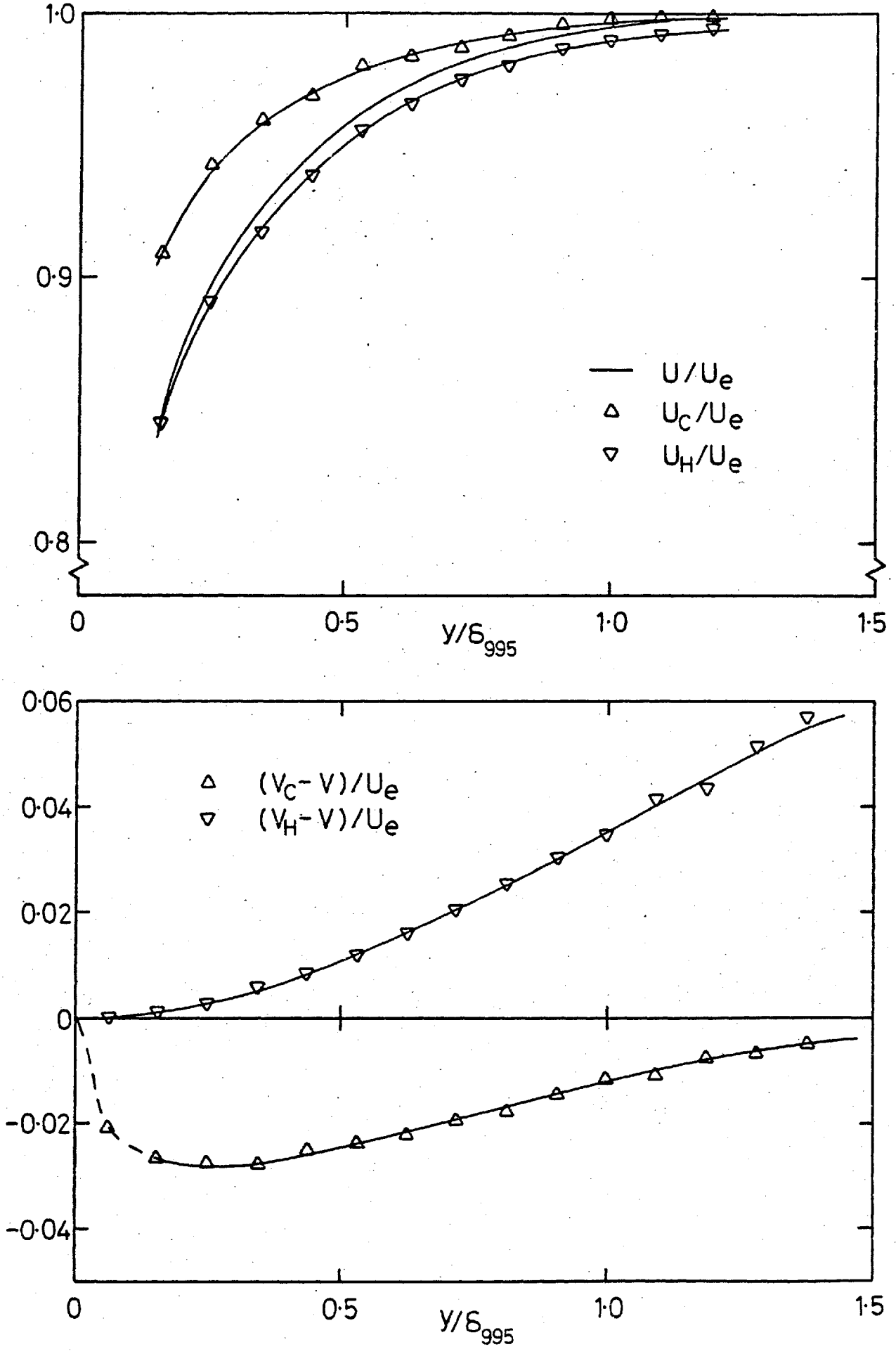

Fig. 4.19f, 15.2 cm grid, X_{LE} = 1.37 m, stn 6. $(u'/U)_e$ = 0.0575, L^u_e/δ_{995} = 1.83

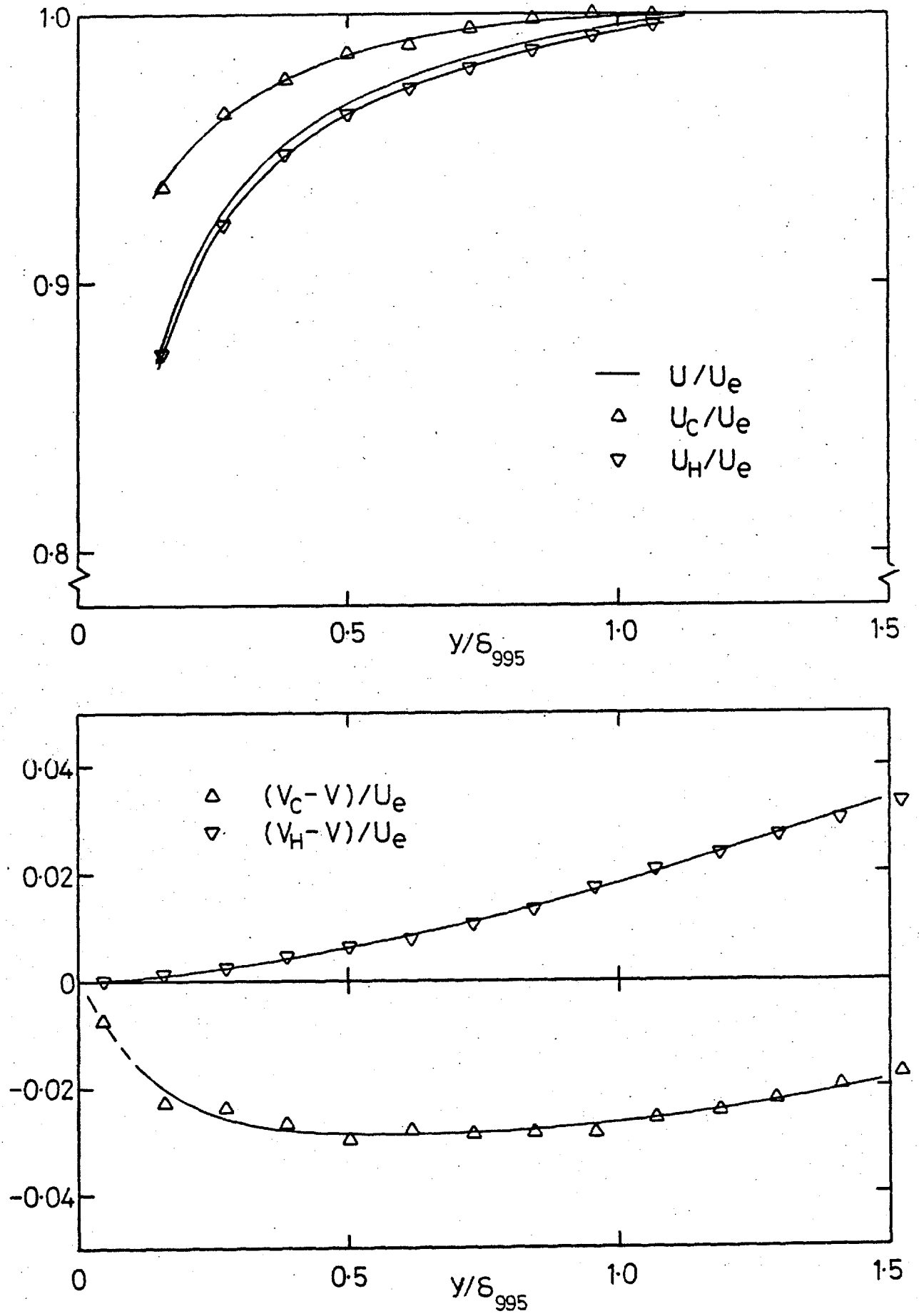

Fig. 4.19g, 15.2 cm grid, X_{LE} = 0.76 m, stn 10. $(u'/U)_e$ = 0.0575, L_e^u/δ_{995} = 1.34

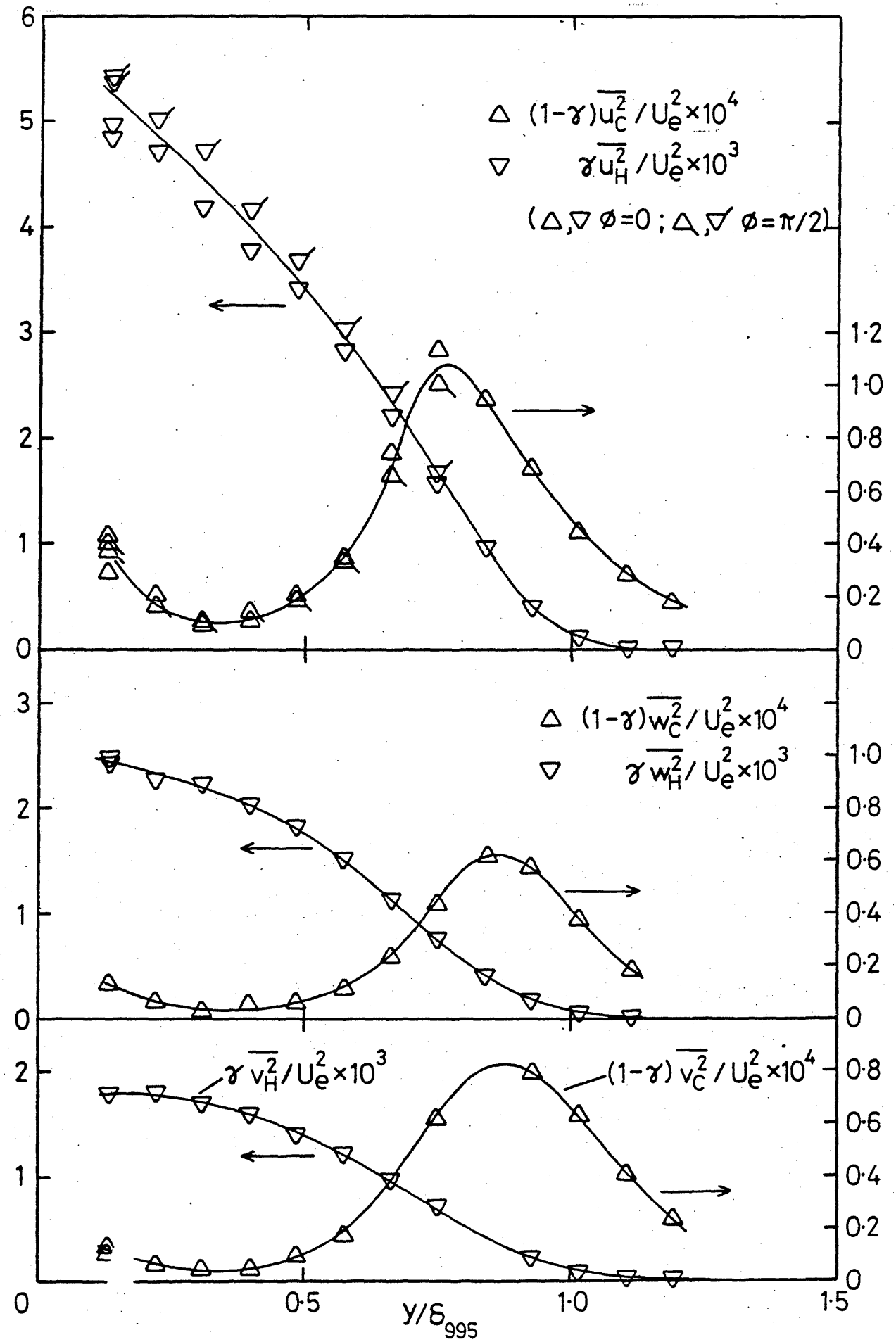

a) No grid, stn 6. (Note different scales for hot and cold zones).

Fig. 4.20 Conditionally-averaged direct-stress profiles

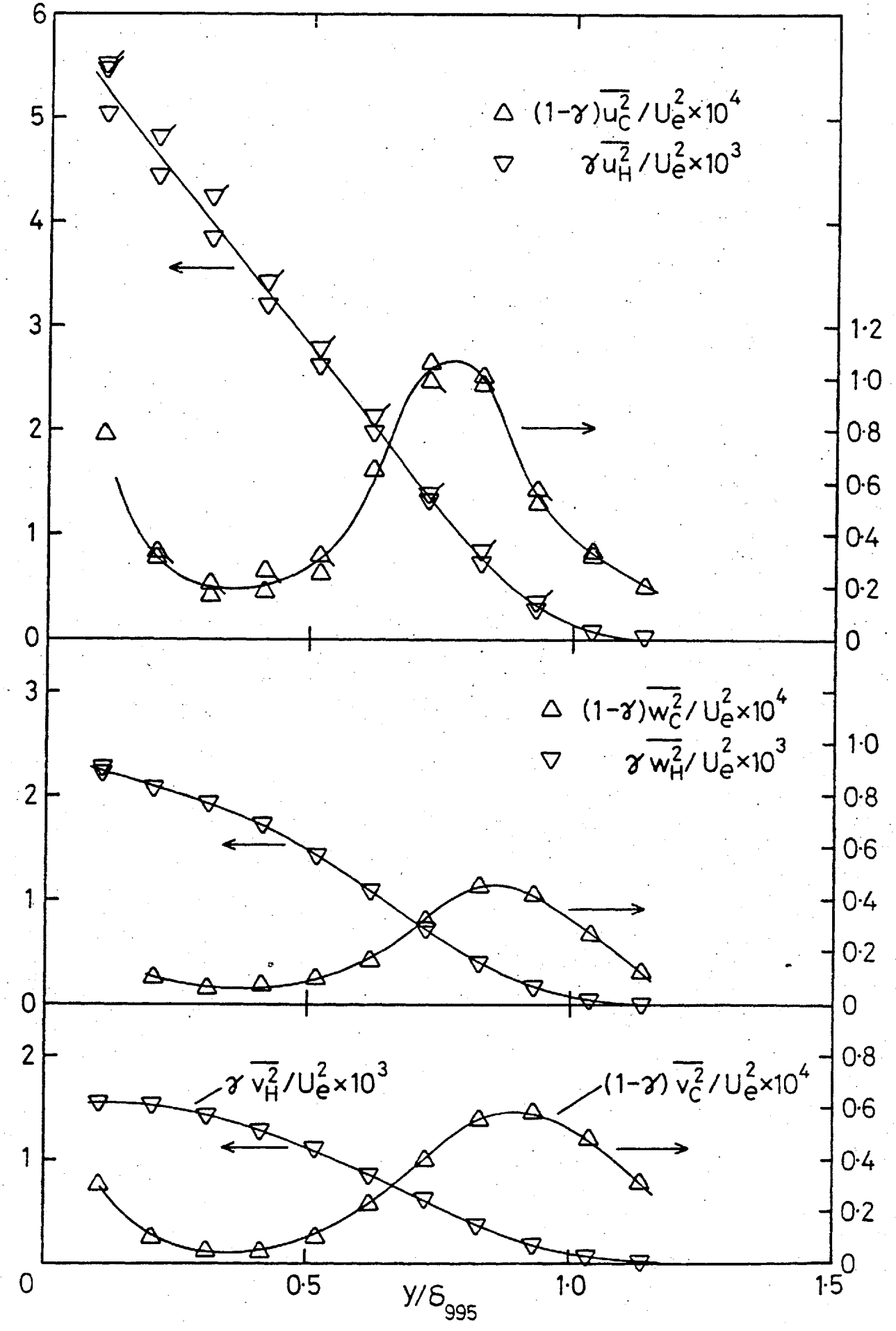

Fig. 4.20b, No grid, stn 14. (Note different scales for hot and cold zones).

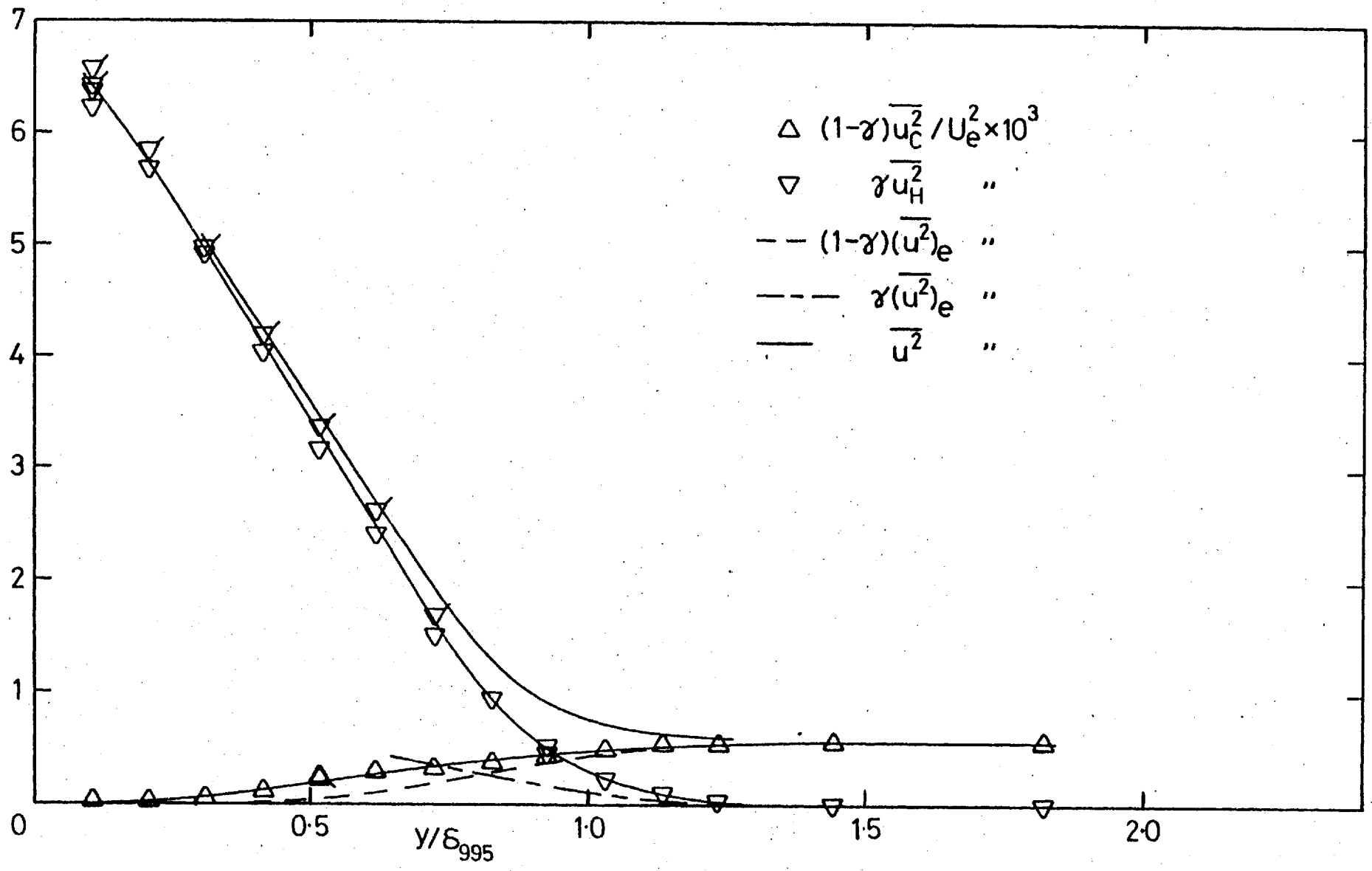

Fig. 4.20c, 7.6 cm grid, X_{LE} = 2.06 m, stn 6. $(u'/U)_e$ = 0.0240, L^u_e/δ_{995} = 1.88. Continued next page.

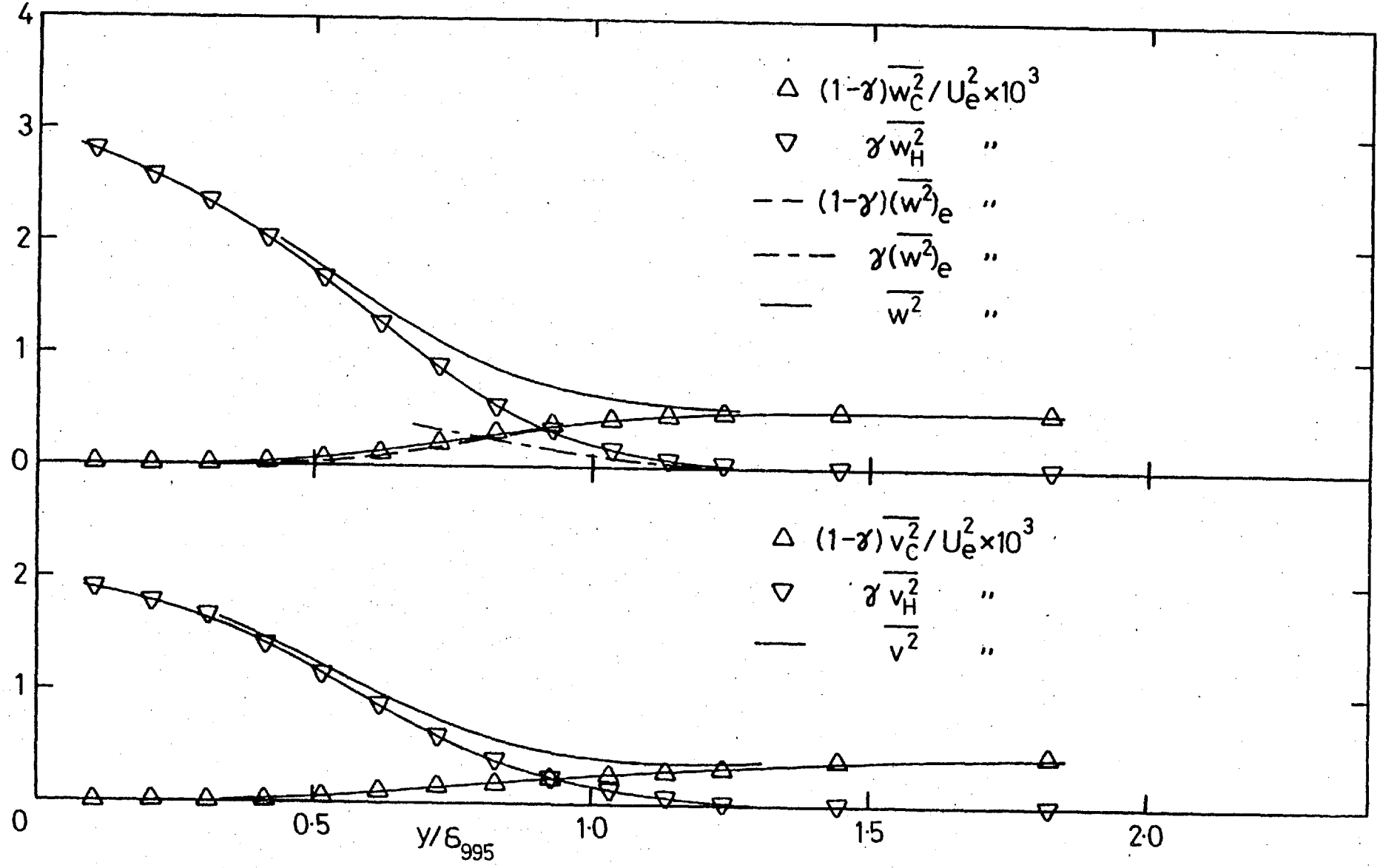

Fig. 4.20c, completed.

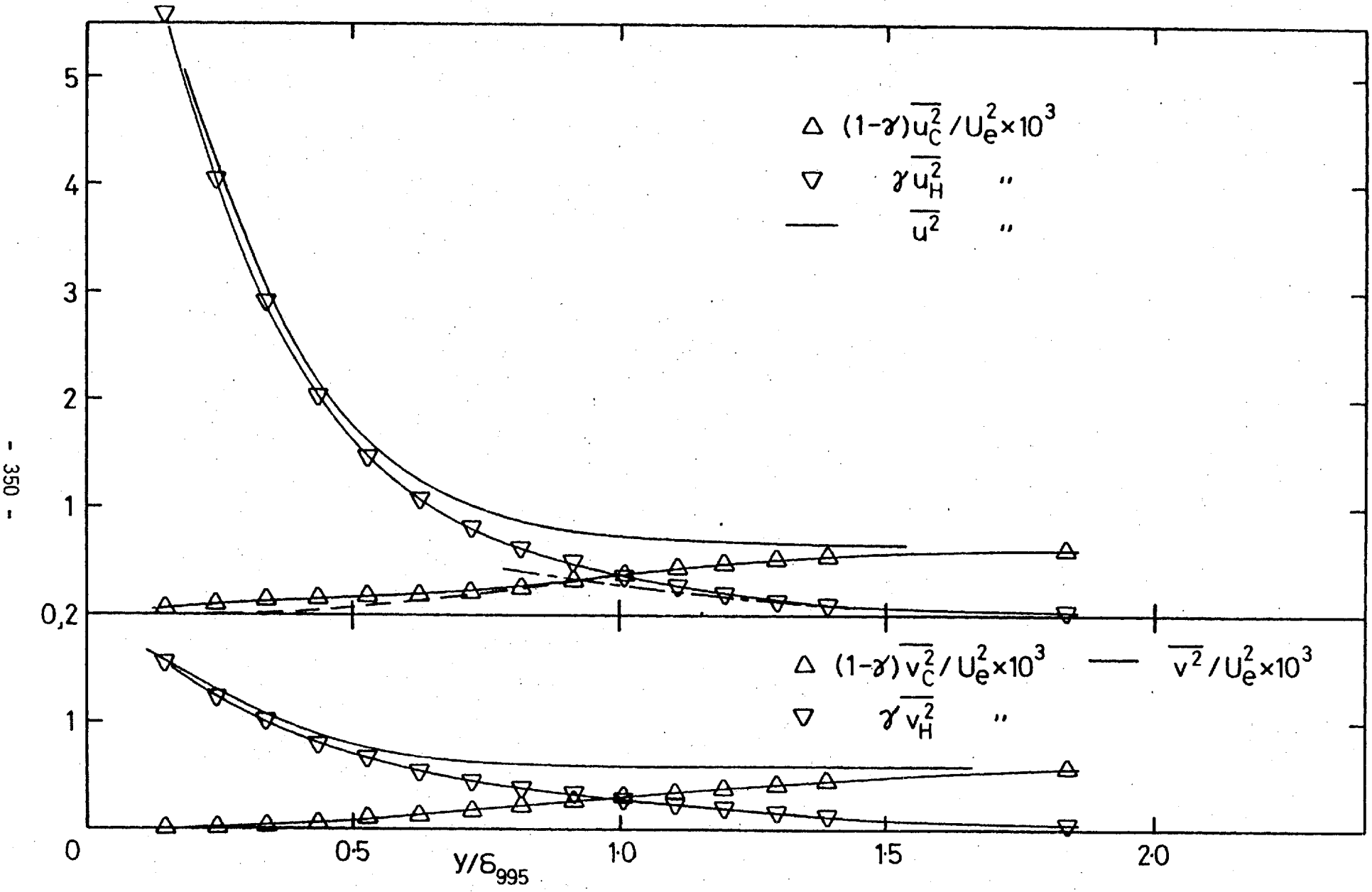

Fig. 4.20d, 7.6 cm grid, X_{LE} = 0.30 m, stn 16. $(u'/U)_e$ = 0.0255, L^u_e/δ_{995} = 0.67. Broken lines as in c).

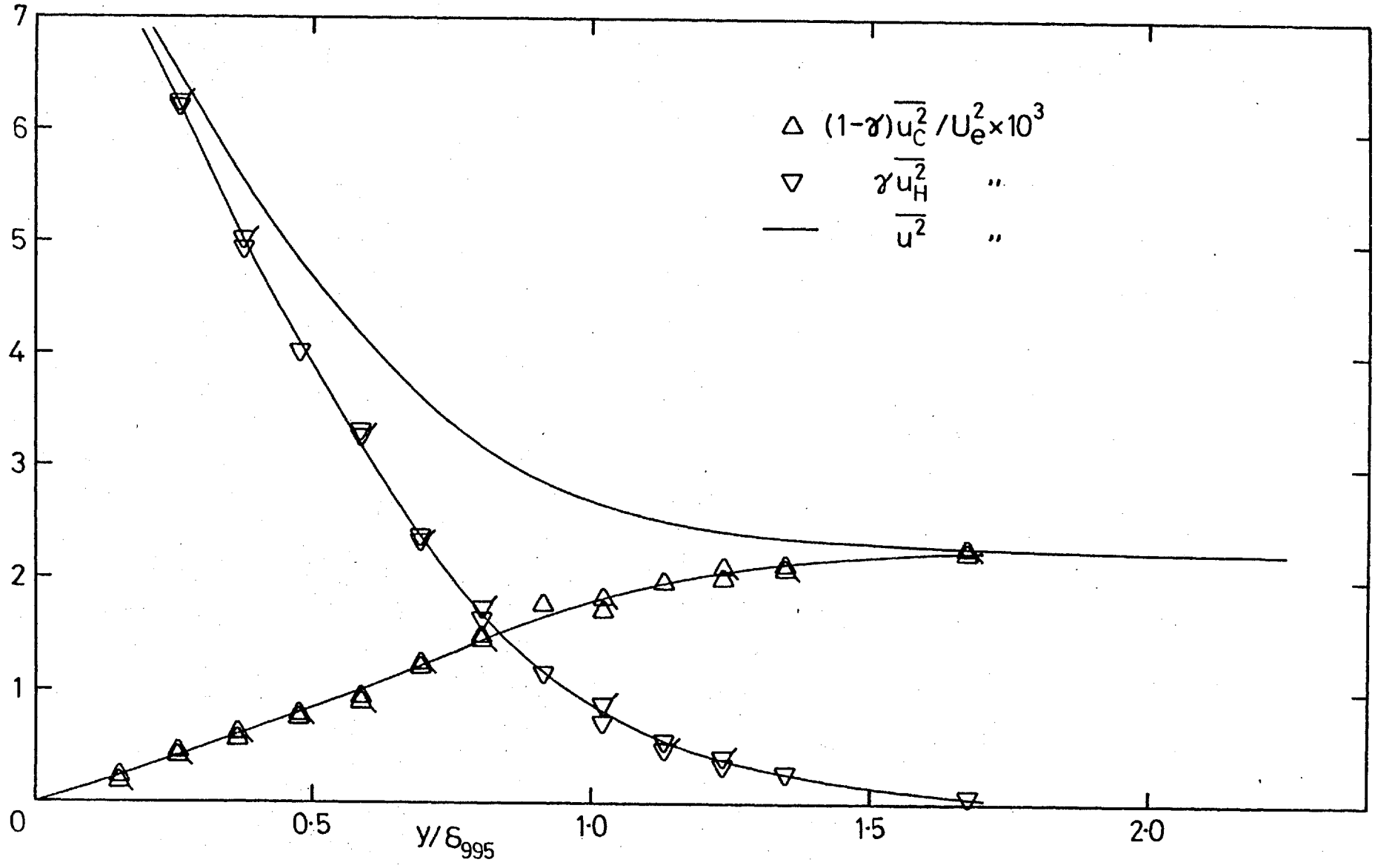

Fig. 4.20e, 15.2 cm grid, X_{LE} = 2.06 m, stn 6. $(u'/U)_e$ = 0.0468, L^u_e/δ_{995} = 2.72. Continued next page.

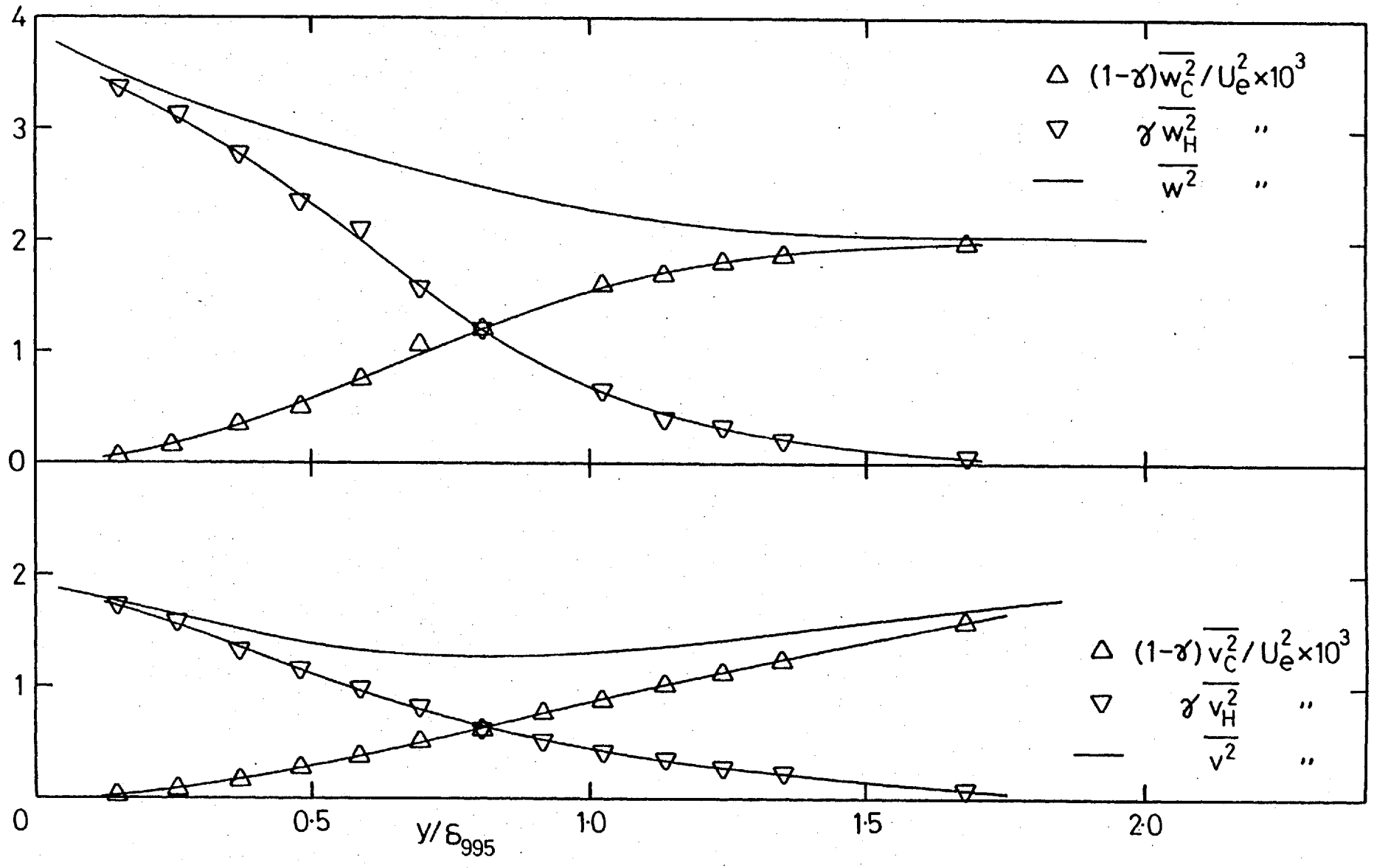

Fig. 4.20e, completed.

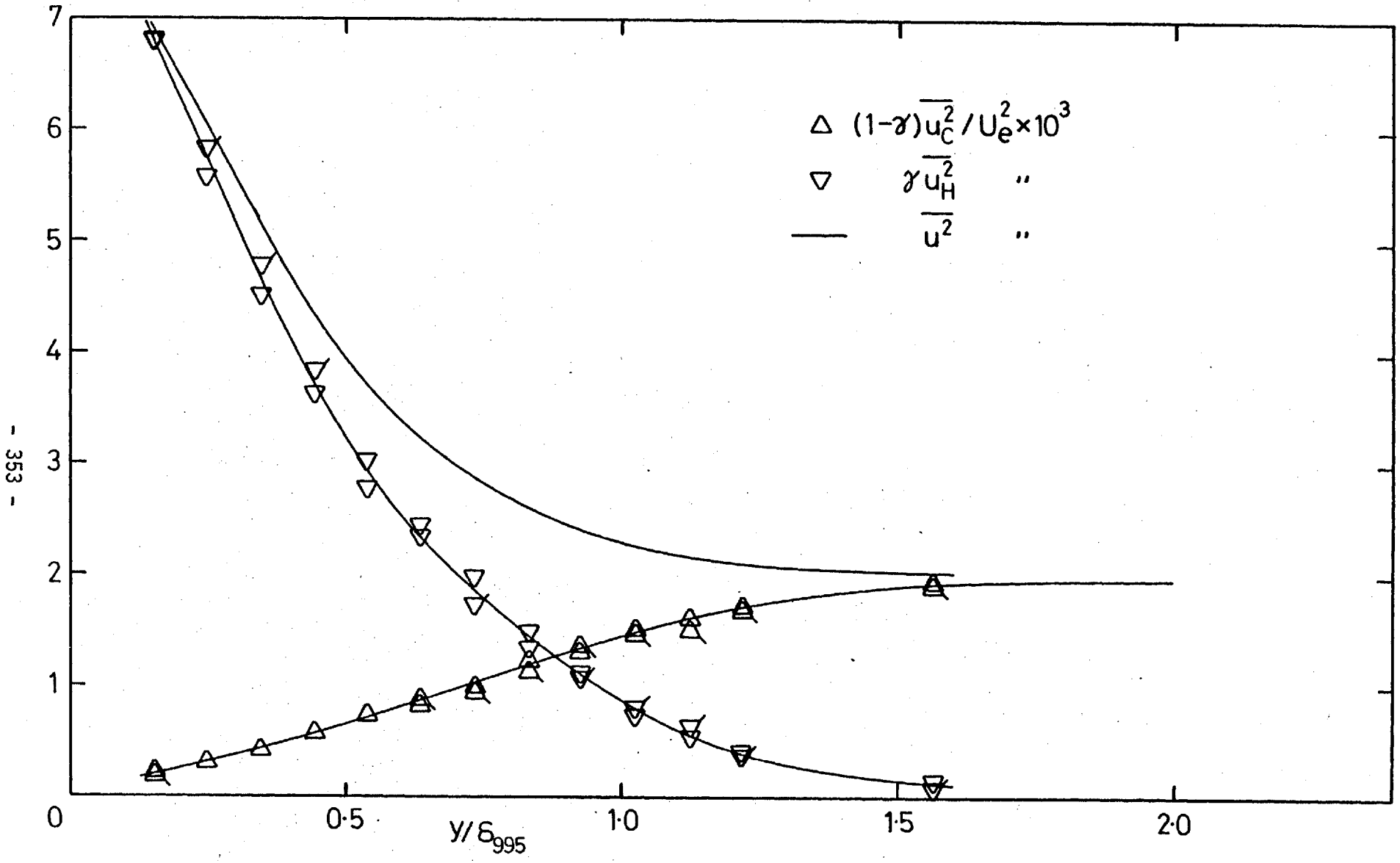

Fig. 4.20f, 15.2 cm grid, X_{LE} = 2.06 m, stn 8. $(u'/U)_e$ = 0.0442, L^u_e/δ_{995} = 2.23. Continued next page.

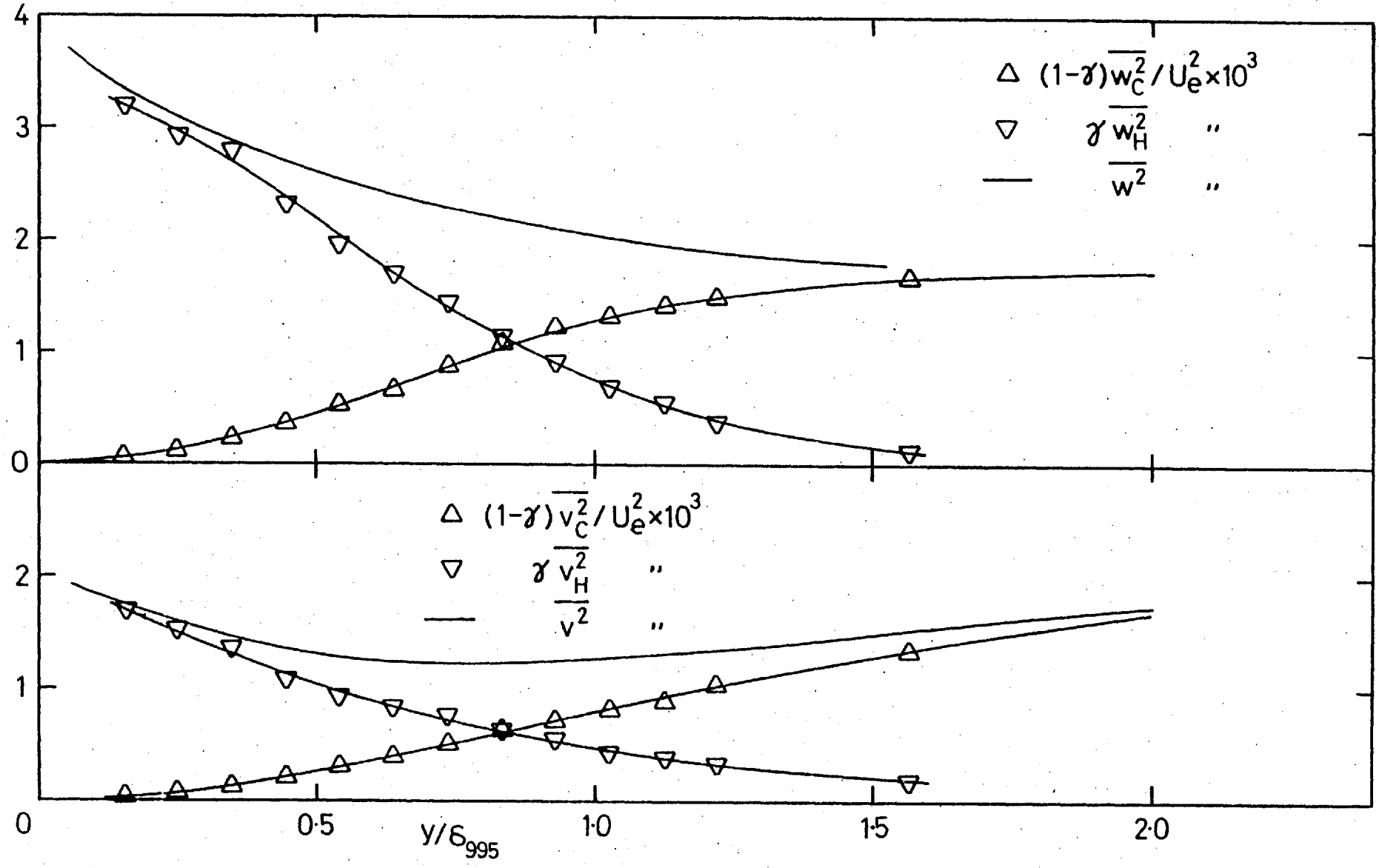

Fig. 4.20f, completed.

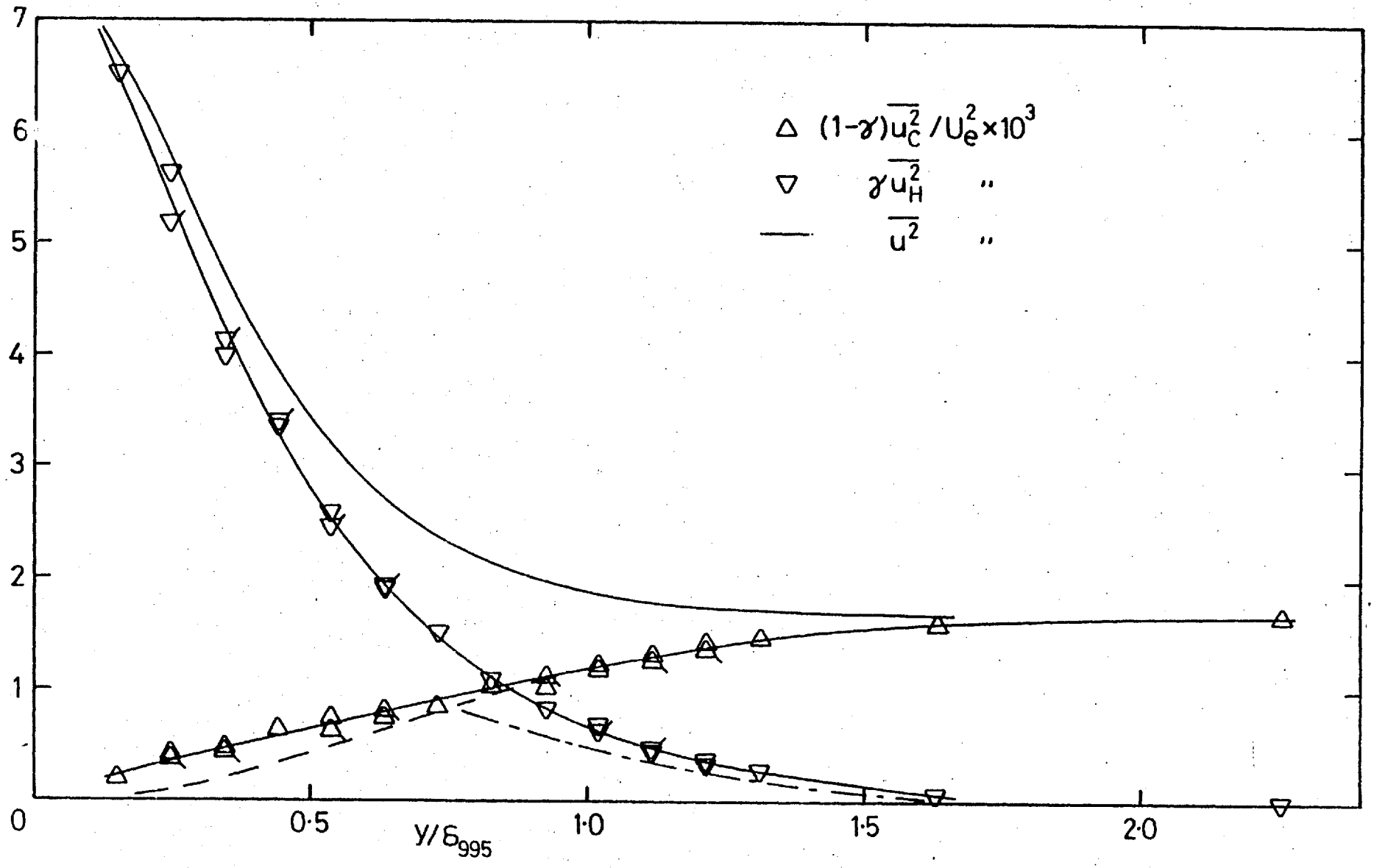

Fig. 4.20g, 15.2 cm grid, X_{LE} = 2.06 m, stn 10. $(u'/U)_e$ = 0.0410, L^u_e/δ_{995} = 1.90. Broken lines as in a).

Continued next page.

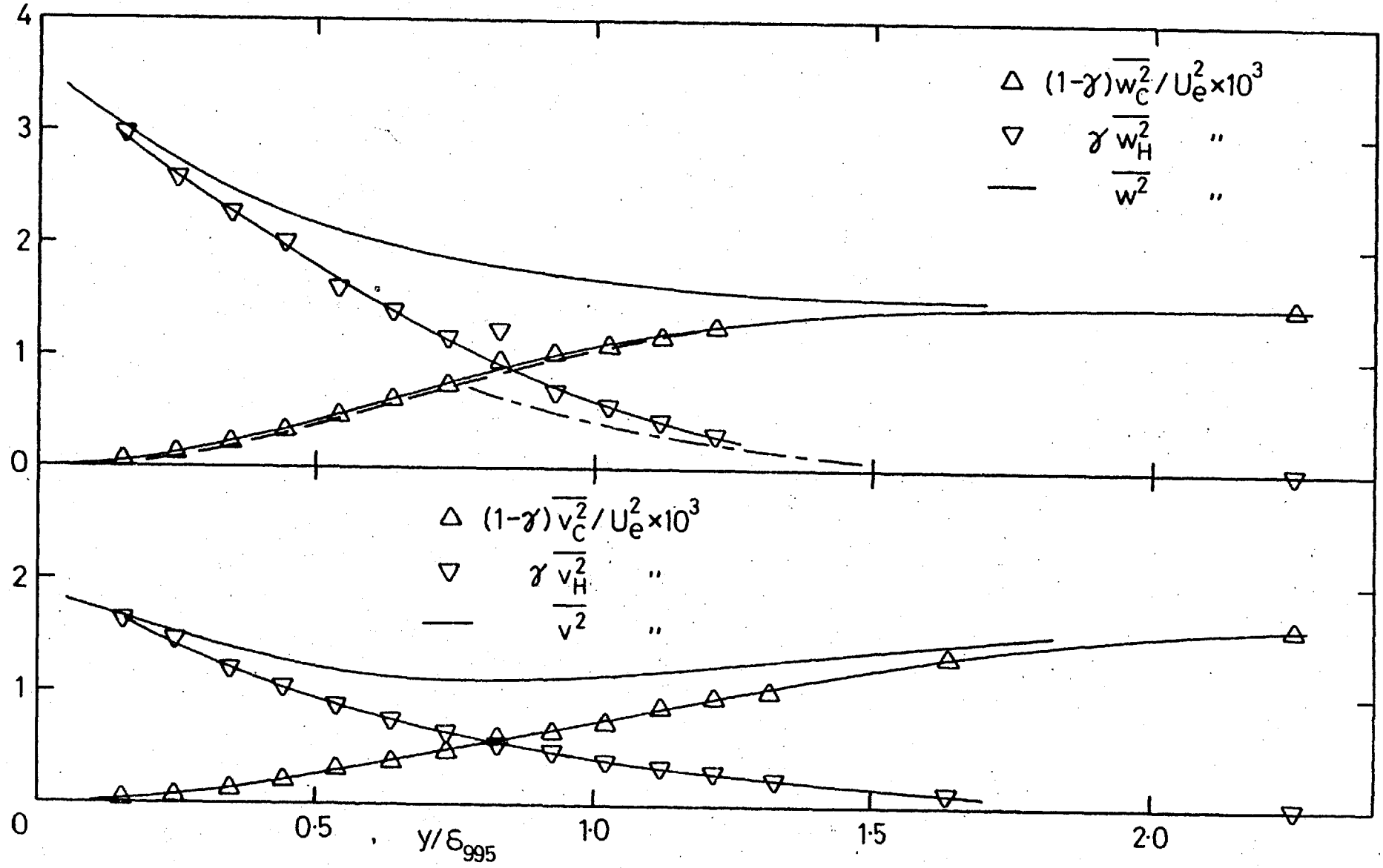

Fig. 4.20g, completed.

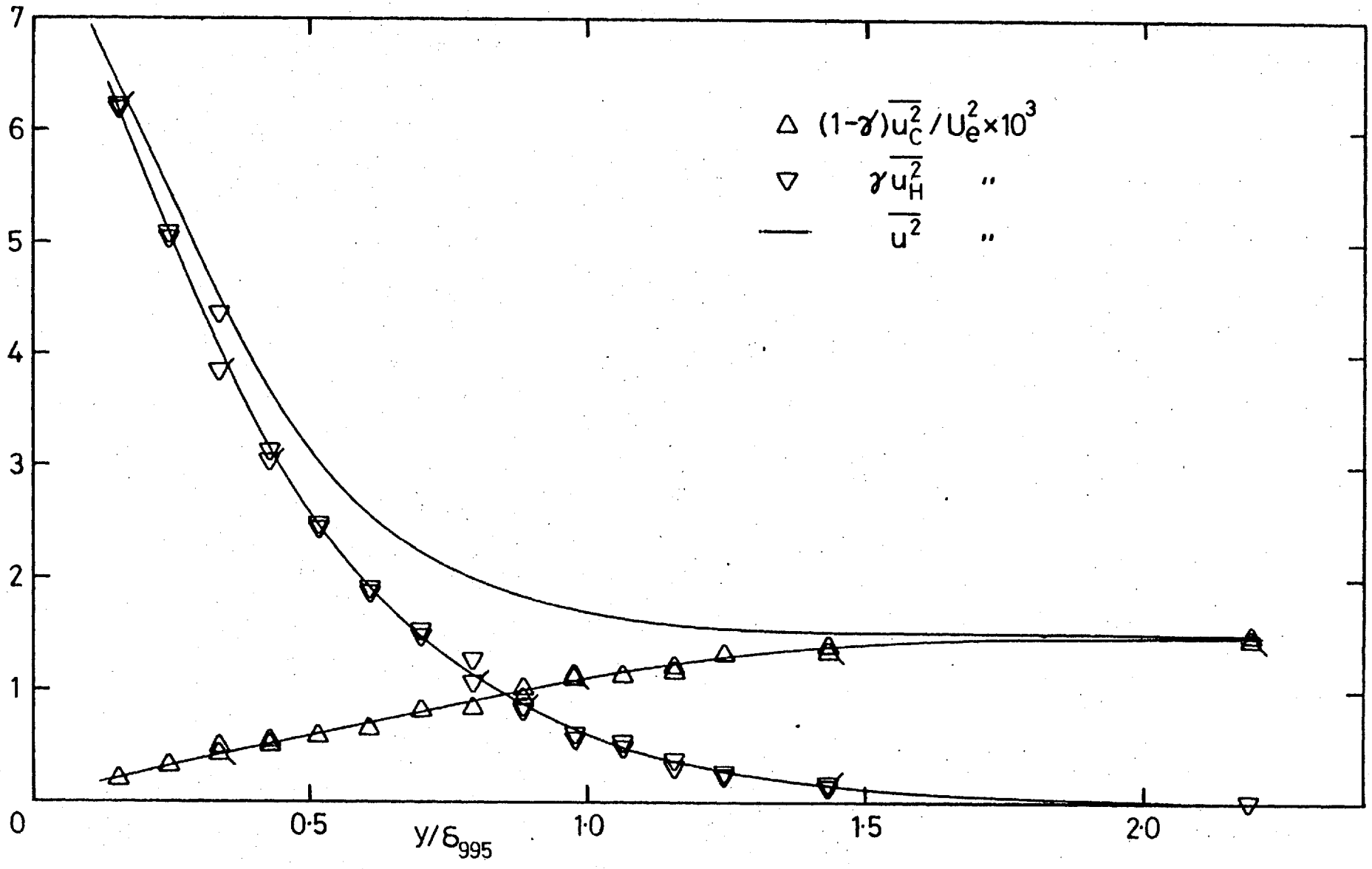

Fig. 4.20h, 15.2 cm grid, X_{LE} = 2.06 m, stn 12. $(u'/U)_e$ = 0.0387, L^u_e/δ_{995} = 1.70. Continued next page.

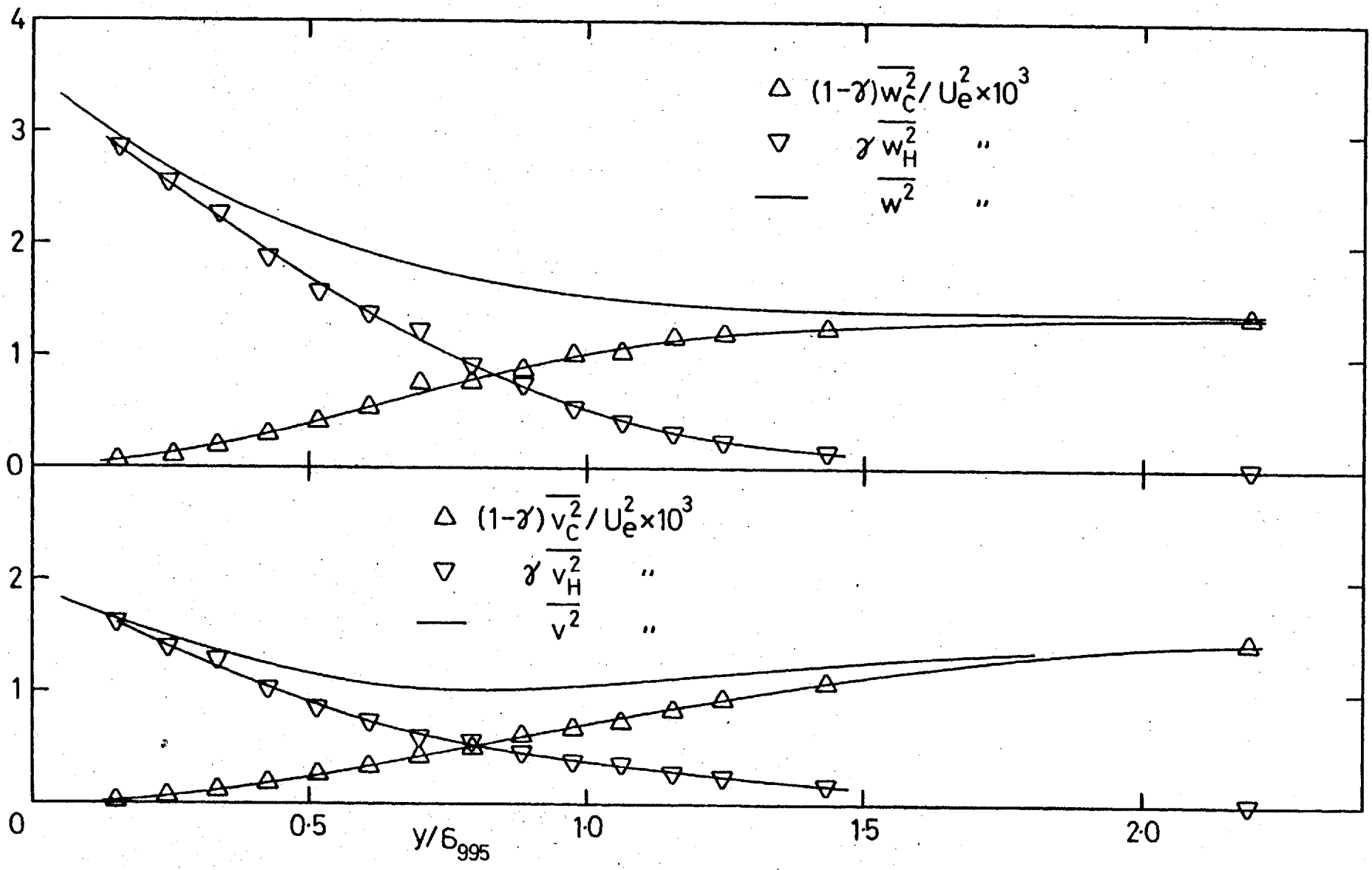

Fig. 4.20h, completed.

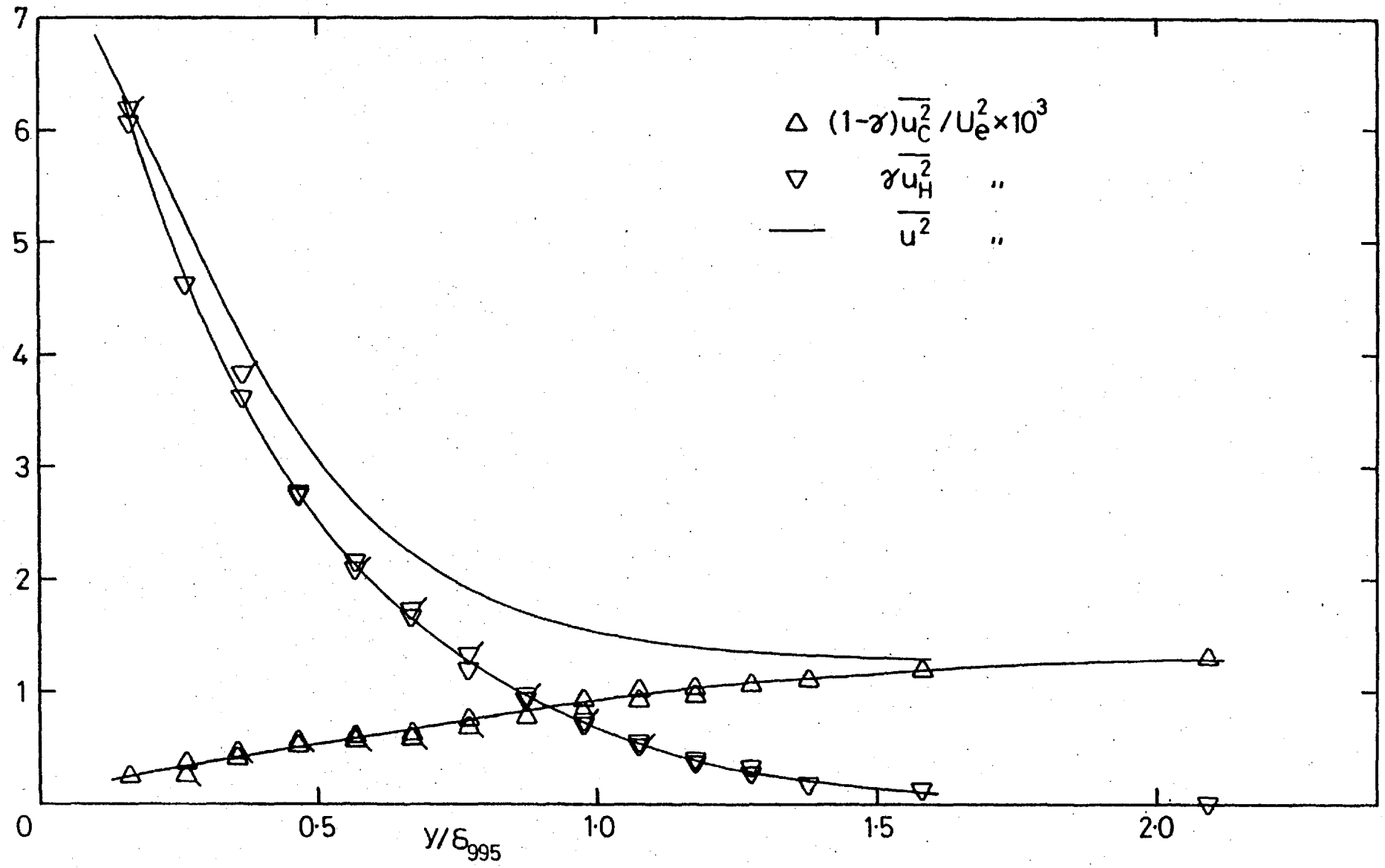

Fig. 4.20i, 15.2 cm grid, X_{LE} = 2.06 m, stn 14. $(u'/U)_e$ = 0.0362, L_e^u/δ_{995} = 1.69. Continued next page.

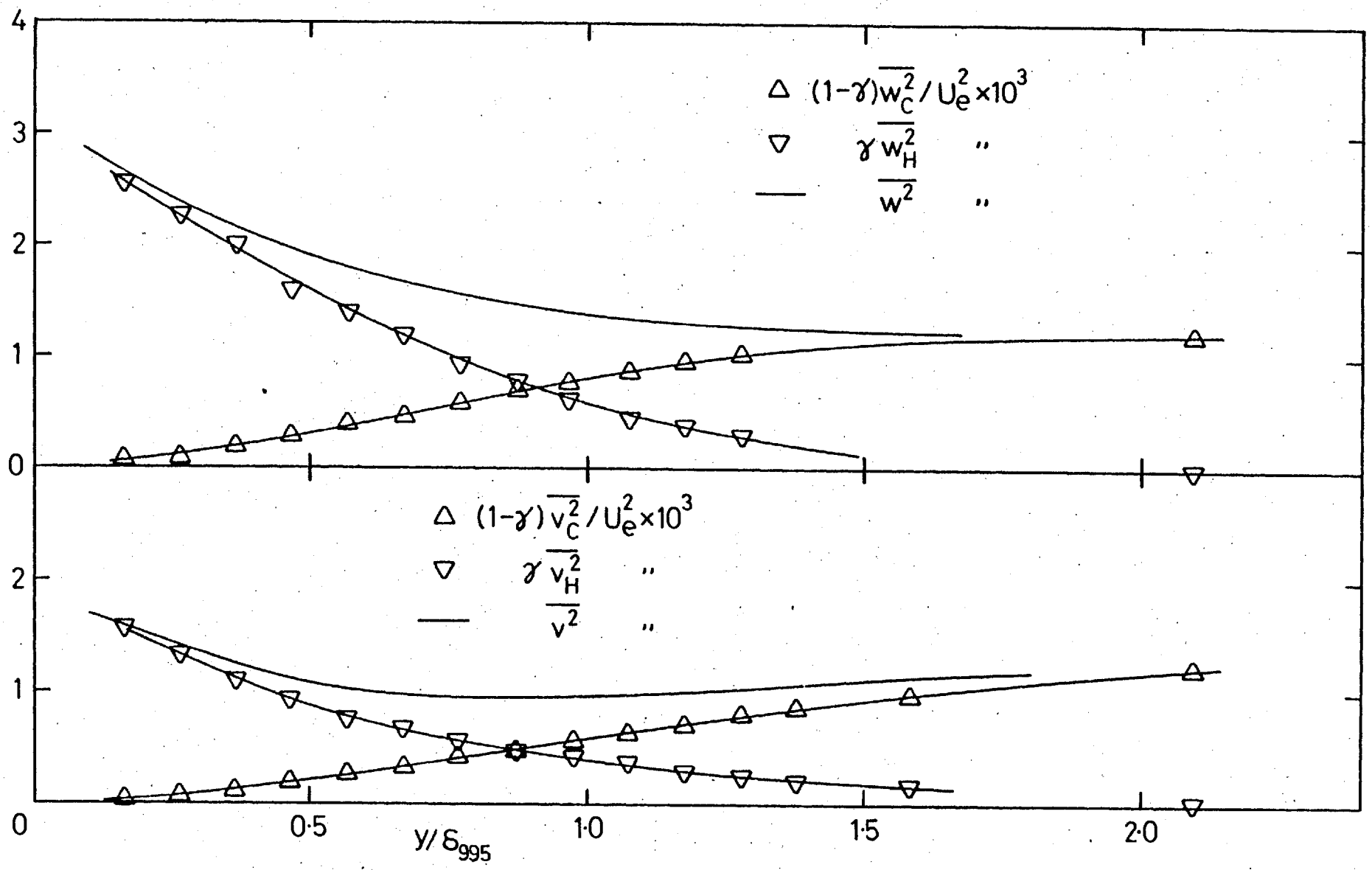

Fig. 4.20i, completed.

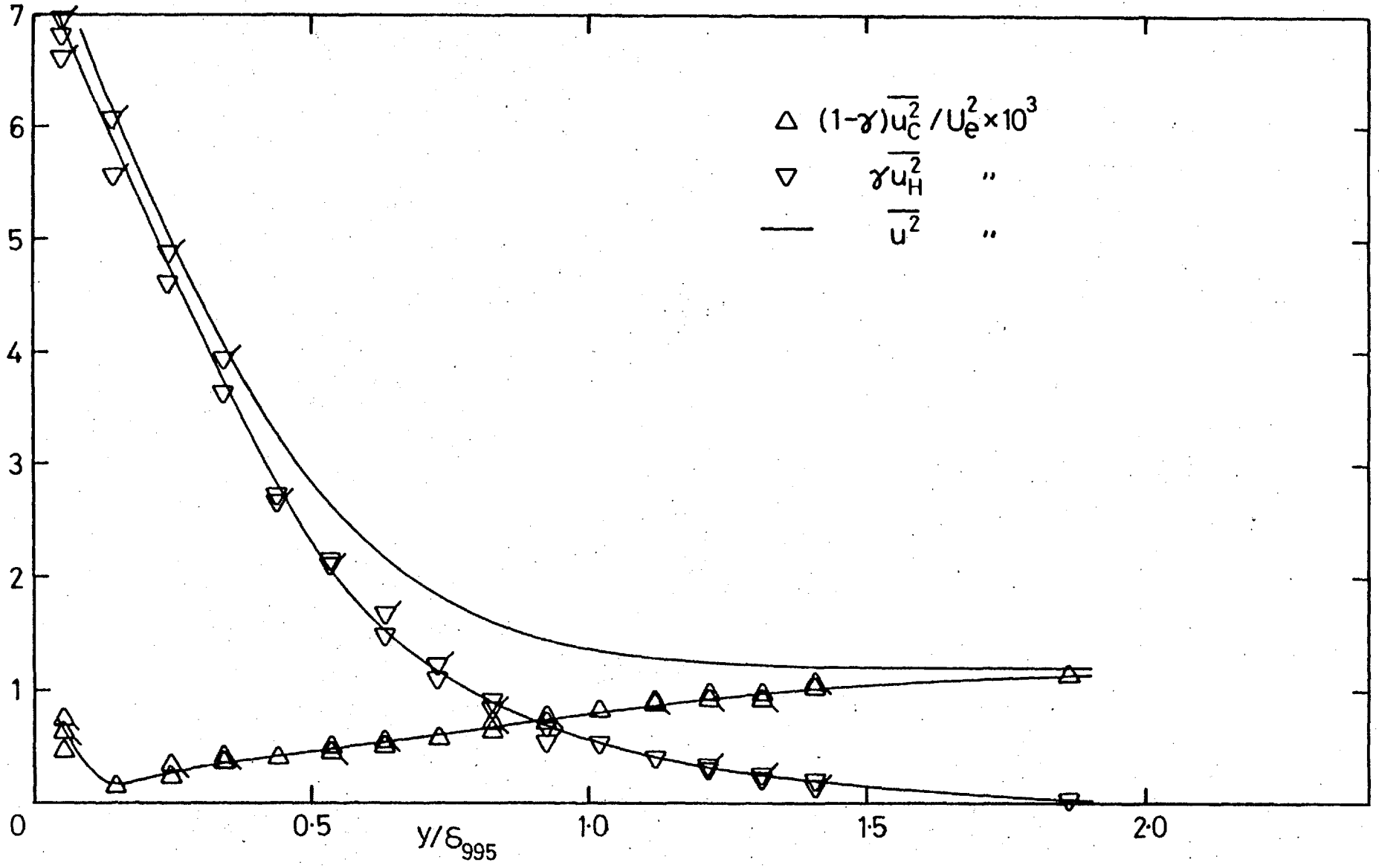

Fig. 4.20j, 15.2 cm grid, X_{LE} = 2.06 m, stn 16. $(u'/U)_e$ = 0.0345, L_e^u/δ_{995} = 1.55. Continued next page.

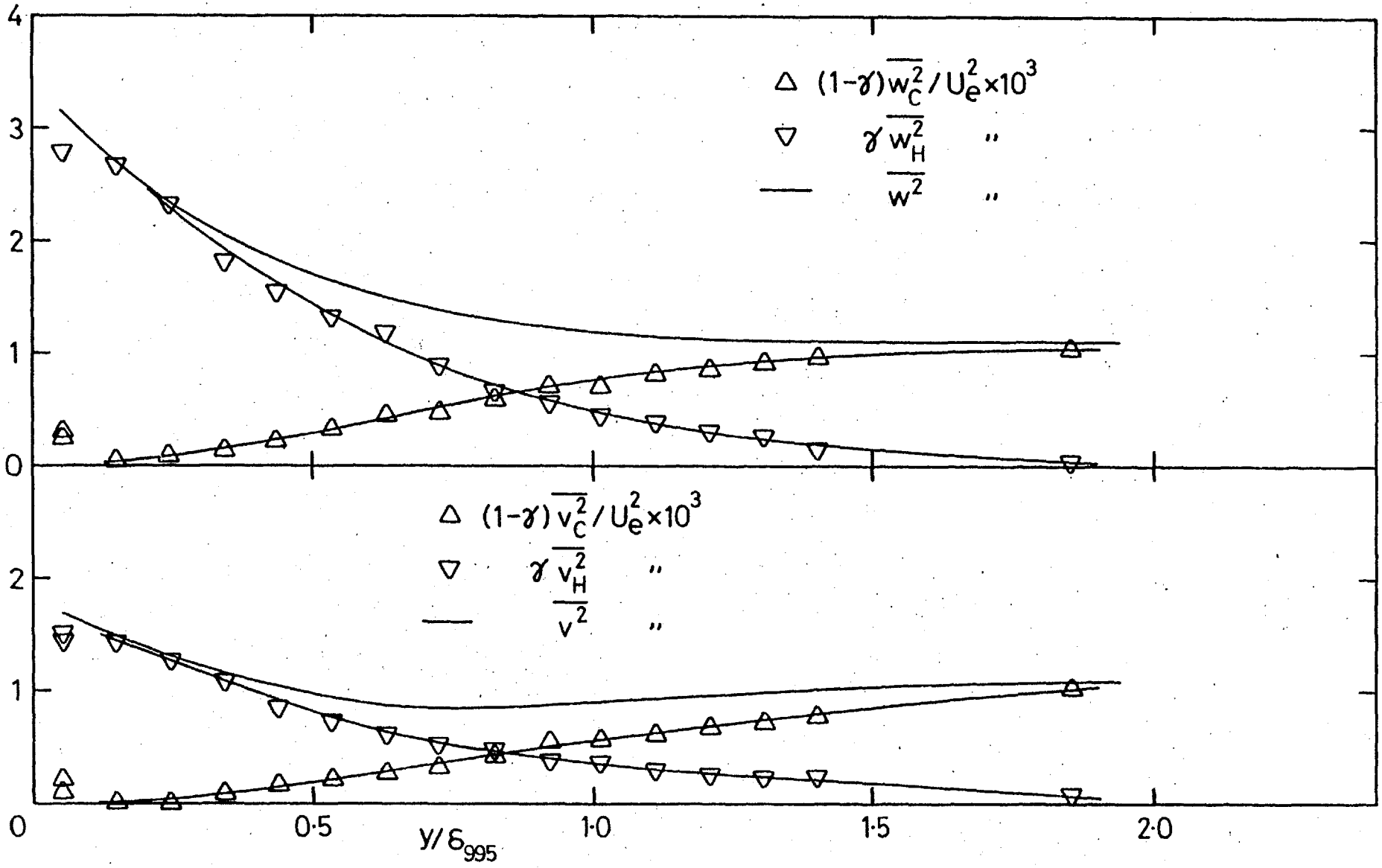

Fig. 4.20j, completed.

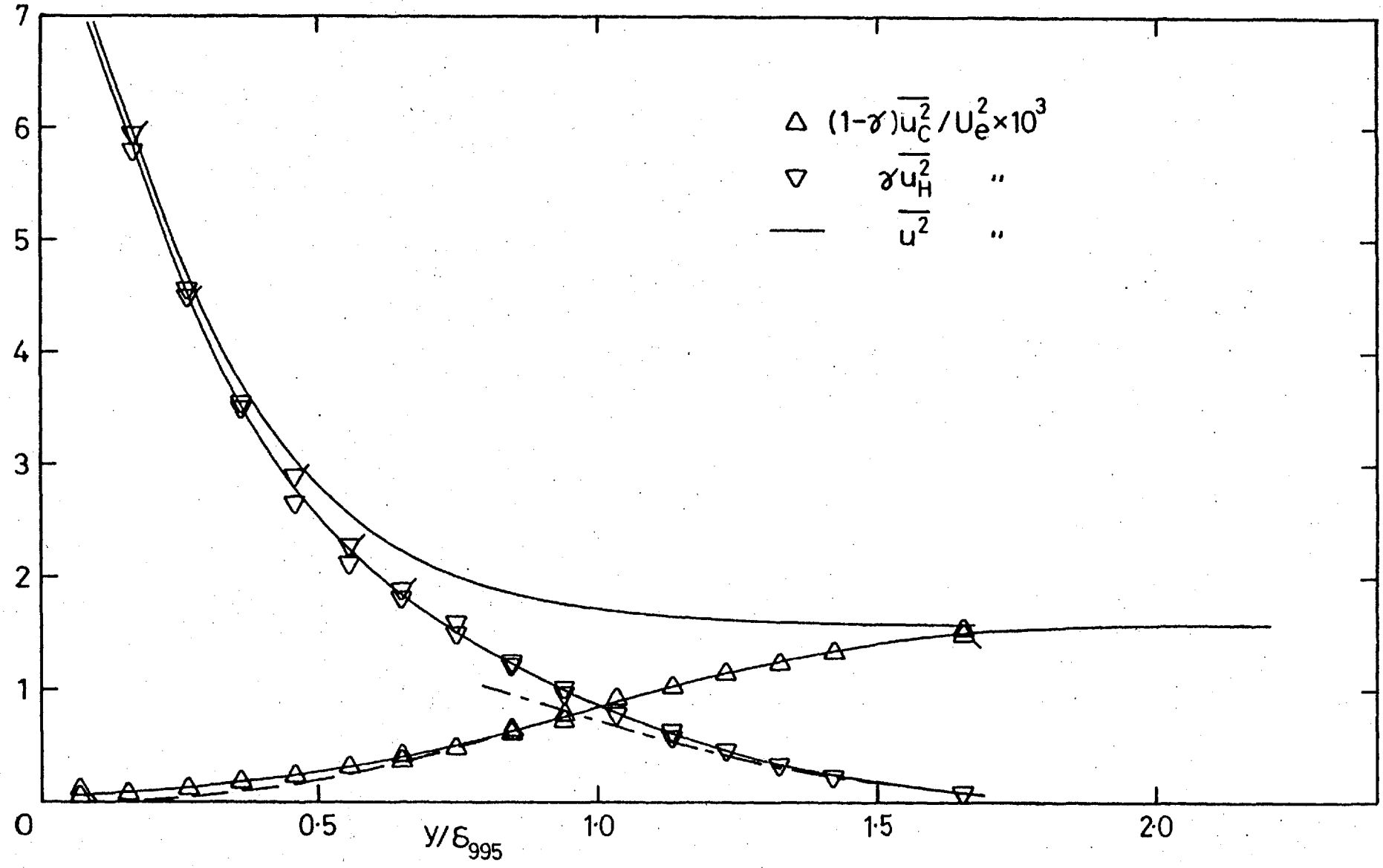

Fig. 4.20k, 7.6 cm grid, X_{LE} = 0.30 m, stn 8. $(u'/U)_e$ = 0.0399, L^u_e/δ_{995} = 0.71. Broken lines as in c).

Continued next page.

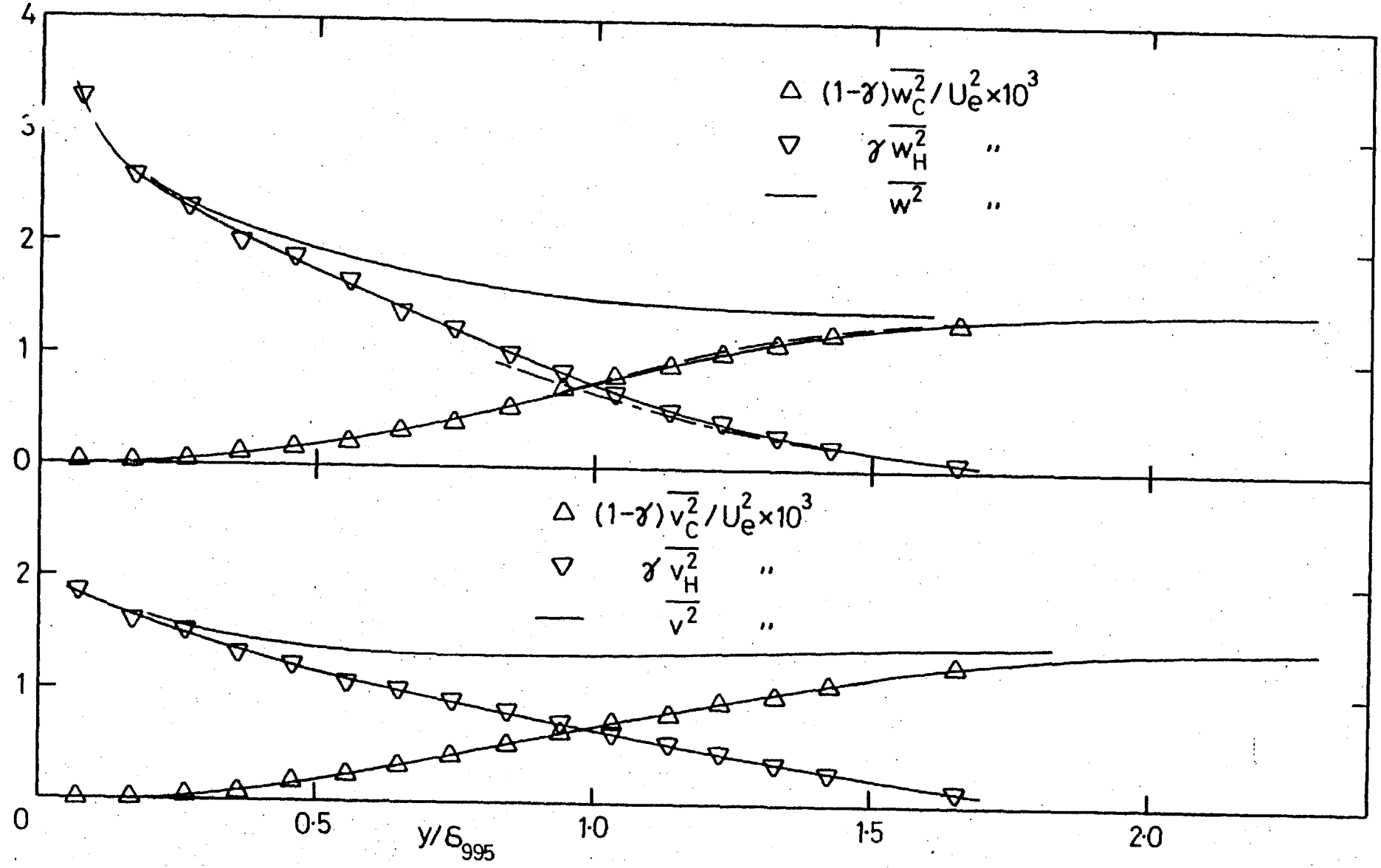

Fig. 4.20k, completed.

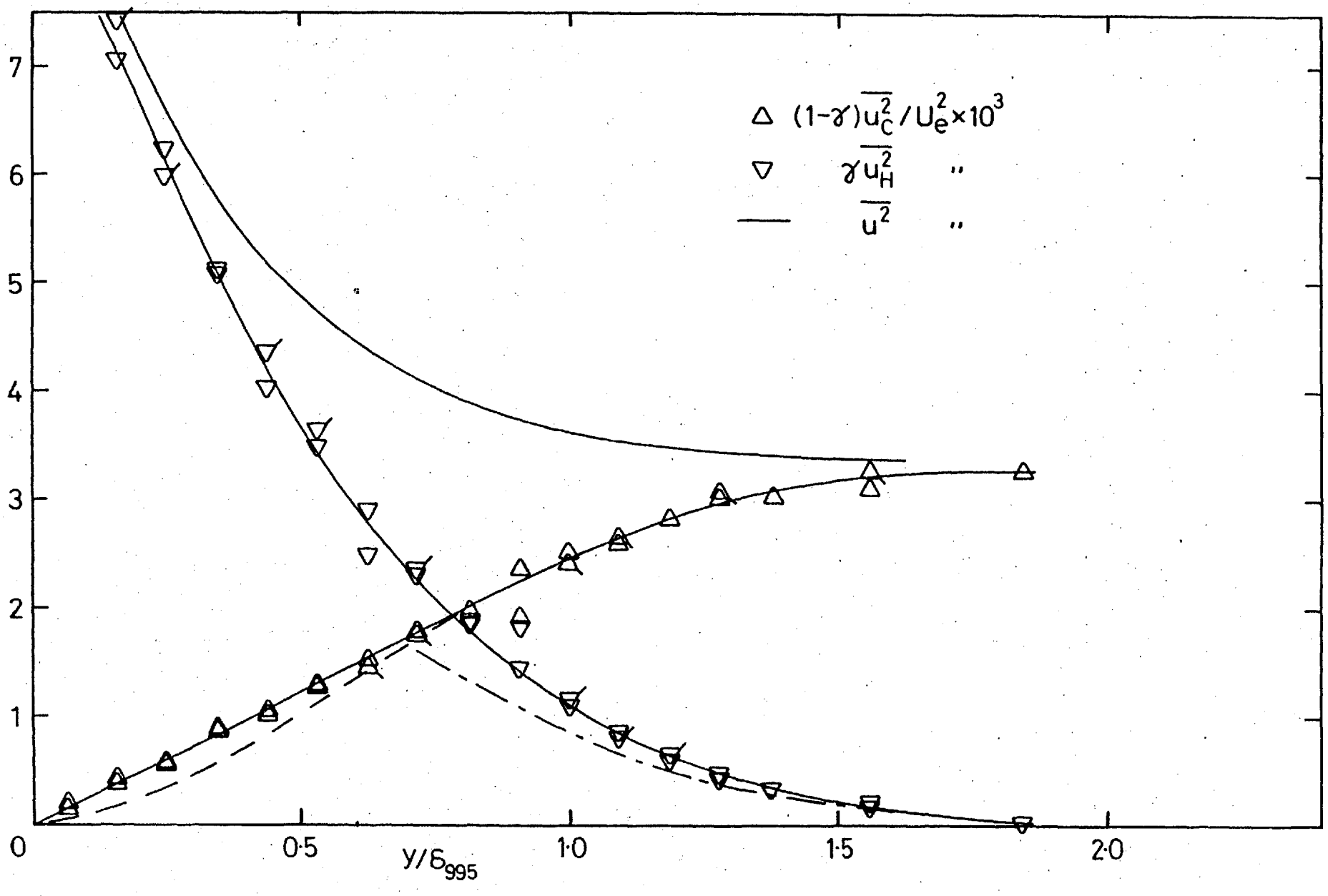

Fig. 4.20ℓ, 15.2 cm grid, X_{LE} = 1.37 m, stn 6. $(u'/U)_e$ = 0.0575, L_e^u/δ_{995} = 1.83. Broken lines as in c).

Continued next page.

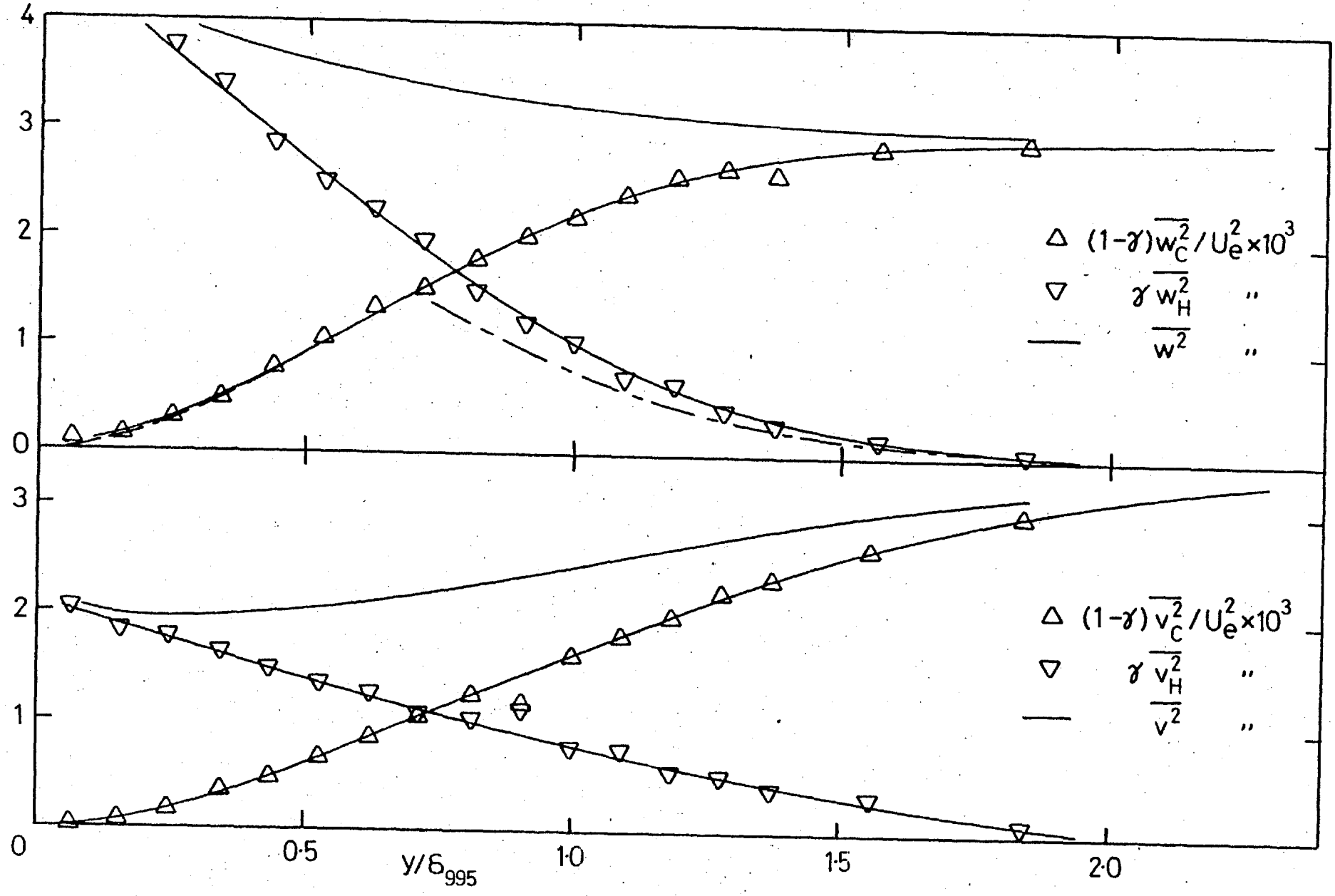

Fig. 4.20ℓ, completed.

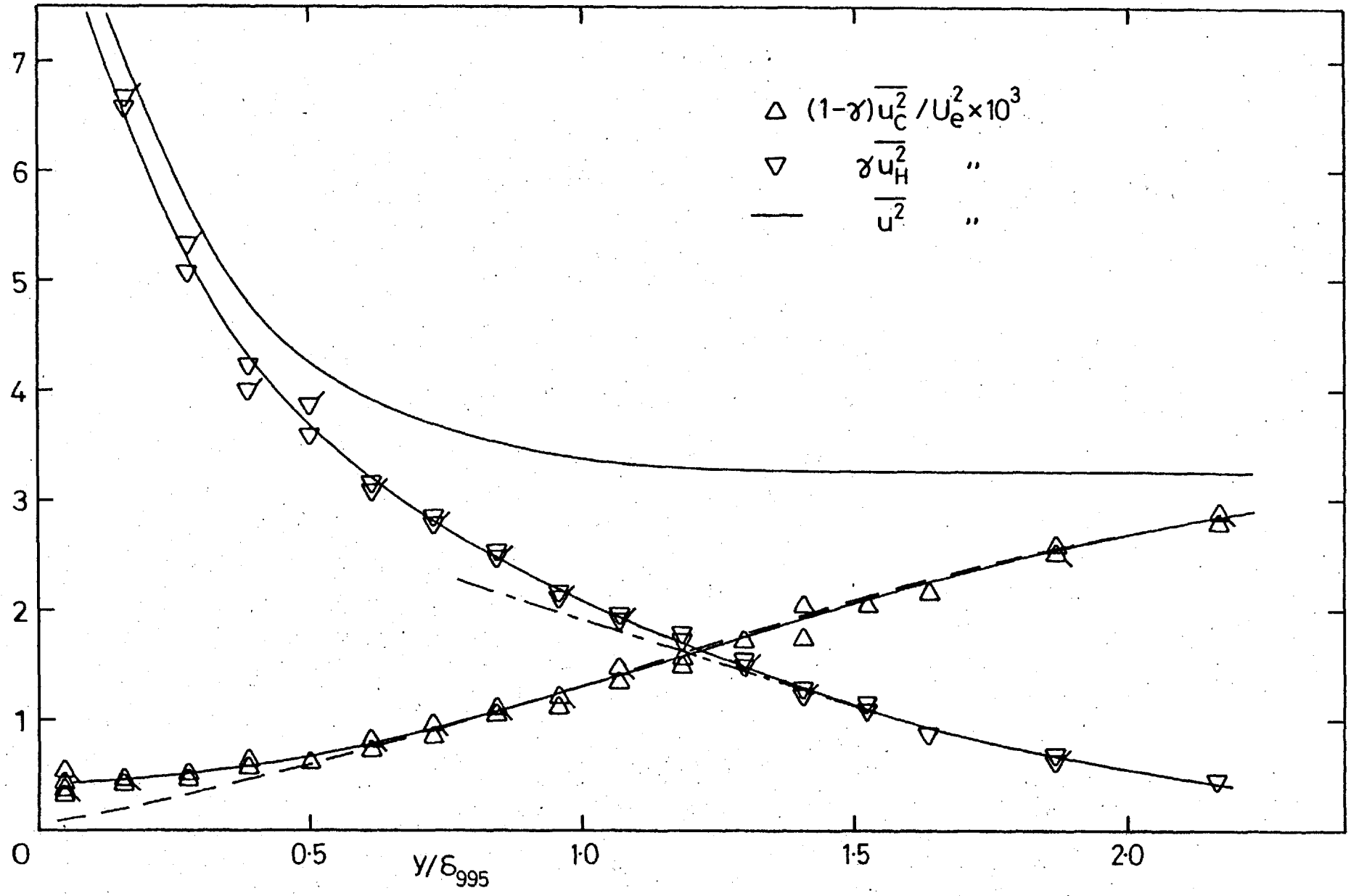

Fig. 4.20m, 15.2 cm grid, X_{LE} = 0.76 m, stn 10. $(u'/U)_e$ = 0.0575, L_e^u/δ_{995} = 1.34. Broken lines as in c).

Continued next page.

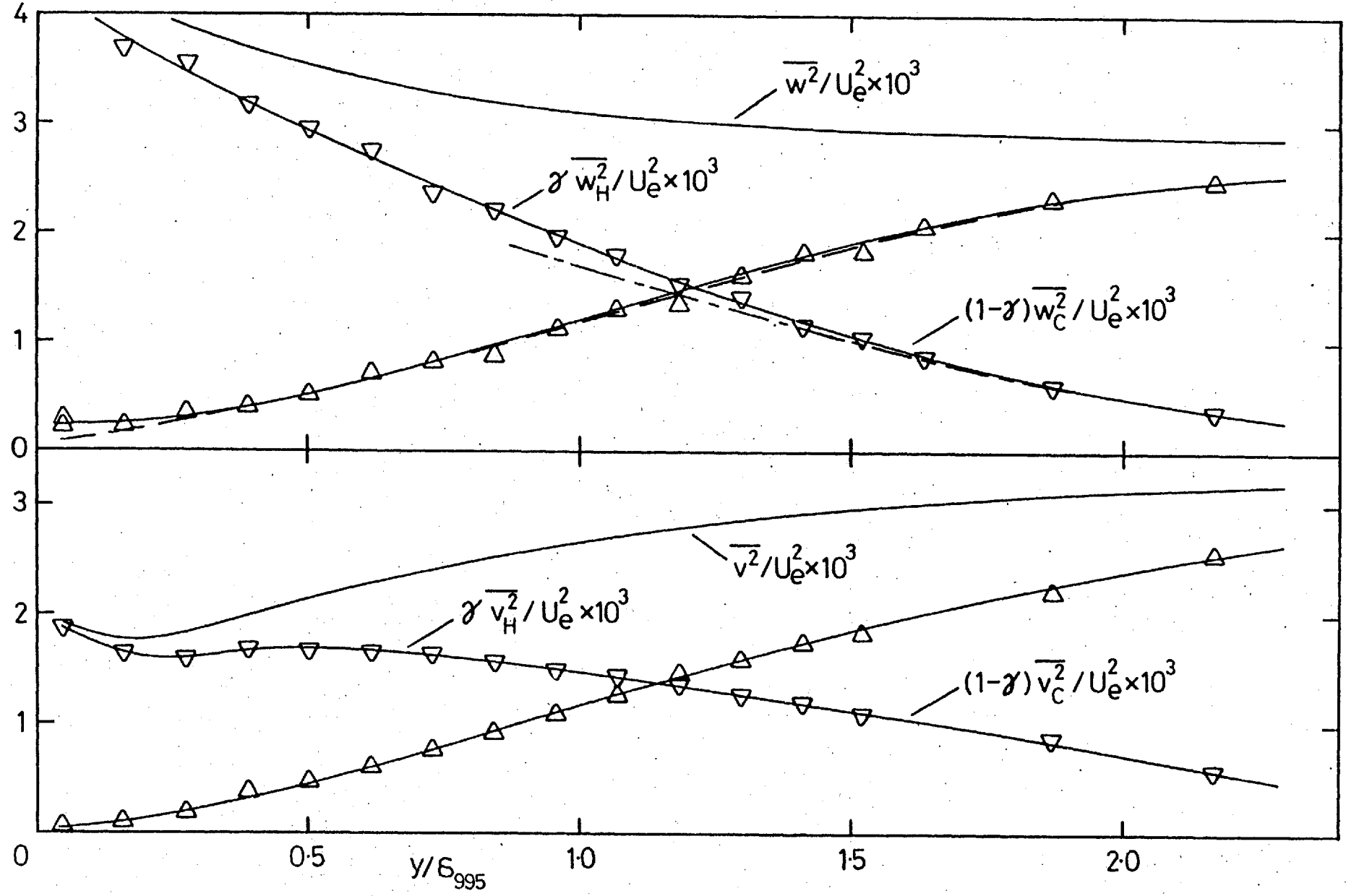

Fig. 4.20m, completed.

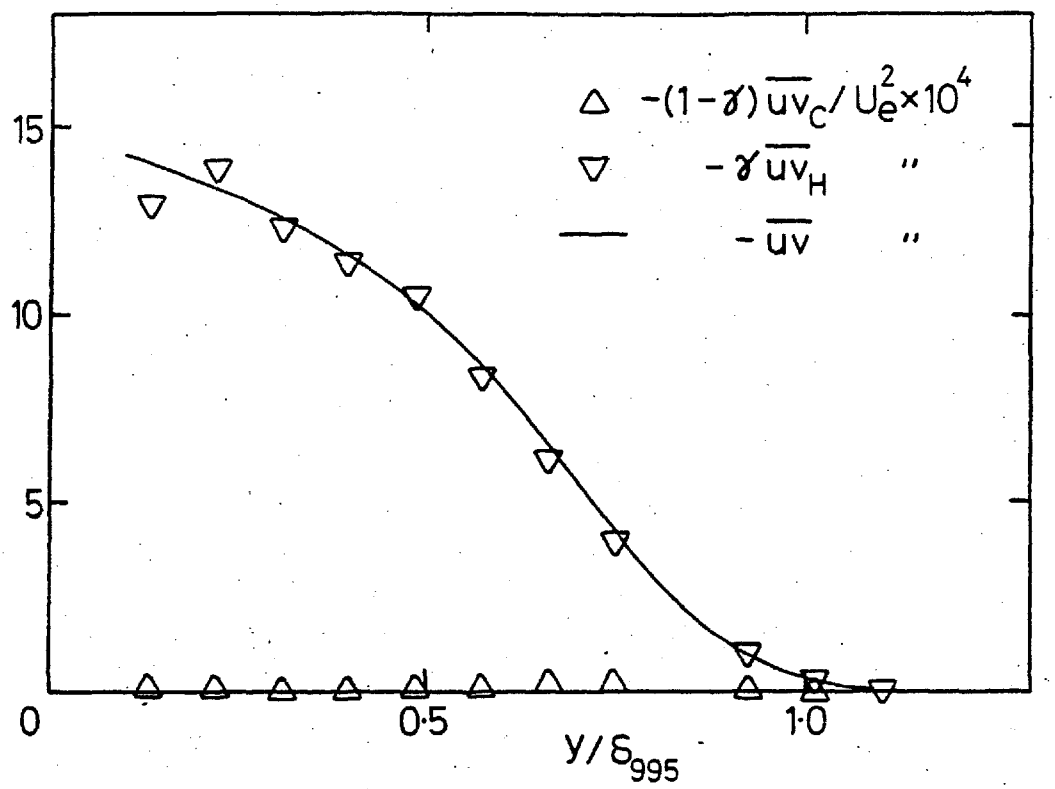

a) No grid, stn 6.

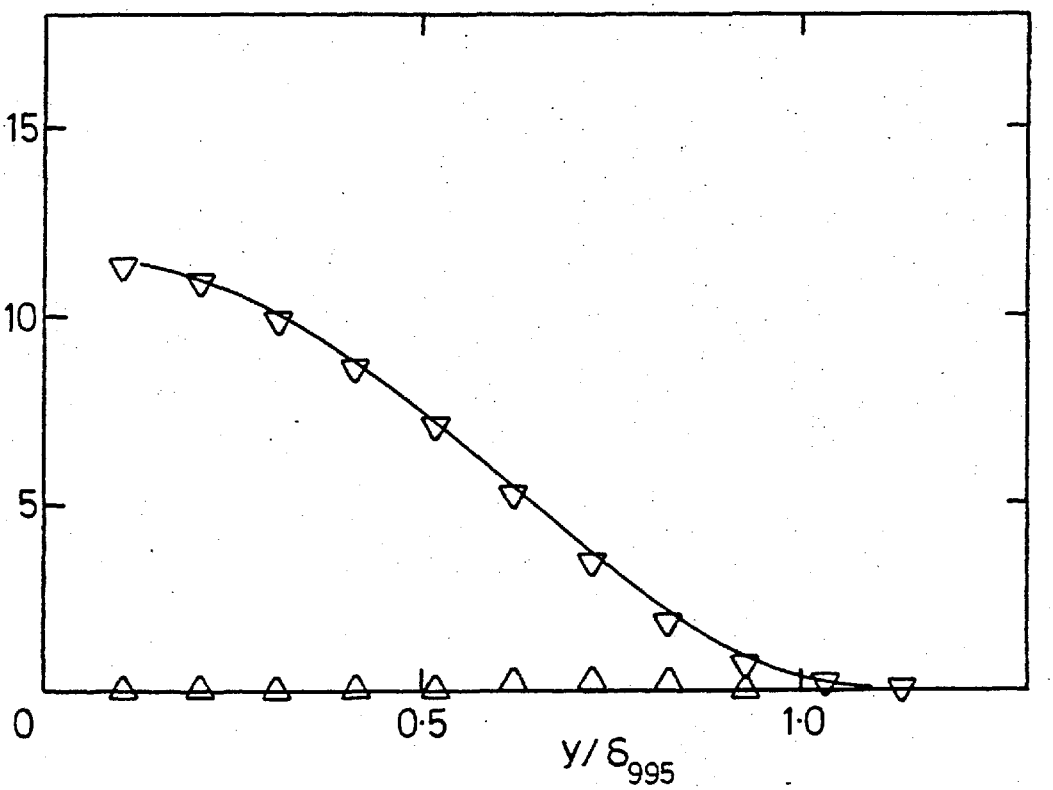

b) No grid, stn 14. Symbols as in a).

Fig. 4.21 Conditionally-averaged shear-stress profiles.

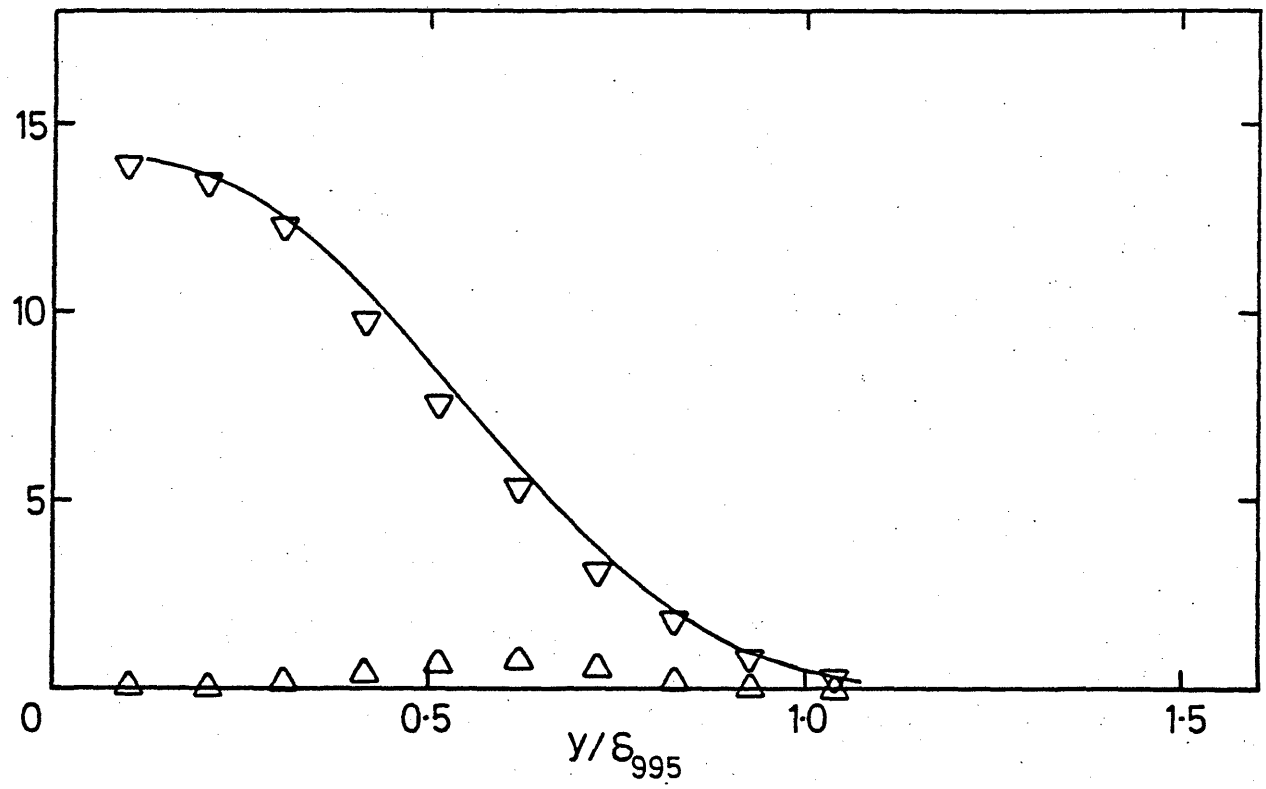

Fig. 4.21c, Zone shear stresses; 7.6 cm grid, X_{LE} = 2.06 m, stn 6. $(u'/U)_e$ = 0.0240, L^u_e/δ_{995} = 1.88. Symbols as in a).

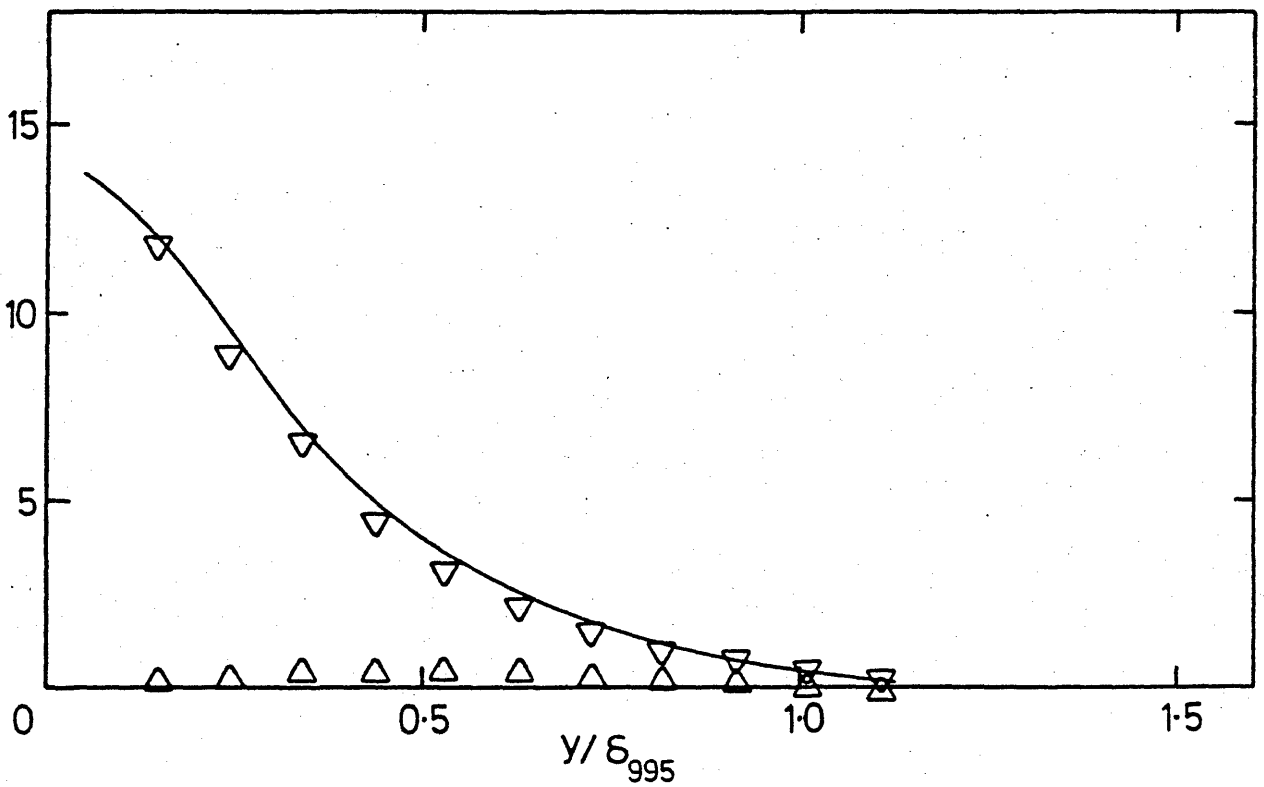

Fig. 4.21d, Zone shear stresses; 7.6 cm grid, X_{LE} = 0.30 m, stn 16. $(u'/U)_e$ = 0.0255, L^u_e/δ_{995} = 0.67. Symbols as in a).

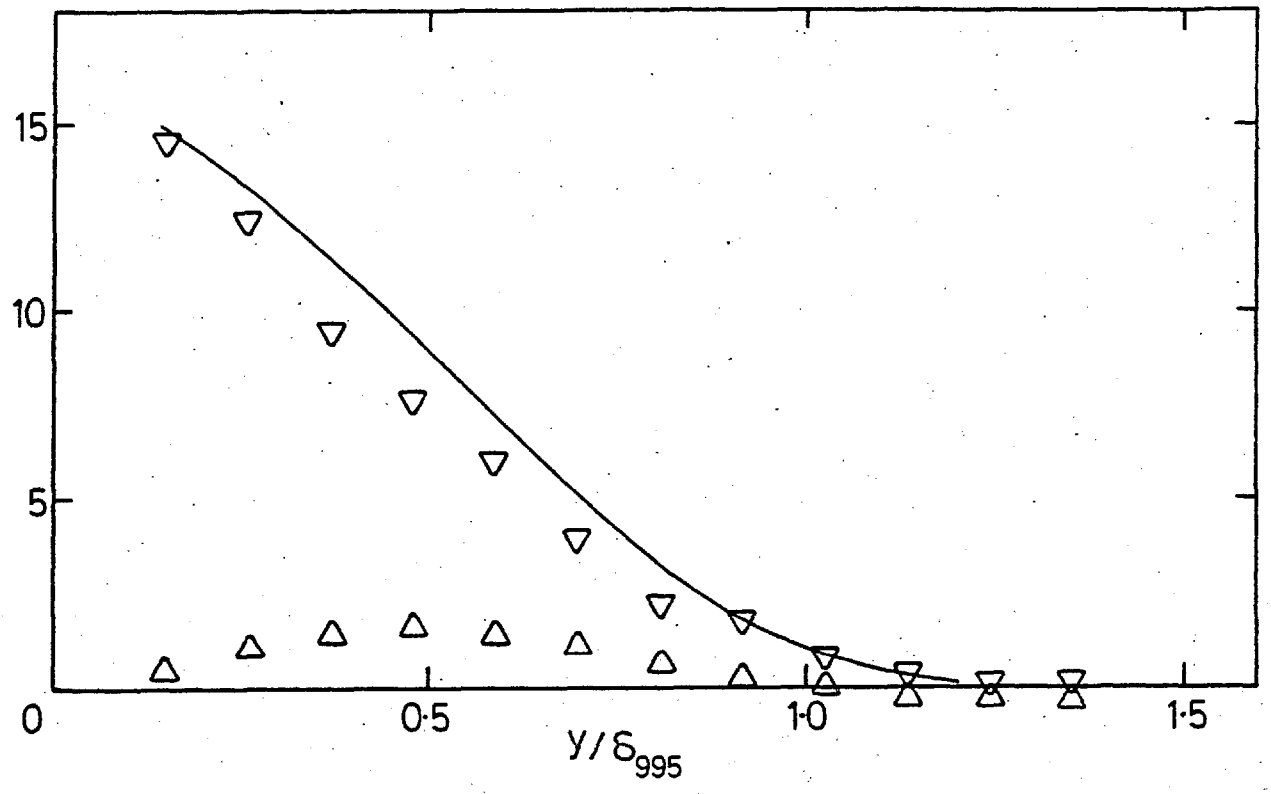

Fig. 4.21e, Zone shear stresses; 15.2 cm grid, X_{LE} = 2.06 m, stn 6.
$(u'/U)_e$ = 0.0468, L^u_e/δ_{995} = 2.72. Symbols as in a).

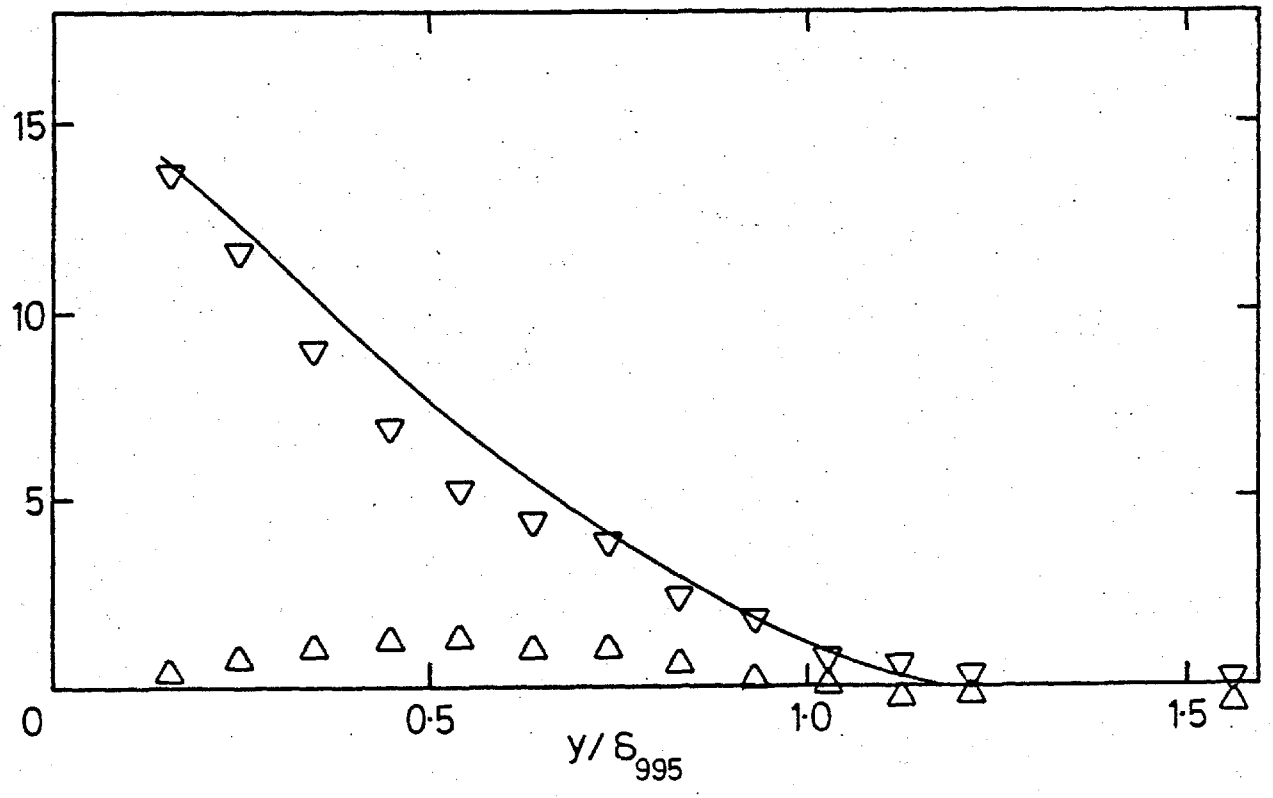

Fig. 4.21f, Zone shear stresses; 15.2 cm grid, X_{LE} = 2.06 m, stn 8.
$(u'/U)_e$ = 0.0442, L^u_e/δ_{995} = 2.23. Symbols as in a).

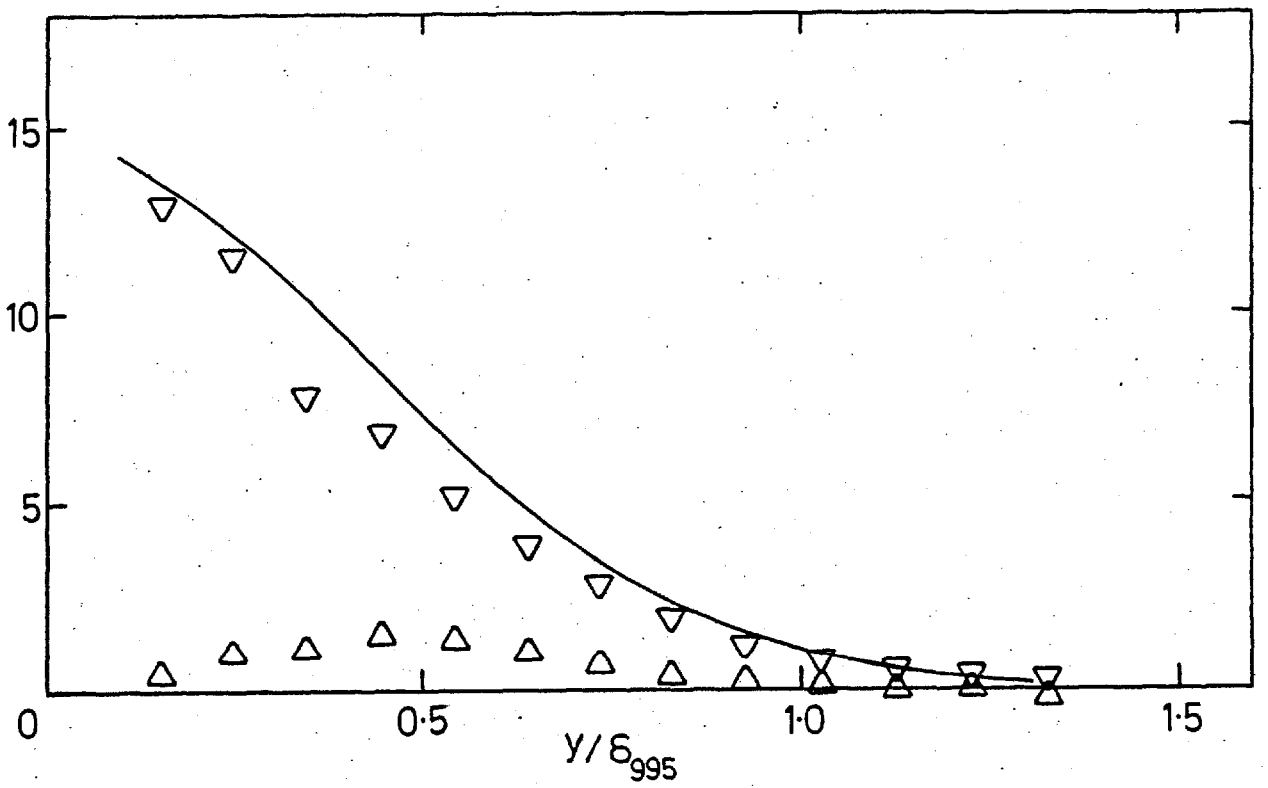

Fig. 4.21g, Zone shear stresses; 15.2 cm grid, X_{LE} = 2.06 m, stn 10. $(u'/U)_e$ = 0.0410, L^u_e/δ_{995} = 1.90. Symbols as in a).

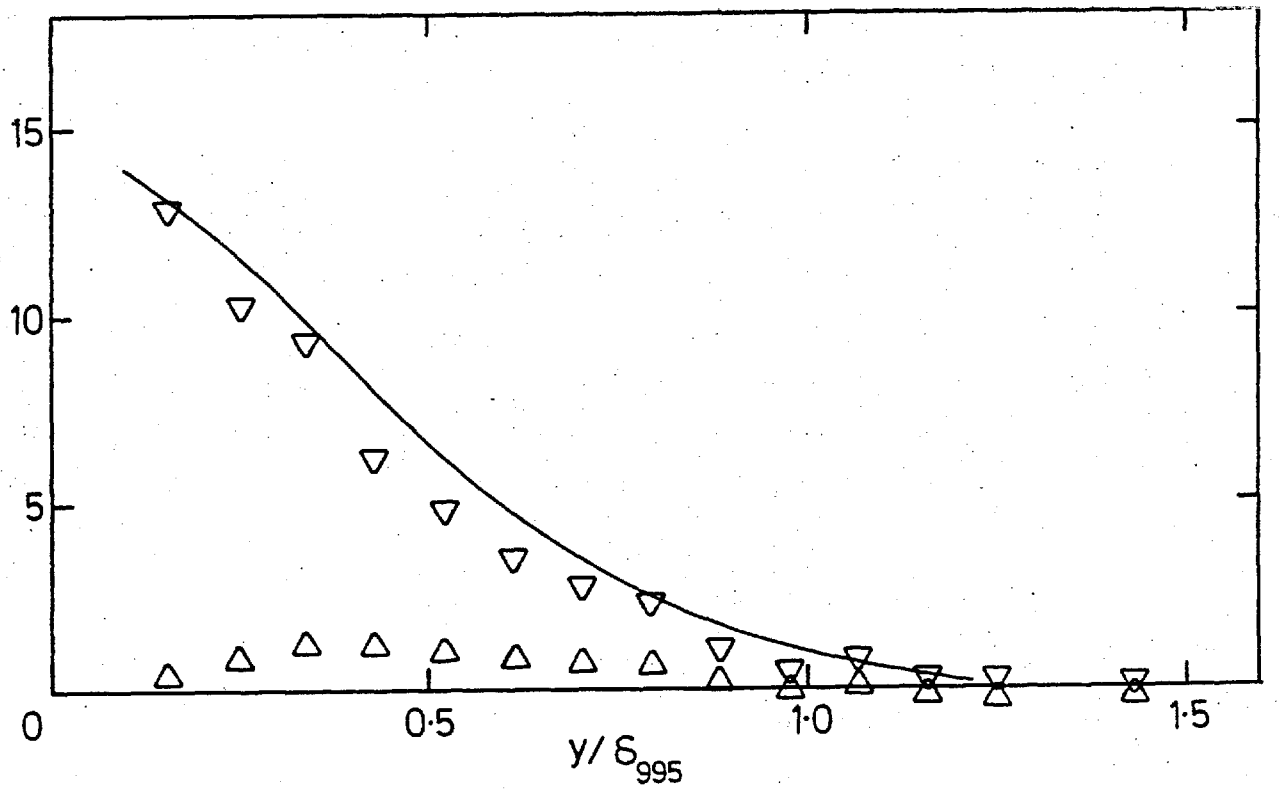

Fig. 4.21h, Zone shear stresses; 15.2 cm grid, X_{LE} = 2.06 m, stn 12. $(u'/U)_e$ = 0.0387, L^u_e/δ_{995} = 1.70. Symbols as in a).

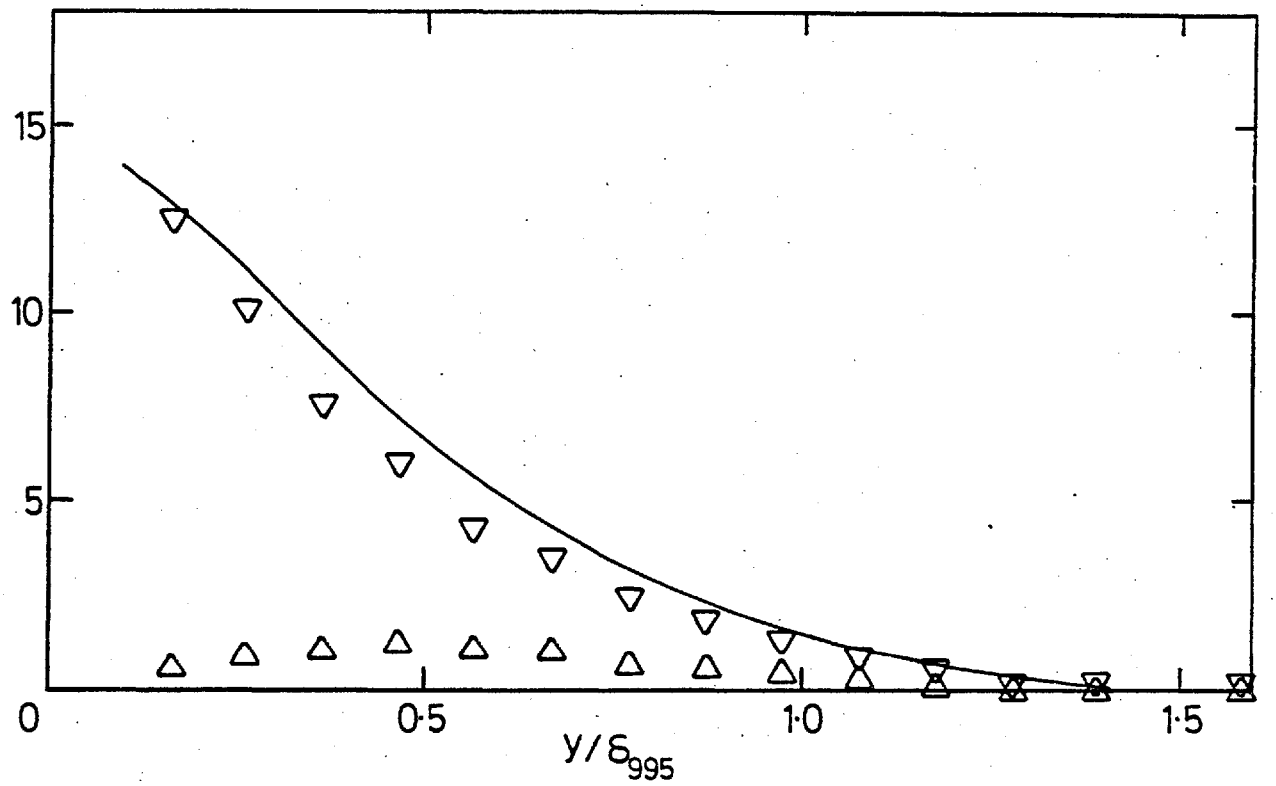

Fig. 4.21i, Zone shear stresses; 15.2 cm grid, X_{LE} = 2.06 m, stn 14. $(u'/U)_e$ = 0.0362, L^u_e/δ_{995} = 1.69. Symbols as in a).

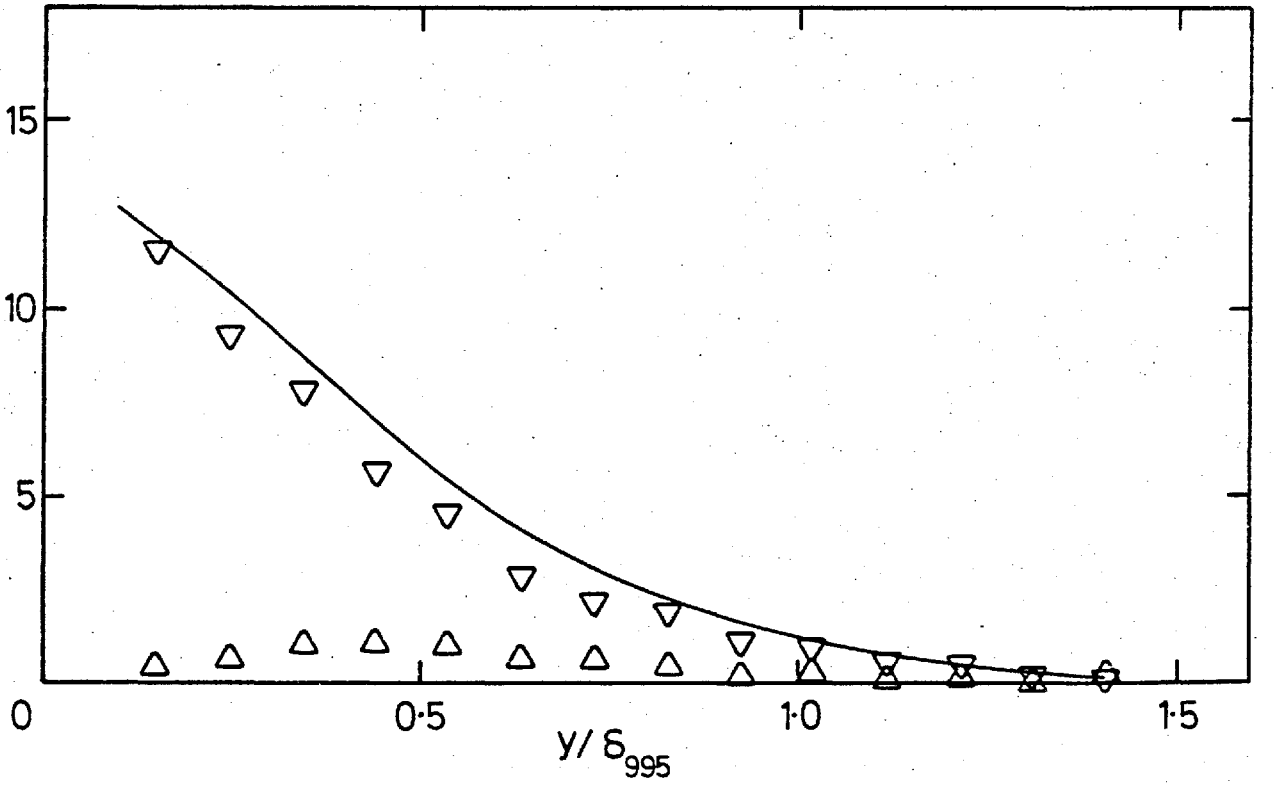

Fig. 4.21j, Zone shear stresses; 15.2 cm grid, X_{LE} = 2.06 m, stn 16. $(u'/U)_e$ = 0.0345, L^u_e/δ_{995} = 1.55. Symbols as in a).

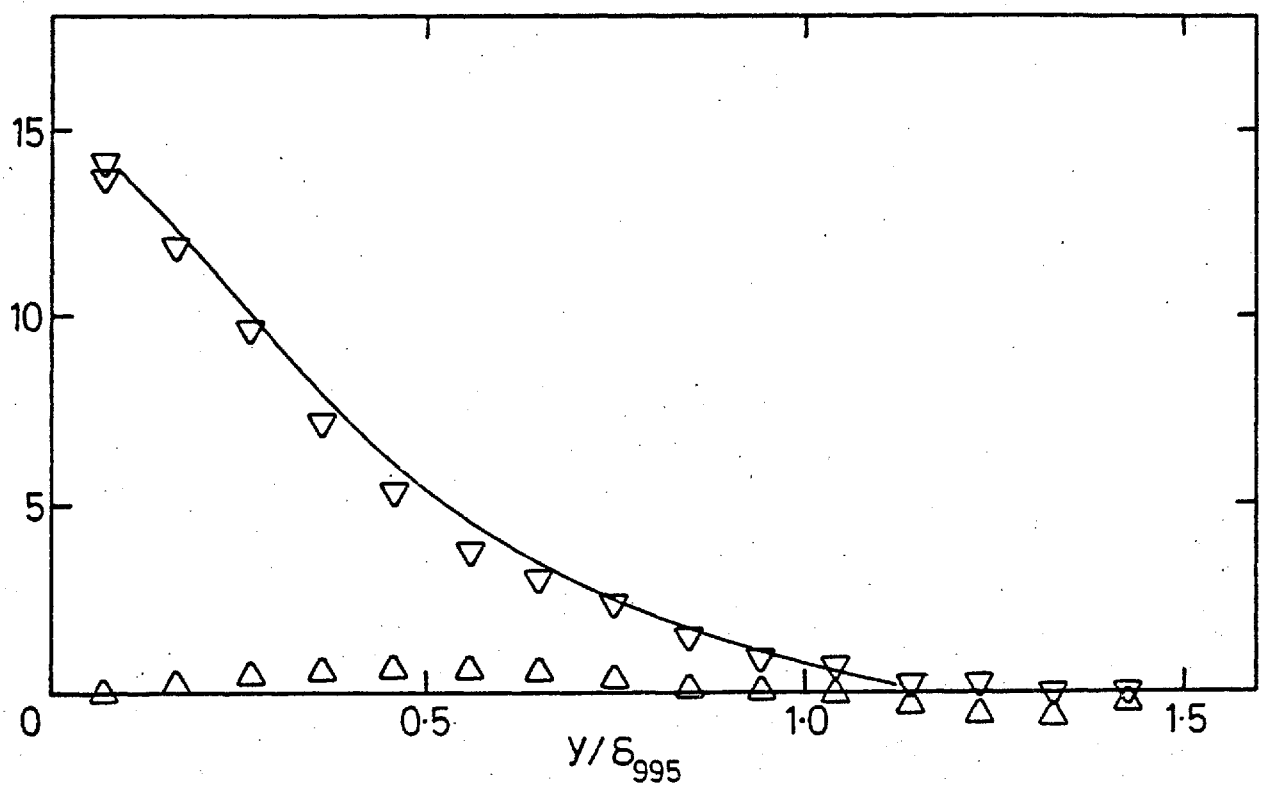

Fig. 4.21k, Zone shear stresses; 7.6 cm grid, X_{LE} = 0.30 m, stn 8. $(u'/U)_e$ = 0.0399, L^u_e/δ_{995} = 0.71. Symbols as in a).

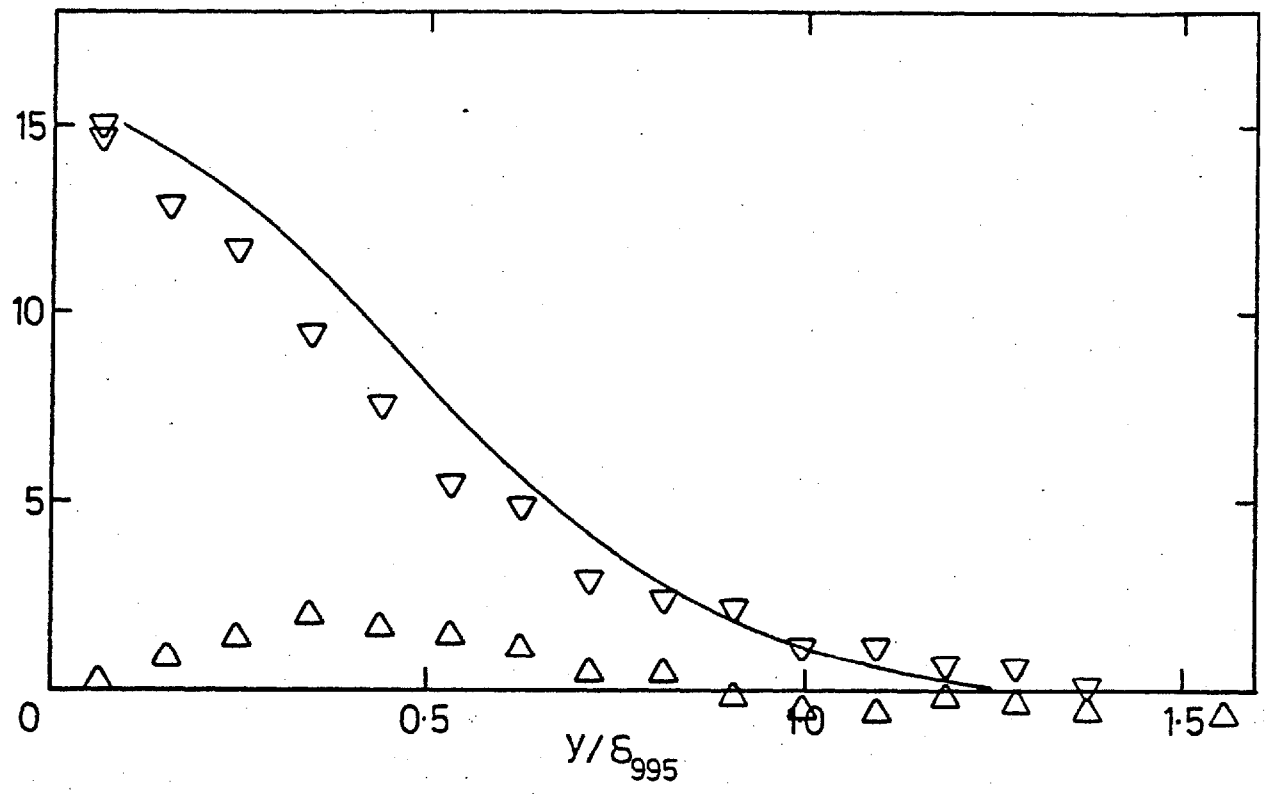

Fig. 4.21ℓ, Zone shear stresses; 15.2 cm grid, X_{LE} = 1.37 m, stn 6.
$(u'/U)_e$ = 0.0575, L^u_e/δ_{995} = 1.83. Symbols as in a).

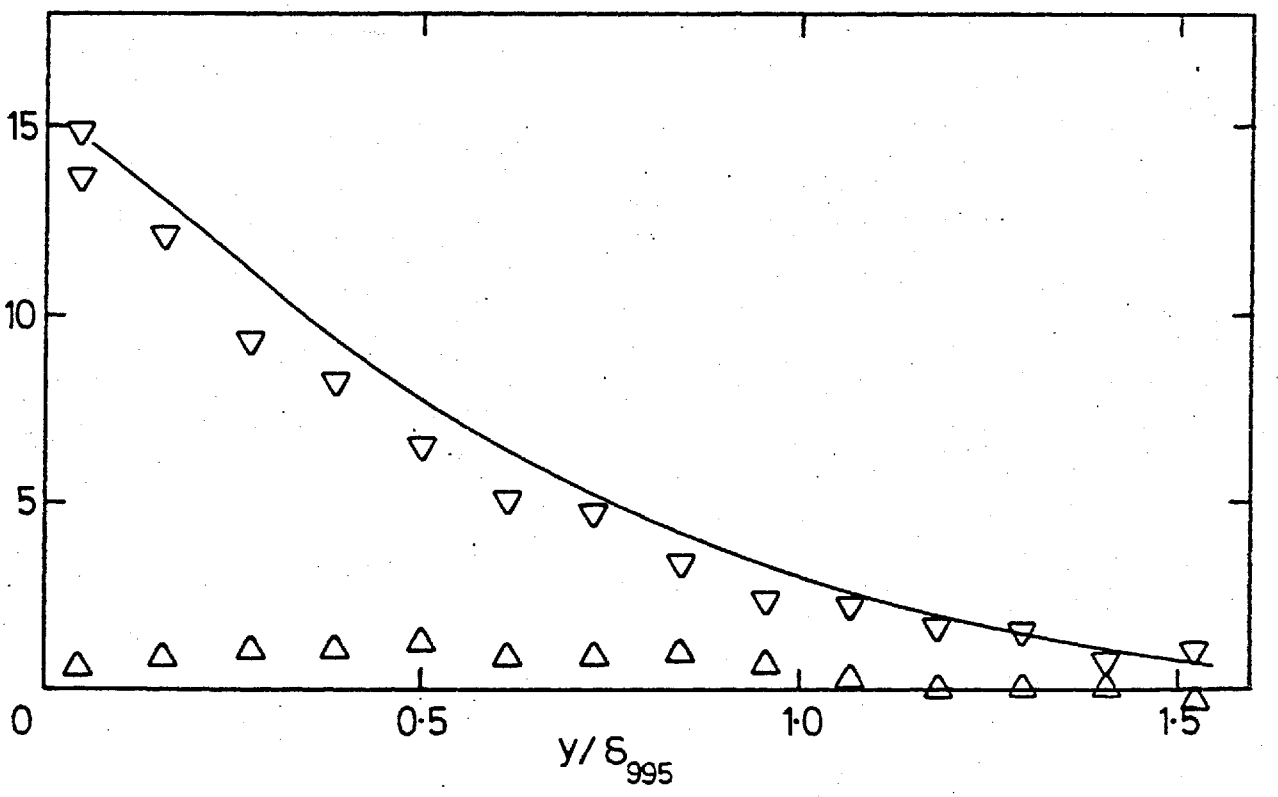

Fig. 4.21m, Zone shear stresses; 15.2 cm grid, X_{LE} = 0.76 m, stn 10.
$(u'/U)_e$ = 0.0575, L^u_e/δ_{995} = 1.34. Symbols as in a).

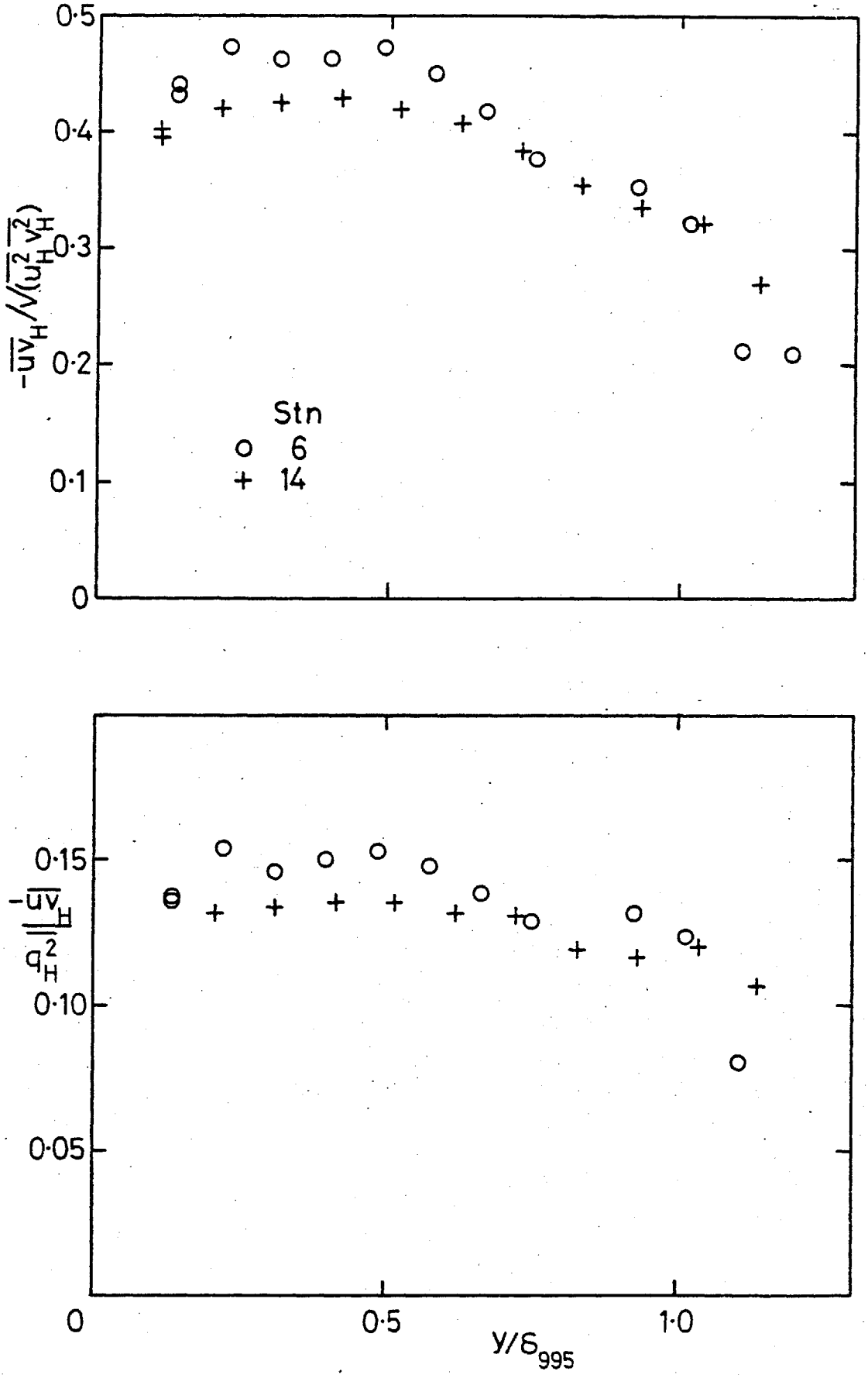

a) No grid.

Fig. 4.22 Hot-zone shear-stress correleation coefficient and the ratio $-\overline{uv}_H/\overline{q_H^2}$

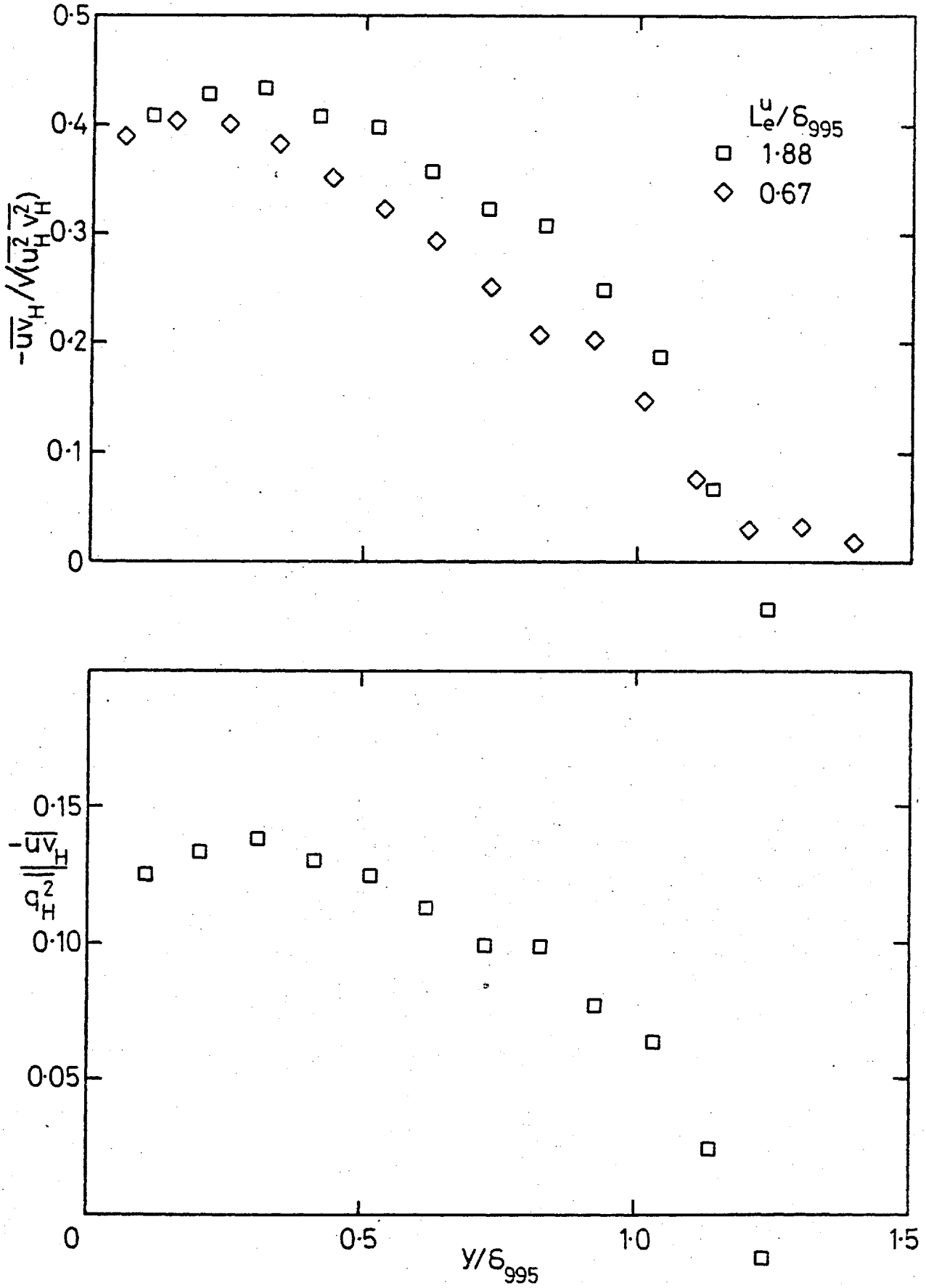

Fig. 4.22b, $(u'/U)_e \approx 0.025$. □

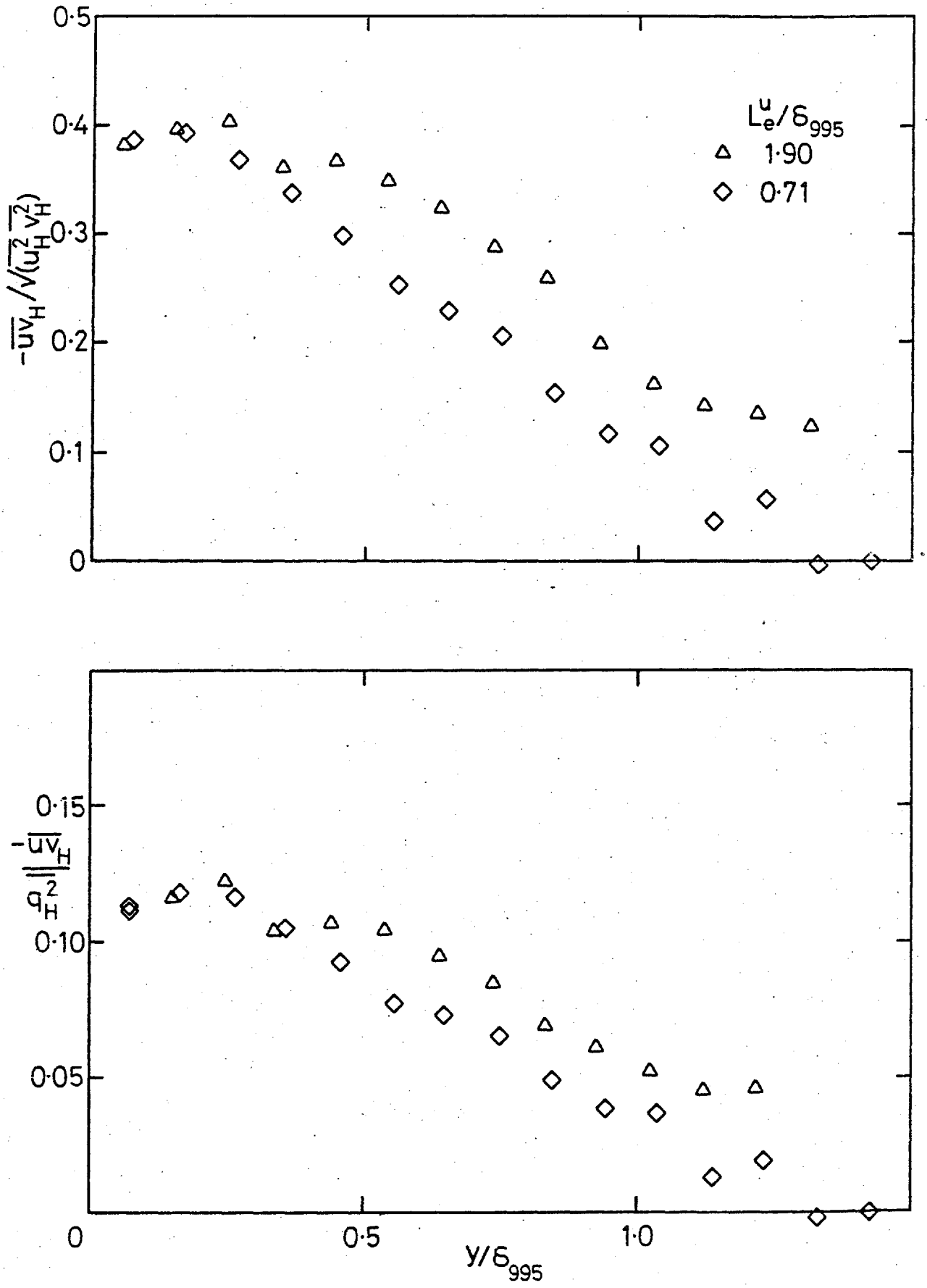

Fig. 4.22c, $(u'/U)_e \approx 0.040$.

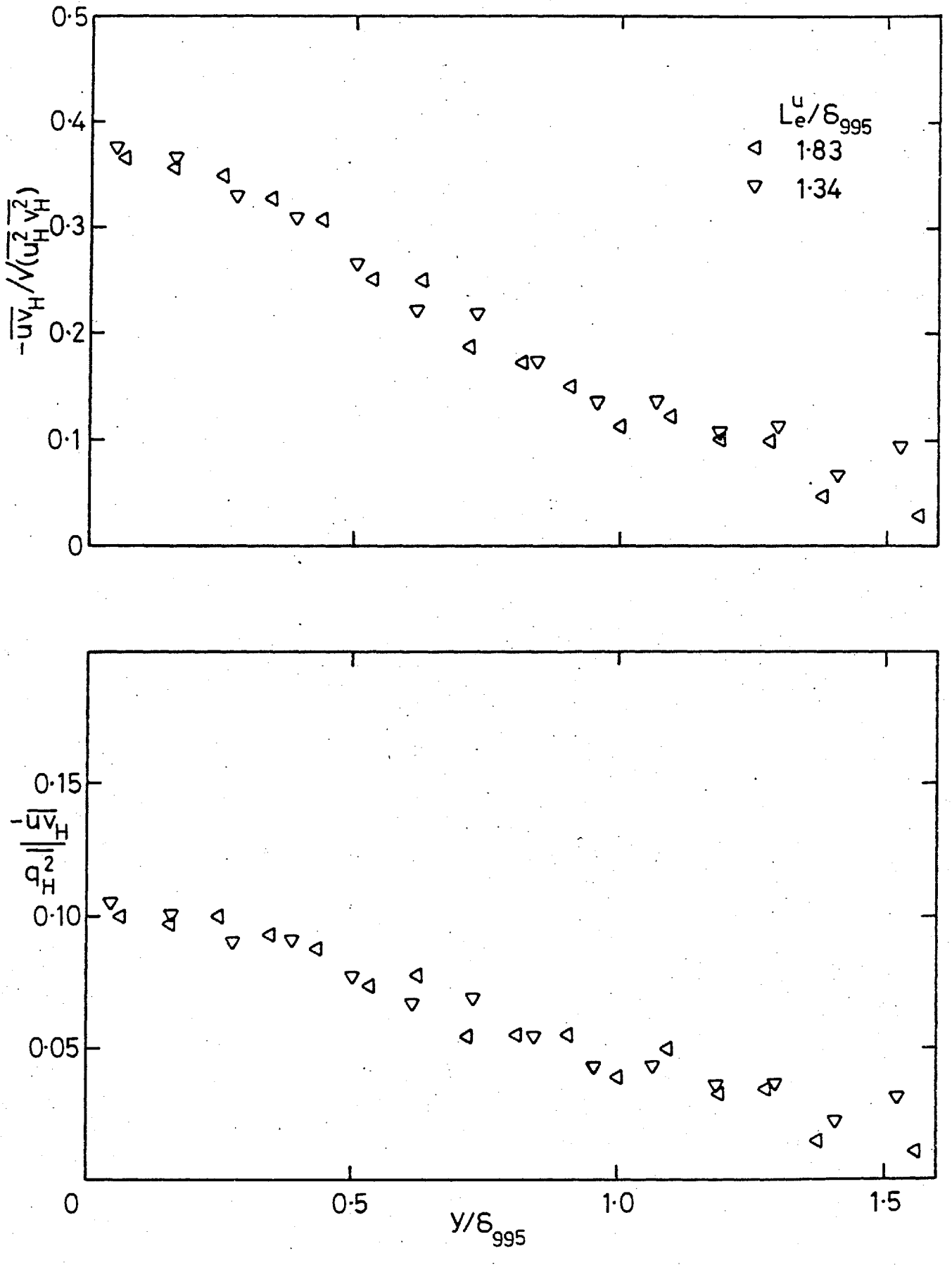

Fig. 4.22d, $(u'/U)_e = 0.0575$.

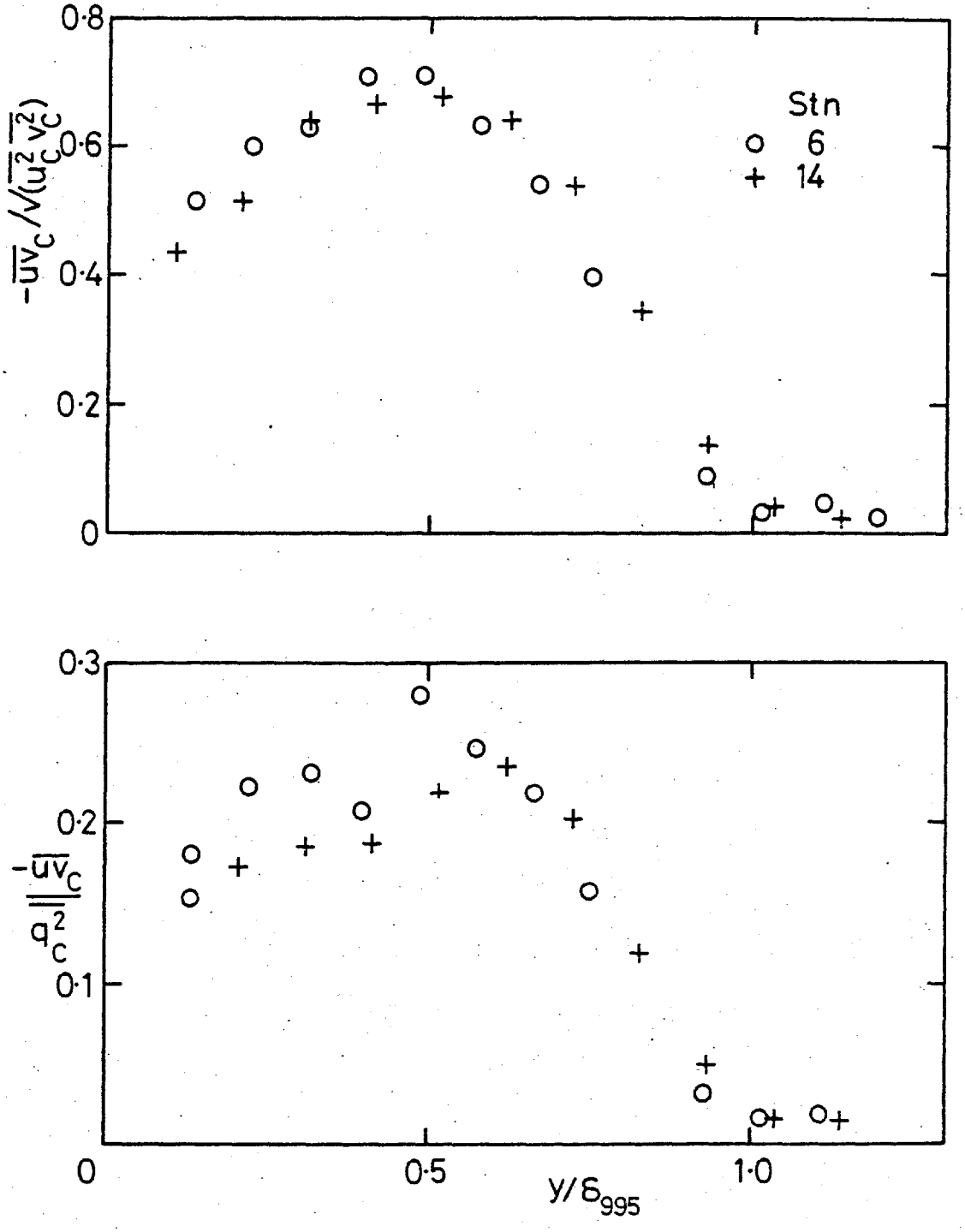

a) No grid.

Fig. 4.23 Cold-zone shear-stress correlation coefficient and the ratio $-\overline{uv}_c/\overline{q_c^2}$

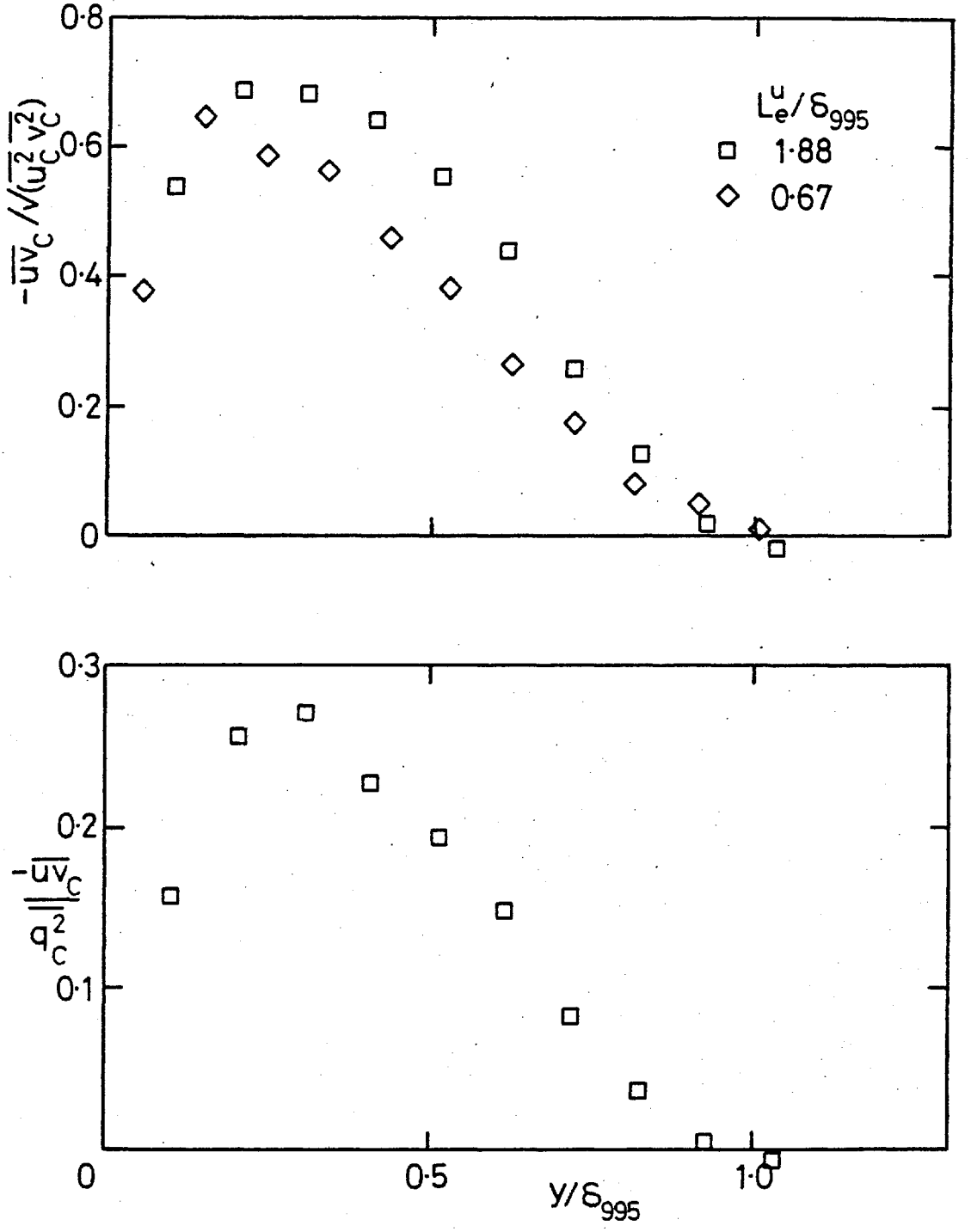

Fig. 4.23b, $(u'/U)_e \approx 0.025$.

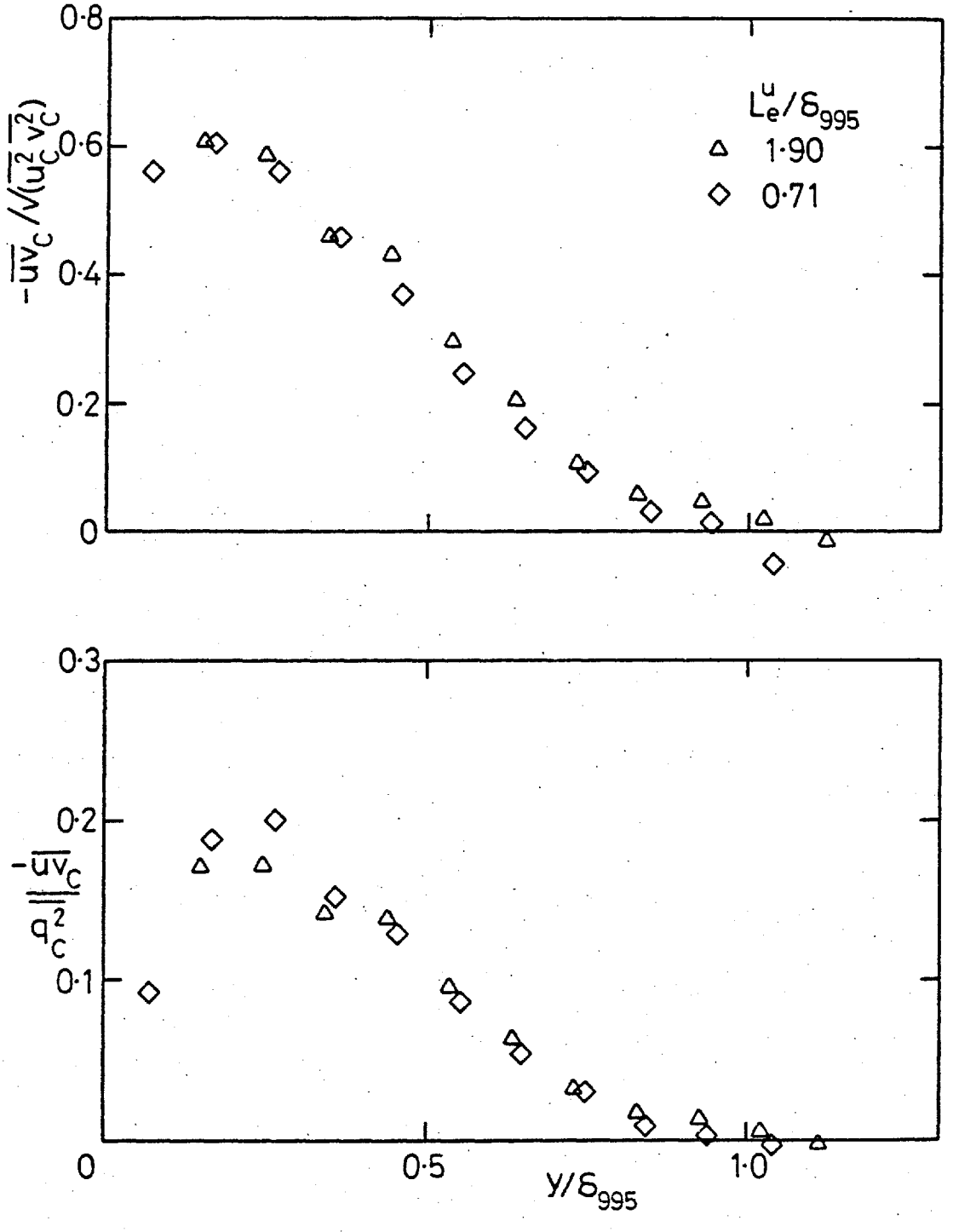

Fig. 4.23c, $(u'/U)_e \approx 0.040$.

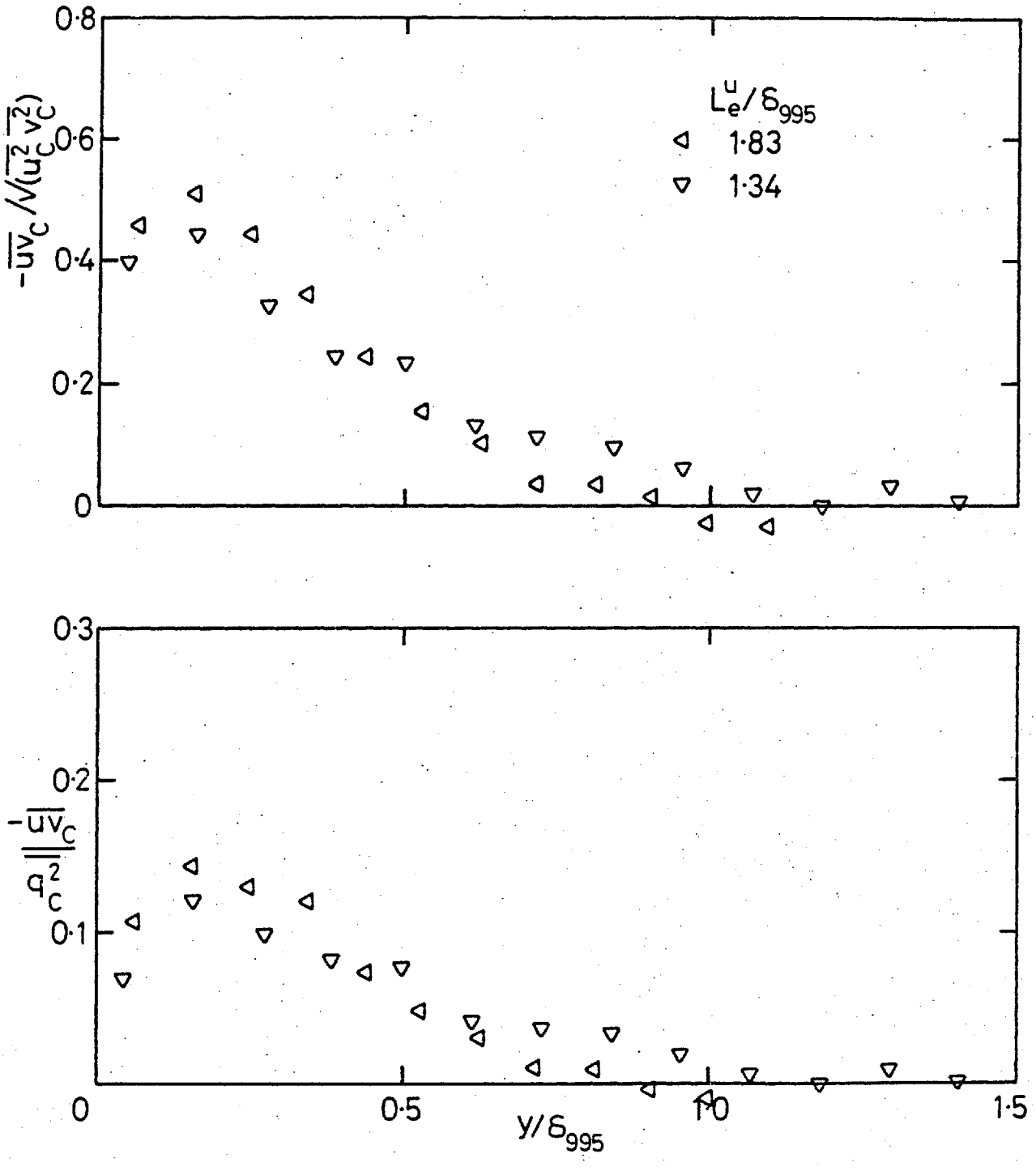

Fig. 4.23d, $(u'/U)_e$ = 0.0575.

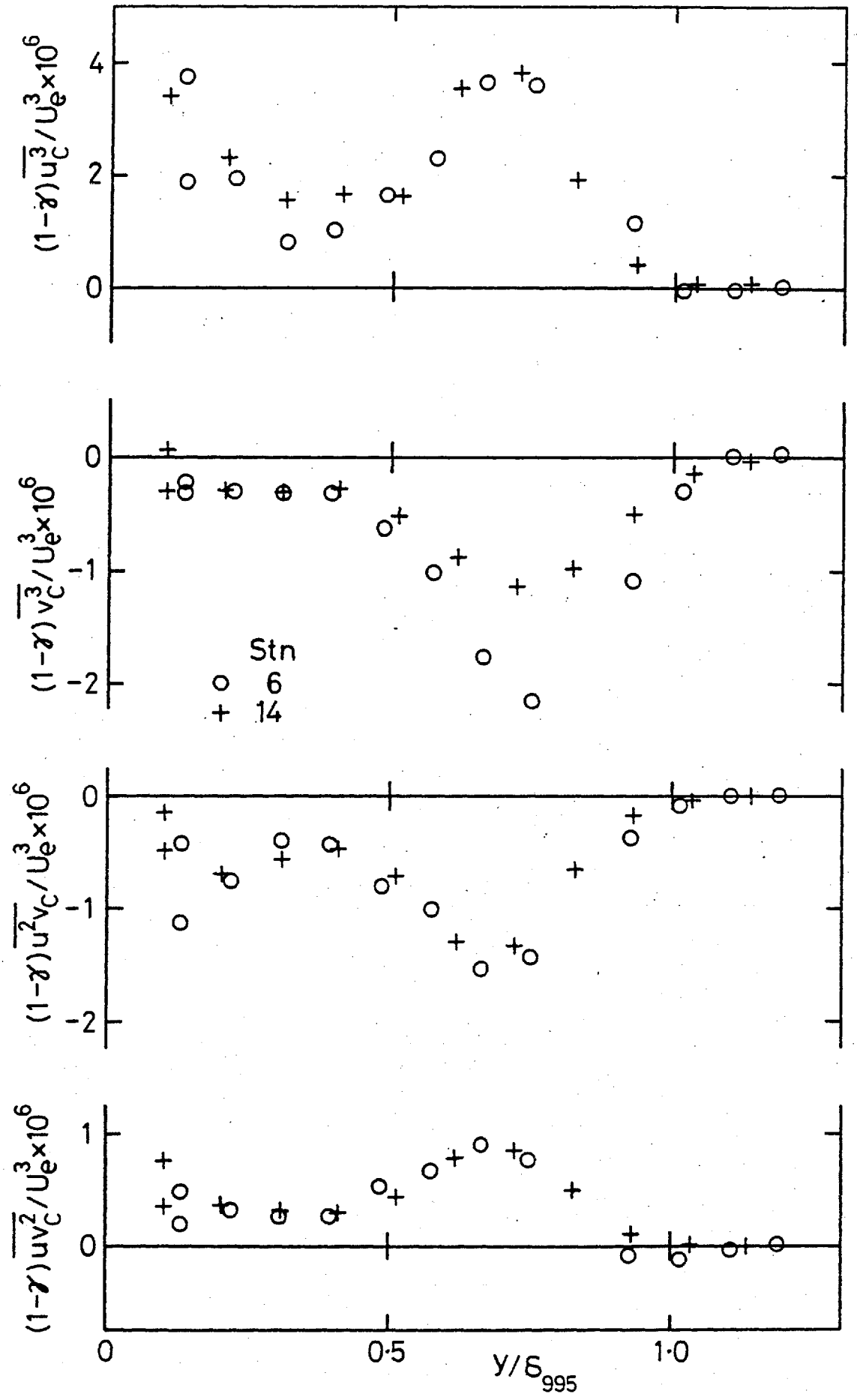

Fig. 4.24 Cold-zone triple products, no grid.

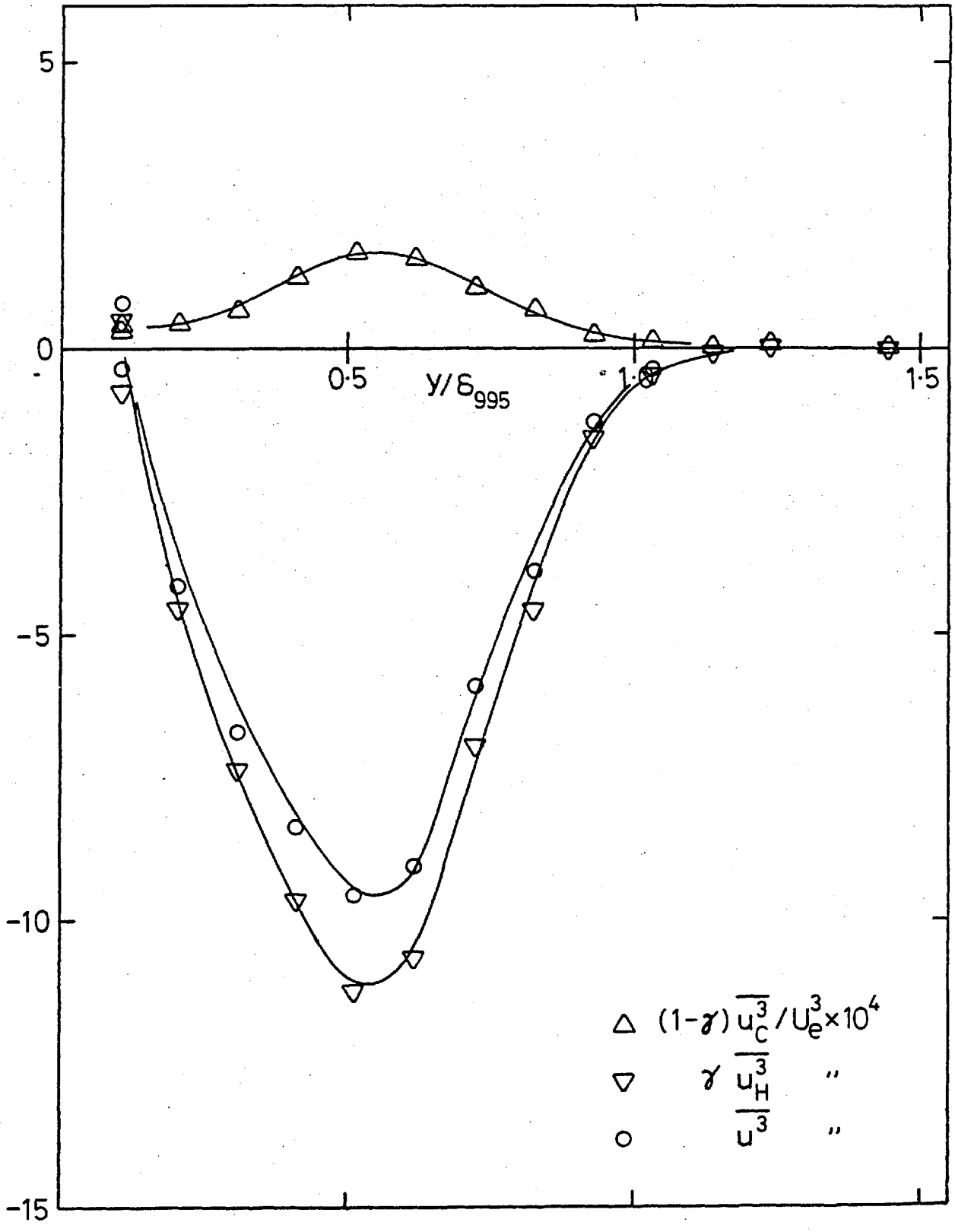

a) $(u'/U)_e$ = 0.0240, L_e^u/δ_{995} = 1.88.

Fig. 4.25 Zonal contributions to $\overline{u^3}$

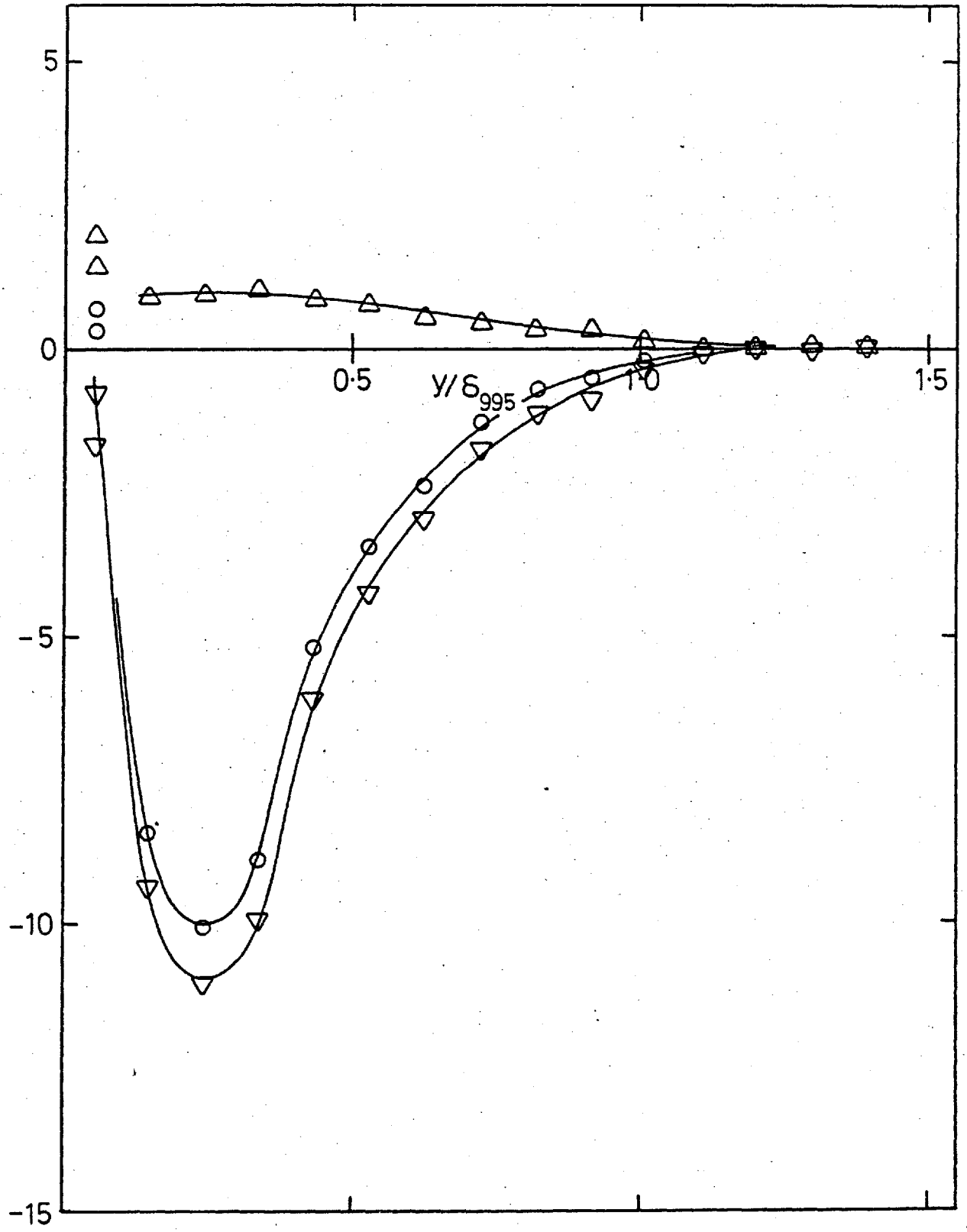

Fig. 4.25b, Contributions to $\overline{u^3}$; $(u'/U)_e = 0.0255$, $L^u_e/\delta_{995} = 0.67$.
Symbols as in a).

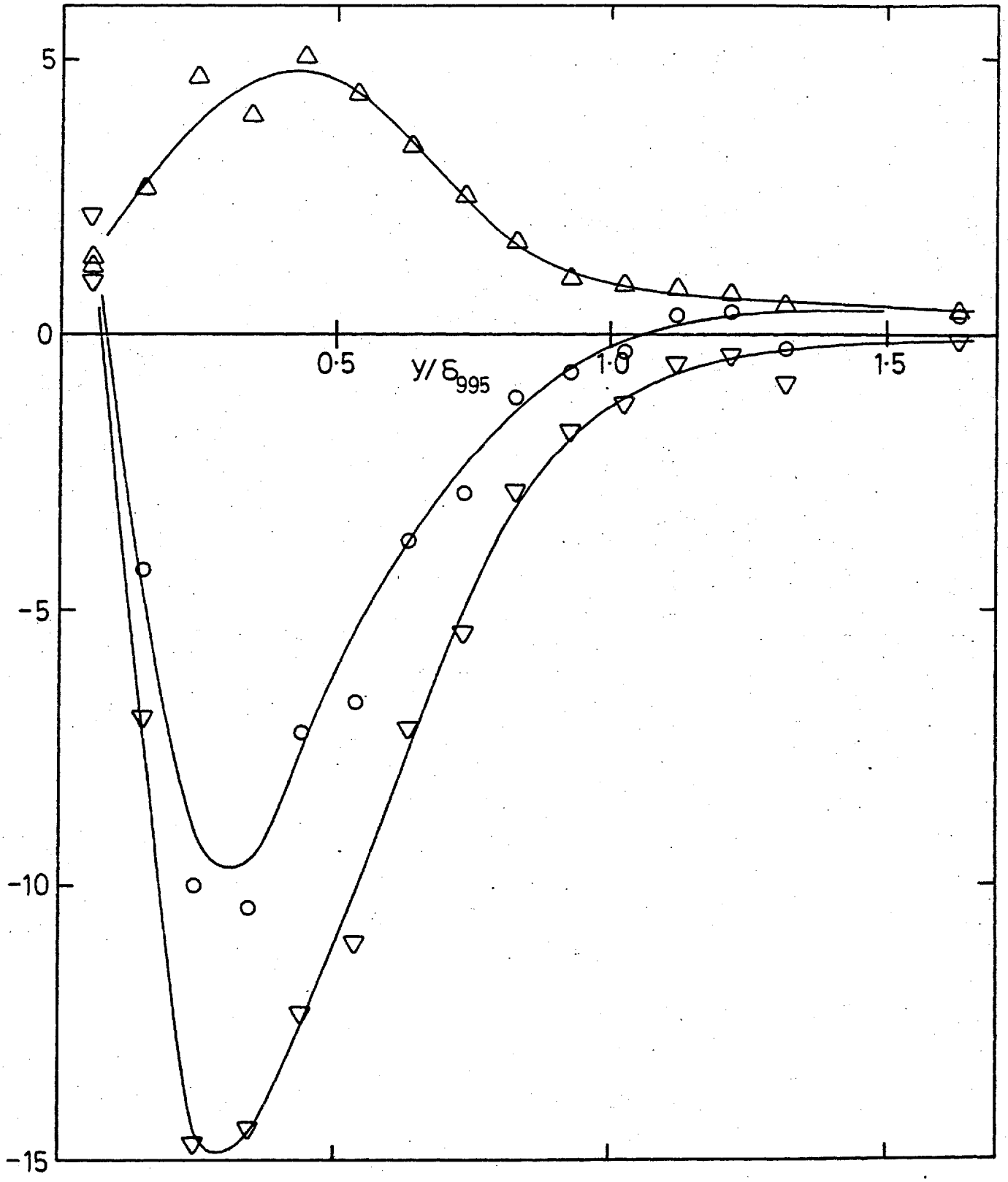

Fig. 4.25c, Contributions to $\overline{u^3}$; $(u'/U)_e = 0.0410$, $L_e^u/\delta_{995} = 1.90$.
Symbols as in a).

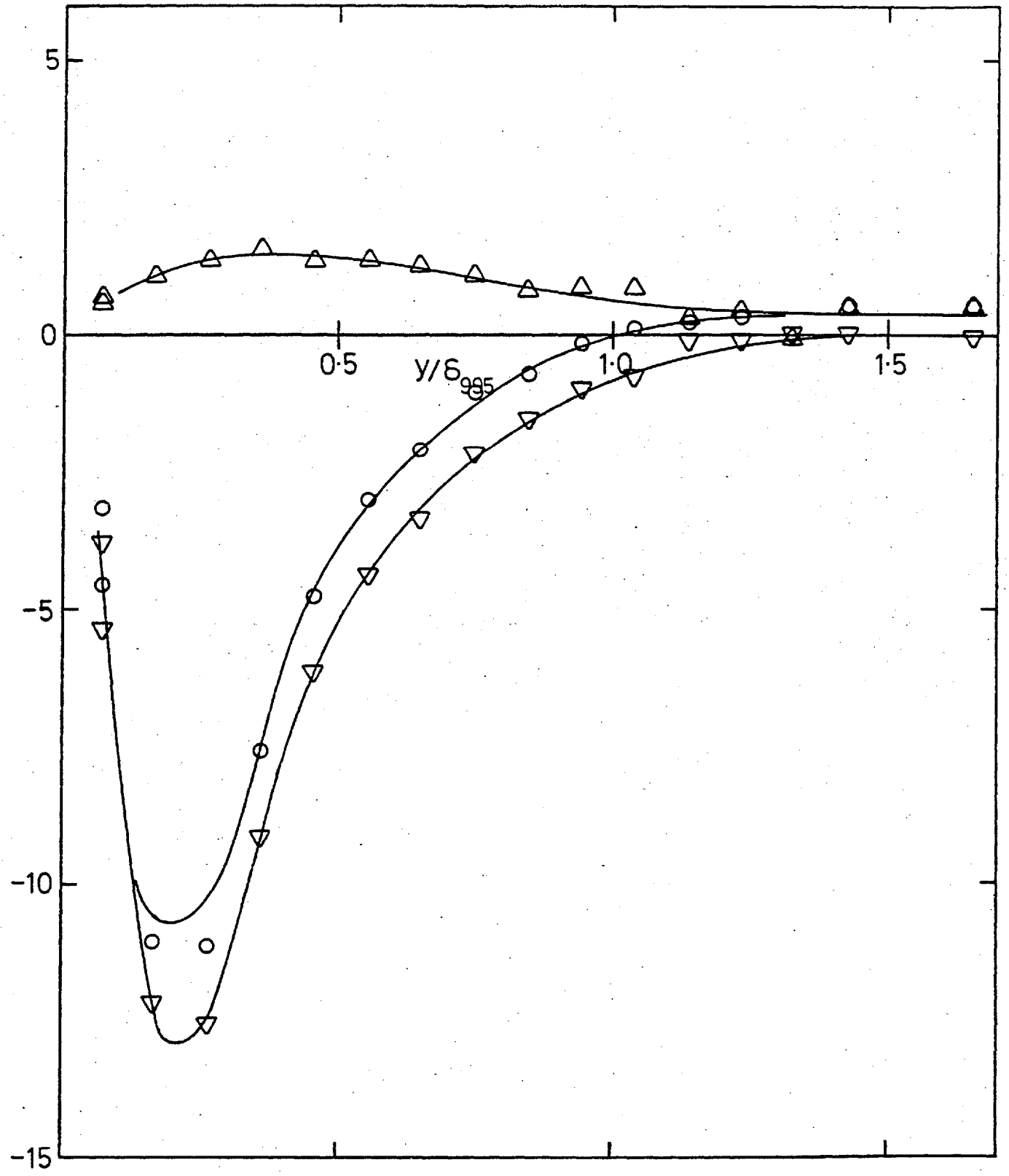

Fig. 4.25d, Contributions to $\overline{u^3}$; $(u'/U)_e = 0.0399$, $L^u_e/\delta_{995} = 0.71$.
Symbols as in a).

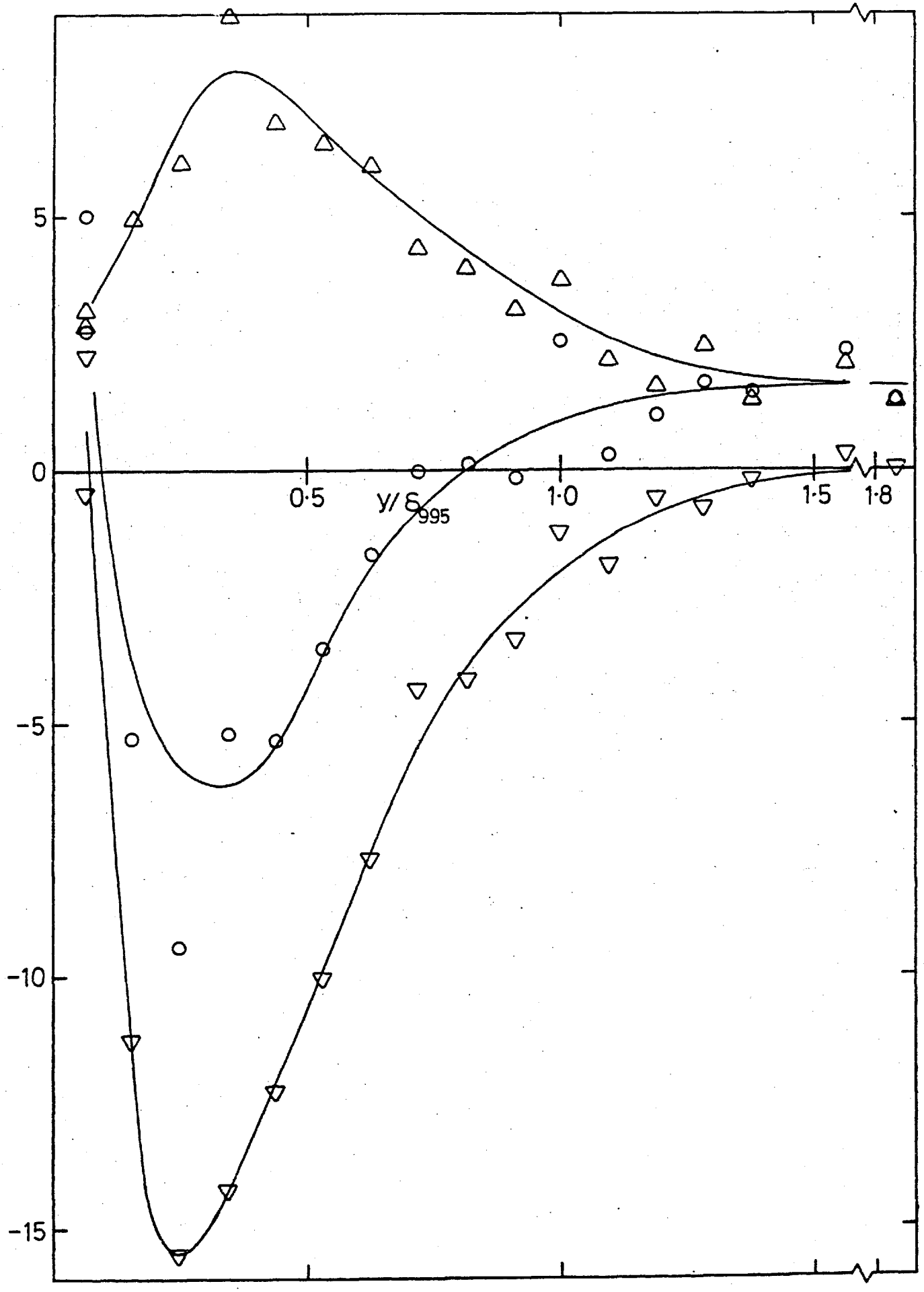

Fig. 4.25e, Contributions to $\overline{u^3}$; $(u'/U)_e = 0.0575$, $L_e^u/\delta_{995} = 1.83$.

Symbols as in a).

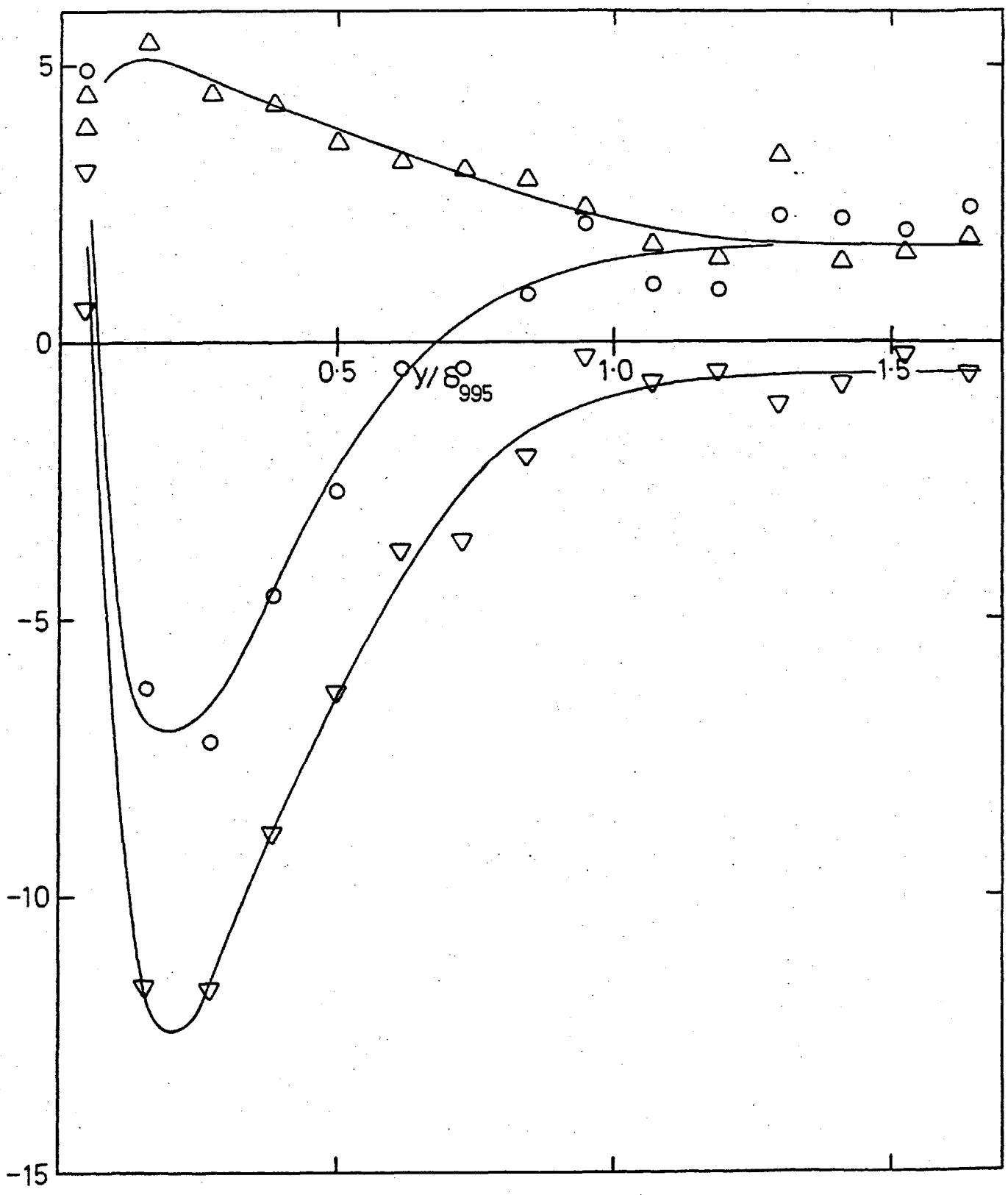

Fig. 4.25f, Contributions to $\overline{u^3}$; $(u'/U)_e = 0.0575$, $L^u_e/\delta_{995} = 1.34$.
Symbols as in a).

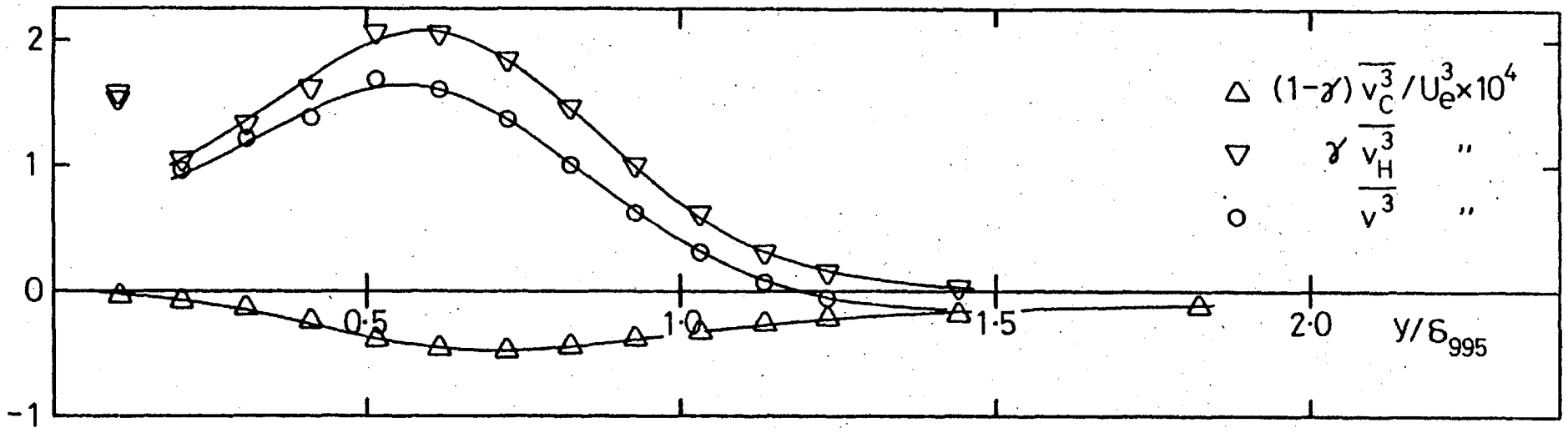

a) $(u'/U)_e$ = 0.0240, L^u_e/δ_{995} = 1.88

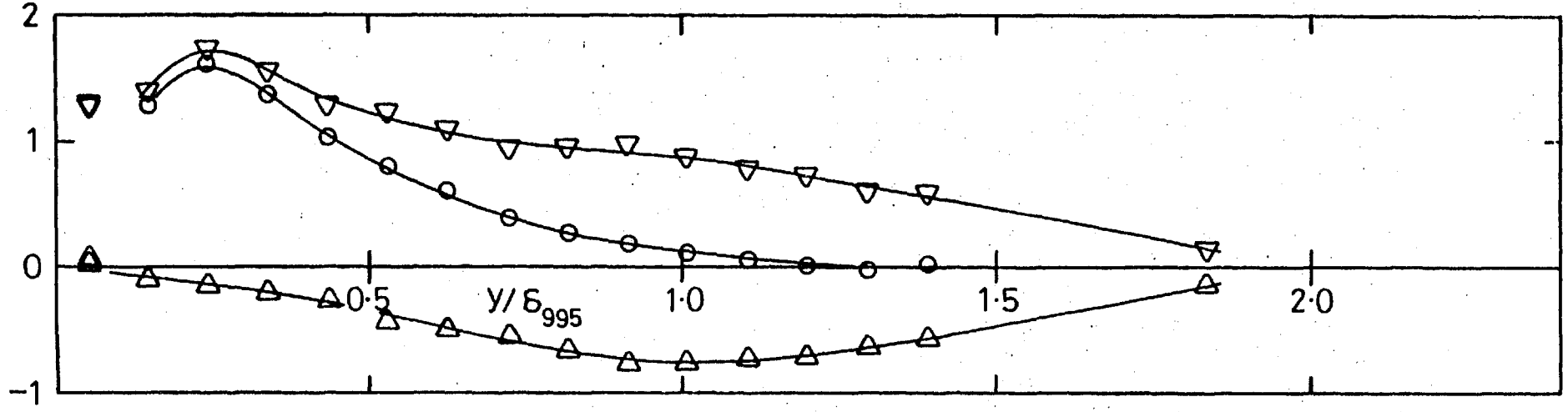

b) $(u'/U)_e$ = 0.0255, L^u_e/δ_{995} = 0.67. Symbols as in a).

Fig. 4.26 Zonal contributions to $\overline{v^3}$.

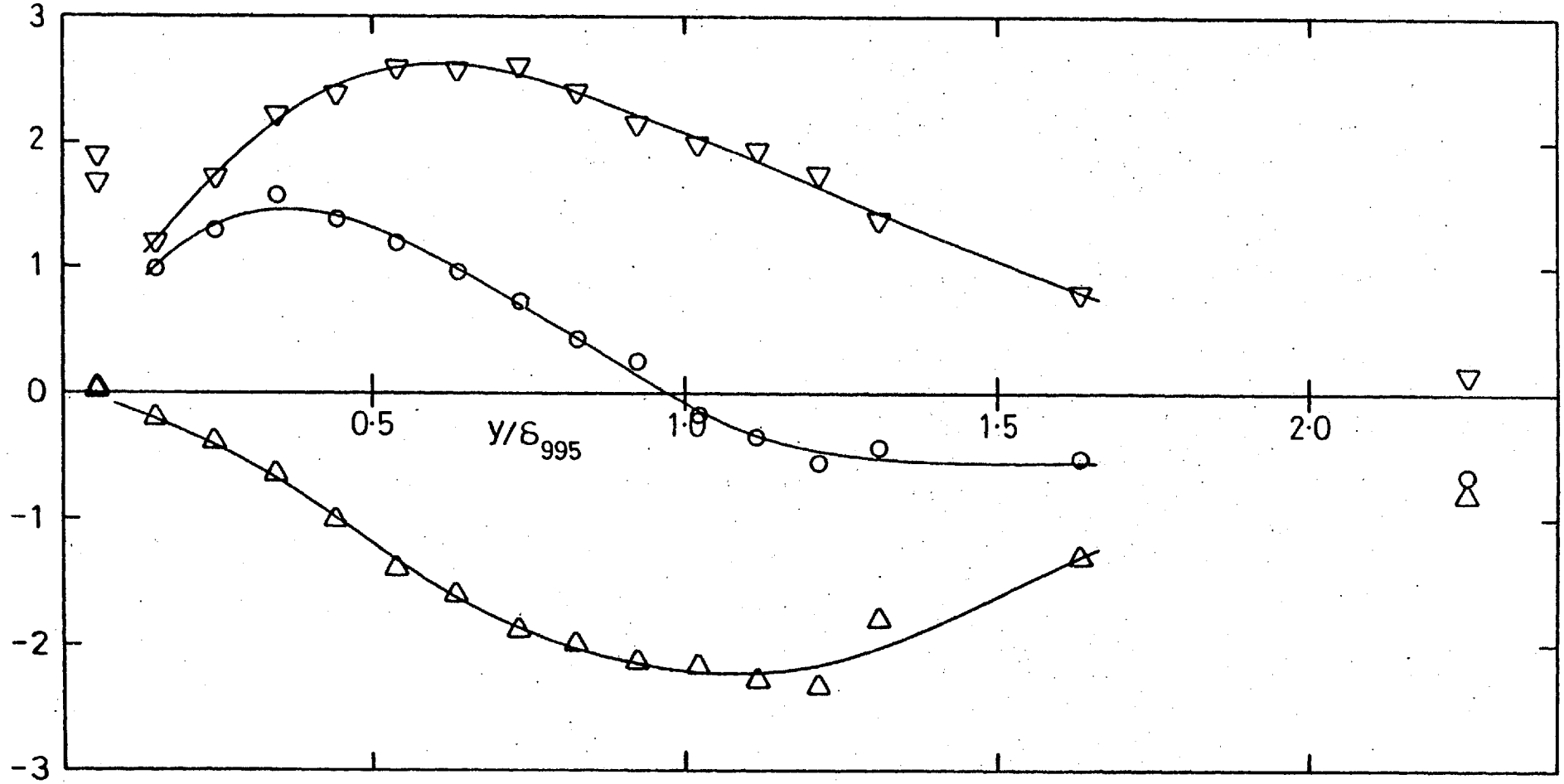

Fig. 4.26c, Contributions to $\overline{v^3}$; $(u'/U)_e = 0.0410$, $L^u_e/\delta_{995} = 1.90$. Symbols as in a).

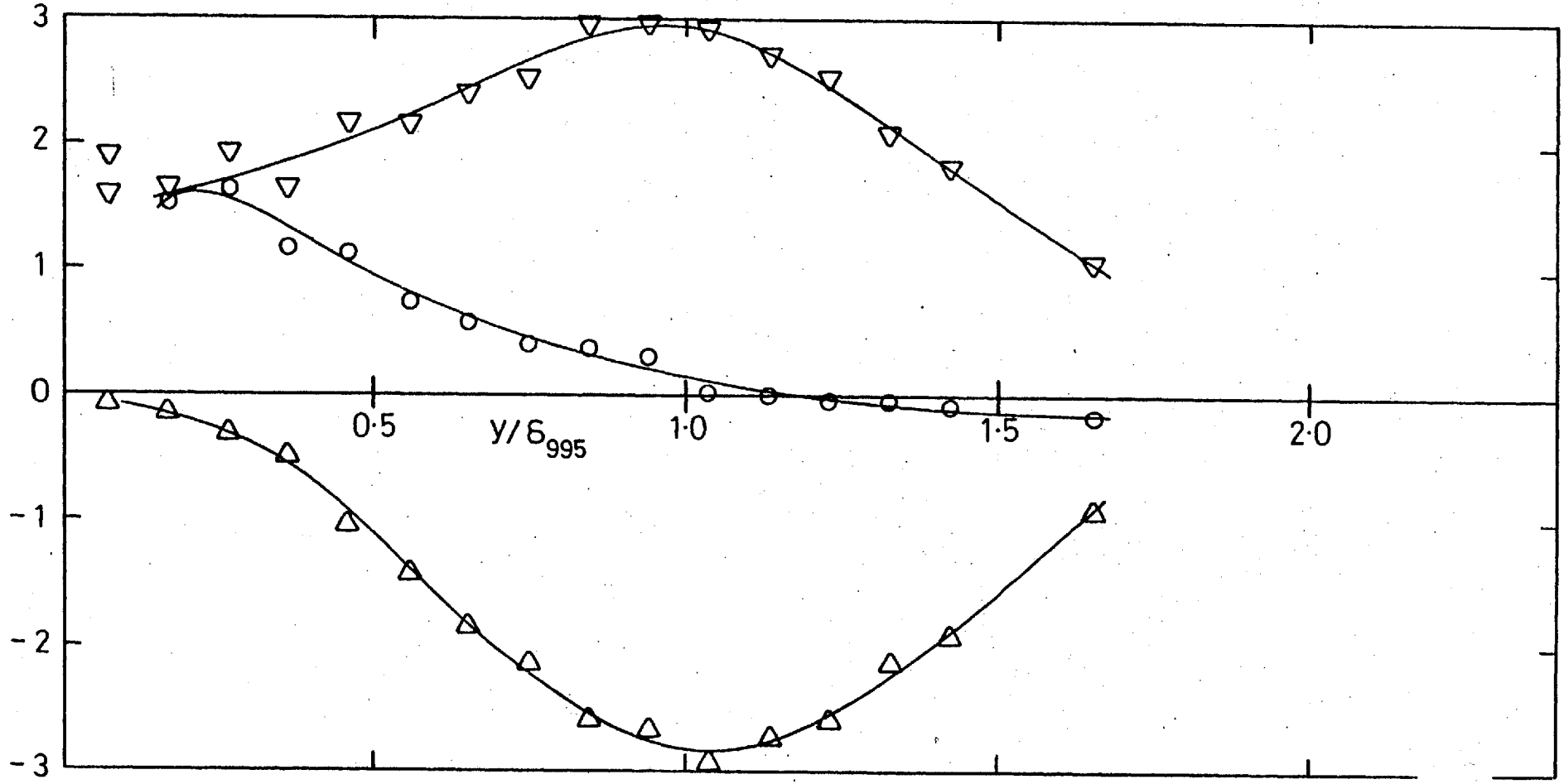

Fig. 4.26d, Contributions to $\overline{v^3}$; $(u'/U)_e = 0.0399$, $L^u_e/\delta_{995} = 0.71$. Symbols as in a).

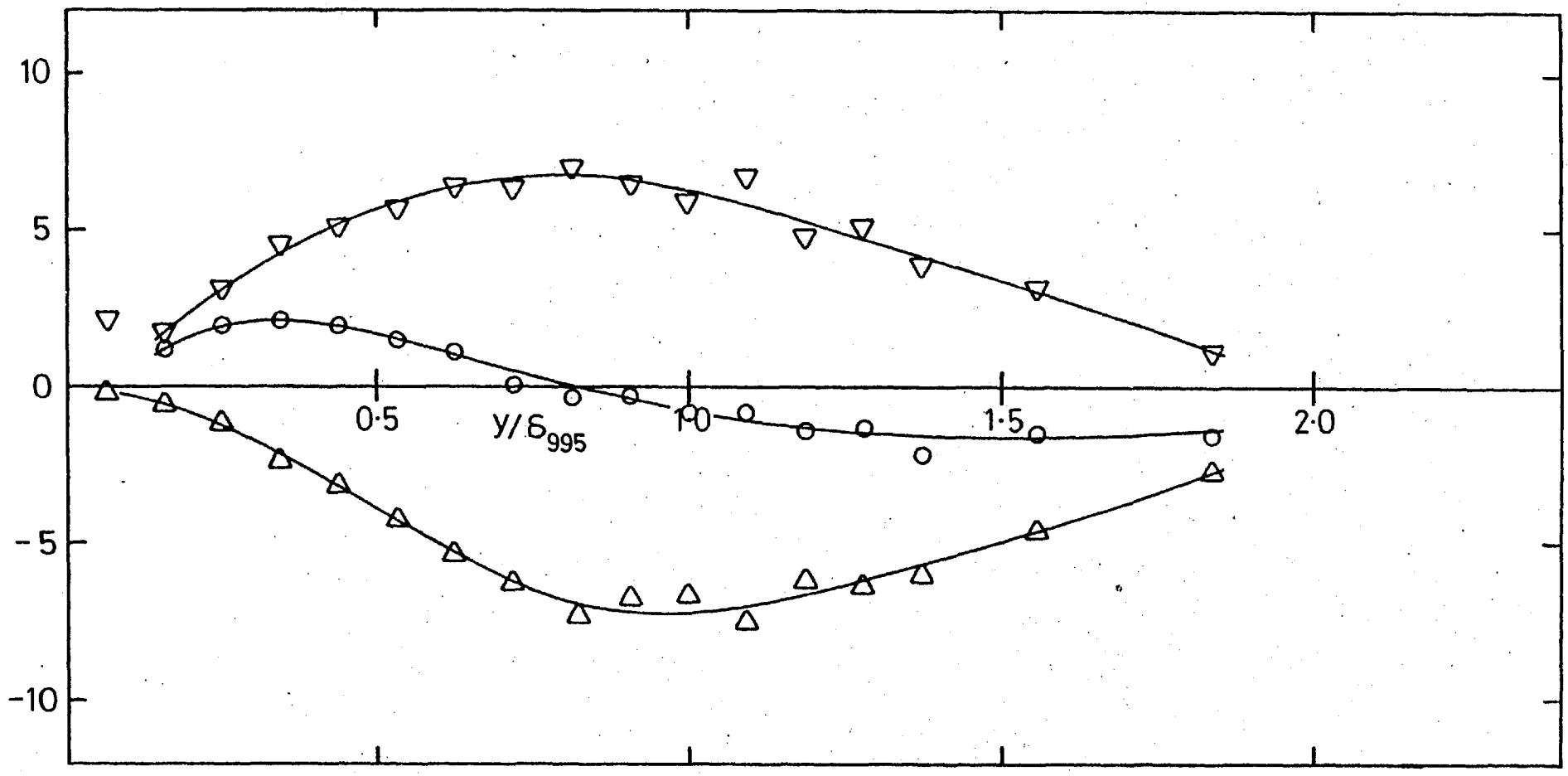

Fig. 4.26e, Contributions to $\overline{v^3}$; $(u'/U)_e = 0.0575$, $L^u_e/\delta_{995} = 1.83$. Symbols as in a). Note new scale.

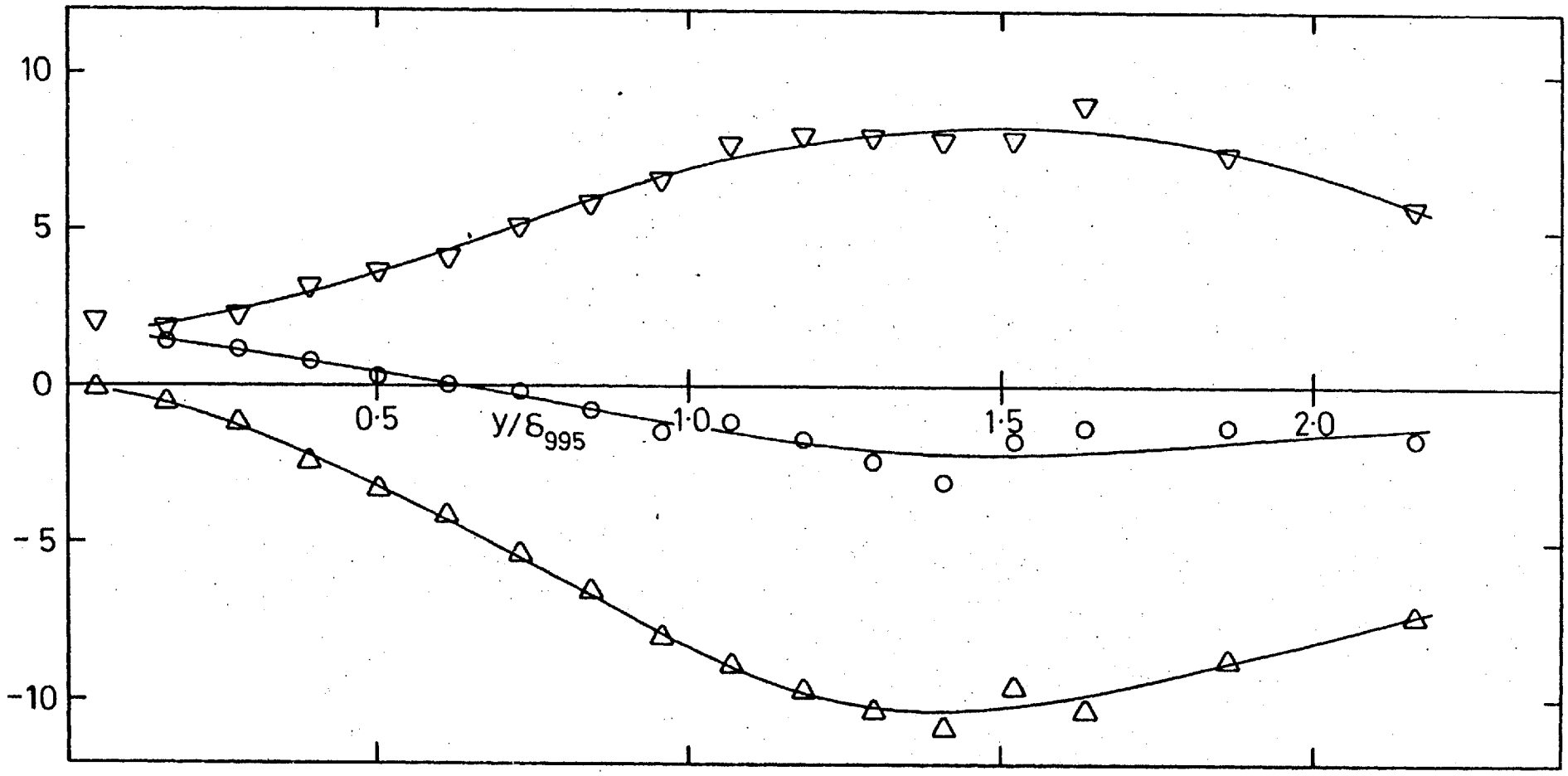

Fig. 4.26f, Contributions to $\overline{v^3}$; $(u'/U)_e = 0.0575$, $L^u_e/\delta_{995} = 1.34$. Symbols as in a). Note new scale.

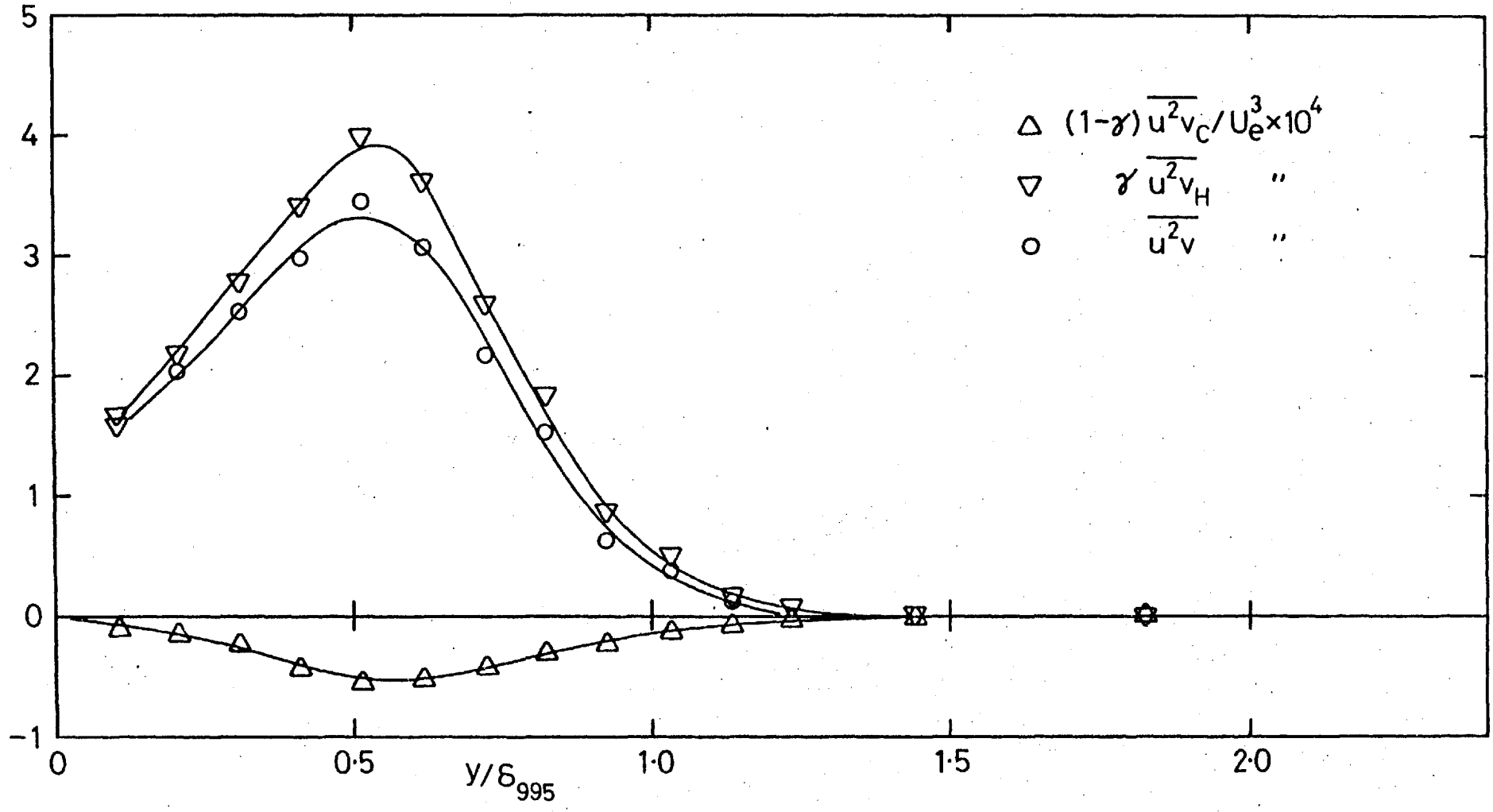

a) $(u'/U)_e = 0.0240$, $L^u_e/\delta_{995} = 1.88$.

Fig. 4.27 Zonal contributions to $\overline{u^2v}$.

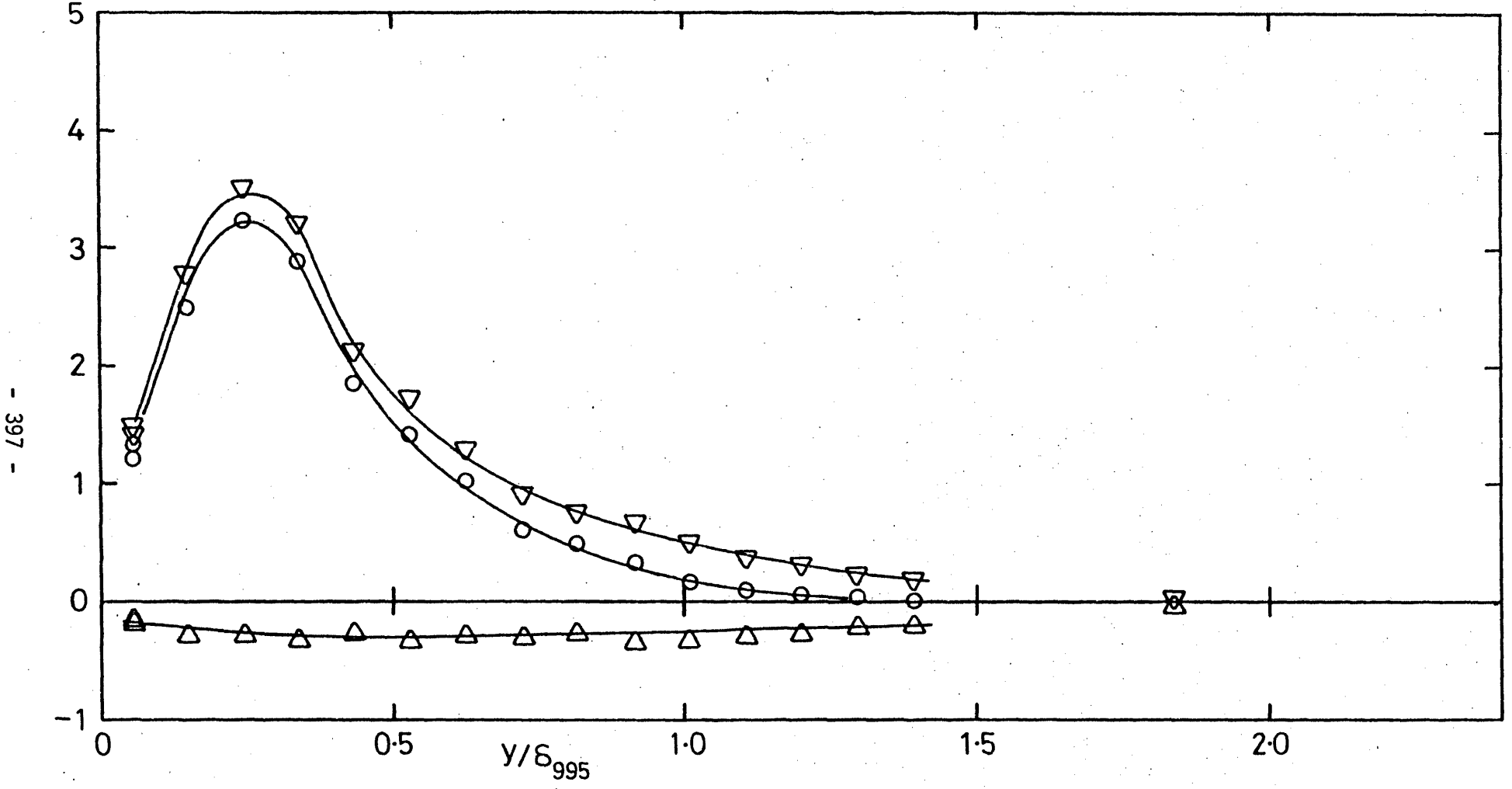

Fig. 4.27b, Contributions to $\overline{u^2v}$; $(u'/U)_e = 0.255$, $L^u_e/\delta_{995} = 0.67$. Symbols as in a).

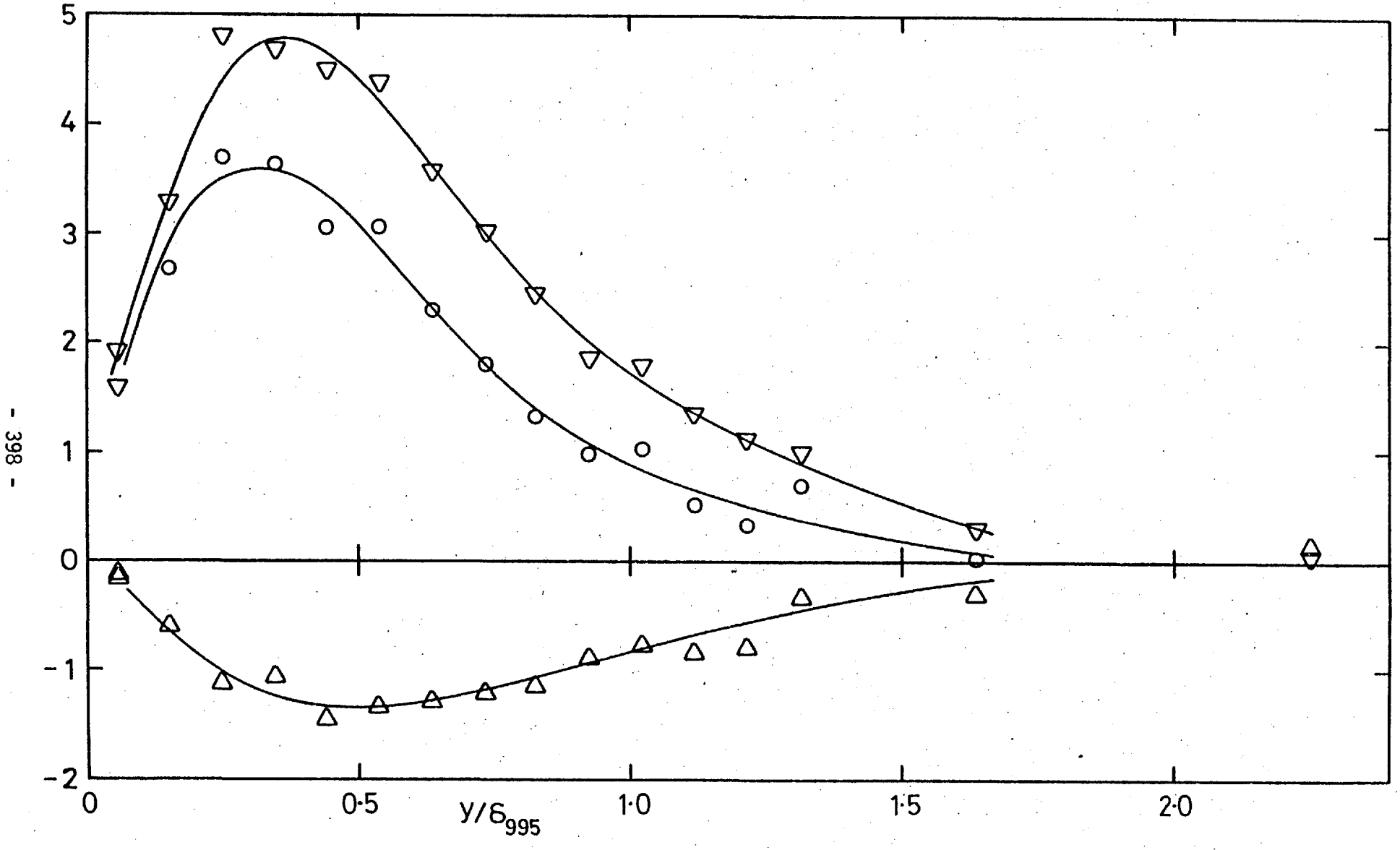

Fig. 4.27c, Contributions to $\overline{u^2 v}$; $(u'/U)_e = 0.0410$, $L^u_e/\delta_{995} = 1.90$. Symbols as in a).

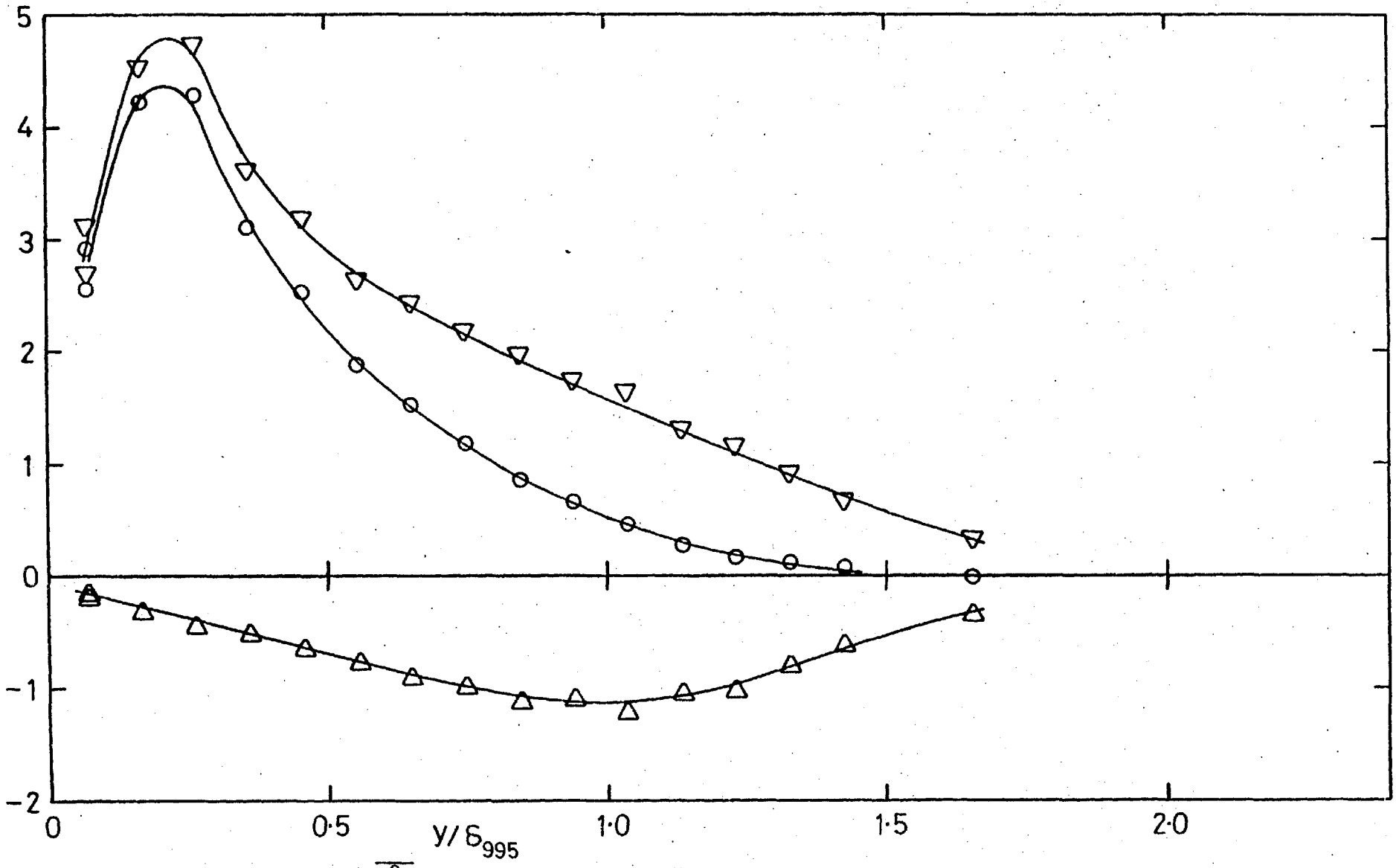

Fig. 4.27d, Contributions to $\overline{u^2v}$; $(u'/U)_e$ = 0.0399, L^u_e/δ_{995} = 0.71. Symbols as in a).

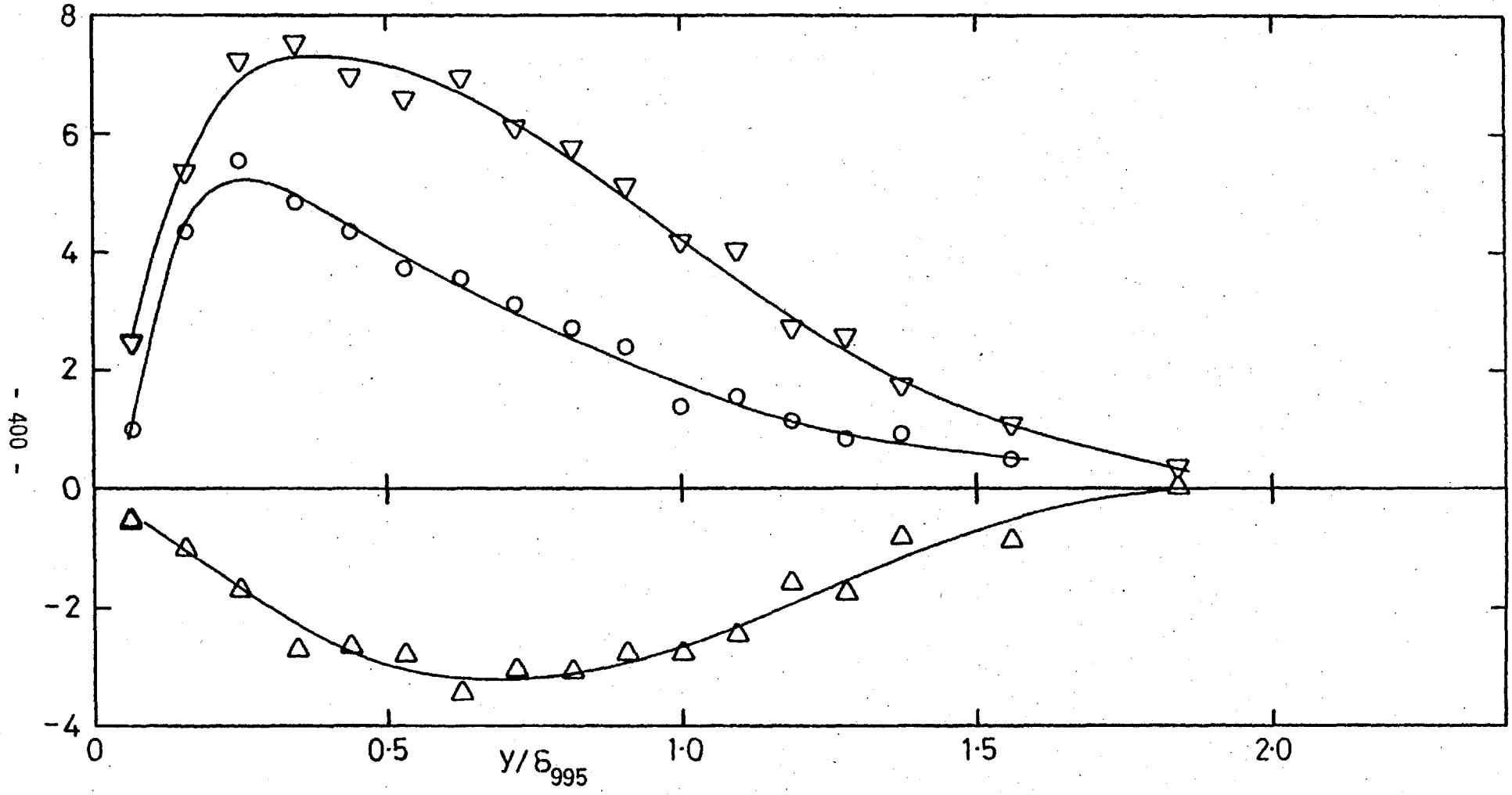

Fig. 4.27e, Contributions to $\overline{u^2v}$; $(u'/U)_e = 0.0575$, $L^u_e/\delta_{995} = 1.83$. Symbols as in a). Note new scale.

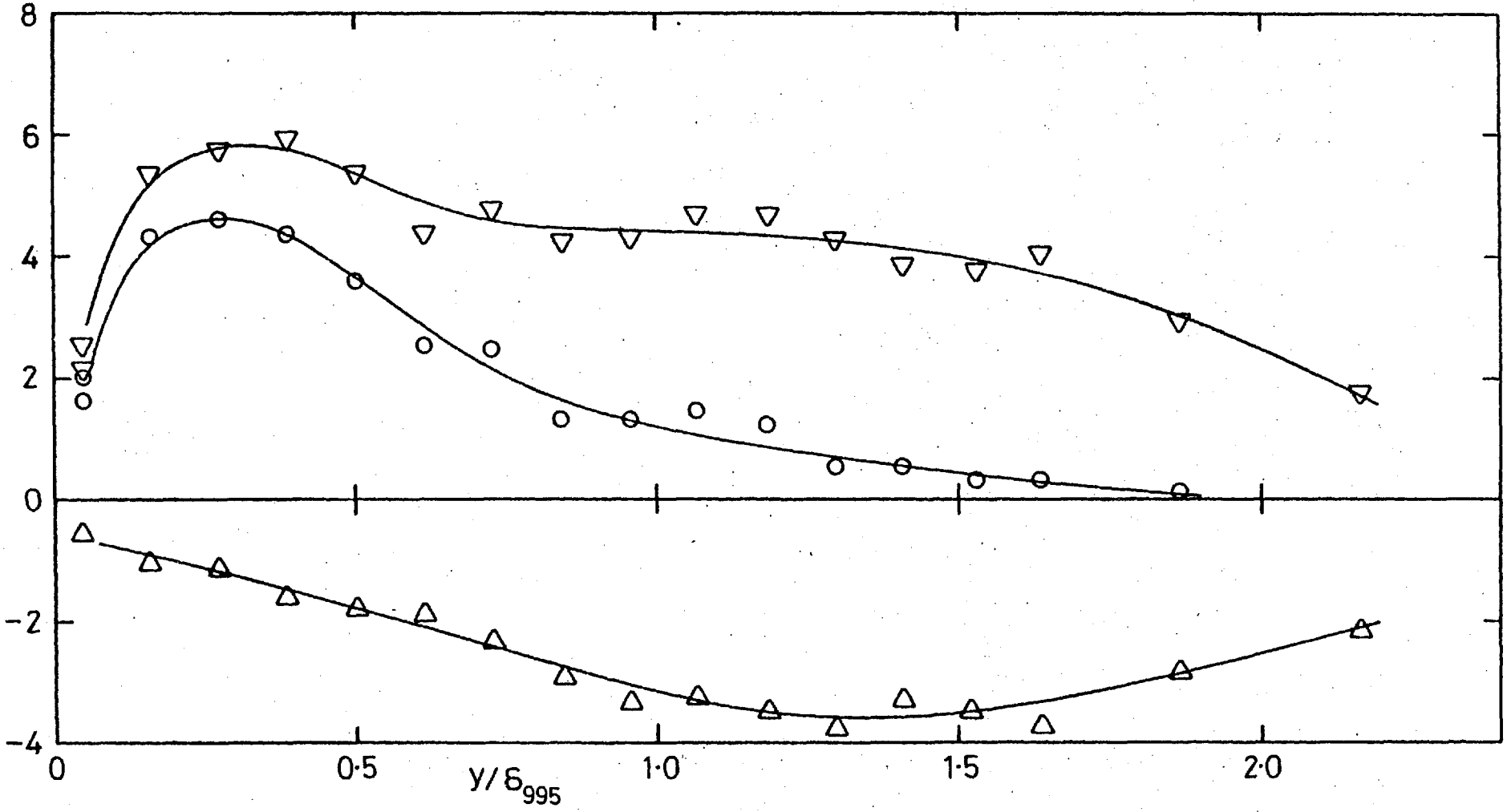

Fig. 4.27f, Contributions to $\overline{u^2v}$; $(u'/U)_e$ = 0.0575, L^u_e/δ_{995} = 1.34. Symbols as in a). Note new scale.

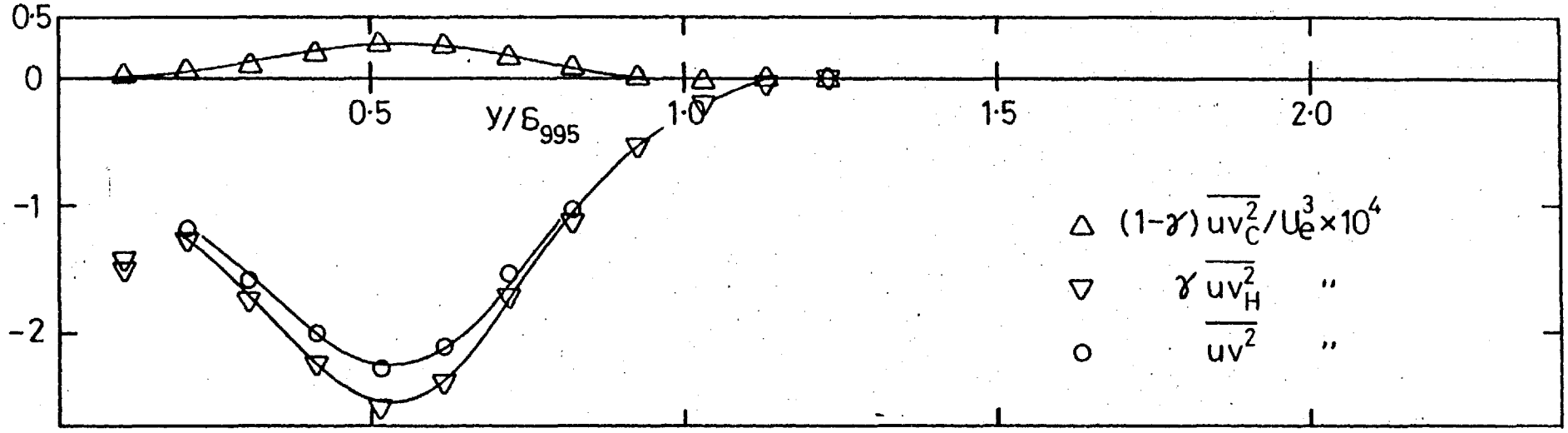

a) $(u'/U)_e$ = 0.0240, L^u_e/δ_{995} = 1.88.

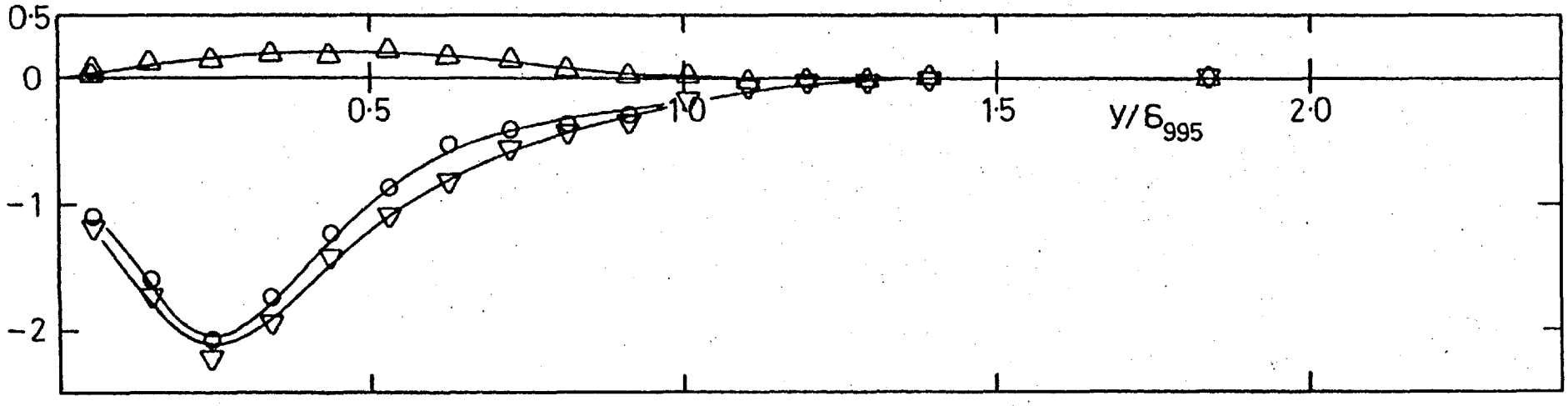

b) $(u'/U)_e$ = 0.0255, L^u_e/δ_{995} = 0.67. Symbols as in a).

Fig. 4.28 Zonal contributions to $\overline{uv^2}$.

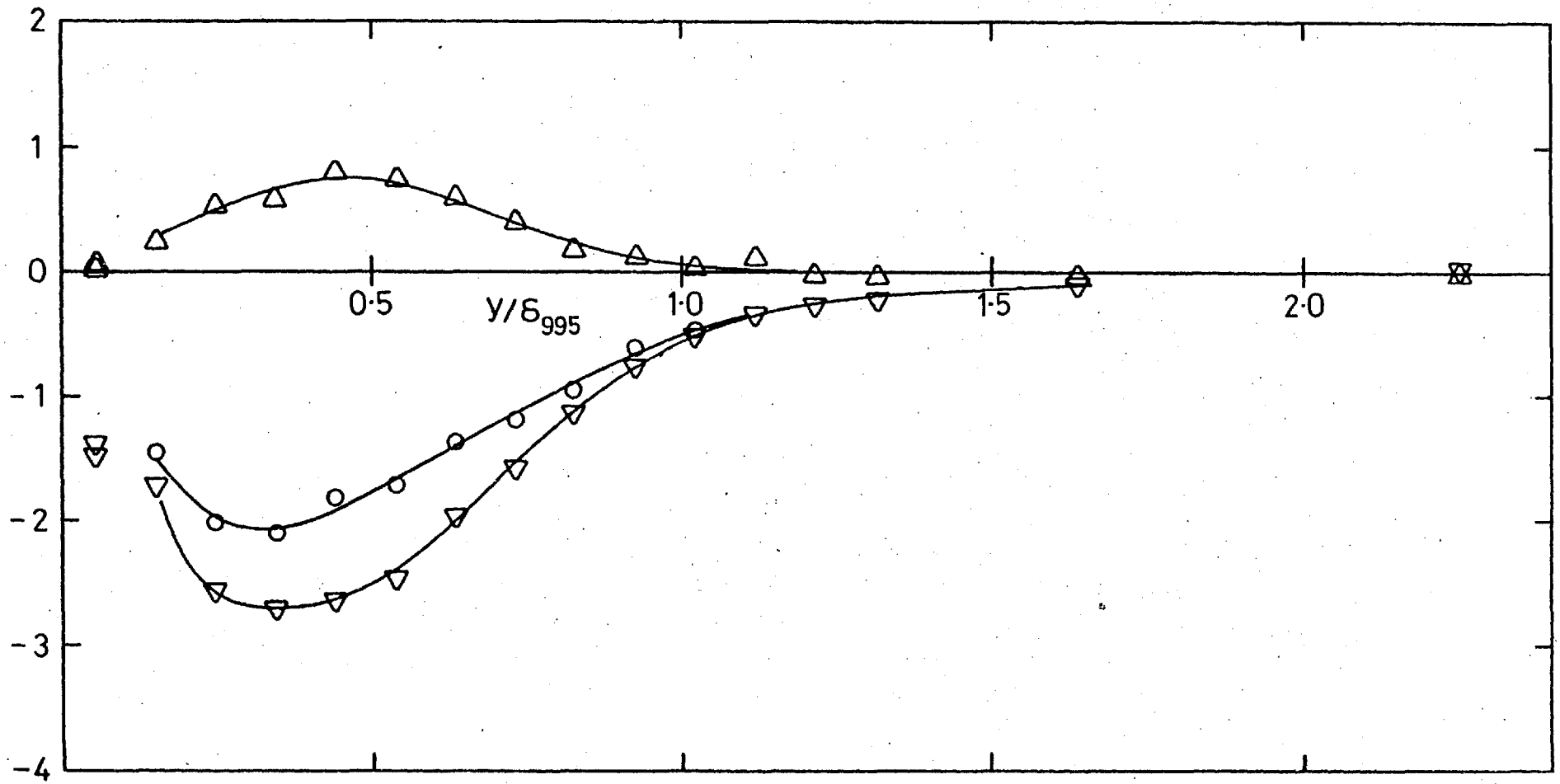

Fig. 4.28c, Contributions to $\overline{uv^2}$; $(u'/U)_e$ = 0.0410, L^u_e/δ_{995} = 1.90. Symbols as in a).

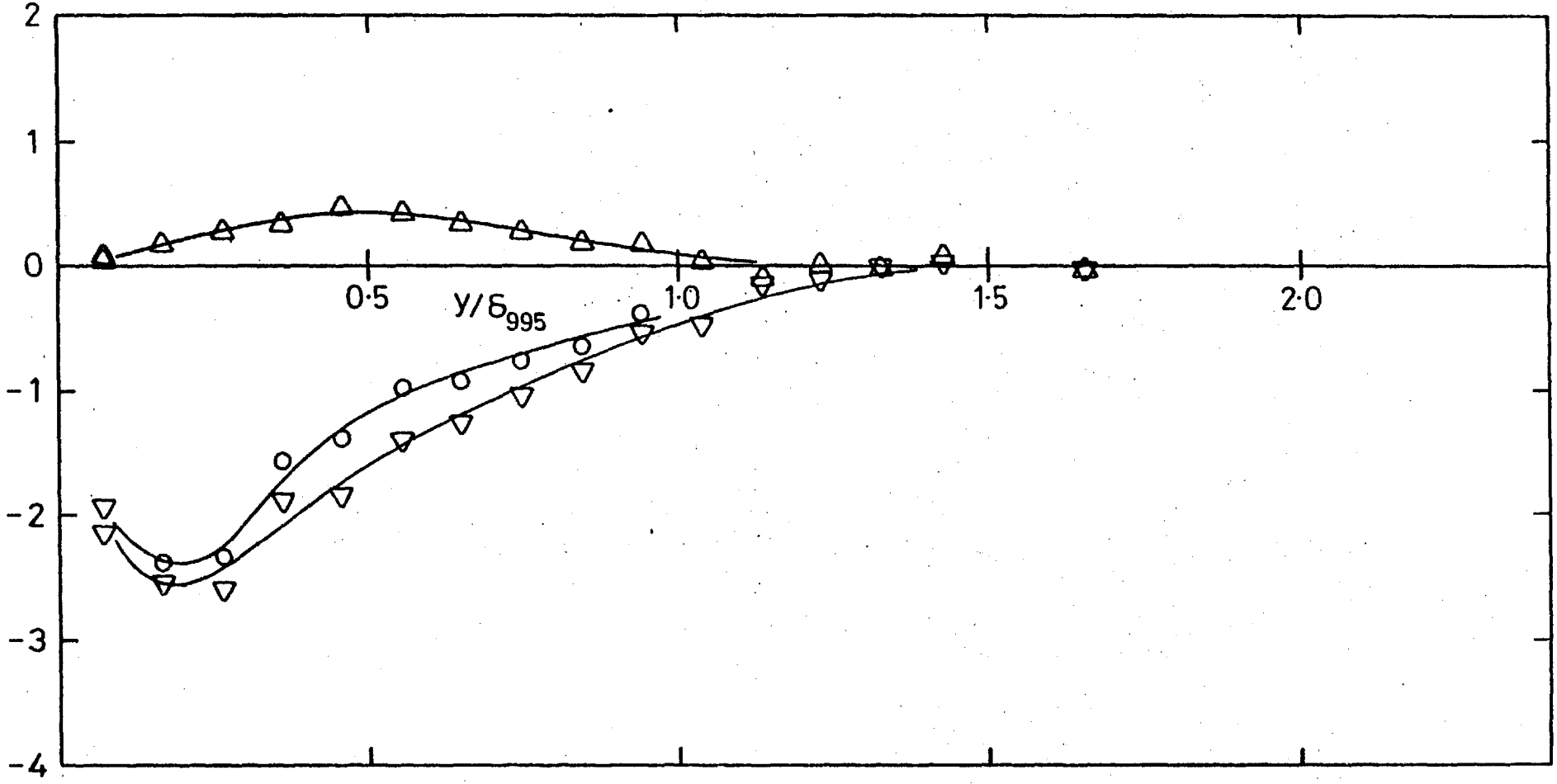

Fig. 4.28d, Contributions to $\overline{uv^2}$; $(u'/U)_e = 0.0399$, $L^u_e/\delta_{995} = 0.71$. Symbols as in a).

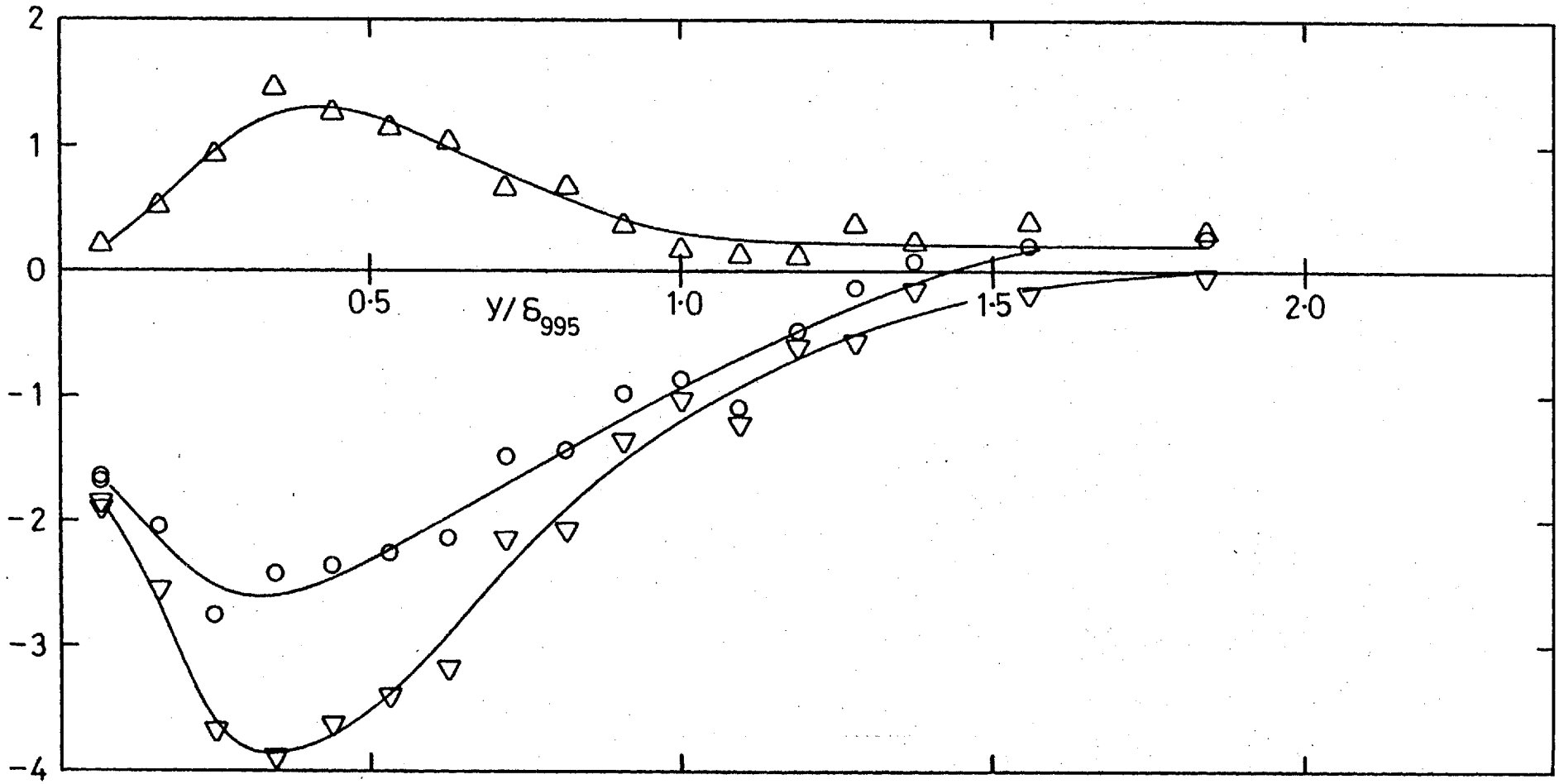

Fig. 4.28e, Contributions to $\overline{uv^2}$; $(u'/U)_e = 0.0575$, $L^u_e/\delta_{995} = 1.83$. Symbols as in a).

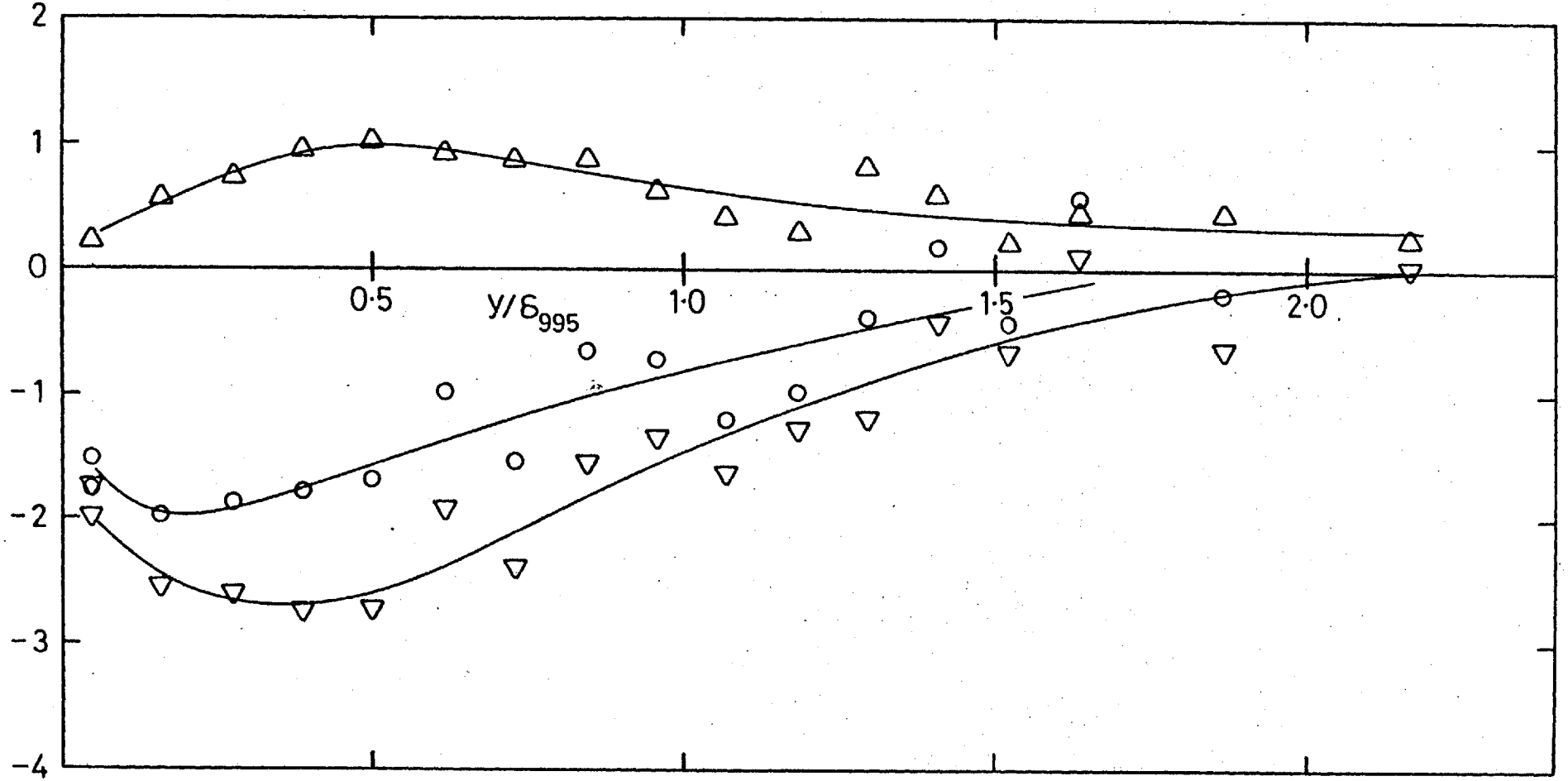

Fig. 4.28f, Contributions to $\overline{uv^2}$; $(u'/U)_e = 0.0575$, $L^u_e/\delta_{995} = 1.34$. Symbols as in a).

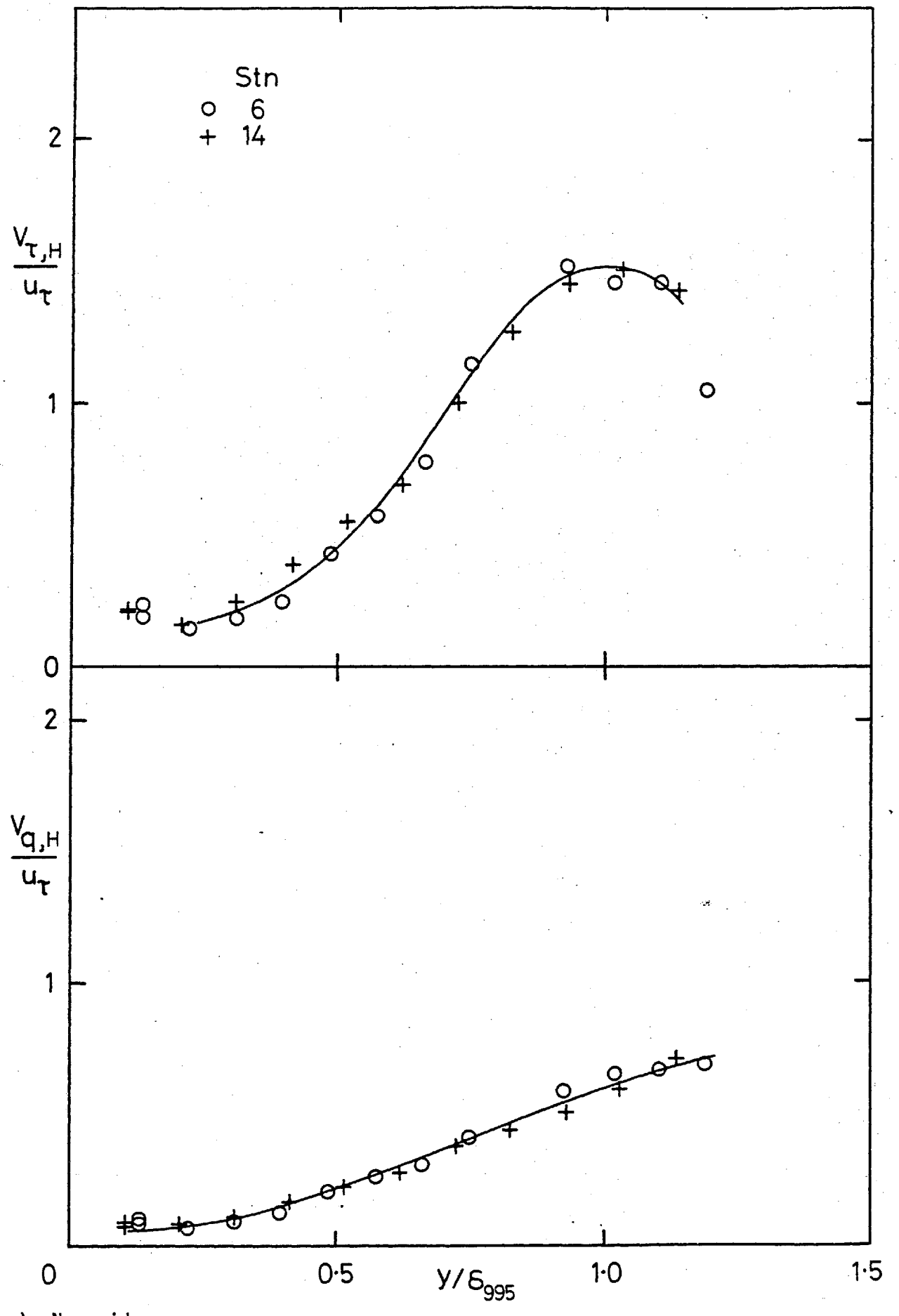

a) No grid.

Fig. 4.29 Hot-zone transport velocities $V_{\tau,H}$ and $V_{q,H}$

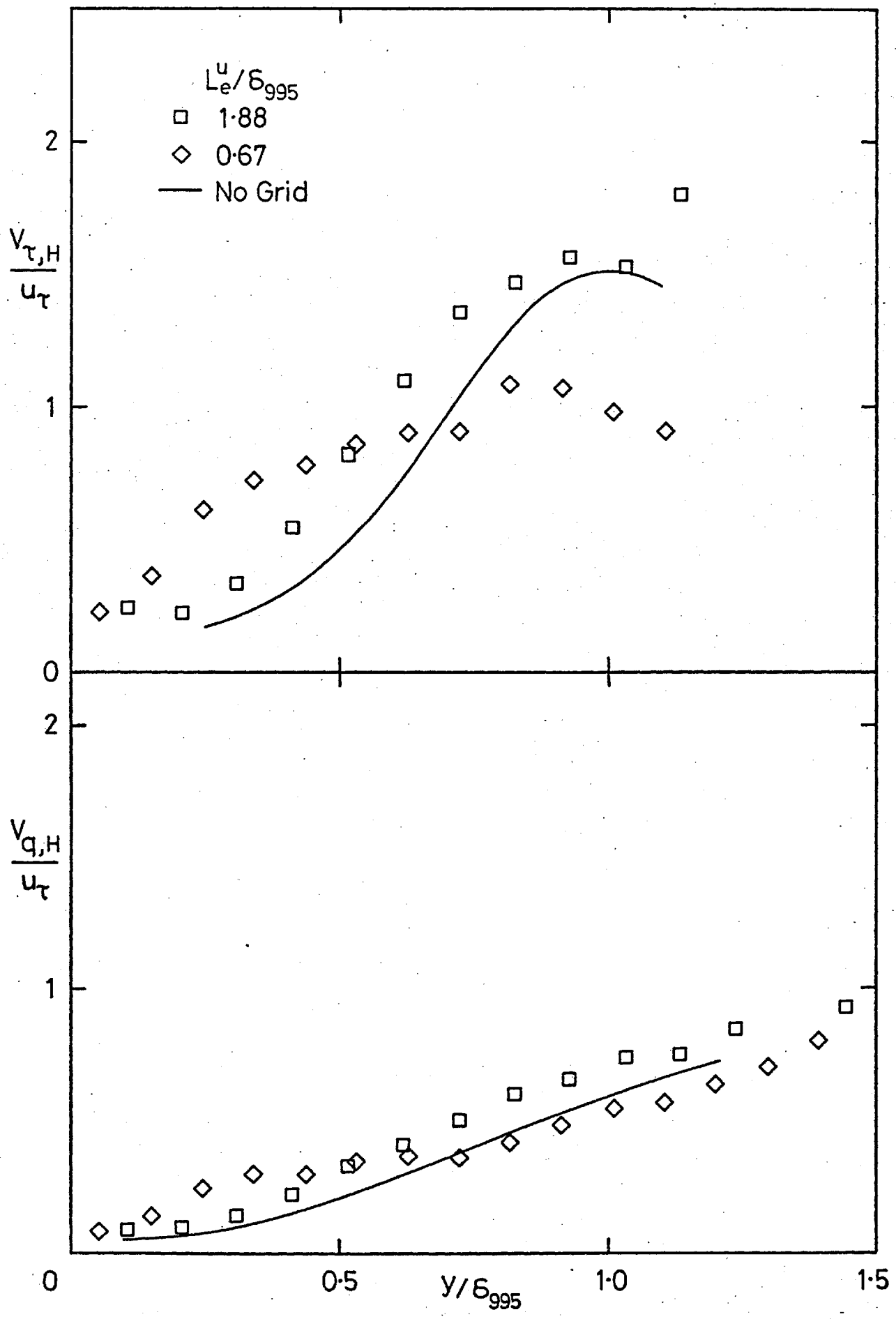

Fig. 4.29b, $(u'/U)_e \approx 0.025$.

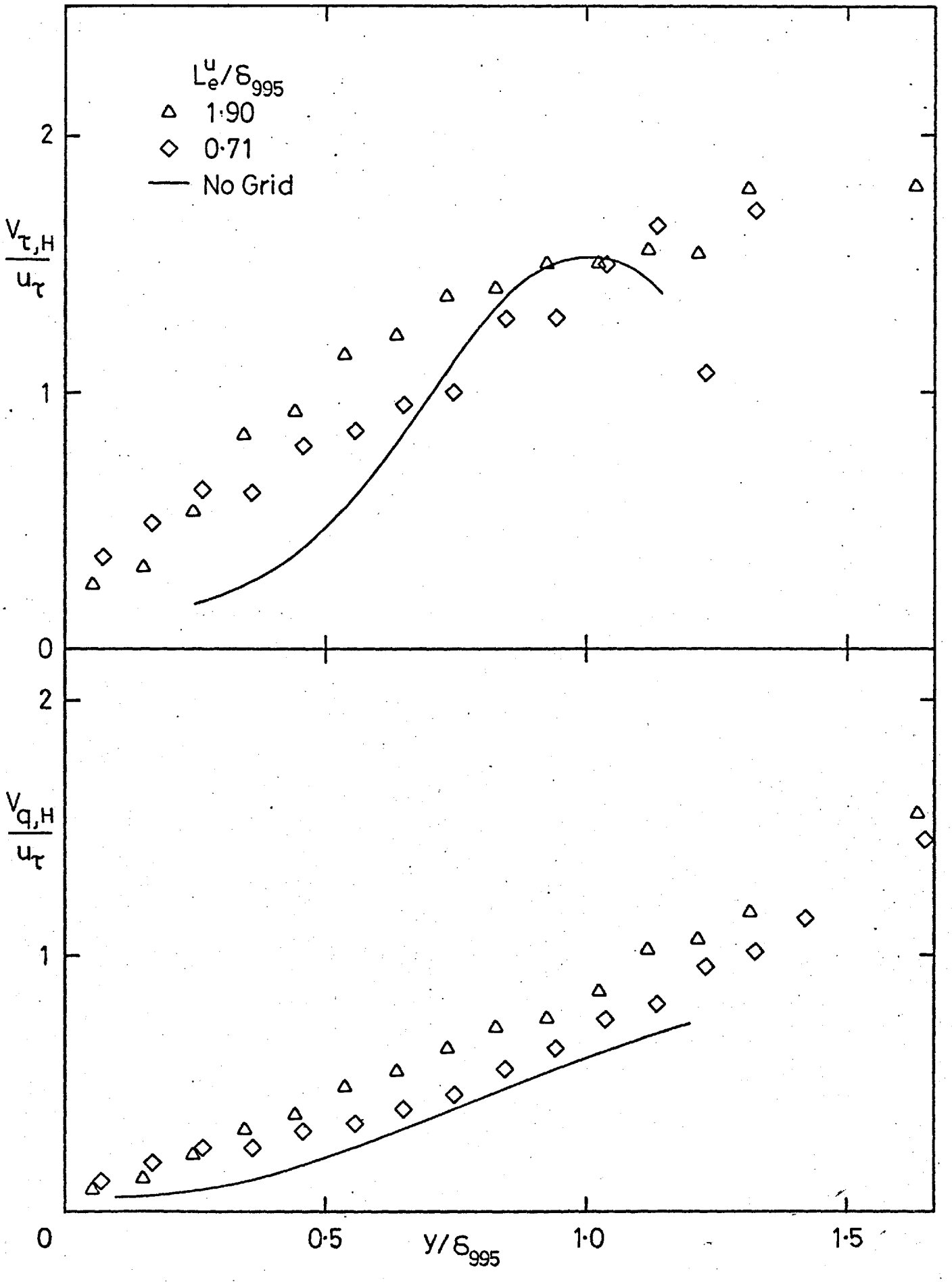

Fig. 4.29c, $(u'/U)_e \approx 0.040$.

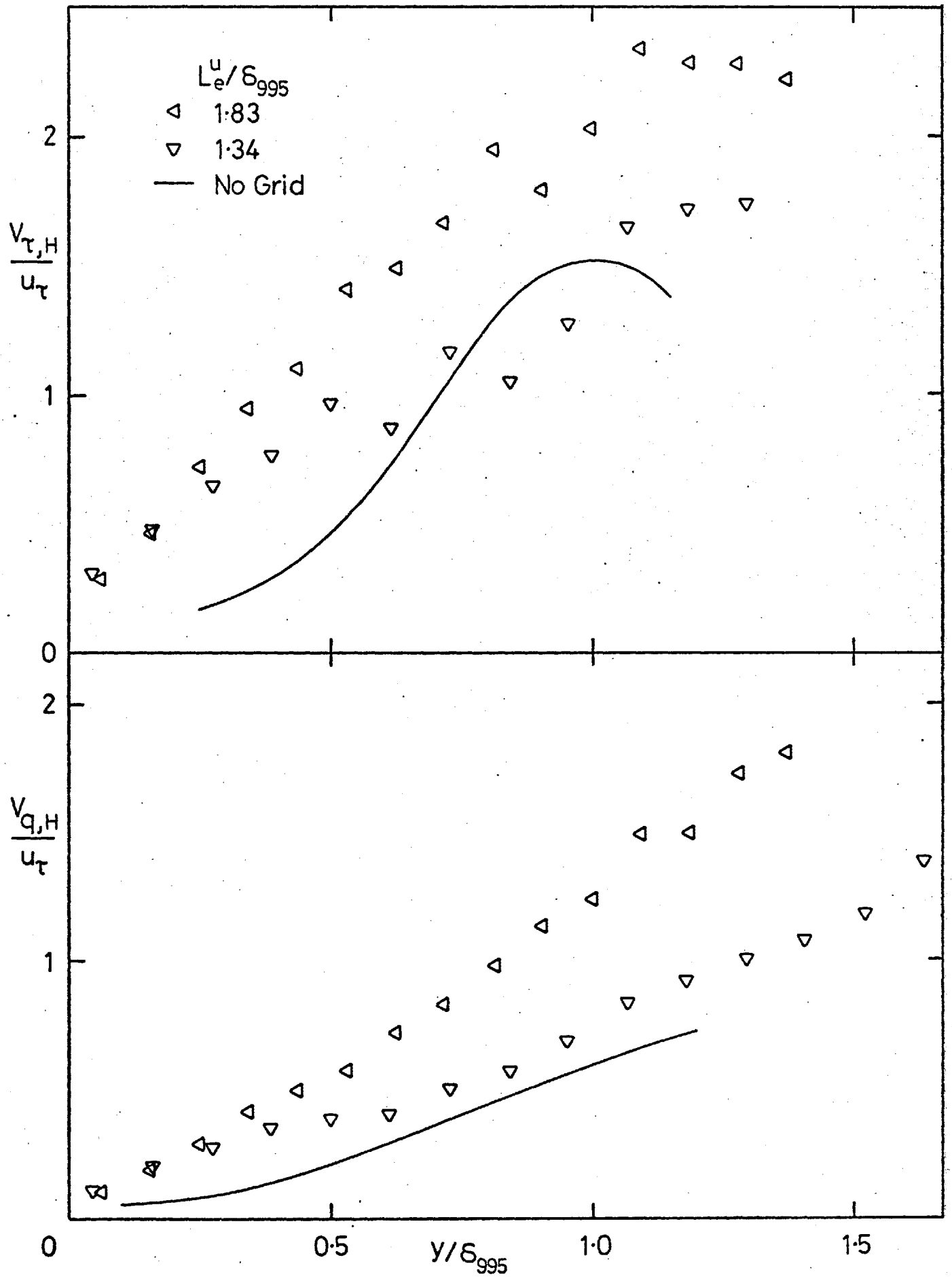

Fig. 4.29d, $(u'/U)_e = 0.0575$.

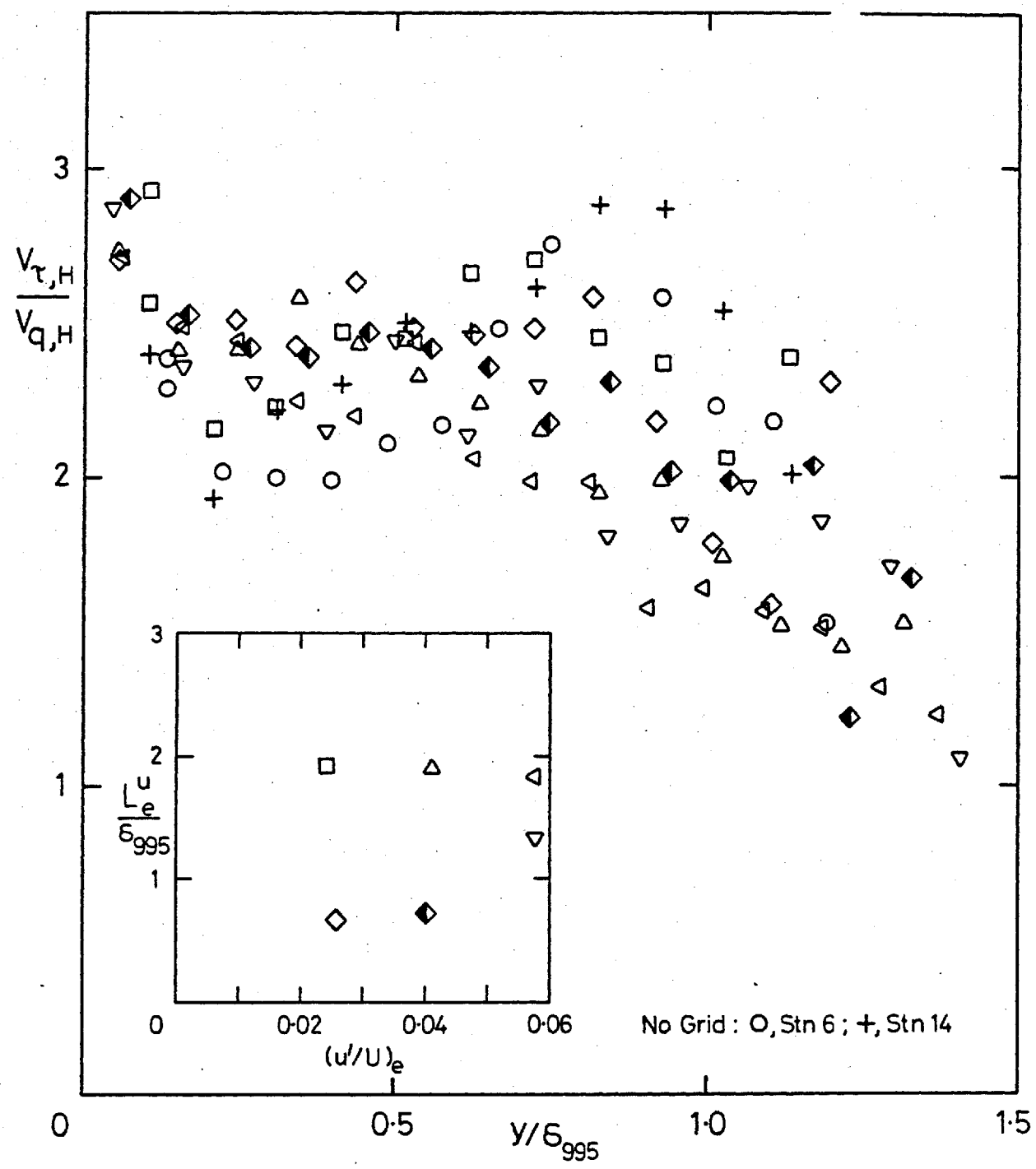

Fig. 4.30 Ratio of hot-zone transport velocities, $V_{\tau,H}/V_{q,H}$.

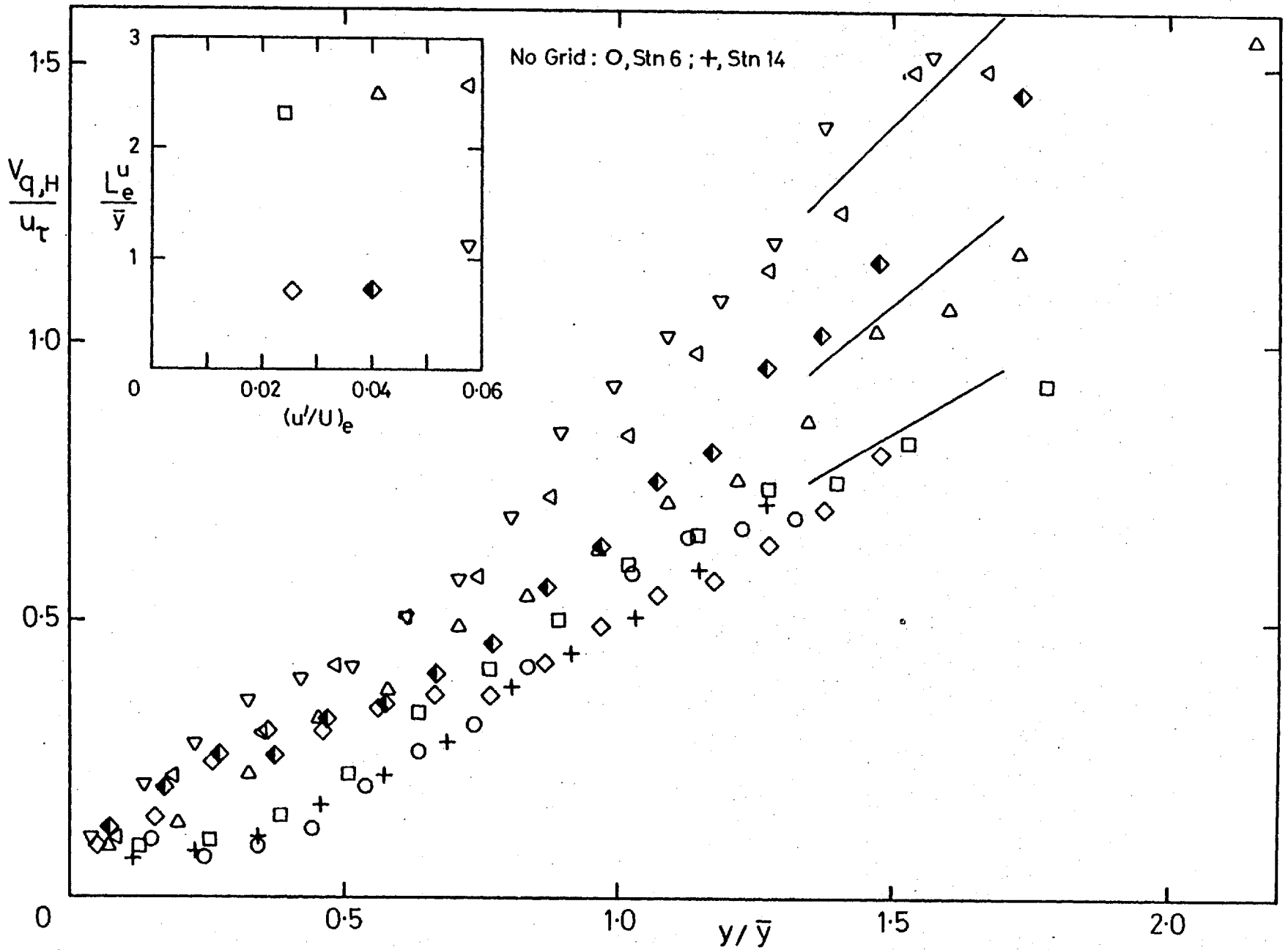

Fig. 4.31 Hot-zone transport velocity $V_{q,H}$ plotted against $y/\bar{y}$

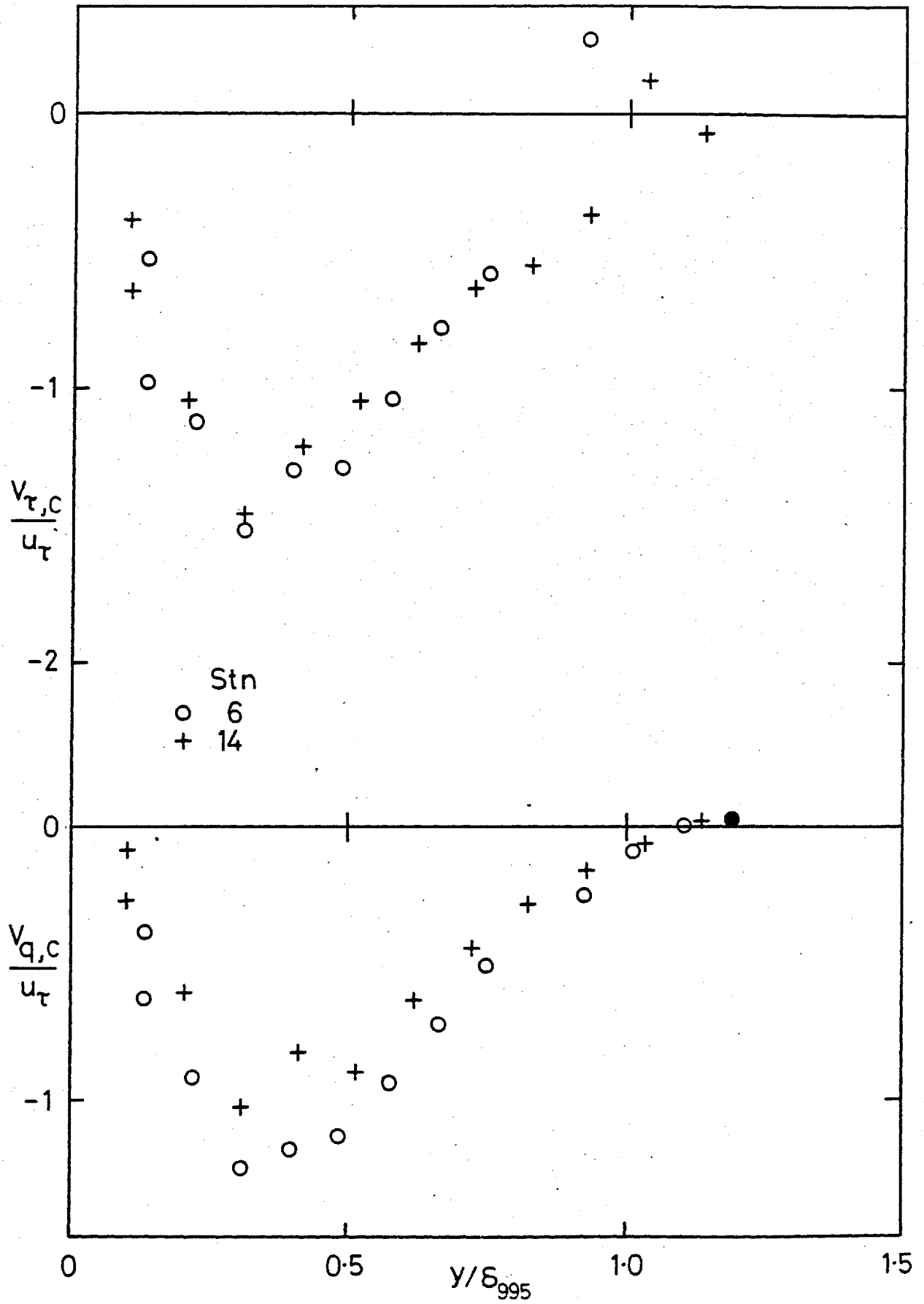

a) No grid.

Fig. 4.32 Cold-zone transport velocities $V_{\tau,C}$ and $V_{q,C}$.

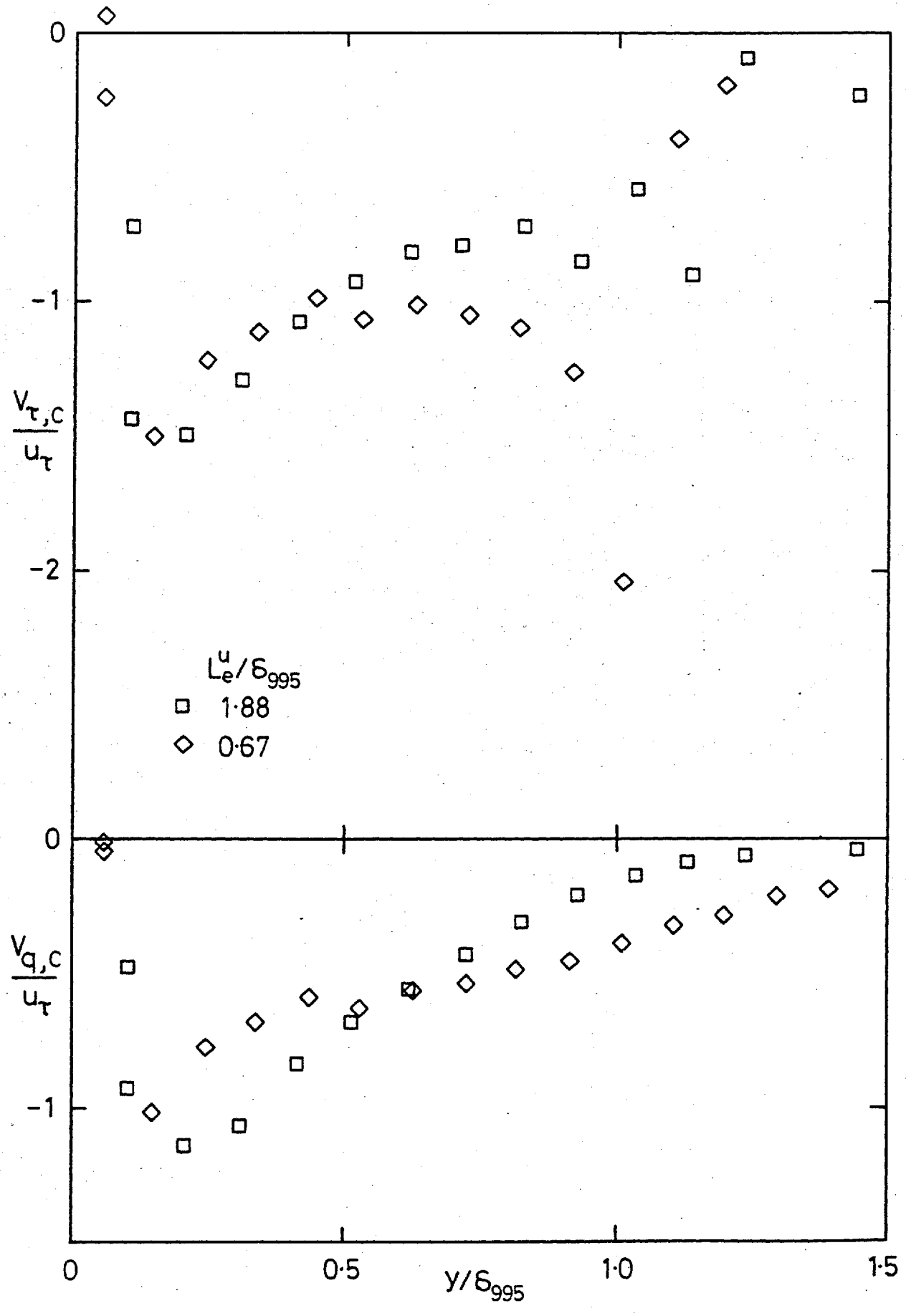

Fig. 4.32b, $(u'/U)_e \approx 0.025$.

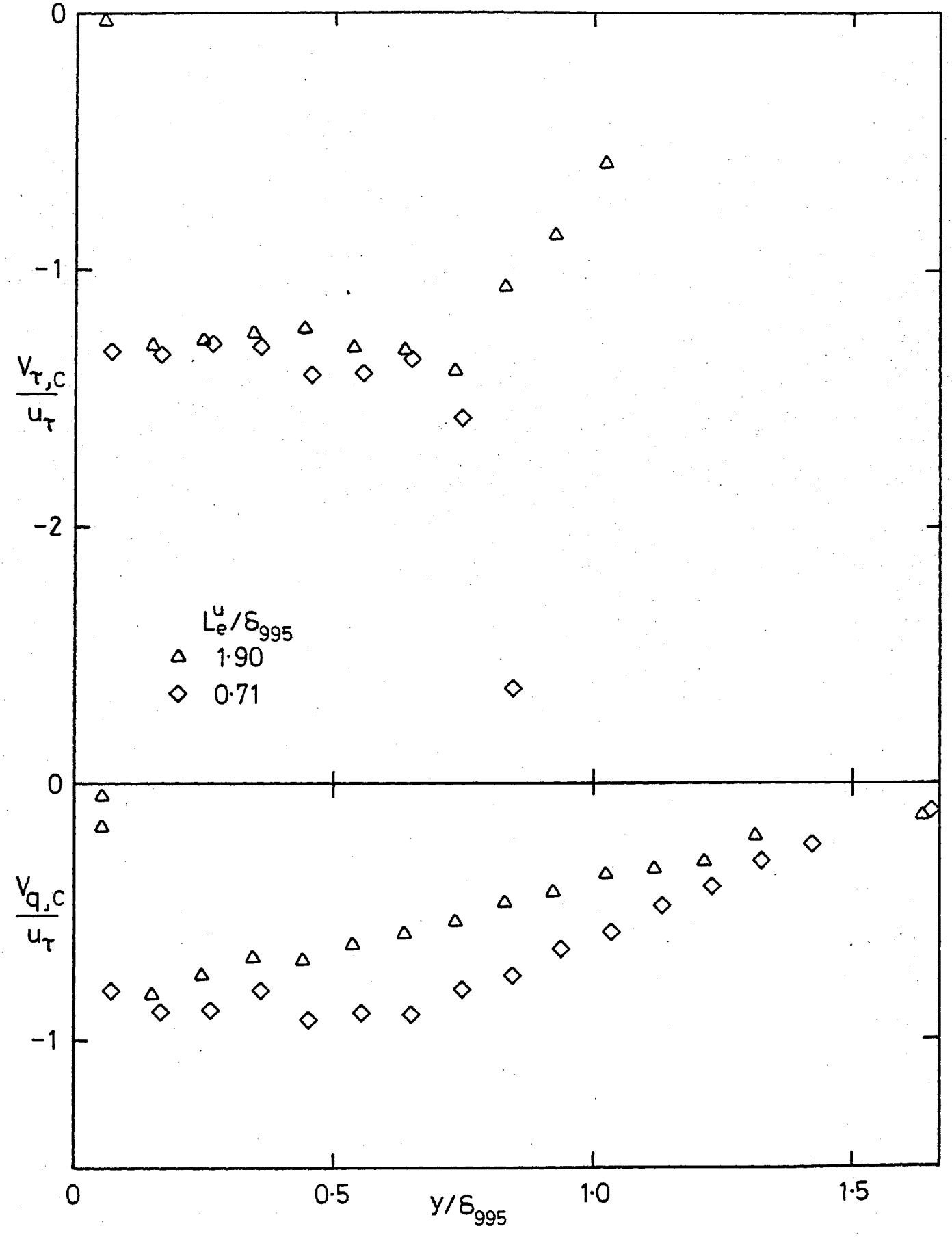

Fig. 4.32c, $(u'/U)_e \simeq 0.040$.

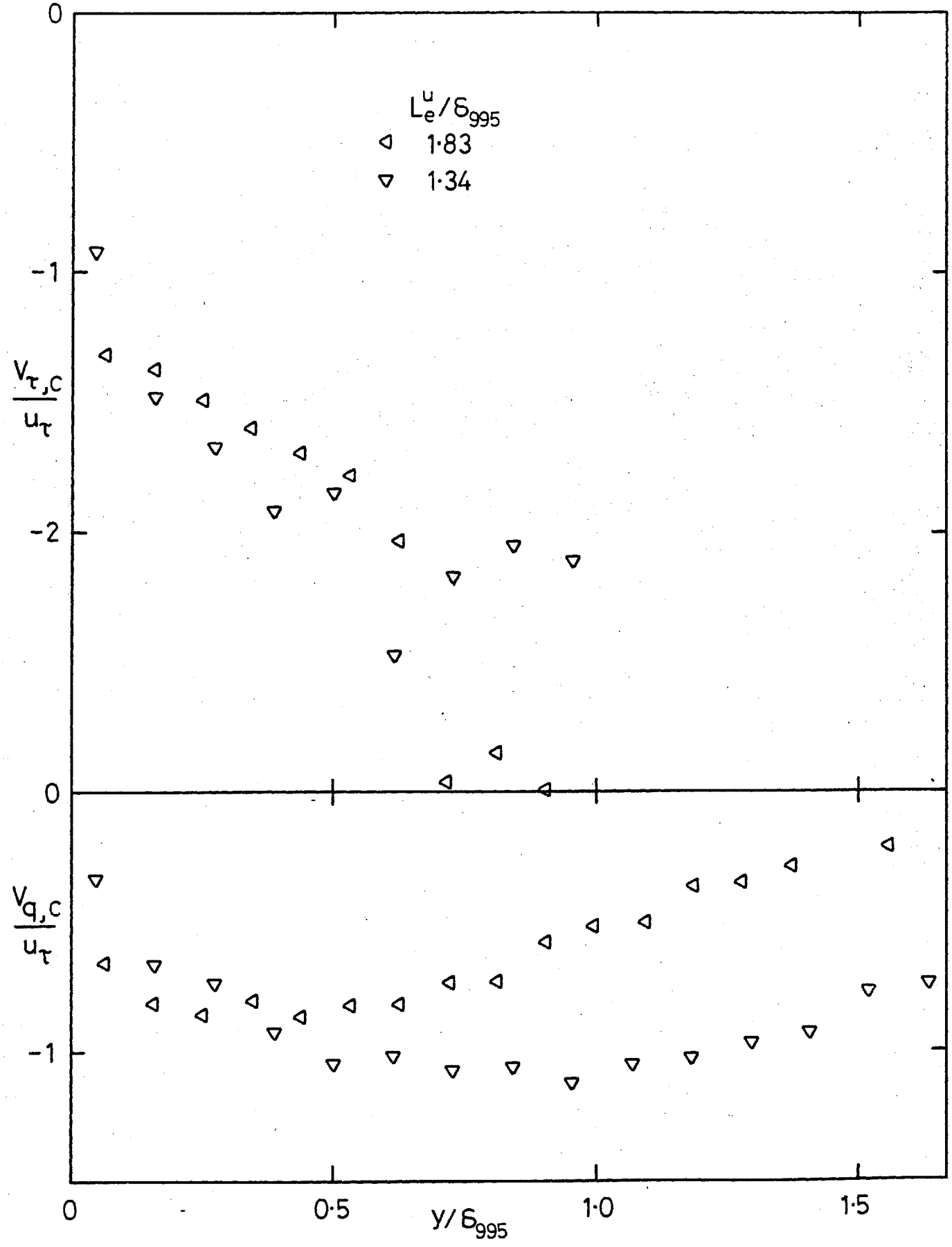

Fig. 4.32d, $(u'/U)_e = 0.0575$.

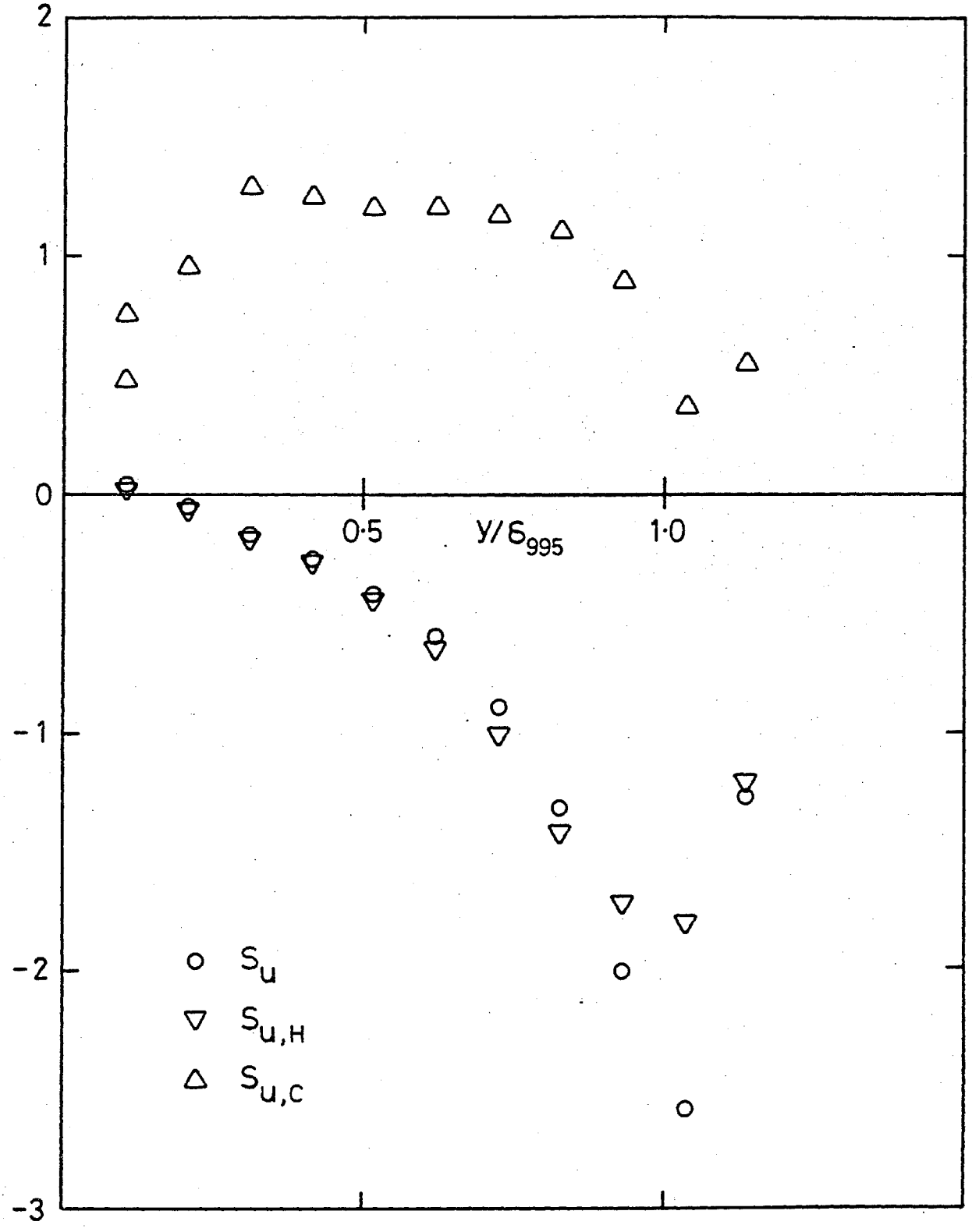

a) No grid, stn 14.

Fig. 4.33 Skewness of u.

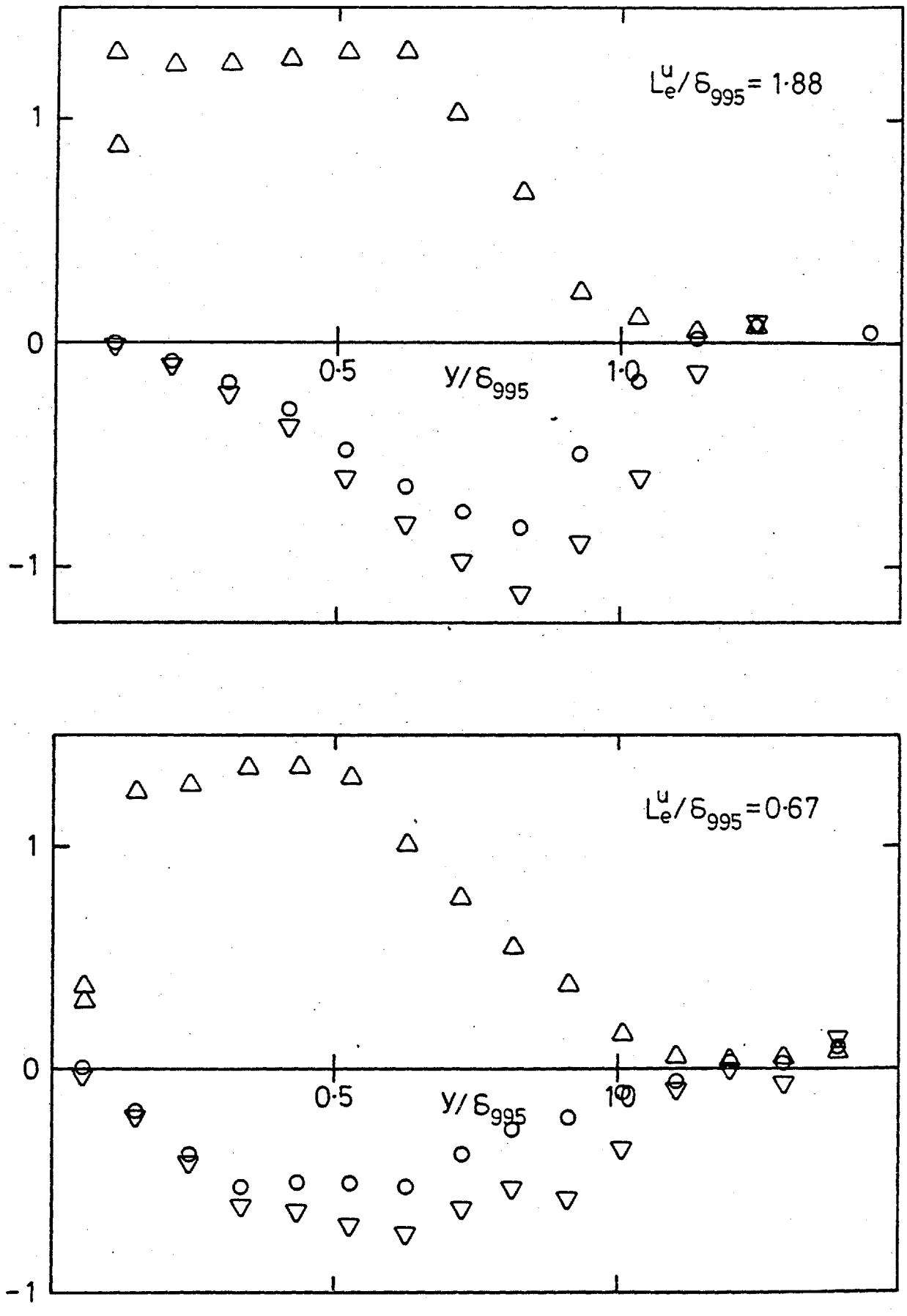

Fig. 4.33b, Skewness of u; $(u'/U)_e \approx 0.025$. Symbols as in a).

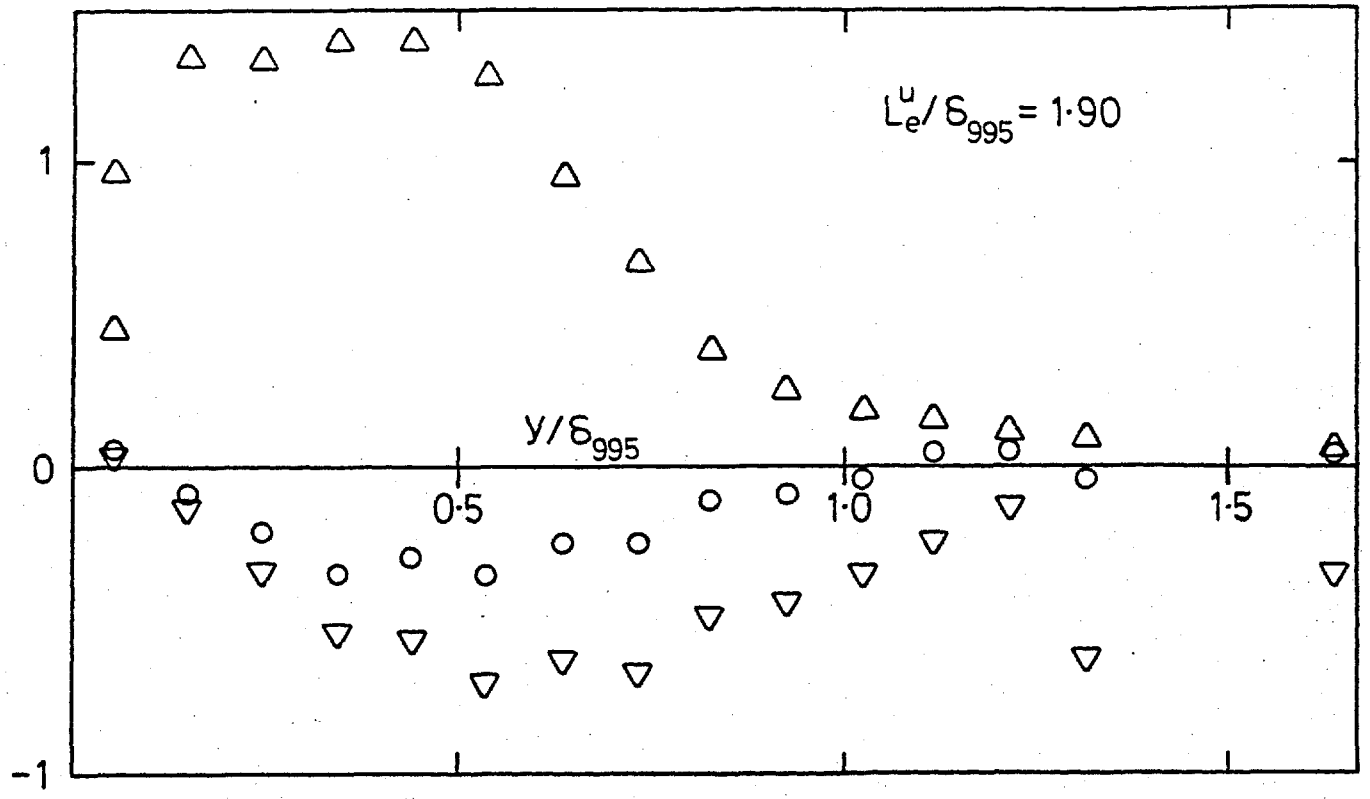

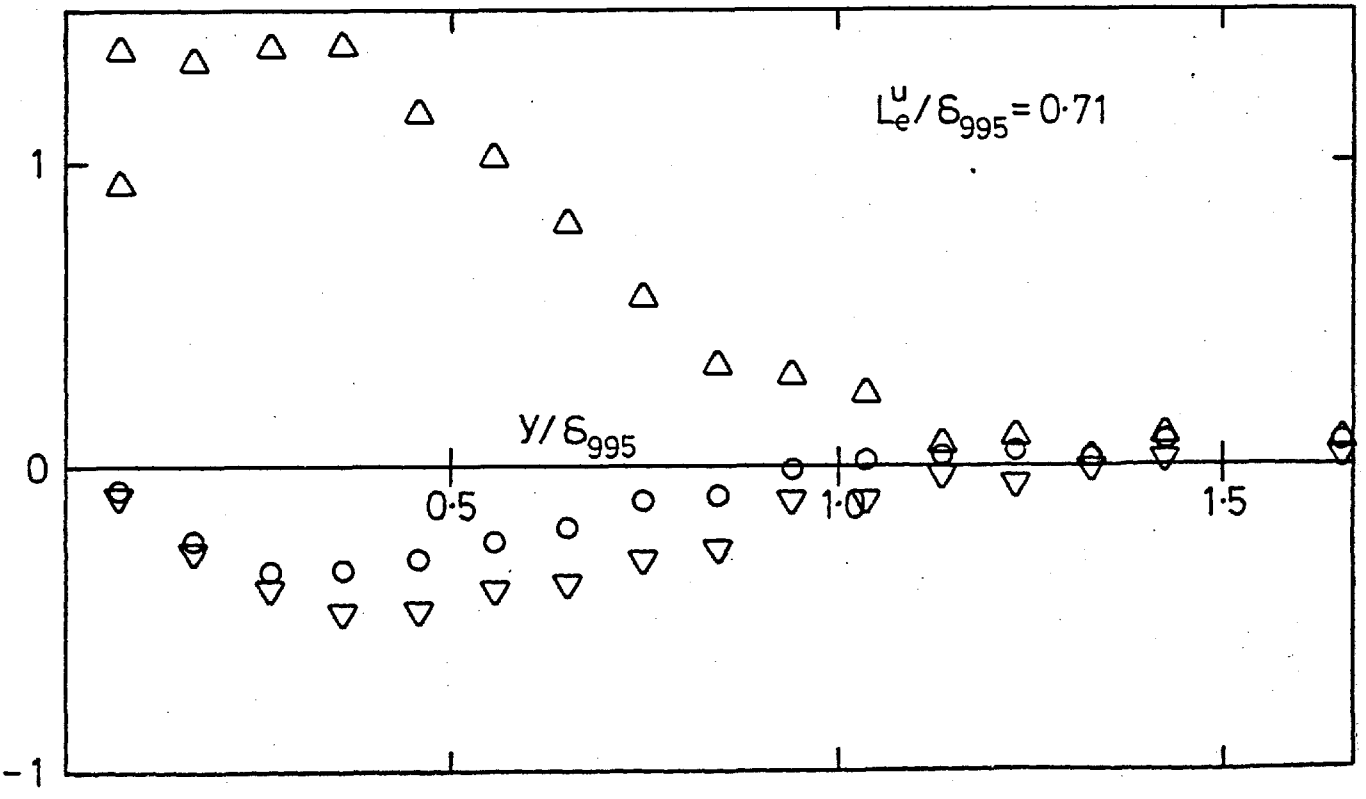

Fig. 4.33c, Skewness of u; $(u'/U)_e \approx 0.040$. Symbols as in a).

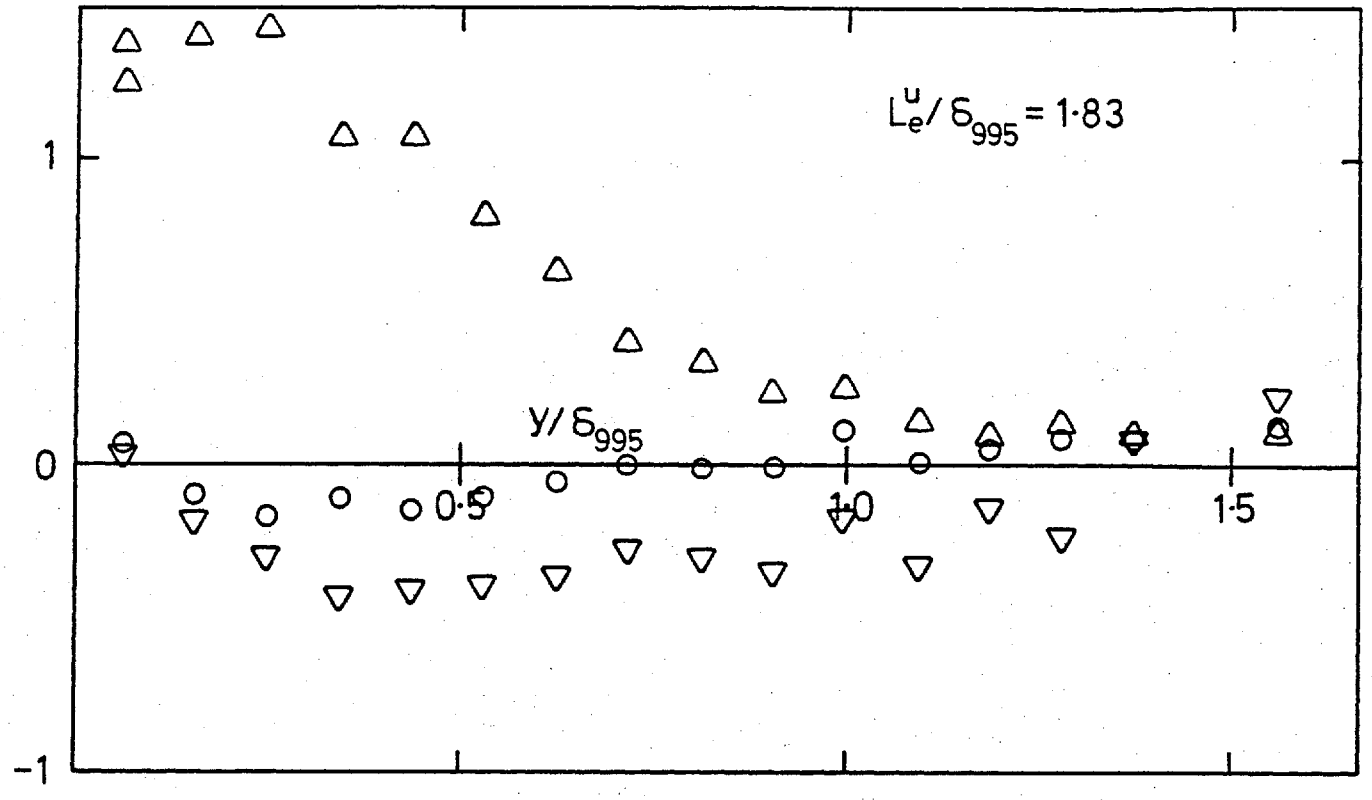

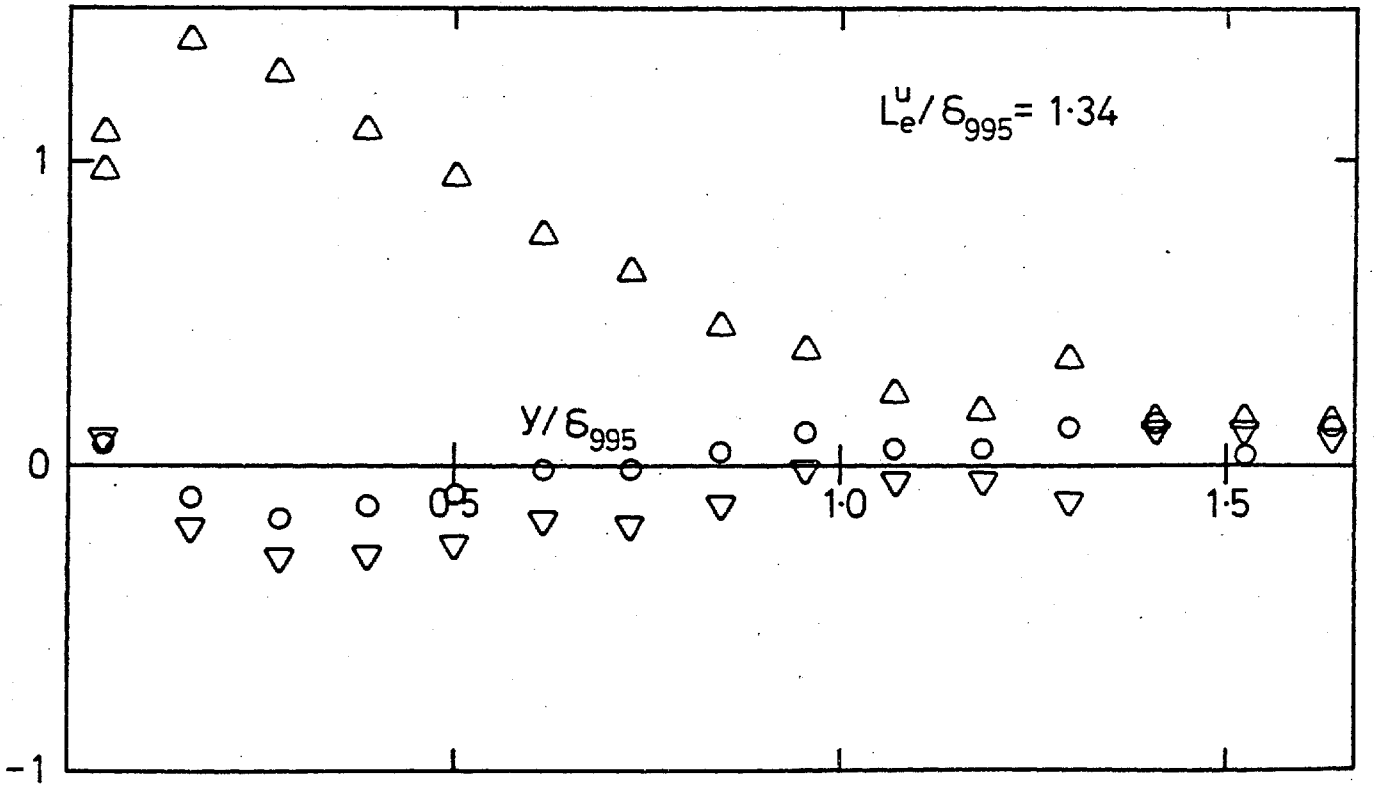

Fig. 4.33d, Skewness of u; $(u'/U)_e$ = 0.0575. Symbols as in a).

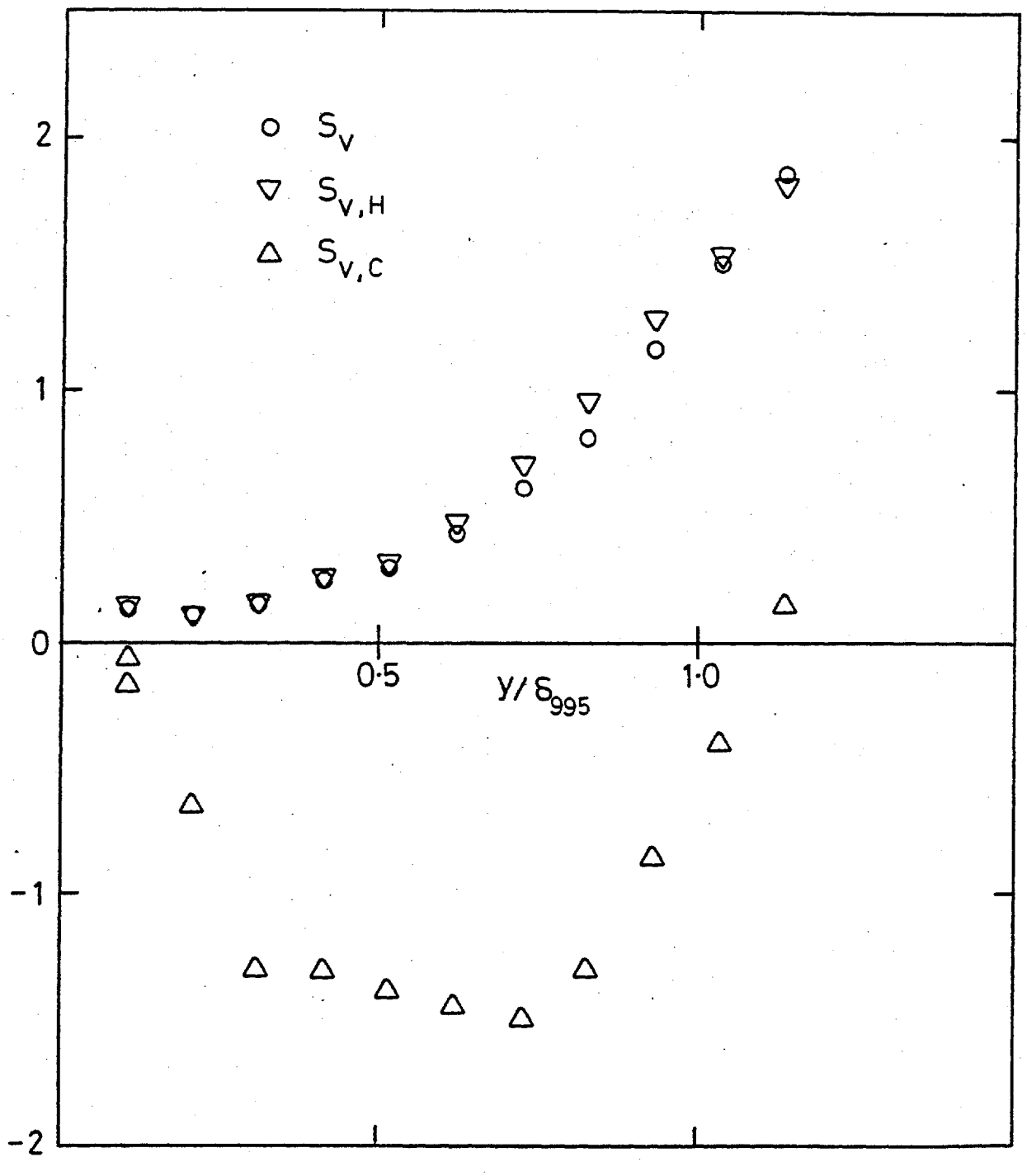

a) No grid, stn 14.

Fig. 4.34 Skewness of v.

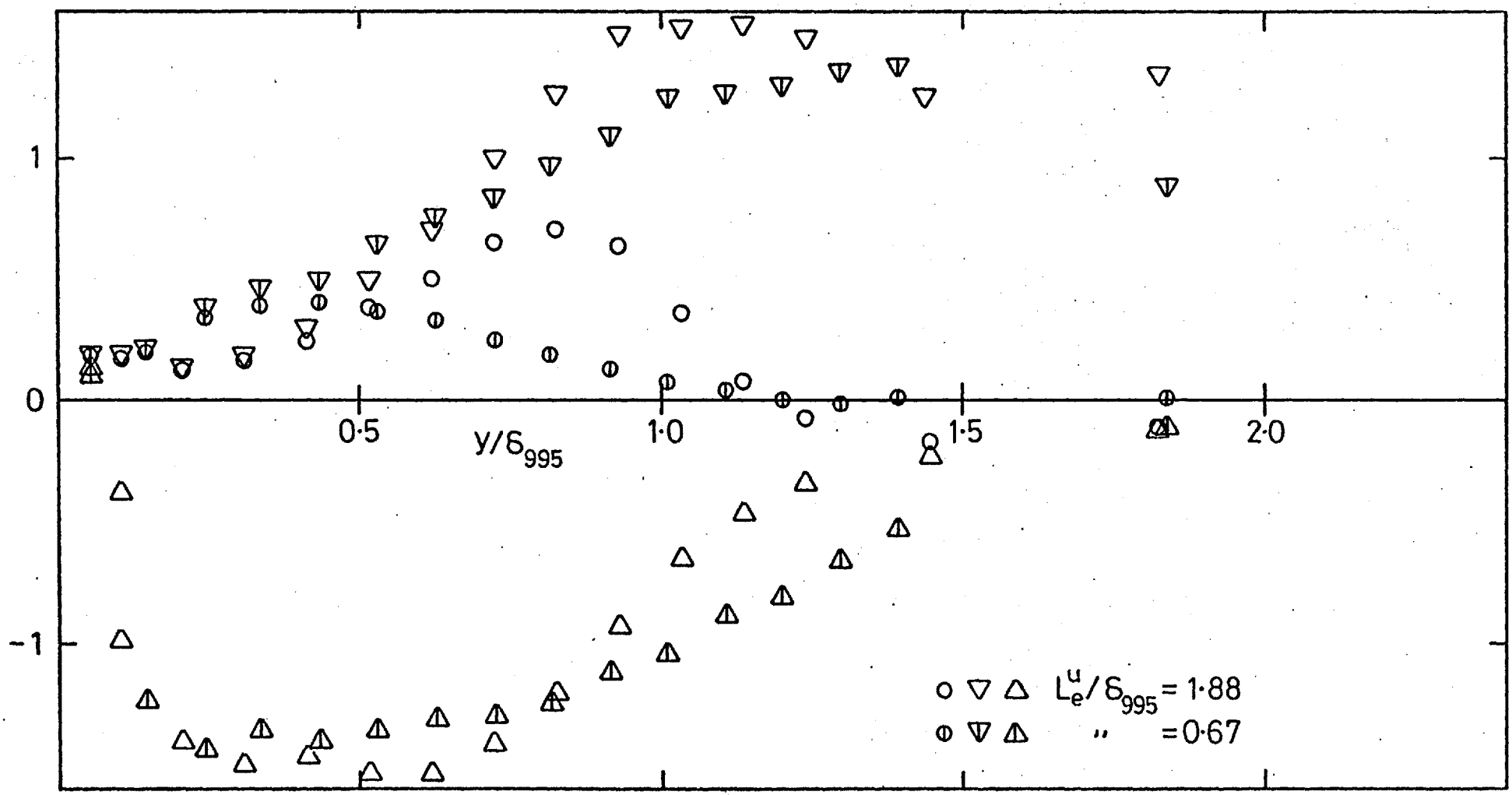

Fig. 4.34b, Skewness of v; $(u'/U)_e \approx 0.025$. Symbols as in a).

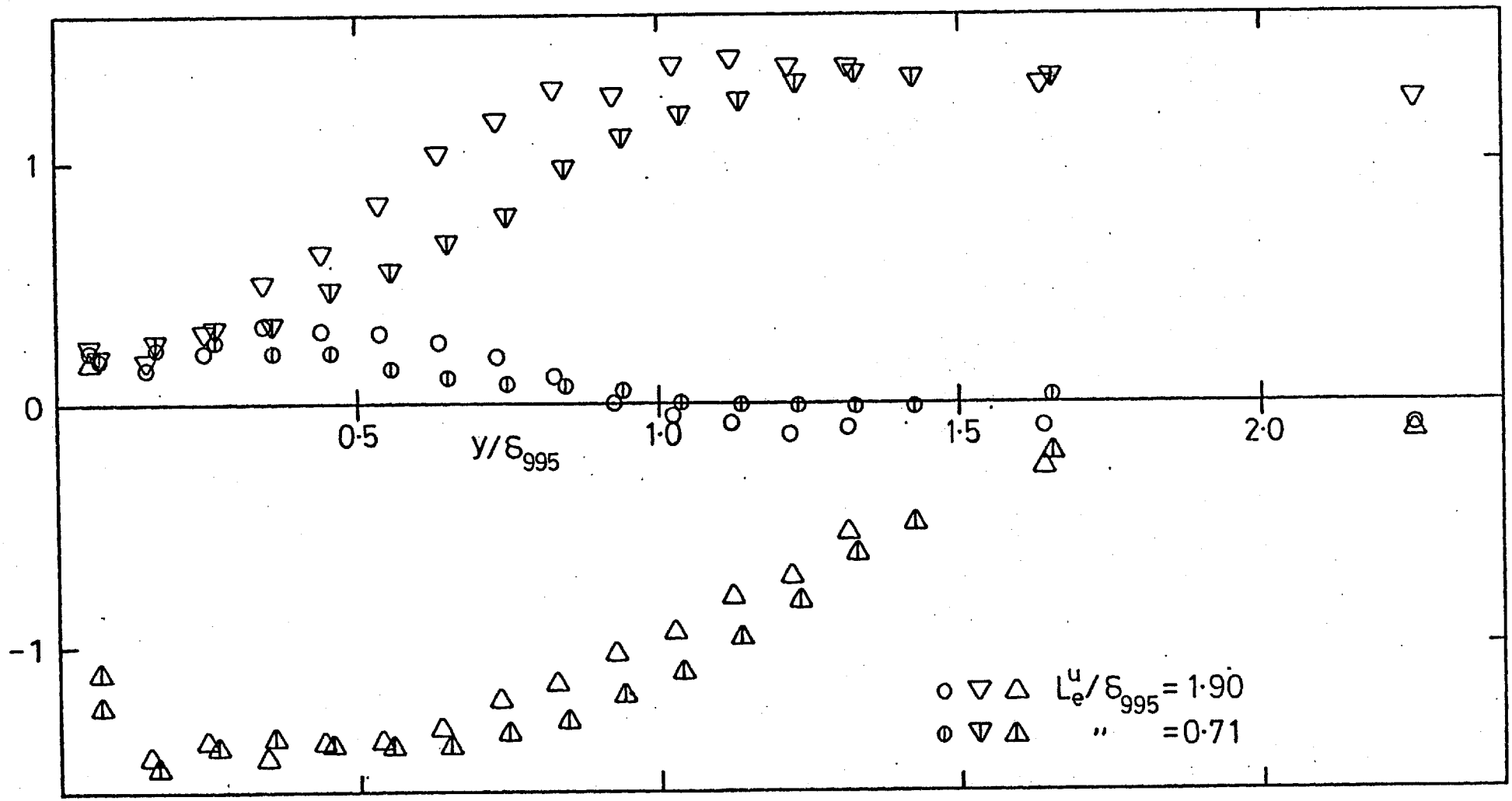

Fig. 4.34c, Skewness of v; $(u'/U)_e \approx 0.040$. Symbols as in a).

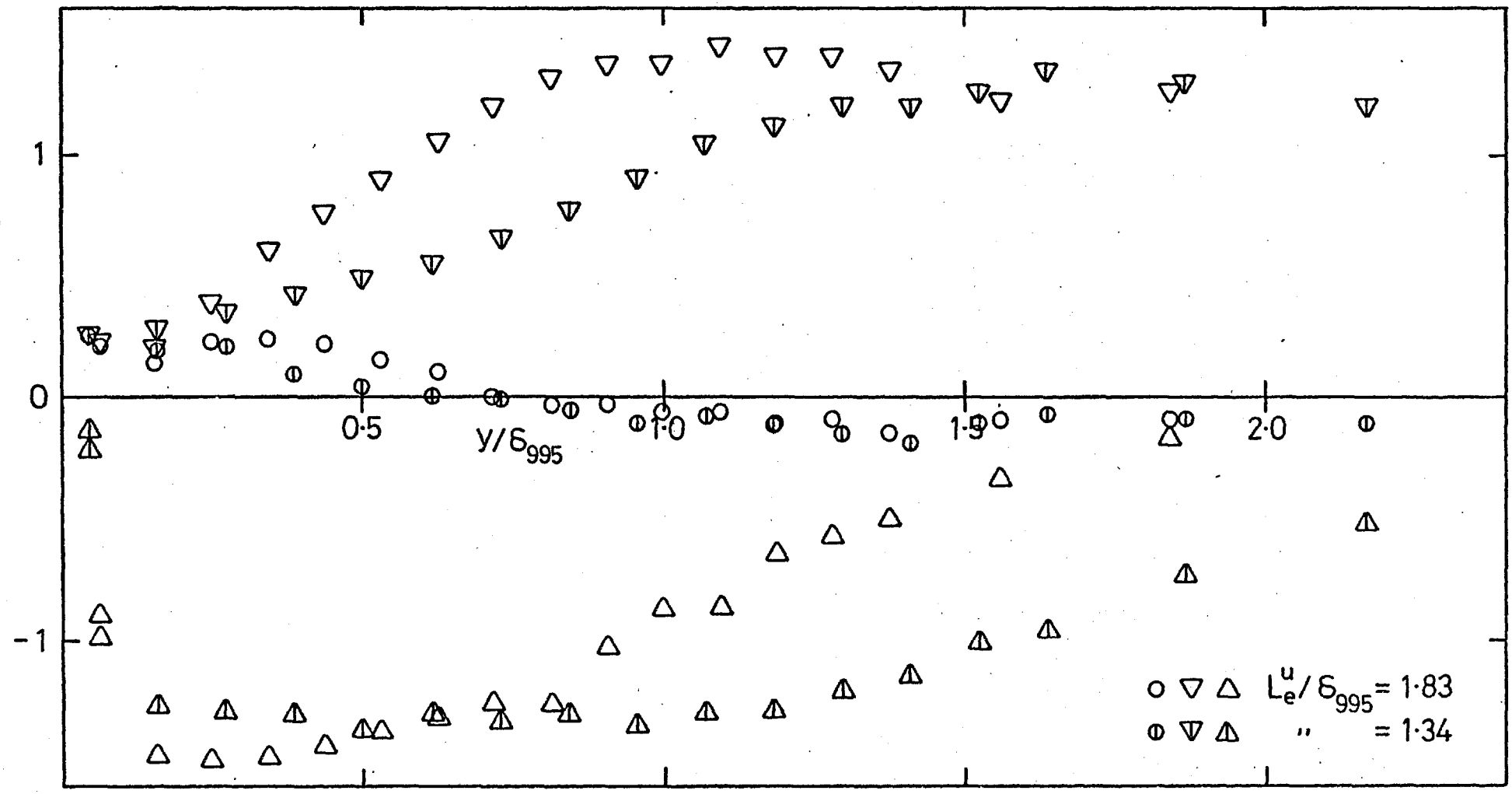

Fig. 4.34d, Skewness of v; $(u'/U)_e$ = 0.0575. Symbols as in a).

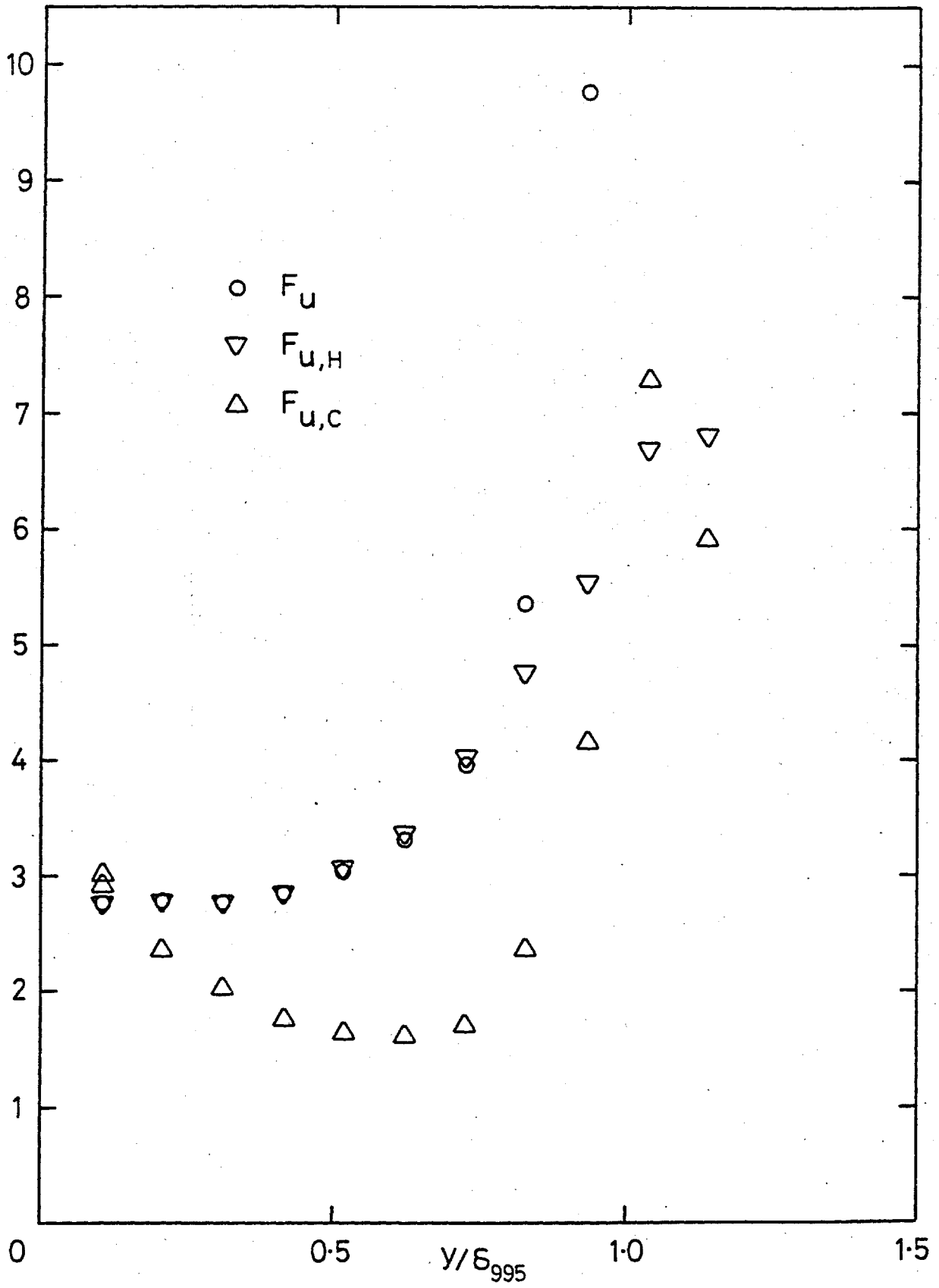

a) No grid, stn 14.

Fig. 4.35 Flatness of u.

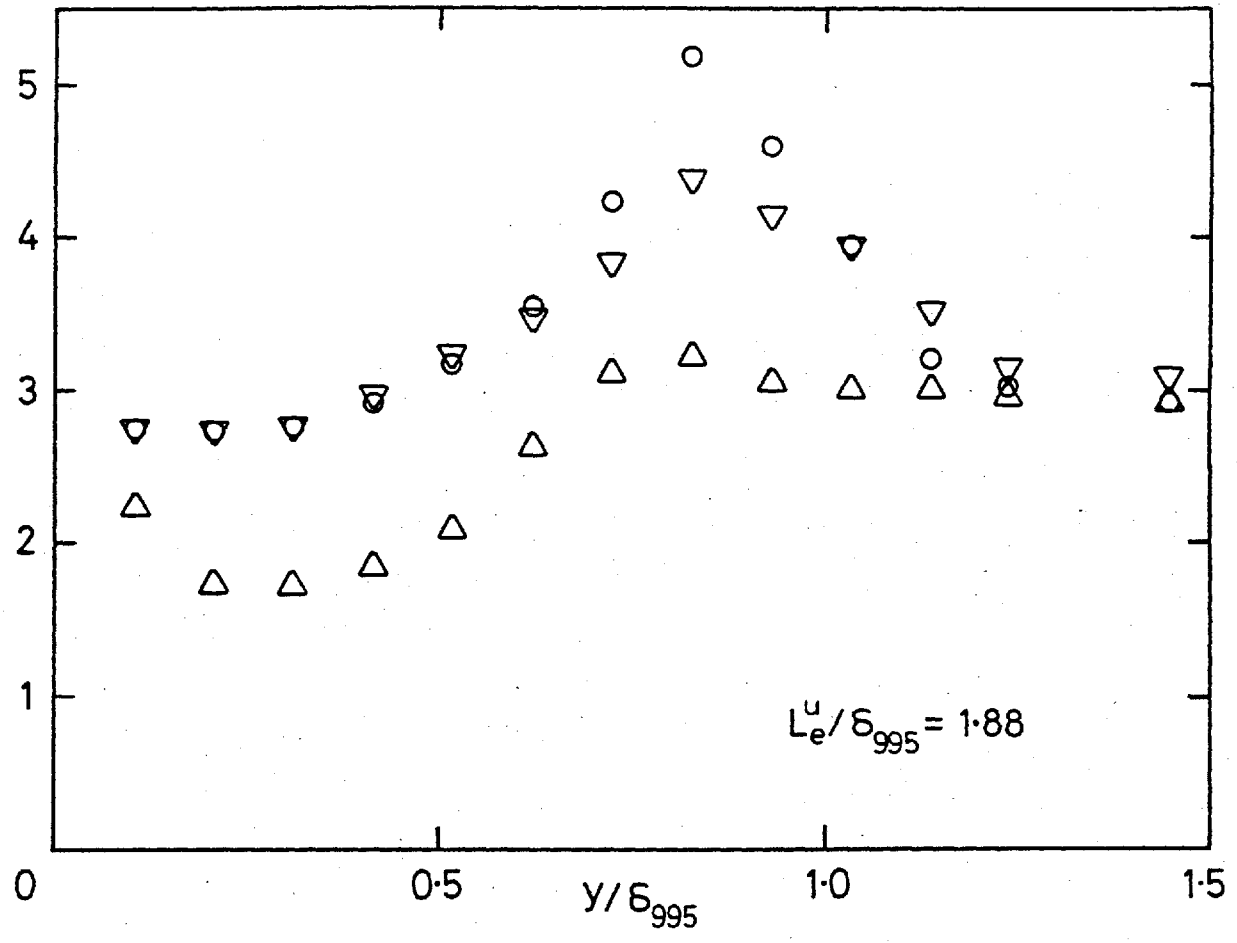

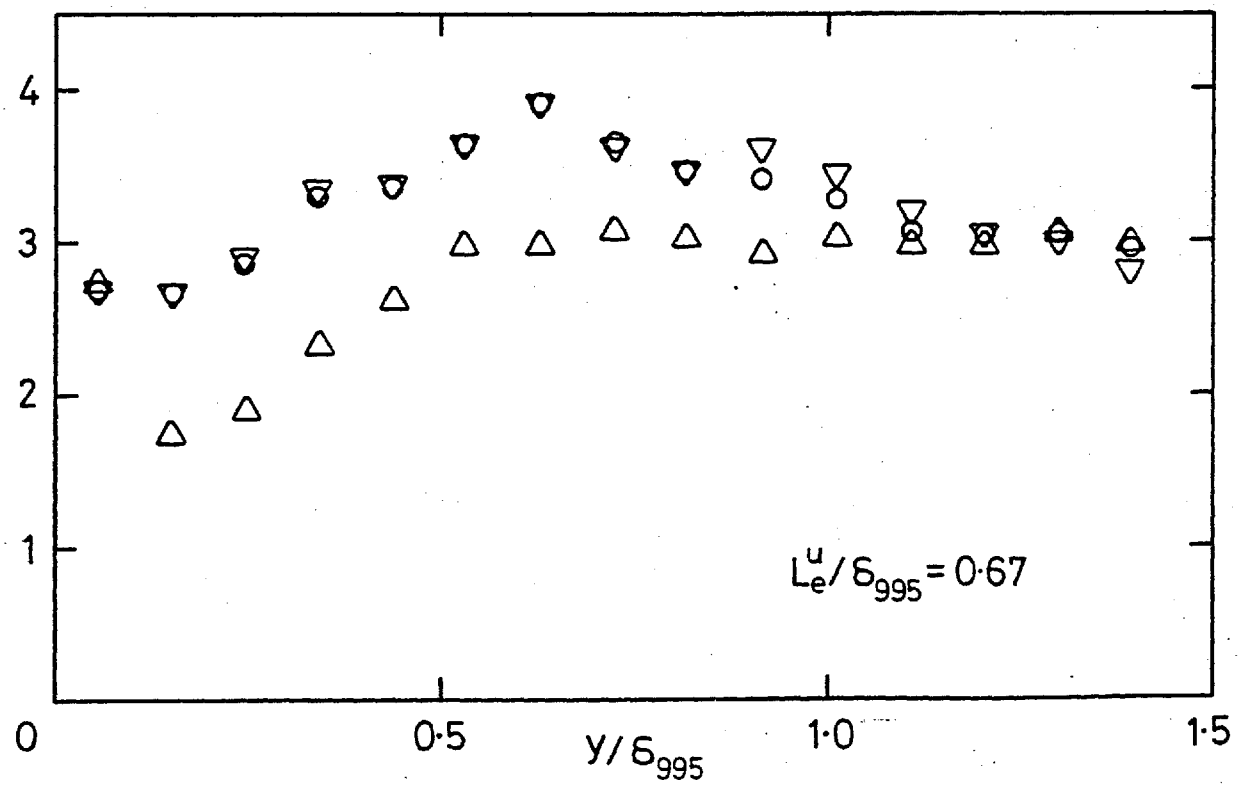

Fig. 4.35b, Flatness of u; $(u'/U)_e \approx 0.025$. Symbols as in a).

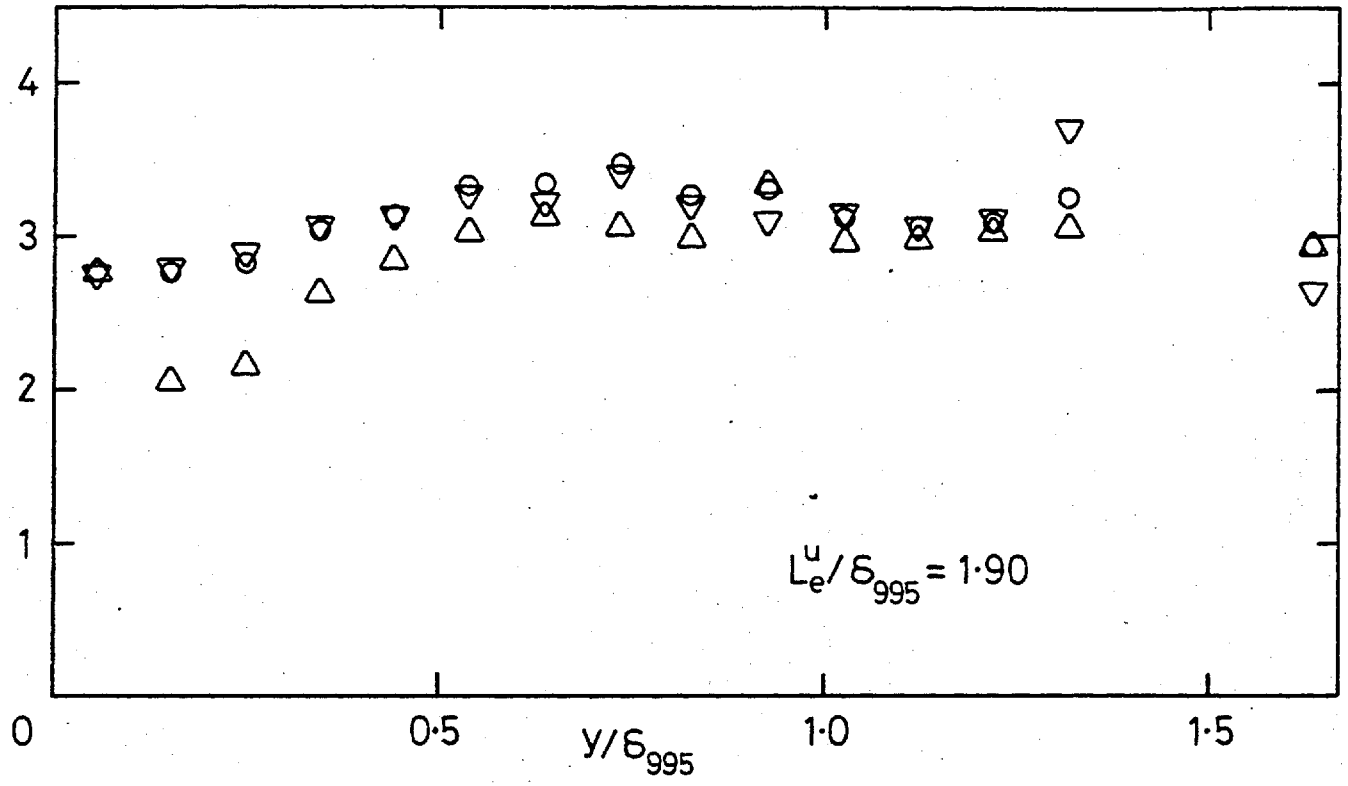

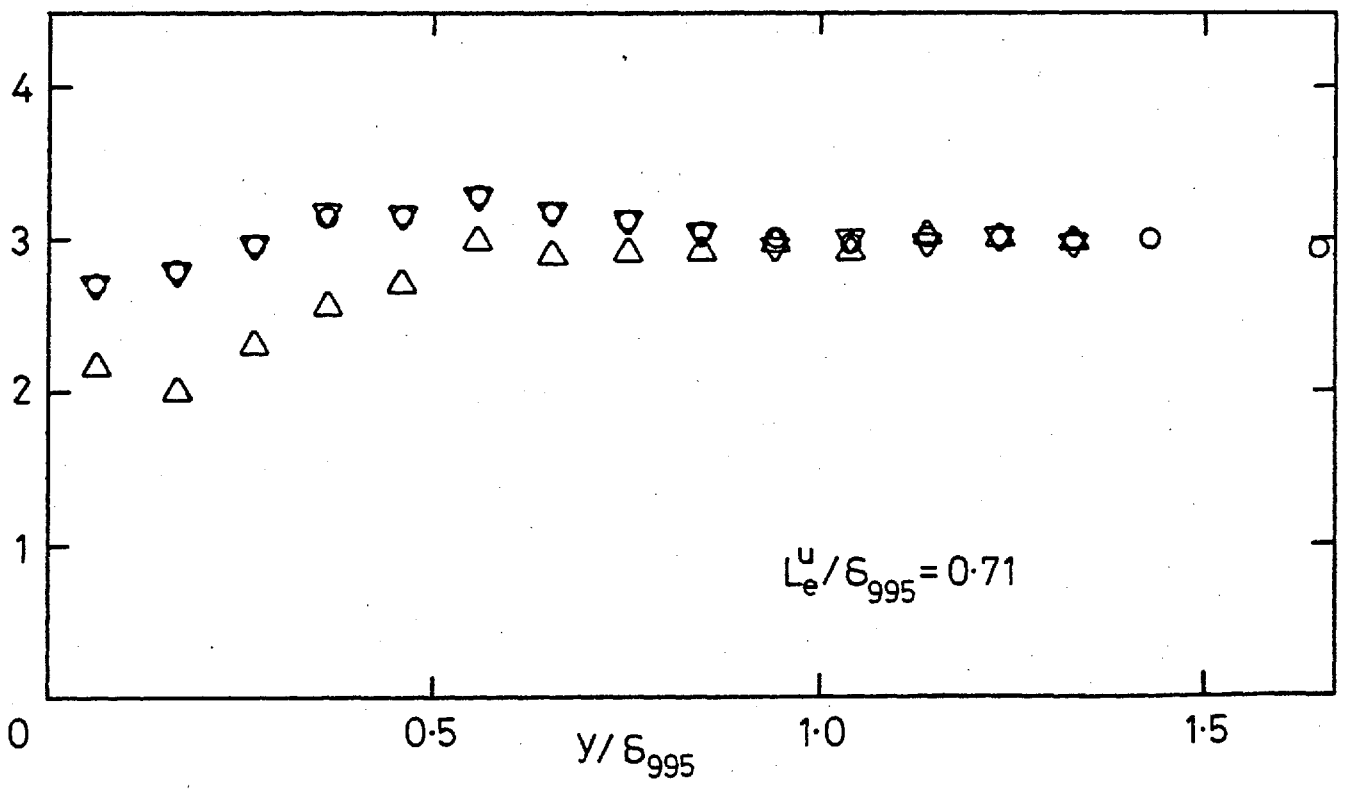

Fig. 4.35c, Flatness of u; $(u'/U)_e \approx 0.040$. Symbols as in a).

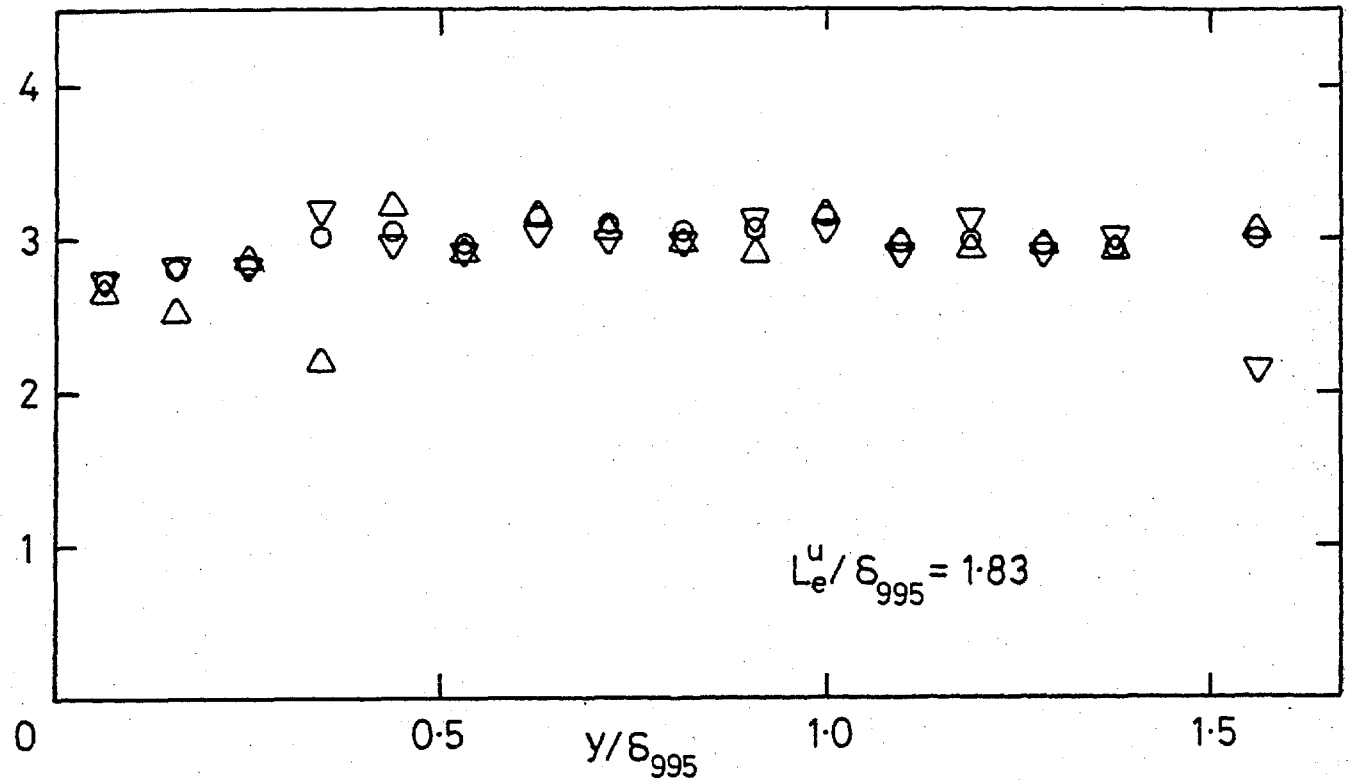

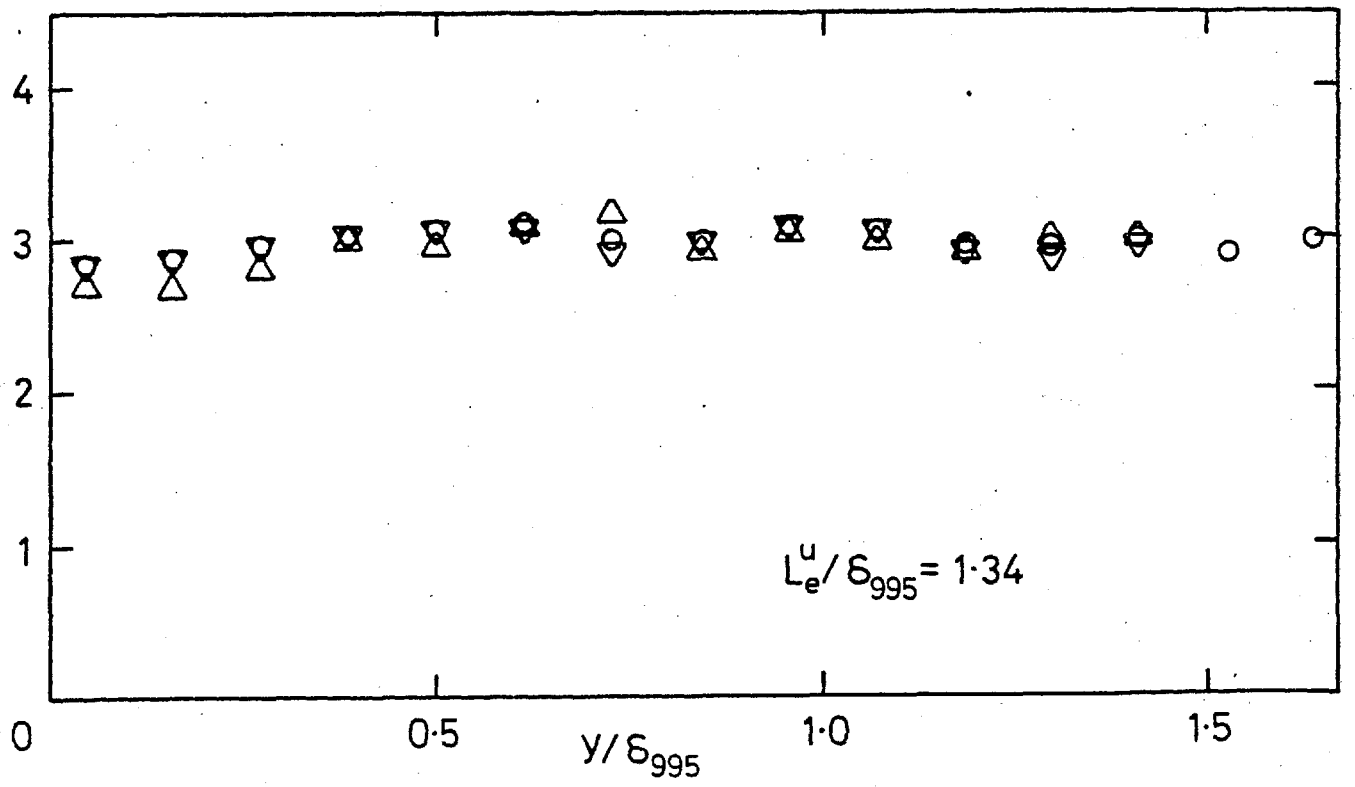

Fig. 4.35d, Flatness of u; $(u'/U)_e = 0.0575$. Symbols as in a).

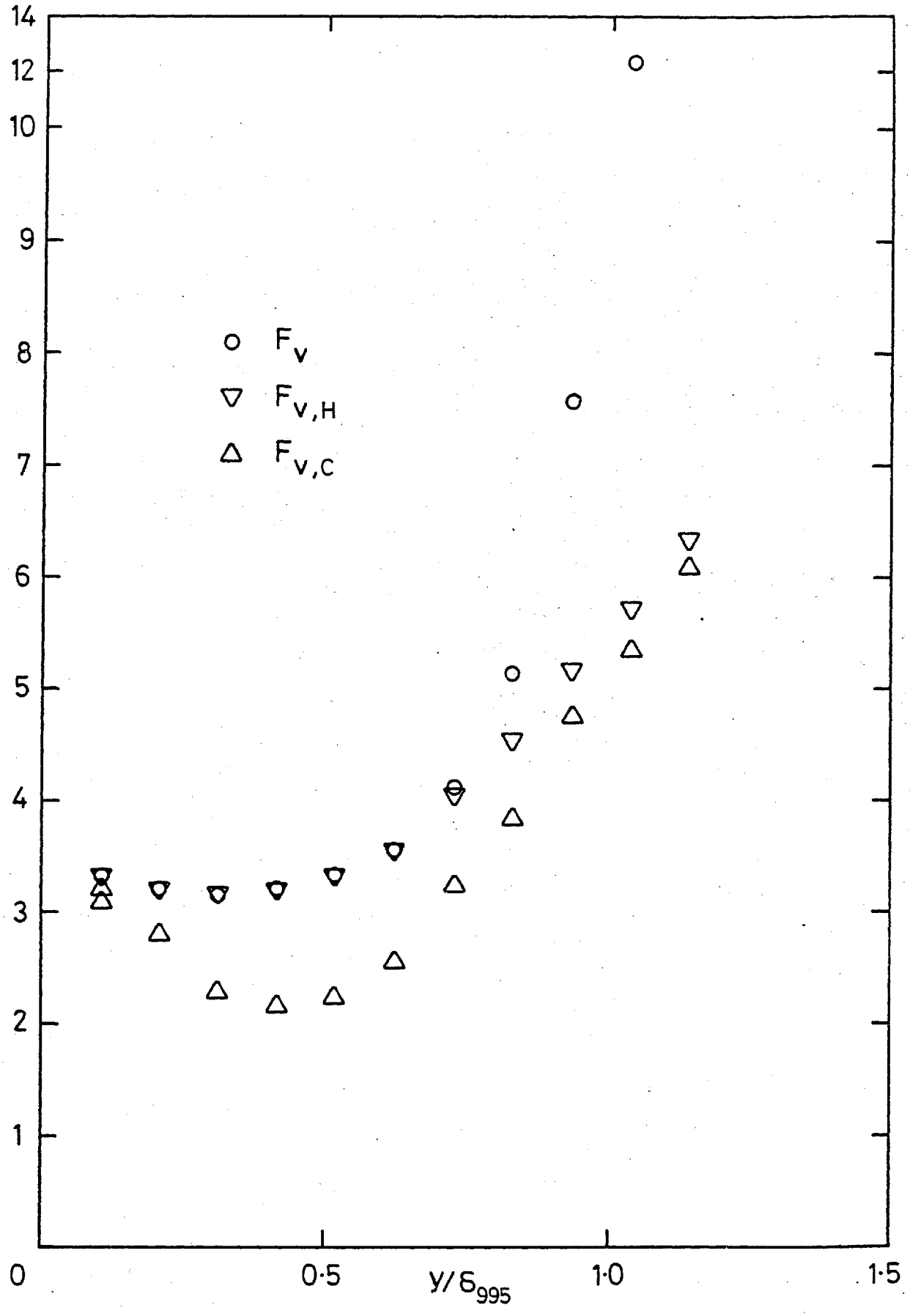

a) No grid, stn 14.

Fig. 4.36 Flatness of v.

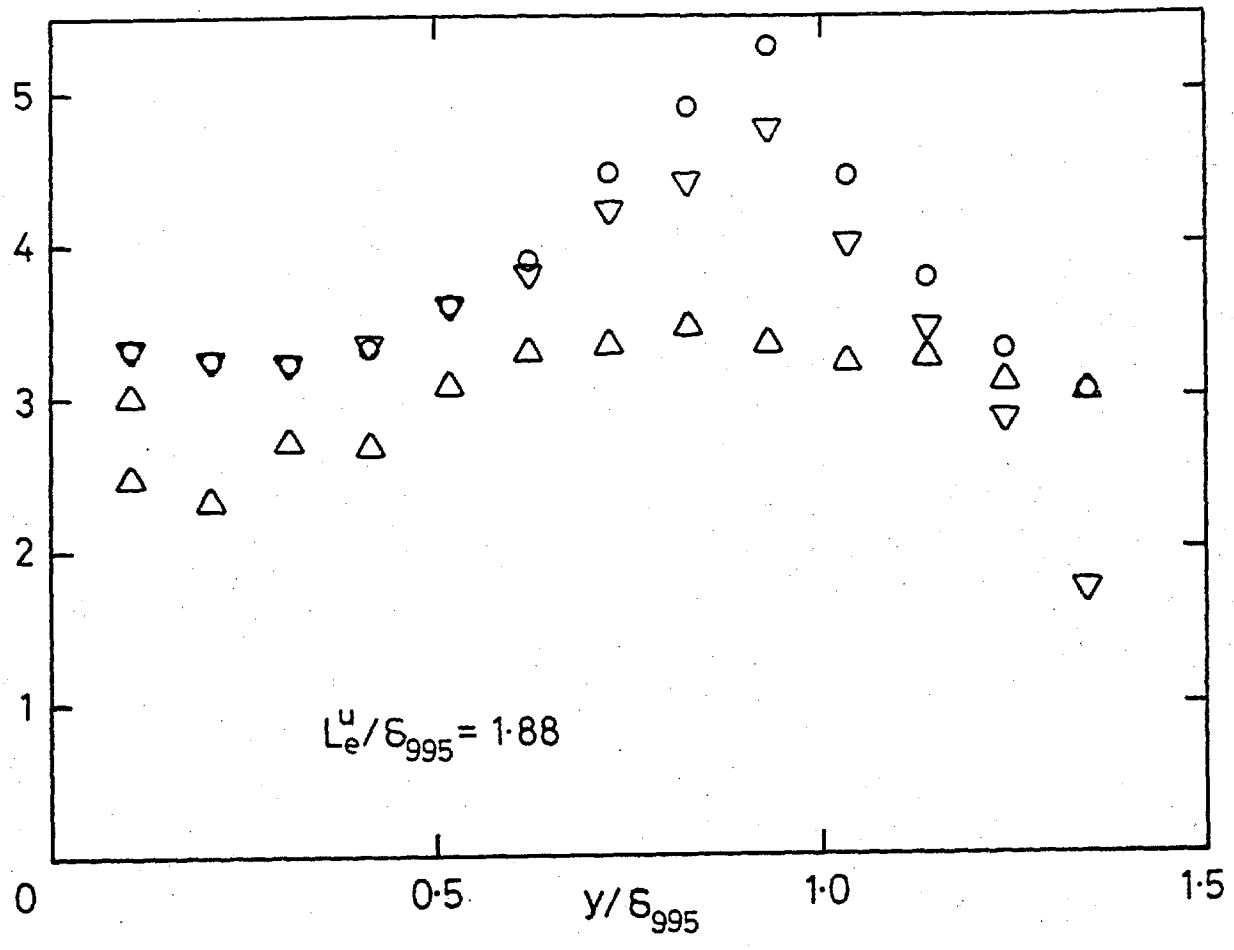

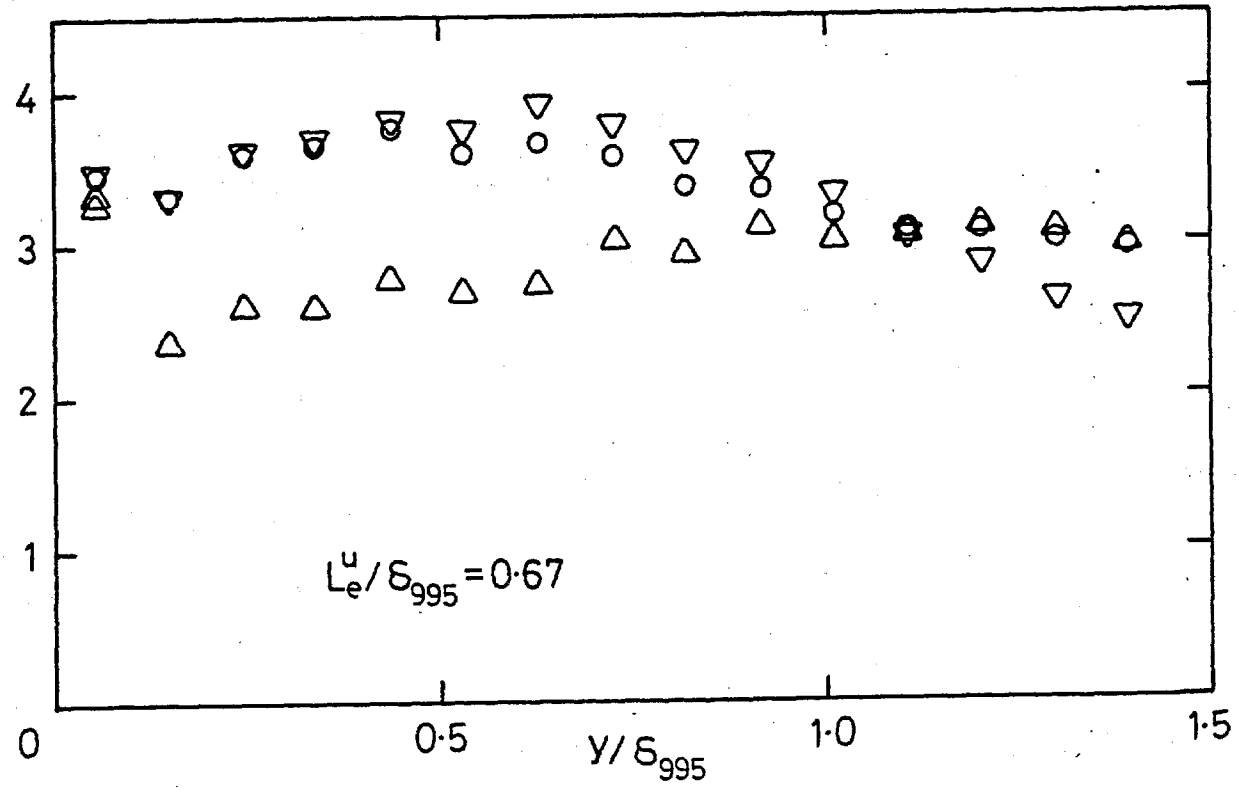

Fig. 4.36b, Flatness of v; $(u'/U)_e \approx 0.025$. Symbols as in a).

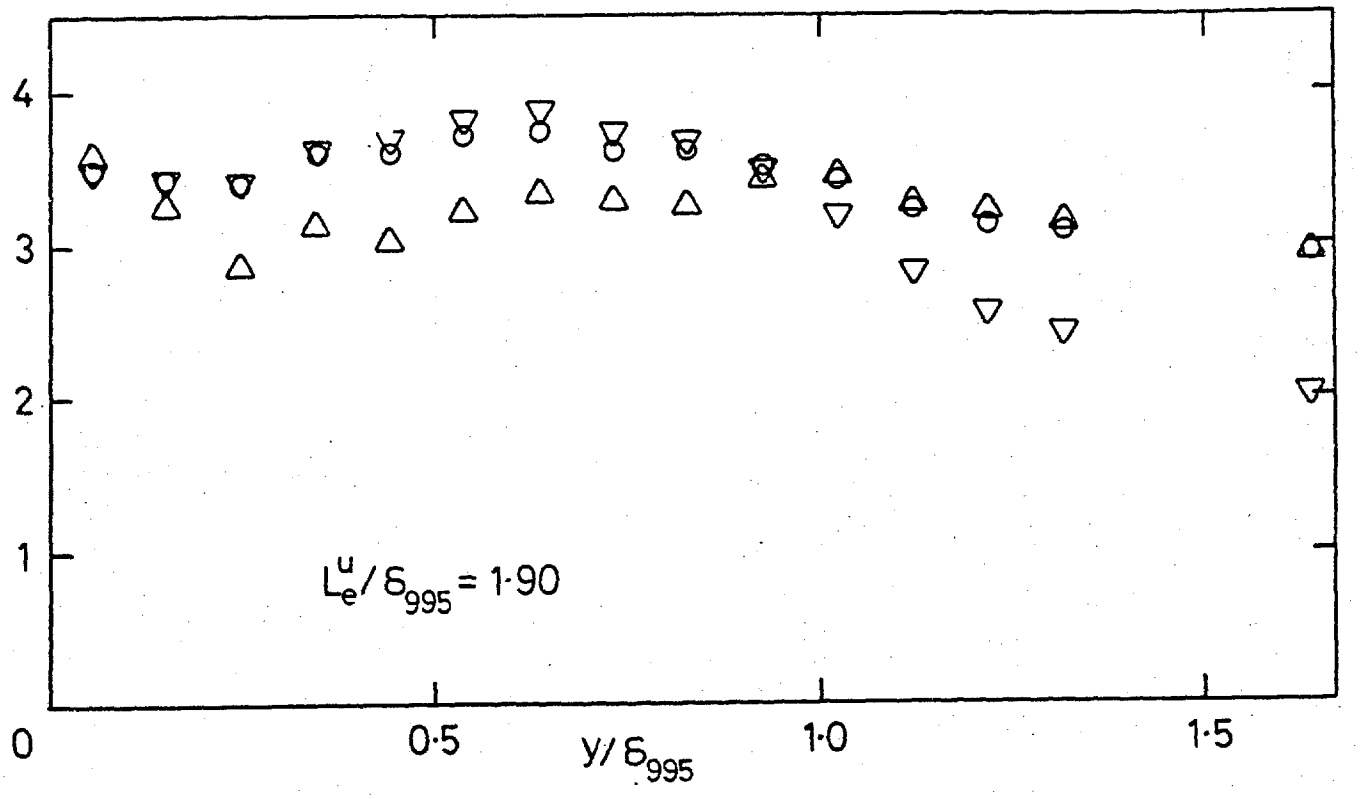

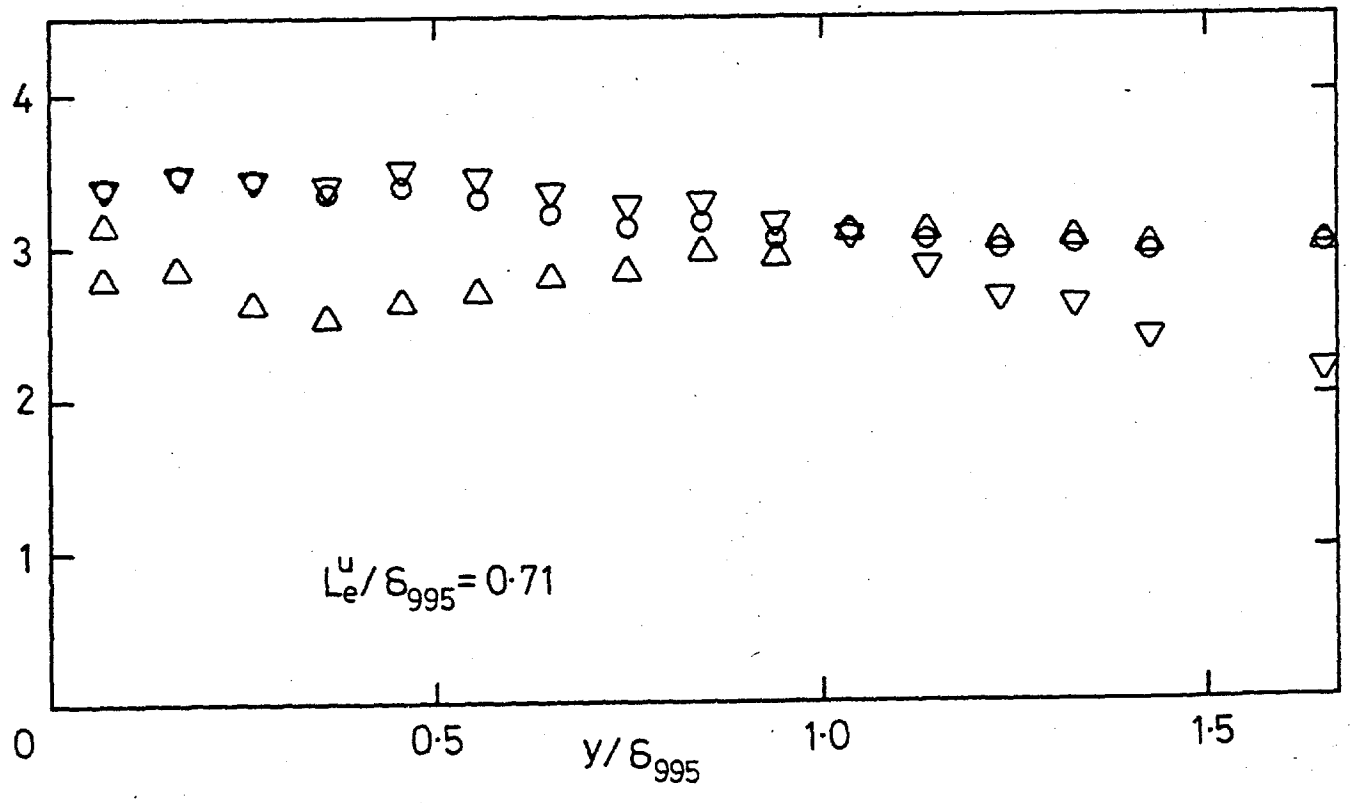

Fig. 4.36c, Flatness of v; $(u'/U)_e \approx 0.040$. Symbols as in a).

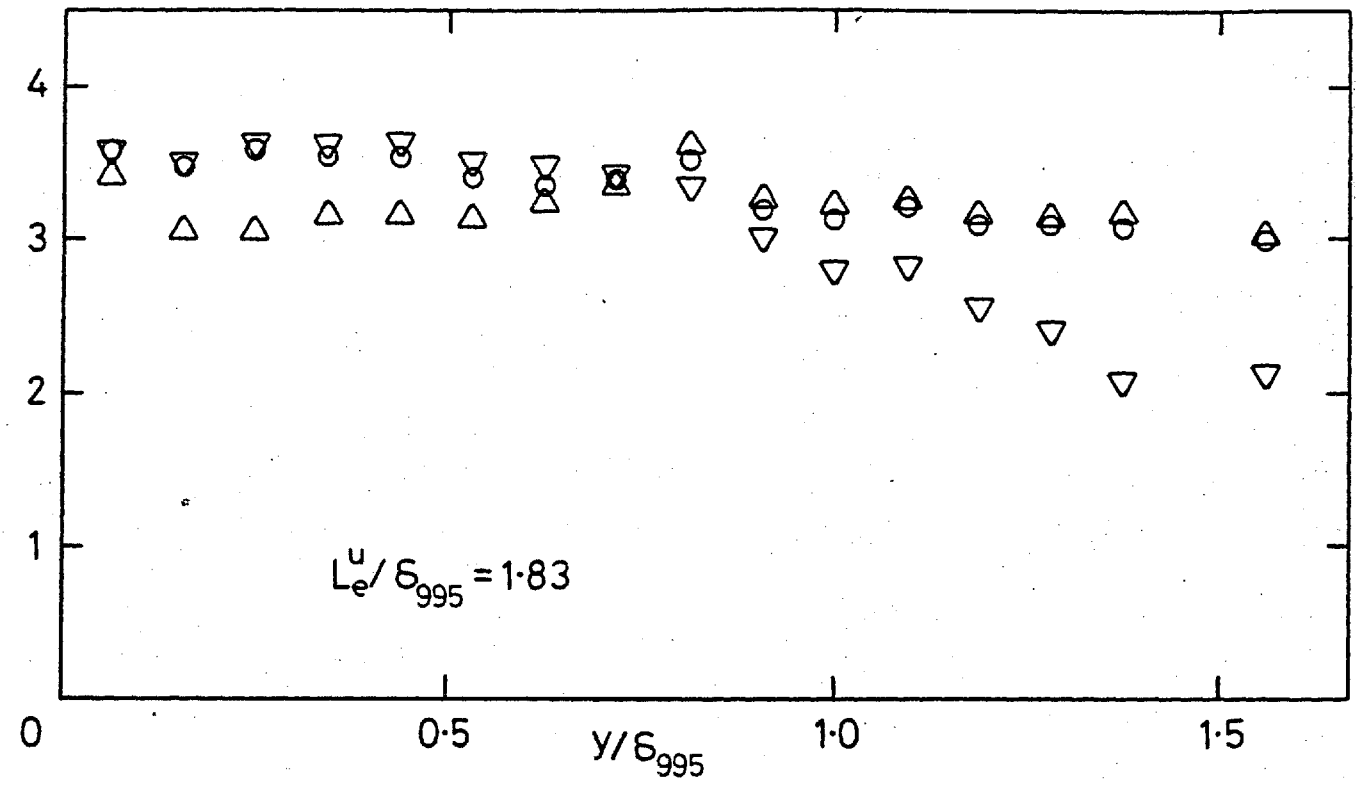

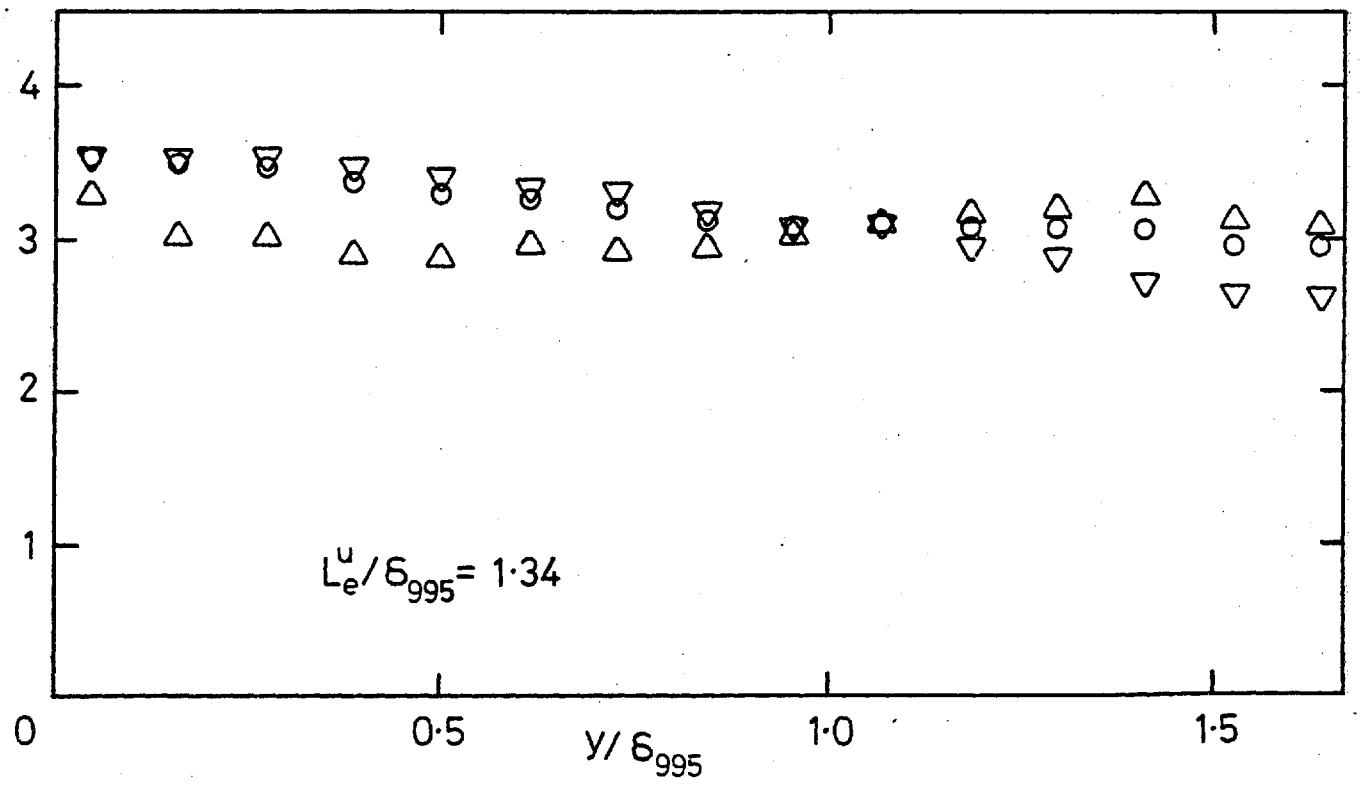

Fig. 4.36d, Flatness of v; $(u'/U)_e$ = 0.0575. Symbols as in a).

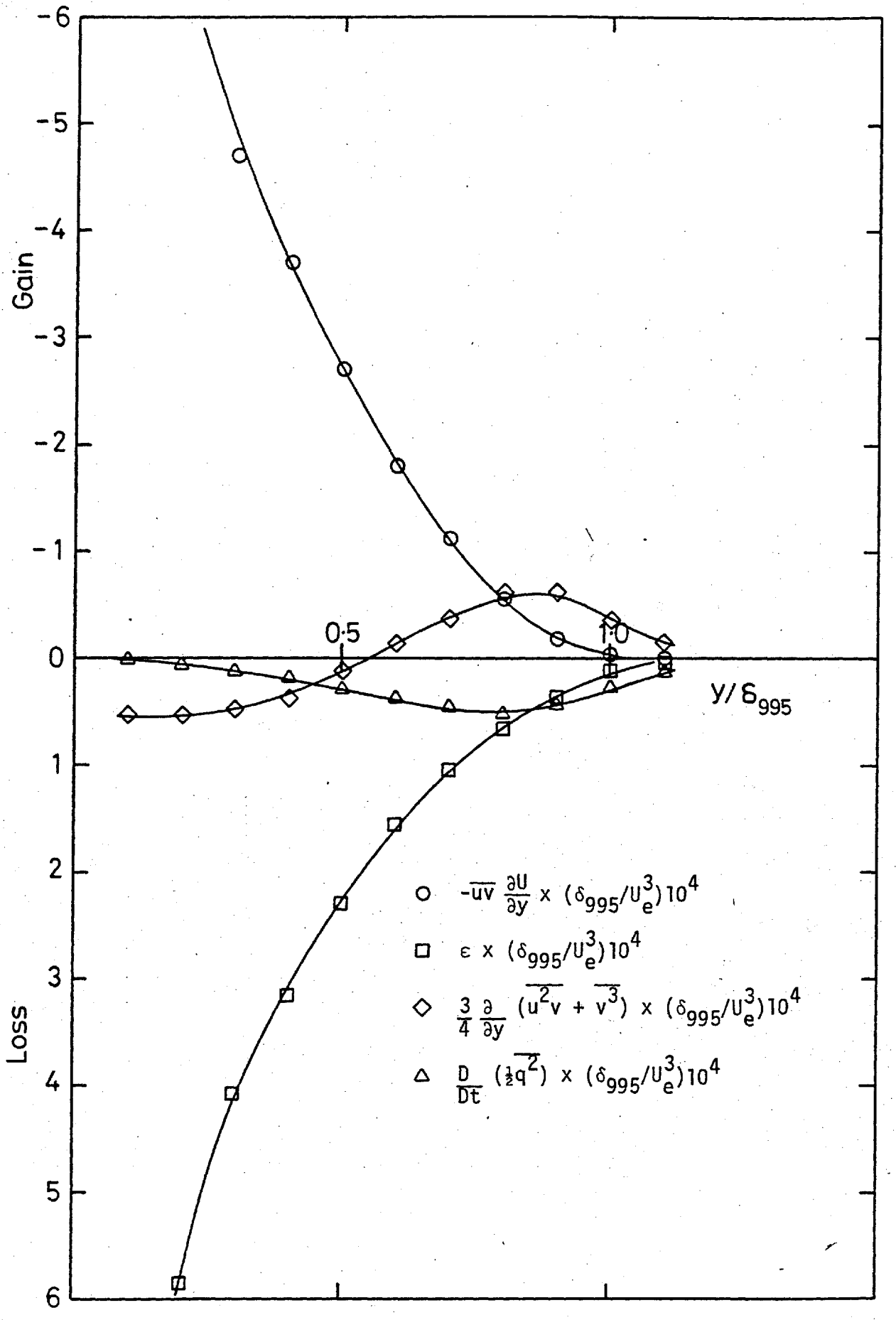

a) No grid, stn 14.

Fig. 4.37 Balances of the turbulent kinetic energy transport equation.

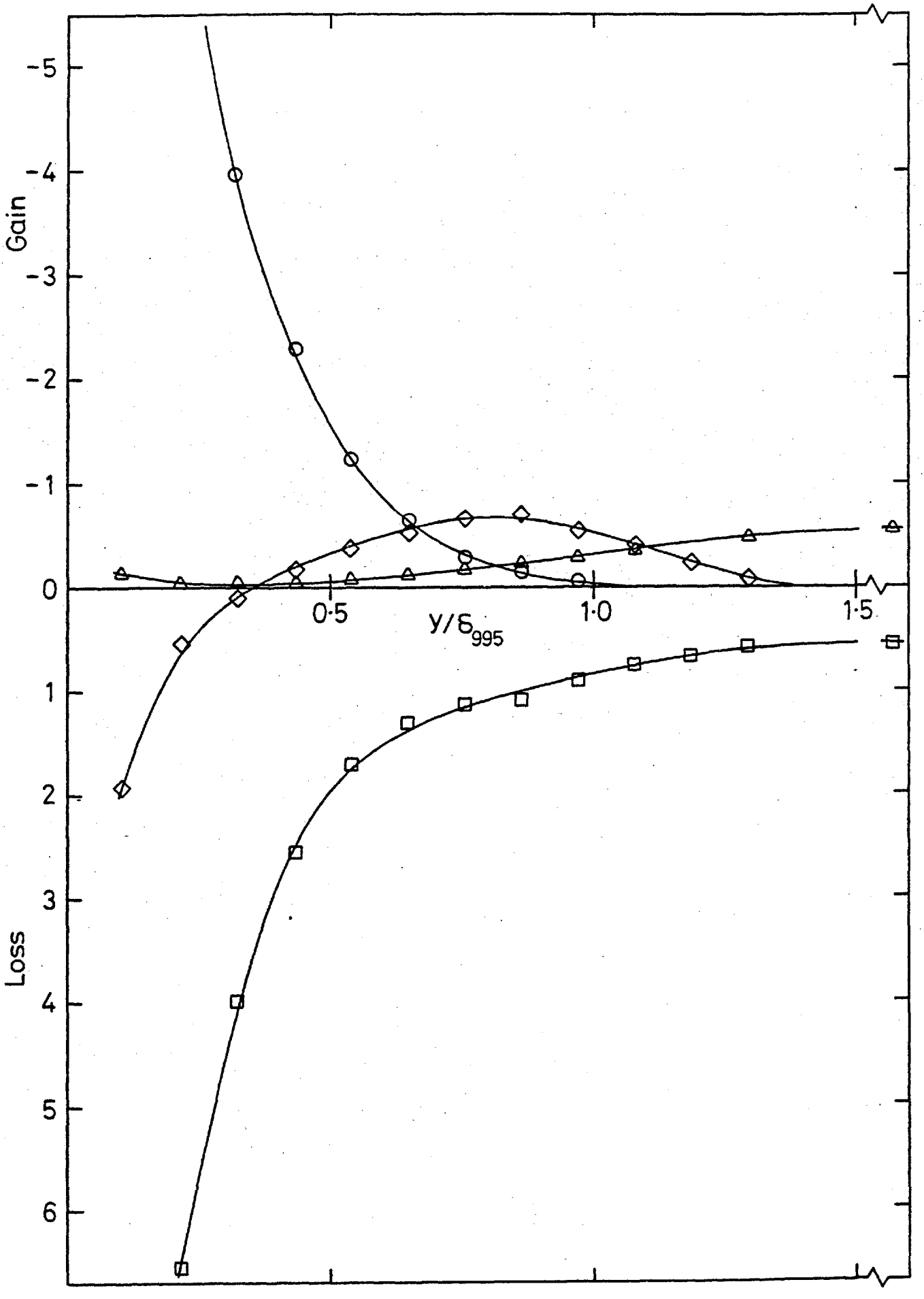

Fig. 4.37b, 15.2 cm grid, X_{LE} = 2.06 m, stn 8. Symbols as in a).

$(u'/U)_e$ = 0.0442, L^u_e/δ_{995} = 2.23.

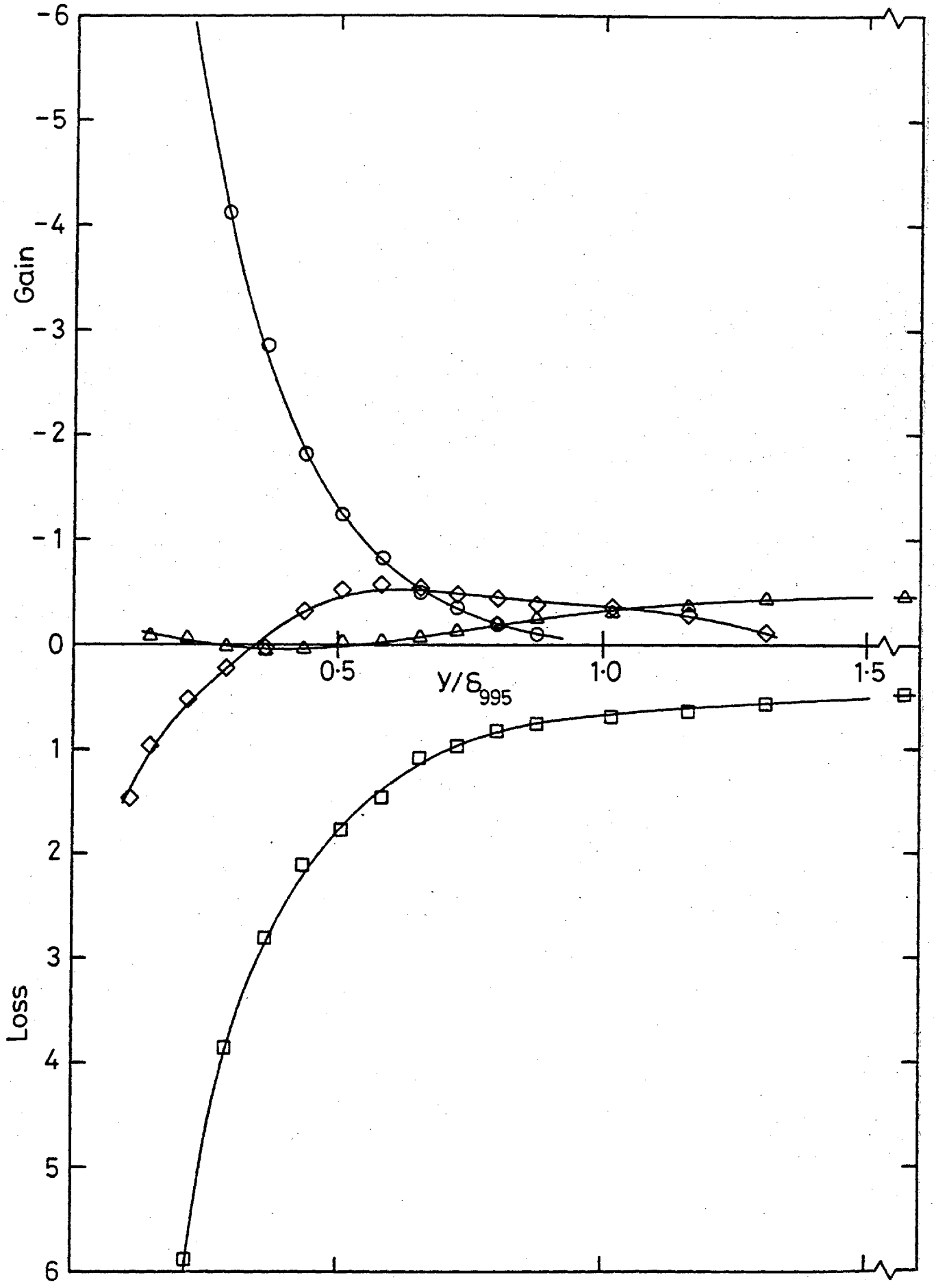

Fig. 4.37c, 15.2 cm grid, X_{LE} = 2.06 m, stn 14. Symbols as in a).
$(u'/U)_e$ = 0.0362, L^u_e/δ_{995} = 1.69.

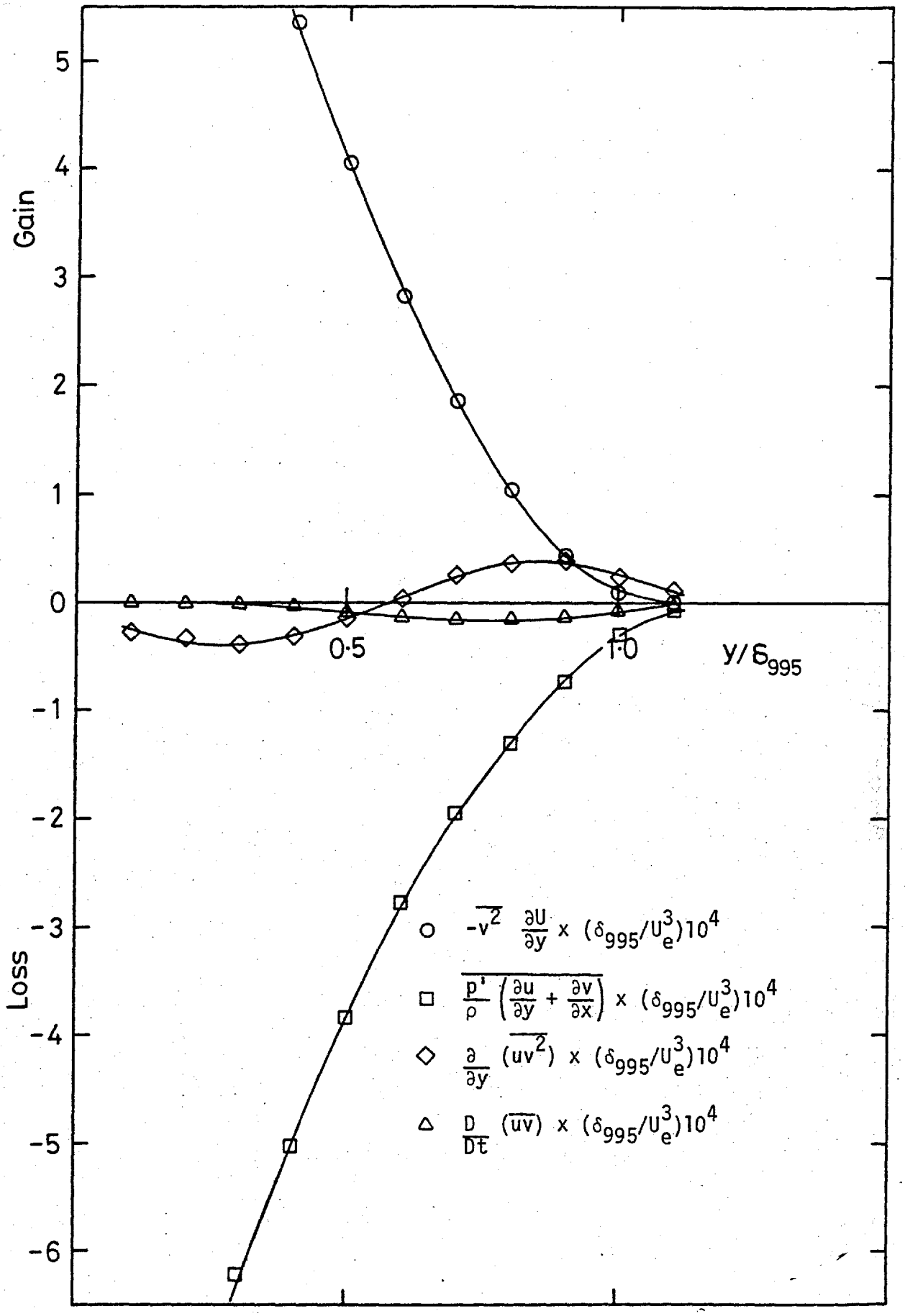

a) No grid, stn 14.

Fig. 4.38 Balances of the turbulent shear stress transport equation.

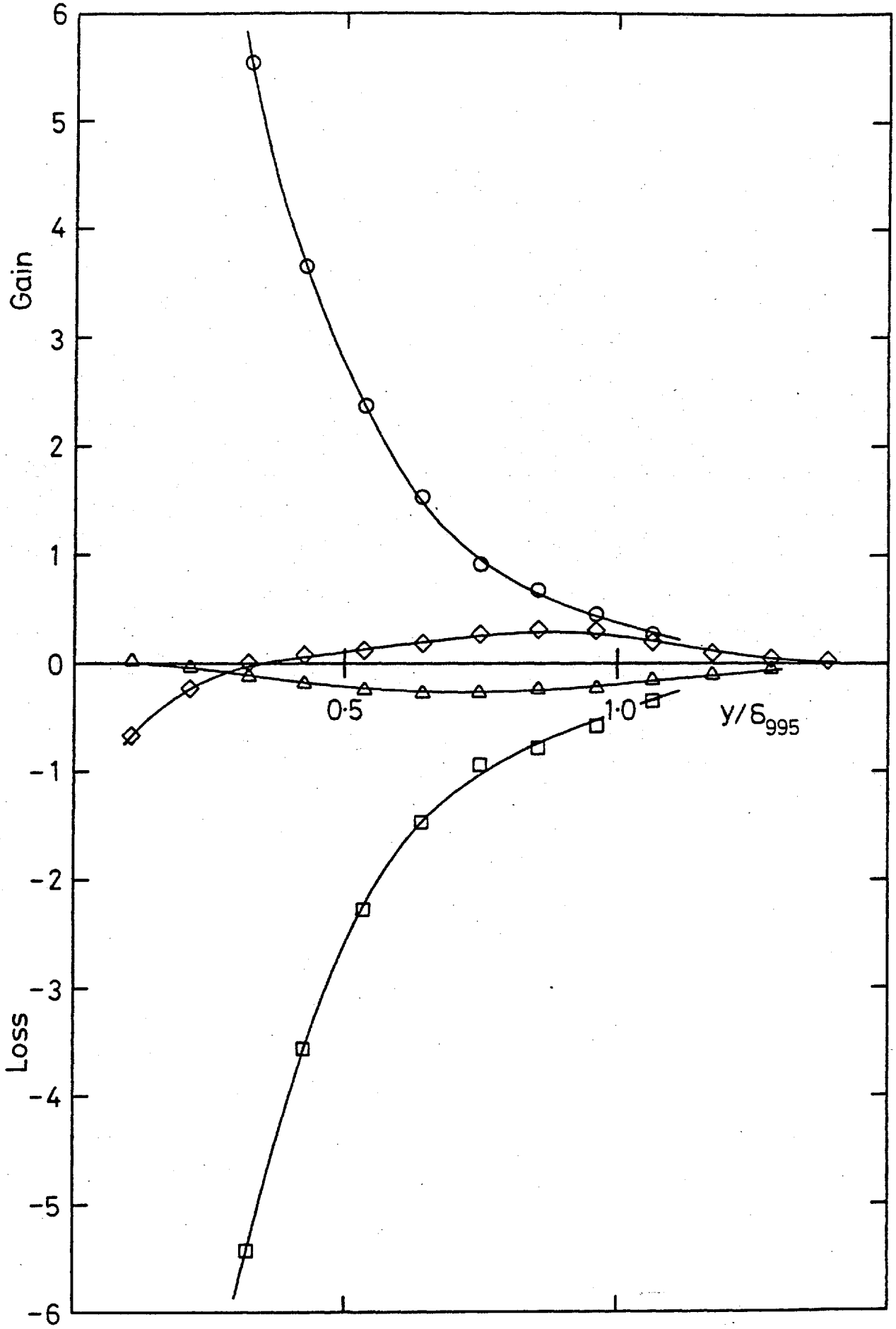

Fig. 4.38b, 15.2 cm grid, X_{LE} = 2.06 m, stn 8. Symbols as in a).
$(u'/U)_e$ = 0.0442, L^u_e/δ_{995} = 2.23.

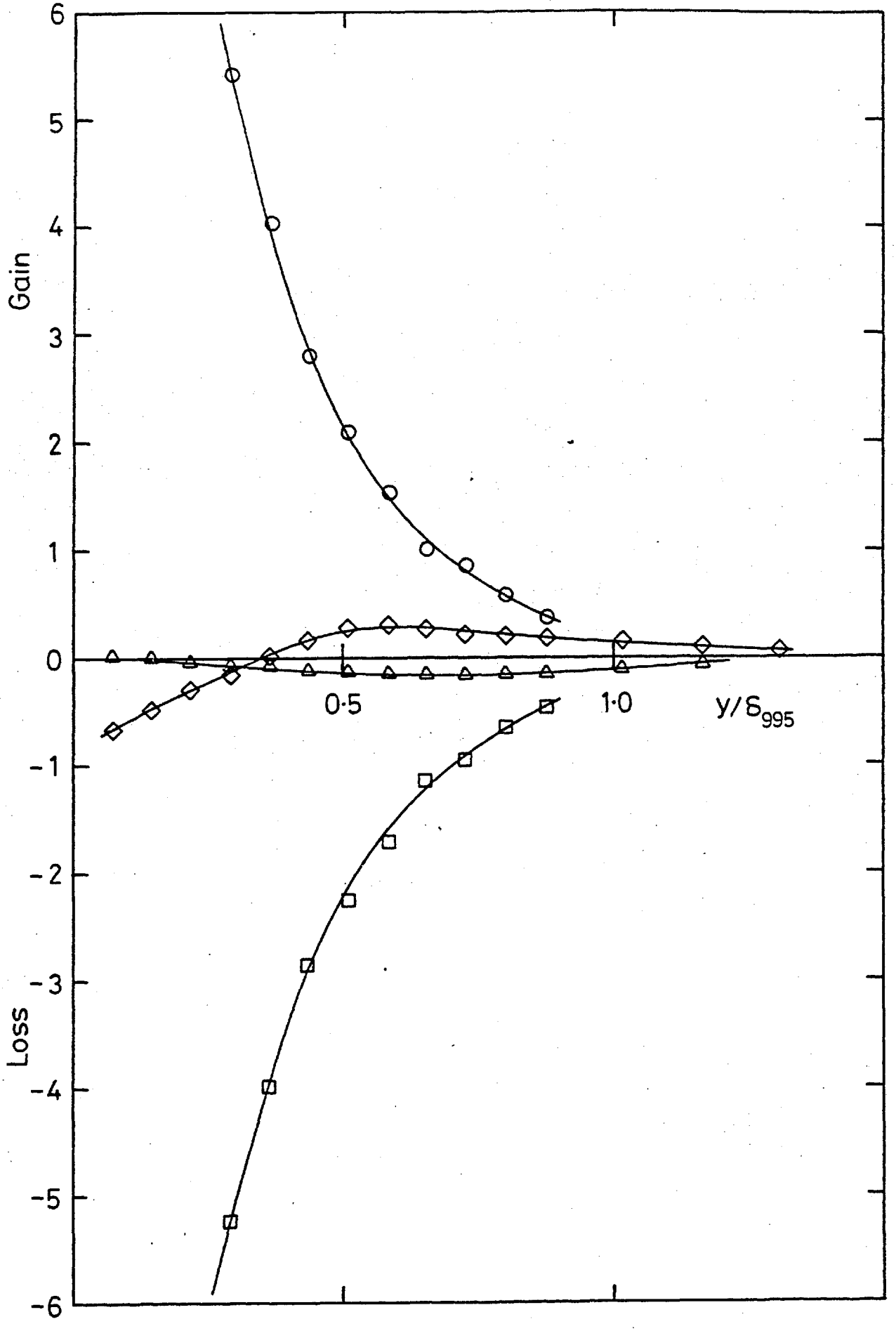

Fig. 4.38c, 15.2 cm grid, X_{LE} = 2.06 m, stn 14. Symbols as in a).
$(u'/U)_e$ = 0.0362, L^u_e/δ_{995} = 1.69.

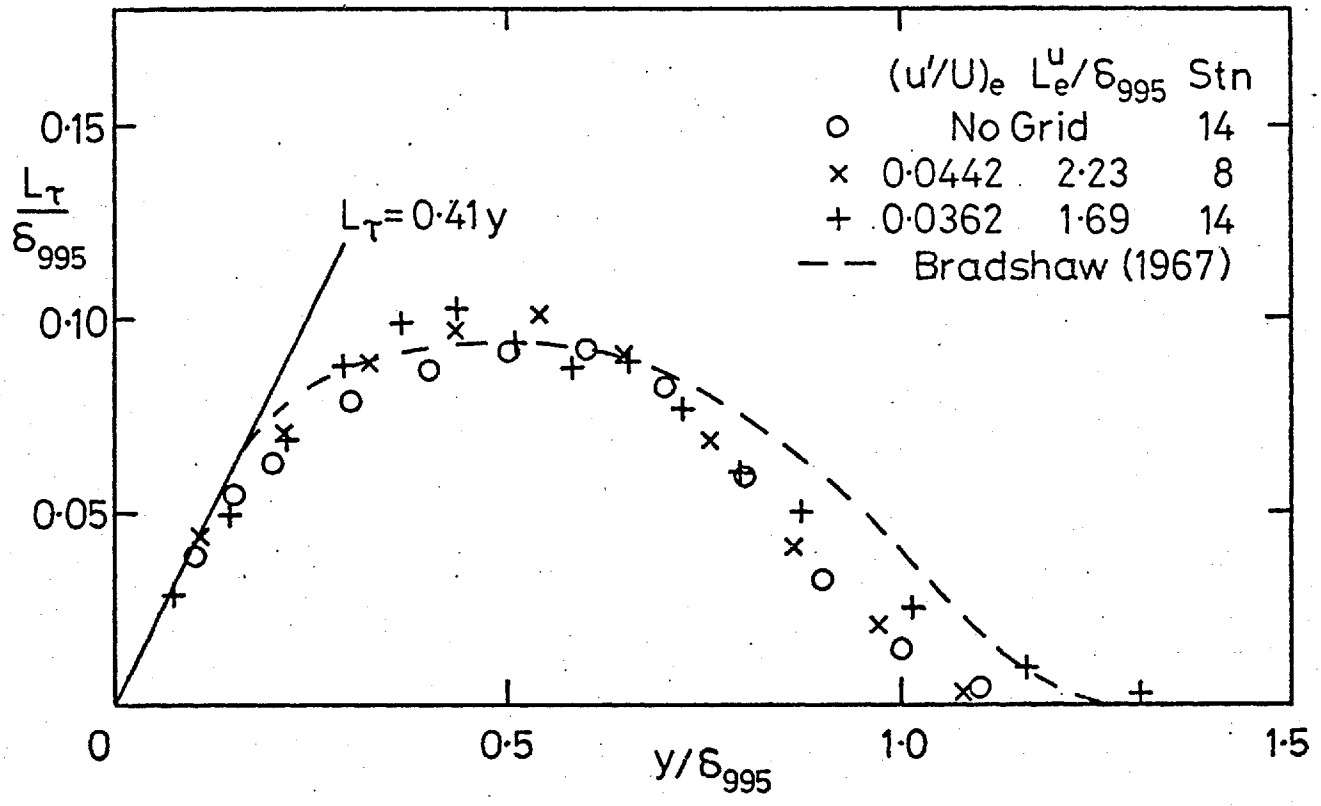

Fig. 4.39 Dissipation length scale $L_\tau \equiv (-\overline{uv})^{3/2}/\varepsilon$.

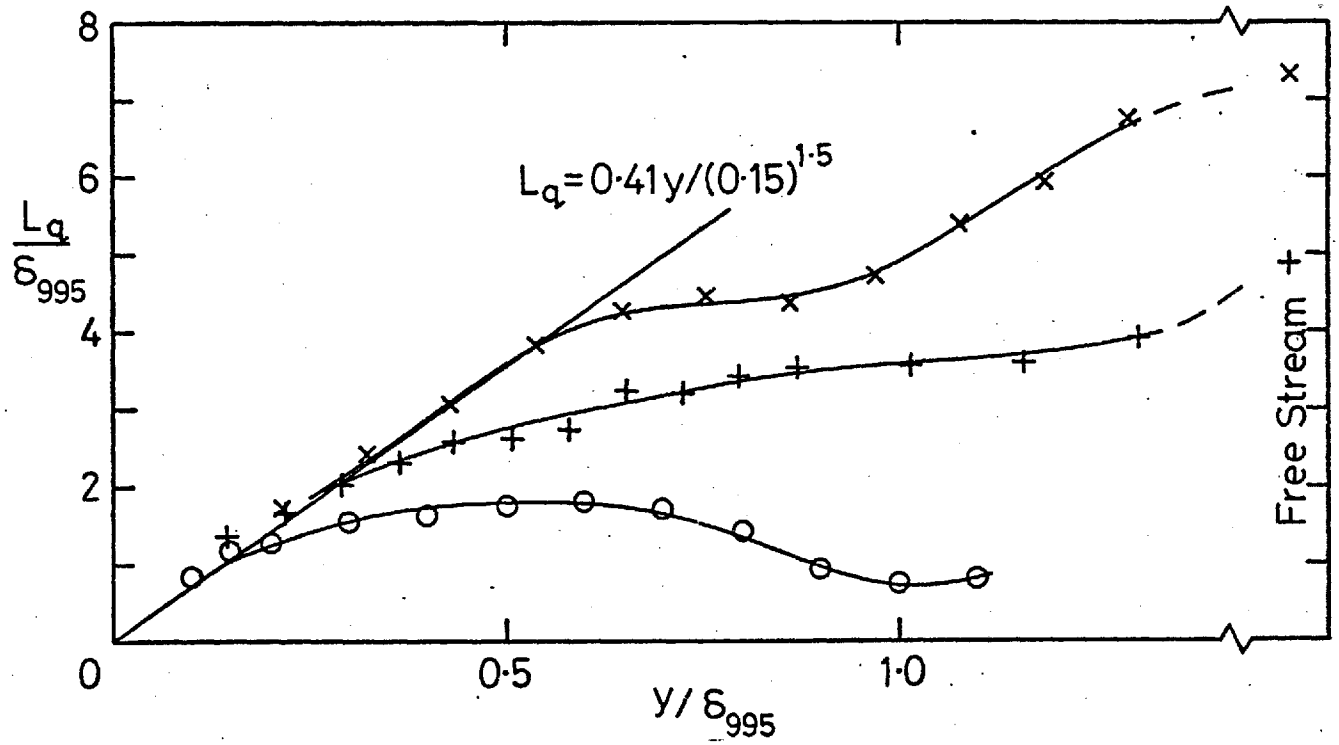

Fig. 4.40 Dissipation length scale $L_q \equiv (\overline{q^2})^{3/2}/\varepsilon$.

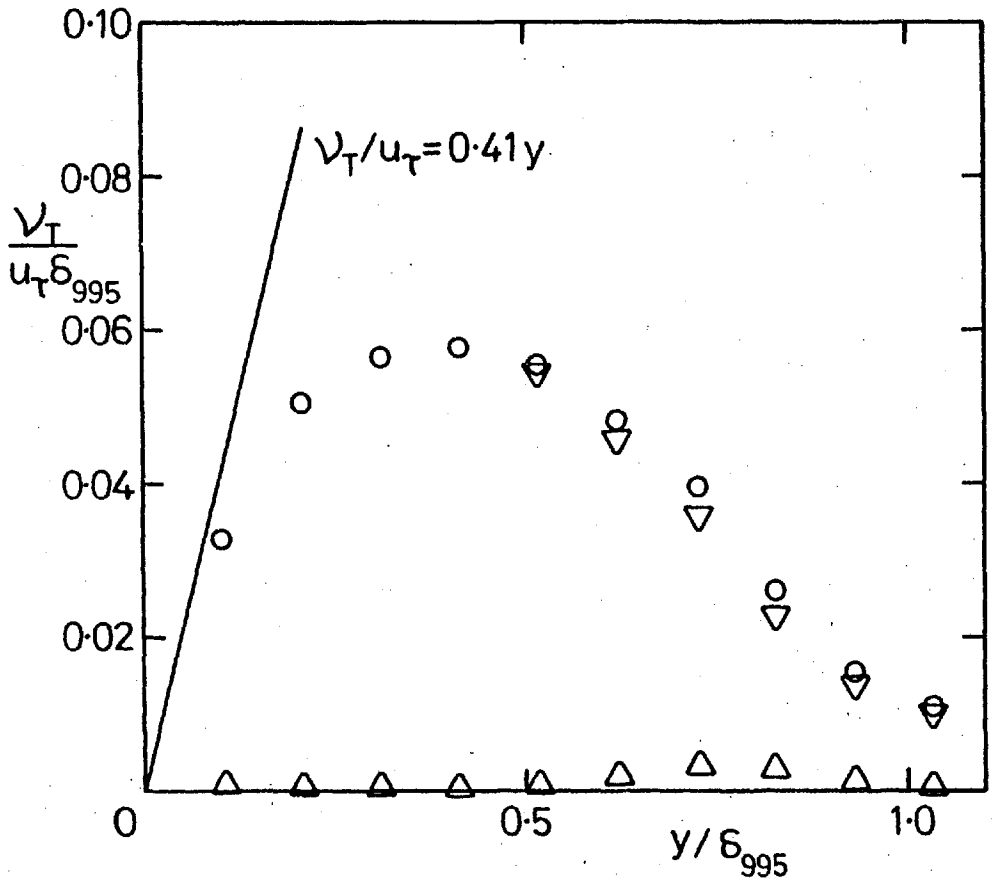

a) No grid (stn 14). $U_e\delta^*/(u_\tau\delta_{995}) = 3.96$.

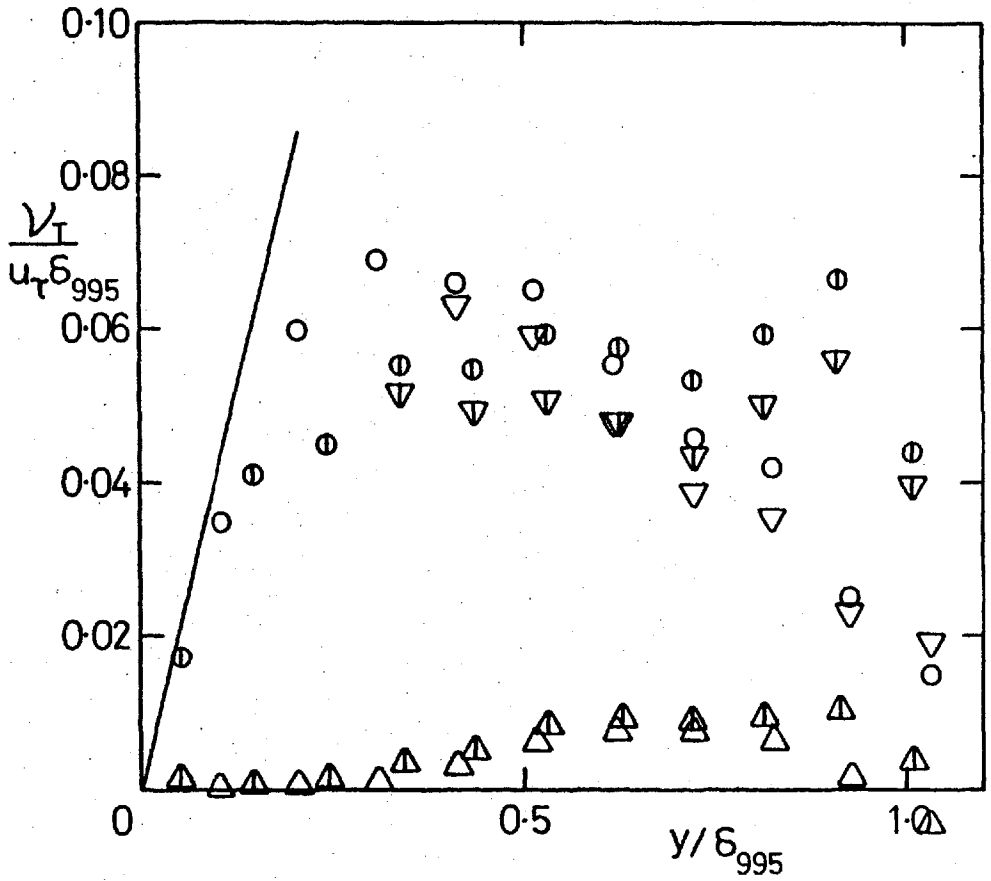

b) $(u'/U)_e \approx 0.025$. Unbarred, $L^u_e/\delta_{995} = 1.88$

Barred, $L^u_e/\delta_{995} = 0.67$

Fig. 4.41 Eddy viscosity.

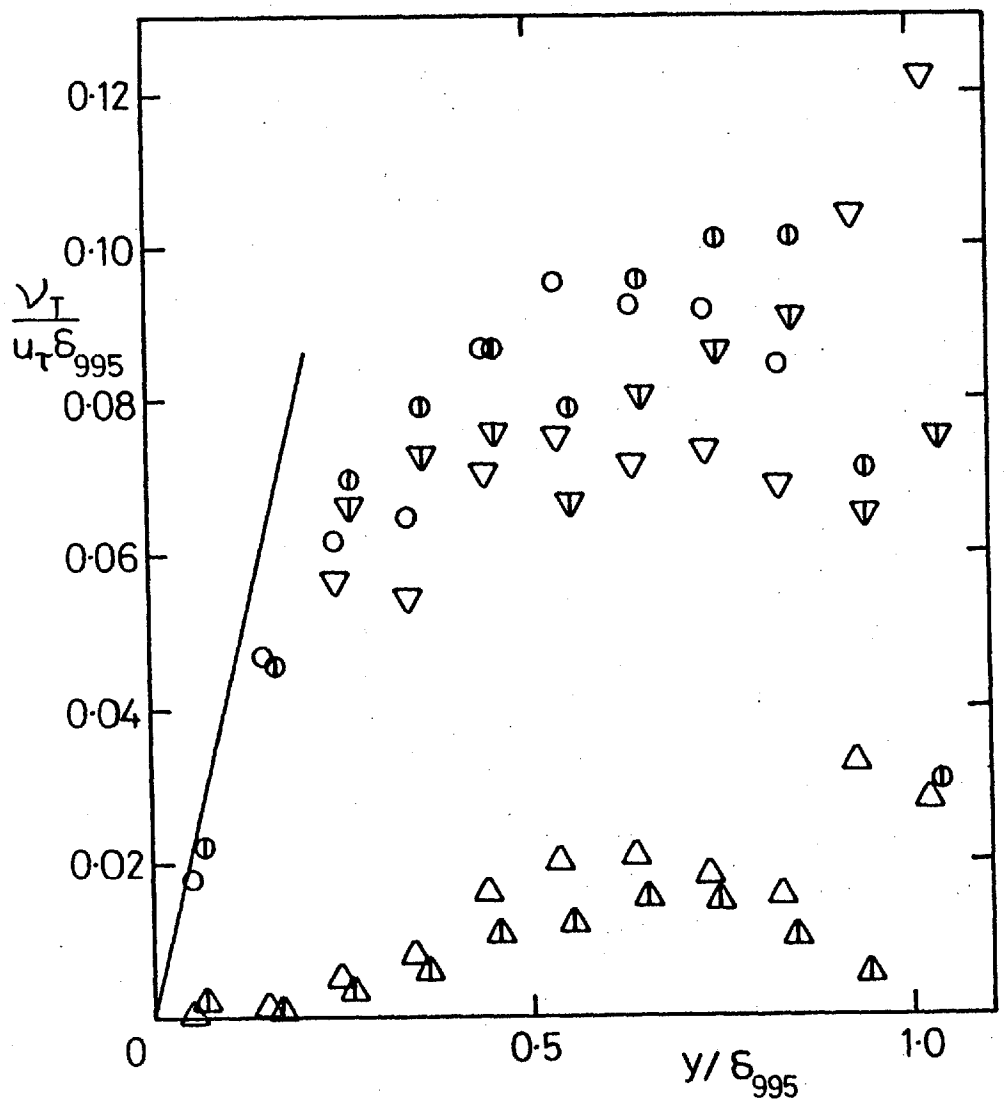

Fig. 4.41c, $(u'/U)_e \approx 0.040$. Unbarred, $L^u_e/\delta_{995} = 1.90$
Barred, $L^u_e/\delta_{995} = 0.71$

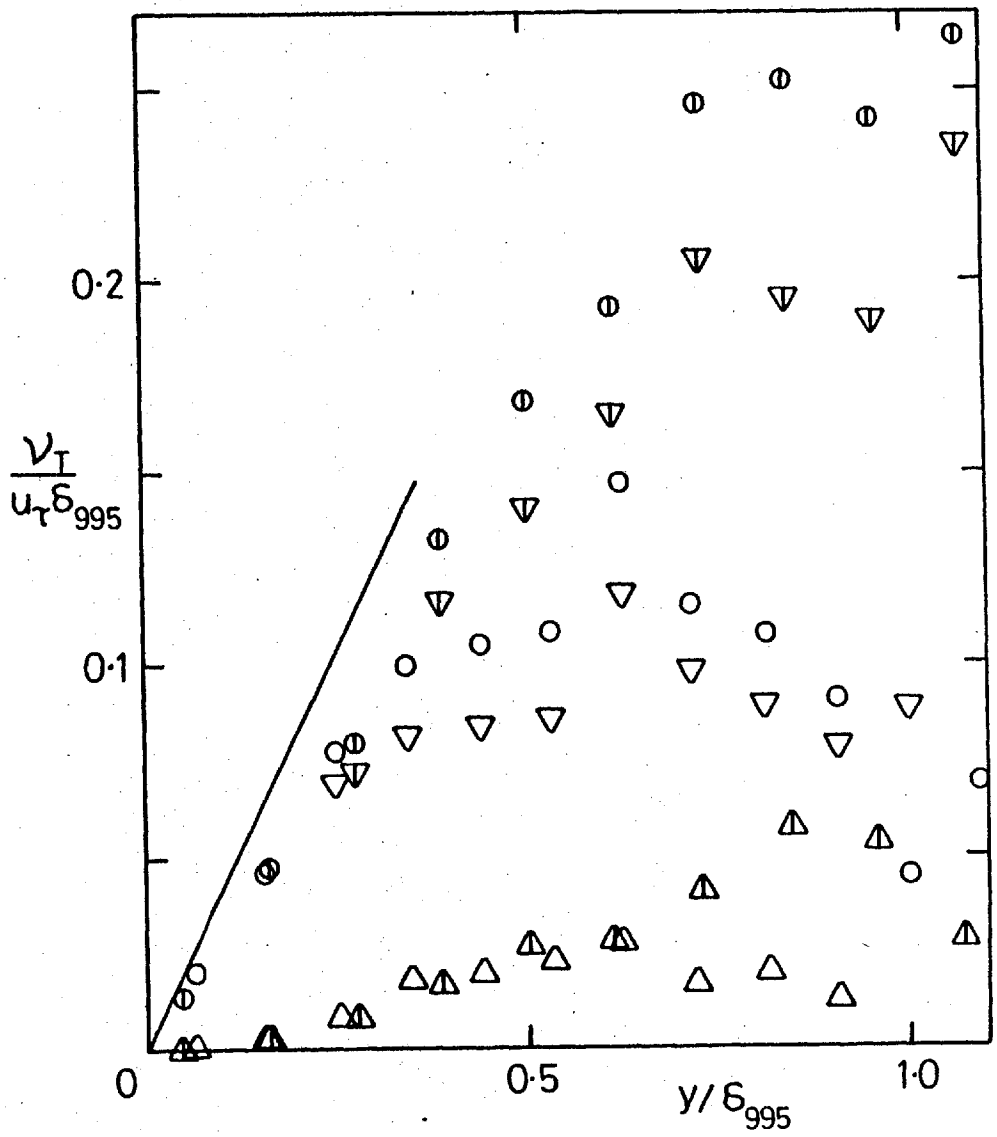

Fig. 4.41d, $(u'/U)_e = 0.0575$. Unbarred, $L^u_e/\delta_{995} = 1.83$
Barred, $L^u_e/\delta_{995} = 1.34$

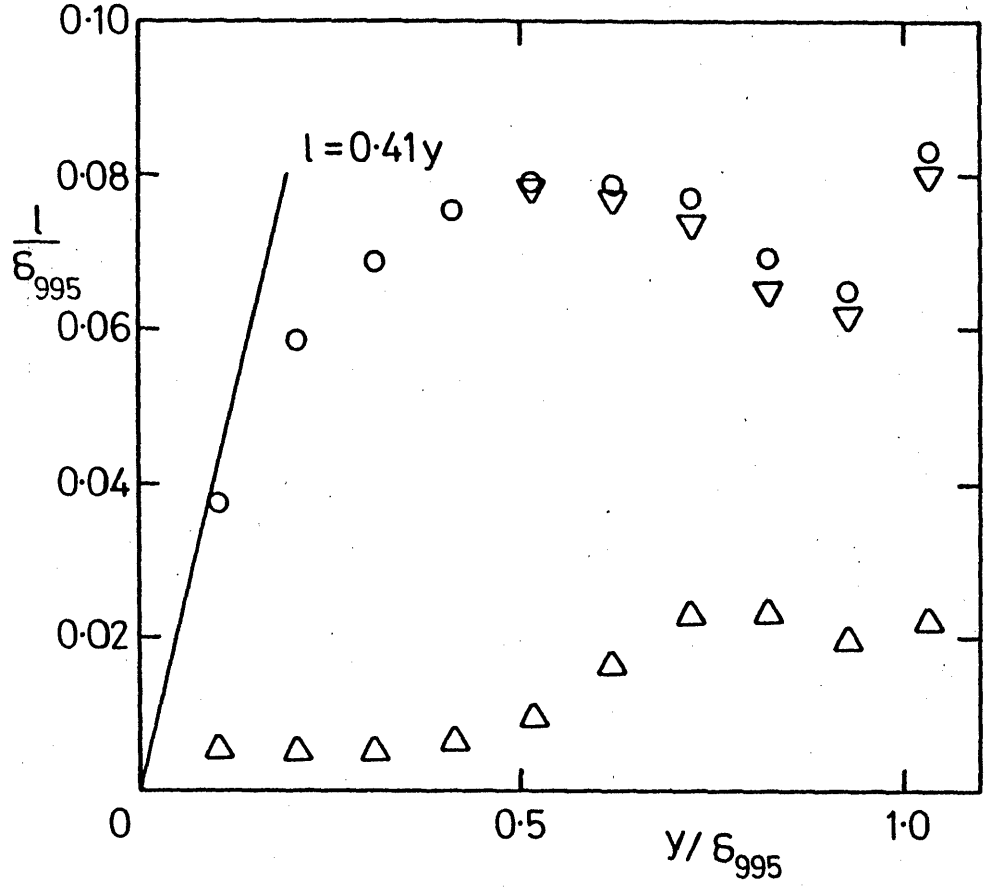

a) No grid.

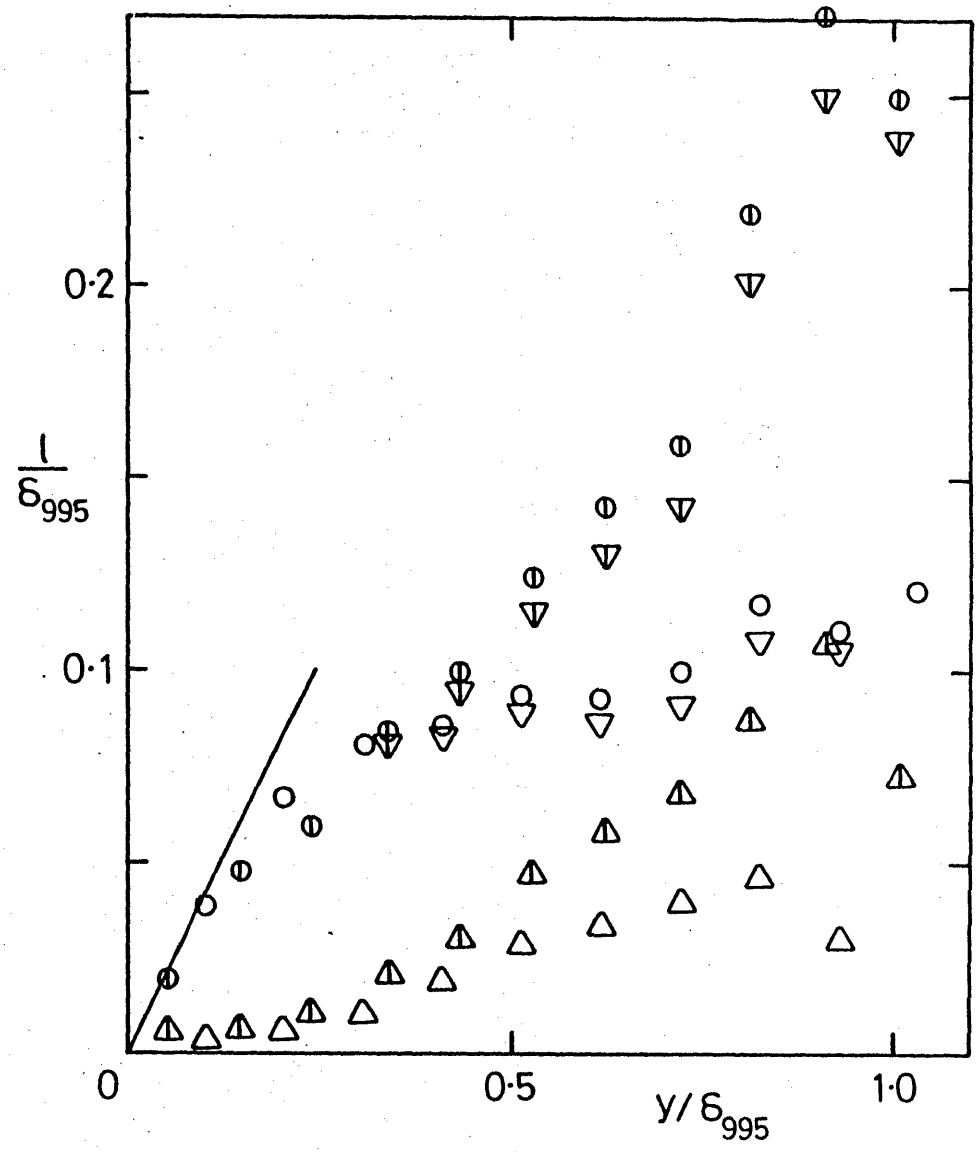

b) $(u'/U)_e \approx 0.025$. Unbarred, $L^u_e/\delta_{995} = 1.88$

Barred, $L^u_e/\delta_{995} = 0.67$

Fig. 4.42 Mixing length.

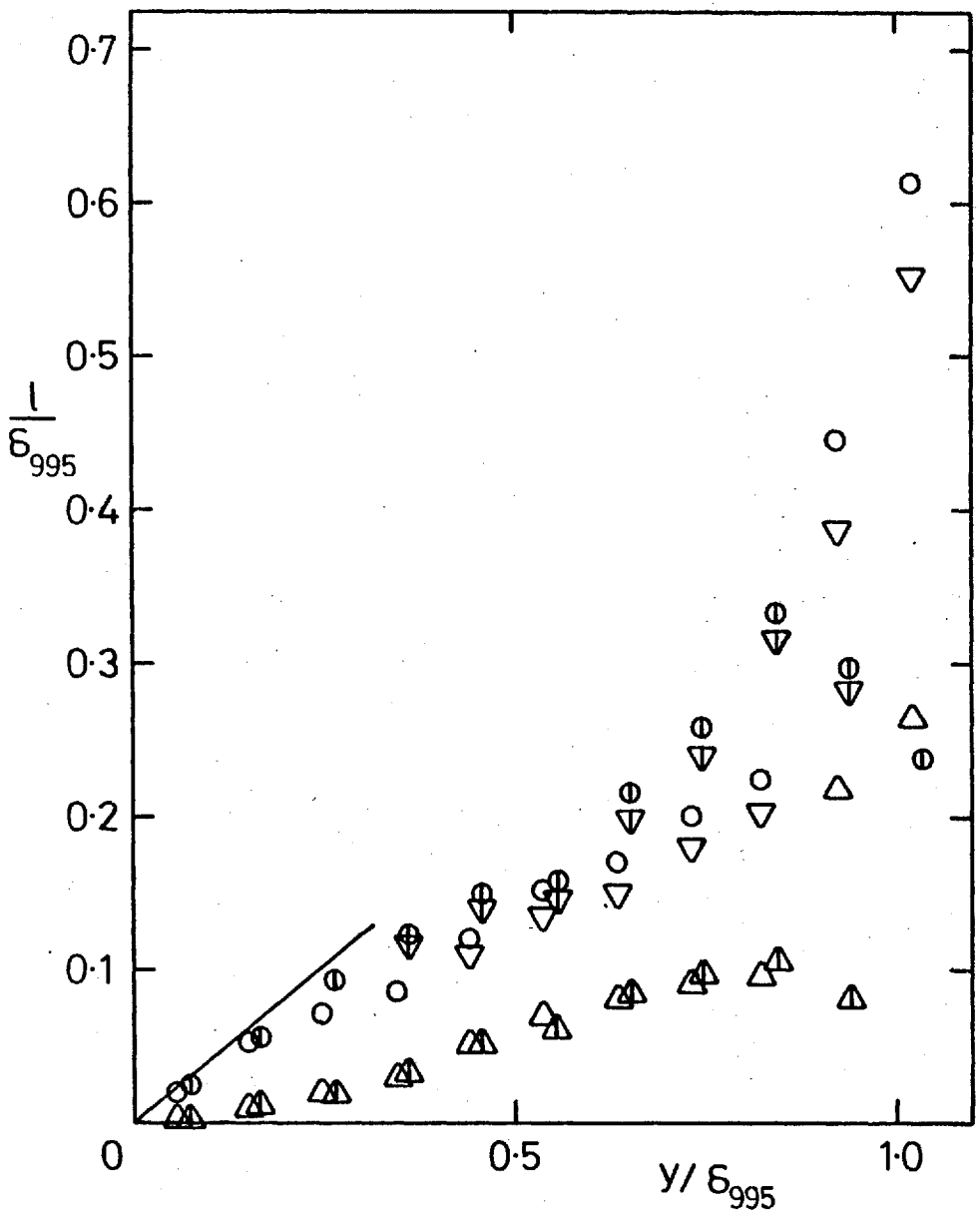

Fig. 4.42c, $(u'/U)_e \approx 0.040$. Unbarred, $L^u_e/\delta_{995} = 1.90$

Barred, $L^u_e/\delta_{995} = 0.71$

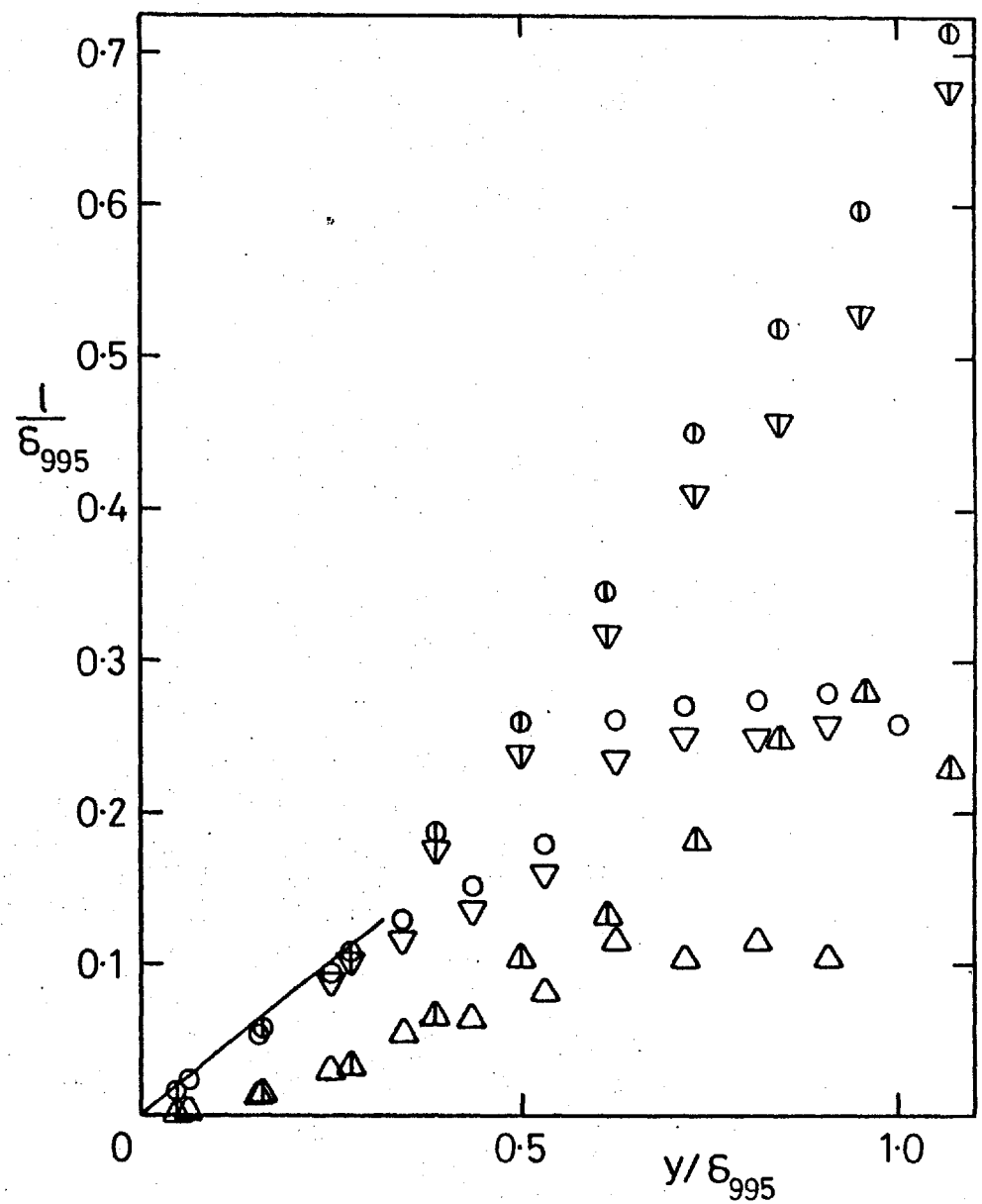

Fig. 4.42d, $(u'/U)_e = 0.0575$. Unbarred, $L^u_e/\delta_{995} = 1.83$

Barred, $L^u_e/\delta_{995} = 1.34$

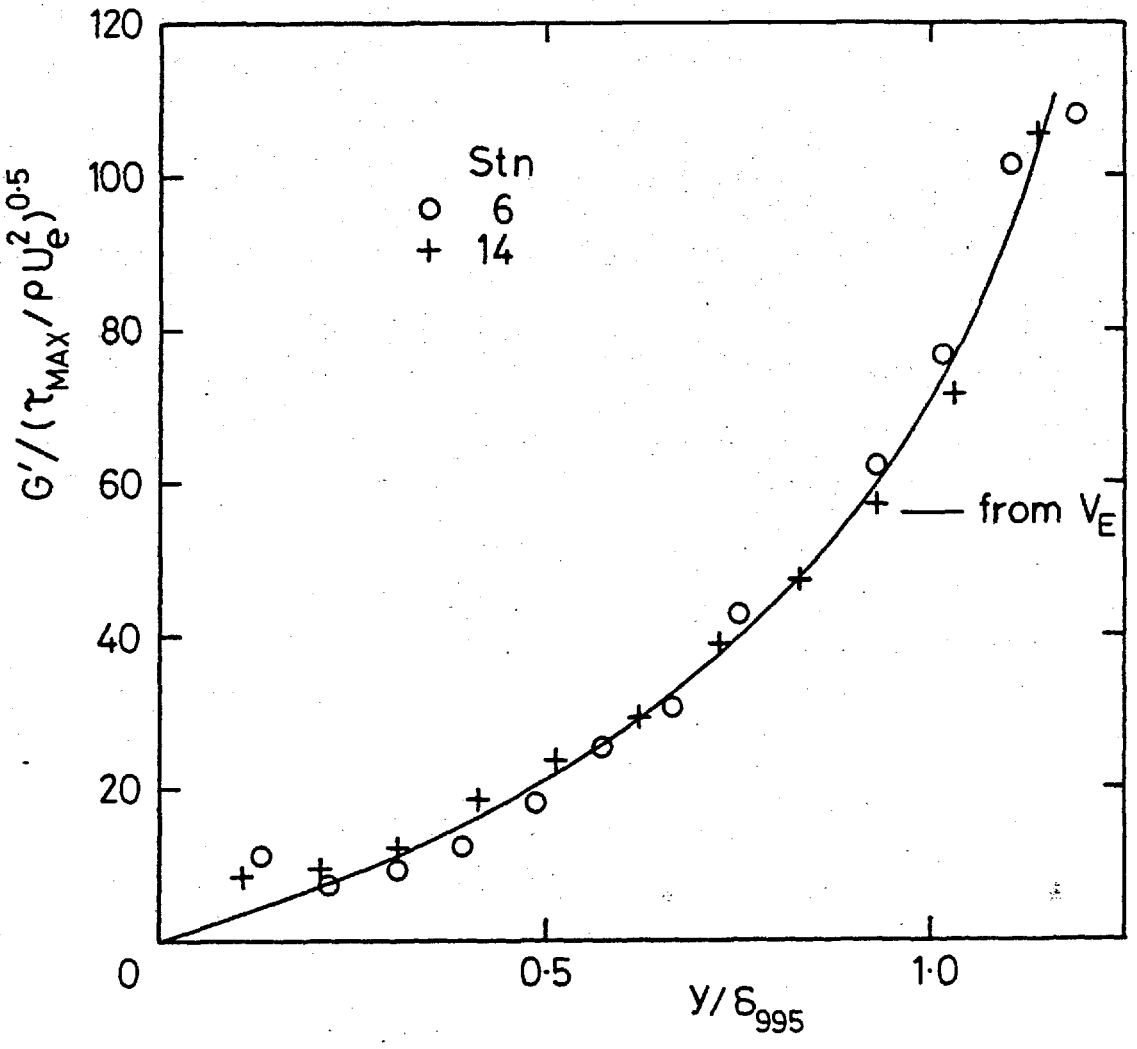

a) No grid.

Fig. 4.43 Diffusion function, G.

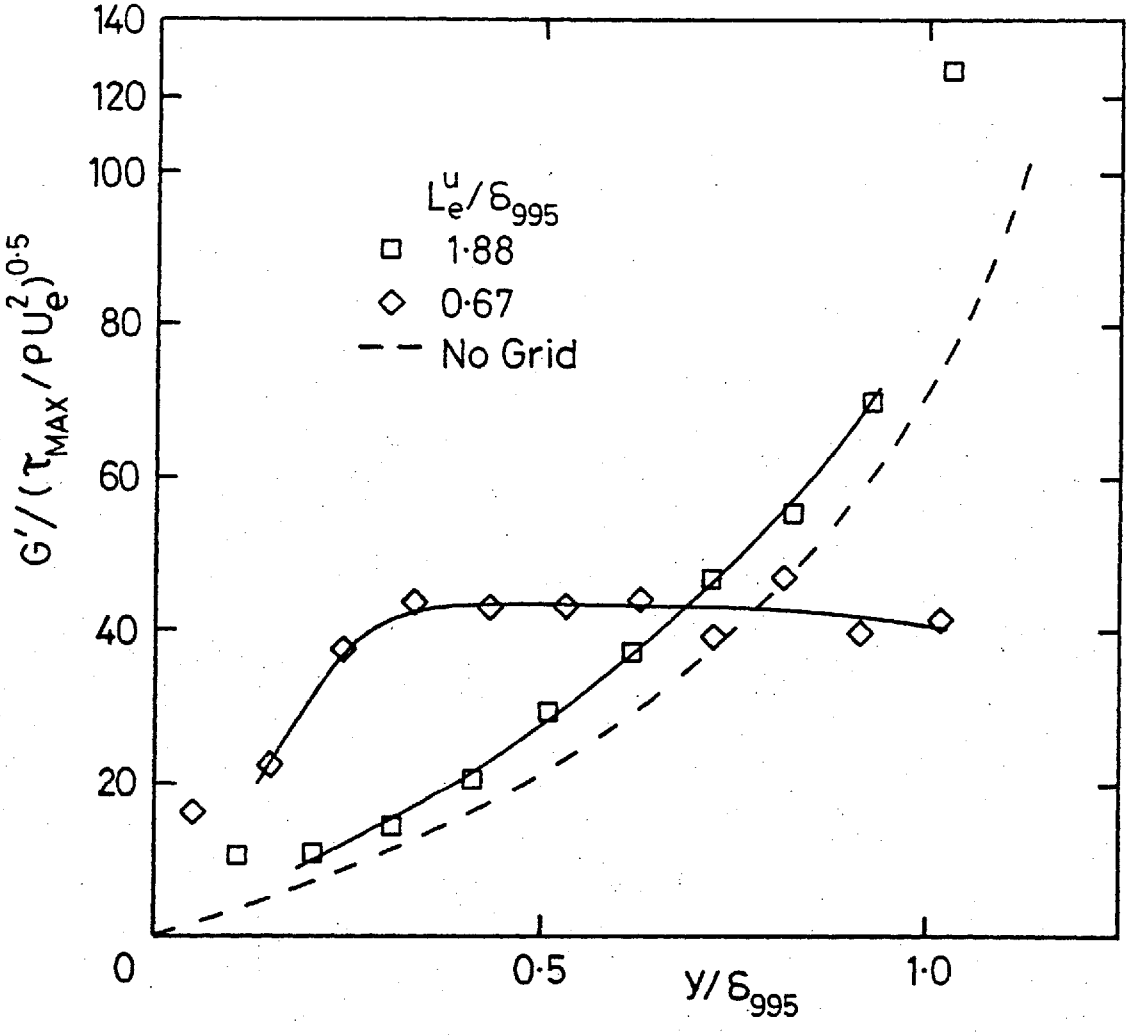

Fig. 4.43b, $(u'/U)_e \approx 0.025$.

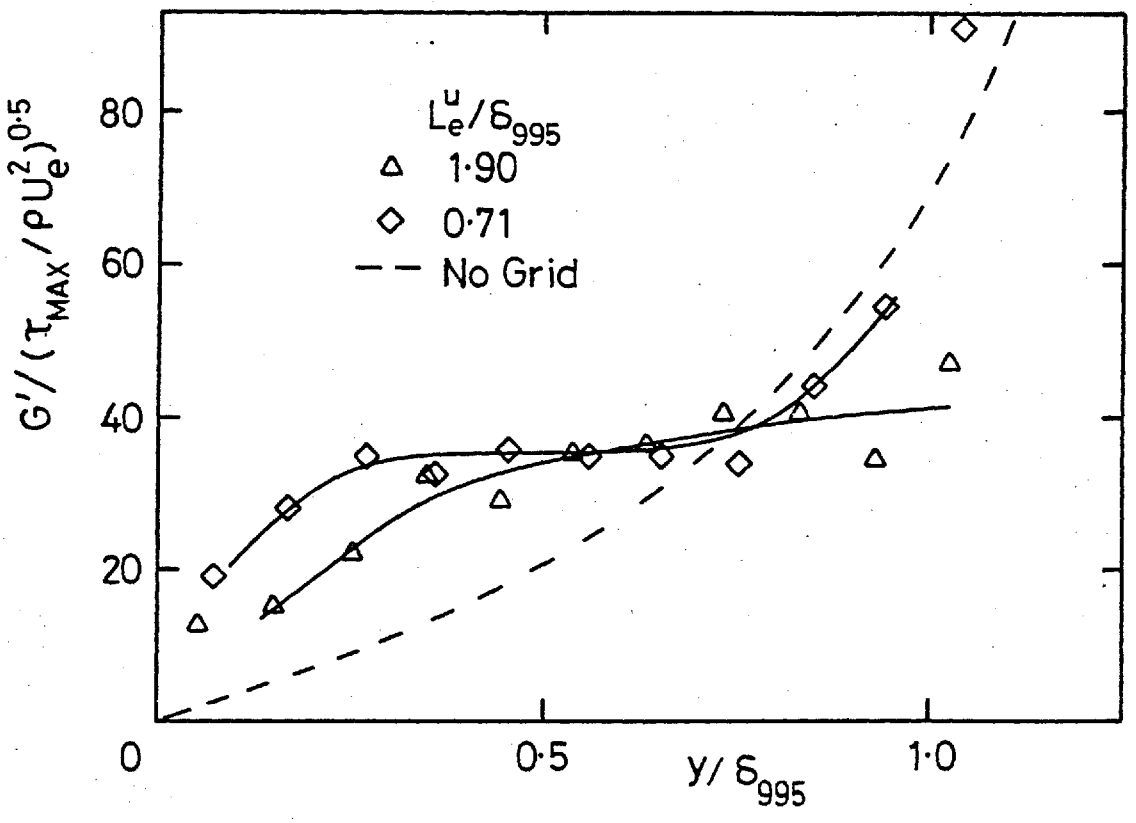

Fig. 4.43c, $(u'/U)_e \approx 0.040$.

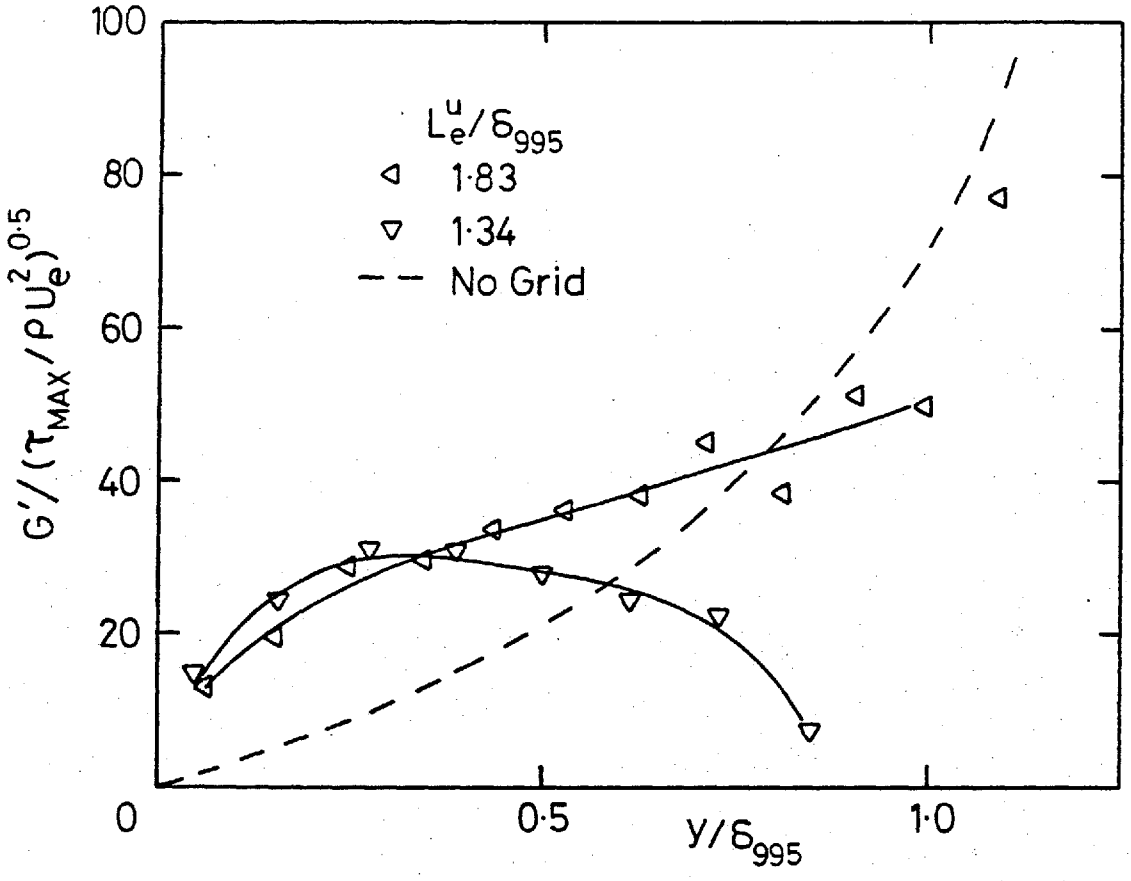

Fig. 4.43d, $(u'/U)_e = 0.0575$.

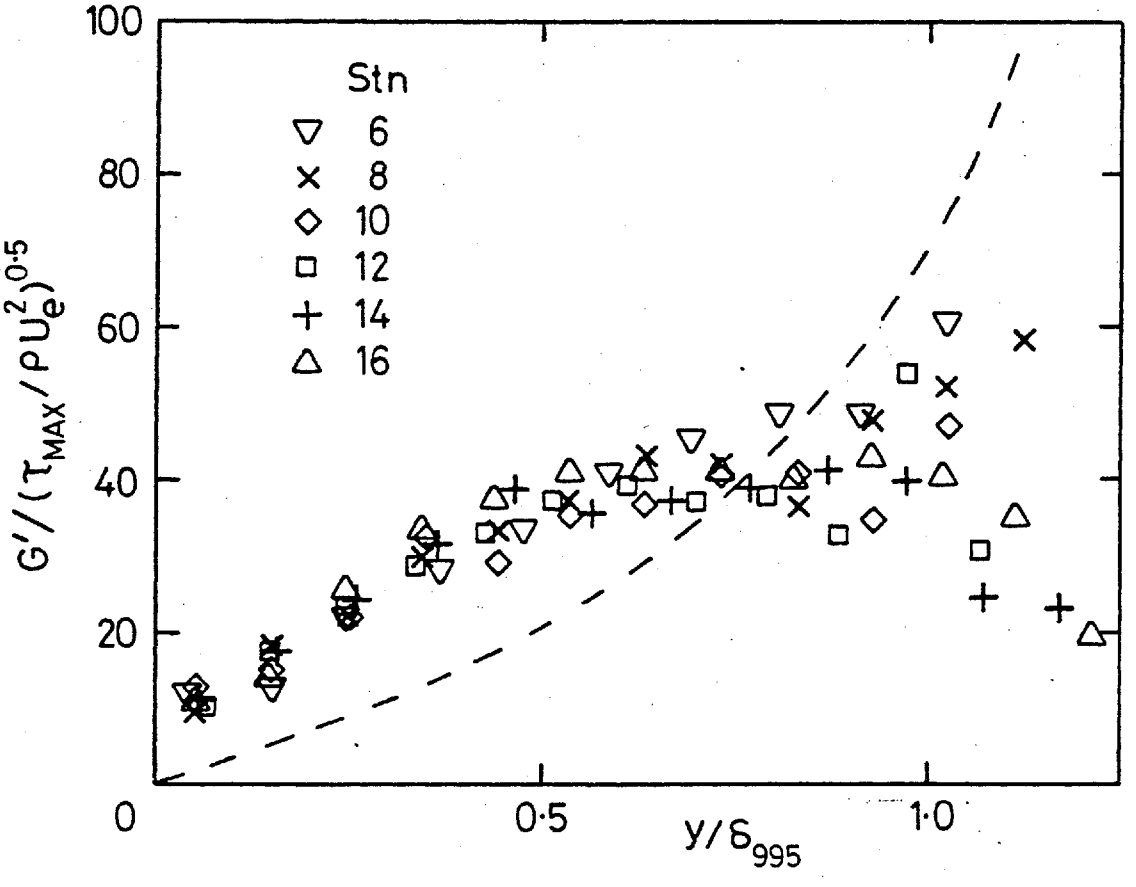

Fig. 4.43e, 15.2 cm grid, X_{LE} = 2.06 m, stns 6, 8, 10, 12, 14, 16.

CHAPTER 5

CONCLUSION

Results of an experimental investigation into the effects of approximately homogeneous, nearly isotropic free-stream turbulence on a closely two-dimensional, nearly constant-pressure incompressible turbulent boundary layer have been presented, for the Reynolds number range $1600 \lesssim Re_\theta \lesssim 5900$. Free-stream turbulence was satisfactorily generated using square-mesh square-bar biplane grids. Some other configurations, notably square-mesh square-bar monoplane grids and square-mesh rectangular-bar biplane grids, were found to give non-uniform and unsteady (i.e. low frequency fluctuations of the "mean") flow well downstream. As a consequence of the large fluctuations that exist close behind turbulence grids the present measurements were made on a flat plate mounted downstream of the grid in preference to, say, a working-section side wall. A useful contribution to the present thesis has been provided by a collaborative experimental investigation into the effect of boundary impermeability on (unsheared) approximately homogeneous nearly isotropic turbulence, separately reported by Thomas & Hancock (1977) and included as appendix 1. That investigation has been discussed as part of the literature review of chapter 1.

In quantifying the observed effects of free-stream turbulence, a single velocity scale and a single (dissipation) length scale of the free-stream energy-containing eddies have been used. Thus the results can be expected to be quantitatively reliable elsewhere only when the free-stream turbulence has energy-containing spectra typical of approximately homogeneous, approximately isotropic turbulence. Grossly different free-stream spectra would almost certainly have a different quantitative effect on the boundary layer. The present mean flow and turbulence investigations have covered ranges of free-stream intensity, $(u'/U)_e$, and length scale

ratio, L_e^u/δ_{995}, shown in figures 3.28 and 4.1. In particular, the latter parameter, which was previously considered to be far less important than the former, has been shown to also have a large effect on both the mean flow and the turbulence structure. Strongly anisotropic free-stream turbulence would in principle need to be described by at least one additional velocity scale and probably by an additional length scale.

Restrictions imposed by wind tunnel dimensions and fan power have been shown to limit the range of free-stream intensity and length-scale ratio obtainable in high Reynolds number laboratory flows. Such restrictions were partly responsible for the fairly close relationship between these two parameters in previous measurements, as shown in figure 3.2. By careful choice of grid size and plate position downstream of the grid the range of the length scale ratio was nearly the largest obtainable with the wind tunnel used and significantly larger than obtained hitherto.

Effects on mean flow parameters have been deduced by comparisons at constant local Reynolds number based upon momentum thickness. Free-stream turbulence increased the skin-friction ratio C_f/C_{f_o} and the growth rate $d\delta_{995}/dx$, and decreased the shape parameter ratios H/H_o and G/G_o and the strength of Coles (1956) wake component. (The skin-friction measurements were obtained by fitting a portion of the mean velocity profiles to the logarithmic law of the wall and from Preston tubes which assume the existence of an inner layer law. Physical arguments were employed to assert insensitivity of the inner layer mean flow to at least moderate free-stream turbulence effects.) C_f/C_{f_o} has been correlated in terms of a single, strongly non-linear function of an empirically derived parameter, $(u'/U)_e/(L_e^u/\delta_{995} + 2.0)$, as shown in figure 3.49. Low-Reynolds-number ($Re_\theta \lesssim 2000$) effects on C_f/C_{f_o} at large values of $(u'/U)_e/(L_e^u/\delta_{995} + 2.0)$, tentatively based on a single but apparently

trustworthy case, has been quite plausibly attributed entirely to the low-Reynolds-number dependence of the wake component that exists in the absence of free-stream turbulence - that is, low-Reynolds-number effects on C_{f_o}. Overall, the increase in C_f/C_{f_o} was found to be slightly larger than the consensus of previous data but both previous and present data have been shown to be consistent with the linear dependence on $\overline{u_e^2}$ observed experimentally by Meier (1976, 1977) for $(u'/U)_e \lesssim 0.01$.

An intermittency function was satisfactorily generated from temperature fluctuations by the algorithm LAGTHR. This used a frequently up-dated level threshold backed-up by a (bulk) slope test which looked for fairly rapid falls from a current 'hot' burst to a likely 'cold' level. The bandwidth of the compensated temperature wire was compatible with the probe resolution volume and large enough to be sensitive to the fine-scale structure of the interface. Conditionally-averaged velocity fluctuations were measured with respect to conventionally-averaged mean velocities rather than conditionally-averaged mean velocities, providing two distinct advantages. The latter method ignores the low-frequency part of the turbulence, and the former permits the use of the simple addition law given in equation 4.2.1.

Visualization of a smoke-filled turbulent boundary layer has shown that free-stream turbulence causes the interface to be even more ragged, with wisps of smoke extending well beyond the edge of the mean velocity profile. The temperature intermittency measurements also showed greater and more frequent penetration of the free-stream fluid into the boundary layer. Consistent with this, the average length of the eruptions of boundary layer fluid ('hot bursts') was found to be substantially reduced over most of the layer but still of order the boundary layer thickness. The average position

($\overline{y}$) of the interface, which is a scale of the outer layer eddies, remained of the order of the thickness (δ_{995}) of the mean velocity profile. The existence of a highly contorted interface at low Reynolds number, as was shown in the first place by the flow vizualization photographs, explained the low-Reynolds-number effects on C_f/C_{f_o} in so far as such effects are usually associated with the interface becoming less contorted.

The integrity of the boundary layer turbulence measurements has unfortunately been marred by undesirably large errors in $-\overline{uv}$, $\overline{w^3}$ and a few profiles of $\overline{u^2}$ (which showed sensitivity to probe rotation). However, although no cause was firmly established, the available evidence supports the belief that other turbulence quantities, particularly the higher-order products, are not seriously in error and that the conclusions of the present thesis, namely those of chapter 4, have not been seriously impaired.

Conventionally- and conditionally-averaged turbulence measurements confirmed that the interaction is largest in the outer layer. Generally, the boundary layer fluid (i.e. the 'hot' zone) exhibited a structure that was dependent on both the free-stream intensity and the length scale ratio, although the hot-zone structural parameters were found to be better behaved than similar parameters formed from conventional averages. For instance, the ratio of transport velocities $V_{\tau,H}/V_{q,H}$ was found to be at most only weakly dependent upon free-stream turbulence while V_τ/V_q was noted to be strongly dependent. Consistent with the small variation of δ_{05}/δ_{995} the wispy motion of the boundary layer fluid was found to contribute negligible shear stress for $y \gtrsim \delta_{995}$, and it was tentatively suggested that the wispy motion beneath $y \simeq \delta_{995}$ may not locally contain much more shear stress than the external fluid (i.e. the 'cold'zone). In the absence of free-stream turbulence $-\overline{uv}_c/\sqrt{(\overline{u_c^2}.\overline{v_c^2})}$ and $-\overline{uv}_c/\overline{q_c^2}$

exhibited values that were genuinely - and, indeed, unexpectedly - significantly larger than for turbulent motion for a substantial part of the boundary layer. Moreover, the peak values of these quantities were found to decrease only slowly, reaching, respectively, about 0.45 and 0.15 when $(u'/U)_e \approx 0.058$. The cold-zone transport velocities $V_{\tau,C}$ and $V_{q,C}$ were observed to scale roughly on u_τ and $\sqrt{(\overline{v^2})}$ measured at the boundary layer edge.

Increased 'inactive' motion was observed, but was found to be only weakly dependent upon length scale ratio. This was noted to be consistent with the inactive motion due to the free-stream turbulence tending to cancel the length-scale effect seen in the outer layer.

Very brief consideration has been given to adapting the calculation method of Bradshaw et al. (1967). The dissipation length scale based upon the shear stress, L_τ, was found, to the likely accuracy of its measurement, to be independent of free-stream turbulence. Although obviously convenient, the result was surprising, since near the outer edge of the boundary layer, at least, the shear stress cannot be the only scale relevant to dissipation when free-stream turbulence (of scales of order the boundary layer scales) is present. Both $-\overline{uv}/\overline{q^2}$ and $G/\sqrt{(-\overline{uv}_{MAX}/U_e^2)}$ (equation 4.8.10 approximated by equation 4.8.12) generally showed strong and fairly complicated dependence upon the free-stream intensity and the length scale ratio, but were nevertheless reasonably well behaved.

J. Fluid Mech. (1977), *vol.* 82, *part* 3, *pp.* 481–496
Printed in Great Britain

Grid turbulence near a moving wall

By N. H. THOMAS† AND P. E. HANCOCK
Department of Aeronautics, Imperial College, London

(Received 3 November 1976)

Decaying grid turbulence was passed over a wall moving at the stream speed. For the high Reynolds number of the experiment, the field due to the wall constraint on the normal component of the velocity fluctuations is found to extend further into the flow than the influence of the viscous boundary condition on the tangential-component fluctuations. Measurements of the variances, length scales and spectra of the three velocity components of the turbulence are compared with the results of a previous experiment and with the theoretical predictions for an idealization of the flow. A simple model for some departures from the theory is proposed.

1. Introduction

The experiment described below, in which decaying grid turbulence was passed over a wall moving at the stream speed, serves as a realization of the simplest bounded turbulence field: 'turbulence in a box'. For, invoking Taylor's frozen-flow hypothesis and supposing the grid turbulence to be essentially isotropic, we have an analogue of the boundary region established when an infinite flat plate is suddenly inserted, without relative mean motion, into a pre-existing field of homogeneous isotropic turbulence. Hunt & Graham (1978) have described the linearized asymptotic solution valid at large Reynolds number. Physically, this exhibits an outer kinematic region characterized by the length scale L_e of the external turbulence, in which the normal component of the velocity fluctuations is inhibited by the wall constraint, and an inner viscous region of typical thickness $\delta_v \sim (\nu t)^{\frac{1}{2}}$, where ν is the kinematic viscosity and t the elapsed time. The theory is valid for small δ_v/L_e.

The experiment, in which $t = x'/\overline{u}$, where x' is measured from the leading edge of the boundary region and $\overline{u}$ is the uniform mean velocity, affords a substantial test of the Hunt & Graham solution. We describe measurements of the time-averaged variances $(\overline{u'^2}, \overline{v'^2}, \overline{w'^2})$ of the fluctuation velocity components (u', v', w'), the one-dimensional frequency spectra $(\Theta_u, \Theta_v, \Theta_w)$ of these components and the longitudinal integral scales defined by

$$L_u = \frac{\overline{u}}{4\overline{u'^2}}\Theta_u(n=0), \quad L_v = \frac{\overline{u}}{4\overline{v'^2}}\Theta_v(n=0), \quad L_w = \frac{\overline{u}}{4\overline{w'^2}}\Theta_w(n=0),$$

where n is the frequency. The subscript e will denote the values in the external stream. It is shown in § 3 that the normal $(\overline{v'^2})$ component is in quantitative agreement with the theory but the transverse $(\overline{w'^2})$ component is essentially uninfluenced by the wall, in

† Present address: Department of Applied Mathematics and Theoretical Physics, University of Cambridge.

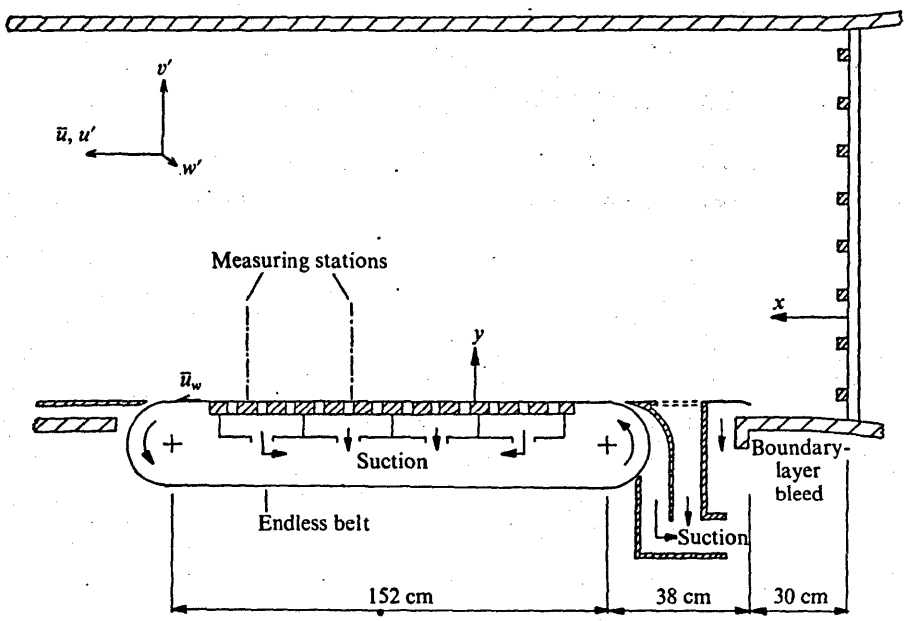

FIGURE 1. Schematic diagram of the wind tunnel, turbulence grid and endless belt arrangement, and definition sketch (the transverse co-ordinate z, not shown, has the centre-plane as origin).

contrast to the theoretically predicted amplification. The local amplification of the longitudinal ($\overline{u'^2}$) component, which is greater than that predicted, grows with increasing downstream distance. A simple explanation, in terms of the streamwise inhomogeneity of the decaying grid turbulence, is proposed in §4.

The present studies, in which the grid Reynolds number R_M was approximately 10^5, where $R_M = M\bar{u}/\nu$ and M is the mesh width, are complementary to those conducted by Uzkan & Reynolds (1967), in which R_M was about 5000. Essentially the same methods of producing a shear-free mean flow were employed (see §2). Uzkan & Reynolds measured the variance and spectrum of the u'-component fluctuation and found a viscous layer with $\delta_v \simeq 1{\cdot}8(\nu x'/\bar{u})^{\frac{1}{2}}$, but no explicit evidence for an outer kinematic region. Now, for large x/M, typically $L_{ue} \simeq 0{\cdot}1(Mx)^{\frac{1}{2}}$, where x is measured from the grid, so if $x \simeq x'$, then $\delta_v/L_{ue} \simeq (300/R_M)^{\frac{1}{2}}$ and is therefore approximately 0·25 for Uzkan & Reynolds' experiment and 0·05 for ours. Further discussion of Uzkan & Reynolds' results is presented in §4.

Hunt & Graham have compared their solution with the results of these moving-wall experiments and with measurements in a decaying turbulent stream by Graham (1975) and Petty (unpublished; see Hunt & Graham) near a flat plate and by Cooke (1971; see Hunt & Graham) near a wind-tunnel wall. Each study showed that outside the conventional mean-flow boundary layer, the v' variance decreased towards the wall as predicted by the theory. Graham's results, obtained near a mean-flow boundary layer of thickness small compared with L_{ue}, compare well with those currently obtained (see §3). This supports the view that, for a sufficiently high Reynolds number, the structure of the outer wall region is independent of the inner region even if the latter is a fully turbulent mean-flow boundary layer.

A practical application of the results is to the effects of free-stream turbulence on

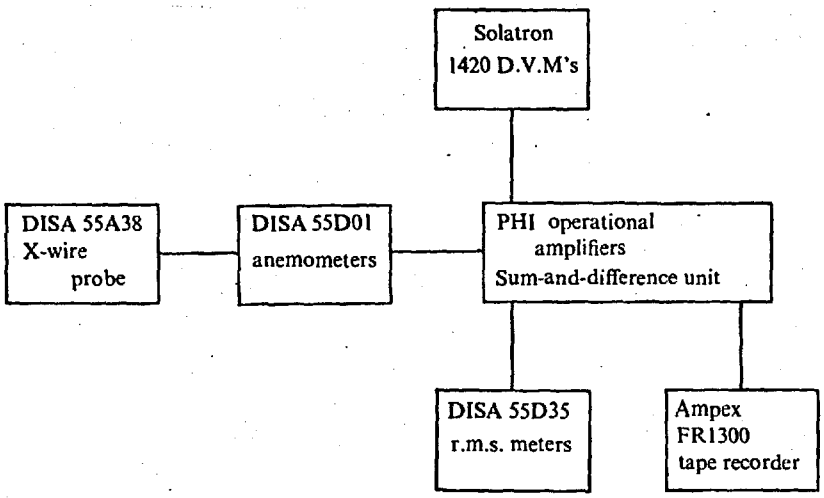

FIGURE 2. Apparatus for the collection and measurement of the turbulence data.

boundary layers when the free-stream length scale, as is usual, exceeds the boundary-layer thickness. In these cases, an outer kinematic region exists and the effective values of the turbulence parameters are not the external-stream values. Recent reviews of the problem of turbulent boundary layers with free-stream turbulence have been given by Green (1972) and Bradshaw (1974).

2. Procedure

The experiments were performed in a low-speed wind tunnel with a 5×4 ft ($1{\cdot}5 \times 1{\cdot}2$ m) working section 7 ft (2·1 m) long, with corner fillets. The floor of the working section was replaced by an endless belt on rollers, with a suction-box assembly upstream (figure 1). The turbulence was generated by biplanar grids of rectangular-section bars with solidities of 0·4. The mesh widths were 3 in. (7·6 cm) and 6 in. (15·2 cm) respectively for the grids hereinafter referred to as grids A and B. The flow was studied at distances 168 cm and 193 cm downstream of grid A and 193 cm downstream of grid B. These stations are referred to below by their nominal downstream distances in grid mesh widths: $22M$, $25M$ and $13M$ respectively. A schematic diagram and definition sketch are shown in figure 1.

The belt, which was smooth except for a diagonal lap joint approximately 0·003 cm thick, was driven by a constant-speed motor at approximately 13 m s^{-1}. The belt speed was measured by a tachometer and also by a stroboscope focused on each roller; no slip was observed. A distribution of suction was applied through the backing plate to hold the belt flat. Frictional heating at this boundary generated a temperature rise of 8° C.

A bleed duct 30 cm downstream of the grid absorbed the tunnel boundary layer. The flow onto the moving belt was controlled by a leading-edge plate with suction through the porous surface and through the gap near the upstream roller (see figure 1). Using a tuft probe for visualization, the camber and incidence of the plate were adjusted to give smooth flow conditions. The size of the suction gap was set to minimize the mean shear at the downstream measurement station. This procedure may have

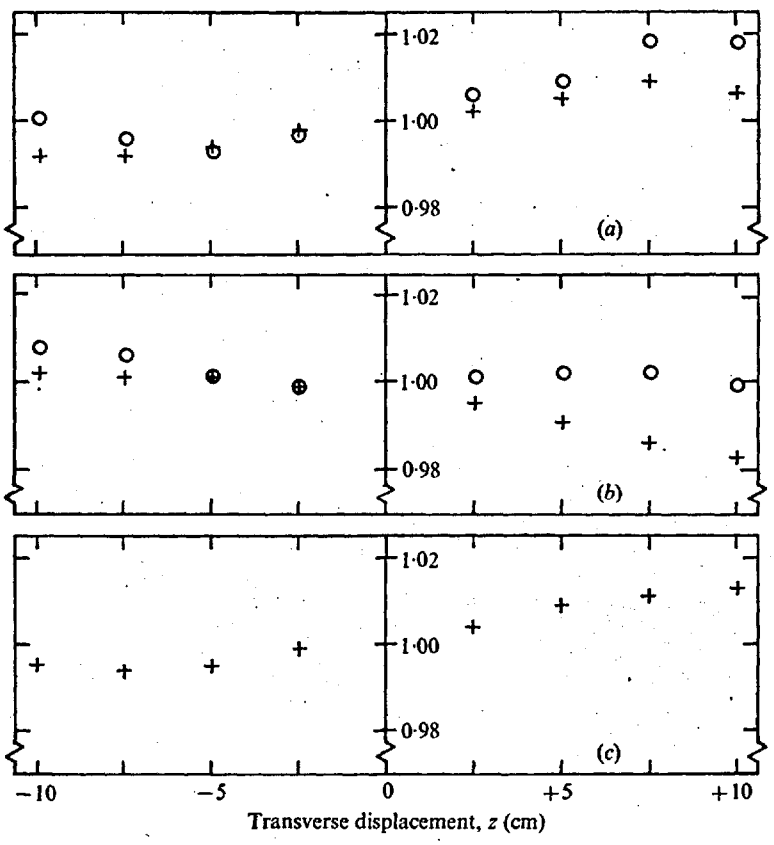

FIGURE 3. Transverse distributions of mean velocity normalized by values on $z = 0$. (*a*) $x/M = 25$, grid A ($M = 3$ in.). (*b*) $x/M = 13$, grid B ($M = 6$ in.). (*c*) $x/M = 22$, grid A. ○, $y = 0{\cdot}5$ cm; +, $y = 7{\cdot}6$ cm.

resulted in small differences in the configurations for the grid A study and the grid B study; the latter was performed at a later date.

The turbulence was measured by hot-wire anemometers. A diagram of the components is presented in figure 2. The probes were calibrated in the flow remote from the tunnel boundaries and 'best fit' King's law relations were used to derive the fluctuation velocities. The mean voltages of the two wires on a given cross-wire probe were matched over the calibration range and a sum-and-difference unit was employed to obtain fluctuating voltages proportional to the longitudinal and lateral components of the turbulence velocity fluctuations, assuming the wires angles to be $\pm 45°$. This assumption proved to be inadequate and corrections were later incorporated into the data reduction procedure; for details see Hancock & Thomas (1977).

The variances of the voltage fluctuations were measured by a commercial r.m.s. meter (figure 2). The recorded signals were later digitally sampled for 20 s at a rate of 2000 s^{-1} and Fourier transformed, using a fast algorithm described by Davies (1974), in blocks of 1024 samples. The effective 'filter' bandwidth was therefore 2 Hz and the total record length was 40 000 data points. No corrections for variations of the hot-wire sensitivities with spatial variations of air temperature were considered, but it was deduced from a comparison of the results of a Pitot-tube traverse and the mean voltage

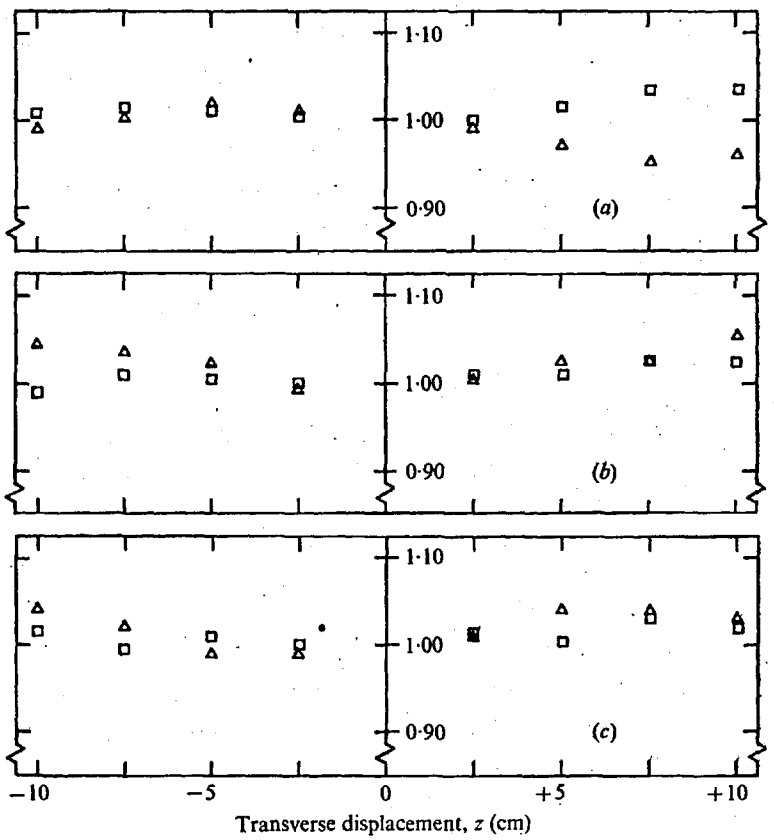

FIGURE 4. Transverse distributions of r.m.s. fluctuation velocities normalized by values on $z = 0$. (*a*) $x/M = 25$, $y = 0{\cdot}5$ cm. (*b*) $x/M = 25$, $y = 7{\cdot}6$ cm. (*c*) $x/M = 22$, $y = 7{\cdot}6$ cm. □, $(\overline{u'^2})^{\frac{1}{2}}$; △, $(\overline{v'^2})^{\frac{1}{2}}$.

outputs of the anemometers that any thermal boundary layer created by the temperature difference between the belt and the stream was essentially confined to a region closer to the wall than the data presented here.

3. Results

Any effects of the streamwise mean velocity variation, estimated as 0·1 % between the measuring stations, are assumed to be negligible. Transverse distributions of mean velocity at heights of 0·2 in. (0·5 cm) and 3 in. (7·6 cm) are shown in figure 3. Variations of less than ± 2 % over ± 10 cm are exhibited. Note that the necessary uniformity of speed at the wall does not suppress variations, presumably caused by the grid, at a height of 0·5 cm.

Figure 4 presents some transverse distributions of the r.m.s. values $(\overline{u'^2})^{\frac{1}{2}}$ and $(\overline{v'^2})^{\frac{1}{2}}$ of the u' and v' fluctuations for grid A only. Variations are typically less than 5 % over distances of ± 10 cm from the centre-plane. The differences between the distributions at heights of 0·5 cm and 7·6 cm at the $25M$ station may be due to a small inclination of the traverse relative to the wall.

Figure 5 shows mean velocity profiles obtained in the central plane at the $13M$ and $25M$ stations with minimized mean shear and with a nominal difference of ± 5 %

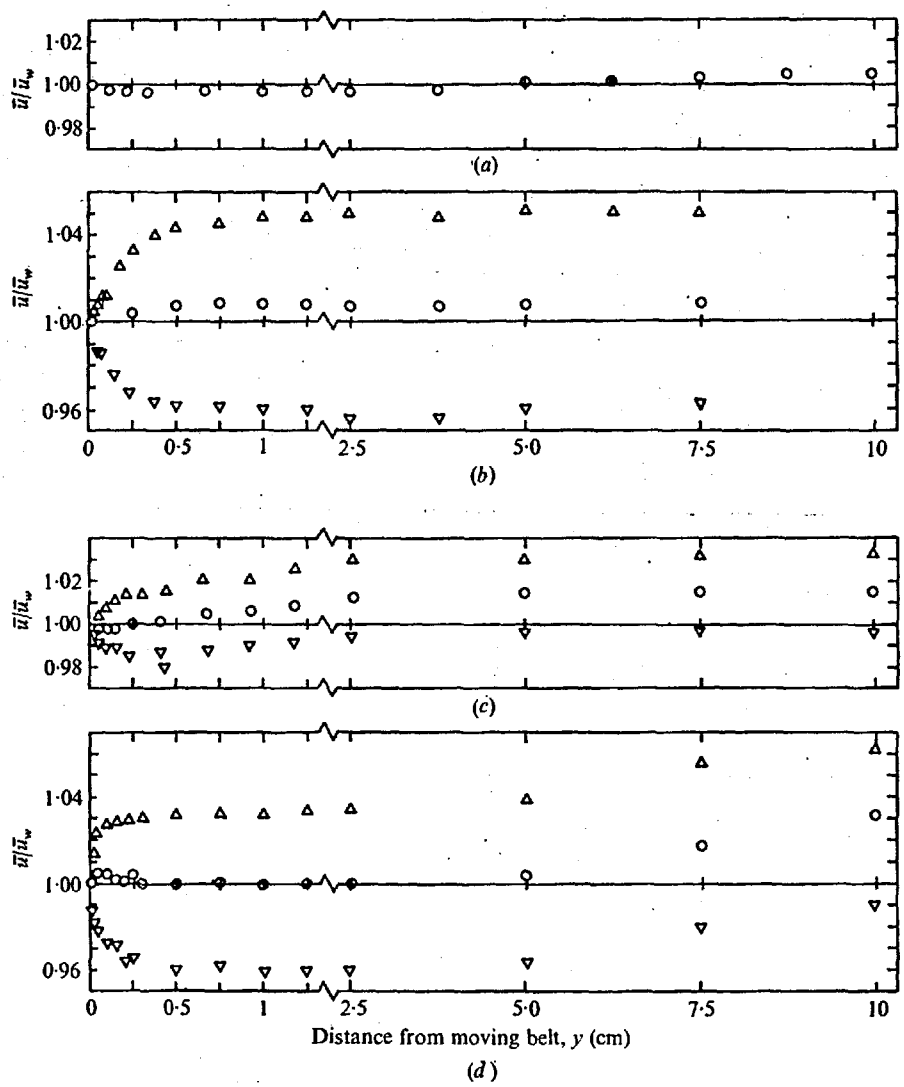

FIGURE 5. Mean velocity profiles at $x = 193$ cm showing the effects of a mismatch between the wall and stream speeds. Grid A experiment ($x/M = 25$): (*a*) without grid; (*b*) with grid. Grid B experiment ($x/M = 13$): (*c*) without grid; (*d*) with grid.

between the wall and stream speeds. For the experiment with grid A, the velocity is uniform to within 1% for $0 < y < 7{\cdot}5$ cm with the grid present and uniform to within $\frac{1}{2}$% for $0 < y < 10$ cm with the grid removed. For the grid B study, there is no significant gradient up to $y = 5$ cm but a 3% change between $y = 5$ cm and $y = 10$ cm. Here the measurement station is at only $13M$ and the gradient may well be due to grid-generated shear. With either grid in the tunnel, the wall shear field produced by deliberately mismatching the speed does not extend beyond $y \simeq 0{\cdot}5$ cm, which is in agreement with our earlier observation on the transverse non-uniformities.

Values of the r.m.s. velocity fluctuations obtained at the $25M$ station with the wall and stream speeds nominally equal and with a ± 5% mismatch between them are shown in figure 6. No significant differences between the three cases can be discerned

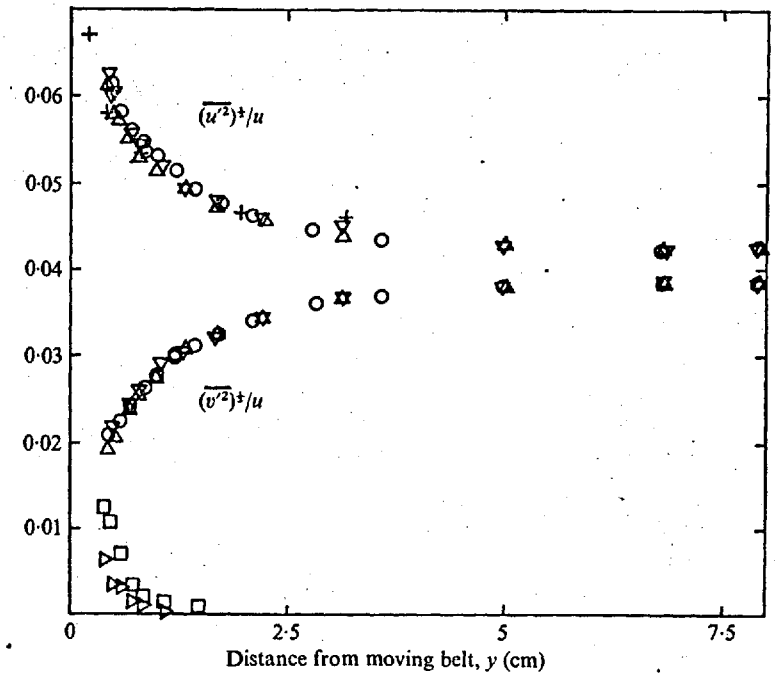

FIGURE 6. Turbulence intensities $(\overline{u'^2})^{\frac{1}{2}}/\overline{u}$ and $(\overline{v'^2})^{\frac{1}{2}}/\overline{u}$ at $x = 193$ cm. Grid A: ○, $\overline{u}_w = \overline{u}_e$; △, $\overline{u}_w = 0{\cdot}95\overline{u}_e$; ▽, $\overline{u}_w = 1{\cdot}05\overline{u}_e$; +, single-wire probe. No grid: □, $(\overline{u'^2})^{\frac{1}{2}}/\overline{u}$; ▷, $(\overline{v'^2})^{\frac{1}{2}}/\overline{u}$.

and we conclude that any influence on the turbulence is confined to the region of significant mean shear. Values of $(\overline{u'^2})^{\frac{1}{2}}$ obtained from a single wire agree to better than 5% with the cross-wire measurements. Figure 6 also shows the r.m.s.profiles obtained in the absence of the grid. This turbulence, probably generated near the leading edge, is presumably uncorrelated with the grid turbulence and contributes an error of less than about 5%.

Figure 7 presents the variances $(\overline{u'^2}, \overline{v'^2}, \overline{w'^2})$ normalized on their external-stream values $(\overline{u_e'^2}, \overline{v_e'^2}, \overline{w_e'^2})$ as functions of y/L_{ue}, where L_{ue} is the external longitudinal integral scale. The results for the normal $(\overline{v'^2})$ component correlate well and are supported by Graham's results for large-scale turbulence streaming past a flat-plate turbulent boundary layer. Figure 7 also shows the theoretical solution of Hunt & Graham. We observe that very good agreement is obtained if the reduced distance is based on the normal-component longitudinal integral scale L_{ve}, which was measured as $0{\cdot}4L_{ue}$ for the present grid turbulence rather than the value $0{\cdot}5L_{ue}$ for the isotropic field assumed in the analysis. Over the range of heights used in the present study, the transverse $(\overline{w'^2})$ component varies only slightly towards the wall, the variation decreasing with downstream distance. Hunt & Graham's solution for homogeneous isotropic external turbulence considerably overpredicts the values near the wall. The longitudinal $(\overline{u'^2})$ component increases towards the wall, the amplification growing significantly with downstream distance. The results at $13M$ are in reasonable agreement with the theory but local scaling is clearly inadequate for a description of the downstream evolution. Further discussion of this behaviour will be given in §4.

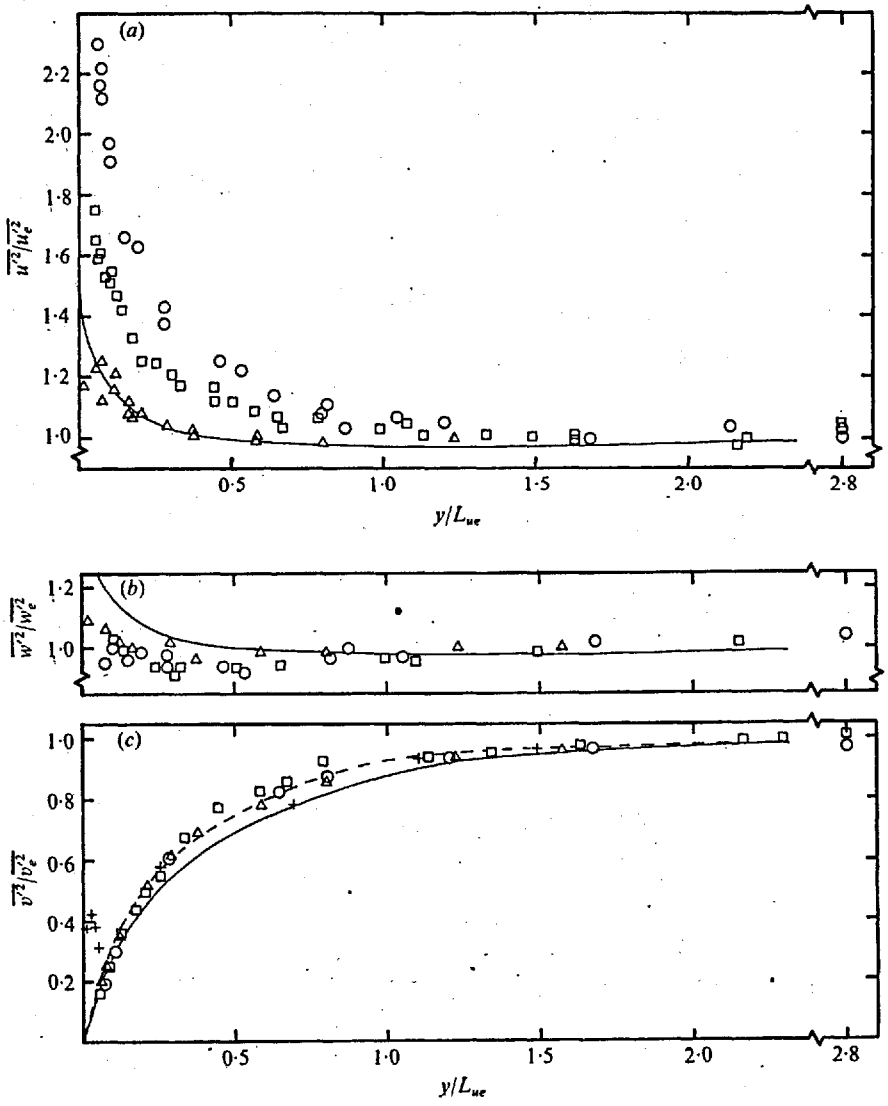

FIGURE 7. Variances of fluctuation velocities normalized on external-stream values as functions of y/L_{ue}. (*a*) $\overline{u'^2}/\overline{u_e'^2}$. (*b*) $\overline{w'^2}/\overline{w_e'^2}$. (*c*) $\overline{v'^2}/\overline{v_e'^2}$. △, $x/M = 13$, $(\overline{u_e'^2})^{\frac{1}{2}}/\overline{u} = 0{\cdot}0775$, $(\overline{w_e'^2})^{\frac{1}{2}}/\overline{u} = 0{\cdot}0700$, $(\overline{v_e'^2})^{\frac{1}{2}}/\overline{u} = 0{\cdot}0700$; □, $x/M = 22$, $(\overline{u_e'^2})^{\frac{1}{2}}/\overline{u} = 0{\cdot}0525$, $(\overline{w_e'^2})^{\frac{1}{2}}/\overline{u} = 0{\cdot}0483$, $(\overline{v_e'^2})^{\frac{1}{2}}/\overline{u} = 0{\cdot}0483$; ○, $x/M = 25$, $(\overline{u_e'^2})^{\frac{1}{2}}/\overline{u} = 0{\cdot}0425$, $(\overline{w_e'^2})^{\frac{1}{2}}/\overline{u} = 0{\cdot}0380$, $(\overline{v_e'^2})^{\frac{1}{2}}/\overline{u} = 0{\cdot}0380$; +, experiment of Graham (1975); ——, theory of Hunt & Graham (1978); – – –, $\overline{v'^2}/\overline{v_e'^2}$ *vs.* $0{\cdot}4y/L_{ve}$.

Length-scale profiles derived from the frequency spectra are shown in figure 8. The scatter hides any trends with downstream distance. The normal-component length scale L_v decreases monotonically towards the wall and appears to extrapolate to zero at the wall, in agreement with the theoretical solution. The transverse-component length scale L_w increases to a measured maximum amplification of 1·6 times the external value at the measurement position nearest the wall. This is consistent with the theory, which predicts a wall scale of twice the external-stream value. The longitudinal-component length scale L_u appears to rise slightly (5 %), then decreases monotonically

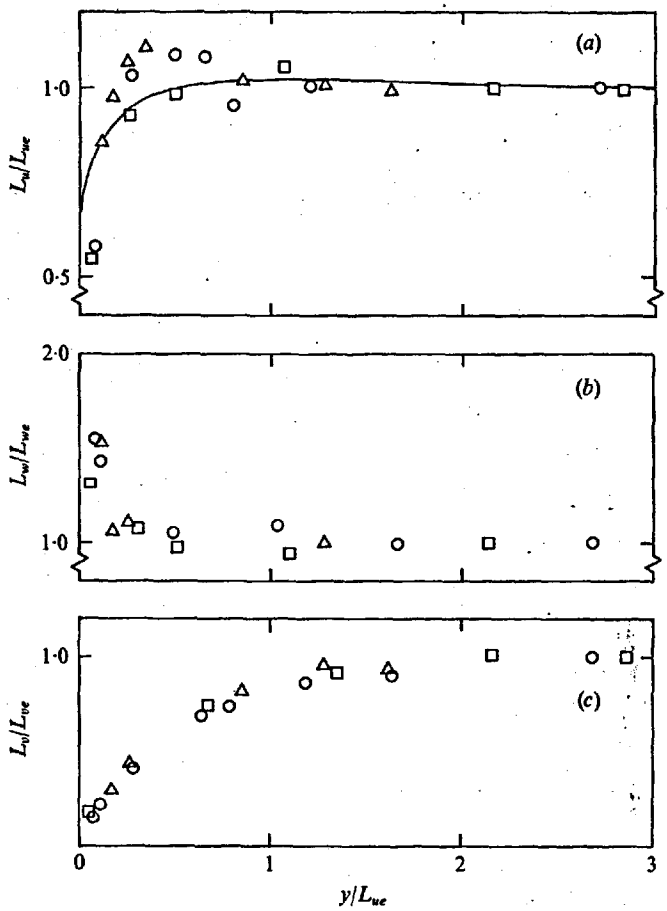

FIGURE 8. Longitudinal integral scales normalized on external-stream values as functions of y/L_{ue}. (*a*) L_u/L_{ue}. (*b*) L_w/L_{we}. (*c*) L_v/L_{ve}. △, $x/M = 13$, $L_{ue}/M = 0{\cdot}393$, $L_{we}/M = 0{\cdot}157$, $L_{ve}/M = 0{\cdot}157$; □, $x/M = 22$, $L_{ue}/M = 0{\cdot}583$, $L_{we}/M = 0{\cdot}233$, $L_{ve}/M = 0{\cdot}233$; ○, $x/M = 25$, $L_{ue}/M = 0{\cdot}633$, $L_{we}/M = 0{\cdot}253$, $L_{ve}/M = 0{\cdot}253$; ——, theory of Hunt & Graham (1978).

to a measured minimum of $0{\cdot}5\,L_{ue}$. The theoretical result is shown to be in reasonable agreement for $y/L_{ue} > 0{\cdot}1$ but the theoretical value at the wall is $\frac{2}{3}L_{ue}$.

One-dimensional frequency spectra are displayed in figure 9. In agreement with the theory, the high frequency ranges are relatively unaffected by the presence of the wall, with the exception of the longitudinal component within an inner region of thickness approximately $0{\cdot}25L_{ue}$, where the energy density grows towards the wall and increases with downstream distance. The dominant characteristic of the low frequency range is the decrease in the normal-component energy towards the wall, which is in good agreement with the theoretical solution. The gain in low frequency energy density of the transverse component also conforms with the theory, but the reduction found in the intermediate frequency range is not predicted. The low frequency energy density of the longitudinal component increases towards the wall and then decreases within the inner region referred to above, while the theoretical solution predicts the low frequency asymptote to be independent of the normal distance y. The results at $13M$ generally support the theory.

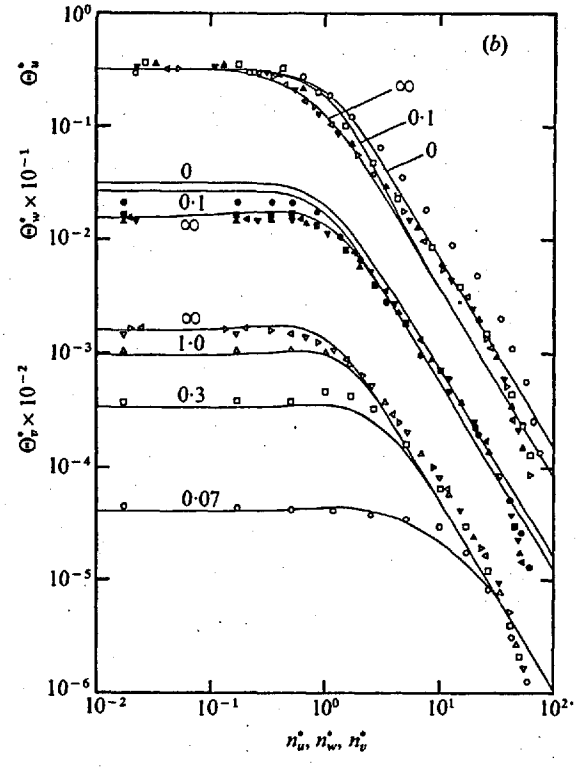

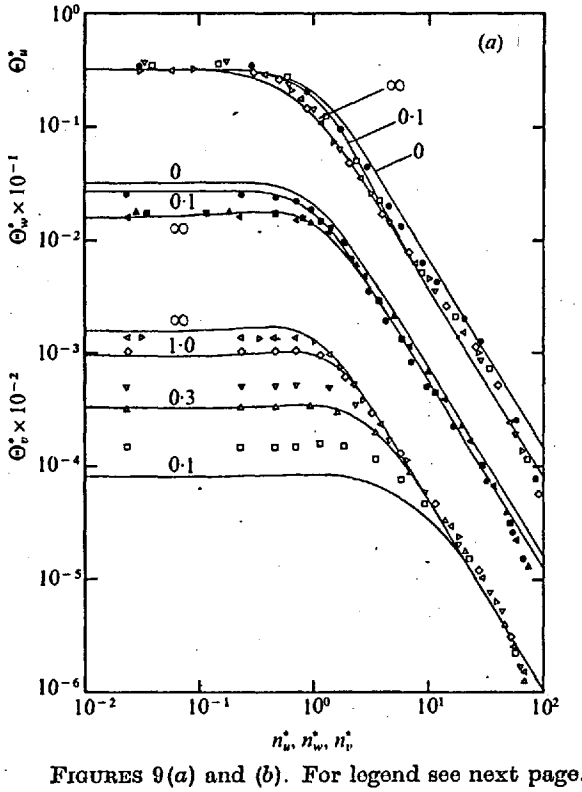

FIGURES 9(*a*) and (*b*). For legend see next page.

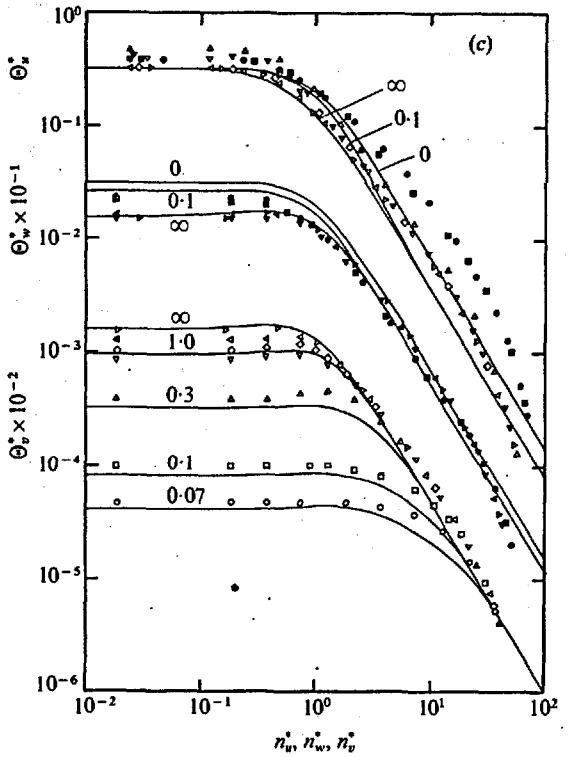

FIGURE 9. Normalized frequency spectra

$$\Theta_u^* = \overline{u}\Theta_u/4\pi\overline{u_e'^2}L_{ue}, \quad \Theta_w^* = \overline{u}\Theta_w/8\pi\overline{w_e'^2}L_{we}, \quad \Theta_v^* = \overline{u}\Theta_v/8\pi\overline{v_e'^2}L_{ve}$$

as functions of the normalized frequencies

$$n_u^* = 2\pi nL_{ue}/\overline{u}, \quad n_w^* = 4\pi nL_{we}/\overline{u}, \quad n_v^* = 4\pi nL_{ve}/\overline{u} \text{ respectively.}$$

(*a*) $x/M = 13$. (*b*) $x/M = 22$. (*c*) $x/M = 25$. ——, theory of Hunt & Graham (1978).

		○	□	△	▽	◇	◁	▷	●	■	▲	▼	◀	▶
y/L_{ue}	(*a*)		0·166	0·255	0·340	0·851	1·28	1·63	0·111	0·170	0·251		1·28	
	(*b*)	0·057	0·256	0·674	1·34		2·16	2·84	0·057	0·297	0·506	1·09	2·14	
	(*c*)	0·047	0·107	0·283	0·647	0·802	1·20	2·78	0·080	0·102		0·497	1·05	2·73

4. Discussion

The present configuration, in contrast to that used by Uzkan & Reynolds, has a bleed duct upstream of the moving wall and this ensures removal of any 'horseshoe' trailing vortex structures arising where the tunnel boundary layer flows between the bars of the grid. Uzkan & Reynolds' measurements do not establish the degree of uniformity of the mean flow close to the surface at the downstream study stations. Cooke's measurements near a wind-tunnel wall may also have been influenced by the presence of horseshoe vortices. On the other hand, the present arrangement may have introduced some small streamline curvature in the entry zone and an associated turbulence distortion field. No flow measurements were taken in this region but the short entry length, the tuft-probe observations and the low turbulence levels obtained at the measuring stations in the absence of the grids suggest that any downstream influence

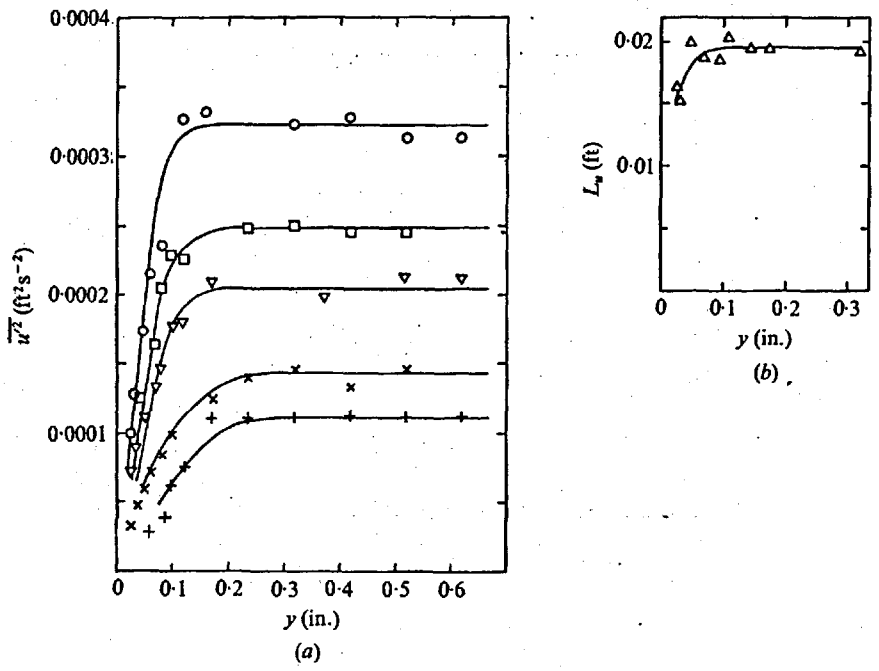

FIGURE 10. Turbulence measurements by Uzkan & Reynolds (1967). (*a*) $\overline{u'^2}$ (from Uzkan & Reynolds 1967, figure 13). $\bar{u} = 0{\cdot}315$ ft s^{-1}: ○, $x/M = 7{\cdot}5$; ▽, 12·5; ×, 15·0; +, 17·5. $\bar{u} = 0{\cdot}330$ ft s^{-1}: □, $x/M = 11{\cdot}5$. (*b*) L_u (from Uzkan & Reynolds 1967, figure 18): △, $x/M = 7{\cdot}5$.

is negligible. Graham's and Petty's measurements near a flat plate are subject to similar uncertainties about the downstream effects of distortion near the leading edge.

Uzkan & Reynolds presented variances, scales and spectra of the longitudinal component obtained in a nominally shear-free water flow at a mesh Reynolds number $R_M \simeq 5000$. Figure 10 reproduces their figure 13 (with the abscissa scale corrected for misprints) and their figure 18. In contrast to the present results, the $\overline{u'^2}$-component profiles decline monotonically towards the wall. Uzkan & Reynolds took this as confirmation of a satisfactory matching of the wall and stream speeds and inferred a viscous scaling for the wall layer, with thickness $\delta_v \simeq 1{\cdot}8(x'\nu/\bar{u})^{\frac{1}{2}}$, where x' is measured from the start of the layer. Their integral-scale profile is comparable with those currently obtained but the absolute values appear to be small, giving $L_{ue}/M \simeq 0{\cdot}12$. An expected value obtained from the survey of Naudascher & Farrell (1970) and giving $L_{ue}/M \simeq 0{\cdot}4$ at $x/M = 16$ indicates that for Uzkan & Reynolds' study $\delta_v/L_{ue} \simeq 0{\cdot}25$. The current results have shown that the total wall-layer thickness is approximately $2L_{ue}$, so it appears that for Uzkan & Reynolds' experiment there was, as they suggested, a substantial outer kinematic field. Using the above expression for δ_v, we find that in the present experiment, in which R_M was approximately 20 times Uzkan & Reynolds' value, $\delta_v/L_{ue} \simeq 0{\cdot}05$. This implies that all our measurements were taken outside the viscous layer, which is consistent with the results obtained. Hunt & Graham discussed a generally successful reconciliation of the two sets of results with arguments stemming from their two-layer analysis. However, their solution does not adequately describe the evolution of the u' component observed in the present experiment, and we now consider this development.

In the absence of gradients of mean velocity, the Reynolds mean momentum equations are

$$\frac{\partial}{\partial x}(\bar{p}+\overline{u'^2})+\frac{\partial}{\partial y}\overline{u'v'}=0, \quad \frac{\partial}{\partial y}(\bar{p}+\overline{v'^2})+\frac{\partial}{\partial x}\overline{u'v'}=0,$$

where $\bar{p}$ is the 'kinematic' pressure. Noting that the spatial derivatives $\partial/\partial x$ and $\partial/\partial y$ operating on the time-averaged variables are of orders $[(\overline{u'^2})^{\frac{1}{2}}/\bar{u}]\ L_{ue}^{-1}$ and L_{ue}^{-1} and neglecting terms $O(\overline{u'^2}/\bar{u}^2)$, these equations may be combined to give

$$\frac{\partial}{\partial x}(\overline{u'^2}-\overline{v'^2})+\frac{\partial}{\partial y}\overline{u'v'}=\frac{\partial}{\partial x}(\overline{u_e'^2}-\overline{v_e'^2}).$$

It is easily demonstrated that this equation holds for any irrotational mean velocity field. However, without additional information it merely relates three components of the Reynolds-stress tensor. Values of $\overline{u'v'}$ calculated from the current experimental data were found to be too small to be reliable. We adopt the strategy of assuming a sufficiently large Reynolds number $Re=(\overline{u_e'^2})^{\frac{1}{2}}L_{ue}/\nu$ for validity of Hunt & Graham's solution for the v' component, which is supported by the present results, and then consider the implied limiting responses of $\overline{u'^2}$ and $\overline{u'v'}$. This essentially heuristic procedure indicates a plausible closure equation for $\overline{u'v'}$ in terms of the known $\overline{v'^2}$ field, with magnitude dependent on Re; the latter is presumably the dominant parameter distinguishing Uzkan & Reynolds' experiment from the present one. We can then calculate the implied evolution of the $\overline{u'^2}$ field.

The continuity equation suggests that $(\overline{v'^2})^{\frac{1}{2}}(y=\delta_v)\sim\delta_v(\overline{u_e'^2})^{\frac{1}{2}}/L_{ue}$, so for a substantial outer region it is necessary that $\delta_v/L_{ue}\ll 1$ and for the v' field to be essentially kinematic everywhere, $(\overline{u_e'^2})^{\frac{1}{2}}\delta^2/\nu L_{ue}\gg 1$, or $Re\,(\delta_v/L_{ue})^2\gg 1$. Uzkan & Reynolds' experimental results show $\delta_v/L_{ue}\simeq 0{\cdot}25$ at $Re\simeq 100$, while the present experiment with grid A gives $\delta_v/L_{ue}\simeq 0{\cdot}05$ at $Re\simeq 2000$ and that with grid B gives $\delta_v/L_{ue}\simeq 0{\cdot}04$ at $Re\simeq 4000$. It appears that for all the experiments $\delta_v/L_{ue}\simeq(6/Re)^{\frac{1}{2}}$.

If $\overline{u'v'}$ is sufficiently small for the approximation

$$\frac{\partial}{\partial x}(\overline{u'^2}-\overline{u_e'^2})=\frac{\partial}{\partial x}(\overline{v'^2}-\overline{v_e'^2})$$

to be valid then the decay rate of $\overline{u'^2}$ is reduced near the wall, which is consistent with the present results. On the other hand, Uzkan & Reynolds' results for the outer region show $\overline{u'^2}\simeq\overline{u_e'^2}$, in which case the equation approximates to

$$\frac{\partial}{\partial y}\overline{u'v'}=\frac{\partial}{\partial x}(\overline{v'^2}-\overline{v_e'^2}).$$

Taking both these limits into consideration, we propose as a closure equation

$$\frac{\partial}{\partial y}\overline{u'v'}=f(Re)\frac{\partial}{\partial x}(\overline{v'^2}-\overline{v_e'^2}),$$

where $f(Re\to\infty)\to 0$ and $f(Re\simeq 100)\simeq 1$. For an estimation of the form of $f(Re)$, we assume a viscous scale for $\overline{u'v'}$ given by $(\overline{u'^2v'^2})^{\frac{1}{2}}(y=\delta_v)\simeq\overline{u_e'^2}\,\delta_v/L_{ue}$, which is proportional to $Re^{-\frac{1}{2}}\overline{u_e'^2}$. This suggests that the magnitude of $\overline{u'v'}$ is an order smaller than in a fully turbulent shear layer and so accounts for the unreliability of the present

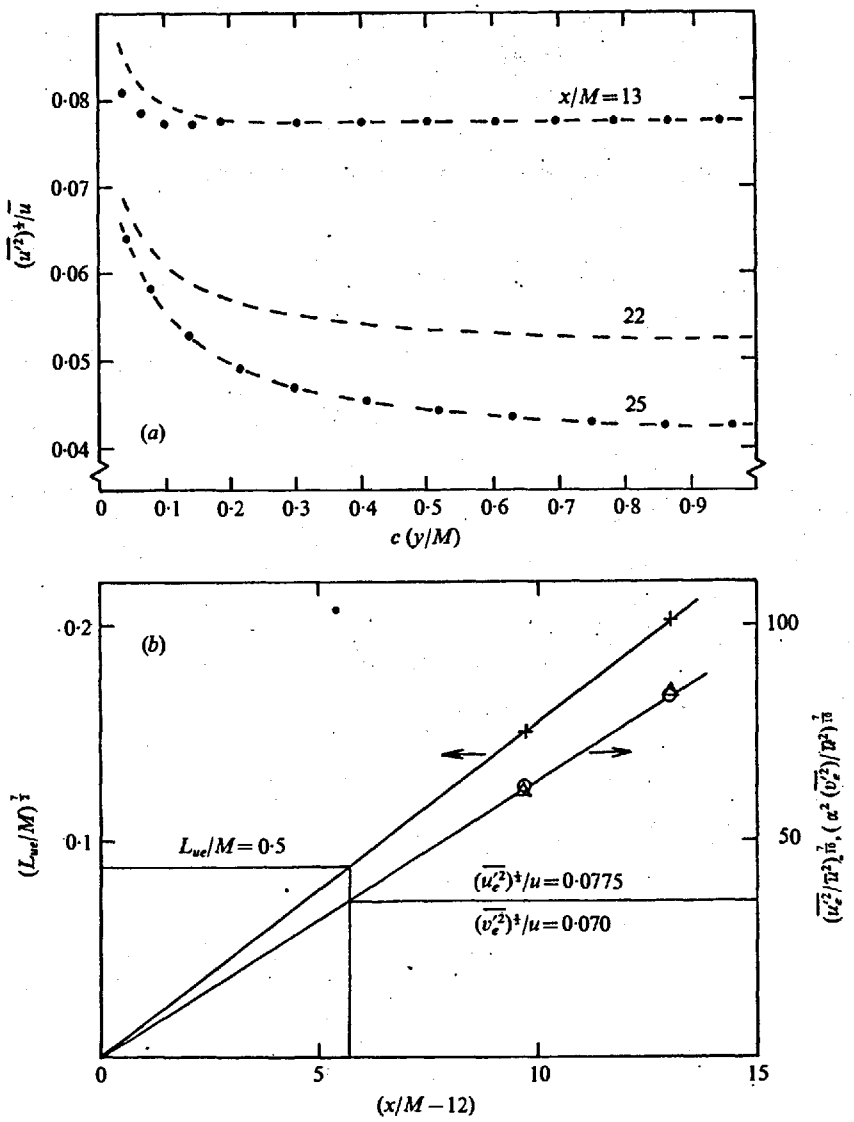

FIGURE 11. (*a*) Turbulence intensity $(\overline{u'^2})^{\frac{1}{2}}/\bar{u}$: ●, calculated from the model equation; – –, experimental values; $c = 1$ for grid A, $c = (L_{ue}/M)_A (L_{ue}/M)_B^{-1}$ for grid B. (*b*) Energy decay and length-scale growth for the turbulence generated by grid A compared with the Kolmogorov '$\frac{10}{7}$' decay law: ○, $\overline{u_e'^2}/\bar{u}^2$; △, $\overline{v_e'^2}/\bar{u}^2$; $\alpha = (\overline{u_e'^2}/\overline{v_e'^2})^{\frac{1}{2}} = 1·11$.

experimental values. The assumed scaling indicates that an appropriate choice is $f \propto Re^{-\frac{1}{2}}$ and substitution in the closure proposal yields

$$\frac{\partial}{\partial y}\overline{u'v'} \simeq 10Re^{-\frac{1}{2}}\frac{\partial}{\partial x}(\overline{v'^2} - \overline{v_e'^2}).$$

Figure 11 (*a*) shows the calculated values of $(\overline{u'^2})^{\frac{1}{2}}/\bar{u}$ at $x/M = 25$ for $Re = 2000$ obtained using the faired experimental profile at $x/M = 22$ as the initial curve. Excellent agreement with the experimental results is demonstrated. Figure 11 (*b*) shows

that, in the external stream, the variances and the length scales of the turbulence generated by grid A are described near the test stations by the Kolmogorov '$\frac{10}{7}$' energy decay law (Comte-Bellot & Corrsin 1966) with a single virtual origin at $x/M \simeq 12$. Extrapolation suggests that the external-stream variances found at $x/M = 13$ with grid B would be obtained at $x/M = 18$ with grid A and that the length scale would be $0{\cdot}5M$. As a further test of the model, figure 11(a) shows the inferred profile at $x/M = 18$ calculated from the data at $x/M = 22$, and the experimental results obtained with grid B. The normal co-ordinate y has been stretched in an effort to accommodate the different length scales. Although a comparison is not strictly admissible, the model follows the experimental trends: the amplification and the boundary-region thickness of the u' component are reduced.

The u'-component spectra demonstrated that the transferred energy resides in the intermediate and high frequency ranges. A reduction of this energy with decreasing Re, as supposed in the model, is consistent with these spectral observations. The model does not explain the departures from the theory of the w' component, but the spectra showed that these occur mainly in the intermediate and high frequency ranges, so they may be related to the development of the u' component.

5. Conclusions

At high Reynolds numbers, the outer region of a turbulent boundary region with zero mean shear scales on the external turbulence parameters. The normal fluctuating component is inhibited within a layer of characteristic thickness about twice the external longitudinal integral length scale. The profiles of this component are in good agreement with the theoretical solution given by Hunt & Graham. The amplification of the longitudinal component is also in accordance with the theory and in marked contrast to the essentially viscous response observed by Uzkan & Reynolds at about one-tenth of the present mesh Reynolds number. In terms of the microscale Reynolds number $R_\lambda = (\overline{u_e'^2})^{\frac{1}{2}} \lambda/\nu$, the present experiment, with $R_\lambda \simeq 120$, as opposed to Uzkan & Reynolds' experiment, with $R_\lambda \simeq 25$, should be typical of all high Reynolds number flows, with $R_\lambda > 100$, say. The longitudinal component shows a downstream development not predicted by the theory but plausibly described by a model of the dynamical equation incorporating Uzkan & Reynolds' experimental results. The lateral component appears to be only weakly influenced by the wall and its behaviour remains to be explained.

The integral length scales of the three fluctuating components are generally in agreement with the theoretical solution, with the exception of the longitudinal component near the wall. The latter is smaller than is predicted.

The spectra tend to confirm the *prima facie* expectation that the smaller eddies will be less influenced by the wall than the larger ones. The normal-component spectra are in good agreement with the theory. The increase in the longitudinal-component variance is associated with the intermediate and higher frequency ranges, as is the reduced variance of the lateral component. The generally reasonable agreement in the low frequency ranges is satisfying since the premises of the theory, such as second-order weak interactions, are more adequately met.

We are grateful to Dr P. W. Bearman and Mr P. Bradshaw for their valuable advice during this study. Acknowledgement is made to the Science Research Council, who supported this work. P. E. Hancock was in receipt of a Science Research Council maintenance grant.

REFERENCES

BRADSHAW, P. 1974 Effects of free-stream turbulence on turbulent shear layers. *Imperial College Aero. Rep.* no. 74-10.

COMTE-BELLOT, G. & CORRSIN, S. 1966 The use of a contraction to improve the isotropy of grid-generated turbulence. *J. Fluid Mech.* **25**, 657.

DAVIES, M. E. 1974 Spectral analysis programs Powspec and Cophase. *Imperial College Aero. Tech. Note* no. 74-103.

GRAHAM, J. M. R. 1975 Turbulent flow past a long flat plate. *Imperial College Aero. Tech. Note* no. 75–101.

GREEN, J. E. 1972 On the influence of free stream turbulence on a turbulent boundary layer as it relates to wind tunnel testing at subsonic speeds. *R.A.E. Tech. Rep.* no. 72201.

HANCOCK, P. E. & THOMAS, N. H. 1977 Grid turbulence near a moving wall. *Imperial College Aero. Note* (to be published).

HUNT, J. C. R. & GRAHAM, J. M. R. 1978 Free-stream turbulence near plane boundaries. To be published.

NAUDASCHER, E. & FARELL, C. 1970 Unified analysis of grid turbulence. *Trans. A.S.C.E.* **96** (EM2), 121.

UZKAN, T. & REYNOLDS, W. C. 1967 A shear-free turbulent boundary layer. *J. Fluid Mech.* **28**, 803.

APPENDIX 2

HODOGRAPHS FOR LEADING EDGE SHAPES

A2.1 Sharp leading edge

Figure A2.1a illustrates the stagnation streamline AB, the streamline BCD defining the leading edge shape itself, and the flat plate DE. α is the apex half angle. Figure A2.1b shows the streamline ABCDE in the complex velocity plane, q. Applying the transformation

$$p = q^{\pi/2\alpha} \tag{A2.1.1}$$

gives the streamline pattern shown in figure A2.1c where the streamline bifurcation angles at B are $\pm\pi/2$. The simplification that 'length AB = length DE' and BCD be semi-circular was made to the p-plane streamline pattern. Putting $U_e = 1$ and transforming as follows

$$t = 1/(p - 1) \tag{A2.1.2}$$

$$s = t + 1/t \tag{A2.1.3}$$

gives the pattern shown in figure A2.1e. Thus,

$$q = \left(\frac{\sqrt{s + 2} + \sqrt{s - 2}}{\sqrt{s + 2} - \sqrt{s - 2}} + 1 \right)^{2\alpha/\pi} \tag{A2.1.4}$$

Now $q^* = dW/dz$ where $W = \phi + i\psi$ is the complex potential. (q^* is the complex conjugate of q.) Replacing s by W and putting $\psi = 0$ gives

$$dz = \frac{1}{2} (\phi + 2 - i \sqrt{\phi + 2}\ \sqrt{\phi - 2})^{-2\alpha/\pi}\, d\phi, \tag{A2.1.5}$$

and on using $4\cos^2\theta = \phi + 2$ yields

$$dx = (\cos\theta)^{(1-2\alpha/\pi)} \cos\left(\frac{2\alpha\theta}{\pi}\right) \sin\theta\, d\theta, \tag{A2.1.6}$$

and

$$dy = (\cos\theta)^{(1-2\alpha/\pi)} \sin\left(\frac{2\alpha\theta}{\pi}\right) \sin\theta\, d\theta. \tag{A2.1.7}$$

$\theta = 0$ and $\pi/2$ correspond to the points B and D respectively.

Equations A2.1.6 and A2.1.7 were integrated numerically using the trapesoidal rule with sufficiently small increment

(most important near point B) for $\alpha = 10^o$ (leading edge A) and $\alpha = 25^o$ (leading edge B). The profile shapes and coordinates are given in figure A2.3. The maximum velocity occurs at D and is given by $U_D = U_e \times 2^{2\alpha/\pi}$; for $\alpha = 10^o$ $U_D/U_e = 1.08$ and for $\alpha = 25^o$ $U_D/U_e = 1.21$.

A2.2 Rounded leading edge

Figure A2.2a illustrates the stagnation streamline AB, the streamline BCD defining the leading edge shape itself, and the flate plate DE. Figure A2.2b shows the streamline ABCDE in the complex velocity plane, q. The parameter η is defined by $\eta = U_D/U_e$ where U_D is the velocity at D. Putting $U_e = 1$ and transforming as follows

$$p = q - 1$$

$$t = 1/p$$

gives the streamline pattern shown in figure A2.2C. Transforming by

$$t' = t + \frac{1}{2}\left(1 - \frac{1}{\eta - 1}\right)$$

and, assuming BCD to be semi-circular, transforming again using

$$s = t' + \frac{a}{t'}$$

gives the streamline pattern shown in figure A2.2d, where

$$a = \frac{1}{2}\left(1 + \frac{1}{\eta - 1}\right)^2 .$$

Hence $$q = 1 + (\eta - 1)\left(\frac{\sqrt{s + 2a} - \sqrt{s - 2a}}{\sqrt{s + 2a} + (\eta - 1)\sqrt{s - 2a}}\right).$$

Putting $s = W = \phi + i\psi$ and considering only $\psi = 0$ gives, after some manipulation

$$dx = \frac{1}{\eta}\, d\phi,$$

and $$dy = \left(\frac{\eta - 1}{\eta}\right)\sqrt{\frac{2 - \phi}{\phi + 2}}\, d\phi \cdot$$

for which an explicit solution exists,

$$y = (\eta - 1)\left[\sqrt{x\left(\frac{4}{\eta} - x\right)} + \frac{4}{\eta}\tan^{-1}\left(\sqrt{x\left(\frac{4}{\eta} - 1\right)}\right)\right] ,$$

where $0 \leq x \leq 4/\eta$. The Rounded leading edge (leading edge C) was designed to 'match' leading edge A by specifying $\eta = 1.08$. The profile shape and coordinates are given in figure A2.3.

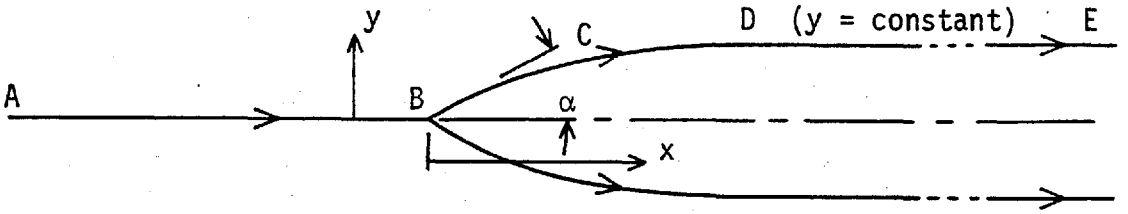

a) Stagnation (AB) and leading edge (BCD) streamlines (z-plane)

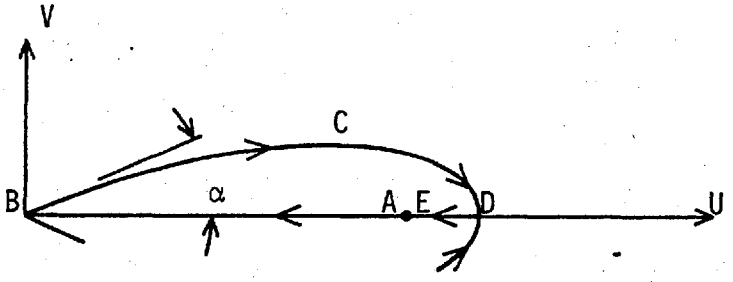

b) Velocity plane (q-plane)

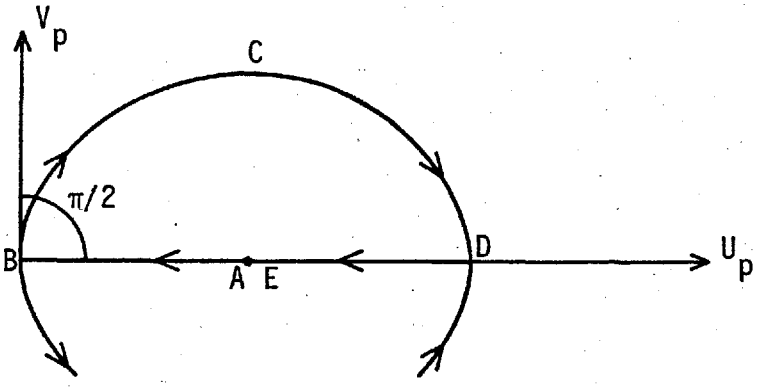

c) p-plane

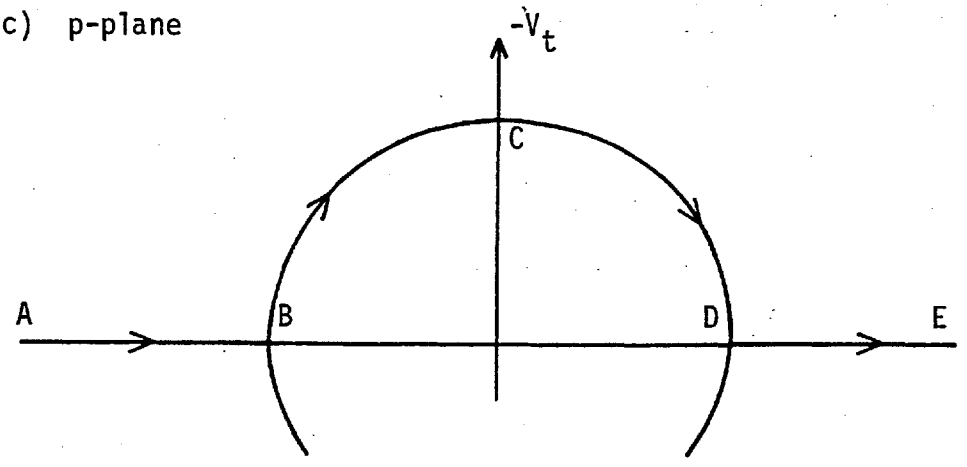

d) t-plane

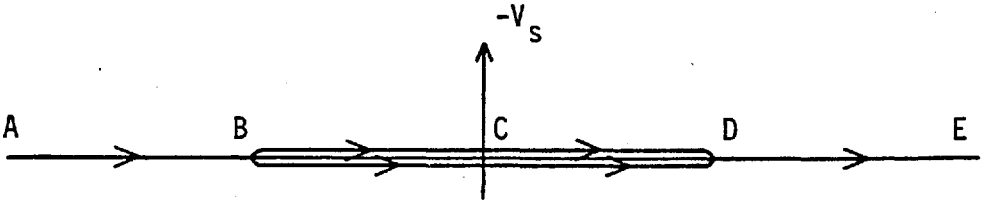

e) s-plane

Fig. A2.1 Hodograph for sharp leading edge.

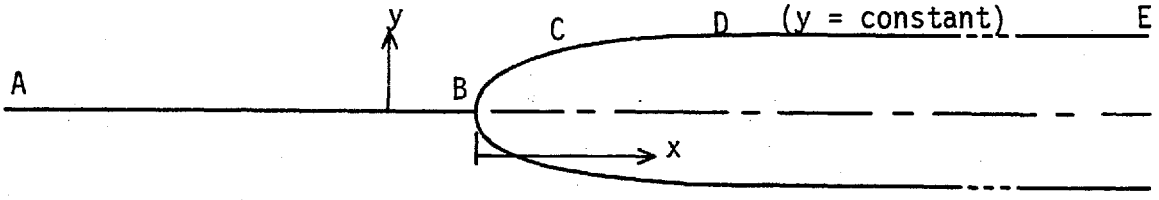

a) Stagnation (AB) and leading edge (BCD) streamlines (z-plane)

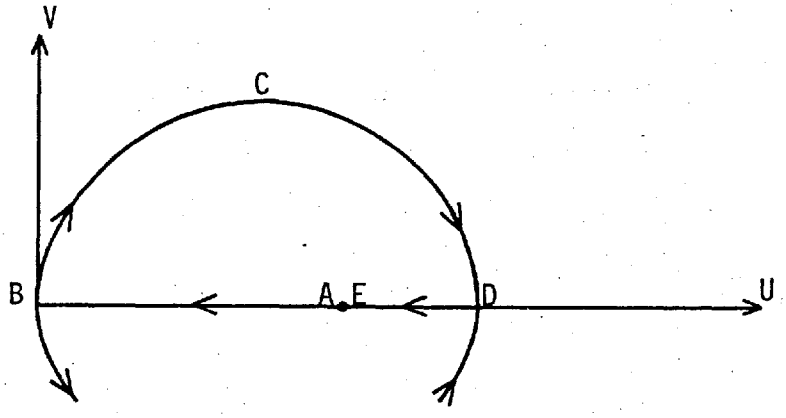

b) Velocity plane (q-plane)

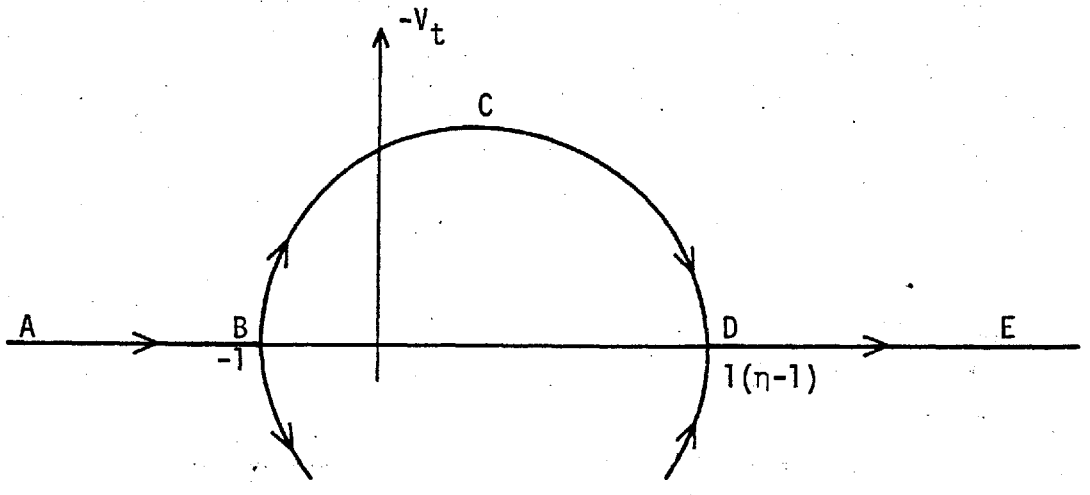

c) t-plane

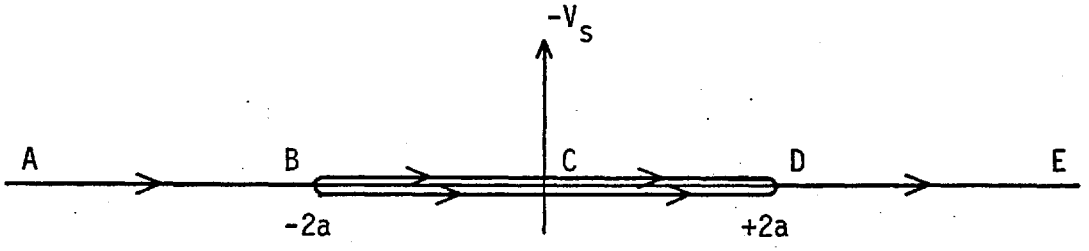

d) s-plane

Fig. A2.2 Hodograph for rounded leading edge

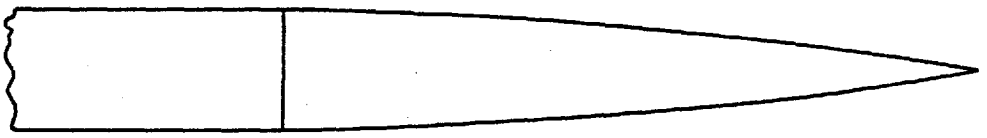

a) $\alpha = 10^{o}$

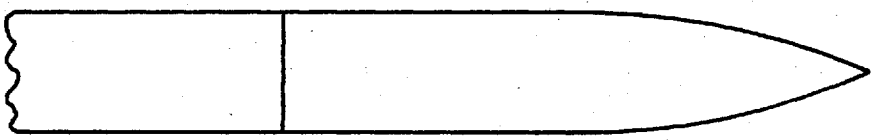

b) $\alpha = 25^{o}$

c) Rounded

Leading edge a):

x(mm)	0	2.90	7.09	15.9	24.9	34.1	43.5	53.0
y(mm)	0	0.46	1.07	2.22	3.28	4.24	5.12	5.89
	62.6	72.2	82.0	91.4				
	6.57	7.13	7.56	7.77				

Leading edge b):

x(mm)	0	3.07	4.93	7.24	9.73	12.4	15.1	17.9
y(mm)	0	1.27	1.80	2.74	3.51	4.27	4.98	5.64
	20.6	23.2	25.6	29.6	32.2	33.1	76.2	
	6.20	6.68	7.06	7.54	7.75	7.77	7.77	

Leading edge c):

x(mm)	0	0.25	1.27	2.54	5.08	7.62	12.7	17.8
y(mm)	0	0.64	1.42	1.98	2.79	3.40	4.32	5.05
	25.4	38.1	50.8	66.0				
	5.87	6.88	7.52	7.77				

Fig. A2.3 Leading-edge profiles.

APPENDIX 3

EFFECT OF HOT-WIRE ANGLE ERRORS ON MEAN VELOCITY AND MOMENTS OF FLUCTUATING VELOCITY

Generally, an error in one or both wire angles implies an error in U and V (or U and W). Here, U and V are used to denote total instantaneous velocities. In the present case the equation

$$E^2_{1,2} = E^2_{0,1,2} + B_{1,2}\,(U \pm V \tan \psi_{eff_{1,2}})^{0.45} \qquad \text{(A3.1)}$$

was used to evaluate U and V. Thus the corrected and uncorrected velocities are related by

$$U'' \pm V'' \tan \psi''_{1,2} = U' \pm V' \tan \psi'_{1,2}\ , \qquad \text{(A3.2)}$$

where double and single primes denote corrected and uncorrected quantities respectively. Effective wire angles are assumed throughout. It follows from equation A3.2 that

$$u'' \pm v'' \tan \psi''_{1,2} = u' \pm v' \tan \psi'_{1,2} \qquad \text{(A3.3)}$$

From equations A3.2 and A3.3

$$U'' = U' + V' \times C_1 \qquad V'' = V' \times C_2\ , \qquad \text{(A3.4a,b)}$$

and

$$u'' = u' + v' \times C_1 \qquad v'' = v' \times C_2\ , \qquad \text{(A3.5a,b)}$$

where $C_1 = (\tan\psi''_2 \tan\psi'_1 - \tan\psi''_1 \tan\psi'_2)/(\tan\psi''_1 + \tan\psi''_2)$, (A3.6)

and $C_2 = (\tan\psi'_1 + \tan\psi'_2)/(\tan\psi''_1 + \tan\psi''_2)$. (A3.7)

So, for example

$$\begin{aligned}
\overline{u^{2''}} &= \overline{u^{2'}} + C_1^2\,\overline{v^{2'}} + 2C_1\,\overline{uv'} \\
\overline{v^{2''}} &= C_2^2\,\overline{v^{2'}} \\
\overline{uv''} &= C_2\,\overline{uv'} + C_1 C_2\,\overline{v^{2'}}
\end{aligned} \qquad \text{(A3.8)}$$

and

$$\begin{aligned}
\overline{u^{3''}} &= \overline{u^{3'}} + 3C_1\,\overline{u^2 v'} + 3C_1^2\,\overline{uv^{2'}} + C_1^3\,\overline{v^{3'}} \\
\overline{u^2 v''} &= C_2\,\overline{u^2 v'} + 2C_1 C_2\,\overline{uv^{2'}} + C_1^2 C_2\,\overline{v^{3'}} \\
\overline{uv^{2''}} &= C_2^2\,\overline{uv^{2'}} + C_1 C_2\,\overline{v^{3'}} \\
\overline{v^{3''}} &= C_2^3\,\overline{v^{3'}} \\
&\text{etc.}
\end{aligned} \qquad \text{(A3.9)}$$

Note that $B_{1,2}$ are dependent upon probe alignment and were always evaluated (in the free-stream) for each setting of the probe rotation (ϕ) whereas $\psi_{eff_{1,2}}$ were not. When $B_{1,2}$ are not evaluated in the measuring position the above analysis should be repeated using $U''\cos\psi''_{1,2} \pm V''\sin\psi''_{1,2} = U'\cos\psi'_{1,2} \pm V'\sin\psi_{1,2}$.

APPENDIX 4

MEASUREMENT OF MOMENTS OF FLUCTUATING VELOCITY CONTAINING NORMAL AND TRANSVERSE COMPONENTS : a method of measuring probe rotation ϕ.

A X-wire probe with its body aligned parallel with the x-axis is sensitive to the velocity fluctuations

u, and $(v \cos\phi + w \sin\phi)$.

ϕ is the angle of rotation of the probe about its body axis. Thus, the second-order products become

$$\overline{u^2} \quad , \quad (\overline{uv} \cos\phi + \overline{uw} \sin\phi),$$

$$\text{and } (\overline{v^2} \cos^2\phi + 2\overline{vw} \cos\phi \sin\phi + \overline{w^2} \sin^2\phi),$$

and the third-order products become

$$\overline{u^3} \quad , \quad (\overline{u^2v} \cos\phi + \overline{u^2w} \sin\phi),$$

$$(\overline{uv^2} \cos^2\phi + 2\overline{uvw} \cos\phi \sin\phi + \overline{uw^2} \sin^2\phi),$$

$$\text{and } (\overline{v^3} \cos^3\phi + 3\overline{v^2w} \cos^2\phi \sin\phi + 3\overline{vw^2} \cos\phi \sin^2\phi + \overline{w^3} \sin^3\phi),$$

and so on for still higher products. Assuming that $\overline{v^2}$ and $\overline{w^2}$ are already known ($\phi = 0$ and $\phi = \pi/2$ respectively) the evaluation of $\overline{vw}$ requires only one additional value of ϕ. When $\overline{u^2v}$, $\overline{v^3}$, $\overline{u^2w}$ and $\overline{w^3}$ are known, $\overline{v^2w}$ and $\overline{vw^2}$ require two additional but different values of ϕ. It is usual to choose ϕ close to $\pm\pi/4$. In the case of a two-dimensional flow or flow on a plane of symmetry $\overline{uw}$, $\overline{vw}$, $\overline{u^2w}$, $\overline{uvw}$ and $\overline{v^2w}$ would be expected to be zero.

A small number of measurements of $\overline{vw^2}$ were made but as the data was rather scattered and confused by erroneous measurements of $\overline{w^3}$ (discussed in chapter 4) they are not presented. However, it seems worth recording the method by which ϕ was measured.

Rather than measure ϕ geometrically, it having been set approximately to $+45^\circ$ or -45°, ϕ was measured using a method similar to that used to measure the effective wire angles, $\psi_{eff_{1,2}}$ (with $\phi = \pi/2$). In the present sense ϕ is <u>not</u> an effective angle for the same reasons that ψ_{eff} is an effective angle although such a method does average-

out any slight curvature of the hot-wires. Furthermore, in the analysis of the measurements presented in the main body of the thesis, it has been assumed that the hot-wires were parallel in the sense that ϕ was assumed equal for both. Obviously it is unlikely that ϕ will be exactly the same for each wire. In the example given later the error in assuming ϕ to be equal for both wires is negligible.

Consider the probe to be aligned parallel with the x-axis, rotated about its own axis so that $\phi \approx 45^{o}$ (say), and positioned in the free stream. Rotating the probe about the y-axis by an angle $\Delta\eta$ - in the present case $\Delta\eta = \pm 4.67n$ where n = 1, 2, 3 - gives a velocity, U', along the probe axis

$$U' = U \cos\Delta\eta \tag{A4.1}$$

and a velocity, W', normal to the probe axis and parallel to the plate

$$W' = U \sin\Delta\eta \tag{A4.2}$$

Resolving this latter component with components V" and W" respectively in the plane of the wires and perpendicular to this plane, gives

$$V'' = W' \sin\phi, \tag{A4.3}$$

$$W'' = W' \cos\phi. \tag{A4.4}$$

The effective cooling velocity, U_{eff}, is then

$$U_{eff_{1,2}} = \left[W''^{2} + (U' \cos\psi_{eff_{1,2}} + V'' \sin\psi_{eff_{1,2}})^{2} \right]^{\frac{1}{2}} \tag{A4.5}$$

where $\psi_{eff_{1,2}}$ are the effective wire angles determined in the normal way (with $\phi = \pi/2$) and, if necessary, corrected for "pitch" as described in subsection 2.4.3. In the present discussion it is important in order to avoid confusion to retain signs for $\psi_{eff_{1,2}}$. Hence the sign of V" is shown only as positive. Substituting for U', V" and W"

$$U_{eff}^{2} = U^{2} \left[\sin^{2}\Delta\eta.\cos^{2}\phi + (\cos\Delta\eta.\cos\psi_{eff} + \sin\Delta\eta.\sin\phi.\sin\psi_{eff})^{2} \right] \tag{A4.6}$$

where suffices 1, 2 are understood. Using the identity $\cos^{2} + \sin^{2} \equiv 1$ this equation may be reduced to

$$U_{eff}^{2} = U^{2} \left[1 - (\sin\psi_{eff}.\cos\Delta\eta - \sin\phi.\cos\psi_{eff}.\sin\Delta\eta)^{2} \right] \tag{A4.7}$$

The author is indebted for assistance in this last step to Dr. A. Nakayama who has considered the same method of measuring ϕ but used a simpler method of determing U_{eff}. Substituting this last equation into the equation

$$E^2 = E_o^2 + \frac{B}{(\cos\psi_{eff})^n} (U_{eff})^n \qquad \text{(A4.8)}$$

gives

$$\frac{1}{\sin\psi_{eff}} \left[1 - \left(\frac{E^2 - E_o^2}{B\, U^n} \right)^{\frac{2}{n}} \cos^2\psi_{eff} \right]^{\frac{1}{2}} - \cos\Delta\eta = - \left(\frac{\sin\phi}{\tan\psi_{eff}} \right) \sin\Delta\eta \qquad \text{(A4.9)}$$

whereupon $(\sin\phi/\tan\psi_{eff})$ and hence ϕ may be determined. An example is shown in figure A4.1.

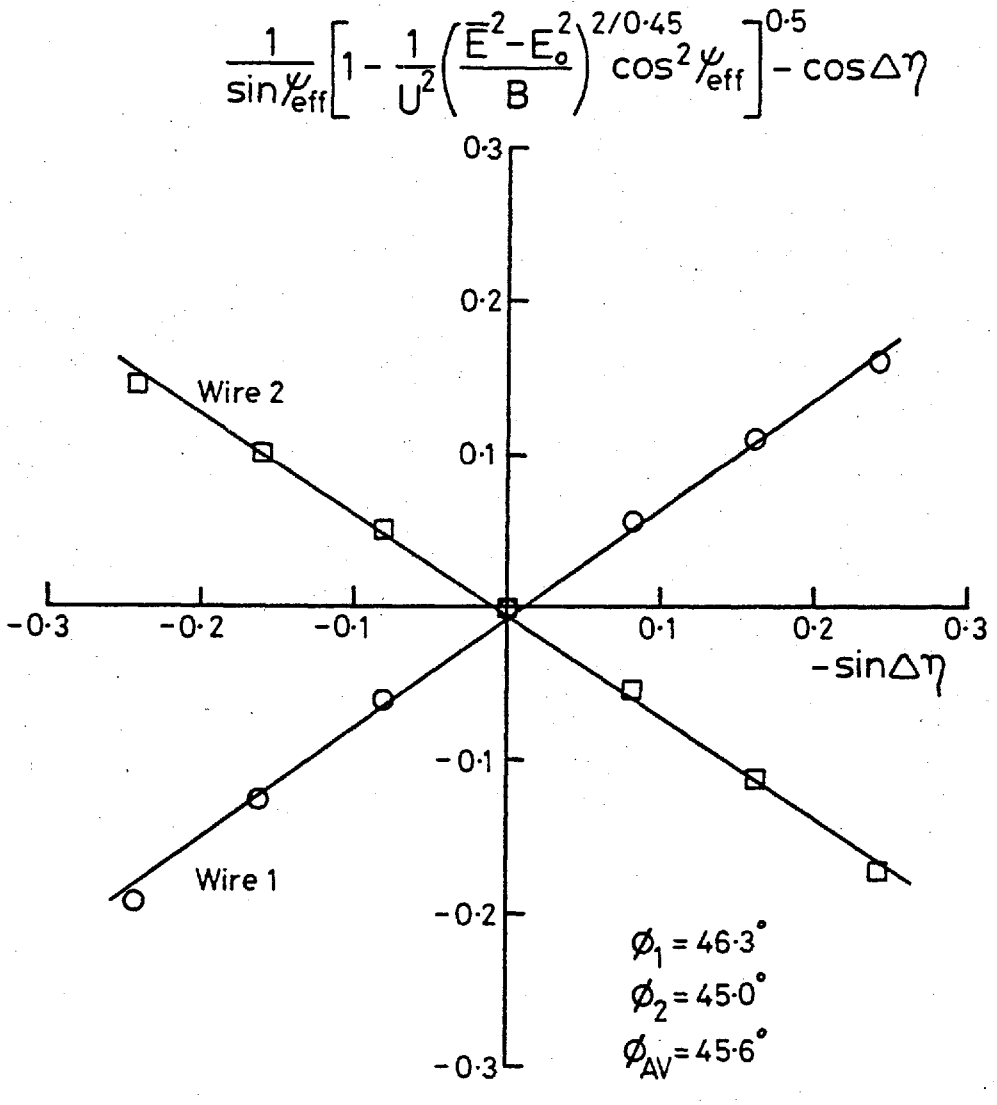

Fig. A4.1 Measurement of probe rotation ϕ. (Probe B in table 4.1).

APPENDIX 5

SUMMARY OF MEAN FLOW MEASUREMENTS FOR FREE-STREMM TURBULENCE GENERATORS CONSISTING OF A SINGLE ROW OF SQUARE BARS

Only three mean velocity profiles were obtained with the free-stream turbulence generator consisting of a single row of square bars. These are shown in figures A5.1 to A5.3, and the free-stream and boundary layer parameters are given in table A5.1. Figures A5.4 and A5.5 show the effect of free-stream turbulence generated by a single row of bars on the shape parameter H and on C_f, each compared at constant Re_θ. The spectrum measurements (chapter 3) downstream of the square-mesh biplane grids suggest that the 'irregular' portion of the spectra measured downstream of the grids of a single row of bars amounts to about 7% of $\overline{u^2}$. If this irregular portion of the spectra results in an effect on the boundary layer of the order of 7% of the total effect (due to the presence of the free-stream turbulence) large discrepancies between measurements obtained for either a biplane grid or a single row of bars are not to be expected.

STN	u'/U_e	L_e^u/δ_{995}	δ_{995}	δ^*	θ	U_e	Re_θ	$\frac{u_\tau \delta_{995}}{\nu}$	$C_f^{(1)}$	$C_f^{(2)}$	H	$\frac{k\Delta U}{2u_\tau}$	$\frac{y_{\Delta U}}{\delta_{995}}$	PROFILE NUMBER
7.6cm GENERATOR			X_{LE} = 0.305m			NO HEATING WIRES AT LEADING EDGE								
12	.0350	0.96	55.0	4.66	3.65	16.60	3980	2520	.00352	.00347	1.277	0.05	0.35	23
7.6cm GENERATOR			X_{LE} = 2.06m			NO HEATING WIRES AT LEADING EDGE								
12	.0226	1.80	38.1	4.91	3.65	16.45	3970	1660	.00321	.00321	1.344	0.35	0.84	14
15.2cm GENERATOR			X_{LE} = 2.06m			NO HEATING WIRES AT LEADING EDGE								
12	.0476	2.61	51.7	4.82	3.75	16.11	3990	2300	.00348	.00345	1.284	0.08	0.5	13

$C_f^{(1)}$ FROM LOG-LAW FIT

$C_f^{(2)}$ FROM PRESTON TUBE

TABLE A5.1 Boundary layer mean flow and free-stream turbulence parameters (Generators of a single row of square bars)

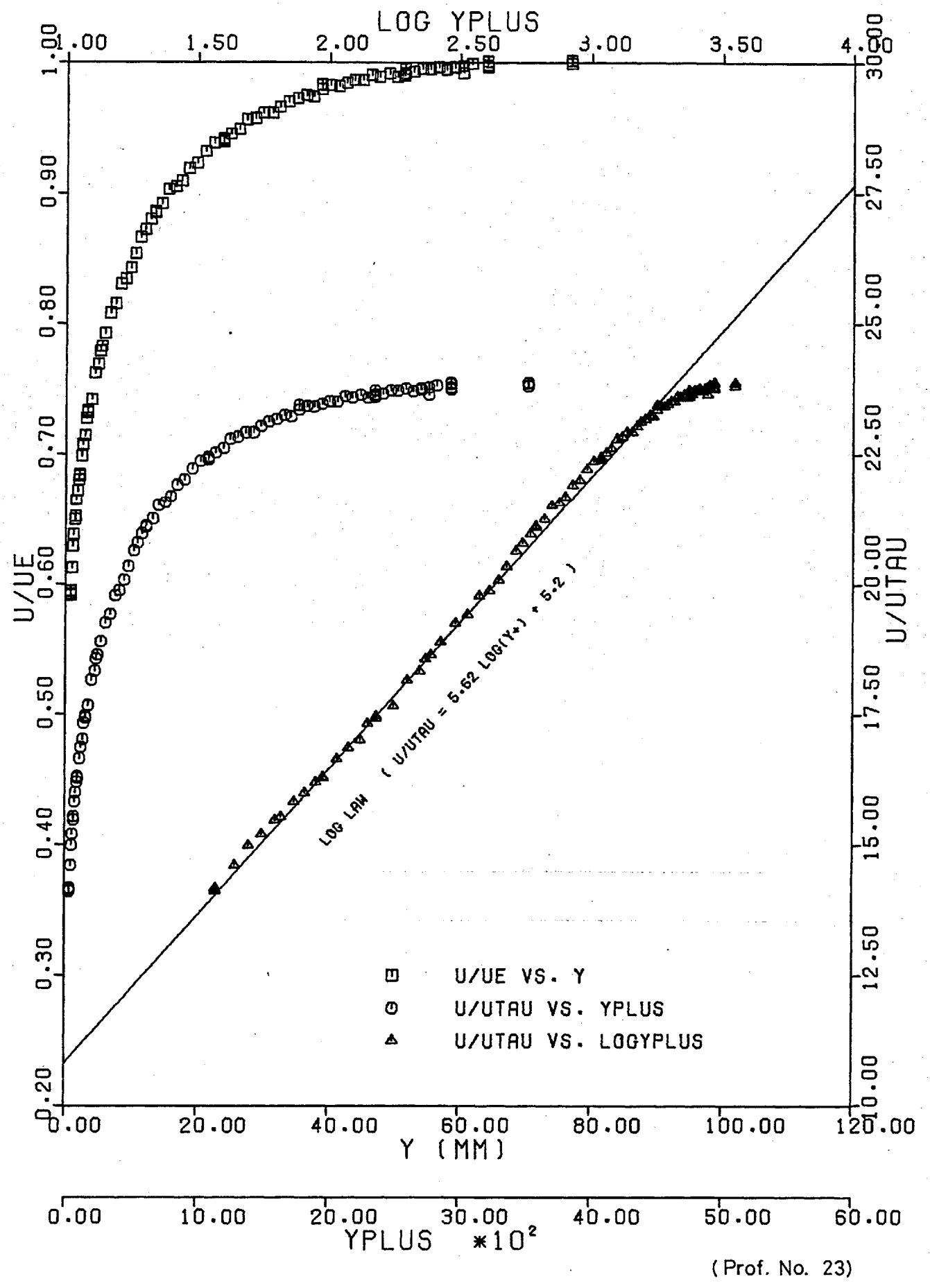

Fig. A5.1. Velocity Profile. 7·6cm Generator, X_{LE}=0·30m, Stn 12.

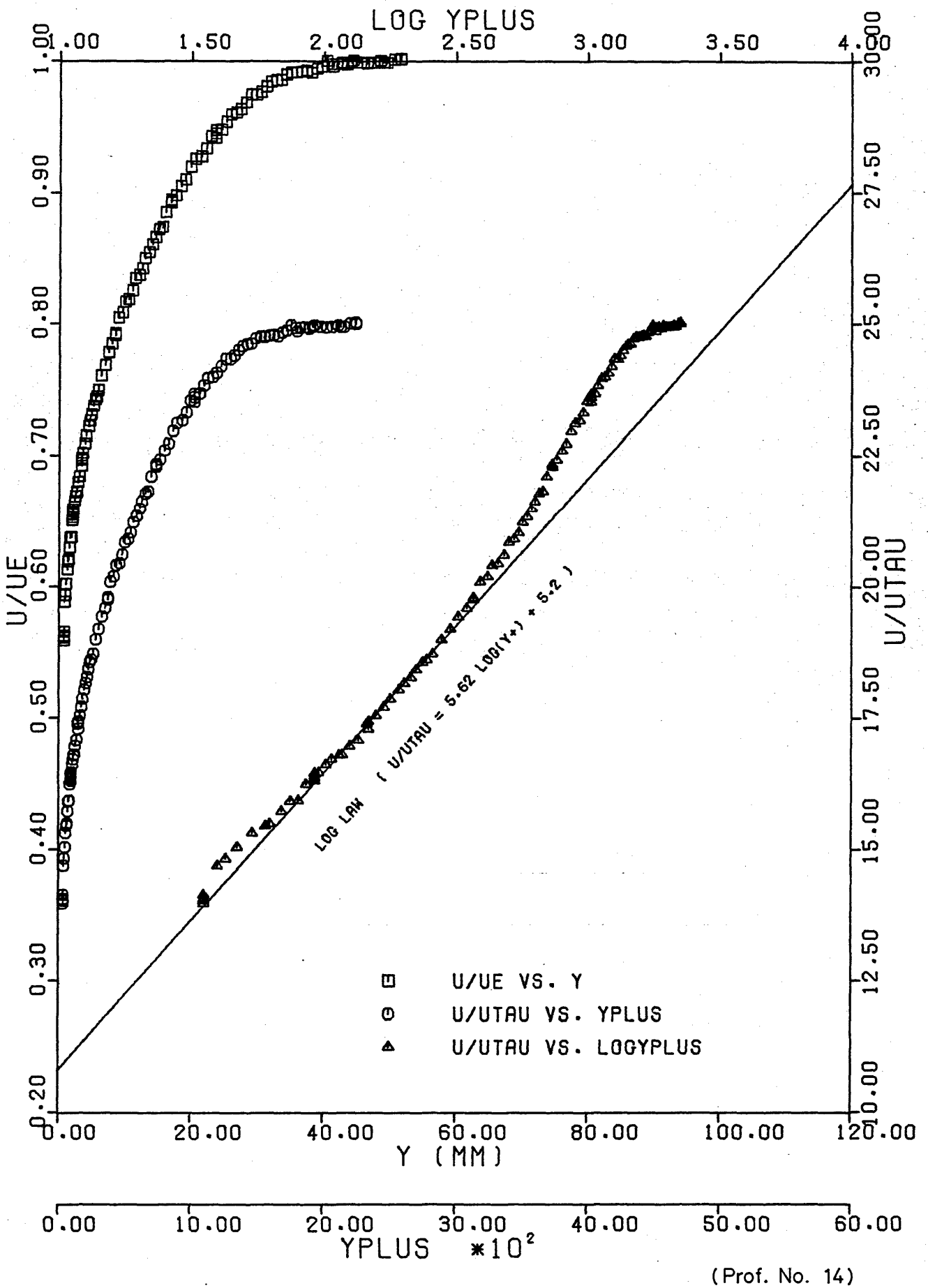

Fig. A5.2. Velocity Profile. 7·6cm Generator, X_{LE} = 2·06m, Stn 12.

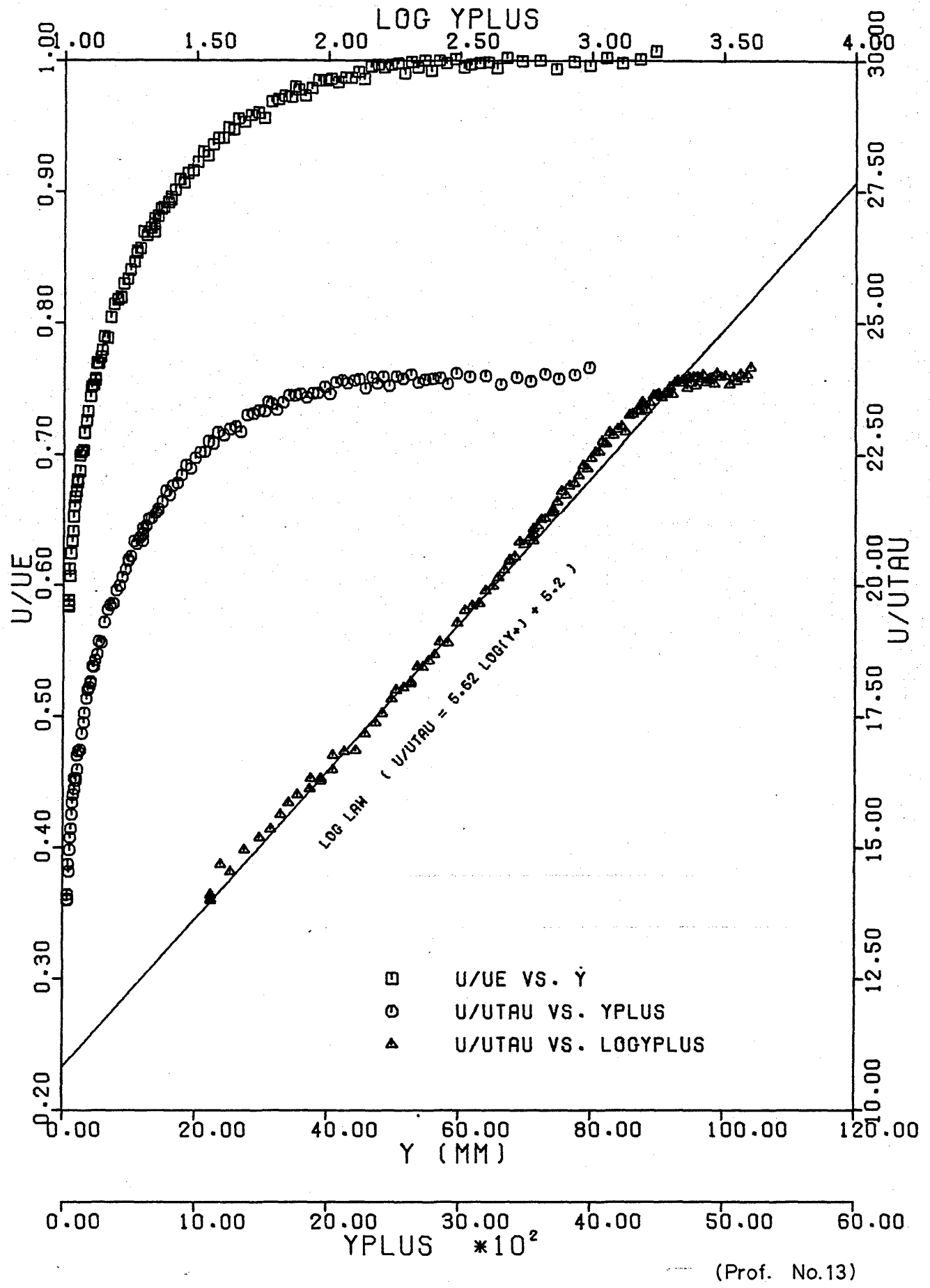

Fig. A5.3. Velocity Profile. 15·2cm Generator, X_{LE}=2·06m, Stn 12.

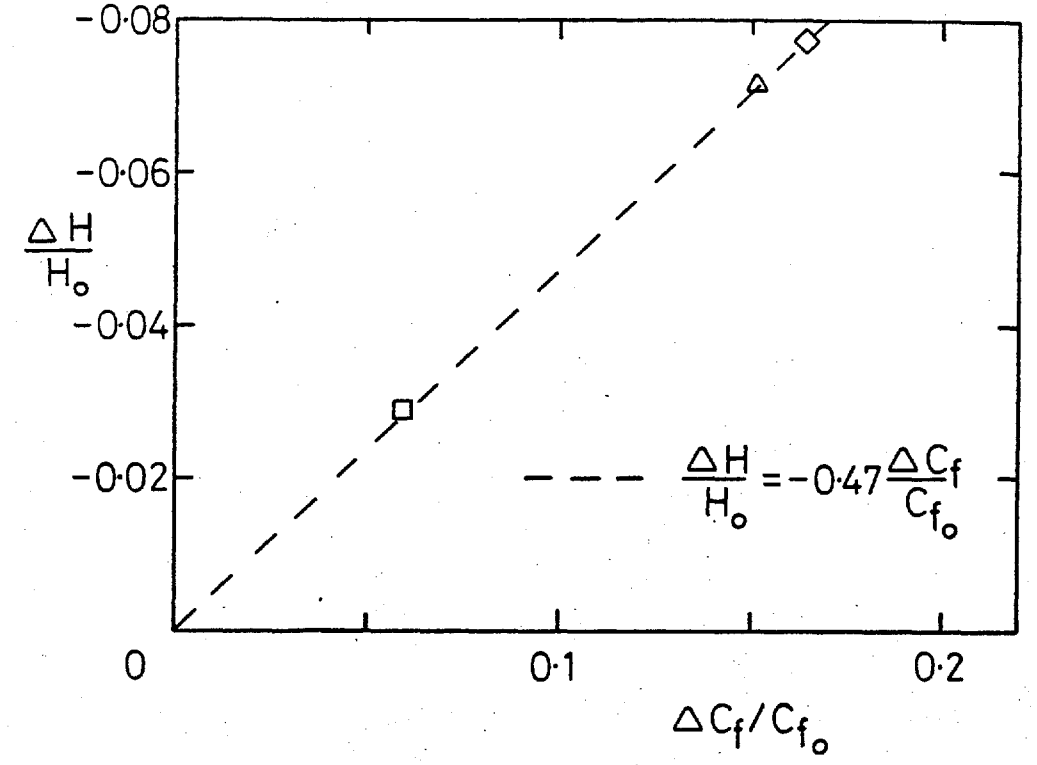

Fig. A5.4 Correlation between $\Delta H/H_o$ and $\Delta C_f/C_{f_o}$

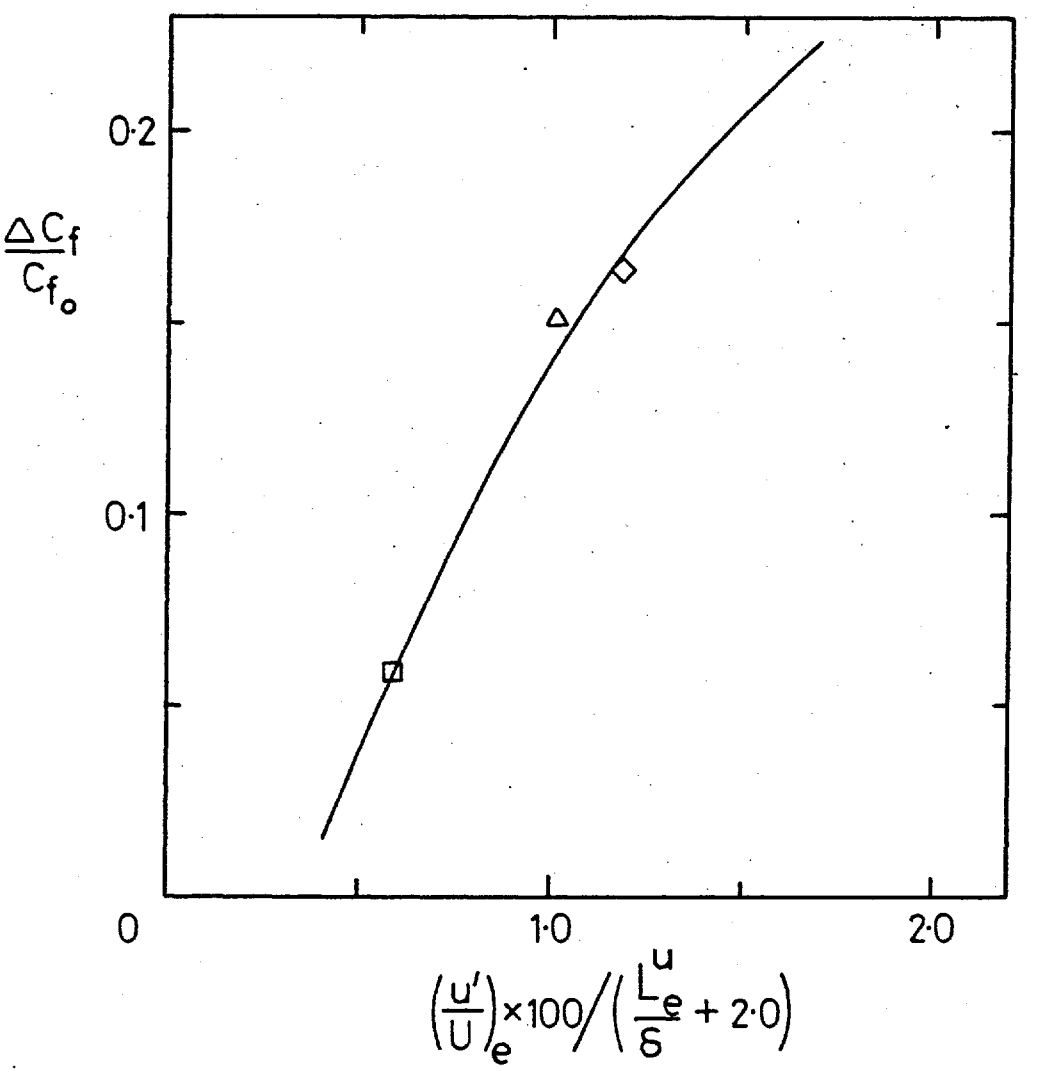

Fig. A5.5 Correlation of $\Delta C_f/C_{f_o}$ with $(u'/U)_e$ and L_e^u/δ_{995}. Full line, correlation of Fig. 3.49.

APPENDIX 6

LISTING OF THE INTERMITTENCY (FORTRAN) SUBROUTINE 'LAGTHR'

```
560.          SUBROUTINE LAGTHR                                          LAGTHR
561.         REAL IZJ, IZAP                                              LAGTHR
562.         REAL IZJ1,IZJ2                                              PEH3
563.         COMMON/ /ICH(1536),ID(512),NCH,NRI,NP,ACO,AVE,DT1,IDAC,II,NR,  LAGTHR
            1IN(10),JK,IPRIN,NPCH,NPCH1,NPCH2.                           LAGTHR
            2,SHZ                                                        PEH3
564.         COMMON/BB/I1,I2,NTH1,NTH2,NTH3,NTH4,NP2,NP3                 HOTAV
565.         COMMON/UV/U(512),V(512),TEMPL(20),IZAP(512),XX(6)           LAGTHR
            1,XXX(6)                                                     HOTCONV
566.           DIMENSION TTLAG(532),TB(20)                               LAGTHR
567.           EQUIVALENCE(TTLAG(1),TEMPL(1))                            LAGTHR
      C                                                                  LAGTHR
      C  -- IZAP(I) IS USED FOR INTERMITTENCY DETERMINATION              LAGTHR
      C  -- IT IS AT PRESENT THE SAME AS @TEMP@ - SEE COMMON BLOCK       LAGTHR
      C                                                                  LAGTHR
      C  TEST ON TEMP LEVEL  THEN SLOPE.                                 LAGTHR
      C  PT IS @HOT@ IF TEMP.GT.(TMIN2+TH2) ,                            LAGTHR
      C WHERE  TMIN2 IS MIN TEMP IN LAST COLD BURST BUT ONE              LAGTHR
      C  STARTER VALUE FOR TMIN2 IS MEAN TEMP (AVE) .                    LAGTHR
      C                                                                  LAGTHR
      C  IF  IN @HOT@ BURST ,TEMP(J) DROPS MORE THAN TH3D BELOW TEMP(J-NLAG)  LAGTHR
      C    PT. J IS CALLED @COLD@ AND THRESHOLD THA SET TO TEMP(J-NLAG)  LAGTHR
      C   UNLESS THIS IS ABOVE (TRCT5 +TH4) ,                           LAGTHR
      C   WHERE TRCT5 IS MIN TEMP OVER LAST NB5 RECS.                   LAGTHR
      C  ARRAY TTLAG HOLDS TEMP OF CURRENT REC IN TTLAG(21) TO TTLAG(532)  LAGTHR
      C    AND THE LAST 20 PTS OF PREVIOUS REC IN TTLAG(1) TO TTLAG(20).  LAGTHR
      C                                                                  LAGTHR
      C TMIN2  RESET TO (TRAR-TH2) IF SUSPICIOUSLY LONG HOT BURST,       LAGTHR
      C    AND TO  PRESENT TEMP IF SUSPICOIUSLY LONG COLD BURST.         LAGTHR
```

```
      C     OTHER VARIABLES INCLUDE -                                                  LAGTHR
      C         N1=LENGTH OF CURRENT HOT BURST                                         LAGTHR
      C         N2 =  DITTO COLD                                                       LAGTHR
      C         T1= HOT-ZONE-MEAN DEVIATION OF TEMP FROM COLD                          LAGTHR
      C         T2=  R.M.S. DITTO                                                      LAGTHR
      C         TBAR= OVERALL (CUM) MEAN TEMP  (ABOVE TCALIB)                          LAGTHR
      C         NTH2C= NO. OF TIMES THRESHOLD CHANGED IN COLD                          LAGTHR
      C         NTH2H=  DITTO IN LONG HOT BURSTS                                       LAGTHR
      C         TB(N)=  MIN TEMP OF THE REC N BEFORE THIS                              LAGTHR
      C                                                                                LAGTHR
  568.         IF(LK.GT.1 ) GO TO 100                                                  LAGTHR
      C                                                                                LAGTHR
      C  FIRST REC - READ THRESHOLDS FROM CARDS AND SET COUNTERS TO ZERO.              LAGTHR
  569.         READ 10,NU,NL,NLAG,NB5,TH2,TH3U,TH3D,TH4                                LAGTHR
               1,RC                                                                    LAGTHR
  570.         PRINT 11,NU,NL,NLAG,NB5,TH2,TH3U,TH3D,TH4,RC                            PEH3
  571.    11   FORMAT(1X,4I5,4F10.3,2F10.6)                                           PEH3
  572.    10   FORMAT(4I5,4F10.3,2F10.6)                                              PEH3
  573.         IF(NLAG.GT.20 .OR. NB5.GT.20) GO TO 300                                 PEH3
  574.         NTH2S    =NTH2C=NTH2H=0                                                 LAGTHR
  575.           ST=0.                                                                 LAGTHR
  576.         NPTS=1                                                                  LAGTHR
  577.          NNTH3=NNTH2=NNTH4=NNP2=NNP3=0                                          LAGTHR
  578.         NI1=0                                                                   LAGTHR
  579.         N1=N2=0                                                                 LAGTHR
  580.         TH=TH2 +AVE                                                             LAGTHR
  581.         ICL=0                                                                   LAGTHR
  582.         TBAR=TMIN0=TMIN1=TMIN2=AVE                                              LAGTHR
  583.            TBC15=0.                                                             LAGTHR
      C        THIS LOW SETTING OF TBOT5 MAKES TH3 IGNORED FOR 1ST REC                 LAGTHR
  584.            NT=1                                                                 LAGTHR
  585.            TSQU=0.                                                              LAGTHR
  586.          TSD2L=0.                                                               LAGTHR
```

```
      DO 15 J=1,20                                                      LAGTHR
      TR(J)=1.0E6                                                       LAGTHR
 15   TTLAG(J)=IZAP(J)                                                  LAGTHR
      IZJ1=IZAP(3)                                                      PEH3
C                                                                       LAGTHR
 100  CONTINUE                                                          LAGTHR
      IC(1)=ICL                                                         LAGTHR
      I1=I2=0                                                           LAGTHR
      NTH3=NTH2=NTH4=NP3=NP2=0                                          LAGTHR
        TBOTO=IZAP(1)                                                   LAGTHR
C-------------                                                          LAGTHR
      IZAP(1)=IZJ1                                                      PEH3
 120    DO 180 J=2,NPCH1                                                LAGTHR
      IZJ2=IZAP(J)                                                      PEH3
      IZAP(J)=IZAP(J)+(IZAP(J+1)-IZJ1)*RC*SHZ/2.0                       PEH3
      IZJ1=IZJ2                                                         PEH3
       IZJ=IZAP(J)                                                      LAGTHR
         ST=SI+IZJ                                                      LAGTHR
      TBOTO=AMIN1(TBOTO,IZJ)                                            LAGTHR
       TLAG=TTLAG(J+20-NLAG)                                            LAGTHR
C                                                                       LAGTHR
 130  IF(IZJ-THA)132,132,136                                            PEH3
 132  IF(IZJ+TH2-THA)136,134,134                                        PEH3
 136  THA=IZJ+TH2                                                       PEH3
 134  IF(N1.NE.1) GO TO 131                                             PEH3
      IC(J-1)=-1                                                        PEH3
      NTH2=NTH2-1                                                       PEH3
      NP2=NP2+1                                                         PEH3
      NTH2S=NTH2S+1                                                     PEH3
      TSDL=TSDU-DU                                                      PEH3
      TSD2U=TSD2U-DU*DU                                                 PEH3
C                                                                       LAGTHR
 131  GO TO 140                                                         PEH3
C                                                                       PEH3
```

```
      C  CHECK THAT NO OF HOT POINTS GREATER THAN NLAG BEFORE PROCEEDING                PEH3
      C  WITH SLOPE CHECK                                                              PEH3
616.   139  IF(N1.LT.NLAG) GO TO 160                                                   PEH3
      C                                                                                LAGTHR
      C  HOT BY LEVEL -CHECK SLOPE                                                     LAGTHR
617.   135   IF(IZJ-TLAG+TH3C) 137,137,160                                            LAGTHR
      C     FAST FALL - CALL PT. @COLD@ AND RESET THRESOLD TO (TEMP(J)+TH2)            LAGTHR
      C    UNLESS THAT WOULD BE UNREASONABLY HIGH.                                     LAGTHR
618.   137   IF(IZJ-TBOT5-TH4)138,138,163                                             LAGTHR
619.   138   TMIN2=TMIN1=TMIN0=IZJ                                                    LAGTHR
620.         THA=TMIN2+TH2                                                            LAGTHR
621.         N2=0                                                                     LAGTHR
622.         GO TO 142                                                                LAGTHR
      C                                                                                LAGTHR
      C --- COLD---                                                                    LAGTHR
623.    140 NP2=NP2 +1                                                                LAGTHR
624.        ID(J)=0                                                                   LAGTHR
625.           GO TO 145                                                              LAGTHR
626.   142   NP3=NP3+1                                                                LAGTHR
627.        ID(J)=-2                                                                  PEH3
628.    145  N1=0                                                                     LAGTHR
629.        N2=N2+1                                                                   LAGTHR
630.        IF(N2.NE.1) GO TO 146                                                     LAGTHR
      C FIRST PT OF COLD BURST                                                         LAGTHR
631.         TMIN0=IZJ                                                                LAGTHR
632.         I2=I2+1                                                                  LAGTHR
633.   146   IF(N2.LT.NL)GO TO 150                                                    LAGTHR
      C  SUSPICIOUSLY LONG COLD BURST -RESET THRESHOLD                                 LAGTHR
634.          NTH2C=NTH2C+1                                                           LAGTHR
635.          N2=1                                                                    LAGTHR
636.        ID(J)=0                                                                   LAGTHR
637.          TMIN2=TMIN1=TMIN0=IZJ                                                   LAGTHR
638.          THA=TMIN2+TH2                                                           LAGTHR
      C  FIND MIN TEMP OF THIS COLD BURST                                              LAGTHR
639.   150    TMIN0=AMIN1(TMIN0,IZJ)                                                  LAGTHR
640.          GO TO 180                                                               LAGTHR
```

```
      C                                                                 LAGTHR
      C----HCT---                                                       LAGTHR
641.    160 NTH2=NTH2 +1                                                LAGTHR
642.        IC(J)=1                                                     LAGTHR
643.        GC TC 165                                                   LAGTHR
644.   162   NTH3=NTH3+1                                                LAGTHR
645.         IC(J)=1                                                    LAGTHR
646.        GC TO 165                                                   LAGTHR
647.   163   NTH4=NTH4+1                                                LAGTHR
648.        IC(J)=1                                                     LAGTHR
649.   165    N2=0                                                      LAGTHR
650.        N1=N1+1                                                     LAGTHR
651.            DU=IZJ-TMIN2                                           LAGTHR
652.           TSDU=TSDU+DU                                            LAGTHR
653.           TSD2U=TSD2U+DU*DU                                       LAGTHR
654.        IF(N1.GT.1) GO TO 170                                       LAGTHR
      C FIRST PT OF HOT BURST -RESET LEVEL THRESHOLD                    LAGTHR
655.        TMIN3=TMIN2                                                 PEH3
656.        IF(TMIN0.LT.TMIN1) TMIN1=TMIN0                              PEH3
657.        TMIN2=TMIN1                                                 LAGTHR
658.        TMIN1=TMIN0                                                 LAGTHR
659.        THA=TMIN2+TH2                                               LAGTHR
660.        I1=I1+1                                                     LAGTHR
661.   170    IF(N1.LT.NU)GO TC 180                                     LAGTHR
      C  SUSPICIOSLY LONG HOT BURST -                                   LAGTHR
      C      RESET THRESHOLD TO TBAR                                    LAGTHR
662.        NTH2H=NTH2H+1                                               LAGTHR
663.          IC(J)=1                                                   LAGTHR
664.        N1=1                                                        LAGTHR
665.        TMIN2=TMIN1=TMIN0=TBAR-TH2                                  LAGTHR
666.        THA=TBAR                                                    LAGTHR
667.   180   CONTINUE                                                   LAGTHR
```

```
      C---------+---------
  668.          NT=NT+NTH2+NTH3+NTH4                                    LAGTHR
  669.             T1=TSDU/NT                                           LAGTHR
  670.           T2=SQRT(TSD2U/NT)                                      LAGTHR
      C  MOVE DOWN STACK TB OF MINIMA                                   LAGTHR
  671.          DO 190 NB=1,NB5                                         LAGTHR
  672.          N=NB5+1-NB                                              LAGTHR
  673.  190     TB(N+1)=TB(N)                                           LAGTHR
  674.  192     TB(1)=TBOT5=TBOT0                                       LAGTHR
  675.          DO 195 NB=1,NB5                                         LAGTHR
  676.  195    TBOT5=AMIN1(TBOT5,TB(NB))                                LAGTHR
      C HOLD LAST 20 PTS OF TEMP FOR FUTURE USE                         LAGTHR
  677.          DO 199 J=1,20                                           LAGTHR
  678.  199    TTLAG(21-J)= IZAP(NPCH1-J)                              LAGTHR
  679.          ICL=IC(NPCH1)                                           LAGTHR
      C  CUMLLATIVE COUNTERS                                            LAGTHR
  680.        NPTS=NPTS+NPCH                                            LAGTHR
  681.        GAM=FLOAT(NT)/FLOAT(NPTS)                                 PEH3
  682.        TBAR=ST/NPTS                                              LAGTHR
  683.        NNP2=NNP2+NP2                                             LAGTHR
  684.        NNP3=NNP3+NP3                                             LAGTHR
  685.        NNTH3=NNTH3+NTH3                                          LAGTHR
  686.        NNTH2=NNTH2+NTH2                                          LAGTHR
  687.          NNTH4=NNTH4+NTH4                                        LAGTHR
  688.         NI1=NI1+I1                                               LAGTHR
      C                                                                 LAGTHR
  689.          IF(IPRIN.EQ.0)RETURN                                    LAGTHR
```

```
      C
690.        ENTRY THROUT                                                    HOTAV
      C OUTPUT                                                              HOTAV
691.         WRITE(6,230)NPCH ,NLAG,NU,NL,NB5                              LAGTHR
692.   230   FORMAT(@ CURRENT TEMP PARAMS -@/ 10X,@NPCH2,NLAG,NU,NL,NB5 @,5I6)  LAGTHR
693.         WRITE(6,250)JK,TH2,TMIN2,TH3U,TH3D,TH4,TBOT5                  LAGTHR
694.         WRITE(6,255) GAM,NNTH2,NNTH3,NNTH4,NNP2,NNP3,NT,NPTS,NII      LAGTHR
695.         WRITE(6,260) NTH2S, NTH2H,NTH2C                               LAGTHR
696.         WRITE(6,270) TBAR,T1,T2                                       LAGTHR
697.          RETURN                                                       LAGTHR
      C                                                                    LAGTHR
698.   250   FORMAT(/@ REC NO@,I5, @ CURRENT THRESHOLD LEVEL@,             LAGTHR
           *   ,F10.4,@ ABOVE@,F10.4,/20X,@JUMP LEVELS (TH3UP,TH3DOWN)=@,  LAGTHR
           *     2F10.4,                                                  LAGTHR
           * 2X,@GROSS LEVEL=@,F10.4,@ABOVE@,F10.4)                       LAGTHR
699.   255   FORMAT(@ CUM CTS..GAMMA=@,F10.4,@ PTS HOT ON LEVEL/SLOPE/@,  LAGTHR
           2   ,@GROSS LEVEL =@ ,3I8 /10X,@ PTS COLD ON LEV/SLOPE=@,2I8 /10X,  LAGTHR
           2     @TOTAL HOT PTS=@,I8,@ TOTAL PTS=@,I8,@ BURSTS=@,I8)      LAGTHR
      C                                                                    LAGTHR
700.   260     FORMAT(@ CUM ADJUSTMENT COUNTS...SPIKES,LONG HOT,LONG COLD@,3I8)  LAGTHR
701.   270   FORMAT(@ CUM MEAN TEMP,...HOT ZONE ABOVE COLD LEVEL (MEAN,RMS)@,  PEH3
           1 3F12.4)                                                       PEH3
      C                                                                    LAGTHR
702.   300     PRINT 301,NLAG,NB5                                          LAGTHR
703.   301     FORMAT(//@ XXX PARAMETERS NLAG,NB5 =@,2I10,@ TOO BIG @       LAGTHR
           3,@FOR SUBR. LAGTHR@/@ ANALYSIS CONTINUES WITHOUT INTERMITTENCY@/)  LAGTHR
704.          IN(2)=0                                                      LAGTHR
705.          RETURN                                                       LAGTHR
706.              END                                                      LAGTHR
```

APPENDIX 7

EQUATIONS OF MOTION

The discussion included in this appendix is intended only to furnish the immediate needs of the present thesis and will not be rigorous or complete. For a more detailed discussion see, for example, Townsend (1976). Only the 'Eulerian' equations of motion of a constant-property Newtonian fluid are given, expressed in terms of velocity components at a fixed point. Tensor notation will be used to enable compactness.

The continuity equation which expresses the conservation of mass is

$$\frac{\partial}{\partial x_i} (U_i + u_i) = 0 \qquad \text{(A7.1)}$$

Ensemble or time averaging gives

$$\frac{\partial U_i}{\partial x_i} = 0 \qquad \text{and} \qquad \frac{\partial u_i}{\partial x_i} = 0. \qquad \text{(A7.2 a,b)}$$

The Navier-Stokes momentum equations are

$$\frac{\partial}{\partial t} (U_i + u_i) + (U_\ell + u_\ell) \frac{\partial}{\partial x_\ell} (U_i + u_i)$$

$$= - \frac{1}{\rho} \frac{\partial}{\partial x_i} (p + p') + \nu \frac{\partial^2}{\partial x_\ell^2} (U_i + u_i) + f_i \qquad \text{(A7.3)}$$

where the f_i are body forces. Ensemble averaging equation A7.3, employing the continuity equation, and slightly rearranging, leads to

$$\frac{DU_i}{Dt} = - \frac{1}{\rho} \frac{\partial p}{\partial x_i} - \frac{\partial \overline{u_\ell u_i}}{\partial x_\ell} + \nu \frac{\partial^2 U_i}{\partial x_\ell^2} + \overline{f}_i \ , \qquad \text{(A7.4)}$$

where $$\frac{D}{Dt} \equiv \frac{\partial}{\partial t} + U_\ell \frac{\partial}{\partial x_\ell} \ . \qquad \text{(A7.5)}$$

$\overline{u_\ell u_i}$ are the (kinematic) Reynolds stresses and represent the ensemble or time averaged transfer of fluctuating momentum u_i by the fluctuating velocity u_ℓ.

Transport equations for $\overline{u_i u_j}$ may be obtained by multiplying

equation A7.3 by u_j, adding it to the equation for $(U_j + u_j)$ multiplied by u_i, and averaging. The result may be written as

$$\frac{D}{Dt}\overline{u_i u_j} = -\left(\overline{u_i u_\ell}\frac{\partial U_j}{\partial x_\ell} + \overline{u_j u_\ell}\frac{\partial U_i}{\partial x_\ell}\right)$$

$$+ \overline{\frac{p'}{\rho}\left(\frac{\partial u_i}{\partial x_j} + \frac{\partial u_j}{\partial x_i}\right)}$$

$$- \frac{\partial}{\partial x_\ell}\left(\overline{u_i u_j u_\ell}\right) \qquad \text{(A7.8)}$$

$$- \frac{1}{\rho}\left(\frac{\partial}{\partial x_i}\overline{p' u_j} + \frac{\partial}{\partial x_j}\overline{p' u_i}\right)$$

$$+ \nu\left(\overline{u_i \frac{\partial^2 u_j}{\partial x_\ell^2}} + \overline{u_j \frac{\partial^2 u_i}{\partial x_\ell^2}}\right).$$

REFERENCES

AHMAD, Q., LUXTON, R. and ANTONIA, R.A. 1976
Characteristics of a turbulent boundary layer with external turbulent uniform shear flow.
J. Fluid Mech., 77, 369.

ANDREOPOULOS, J. 1978
Symmetric and asymmetric near wake of a flat plate.
Ph.D. Thesis, Imperial College, University of London.

ANTONIA, R.A. 1972
Conditionally-sampled measurements near the outer edge of a turbulent boundary layer.
J. Fluid Mech., 56, 1.

ANTONIA, R.A. and BRADSHAW, P. 1971
Conditional sampling of turbulent shear flows.
Imperial College Aero Report 71-04.

ANTONIA, R.A., DAHN, H.Q. and PRABHU, A. 1977
Response of a turbulent boundary layer to a step change in surface heat flux.
J. Fluid Mech., 80, 153.

ANTONIA, R.A. and LUXTON, R. 1971
The response of a turbulent boundary layer to a step change in surface roughness : Part 1 Smooth-to-rough.
J. Fluid Mech., 48, 721.

ANTONIA, R.A., PRABHU, A. and STEPHENSON, S.E. 1975
Conditionally sampled measurements in a heated turbulent jet.
J. Fluid Mech., 72, 485.

ARNAL, D. 1977
Influence de la turbulence de l'ecoulement general sur les couches limites turbulentes en fluid incompressible.
ONERA Tech. Note 1977-1.

ARNAL, D., COUSTEIX, J. and MICHEL, R. 1976
Couche limite se developpant avec gradient de pression positif dans un ecoulement turbulent.
ONERA T.P. 1976-24.

BARRACK, P.G.L. 1977
The effect of free-stream turbulence on the stalling characteristics of a family of NACA 23000-series aerofoil sections.
M.Sc. Thesis, Imperial College, University of London.

BATCHELOR, G.K. 1953
The theory of homogeneous turbulence.
Cambridge University Press.

BAYLEY, F.J. and MILLIGAN, R.W. 1977
The effects of free-stream turbulence upon heat transfer to turbine blading.
ARC 37568.

BEARMAN, P.W. 1971
Corrections for the effect of ambient temperature drift on hot-wire measurements.
Disa Information, No. 11.

BENEK, J.A. 1977
Effects of acoustic and vortical disturbances on the turbulent boundary layer at free-stream Mach No. 0.5.
AEDC TR-77-73.

BRADBURY, L.J.S. 1964
A simple circuit for the measurement of intermittency factor in turbulent flow.
Aero. Quarterly 15, 281.

BRADBURY, L.J.S. and CASTRO, I.P. 1972
Some comments on heat transfer laws for fine wires.
J. Fluid Mech., 51, 487.

BRADSHAW, P. 1967
The turbulence structure of equilibrium boundary layers.
J. Fluid Mech., 29, 625.

BRADSHAW, P. 1967
'Inactive' motion and pressure fluctuations in turbulent boundary layers.
J. Fluid Mech., 30, 241.

BRADSHAW, P. 1971
An introduction to turbulence and its measurement.
Pergamon Press.

BRADSHAW, P. 1974
Effects of free-stream turbulence on turbulent shear layers.
Imperial College Aero. Report 74-10, and ARC 35648.

BRADSHAW, P. Ed. 1976
Turbulence.
Springer-Verlag.

BRADSHAW, P. 1976
Interacting shear layers in turbomachines and diffusers.
Project SQUID Workshop : Turbulence in internal flows, Ed. S.N.B. Murthy,
Hemisphere Publishing Corporation.

BRADSHAW, P. 1977
Effects of external disturbances on the spreading rate of a plane
turbulent jet.
J. Fluid Mech. 80, 795.

BRADSHAW, P., FERRISS, D.H. and ATWELL, N.P. 1967
Calculation of boundary-layer development using the turbulent energy
equation.
J. Fluid Mech., 28, 593.

BRADSHAW, P. and MURLIS, J. 1974
On the measurement of intermittency in turbulent flow.
Imperial College Aero. Report 74-04.

BREDERODE, V. 1973
VELPROF - a boundary layer data analysis program.
Imperial College Aero. Tech. Note 73-107.

BREDERODE, V. and BRADSHAW, P. 1974
A note on the emperical constants appearing in the logarithmic law for turbulent wall flows.
Imperial College Aero. Report 74-03.

BROWN, A.C. and BURTON, R.C. 1977
The effects of free-stream turbulence intensity and velocity distribution on heat transfer to curved surfaces.
ASME Paper No. 77-GT-48.

BROWN, G.L. and ROSHKO, A. 1974
On density effects and large structure in turbulent mixing layers.
J. Fluid Mech., 64, 775.

CASTRO, I.P. 1973
A highly distorted turbulent free shear layer.
Ph.D. Thesis, Imperial College, University of London.

CHAMPAGNE, F.H. 1978
The fine-scale structure of the turbulent velocity field.
J. Fluid Mech., 86, 67.

CHANDRSUDA, C. 1975
A reattaching turbulent shear layer in incompressible flow.
Ph.D. Thesis, Imperial College, University of London.

CHANDRSUDA, C., MEHTA, R.D., WEIR, A.D. and BRADSHAW, P. 1978
Effects of free-stream turbulence on large structures in turbulent mixing layers.
J. Fluid Mech., 85, 693.

CHARNAY, G. 1974
Characteristiques d'une couche limit turbulente evoluant en presence d'un ecoulement exterior turbulent.
Ph.D. Thesis, Universite de Lyon.

CHARNAY, G., COMTE-BELLOT, G. and MATHIEU, J. 1971
Development of a turbulent boundary layer on a flat plate in an external turbulent flow.
AGARD Conference Proceedings No. 93.

CHARNAY, G., MATHIEU, J. and COMTE-BELLOT, G. 1976
Response of a turbulent boundary layer to random fluctuations in the external stream.
Physics of Fluids, 19, 1261.

CHEN, C-H. P., and BLACKWELDER, R.F. 1978
Large-scale motion in a turbulent boundary layer : a study using temperature contamination.
J. Fluid Mech., 89, 1.

CHERRY, N.J. 1980
The effects of stream turbulence on a separated flow with reattachment.
Ph.D. Thesis, Imperial College, University of London.

COLES, D. 1956
The law of the wake in the turbulent boundary layer.
J. Fluid Mech., 1, 191.

COLES, D. 1962
The turbulent boundary layer in a compressible fluid.
RAND Corp. Report R-403-PR.

COLES, D. 1968
The young person's guide to the data.
Proc. AFOSR-IFP-Stanford Conference on Computation of Turbulent Boundary Layers, 2, 1.

COMTE-BELLOT, G. 1976
Hot-wire anemometry.
Ann. Review of Fluid Mech., 8, 209.

COMTE-BELLOT, G. and CORRSIN, S. 1966
The use of a contraction to improve the isotropy of grid turbulence.
J. Fluid Mech., 25, 657.

CONSIGNY, H., CHAN, C.K. and RICHARDS, B.E. 1979
The effect of pressure gradient and external turbulence on heat transfer to a cold flat plate.
VKI Tech. Note 128.

CORRSIN, S. and KISTLER, A.L. 1955
Free-stream boundaries of turbulent flows.
NACA Report 1244.

COUSTEIX, J., DESSOPPER, A. and HOUDEVILLE, R. 1977
Structure and development of a turbulent boundary layer in an oscillatory external flow.
Proc. Symposium on Turbulent Shear Flows, Pennsylvania State University.

DAVIES, M.E. 1974
Spectral analysis programs Powspec and Cophase.
Imperial College Aero. Tech. Note 74-103.

DAVIES, M.E. 1975
Wakes of oscillating bluff bodies.
Ph.D. Thesis, Imperial College, University of London.

DEAN, R.B. 1974
Reynolds number dependence of skin friction in a two-dimensional rectangular duct flow and a discussion of the 'Law of the Wake'.
Imperial College Aero. Report 74-11.

DEAN, R.B. and BRADSHAW, P. 1976
Measurements of interacting turbulent shear layers in a duct.
J. Fluid Mech., 78, 641.

DURBIN, P. 1977
Distortion of turbulence by a constant-shear layer adjacent to a wall.
Unpublished Paper, Dept. of Applied Mathematics and Theoretical Physics, University of Cambridge.

EDWARDS, A. and FURBER, B.N. 1956
The influence of free-stream turbulence on heat transfer by convection from an isolated region on a plane surface in parallel air flow.
Proc. Inst. of Mech. Engrs, 170, 941.

EVANS, B.J. 1971
Effect of free-stream turbulence on blade performance in a compressor cascade.
ARC 33135.

EVANS, R.L., 1972
Free-stream turbulence effects on the turbulent boundary layer.
Dept. of Engineering, University of Cambridge, Report CUED/A Turbo/TR41.

EVANS, R.L. 1976
Some turbulence and unsteadiness effects in turbomachinery.
Project SQUID Workshop : Turbulence in Internal Flows, Ed.S.N.B. Murthy, Hemisphere Publishing Corporation.

EVANS, R.L. and HORLOCK, J.H. 1973
Calculation of the development of turbulent boundary layers with a turbulent free-stream.
Dept. of Engineering, University of Cambridge, Report CUED/A Turbo/TR53.

FAVRE, A., GAVIGLIO, J. and DUMAS, R. 1954
Nouvelles measures dans la couche limite d'une plaque plane des intensities de turbulence et des correlations dans de temps spectres.
La Recherche Aeronautique, No. 38, 7.

FEILER, C.E. and YEAGER, E.B. 1962
Effect of large-amplitude oscillations on heat transfer.
NASA Tech. Report R-142.

FERNHOLZ, H. 1964
Three-dimensional disturbances in a two-dimensional imcompressible turbulent boundary layer.
ARC R & M 3368.

FIEDLER, H. and HEAD, M.R. 1966
Intermittency measurements in the turbulent boundary layer.
J. Fluid Mech., 25, 719.

FINK, L.E. 1977
Influence of external turbulence on mixing of axisymmetric coaxial jets.
Proc. Symposium on Turbulent Shear Flows, Pennsylvania State University.

FINLEY, P.J., PHOE, K.C. and POH, C.J. 1966
Velocity measurements in a thin turbulent water layer.
Houille Blanche, 21, 713.

GRAHAM, J.M.R. 1975
Turbulent flow past a long flat plate.
Imperial College Aero. Tech. Note 75-101.

GREEN, J.E. 1972
On the influence of free stream turbulence on a turbulent boundary layer as it relates to wind tunnel testing at subsonic speeds.
RAE Tech. Report 72201.

HEDLEY, T.B. and KEFFER, J.F. 1974, a
Turbulent/non-turbulent decisions in an intermittent flow.
J. Fluid Mech., 64, 625.

HEDLEY, T.B. and KEFFER, J.F. 1974, b
Some turbulent/non-turbulent properties of the outer intermittent region of a boundary layer.
J. Fluid Mech., 64, 645.

HINZE, J.O. 1959, 1975
Turbulence.
McGraw-Hill, New York.

HIRST, A.E. and REYNOLDS, W.C. 1968
An integral prediction method for turbulent boundary layers using the turbulent kinetic energy equation.
Proc. AFOSR-IFP-Stanford Conference on Computation of Turbulent Boundary Layers, 1, 213.

HOFFMANN, P.H. 1978
Private Communication.
Imperial College Aero. Dept.

HUFFMAN, G.D., ZIMMERMAN, D.R. and BENNETT, W.A. 1972
The effect of free-stream turbulence level on turbulent boundary layer behaviour.
AGARD Proc. of Meeting on Boundary Layer Effects in Turbomachines, 164, 91. Also, Detroit Diesel Allison Report.

HUFFMAN, G.D. 1977
Private Communication.

HUNT, J.C.R. and GRAHAM, J.M.R. 1978
Free-stream turbulence near plane boundaries.
J. Fluid Mech., 84, 209.

JOHNSON, D.S. 1959
Velocity and temperature fluctuation measurements in a turbulent boundary layer downstream of a stepwise discontinuity in wall temperature.
J. Applied Mech., Trans. ASME, 81, 325.

JONES, W.P. and LAUNDER, B.E. 1972
The prediction of laminarization with a two-equation model of turbulence.
Int. J. of Heat and Mass Transfer, 15, 301.

JUNKHAN, G.H. and SEROVY, G.K. 1967
Effects of free-stream turbulence and pressure gradient on flat plate boundary layer velocity profiles, and on heat transfer.
J. of Heat Transfer, Trans. ASME, 89, 169.

KAPLAN, R.E. and LAUFER, J. 1968
The intermittently turbulent region of a turbulent boundary layer.
Proc. 12th Int. Cong. Applied Mech. University of Stanford.

KARLSSON, S.K.F. 1959
An unsteady turbulent boundary layer.
J. Fluid Mech., 5, 622.

KEARNEY, D.W., KAYS, W.M., MOFFAT, R.J. and LOYD, R.J. 1970
Effects of free-stream turbulence on heat transfer to a strongly accelerated turbulent boundary layer.
Proc. of 22nd Meeting of Heat Transfer and Fluid Mech. Inst., Naval Postgraduate School, Monterey, California.

KESTIN, J. 1966
The effect of free-stream turbulence on heat transfer rates.
Advances in Heat Transfer, 3, 1.

KESTIN, J., MAEDER, P.F. and WANG, H.E. 1961
Influence of turbulence on the transfer of heat from plates with and without a pressure gradient.
Int. Developments in Heat Transfer, International Heat Transfer Conference, University of Colorado and London, England, ASME, 432.

KLEBANOFF, P.S. 1955
Characteristics of turbulence in a boundary layer with zero pressure gradient.
NACA Report 1247.

KLINE, S.J., LISIN, A.V. and WAITMAN, B.A. 1960
Preliminary experimental investigations of the effect of free-stream turbulence on turbulent boundary layer growth.
NASA Tech. Note D368.

KOMODA, H. 1957
On the effect of free-stream turbulence on the structure of a turbulent wake.
J. Japanese Soc. Aero. Eng., 274.

KOTSOVINOS, N.E. 1976
A note on the spreading rate and virtual origin of a plane turbulent jet.
J. Fluid Mech., 77, 305.

KOVASZNAY, L.S.G., KIBENS, V. and BLACKWELDER, R.F. 1970
Large-scale motion in the intermittent region of a turbulent boundary layer.
J. Fluid Mech., 41, 283.

KULIK, R.A., LEITHEM, J.J. and WEINSTEIN, H. 1969
Effect of free-stream turbulence on coaxial mixing.
NASA CR-1336.

LEUCHTER, O. 1976
Effects of free-stream turbulence and initial boundary layers on the development of turbulent mixing layers.
Project SQUID Workshop : Turbulence in Internal Flows, Ed.S.N.B. Murthy, Hemisphere Publishing Corporation.

LUDWIEG, H. and TILLMANN, W. 1950
Investigations of the wall-shearing stress in turbulent boundary layers.
NACA Tech. Note 1285.

MACMILLAN, F.A. 1957
Experiments on Pitot-tubes in shear flow.
ARC R & M 3028.

MASUDA, S., SASAKI, N., ARIGA, I. and WATANABE, I. 1972
Effects of free-stream velocity profiles on a turbulent boundary layer, with some reference to the effects of free-stream turbulence.
2nd Int. JSME Symposium Fluid Machinery and Fluidics, Tokyo.

McDONALD, H. and KRESKOVSKY, J.P. 1974
Effects of free-stream turbulence on the turbulent boundary layer.
Int. J. of Heat and Mass Transfer, 17, 705.

McKEOUGH, P.J. 1976
Effects of turbulence on aerofoils at high incidence.
Ph.D. Thesis, Imperial College, University of London.

MEIER, H.U. 1976
The response of turbulent boundary layers to small turbulence levels in the external free stream.
DFVLR Report IB 251-76 A17. Also 10th Cong. of ICAS, Ottawa.

MEIER, H.U. 1977
The effects of velocity fluctuations and non-uniformities in the free stream on the boundary layer development.
Proc. Symposium on Turbulent Shear Flows, Pennsylvania State University.

MEIER, H.U. and KREPLIN, H.P. 1978
The influence of turbulent velocity fluctuations and integral length scale of low speed wind tunnel flow on boundary layer development.
AIAA Paper 78-800.

MILLIGAN, C.B. and KLEIN, A.L. 1933
The effect of turbulence; an investigation of maximum lift coefficient and turbulence in wind tunnels and in flight.
Aircraft Engineering, August.

MURLIS, J. 1975
The structure of a turbulent boundary layer at low Reynolds numbers.
Ph.D. Thesis, Imperial College, University of London.

MOHAMMADIAN, S., SAIY, M. and PEERLESS, S.J. 1976
Fluid mixing with unequal free stream turbulence intensities.
J. Fluids Eng., Trans. ASME, 98, 229.

NASH, J.F. and MACDONALD, A.G.J. 1967
A turbulent skin-friction law for use at subsonic and transonic speeds.
ARC C.P. 948.

PATEL, R.P. 1978
Effects of stream turbulence on free shear flows.
Aero. Quarterly, 29, 33.

PATEL, V.C. 1965
Calibration of the Preston tube and limitations on its use in pressure gradients.
J. Fluid Mech., 23, 185.

PEERLESS, S.J. 1971
Turbulent mixing of gas streams : a theoretical and experimental investigation of the effects of free-stream turbulence on the development of the plane mixing layer.
Ph.D. Thesis, Imperial College, University of London.

PFEIL, H. and PACHE, W. 1977
Messungen von strömungsgrenzschichten unter Turbomaschinenbedingungen.
Z. Flugwiss. Weltraumforsch., 1, 267.

PICHAL, M. 1966
Die turbulente Grenzschicht an einer ebenen Platte in der hochturbulenten Stromung.
Proc. 11th Int. Cong. Applied Mech., 896, Munich.

RAGHUNATHAN, S., COLL, J.B. and MABEY, D.G. 1979
Flat plate turbulent boundary layers subjected to large pressure fluctuations.
AIAA J., 17, 105.

REYNOLDS, W.C., KAYS, W.M. and KLINE, S.J. 1958
Heat transfer in the turbulent incompressible boundary layer - I - constant wall temperature.
NASA Memo. 12-1-58W.

ROBERTSON, J.M. and HOLT, C.F. 1972
Stream turbulence effects on the turbulent boundary layer.
Proc. ASCE, 98, HY6, 1093.

ROTTA, J.C. 1962
Turbulent boundary layers in incompressible flow.
Progress in Aero. Sci., 2, 1.

SAIY, M. 1974
Turbulent mixing of gas streams : an experimental and computational investigation of turbulence in plane two-stream mixing layers with various levels of free-stream turbulence.
Ph.D. Thesis, Imperial College, University of London.

SCHLICHTING, H. 1968
Boundary layer theory.
McGraw-Hill.

SCHLICHTING, H. and DAS, A. 1970
On the influence of turbulence level on the aerodynamic losses of axial turbomachines.
Flow Research on Blading, 243, Ed. by L.S. Dzung, Elsevier Publishing Company.

SHABAKA, I.M.M.A. 1979
Turbulent flow in an idealized wing-body junction.
Ph.D. Thesis, Imperial College, University of London.

SIMONICH, J.C. and BRADSHAW, P. 1978
Effect of free-stream turbulence on heat transfer through a turbulent boundary layer.
J. of Heat Transfer, Trans. ASME, 100, 671.

SLANCIAUSKAS, A. and PEDISIUS, A. 1979
Effect of free-stream turbulence on the heat transfer in the turbulent boundary layer.
Proc. 6th Int. Heat Transfer Conf., 573, Toronto.

SMITS, A.J., YOUNG, S.T.B. and BRADSHAW, P. 1979, a
The effect of short regions of high surface curvature on turbulent boundary layers.
J. Fluid Mech., 94, 209.

SMITS, A.J., EATON, J.A. and BRADSHAW, P. 1979, b
The response of a turbulent boundary layer to lateral divergence.
J. Fluid Mech., 94, 243.

SUGAWARA, S., SATO, T., KOMATSU, H. and OSAKA, H. 1958
The effects of free-stream turbulence on heat transfer from a flat plate.
NACA Tech. Memo. 1441.

SUNYACH, M. 1971
Contribution a l'etude des frontieres d'ecoulements turbulents libres.
D.Sc. Thesis, Universite de Lyon.

THOMAS, R.M. 1973
Conditional sampling and other measurements in a plane turbulent wake.
J. Fluid Mech., 57, 549.

THOMAS, N.H. and HANCOCK, P.E. 1977
Grid turbulence near a moving wall.
J. Fluid Mech., 82, 481.

TOWNSEND, A.A. 1961
Equilibrium layers and wall turbulence.
J. Fluid Mech., 11, 97.

TOWNSEND, A.A. 1976
The structure of turbulent shear flow.
Cambridge University Press.

TSUJI, Y. and IIDA, S. 1972
Influence of free stream turbulence on mean velocities of turbulent boundary layer without pressure gradient.
Trans. Japanese Soc. for Aero. and Space Sc., 15, 105.

UZKAN, T. and REYNOLDS, W.C. 1967
A shear-free turbulent boundary layer.
J. Fluid Mech., 28, 803.

WEEKS, D.J. and HODGES, J. 1977
An experimental investigation into the influence of acoustic disturbances on the development of a turbulent boundary layer.
RAE Tech. Report 77035.

WEIR, A.D. 1976
Program TUVTER : an aid to selecting intermittency criterion.
Imperial College Aero. Tech. Note 76-103.

WEIR, A.D. and BRADSHAW, P. 1974
Apparatus and programs for digital analysis of fluctuating quantities in turbulent flow.
Imperial College Aero. Report 74-09

WEIR, A.D. and BRADSHAW, P. 1977
The interaction of two parallel free shear layers.
Proc. Symposium Turbulent Shear Flows, Pennsylvania State University.

WIEGHARDT, K. 1944
Uber die turbulente Stromung in Rohr und langs einer Platte.
ZAMM, 24, 294.

WONG, F.Y.F. 1970
Shear flow over a rearward facing step.
M.Sc. Thesis, Imperial College, University of London.

WYGNANSKI, I. and FIEDLER, H.E. 1970
The two-dimensional mixing region.
J. Fluid Mech., 41, 327.